# Electrochemical Studies of the Oxygen Evolution Reaction at Mn, Ni/Co Mixed Oxide Electrodes in Aqueous Alkaline Solution



Luis Andrés Romeral Fernández

A thesis submitted to the University of Dublin, Trinity College for the Degree of Doctor of Philosophy

Supervisor: Prof. M.E.G. Lyons

School of Chemistry

2019

## Declaration

This thesis is submitted by the undersigned for the degree of Doctor of Philosophy at the University of Dublin. I declare that this thesis has not been submitted as an exercise for a degree at this or any other university and is entirely my own work.

I agree to deposit this thesis in the University's open access institutional repository or allow the Library to do so on my behalf, subject to Irish Copyright Legislation and Trinity College Library conditions of use and acknowledgement.

_____

Luis Romeral

March 2019

**Acknowledgements**

I would like to extend my sincere thanks to my supervisor Prof. M.E.G. Lyons for offering me the opportunity to carry out my PhD and for sharing his wealth of fundamental electrochemistry and kinetic knowledge which has guided me in the correct direction during both practical and write-up stages of the present work. His clear passion and love for physical electrochemistry subject has shone throughout my PhD experience for which I am grateful. I initially joined his group for a six-month undergrad final year research project back in January 2014. I thoroughly enjoyed my time spent in the group then and was fortunate to be able to return to the group full-time in September 2014.

Gratitude is also due to all the members of the Lyons group especially to Dr. Ian Godwin, for his invaluable support right from the start of my PhD, and the members of the School of Chemistry in both the professional and social sense for making my PhD a remarkable experience.

Dr. Elena Calatrava y Mr. Aron Gutiérrez, with whom I've been knocking around College for over 5 years now, also deserve a mention. Also, to Mr. Pau Coll and Mr. Fionn Cronin for their authentic friendship.

I would like to thank my parents Joana and Jose Luis and my younger brother Xavier for their support and understanding during all my PhD. I would also like to mention all the other family members for their support. I also must thank my quelcom, Berta, for the emotional, personal support and for the time spent together. Gracias Berta.

**Abstract**

There has been an abundance of publications over the last twenty years on electrode materials proposed to be suitable catalysts for the oxygen evolution reaction (OER) in alkaline solutions. Although it is widely accepted that $RuO_2$ and $IrO_2$ anodes exhibit the most efficient electrocatalyst performance towards the reaction, their high cost renders prohibitive the widespread adoption of this material for industrial applications. Amongst the more cost-effective materials that have been proposed as OER anodes are, various inter-metallic alloys, typically containing Ni, Co or Fe, and transition mixed oxides, including spinels (particularly nickelites, cobalites and ferrites) and perovskites. In view of this, the present work investigates the redox, the electrocatalytic and the mechanistic properties of two types of electrodes based on transition metal oxides were examined for the oxygen evolution reaction. The oxide materials were repetitive potential multi-cycled prepared hydrous manganese oxide electrodes and thermally prepared nickel cobalt mixed oxide electrodes. The electrocatalytic properties of both were described for potential use in the industrially and commercially significant OER, which is a rate determining step for hydrogen production via alkaline water electrolysis. Thus, the "backbone" of the present work is to be found in the steady-state polarisation and electrochemical impedance measurements. The aim of these measurements was to obtain experimental values for the OER Tafel slope and the $OH^-$ ion reaction order for these electrodes in aqueous alkaline solution, with a view to perform classical kinetic mechanistic analyses, to identify the operative oxygen evolution pathway for each of these anodes. In addition, steady-state polarisation measurements were used to quantify and compare the OER catalytic activity of electrodes at a given applied potential. Electrochemical impedance spectroscopy (EIS) measurements have demonstrated that the OER Tafel slope, derived from dc or ac measurements are truly characteristic of the kinetics of the reaction. Physical, elemental and morphological characterisation gave further insight into the nature of the modified film surface and enabled one to relate the electrocatalytic activity of these anodes with physical aspects such as surface morphology and surface composition. It was also noted that knowledge of the chemical and structural properties of the underlying oxide phase is crucial in understanding the OER; the amphoteric character of the anodic oxides implies that it is more realistic to investigate the oxygen evolution active sites in terms of anionic surface complexes rather than using the traditional viewpoint of

stoichiometric units of the bulk oxide material. We noted that the chemistry of the surfaquo group determines the chemistry of the OER active catalytic site.

Concluding, this work has demonstrated that manganese and nickel cobalt mixed oxides display very promising potential as inexpensive materials for electrochemical oxygen evolution in alkaline solutions due to their relatively low overpotential values and high stability in strong alkaline solutions. Particularly, the nickel cobalt mixed oxide electrode with 60 % M Co content, annealed at 400°C in air, exhibit the best OER catalytic activity in alkaline solutions among all the other electrodes studied in this thesis.

# Table of Contents

## CHAPTER 1 – INTRODUCTION AND LITERATURE REVIEW


1.1 Review of Relevant Electrochemical Theory . . . . . 1

1.1.1 Introduction to the Classical Theory of Electrical Conduction . . . . 1

1.1.2 Introduction to Chemical Interfaces . . . . . 3

1.1.3 General Concepts of Phase Potentials . . . . . 4

1.1.3.1 Metal / Electrolyte Interphase . . . . . 4

1.1.3.2 Metal / Electrolyte Interactions . . . . . 8

1.1.4 Concepts of Electrode / Solution Interface . . . . . 11

1.1.4.1 Structural Models of the Electrode / Solution Interface . . . 18

1.1.4.2 The Oxide / Solution Interphase . . . . . 34

1.2 Electrode Kinetics . . . . . 42

1.2.1 Fundamentals of the Electrode Kinetics . . . . . 42

1.2.2 Single-Step Electrode Processes. . . . . 46

1.2.3 Surface Coverage Considerations and Adsorbed Isotherms . . . 54

1.2.4 Multistep Kinetics . . . . . 60

1.2.5 Tafel Slope . . . . . 63

1.2.6 Electrochemical Reaction Order Determination . . . . 70

1.2.7 Modified Nernst Equation for the Account of the pH . . . . 73

1.2.8 Effects of the Double Layer and Mass Transport on the Electrode Kinetics . 77

1.3 Electrocatalysis . . . . . 81

1.3.1 Basic Concepts of the Electrocatalysis . . . . . 81

1.3.2 Hydrogen Evolution Reaction . . . . . 86

1.3.3 Further Observations on Electrocatalysis . . . . . 90

1.4 The Surface Electrochemistry of Nickel, Iron, Cobalt and Manganese . . 93

1.4.1 Nickel . . . . . 94

1.4.2 Iron . . . . . 103

1.4.3 Cobalt . . . . . 107

1.4.4 Manganese . . . . . 111

1.5 The Oxygen Evolution Reaction . . . . . 118

1.5.1 Introduction to the Oxygen Evolution Reaction . . . . 118

1.5.2 Difficulties of the Anodic Oxygen Evolution Reaction . . . 119

1.5.3 General Comments on the Oxygen Evolution Reaction . . . 121

1.5.4 Introduction to Synergy . . . . . 123

1.5.4.1 Nickel Cobalt Mixed Oxides . . . . . 124

1.5.5 Reaction Pathways for the Oxygen Evolution Reaction . . . 128

1.6 Motivations and Objectives . . . . . 133

1.7 References Chapter 1 . . . . . 136

**CHAPTER 2 – CONCEPTS OF EXPERIMENTAL TECHNIQUES**

2.1 Introduction . . . . . 147

2.2 Steady-State Polarization Measurements . . . . . 147

2.3 Cyclic Voltammetry . . . . . 150

2.4 X-ray Powder Diffraction . . . . . 152

2.5 X-ray Photoelectron Spectroscopy . . . . . 159

2.5.1 Elemental Analysis of Peak Lines and Intensities . . . . 160

2.6 Scanning Electron Microscopy . . . . . 162

2.7 Miscellaneous Surface Characterisation . . . . . 164

2.7.1 Contact Angle . . . . . 164

2.7.2 Thermogravimetric Analysis . . . . . 165

2.8 References Chapter 2 . . . . . 167

**CHAPTER 3 – EXPERIMENTAL METHODOLOGY AND PROCEDURE**

3.1 Introduction . . . . . 169

3.2 General Reagents and Solutions . . . . . 169

3.3 Electrode Materials and Instrumentation . . . . . 169

3.3.1 Electrochemical Cell . . . . . 169

3.3.2 Electrodes . . . . . 170

3.3.2.1 Working Electrode . . . . . 171

3.3.2.2 Counter Electrode . . . . . 173

3.3.2.3 Reference Electrode . . . . . 174

3.3.3 Electrochemical Analysis . . . . . 179

3.3.4 X-ray Powder Diffraction Spectroscopy . . . . . 179

3.3.5 Scanning Electron Microscope . . . . . 180

3.3.6 Energy Dispersive X-ray . . . . . 181

3.3.7 X-Ray Photoelectron Spectroscopy . . . . . 181

3.3.8 Thermogravimetric Analysis . . . . . 181

3.3.9 UV-Vis Spectroscopy . . . . . 182

3.3.10 Contact Angle . . . . . 183

3.4 Determination of iR Compensation . . . . . 183

3.5 The Benefits of Potential Step Method . . . . . 190

3.6 Electrochemical Impedance Spectroscopy . . . . . 193

3.6.1 AC Circuit Theory and Implementation . . . . . 195

3.6.2 The Nyquist Diagram . . . . . 200

3.6.3 The Bode Diagram . . . . . 203

3.6.4 Practical Considerations . . . . . 204

3.6.5 Extracting Electrochemical Parameters from EIS Raw Data . . . 205

3.6.6 Kramers-Kronig Transforms . . . . . 216

3.6.7 Impedance Spectroscopy Uncompensated Resistance . . . . 218

3.7 References Chapter 3 . . . . . 220

**CHAPTER 4 – THE REDOX AND ELECTROCATALYTIC BEHAVIOUR OF HYDROUS MANGANESE OXYHYDROXIDE FILMS**

4.1 Introduction . . . . . 222

4.2 Oxide Growth and Surface Redox Chemistry . . . . . 222

4.3 Factors Affecting the Development of Charge Storage Capacity. . . . 237

4.4 The Influence of the Solution pH on the Voltammetric Response . . 245

4.5 Kinetic Analysis . . . . . 250

4.6 Open Circuit Decay Measurements . . . . . 264

4.7 Double Layer Capacitance Study . . . . . 269

4.8 Electrocatalytic Behaviour of an Aged Manganese Electrode . . . 272

4.9 References Chapter 4 . . . . . 277

**CHAPTER 5 – THE REDOX AND ELECTROCATALYTIC BEHAVIOUR OF THERMALLY PREPARED NICKEL COBALT MIXED OXIDE FILMS**

5.1 Introduction . . . . . 279

5.2 Brief Electrochemical Study of Nickel Oxide and Cobalt Oxide for OER . 279

5.2.1 Nickel Oxide . . . . . 280

5.2.2 Cobalt Oxide . . . . . 282

5.3 Annealing Temperature Effect on Nickel Cobalt Mixed Oxide Electrodes . 284
5.3.1 Structural Analysis . . . . . 285
5.3.2 Degree of Crystallinity . . . . . 292
5.3.3 Crystallite Size . . . . . 293
5.3.4 Surface Morphology . . . . . 299
5.3.5 Electrochemical Evaluation . . . . . 300
5.4 The Effect of Cobalt Oxide on the OER of Nickel Cobalt Mixed Oxide Electrodes . . . . . 307
5.4.1 Introduction . . . . . 307
5.4.2 Physical Characterisation of Nickel Cobalt Mixed Oxide Electrodes . . 307
5.4.2.1 X-ray Powder Diffraction Spectroscopy Analysis . . . . 307
5.4.2.2 X-ray Photoelectron Spectroscopy Analysis . . . . . 311
5.4.3 Scanning Electron Microscope – Energy Dispersive X-ray . . . 317
5.4.4 Contact Angle Analysis . . . . . 330
5.5 The Influence of Cobalt Oxide on the Electrochemical Behaviour of Nickel Cobalt Mixed Oxide Electrodes . . . . . 332
5.5.1 The Surface Redox Chemistry . . . . . 332
5.5.2 The Influence of the pH on the Voltammetric Response . . . 336
5.5.3 The Kinetic Analysis . . . . . 340
5.6 Open Circuit Decay Measurements . . . . . 349
5.7 Double Layer Capacitance Study . . . . . 352
5.8 References Chapter 5 . . . . . 356

**CHAPTER 6 – IMPEDANCE STUDIES ON HYDROUS MANGANESE OXYHYDROXIDE AND THERMALLY PREPARED NICKEL COBALT OXIDE ELECTRODES**

6.1 Introduction . . . . . 359

6.2 Appropriate Equivalent Circuit Model Discussion . . . . 359

6.3 Electrochemical Impedance Spectroscopy Studies of Oxygen Evolution on Manganese Oxide Electrodes . . . . 363

6.4 Electrochemical Impedance Spectroscopy Studies of Oxygen Evolution on Nickel Cobalt Oxide Electrodes . . . . 376

6.5 Derivation of Tafel Slopes from Impedance Data . . . . 388

6.6 References Chapter 6 . . . . . 392

**CHAPTER 7 – CONCLUSIONS AND FUTURE WORK**

7.1 Conclusions . . . . . 393

7.2 Future Work . . . . . 397

# CHAPTER 1

# INTRODUCTION
# AND
# LITERATURE REVIEW

## 1.1 Review of Relevant Electrochemical Theory

Since this work deals with the surface electrochemistry of transition metal oxides in aqueous solutions, it seems pertinent to describe, from the basics to more complex conceptions, the aspects behind an electrochemical system. In view of the matters previously mentioned and since the electrochemical measurements presented in this thesis involve an electrode-electrolyte interface; this chapter will begin with a description of concepts such as the structure of, and electron transfer kinetics at, the interface between an electrode and an electrolyte solution.

Further, it is also important to note that a variety of electrochemical techniques and several physical and chemical characterisation techniques were performed throughout this work. These measurements aimed to both probe and study the catalytic behaviour of various first-row transition metal oxides in alkaline solutions. The properties and theory behind these techniques will also be described in the present chapter.

This work also puts an emphasis on the performance of various transition metal oxides for the electrochemical water oxidation or oxygen evolution reaction (OER). For this purpose, materials such as manganese oxide prepared *via* repetitive potential multicycling of a Mn metal electrode in an alkaline solution and thermally decomposed nickel cobalt mixed oxide with different nickel/cobalt molar ratios, were used as working electrodes and their redox and electrocatalytic characteristics subjected to analysis.

The electrochemical theory presented in the upcoming sections of this thesis is adapted from well-established textbooks written by Fisher[1], Bard and Faulkner[2], and the Southampton Electrochemistry Group.

### 1.1.1 Introduction to the Classical Theory of Electrical Conduction

As a general concept, when no current passes through a conductive material, no net movement of charges carriers occurs and, therefore, the electric field inside that material is equal to zero.

Assuming a local relationship, the *current density J* (current per unit of area) can be described as the result of the product of the electric field *E* and the electrical conductivity, $\sigma$.

$$J(x) = \sigma E(x) \tag{1.1.1}$$

The magnitude of the electrical conductivity determines whether a material is a conductor (high $\sigma$ value), an insulator (low $\sigma$ value) or a semiconductor (intermediate $\sigma$ value). To put it in context, metals such as silver and gold, are considered to be conductor materials, with high electrical conductivity in the order of $10^6$ - $10^8$ $Sm^{-1}$ whereas insulator materials, such as porcelain or diamond, exhibit conductivities typically lower than $10^{-6}$ $Sm^{-1}$. Semiconductors, such as silicon or germanium, exhibit intermediate conductivities typically in the range of $10^{-6} < \sigma < 10^6$ Ω-m. [3]

The Drude model based on classical physics is the simplest formalism by which conductivity can be understood. This theory states that, when an electric field crosses a metal material, the electrons in the material accelerate in the same direction in response, seeking to eliminate the electric field. These electrons possess a weak atomic bond and are mobile. The Drude theory considers that during this uniform movement, part of the mobile or free electrons in the material collide with ion cores and other "scattered" electrons. These collisions produce random dispersion of electrons, known as "scattered" electrons, which can also collide with other electrons in motion. It should be mentioned that the extent of electron/ion and electron/electron collisions will be determined by the physical nature of the material medium (atomic number, density, lattice structure, etc.) The latter determines the electrical resistivity of materials. Focusing on a single collision between electrons, the velocity of an electron after a collision *C* can be represented by eqn. 1.1.2:

$$v(t) = v_C - \frac{eE}{m}(t - t_C) \tag{1.1.2}$$

The first term represents the velocity of the electron just after the collision whereas the second term represents its acceleration. If one considers the direction of the $v_C$ to be random, then the average $v_C$ of the total conduction electrones will tend to zero. At this point the average current density can be defined as:

$$J = ne\mu E = \frac{ne^2\tau}{m}E \tag{1.1.3}$$

where n is the number of conduction electrons per unit of volume and the parameter $\mu = \frac{e\tau E}{m}$ is defined as the mobility of electrons. Consequently, the Drude conductivity formula can be described as

$$\sigma = \frac{ne^2\tau}{m} \tag{1.1.4}$$

where $\tau$ is the mean free time between collisions, $m$ is the effective mass, and $e$ refers to the electronic charge.

### 1.1.2 Introduction to Chemical Interfaces

Before probing more deeply into electrode/solution interfaces it is first necessary to differentiate between two essential concepts: interface and interphase.

The general definition of an interface region refers to a surface in contact with another phase, which is defined within an atomic layer. Interphase, on the other hand, is that region at which the phase boundary between two chemically distinct phases whose properties, both chemical and physical, differ from their respective bulk phases. It is in this region where the electromagnetic forces segregate positive and negative ions, produce adsorption and dipole orientation.

Many types of interface regions exist, *e.g*. liquid/liquid, gas/ liquid, solid/liquid, and even solid/solid. Particularly, the solid / liquid, and by extension, the solid electrode (metal)/aqueous electrolyte solution (*e.g*. $NaOH_{(aq)}$), is the most relevant interface in this thesis. Note that the nature of charge carrier conductivity changes at the solid/ionic solution interface. In the solid electrode the charge carriers are electrons (and perhaps holes if the material is a semiconductor). In the adjacent ionic solution, the charge carriers are charged positive and negative ions.

Usually, the interface where an electromagnetic field exists is known as the *electrical double layer*. As outlined above, this interface consists of a distribution of positive and negative ions (which produces the formation of a charged surface), solvent molecules and of electrons at the interface between a solid electrode and an electrolytic solution. The

separation between charged surfaces is typically of the order of an atomic diameter. Hence, the electric field strength across the interface is typically $10^8$ V $cm^{-1}$. Certainly, ion distribution is not the only factor influencing the formation of charge. In this sense, Pauli repulsion, carrier concentration gradients, electromagnetic induction, and thermal effects also play an important role here. A deep description of the latter factors is beyond the scope of this section. However, the study of the electromagnetic field along with the ion distribution associated with it is vital to understanding the dynamics and kinetics that govern the principals of electrochemical reactions. Thus, this chapter will introduce the various electrode phenomena and the formation of the *electrical double layer* to describe the various potentials involved in systems comprising several electrical conducting phases and interfaces.

A summary of the general features of the metal and oxide solution interphases will be presented in the following sections. Later in this chapter, attention will be given to the present state of knowledge in the field, particularly regarding the anodic oxygen evolution reaction in alkaline solution.

### 1.1.3 General Concepts of Phase Potentials

#### 1.1.3.1 Metal / Electrolyte Interphase

In the theory of chemical thermodynamics, the *chemical potential* or partial molar free energy $\mu_i^\alpha$ of an ionic species *i*, present in a phase $\alpha$ where there is no surface charge nor electrical potential flowing within this phase, is defined as:

$$\mu_i^\alpha = -\left(\frac{\partial G^\alpha}{\partial n_i}\right)_{T,P,n_{j\neq i}} \tag{1.1.5}$$

where $n_i$ is the number of moles of ionic species *i* in phase $\alpha$ at a given temperature and pressure. Hence the chemical potential is a thermodynamic function expressing the ability of an uncharged atom or molecule in a chemical system to perform physical work.

The *chemical potential* $\mu_i^\alpha$ arises from chemical forces within the phase as a result of an electron interaction between single nuclei and the atoms in its vicinity. If, however, phase $\alpha$ is assumed to have an inner potential $\phi^\alpha$, also referred as *Galvani potential*, and an excess surface charge, with the species *i* possessing a charge of $z_iF$ per mole, it is necessary to define an *electrochemical potential* $\bar{\mu}_i^\alpha$ of an element *i* in a phase $\alpha$ as:

$$\bar{\mu}_i^{\alpha} = \mu_i^{\alpha} + z_i F \phi^{\alpha} \qquad (1.1.6)$$

While the first term of eqn. 1.1.6 refers to the previously mentioned chemical potential $\mu_i^{\alpha}$ (see eqn. 1.1.5), the second one considers the free energy change brought about by altering the inner potential $\phi^{\alpha}$ within the $\alpha$ phase.

In order to clarify this concept, we consider the interface $M/M^{z+}$, $OH^-$ (aq) as an example of how an interface is charged. Focusing on the metal surface, the positive metal ions situated in the vicinity of the solid permeate the metal surface with free electrons. In addition, both $OH^-$ and water molecules adjacent to the electrode surface interact with the metal producing a layer of oriented dipoles, typically of the order of ca.1 nm.[4] All these interactions arise from *Coulombic interactions* when two conductor phases are placed in contact. These are possible paths for the formation of an electrical charge density which resides on the surface of phase $\alpha$.

It is also relevant to introduce the concept of charge $q$. By employing the Gauss law and considering a finite uniform volume with an imaginary surface area (the Gaussian surface) and assuming that for every surface point the electric field is being kept constant, one can represent the total amount of net charge $q$ by performing a surface integral of the electric field over the surface:

$$q = \varepsilon_o \oint E \; dS \qquad (1.1.7)$$

where $\varepsilon_o$ is the permittivity of vacuum ($8.854 \cdot 10^{-12}$ F $m^{-1}$), E is the electric field and $dS$ represents an infinitesimal surface area. If there is no current flow, then E is equal to zero over the Gaussian surface and hence the net charge is also zero. Using the example of a charged interface $M/M^{z+}$, $OH^-$ (aq) which demonstrates a charge distribution over a surface without a current flow, one must infer that the excess charge resides only on the surface of the conducting phase. In contrast however, the excess charge in a semiconductor material however, does not reside on the surface. Instead it is distributed in a space *charge region of finite thickness*. If the charge carriers possess a significant volume, thermal processes will impede the formation of a compact layer on the surface. Thus, a positive gradient of change carriers with respect to the bulk will be formed. Because of this charge, the distribution region has, in fact, a finite volume, which implies that the resulting electric field will compromise the electrochemical potential. Opposite, in a pure conductor phase

(metals), the thickness of this region can be assumed as negligible due to the high electronic conductivity that metals possess. Consequently, the interphase region encompasses the solution phase close to the metal surface. Fig. 1.1.1 may serve as a clarification for these concepts. In case of an eventual excess charge variation, the new excess charge would be distributed uniformly over the entire boundary of the phase in order to maintain a neutral charge inside the surface.

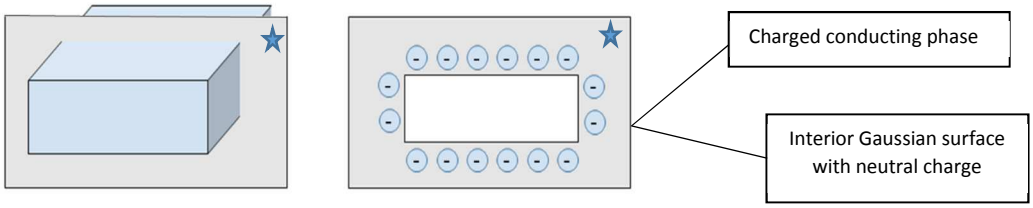



Figure 1.1.1 Cross-section of a three-dimensional conducting phase containing a Gaussian enclosure and illustration of the excess charge on the surface of the phase.

However, electrochemical measurements usually involve systems with various types of phases. The most common of these systems comprises two conductive phases, thus being a solid phase, the electrode, and a liquid phase, the electrolyte. This type of systems ought to be analysed in more detail hereafter.

It might be useful at this point to introduce the concepts of polarizable and non-polarizable interfaces. In this sense, and on the one hand, an electrode in which no charge transfer occurs through the metal solution interface, regardless of any external potential, is called *ideal polarisable electrode* (IPE). On the other hand, the electrode which shows large changes on potential upon the passage of infinitesimal current is called ideal non-polarisable electrode (INPE). At INPE, electrons cross very easily across the interface and electrochemical equilibrium is rapidly achieved. In the event an external potential is applied to the electrode, the electrons continue to flow at a fast rate and there will be no charge execs created on the interface. Contrary, if the electrode is ideally polarizable, the electron transfer across the interface is difficult and thus when an external potential is applied, an excess surface charge develops as a result of the difficulty of electrons to pass through the electrode. Since charge cannot cross the IPE interface, or only does it with difficulty, the behaviour of the electrode solution interface is analogous to a capacitor. Fig. 1.1.2 shows the typical current response of IPE and INPE as a result of potential variation.

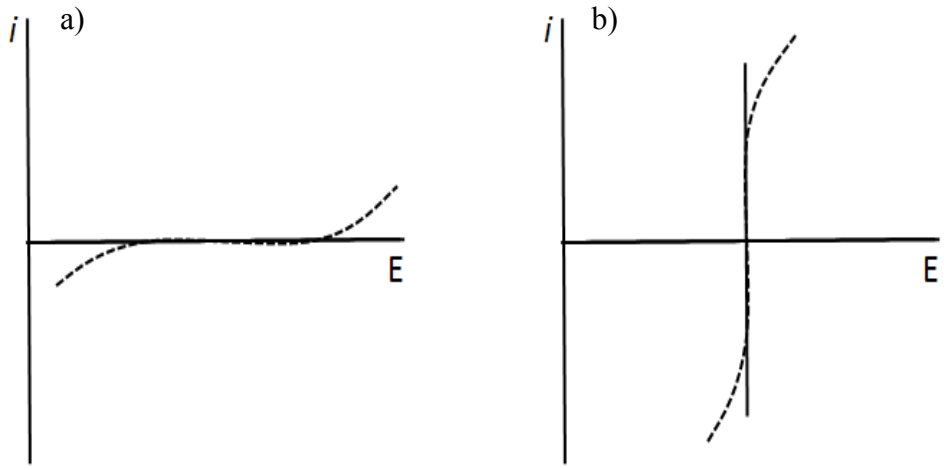



Figure 1.1.2 Typical current-potential curves for ideal a) polarizable and b) non-polarizable electrodes. Dashed lines represent the current response at potential changes.

It should be noted that no real electrode exhibits ideal polarizability over the whole potential range that can be applied before solvent breakdown as seen in fig. 1.1.2. In practice, if enough potential is applied, charge transfer occurs. However, it occurs at a very low rate and requires application of a large potential. These types of electrodes are considered ideal polarisable *de facto*.

Electrochemical measurements taking place between conducting phases usually involved the analysis of the electrical current response $i$ as a function of the applied potential $E$ for a given electrode in solution. Since several different potential interactions are involved during these measurements, it is important to understand the exact meaning of the applied potential.

### 1.1.3.2 Metal / Electrolyte Interactions

The metal/solution interphase has been more thoroughly investigated and comprehensively reviewed than any other interphase. The moment two conducting phases are placed in contact, the formation of different potentials arises and the electrical conditions between the phases become more complex. Fig.1.1.3a) displays a metal sphere of macroscopic size surrounded by a layer of uncharged electrolyte suspended in a vacuum while the representation of the potential changes of a given single positive charge brought from the infinite to a certain distance of a metal phase is shown in fig.1.1.3b).

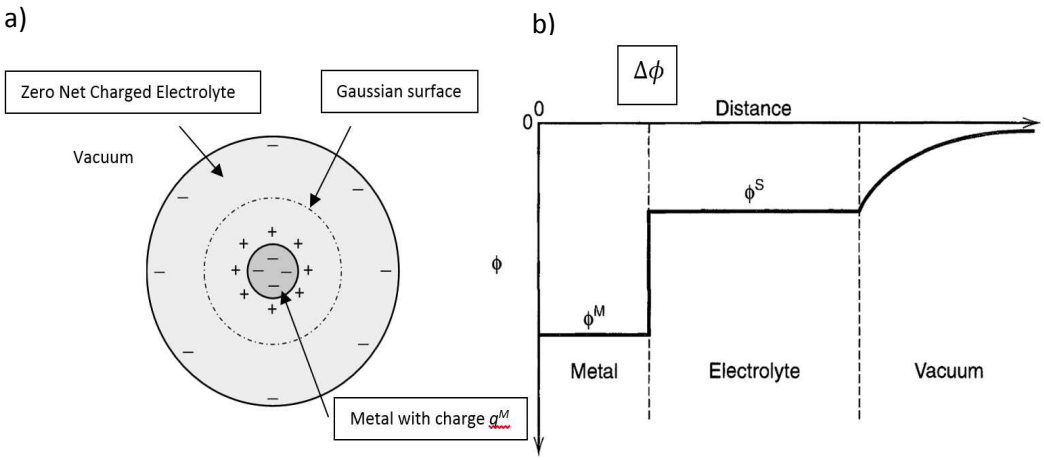



Figure 1.1.3 a) Cross section view of a sphere metal surrounded by electrolyte, b) Display of potential *vs.* distance of a positive charge during its journey form the infinite to the vicinity of the metal.

A system where the net charge is zero is considered to be in *electrical equilibrium*. This only occurs if no electrical current is applied to the phase. Hence, the entire phase is considered to have an *equipotential volume.* The potential at a given point *P* in a conducting phase is known as *Galvani potential* and refers to the work required to move a unit positive charge from an infinite distance to a point *P.* This potential can be expressed as:

$$\phi\,(P) = -\int_{\infty}^{P} E\,dl \tag{1.1.8}$$

where *dl* is an infinitesimal tangent to the path in the direction of the movement. The requirement to reach equilibrium conditions between two phases implies the difference between the inner potentials $\phi^M$ and $\phi^S$ to be zero. The difference between these inner

potentials is known as *Galvani potential difference,* $\Delta\phi$, and mainly depends on the charge imbalance produced by adsorbed ions, surface states, ionic species in the solution phase, and the charge in the metal space charge layer:

$$\Delta\phi = \phi^M - \phi^S \tag{1.1.9}$$

Therefore, the electrochemical equilibrium of the species *i* between two different phases *M* and *S* is:

$$\bar{\mu}_i^M = \bar{\mu}_i^S \tag{1.1.10}$$

By definition, the Galvani potential is constant within the phase at equilibrium. In addition, this interface is a factor of primary importance for electrochemical processes since it is in this region where the electron transfer between the redox active species in the electrolyte and the metal electrode occurs. Some effects such as electro-repulsion of reactants produced by local electrical fields which are caused by large changes on the potential in the boundary region may affect the kinetics of electron transfer across the interface; therefore $\Delta\phi$ controls the electron affinity of the two phases. According to Gibbs and Guggenheim[5], it is always possible to calculate the electrostatic potential between two points within the same phase though it is impossible to purely measure this quantity between points situated in different phases. This is mainly due to the fact that if the positive charge traverses two different phases, thus an interface, then the work required will be affected by the local interactions between the single charge and the chemical environment present in both phases. However, in practice, this measurement issue is solved by coupling a reversible interphase, *e.g.* a stable reference electrode, to the interphase under study. Changes in the potential difference across the latter potential can be monitored by using a simple voltmeter.

Despite the *Galvani potential,* $\phi$ can be considered as a single potential, it is useful to separate it into two regions as seen in eqn. 1.1.11 where the contribution of $\psi$ is primarly due to the charge *q* and $\chi$ to the surface dipoles.

$$\phi = \psi + \chi \tag{1.1.11}$$

These two concepts will be discussed in more detail. On the one hand, the Volta potential $\psi$ of a phase, with an excess of surface charge in a vacuum, is described as the electrostatic work required to move that single positive charge from an infinite point of phase β to a point "near" phase $\alpha$. The term "near" is considered to refer to a point between $10^{-5}$ and $10^{-3}$ cm from the electrode surface considering a metallic phase of 1cm dimeter. At this distance image forces and chemical changes on $\alpha$ phase, due to the approaching charge, are negligible.[6] The outer or *Volta potential difference,* $\Delta\psi$, between a metal phase and a liquid phase in contact with vacuum in therefore described as:

$$\Delta\psi = \psi^M - \psi^S \tag{1.1.12}$$

The outer potential arises due to electrostatic forces and becomes zero if the excess charge on the phase is zero. This occurs when the excess charge on the metal $q^M$ and on the solution $q^S$ are equal in magnitude but different in sign:

$$q^M = -q^S \tag{1.1.13}$$

On the other hand, in a metal/vacuum interfacial region, the potential that exists (mainly due to the spreading of electronic charge into the vacuum phase) across the surface of the phase with no excess of surface charge is known as surface potential, $\chi$. Interactive electrostatic forces arise when the positive charge passes through the first layer of atoms in a case of a metal phase or, in the case of a liquid phase, at the moment of crossing the dipole orientated layer on the interface. This surface potential contributes to the total work required to move a positive charge through a surface. As previously mentioned, both metal and liquid phases will experiment a surface potential on its surface. Hence, *potential surface difference*, $\Delta\chi$, between a metal and solution phase can be defined as the differences in the surfaces potentials of each of these phases

$$\Delta\chi = \chi^M - \chi^S \tag{1.1.14}$$

As previously outlined, the complexity of the applied/measured potentials involved in electrochemical measurements is clear. One may try to suggest which of the previous potentials correspond to the real meaning of the potential measured in a conventional electrochemical experiment. According to Bockris,[7] the *measured potential,* $V_{meas}$,

between a metallic electrode of metal *m* and a metallic reference electrode of metal $m_{ref}$ in a solution *s*, where the net current in the system is zero, being

$$V_{meas} = \left(\Delta^{m-s}\phi - \frac{\mu_e^m}{nF}\right) - \left(\Delta^{mref-s}\phi - \frac{\mu_e^{mref}}{nF}\right) = V_m - V_{ref} \quad (1.1.15)$$

where $\Delta^{m-s}\phi$ and $\Delta^{mref-s}\phi$ are the Galvani potential difference between the metal electrode and the electrolyte and the reference electrode with the electrolyte, respectively. F corresponds to the Faraday constant (96,485 C $mol^{-1}$) and n to the number of electrons involved in the reaction.

### 1.1.4 Concepts of Electrode / Solution Interface

As formerly outlined in section 1.1.3, since the charge of a metal phase resides on its surface, the unbalanced charge distribution on the metal creates a segregation of positive and negative charges in the direction of the phase boundary. Typically, these charges are associated with dipolar molecules, polarised atoms or ions. The volume that these particles occupy in the vicinity of the metal surface is called *double layer (DL).* The study of the double layer is closely related to what was defined as ideally polarized electrodes (IPE), those being electrodes on which no charge transfer occurs regardless of any potential applied by an external source. It was also mentioned that under these conditions, the electrical equilibrium between the phases is established. This leads to the possibility of developing various thermodynamic models of the electrical charge distribution on both sides of the double layer.

Most of the models that study the electric double layer are built from measurements of macroscopic equilibrium properties such as the interfacial capacitance and the surface tension are based on electrocapillary studies. In general, they pursue the way these properties change with potential and with activities of various species present in the electrolyte. These works consisted in a mercury droplet surrounded by a conductive electrolyte, *e.g.* KCl. One of the reasons why a mercury droplet is used is that it requires high activation energy for hydrogen evolution, which makes this material behave as an IPE over a range of 2 V in a typical protonic solution. In addition, the mercury droplet is liquid at room temperature, has a sphere shape which provides a homogeneous surface tension, $\gamma$ (to be described later in this chapter), and can be obtained at a high degree of purity. Since the interfacial tension of a liquid - liquid interface is less complex to measure than that of a

solid - liquid, the mercury droplet provides for the ideal material to formulate the theory of the double layer. The first comprehensive investigation on electrocapillary was carried out by Lippmann,[8] who developed a method to measure the *interfacial surface tension,* $\gamma$, as a function of potential drop assuming that no charge transfer across the surface occurs. Lippmann devised a simple apparatus for measuring simultaneously the boundary phase potential between mercury and various aqueous solutions and the boundary tension. It its simplest form, the apparatus consists of a mercury reservoir terminating in a fine capillary which is immersed in the solution. A standard reference electrode serves as the other pole. As progressively more negative potentials are applied to the mercury in the capillary, the interface tension rises, reaches a maximum, and then decreases. The electrocapillary effect is noticed as the variation of the interfacial meniscus. More detail about the electrocapillary curves will be given later. This method is based on eqn.1.1.16:

$$d\gamma = -q_m\, dE - \sum \tau_i\, d\mu_i \tag{1.1.16}$$

Electrocapillary studies assume no charge transfer across the surface takes place as a function of electrolyte concentration as seen in:

$$d\gamma = -q_m\, dE - \frac{q_m}{z_j F} d\mu_j \sum \Gamma_i\ d\mu_i \tag{1.1.17}$$

where $q_m$ is the surface charge density on the metal and E is the applied potential. $\Gamma_i$ is the *Gibbs surface excess* and represents the surface excess concentration of species *i* in the interphase compared to the bulk solution:

$$\Gamma_i = \int_0^\infty c_i(x)\, dx \tag{1.1.18}$$

It should be noted that the subscript *j* refers to an ionic compound that crosses the interface with ease whereas *i* passes across it with difficulty due to its bigger molecular size, stronger electromagnetic interactions, *etc*. For fixed solution composition $d\mu_i = 0, d\mu_i = 0$ and the electrocapillary equation (eqn. 1.1.17) reduces to the *Lippmann eqn.*:

$$\left(\frac{d\gamma}{dE}\right)_{P,T,\mu_I} = -q_m = q_{sol} \tag{1.1.19}$$

The interfacial tension is a measurable parameter. A typical set of electrocapillary curves for various electrolytes is present in fig. 1.1.4. It is obvious from fig. 1.1.4 that the curves

are usually characteristically parabolic and heavily dependent on the electrolyte composition.

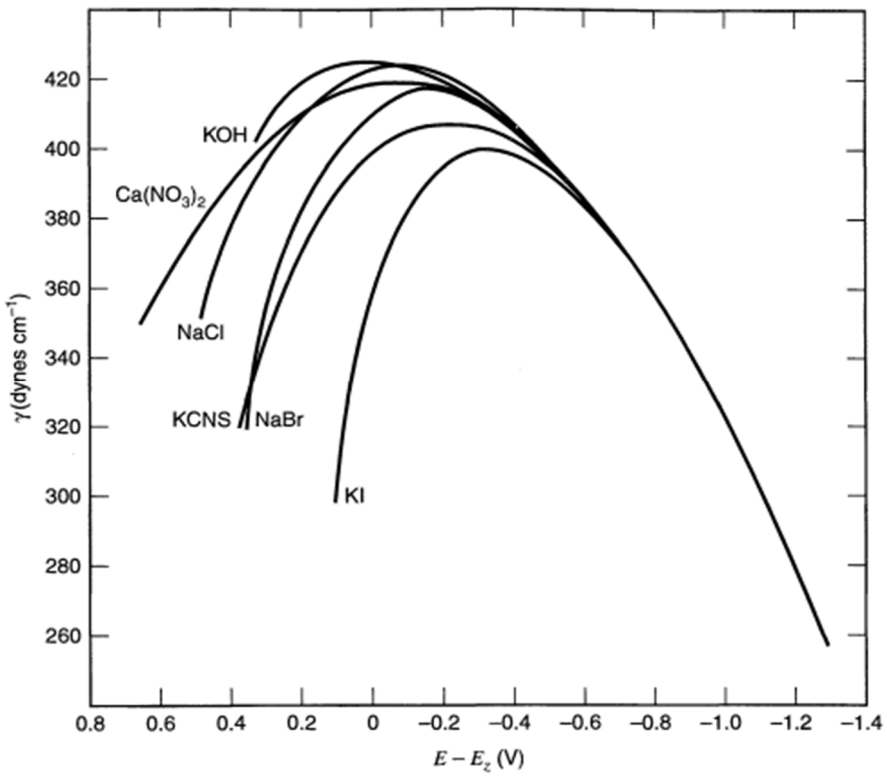



Figure 1.1.4 Electrocapillary curves for mercury in contact with aqueous solutions of different electrolytes at 18°C. The potential is plotted with respect to the p.z.c for NaF. Reproduced from Ref. [9]

A common aspect of all the curves is the existence of a maximum point in the surface tension. The potential at which this occurs is known as the *electrocapillary maximum* (*ECM):*

$$\left(\frac{\partial \gamma}{\partial E}\right)_{P,T,\mu_I} = -q_m = 0 \qquad (1.1.20)$$

Since the slope of the curve at this point is zero, the charge is also zero. The potential is this scenario is defined as the potential of zero charge (p.z.c) where:

$$\sigma^m = \sigma^s = 0 \qquad (1.1.21)$$

In order to explain the general shape of the curves, it is necessary to consider the adsorption effects on the electrode-electrolyte interface. Further, a brief description of the adsorption phenomena needs to be presented.

Adsorption is the formation of some type of bound between the adsorbate, commonly dipolar molecules, polarised atoms or ions, and the electrode surface. The interaction may be merely electrostatic, *e.g*. anions or cations with opposite charge to that of the surface, or due to the formation of a covalent bond. Moreover, dipole molecules *e.g*. water molecules, can be attracted to the electrode surface. The extent of the adsorption is usually expressed as *surface coverage*, $\theta$, and determines the fraction of the surface covered by adsorbate. It is relevant to point out that the surface coverage depends on the electrode surface, the solvent, the electrolyte and the adsorbate structure. The effective interaction between the adsorbed specie and the electrode surface generally depends on two parameters. The first one is the number of molecules adsorbed, since the single specie-electrode interaction varies when approached by another specie. The second one is the strength of their bound with the electrode surface. Hence, two types of adsorption phenomena may occur. The first one, or non-specific adsorption, refers to the process of build-up ions on the interface solution side. This type of adsorption is governed by long range electrostatic forces.[2] Apart from the magnitude of the charge on such ions, the chemically identity of such species is unimportant with regards to their adsorption characteristics – hence their "non-specificity". Moreover, in aqueous solutions, non-specifically adsorbed ions tend to be solvated. On the other hand, the second type, or specifically adsorbed species, are bound to the electrode surface by short range forces and therefore the chemical identity of the adsorbate is significant. These short-range forces are quantum mechanical in origin, and are not fully understood, with computer simulation latterly being applied to the problem of their elucidation.

Hence, if a more negative potential with respect the p.z.c is applied to the electrode, its surface develops a negative excess charge, whereas if a positive potential is applied it creates a positive surface charge. Variations on the potential with respect the p.z.c cause a decrease on the surface tension as seen in fig. 1.1.4. This is attributed to an increment of mutual repulsion between adsorbed ions on the surface, which occurs as a consequence of increased adsorption as the potential moves away from the p.z.c. Referring to the differences between anodic and cathodic curve shapes, it can be observed that the surface tension for potentials of less than the p.z.c is the same regardless of the electrolyte composition, whereas for higher potentials the surface tension tends to be dependent on the electrolyte composition. The former is an indicative of non-specific adsorption between the electrolyte ions and the electrode surface while the latter suggests a specific adsorption

since the behaviour of the systems in this potential region depends specifically on the identity of the ions in solution. The differences in electrocapillary curves occur at positive potentials where the presence of anions in the solution side of the interface is at its maximum. The manifestation of specific adsorption of anions in these potentials justifies this behaviour. The separation of charge perpendicular to the surface characterises its ability to store charge in response to a perturbation on the potential giving it the properties of an electrical capacitor. Plots of surface charge can be obtained by differentiating electrocapillary curves. Examples of surface charge with respect to the potential are shown in fig. 1.1.5.

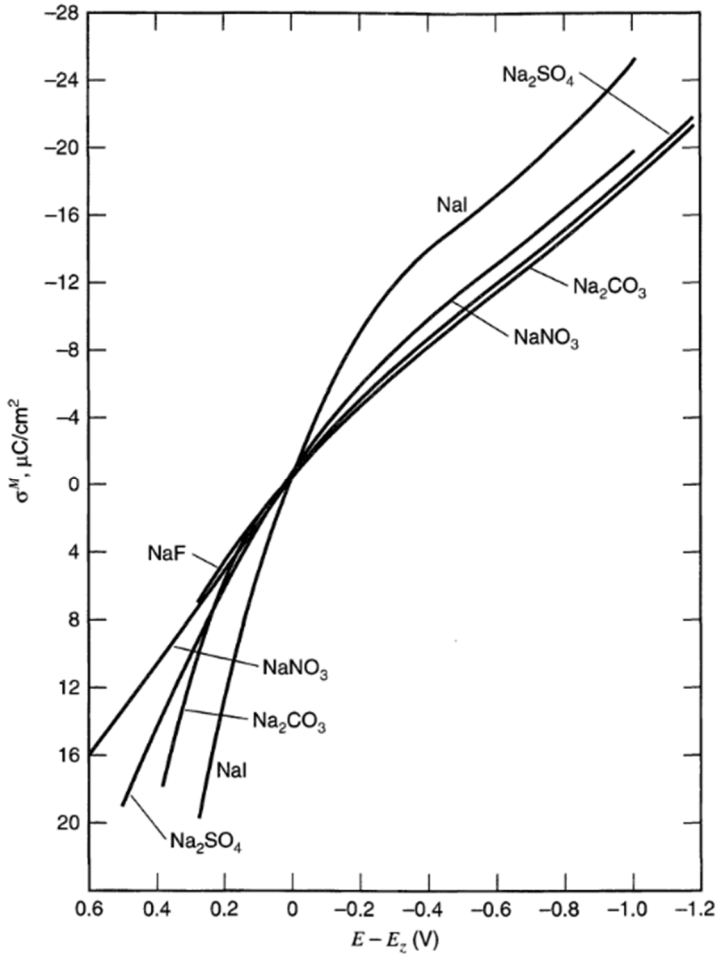



Figure 1.1.5 Electronic charge on mercury surface in contact with aqueous solutions of different electrolytes at 25°C. The potential is plotted with respect to the p.z.c for NaF. Reproduced from Ref. [9]

It becomes obvious from fig. 1.1.5 that the behaviour of the charge density is not linear with respect to the potential, as it should be for an ideal capacitor. Consequently, it is

necessary to define a *differential capacitance*, *C*. The differentiation of the Lippmann equation with respect to potential yields an expression for the *differential capacitance* $C_{diff}$ of the interphase:

$$C_{diff} = \left(\frac{d\sigma^M}{dE}\right)_{P,T,\mu_i} = -\left(\frac{d^2\gamma}{dE^2}\right)_{P,T,\mu_i} \qquad (1.1.22)$$

In the case of a mercury-solution interface the differential capacitance is obtained by performing a second graphical differentiation of the electrocapillary curve. For solid electrodes, however, $C_{diff}$ can be measured using ac electrochemical impedance spectroscopy. A schematic representation of the variation of differential capacity with potential for various electrolyte concentrations for the previous system is outlined in fig. 1.1.6.

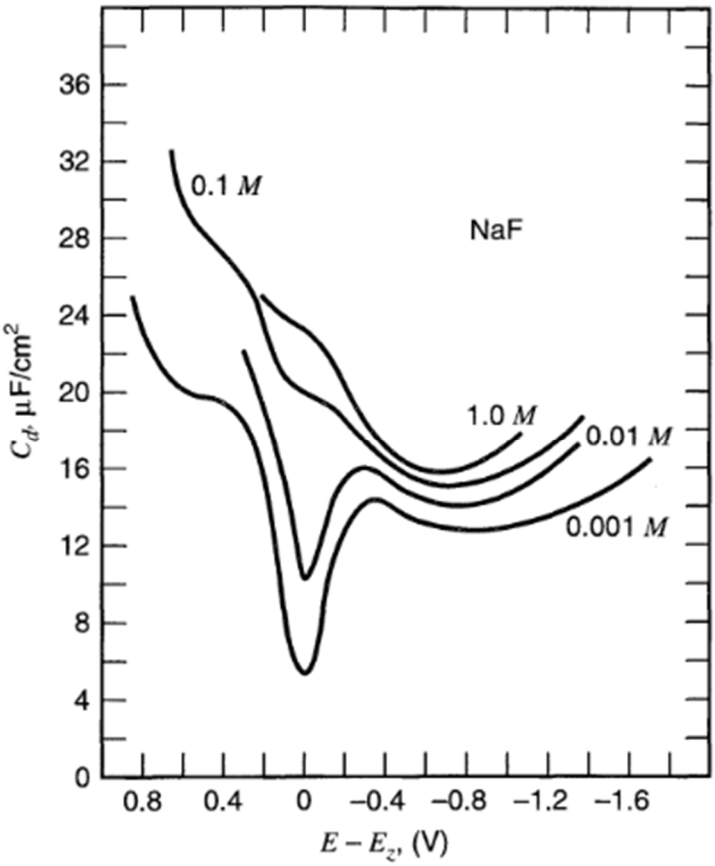



Figure 1.1.6 Differential capacitance *vs*. potential for NaF solutions in contact with mercury at 25°C. Reproduced from Ref. [9]

In general, the curves of interfacial capacitance against potential exhibit a minimum value of p.z.c in dilute solutions, whereas a maximum is evident at higher electrolyte

concentrations. More detailed considerations about the shape of the curves will be discussed in further sections of this thesis.

The $C_{diff}$ variation with respect to *E* leads to the introduction of the *integral capacitance K* , which represents the ratio of the total charge density of the metal at a given potential and defined as:

$$K = \frac{\sigma^M}{E - E_{p.z.c}} \tag{1.1.23}$$

where $E_{p.z.c}$ is the potential of zero charge. Therefore, *K* may be analogously interpreted to an ordinary parallel plate capacitor. The integral and the differential capacities are related as follows:

$$C_{diff} = K + \left(E - E_{p.z.c}\right) \frac{dK}{dE} \tag{1.1.24}$$

It is clear from eqn. 1.1.24 that $C_{diff} = K$ at the p.z.c.

Returning to the electrocapillary (eqn. 1.1.19), the relative surface excess of neutral molecules *i* on the interface in solution is obtained from the measurement of the dependence of the interfacial tension on the concentration of that component:

$$\Gamma_i = -\left(\frac{d\gamma}{d\mu_i}\right)_{P,T,\mu_{i\neq j}} \tag{1.1.25}$$

For ideal solutions the chemical potential is related to the bulk concentration through:

$$\mu_i = \mu_i{}^0 + RT\, ln\, a_i \tag{1.1.26}$$

where $a_i$ represents the thermodynamic activity of the compound *i* in solution. Differentiating eqn. 1.1.26 at constant temperature yields to:

$$d\mu_i = RT\ \ dln\, a_i \tag{1.1.27}$$

The utilisation of eqns. 1.1.25 and 1.1.26 results in an alternative expression for $\Gamma_i$ [10],

$$\Gamma_i = -\frac{1}{RT}\left(\frac{d\gamma}{dln\, a_i}\right)_{P,T,\mu_{i\neq j}} \tag{1.1.28}$$

Eqn. 1.1.28 predicts that when a compound is enriched at the interface ($\Gamma_i > 0$), and thus, the relative surface excess increases, the surface tension decreases when the solution

concertation is increased. Contrarily, when a compound avoids the surface ($\Gamma_i < 0$), the surface tension increases when the concentration of the given compound increases. The surface excess can be obtained experimentally, using eqn. 1.1.28, by measuring the surface tension as a function of solution concentration. A plot of $\gamma$ *vs.* solution component concertation has a slope given by $\Gamma_i$. It is worth to note that at p.z.c potentials there may be no electrostatic adsorption and hence $(\Gamma_i)_{p.z.c}$ may be regarded as a measure of the degree of specific adsorption of species *i.*

### 1.1.4.1 Structural Models of the Electrode / Solution Interface

As introduced at the start of the previous section, when the separation of charge occurs at the interface between two phases, that interfacial region is often referend to as the electrical double layer. The term "double layer" was first introduced by Helmholtz[11] back in the nineteenth century. He proposed a model that described a typical metal-solution interface considering it as a two-parallel plate capacitor: the metal with its excess charge on the surface constitutes one plate, while the excess counter charge, with equal and opposite polarity than that of the metal charge on the solution side constitutes the other. Such structure may be defined as the relationship between the stored charge density, $\sigma$, and the voltage difference, $\Delta V$, between the pates as:

$$\sigma = \frac{\varepsilon\varepsilon_0}{d}\Delta V \tag{1.1.29}$$

where $\varepsilon$ is the dielectric constant for the medium, $\varepsilon_0$ is the vacuum permittivity ($8.85 \cdot 10^{-14}$ F $cm^{-1}$) and $d$ is the interpolate spacing. The differential capacitance is obtained from a differentiation of eqn. 1.1.29

$$\frac{d\sigma}{dV} = \frac{\varepsilon\varepsilon_0}{d} = C_{diff} \tag{1.1.30}$$

The weakness of this model may be apparent from eqn. 1.1.30 since it predicts the differential capacitance to be constant regardless of the potential and the solution concentration. However, the experimental data presented in the previous section demonstrated that the differential capacitance does vary with potential and ion concertation in a very definite manner. Variations on $C_{diff}$ with potential suggest that either $\varepsilon$ or $d$ depend on these variables. Hence, a more sophisticated model is required. More accurate

models were presented both in 1910 by Gouy[12], and completely independently three years later, by Chapman.[13] A graphical comparison of the two models is presented in figs. 1.1.7 and 1.1.8.

In general, for a conductive metal, an excess charge density $\sigma^M$ is confined into the surface, but the same is not necessarily true for the solution. This becomes more notorious when the concentration of ions in solution, which are charge carriers, is relatively low. In this situation, it might require some significant thickness of the solution phase to counterbalance the excess charge density of the metal. The thickness would be controlled by the electrostatic interactions of the metal with the charge carriers, either repelling or attracting them, according to their polarity and the tendency of thermal processes to randomize them. This model proposes a finite *diffuse layer* where there is no special layer of ion or solvent molecules at the solution interface, but rather a distribution of excess charge which thickness depends on applied potential and ion concertation.

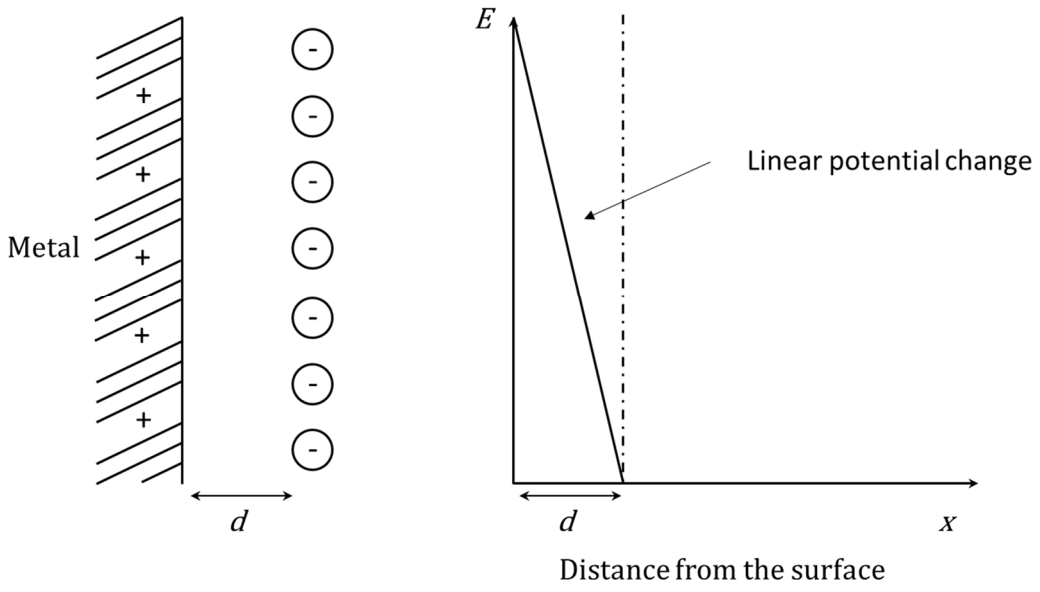



Figure 1.1.7 Helmholtz's parallel plate capacitor model of the double layer showing the distance of closest approach of anion to the metal surface.

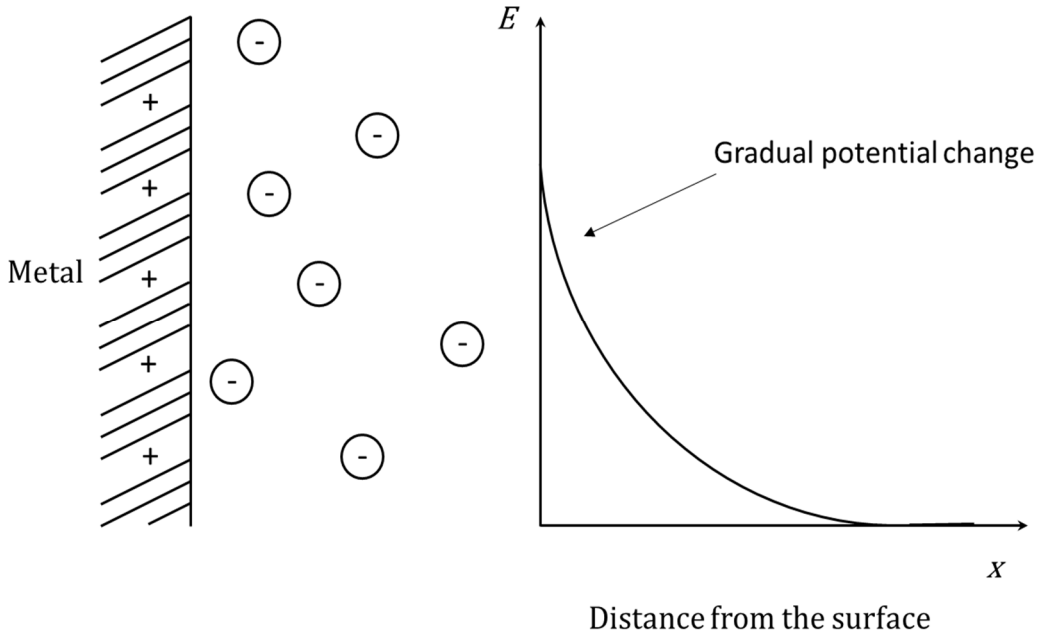



Figure 1.1.8 Gouy - Chapman model of the double layer showing the potential distance relation on the inner layer.

The main concern about this model is that it conceives the ions without a restricted position within the solution. They are considered as point charges[10, 14] that can randomly approach the electrode surface which suggests that, in the case of high polarisation, the separation between charges zones of the metallic and solution phase decreases and tends to zero. This behaviour can be observed in fig. 1.1.8. Certainly, since the ions have a finite size, the proximity of an ion to the electrode surface is limited by its ionic radius and hence cannot approach any closer than that. In the case of solvated ions, the thickness of the primary solution sheath is given by the sum of the ion's radius and the radius of the solvent. Still another increment may be necessary to account for a layer of solvent on the electrode's surface. Therefore, a *plane of closest approach* for the centres of the ions at some finite distance from the electrode surface needs to be considered.

The Gouy - Chapman model was later modified by Stern[15], who added together the earlier models of Helmholtz and Gouy - Chapman proposing that the ions could not approach the electrode surface at distances smaller than its ionic radius. This model is known as Gouy – Chapman - Stern model (GCS) and its representation can be seen in fig. 1.1.9. Stern further proposed that the ions closest to the electrode surface, those accounted for by the Helmholtz element of the model, can be modelistically placed in two main regions: (i) *the*

*inner compact plane* (IHP), also called Helmholtz or Stern layer, and (ii) the *outer Helmholtz plane* (OHP). This idea was then expanded by Grahame.[16] The formation of this layer, especially in metal-solution interfaces, has been a subject to exhaustive discussion not only due to its importance for the electrical double layer theory but also because of its implications on the potential transfer within the interphase[10, 17]. In the case of charged metal surfaces, the layer of oriented water molecules have been studied in three different fashion, those being: (i) the continuum dielectric theory; (ii) the water dipole orientation; and (iii) the H-bounded associated water molecules orientation.[17-18] The second and third of these theories are focused on the solvent orientation in the inner region of the double layer, where the preferred orientation of solvent molecules, either monomers or dimers, on the surface is determined by the surface charge density, whereas the first one of the theories accounts for the displacement of charge in response to an imposed electric field. A more exhaustive discussion of this topic is presented later in this section.

The greatest concentration of charge carriers is found adjacent to the electrode surface, thus in the inner layer, where the electrostatic forces prevail over the thermal processes. Specifically adsorbed ions, usually anions, establish in this region a compact layer of approximately few molecular diameters thick. The total charge density arising from specifically adsorbed ions in this inner layer is given by $\sigma^i$ ($\mu C\ cm^{-2}$).

The detailed nature of the interaction forces between an ion and the electrode surface regarding specific adsorption has not yet been totally resolved. Macdonald and Barlow[19] on one side, and Bockris and Habib[20] on the other side, have provided critical reviews on this area. The progressive reduction of the charge carriers' concentration occurs at greater distances from the electrode surface as the electrostatic forces become weaker. In this scenario, the interaction between the ion and the metal surface is not sufficient to cause the desolvation *ergo* the hydrated ions in contact with the metal are regarded as residing in a layer known as the *outer Helmholtz plane* (OHP).

It is generally accepted that in the case of an aqueous solution the closest approaching solvent ions are separated from the electrode surface by a layer of oriented solvent molecules adsorbed on the metal surface.

Contrary to specific adsorption, where various types of short range interactions exist, the interaction of solvated ions with the metal surface may be accounted for by long range Coulombic forces. In a nutshell, the resultant interaction between the ion and the metal is determined by the competition between the ion - metal and the ion - solvent interactions. In some cases, these interactions develop to a partial charge transfer between the ion and the metal, resulting in the formation of a strong covalent bond. This type of bond is called *chemisorption*. The opposite scenario is known as *physisorption*, where the bond between them is much weaker and does not cause a significant electronic modification of the ion.

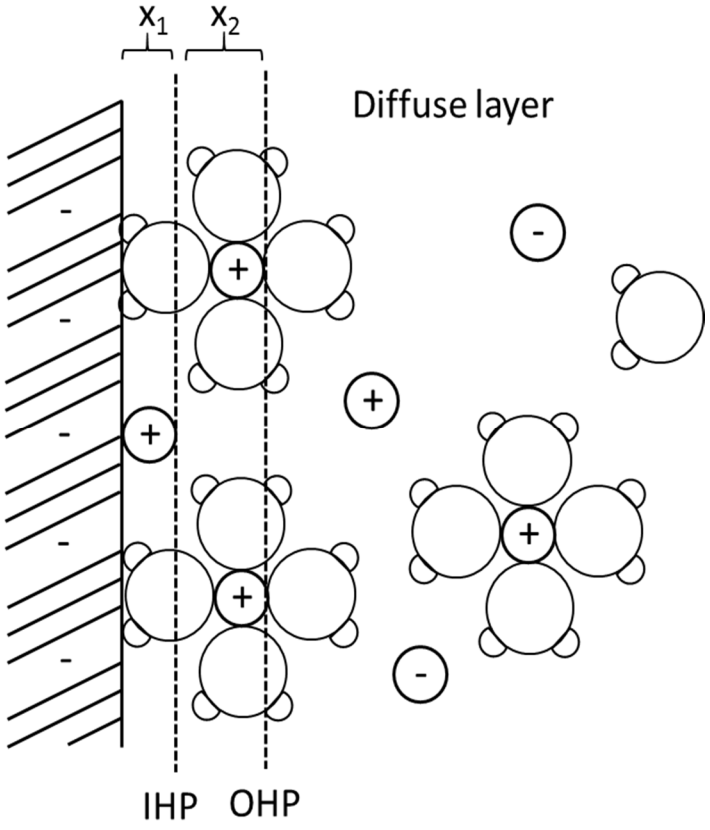



Figure 1.1.9 Gouy - Chapman - Stern model of the double layer region under conditions where cations are specifically adsorbed.

Unlike the specifically adsorbed ions situated at the IHP, the non-specifically adsorbed ions are not all located on the OHP but contained in the diffuse layer which extends from the OHP into the solution bulk. The excess charge density produced by the non-specifically

adsorbed ions in both the OHP and the diffuse layer is $\sigma^d$. Hence, the total excess charge density ion in the solution side of the double layer $\sigma^S$ is given by:

$$\sigma^S = \sigma^i + \sigma^d = -\sigma^M \qquad (1.1.31)$$

The nature of the diffuse layer has its origin in thermal agitation. This thermal agitation provides for a disordering force opposed to the "ordering" Columbic forces of attraction and repulsion. It is worth noting that the arrangement of a *plane of closest approach* produces little impact on the differential capacitance for potentials near p.z.c in systems where the concentration of electrolyte is low. This is due to the thickness of the diffuse layer being larger than the distance from the electrode surface to the OHP. However, as the electrode becomes more charged, a larger number of molecules are gradually more tightly compressed against the boundary in the $x_2$ distance and the whole system begins to coincide with the Helmholtz model.

The model presented in fig. 1.1.9, provides predictions that, broadly speaking, account for a wide variety of real systems.[2] Although discrepancies still exist, the success and the imperfections of the GCS model can be discussed by considering the data in fig. 1.1.6. It has been shown that the minimum capacitance value observed in the vicinity of p.z.c is well predicted by the diffuse layer aspect in the model, whereas the Helmholtz inner layer concept models the roughly constant capacitance region found at potentials between -1.2 V and -0.4 V. Also, as the potential increases, the diffuse layer becomes more compact, developing an increment on the $C_{diff}$ observed at potentials between 0.8 V and 0 V. The lack of accuracy of the GCS is observed comparing the behaviour of the differential capacitance when different electrolyte concentrations are used. The discrepancies between the experimental data and the model can be explained by the fact that the diffusive layer element on the model considers the Debye-Hunkel theory of activity in electrolytes to be of zero order approximation.[10] This approximation neglects the finite size of the ions and can only be accurately applied up to about 0.001 M for 1:1 electrolytes.[21] The problem arises at concentrations greater than 0.001 mol $dm^{-3}$ where the Debye length approaches the dimensions of a solvated ion and, hence, the average distance between solvated ions is greater than the diffuse layer thickness. Bockris[21] suggested that the diffuse layer theory is usually applied to systems where the electrolyte concertation exceeds 100-1000 times the concentration on which the model is based (0.001 mol $dm^{-3}$). The theory also neglects other effects that may arise from the system where the concentration of electrolyte is

higher than 0.001 mol $dm^{-3}$, *e.g.* solvent dielectric saturation or full polarization, ion-ion interactions, ion-pair formation, field-dissociation effects and especially strong nonspecific interactions of the ions with the surface charge on the electrode. The latter effect can be described in terms of *ion condensation* (or counterion condensation) and treated by a model which uses effective parameters such as "*effective surface charge*", to account the ion - surface interaction. Ion condensation may occur when the charge density is increased above a critical value and the ionic concentration on the surface remains constant regardless of the potential applied.[22] It has been observed that the effective surface charge not only depends on the charge of the ions but also on their nature.[23] To avoid confusion, the quantitative values obtained by the GCS model for electrolyte concentrations higher than 0.001 mol $dm^{-3}$ must be always evaluated with prudence.

While the conceptual limitations of the diffuse layer theory can demonstrate the principles for the formation of the differential capacitance minimum peak, the model is not adequate to explain the observation of a capacitance *maxima*, as seen in the curve of 1.0 mol $dm^{-3}$ in fig. 1.1.6. This weakness was already observed by Bockris, Devanathan and Muller and served as the starting point for the development of a new model, known as BDM, in the early 1960s.[24] Unlike the models previously explained, the BDM's success lies primarily in its ability to explain the occurrence of the maximum point found in differential capacitance *vs*. potential graphs, since it takes into consideration the formation of a layer of oriented water molecules on the metal surface. It is relevant to mention that this oriented layer of water molecules affects the shape of potential-distance function in the interface. A more detailed clarification of this concept is presented later in this section.

Regarding the formation of the capacitance hump, Watts-Tobin and Mot[25] suggested an approach to describe the dipole potential difference generated by the compact layer of water molecules on the surface. According to Watts, the presence of a hump in most graphs of $C_{diff}$ *vs.* potential occurs due to an increase in the dielectric constant of the compact layer of water molecules, which results in a change of sign of the average dipole moment of these molecules. Mott *et al*. suggested that, under p.z.c conditions, there was an equality up and down types of water molecules on the metal surface (see fig. 1.1.12 for clarification). Thus, if potential is applied to the electrode, the charge upon the surface changes, which causes all the water molecules to be oriented, up or down, depending on the charge sign of the electrode. This causes a variation on the surface potential, $X_{H_2O}$, with

$q^M$ and since $\frac{dX_{H_2O}}{dq^M}$ has the dimensions of a capacitance, if it is plotted as a function of applied potential, it experiences a maximum at the potential of zero charge as seen in fig. 1.1.4.[26]

Moreover, Bockris *et al.*[26] found that the height of the capacitance maxima was strongly dependent on the radius of the ion of the electrolyte, as represented in fig. 1.1.10. This proves the assumption that the hump is provoked by specific adsorption ions.

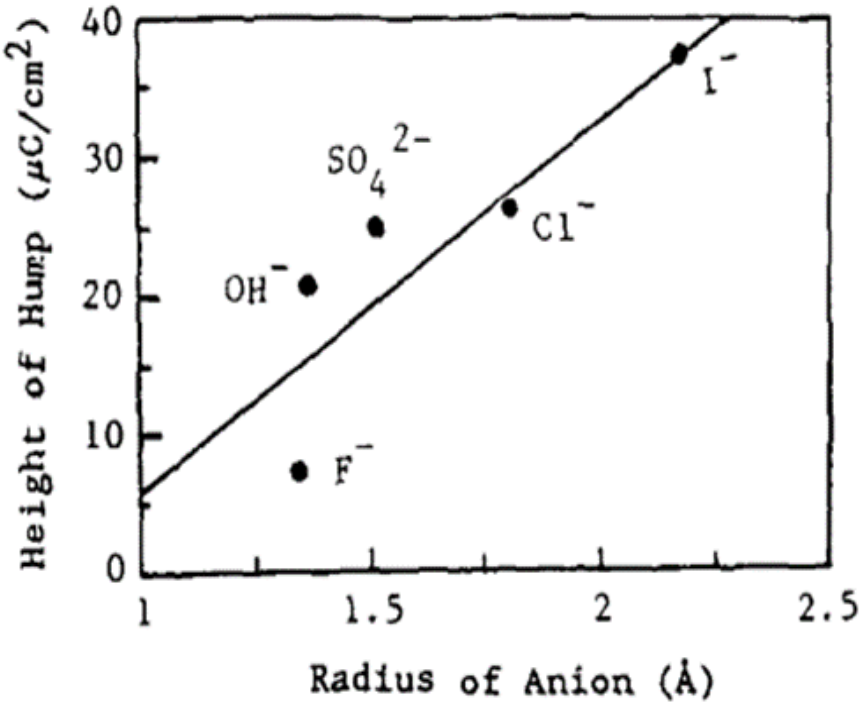



Figure 1.1.10 Capacitance hump as a function of radios of anion. Reproduced from Ref. [26]

Modern pictures of the metal-solution interphase region are essentially based on this BDM model and various aspects of it are pictorially considered in fig. 1.1.11. Although the BDM model implied a substantial improvement on modelling the experimental data with respect to the Gouy - Chapman - Stern model, the issues previously mentioned regarding Debye length in more concentrated electrolytes still remained present in this model. Despite the BDM accounts for the dielectric properties of the interfacial aqueous dilute solutions by assigning fixed dielectric constants $\varepsilon$ to the different regions of the system: 6 for the inner Helmholtz plane, 30 - 40 for the outer Helmholtz plane and approximately 80 for the bulk.[27]

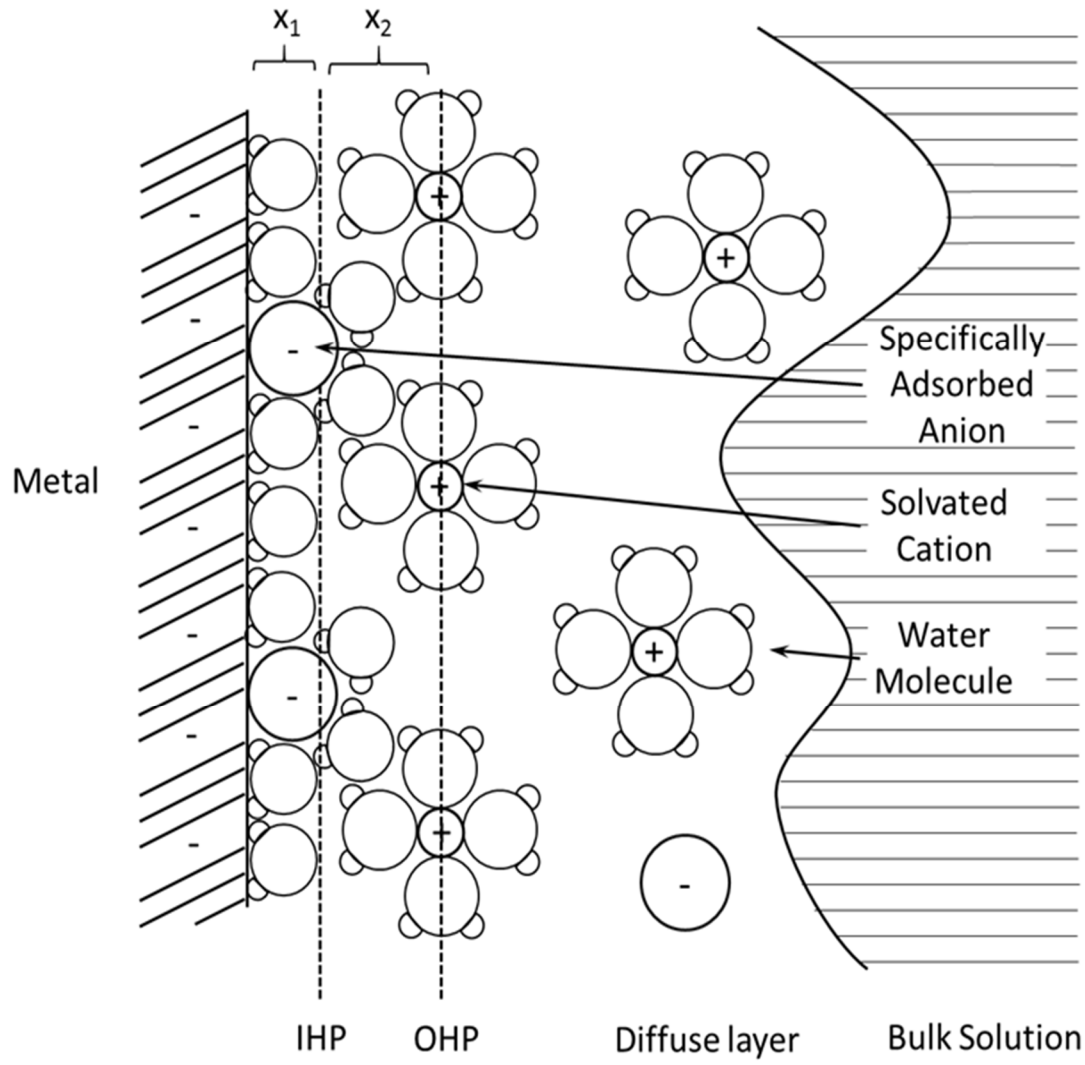



Figure 1.1.11 Schematic representation of the B.D.M. model at a metal solution interphase region.

It was observed that the degree of dielectric saturation and also the structure of the compact layer vary with the solution concertation and the electrode polarisation.[2, 28] It is noteworthy that all the above models share the assumption that both the potential and the charge vary only at the solution contiguous to the metal surface. However, this may not be completely valid.

Most of the efforts over the last forty five years have been focused in developing a more honest correlation between the BDM model and the experimental data.[29] This contributed to the proposal of various multiple state models aiming to evaluate with more precision the inner compact layer and, particularly, the region adjacent to the surface. Toney *et al*.[30]

suggested that for charged electrodes, as the potential is swept from negative to positive, the compact layer of water molecules adjacent to a solid interface is arranged in several layers and that those molecules in the first layer are reoriented from oxygen-up to oxygen-down so the oxygen becomes closer to the surface with the hydrogen facing the bulk solution direction.

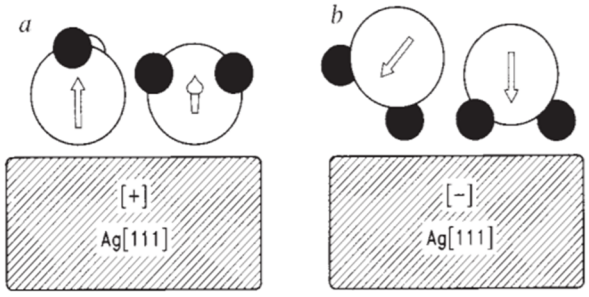



Figure 1.1.12 Possible orientation for water molecules near the electrode surface according with M.F Toney, being a) the positive charged surface and b) the negative surface. The arrows show the directions of the dipole moment. Reproduced form Ref. [30]

Another possible orientation of water molecules on the surface vicinity has been proposed by Watts-Tobin and Mott[25] and is presented in fig. 1.1.13. These authors consider the existence of two orientations of the solvent dipoles adjacent to an electrode surface. On the one hand, Watts-Tobin stated that only two configurations of water molecules can be attached onto the metal surface and that the direction of the dipole vector is given by a three bound-forming on the metal as shown in the fig. 1.1.13. The first configuration is designated as "spin up" and in it the dipole vector points towards the solution bulk while in the second one, the "spin down" configuration, the dipole points towards the surface. The dipole vectors on both configurations are equal in module but opposite in sign, as schematically represented in fig. 1.1.13a. Watts-Tobin observed than the orientation of water molecules on the metal surface in absence of an excess surface charge is weak, so the contribution of the dipole layer to the potential drop across the interface should be neglected. However, if an excess of charge is present on the surface, the water molecules orient themselves in a compact manner onto the surface, which contributes to a significant perturbation on the potential drop across the interface. Watts-Tobin's theory however, neglected the possibility of lateral interactions between water molecules arising from hydrogen bound interactions within the compact layer.

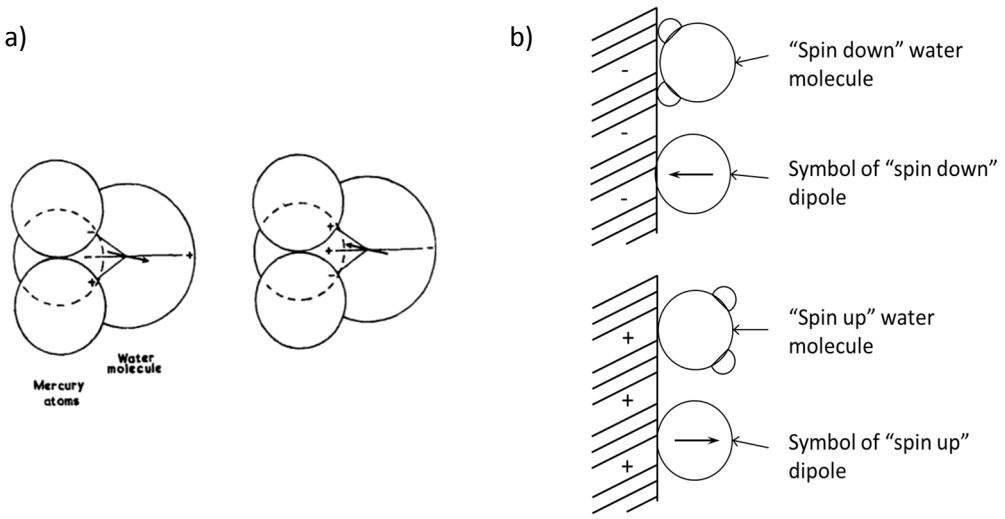



Figure 1.1.13 a) Schematic representation of probable water molecules configuration onto a mercury surface, according to Watts-Tobin. Reproduced from Ref.[25b] b): The "up" and "down" possible configurations of the dipole.

Mott included to the Watts-Tobin model the conception that the only molecules which contribute to the potential drop are placed in a region between the outer Helmholtz plane and the metal and that they do not establish more than a monolayer on the metal. The concept of the two state configuration of water molecules has also been developed by Macdonald and Barlow[31] and by Bockris et. al.[27b]

Modern treatments have, however, abandoned the belief that water dipoles can only be oriented in two discrete configurations.[32] In this sense, Damaskin and Frumkin[33] Bockris and Habib[20b, 34] and Fawcett[35] have developed a three state model while Parsons[36] elaborated a four state model. Fawcett added further postulations to the two-state model proposed by Watts-Tobin and suggested a three-state model assuming that the three orientations of water molecules at the electrode surface may be located either in the same direction than the electric field, against it or perpendicular to it, as shown in fig. 1.1.14. Damaskin and Frumkin took a different approach towards the three-state model. They distinguished two types of water molecules depending on their adsorption to the surface. One type is the *physisorption* water molecules, with weak interaction between each other, which associate together and are freely oriented either in the "up" or "down" direction which is schematically represented in fig. 1.1.15.

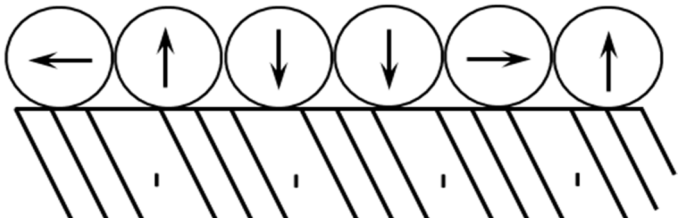


Figure 1.1.14 The Fawcett model of the solvent monolayer at the electrode surface illustrating the orientation of molecules in the up, down and perpendicular positions.

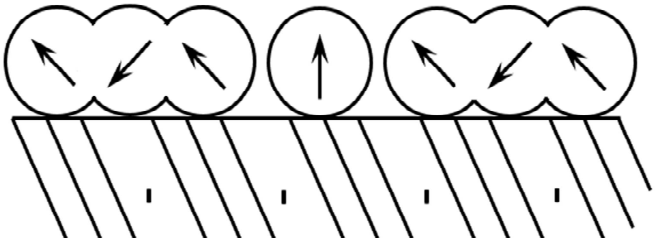


Figure 1.1.15 The three-state model proposed by Damaskin and Frumkin.

These associations have an equal dipole magnitude regardless of their direction. However, there is another kind of molecules, individually distributed on the surface, which are permanently placed with the oxygen atoms attached to the surface. These, due to their strong chemisorption behaviour, do not rotate with the presence of an electric field. In this situation, as the charge changes from zero towards the positive or negative side, the associated molecules are reoriented, whereas the strongly adsorbed ones remain in the same position.[33] The associated water molecules were assumed to reorient themselves altogether at p.z.c, which explains a maximum capacitance at that potential. It was also proposed that a positive increment on the charge causes field induced destruction of the associated groups of water molecules, which leads to an increased polarisation of the double layer. This explains the rising parts observed in experimental $C_{diff}$ *vs.* potential curves *e.g.* in fig. 1.1.6.

Another view for a three state model was presented by Bockris and Habib in 1977.[20a] The proposed model involved an equilibrium between dimers and monomers on the electrode surface. They suggested that under p.z.c conditions and considering a mercury-solution interface, the best approximation of the disposition of water molecules on the metal surface consisted of two-thirds of water dimers (two water molecules combined by hydrogen

bounding) and one-third of monomer water molecules.[37] However, they did not assume that all the water molecules present on the surface were associated onto pairs but also onto trimers, tetramers, *etc*. To relativize the amount of monomer, dimers, trimer, *etc*. on the surface, they calculated the free energy of formation on the surface of these adducts considering the bonding energy and the entropy parameters. According with their results,[37] despite the existence of trimers and tetramers in the layer, their presence can be neglected as their number compared with the monomers or dimers is minor. Parsons[36] developed a four state model of interfacial water molecules as an attempt to improve the Damaskin and Frumkin model. He assumed that instead of strongly adsorbed water molecules onto the surface, as those found in the Damaskin and Frumkin model, there were "free" water molecules coexisting together with dimers on the surface. The former ones can adopt one of the two orientations, either "up" or "down", with equal but opposite dipole direction. The latter ones can also adopt the "up" or "down" orientation but, unlike the free molecules, these orientate themselves with opposite perpendicular dipole moment as seen in fig. 1.1.16.

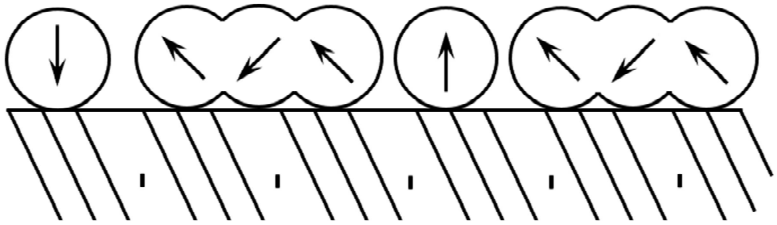


Figure 1.1.16 The four-state model proposed by Parsons.

Even though it has been stated that both the monomers and the dimers have effective dipole moment, the lateral iterations between them and between each of these entities with themselves are neglected in this model. Bockris, however, suggested that a model, referring to Parsons', with a suitable large amount of adjustable parameters such as dipole magnitude, dipole orientation, existence of "free" water molecules and dimers could virtually account for any type of experimental data, which does not validate the model as to be correct nor means that no physical effects have been neglected.[20a, 26]

Two additional linked aspects of the metal solution interphase that have attracted considerable interest are: (i) the way the potential and charge are assumed to vary at the solution side of the interphase, and (ii) the potential distribution in the metal phase. As recently mentioned, in the metal solution interphase several layers of liquid molecules along with ions are attached onto the surface by electromagnetic forces and, as a result, the layers in the vicinity of the metal surface are strongly compacted. The presence of these molecular layers, which have different dielectric properties, causes a non-linearity behaviour in the potential-distance function. In the BDM model, a sharpness change of the potential is observed.[27a] This phenomenon was further discussed by Trasatti[38], who observed that, in the case of metals, the capacity of the inner compact layer under p.z.c conditions is strongly dependent on the electronic structure of the metal. He suggested that the compact layer of water molecules propagates into the solution, by hydrogen bonding, to depths of up to 10 – 20 molecular layers and decays through a disordered region to the bulk. It may be pointed out that the number of layers depend on the H-bound strength in a way that the higher the strength, the more number of layers. Therefore, the propagation of the ordered compact layer, and thus the p.z.c, differs from metal to metal depending on the metal–water strength bond. Trasatti also found that the p.z.c exhibits a linear correlation between the p.z.c and the electronegativity of the metal ion. The p.z.c becomes more positive in terms of potential as the electronic density of the metal increases. A parallel increase was found in the metal–water interaction as the metal becomes more electropositive.[20a, 39] The metal surface has for long been treated as an ideal surface, *e.g.* smooth, perfectly conducting walls whose interactions with the solution occur through electron exchanges and charge image effects, and therefore, the importance of the solid phase has often been neglected. The structure of the metal is often presented on the basis of the "jellium model" and applied to theory of metal surfaces in vacuum. The most remarkable authors who investigated the capacity of the inner layer with respect to the electronegativity of the metal were Badiali and Goodisman,[40] Macdonald[41], Blum *et al*.[42] and Schmickler and Henderson[43] in the early 80s. The theories proposed by these authors have in common three assumptions: (i) that the dielectric constant of the solvent is 90 even up to the electrode surface, (ii) that the solution is a mixture of hard sphere ions and dipoles, as presented in fig. 1.1.17, and (iii) that the metal is considered in terms of the jellium model. This model envisaged the metal as consisting of a skeleton of positive charged metal ions represented by a homogeneous background charge density which drops suddenly to zero at the surface.[32] The electrons on the metal are scattered smoothly across

the ideal surface giving rise to a surface-orientated layer on the boundary of the surface. Fig. 1.1.17 shows that the jellium edge is situated at a distance z = 0 whereas the plane of the outermost metal nuclei is located at a distance of z = 0.5 d. At more negative distances the potential reaches a constant value. Contrary, at a more positive distance of ca. 2 Å, the metal electrons tail out into the vacuum and it is in this point that they can interact with either the adsorbate species or the electrolyte.

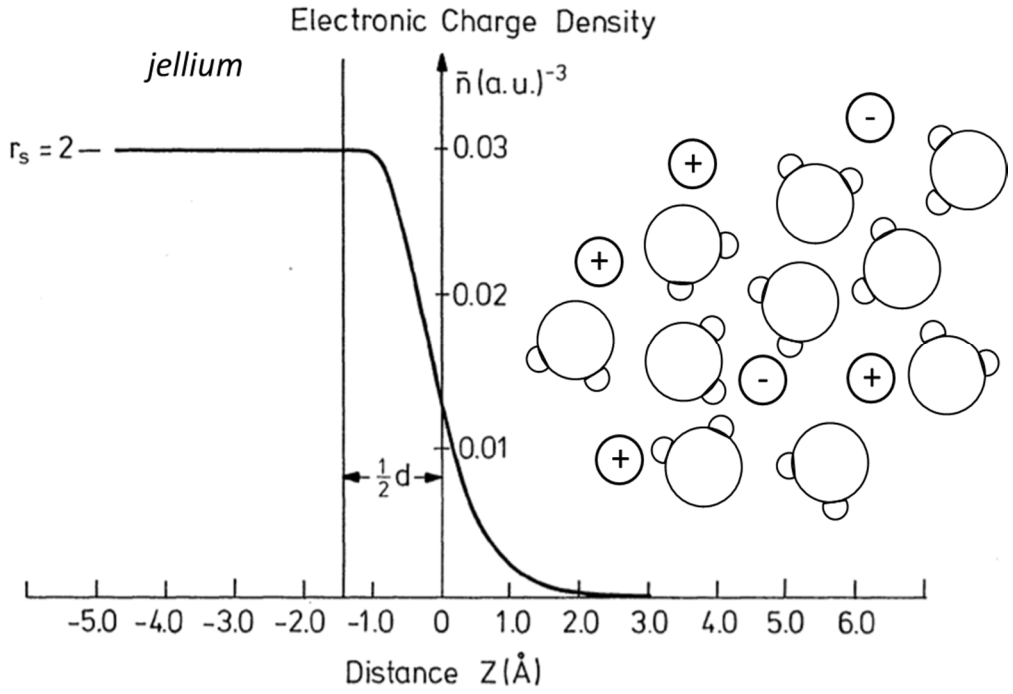



Figure 1.1.17 Surface electronic density as a function of distance perpendicular to the surface. Adapted from Ref.[44]

At this point it is convenient to define *the zeta potential* ($\zeta$) or electrokinetic potential, which is the potential at the shear plane between two charged planes. In many cases, various layers of liquid molecules and ions are tightly compacted onto the metal surface. As a result of this, the shear plane is not exactly at the interface but set at a distance equal to the outer Helmholtz plane and it can be assumed that $\zeta = \phi_{x_2}$.[45]

Many different techniques have been used to investigate the properties of the metal-solution interface.[39, 46] These techniques can be classified into traditional and non-traditional ones as follows.[47]

Traditional techniques are essentially electrochemical in nature[48], such as measurements of potential of zero charge, capacitance variation with potential, interfacial tension, *etc*. These methods provide direct information to be obtained from the interface while indirect information of the interface's structure can be obtained from electrochemical adsorption and kinetic studies.[49]

The latter group of techniques, which are the non-traditional ones, display good sensibility to microscopic parameters of the interphase but lack sufficient molecular specificity. A concise review on this area has been provided by Yeager.[47] Non-traditional techniques have been employed to complement the previous classical electrochemical techniques. These comprise, among others, Auger spectroscopy (AES),[50] electron energy loss spectroscopy (ELS)[51], reflection high-energy electron diffraction (RHEED), ion scattering spectroscopy (ISS)[52], X-ray photoelectron spectroscopy (XPS), specular reflectance spectroscopy[53], ellipsometry spectroscopy.[54] Auger spectroscopy and X-ray photoelectron spectroscopy were used as suitable techniques for chemical identification of surface atoms. Particularly, XPS was employed in interfacial studies in order to distinguish different adoption states of chemisorbed molecules such as Co on Mo.[55] Electron energy loss spectroscopy along with both low energy primary electrons (E ≈ 5 eV) and a high resolution spectrometer ($\Delta E \approx 10\ meV$) was used to detect the vibrational frequencies of surface complexes formed by adsorption and surface phonon in the substrate. Ellipsometry spectroscopy has shown to be a promising technique to study the optical properties of layers such as passivating films on electrode surfaces as function of wavelength, potential and the effective optical thickness of the layers. Ion scattering spectroscopy can be employed to examine the atomic structure of surface layers with various elements such as NiO or $Co_3O_4$. It, however, suffers a lack of resolution when heavy ions with similar masses are analysed. Reflection high-energy electron diffraction probes the surface structure of the metal by using high energy electrons, about 100 keV of magnitude, near grazing incidence. Hence, information on the surface topography, the degree of surface coverage and both symmetry and size of the surface mesh can be obtained. Specular reflectance spectroscopy analysis provided relevant information on the metal surface such as the surface's change densities, the adsorption isotherms, the surface's roughness effects, the electronic characteristics of anodic films and passivating layers on both metals and semiconductors, etc. by analysing the relationship of the reflectance changes as function of potential. The reliability of the experimental data obtained by such studies is highly

dependent on whether the electrode surface can be transferred from an ultra-high vacuum (ca. $10^{-10}$ torr) atmosphere into an aqueous solution and *vice versa* without performing significant chemical changes and surface contamination.

### 1.1.4.2 The Oxide / Solution Interphase

All the concepts and models previously discussed in section 1.1.4.1 refer to the metal-solution interphase. In contrast to metallic electrodes which are identified as good conductors, most metal oxides possess poor conductivity and large electrical resistance, which make them behave as either insulators or semiconductors. The conductivity of a metal oxides lies on both its molecular structure and the magnitude of the band gap.[56]

It is appropriate at this point to review the concept of band gap. Usually the electric properties of solids are described in terms of *the band theory.* This theory involves the behaviour of electrons moving in a region comprised by atomic nuclei and other electrons. According to this theory, if atoms are brought together to construct a crystalline structure, the electronic orbitals of the isolated atoms, either full or partially filled of electrons, and their respective orbitals, fall in continuous bands, which can be divided into the two following groups. The first group is known as *the valence band,* where the outermost electron orbital is completely filled with electrons. The second group is known as *the conduction band* which corresponds to the next highest band to valence band either empty or partially filled with electrons. In general, these bands are separated by a *forbidden region* or *band gap* of energy $E_g$, usually given in units of electron volts, eV.

The conductivity of a solid depends on the distribution of electrons in the conduction band, which is also related to the magnitude of the band gap. On one hand, if the electrons contained in the valence band completely fill one or more bands, thus leaving others empty, there is no contribution to the electrical conductivity and thus the crystal behaves as an insulator. On the other hand, if the electrons partially fill one or more bands, the crystals behave as a conductor. Thus, the difference between a conductor, a semiconductor or an insulator resides on the number of excited electrons into the conduction band, which is determined by the temperature and the magnitude of the band gap. If the energy level that separates the two bands is close to zero, that meaning that the electrons can move from one band to the other with very low activation energy, the material is a conductor. On the contrary, if the band gap is large, 4 – 12 eV, the solid is considered to be an insulator. If

however, the magnitude of the band gap is small, 0 - 4 eV, the material is considered to be a *semiconductor*.[57] In real crystalline materials, however, the conductivity is not only influenced by the band gap but also by: (i) the lattice defects; (ii) the impurities; and (iii) the surface defects.

The following discussion is supported by Electrochemistry at Metal and Semiconductor Electrodes textbook by Sato.[58] Lattice defects in ionic crystals are produced by interstitial ions and ion vacancies. If the imperfection or defect is only present to one lattice side and its immediate neighbour side, it is termed *point defect.* In the case of metal oxides, interstitial metal ions or oxygen vacancies add electron donor levels onto the band gap, whereas the presence of metal vacancies introduces acceptor levels. Such points include (i) vacant lattice sites, and (ii) extra atoms, which are situated in the interstices between regular sides of the lattice. Both (i) and (ii) are also called *vacancies* and *interstitials,* respectively. Impurities and dopant atoms might also introduce either acceptor or donor levels to the band gap, depending on their nature. Generally, a metal oxide material can accommodate all types of point defects but one is usually found to be predominant among the others, depending on both the deviation from stoichiometry and its composition. Many examples of point defects are found in the literature.[59] However, only nickel and cobalt oxides will be described in this introduction as they are materials of crucial importance on this thesis. Nickel and cobalt oxide, typically written as NiO and CoO, both include point defects on their cation lattice and thus they should be written as $Ni_{1-y}$ and $Co_{1-y}O$, respectively, being *y* a small fraction of metal deficiencies. Due to a deviation from their natural stoichiometry in the form of metal deficiency, the predominant nature of defects in these oxides is metal vacancies. Regarding the NiO, these considerations are based on the differences of the self-diffusion coefficient between the nickel and the oxygen.[60] The self-diffusion coefficient of nickel or cobalt is much larger than that of the oxygen and thus it may be assumed that the defects on both oxides are located in the cation lattice.[61] Kroger and Price suggested that the nickel oxide type should only exhibit an excess of oxygen. In addition, it was noted that the *p*-type conductivity of NiO is attributed to the presence of Ni ions vacancies and holes in the lattice which add electron acceptor levels above the valence band.[56, 62] Regarding the cobalt oxide,[62] it has been observed to have a similar defect structure than $Ni_{1-y}O$ but the concentration of these are larger in the cobalt oxide. These defects are mainly due to the presence of electron holes. It has also been noted that point defects on cobalt oxide, are strongly dependent on temperature and oxygen pressure. If its

decomposition pressure is somewhere between $10^{-12}$ atm $O_2$ at 950°C to $10^{-6}$ atm at 1450°C, the CoO is formed in a stoichiometric manner. However, if $O_2$ concentration increases, the oxide becomes metal deficient and, therefore, the presence of cobalt vacancies increase.[63]

References to many other defect structures involving other types of materials can be found in the literature, such as the zirconium dioxide $ZrO_2$,[64] or the Zinc oxide ZnO,[65] respectively. The former is an example of oxygen vacancy and thus it should be written as $ZrO_{2-y}$, whereas the latter is an example of interstitial metal ion and hence should be written as $Zn_{1+y}$. In addition to the defects previously outlined, dopant atoms and dissolved impurities may be also considered. Note that these two are also treated as point defects. In general terms, a dopant is an impurity, that can be found, for instance, in carbon, nickel and cobalt,[66] which is introduced into the lattice of the crystal making a variation on the conduction band and thus, the final electrical properties of the crystal. The above considerations are assumed to be valid only at very low concentrations. It is considered that the point defects do not interact with other point defects. Therefore, they are treated as un-associated points when the concentration of defects is, in terms of mol fraction, between 0.01 - 0.001. At higher defect concentration, however, the point defects tend to associate and interact together into larger units called *clusters*. The formation of these clusters is mainly due to coulombic interactions between point defects with opposite charge sign.[67] These clusters may coexist with single point defects in a dynamic equilibrium.

The following are some other examples of how impurities affect the metal oxide characteristics. In crystalline sodium chloride NaCl, a cation vacancy $V_{Na^+}$ occurs by producing a surface cation $Na^+$. This effect is called *Schottky defect*. Separately, in crystalline silver chloride, AgCl, a pair of cation vacancy and interstitial cation is formed, this effect is known as *Frenkel defect.*

The presence of macroscopic defects in the crystal structures, *e.g.* edges, kinks and steps, also has a significant impact in the electrical properties of the material. Since at such sides the free energies of adsorption reactants/intermediates are higher, the $OH^-$ and $H^+$ ions tend to be more attracted by these areas rather than the standard planar sites. The main difference between these sites and planar sites is the coordination number of the

surrounding atoms, which in the case of the edges, kinks, etc., is higher than the planar ones.

The general properties of the semiconductor-solution interphase have been reviewed by Ahmed[68] and Healy *et al*.[69] It might be suggested that the nature of the interaction between a metal oxide-solution is equal to the metal solution interphase but, however, the oxide-solution interface tends to exhibit various features not possessed by the metal-solution interphase. These include, among others, the presence of an extended *space-charged layer* much closer to the surface than the OHP or the IHP. This layer is basically comprised by either chemisorbed $H^+$ or $OH^-$ ions, with radius of 0.34 Å and 1.1 Å, respectively, and situated within the IHP. However, in real metals, the presence of the space-charged layer also exists, but with a depth thousand times smaller than those found in semiconductors metals. A direct consequence of the presence of this charged layer is that the surface potential and the potential drop across the Helmholtz region both depend on the pH.

It is generally agreed that the surfaces of oxides, whether conductors, semiconductors, or insulators, tends to be covered by hydroxyl groups when the oxide is in contact with an aqueous phase.[68, 70] When this occurs, the water molecules react with the charge centres releasing $H^+$ and $OH^-$. The surface hydration reaction typically takes place by the dissociative addition of water, where the proton attaches to an exposed oxide ion whereas the hydroxyl ion adsorbs onto an adjacent metal ion. It is generally accepted that many oxide surfaces undergo hydroxylation in aqueous solution, forming two types of hydroxyl groups (i) the *acid* $–OH_{(a)}$ and the *base* $–OH_{(b)}$ types.[71] The most widely accepted model for the formation of these Brønsted acid/base groups is the so-called one site / two-pK model which is depicted in fig. 1.1.18. It is known as a "one-side" model because, theoretically, the adsorbed $OH^-$ species is the same in either the acid or the base cases, before ionization occurs. It is relevant to mention that the concentration of these ions is determined by the pH, the solubility product of the oxide and the dissociation constants of their hydroxyl complexes.

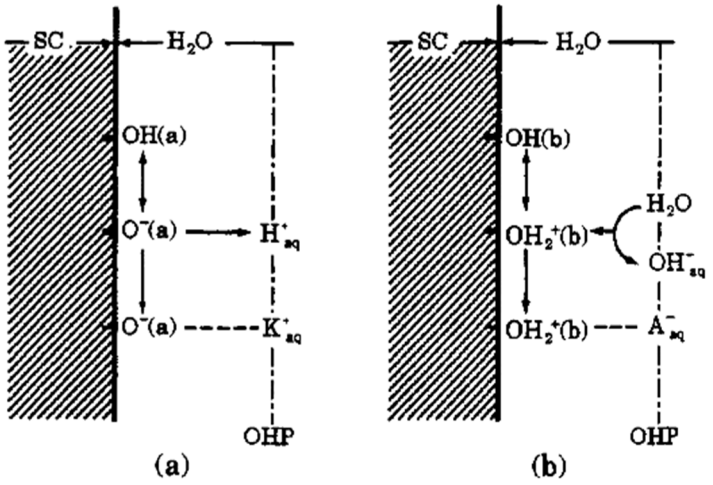



Figure 1.1.18 The one-site / two-pK model for the dissociation of hydroxyl groups at oxide-solution interfaces: (a) dissociation of hydroxyl group of the acid-type, (b) dissociation of hydroxyl group of the base type. $K_{aq}^{+}$ represents the hydrated cation while $A_{aq}^{-}$ represents a hydrated anion. Reproduced from Ref.[72]

For most oxide-solution interphases, the surface hydration reaction process causes the formation of a *reversible double layer* within the compact Helmholtz plane. The reversible double layer varies with pH and is stablished naturally by the dissociation process, involving specifically adsorbed $H^+$ or $OH^-$ ions, taking place in the interface. Hence, an oxide-solution interface under an external *bias* exhibits a combination of both a polarizable and reversible double layer.

The semiconductor–solution interface have been reviewed by Gerisher[73], Myamlin and Pleskov,[74] Ahmed[68] and Pleskov[75]. Theoretical models of this interphase region have been proposed by Dignam *et. al.*[76], Chazalver[77] and Rajeshwar[78].

At the semiconductor - solution interphase, in addition to the presence in the aqueous solutions of an ionic diffuse layer, only present in the dilute solution along with a compact Helmholtz layer, a diffuse three-dimensional space-charge layer takes place in the solid phase as seen in fig. 1.1.19. Moreover, the Helmholtz layers extends in the semiconductor phase mainly due to the presence of surface states.[79] [80] Surface states play an important role in the behaviour of semiconductor electrodes.[81] Tamm[82] defined these surface states as discrete electronic states arising due to termination of the crystal lattice at the boundary. Surface states can also play a significant role in the catalysis of electron transfer reactions

at the semiconductor electrode surface. In the presence of surface states and adsorbed ions, the total semiconductor-solution interface charge can be represented by:

$$\sigma_{total} = \sigma_{sc} + \sigma_{ss} + \sigma_{ad} \tag{1.1.32}$$

where the first term on the right-hand side accounts for the contribution from the excess charge in the space charge layer; the second term arises from the bound charge of the semiconductor surface, which typically is due to surface states on the surface, and the last term accounts for the water molecules adsorbed with an orientated configuration on the surface.

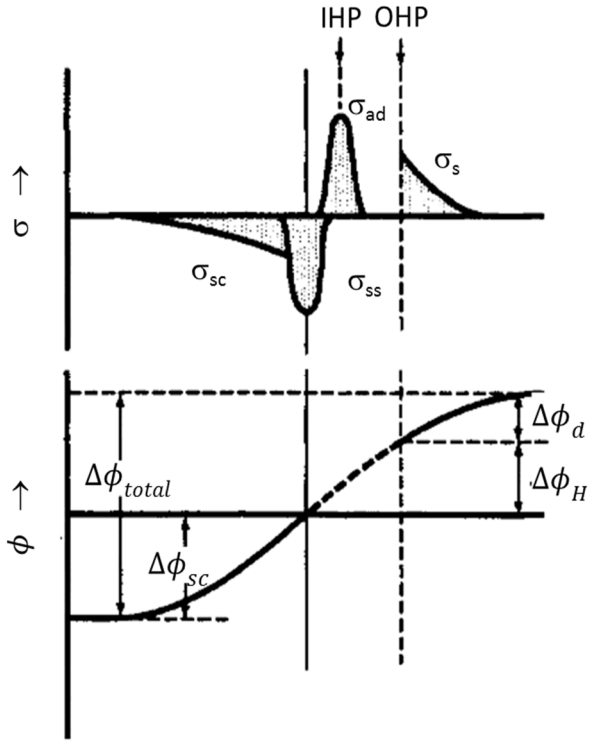



Figure 1.1.19 A schematic representation of the interfacial charge and potential profile in a semiconductor-solution interface, in the presence of surface states and adsorbed ion. Reproduced from Ref.[59]

The Galvani potential difference at a semiconductor-solution interface can be expressed as the sum of the different elements present on the surface, so that:

$$\Delta\phi_{total} = \Delta\phi_d + \Delta\phi_H + \Delta\phi_{sc} \tag{1.1.33}$$

where the first term on the right-hand side accounts for the potential difference between the OHP and the bulk solution, the second one for the potential difference between the

compact layer and the OHP, and the last term refers to the potential difference between the bulk of the semiconductor and its surface. The thickness of these charge layers is in the range of $d_H$ = 0.4 to 0.6 nm in the case of the compact layer, $d_{sc}$ = 10 to 1000 nm for the space charge layer, and $d_d$ = 1 to 10 nm in the case of the diffuse layer. It is important to mention that the thickness of the two last mentioned layers depends on the concentration of charge carriers, $n_1$, in the semiconductor and the ionic solution, respectively. The thickness of these two layers can be estimated using Debye length, $L_D$, for each respective layer, where $L_D$ is given by:

$$L_D = \sqrt{\frac{\varepsilon kT}{e^2 \sum n_i z_i^2}} \tag{1.1.34}$$

where $\varepsilon$ is the dielectric constant, k is the Boltzmann's constant, e is the charge of the carrier and T is the temperature. It is clear from eqn. 1.1.34 that the thickness of both the space charge layer and the diffuse layer are inversely proportional to the sum of the segmental charge densities in the given metal. The Debye length is considered to be about 100 nm in the case of a standard semiconductor material with impurity concentrations in the order of $10^{15}$ cm $^{-3}$ and about 10 nm in dilute 0.01 M ionic solutions. Regarding the differential electric capacity C of this type of semiconductor, interface, it can be represented by various capacities connected in parallel as:

$$\frac{1}{C} = \frac{1}{C_{SC}} + \frac{1}{C_H} + \frac{1}{C_d} \tag{1.1.35}$$

where $C_{sc}$, $C_H$, and $C_d$ are the capacities of the space charge layer, the compact layer, and the diffuse layer, respectively. As seen in eqn. 1.1.35, the total capacity will be determined by the smallest capacity and, therefore, the interfacial capacity of a typical semiconductor electrode may be similar to the capacity of the space charge layer, $C_{sc}$, as this capacitance tends to be between one and two orders of magnitude larger than the other two capacitances.

As a first approximation, the distribution of the electrode potential across the compact Helmholtz layer and the space charge layer can be written as:[74, 83]

$$\frac{\delta \Delta \phi_H}{\delta \Delta \phi_{sc}} = \frac{e\, d_H \sigma_{ss}}{k_B T \varepsilon_H} \tag{1.1.36}$$

where $d_H$ is the compact layer thickness, and $\varepsilon_H$ is the dielectric constant in the compact layer. It has been shown that $\frac{\delta\Delta\phi_H}{\delta\Delta\phi_{sc}} = 1$ at a density, of surface states, $\sigma_{ss}$, of about $10^{13}$ $cm^{-1}$, which represents ca. 1 % of the surface atoms of a semiconductors. At surface state densities above 1 % of surface atom density, $\frac{\delta\Delta\phi_H}{\delta\Delta\phi_{sc}} > 1$, and therefore, almost all the changes in electrode potential difference occurs across the compact layer. It is under these conditions that the interfacial structure of the semiconductor is similar to that of the metal-solution interface. The material is said to be quasi-metallic.

Most of the early investigations on the reversible double layer on oxides have been mostly carried out with suspensions and precipitates of known surface using acid-base titrations methods.[68] In such titration experiments, the amount of acid or base consumed is related to the sum of the amounts of the respective acid or base bounded to the surface. Such bounding may form dissolved aquo complexes. It has been admitted however, that studies involving direct capacitance measurements of oxide electrodes, with the exemption of some conducting oxides of metals such as Pb, Cu, Mn and Ag, tend to be limited by the low conductivity of the material.[84]

Studies in which the titration method is employed tend to be influenced by a variety of secondary processes taking place at the interface. It is widely established that metal oxides are known to adsorb $H^+$ or $OH^-$ ions onto the surface, which largely occurs in two steps, one which is complete after few minutes and another one continuing for a few days or even weeks.[68, 85] The first step is known as the primary equilibrium process and has been attributed to the ionization reaction of surface hydroxyl groups. This type of reaction, in agreement with most proton transfer reactions, is expected to occur instantaneously. In addition, this process leads to the formation of surface metal aquo complexes and the dissociation of surface groups. The second step is known to involve dissolution complexes formation, dissociation of dissolved complex, adsorption of dissolved complexes and precipitation in colloidal form. The methods to minimize complications such as oxide dissolution in solution in secondary processes include either the use of fresh samples of oxides and solutions for each data point, or fast titrations techniques. However, recently[86] there has been a significant progress in quantifying the properties of the oxide-solution interface using techniques such as the Atomic force microscopy (AFM), X-ray standing wave measurements (XSW) and electrochemical impedance spectroscopy (EIS).

## 1.2 Electrode Kinetics

A brief review is now presented on the concepts of the electrode kinetics theory that seem most relevant for the purposes of the present thesis. There exist many exhaustive reviews of electrochemical kinetics[2, 87] and there is no intention of reproducing those in here. On the contrary, the aim of the present section is to identify and discuss the most relevant aspects of the theory in order to facilitate their further utilisation in later chapters of this work, especially when treating experimental data.

### 1.2.1 Fundamentals of the Electrode Kinetics

Electrochemical kinetics might be considered to be a branch of heterogeneous reaction kinetics. However, electrochemical reactions exhibit an additional requirement which differs from those of ordinary heterogeneous chemical reactions, that being that at least one step of the overall electrode reaction comprises a charge transfer reaction in which a charge carrier, whether an ion or electron, is transported from one phase into another across the electrical double layer. Therefore, electrochemical kinetics encompasses the study of the kinetics of electrode reactions.

The beginning point of a quantitative and qualitative insight into electrochemical electron transfer processes can be placed back to 1905, when Tafel[88] firstly observed the relationship between the electrode potential and the rate of reaction manifested by the electrode current density. Nowadays, the structure of modern electrochemistry still remains surprisingly empirical and the fundamental principles of it are based on the semi-empirical equations developed by Tafel, Butler[89], Gruz and Volmer[90], Gurney[91], Frumkin[92], and Parsons[93]. Notwithstanding, in addition to the previous authors this subject has been extensively reviewed by many others scientific researchers.[87a, 94]

The two quantities that determine the magnitude of the potential difference across the interface and the rate of the charge transfer reaction are the *symmetry factor* and the *overpotentials* $\beta$ and $\eta$, respectively. In other words, they determine how electrode potential affects or is affected by the rate. The concepts involving charge transfer and overpotential will be presented first, whereas the symmetry factor will be described later in this section. The charge-transfer reaction is of fundamental importance in electrochemical

kinetics since it is the only reaction directly affected by the electrode potential and the electrolyte concentration following the general reaction:

$$O + ne^- \leftrightarrow R \tag{1.2.1}$$

The hindrance of the charge-transfer reaction provokes the formation of a charge-transfer overpotential $\eta_i$. The overpotential parameter, $\eta$, represents the deviation of the experimental potential from its thermodynamic value and its representation is:

$$\eta = \phi - \phi^0 \tag{1.2.2}$$

where $\phi - \phi^0$ are the electrode potential and the standard electrode potential, respectively. Further discussion about the overpotential parameter will be presented in detail later in this section. Electrochemical reactions share similar features with the heterogeneous process such as the presence of reaction steps. The heterogeneous reactions are composed of three steps. The first one is (i) the transport of the reactants from the electrolyte bulk to the reaction side. This step involves a secondary process which is the adsorption of the reactant onto the solid surface. The reaction side may be either the electrode surface or the metal-electrolyte interphase region. This process is followed by (ii) a surface reaction of the adsorbed species to form the products, and (iii) the transport of the products from the surface to the electrolyte phase. This step is known as the desorption process.

As seen in the previous section, the electric field present on the electrode surface is a factor of fundamental importance since it influences the activity of ions and molecules in the reaction zone and the activation energy for the charge transfer step. The slowest partial reaction step in electrode kinetics is rate determining for the overall process and it is commonly known as the *rate determining step* (RDS). The magnitude of the overpotential is given by the RDS. Generally speaking, the higher the activation energy and the complexity of the reaction of the reaction step, the larger the value of the overpotential.

The electrode reaction rate, or net current, for the total electrode reaction at equation $O + ne^- \leftrightarrow R$ is determined by the rate in steps such as: (i) the mass transfer or diffusion of the reactant from the bulk to the electrode surface, (ii) the electron transfer at the electrode surface, (iii) the chemical reaction following the electron transfer *e.g.* protonation, dimerization decomposition, *etc.*, and (iv) the surface reactions such as adsorption, desorption or crystallisation. There is an overpotential associated with each of these

reaction steps. In this sense, the diffusion or mass transfer overpotential $\eta_d$, arises when the mass transfer of reactants and products to or from the electrode surface is rate determining under current flow conditions. The largest rate of mass transfer of compound O occurs when the concentration on the surface is near zero so that:

$$C^{\infty} - C_{o,x=0} \approx C^{\infty} \tag{1.2.3}$$

where $C^{\infty}$ is the bulk concentration of compound O and $C_{o,x=0}$ is the concentration of compound O at the electrode surface. It is also important to determine the net rate of the electrode reaction $v_{mt}$, which is the rate at which the electroactive species are brought to the electrode surface. It can be represented by the following expression:

$$v_{mt} = \frac{i}{nFA} \tag{1.2.4}$$

The value of the current under these conditions is known as the limiting current $i_L$ and is determined by the maximum rate of mass transport to the electrode surface. It may be represented as:

$$i_L = nFAm_o C^{\infty} \tag{1.2.5}$$

where A is the active surface area and $m_o$ is a proportionality constant known as the mass-transfer coefficient. From eqns. 1.2.4 and 1.2.5 and considering a reduction current as a positive current (*i* might be positive when $C^{\infty} > C_{x=0}$) one obtains:

$$\frac{i}{nFA} = m_o[C^{\infty} - C_{x=0}] \tag{1.2.6}$$

Hence, when the limiting current is flowing, the surface reaction process occurs under steady-state conditions and the surface reaction takes place at the maximum rate possible for the given conditions.

Eqns. 1.2.5 and 1.2.6, can be used to obtain expressions for $C_{x=0}$:

$$\frac{C_{x=0}}{C^{\infty}} = 1 - \frac{i}{i_L} \tag{1.2.7}$$

$$C_{x=0} = \frac{i_L - i}{nFm_o A} \tag{1.2.8}$$

where $C_s$ is the surface concentration of the specie in question and $C^{\infty}$ is the bulk concentration. From the above equations, it results clear that the concentration of compound O at the electrode surface shows linearity with the current and varies from $C^{\infty}$ in the case that $i = 0$ to a negligible value when $i = i_L$. Assuming only diffusion overpotential, the electrode reacts reversibly to the concentration at its surface to produce a potential given by:

$$\phi = \phi^0 + \frac{RT}{nF} \ln C_s \tag{1.2.9}$$

This formula is known as the Nernst equation. A specific section with a dedicated review to it will be presented later in this chapter. Therefore, the diffusion overpotential can be obtained by substituting eqn. 1.2.2 into eqn. 1.2.9, yielding to:

$$\eta_d = \frac{RT}{nF} \ln \frac{C_s}{C^{\infty}} = \frac{RT}{nF} \ln\left(1 - \frac{i}{i_L}\right) \tag{1.2.10}$$

The overpotential of a reaction, in which the rate of the electron transfer between a molecule, ion or atom and the electrode is limited by the relative height of the activation energies for the anodic and cathodic reactions, is denominated activation overpotential, $\eta_a$. Unlike typical heterogeneous reactions, in electrochemical reactions the activation energies are strongly dependent on the electrode potential.

According to eqn. 1.2.2 in the case of an applied potential greater than the equilibrium potential, the activation overpotential becomes positive and oxidation reaction takes place on the electrode surface. Contrary, if the electrode is polarised to a smaller potential than at equilibrium potential, the overpotential is negative, which causes a reduction reaction to occur. The crystallisation overpotential refers to the step in which the energy required to incorporate or to remove a molecule, an ion or an atom to or from the crystal lattice of the electrode surface is rate controlling. This term was first introduced by Fisher[95] and Lorenz[96] and based on concepts from Brandes[97]. Finally, the reaction overpotential, $\eta_r$, is a phenomenon resulting from the presence of a slow rate-determining step in the overall electrode reaction. The chemical step is a reaction in which its rate constant does not depend on the electrode potential. This reaction may proceed homogeneously in a solution or in an adsorbed phase. Effects such as adsorption or desorption of reactants or of products on the electrode surface, hydration or dehydration may control the chemical

reaction rate. As a result of $\eta_r$, the charge transfer equilibrium remains undisturbed during the flow of current on the electrode.

A further contribution to the total overpotential is the resistance or ohmic overpotential, $\eta_{Ohm}$. This contribution affects all electrochemical reactions in which an electrode and an electrolyte are involved and refers to the potential drop across the solution. The current drop can be significant at high current density values, especially with poorly conducting electrolytic solutions. Since the ohmic drop exerts no influence on the kinetics of the electrochemical process, its contribution to the total potential can be minimized by the improvement of the cell design and by the application of automatic post-experimental correction techniques. Regarding the cell design, it has been demonstrated that a considerable improvement on the reduction of the current drop is achieved by correctly positioning a Luggin capillary probe at the reference electrode.[98] A deeper discussion on cell design will be presented later in this chapter.

In view of the electrical nature of an electrochemical system, the main variable in rate studies tends to be related, in a general extent, to the electrode potential behaviour and, in particular, to the different ways of minimizing the overpotential. However, the study of the electrical nature of electrochemical systems is not only limited by the potential behaviour but also by the concentration, pH, electrolyte temperature, stirring rate, surface nature and electrolyte type. Those features may also be studied to obtain quantitative information concerning the nature of an electrode reaction.

Electrochemical reactions might be classified into three types: (i) single-step, (ii) consecutive-step, and (iii) parallel steps. It should be noted that the last two types are also defined as a multistep reaction. A brief introduction to these types of reactions will be presented below.

### 1.2.2 Single-Step Electrode Processes

This type of reactions have been widely reviewed, being Bockris[99], Conway *et al*.[100], Delahay[101] and Vetter[87a] some of those how have more remarkably contributed to its study. Consider a single-step charge transfer reaction such as that presented in eqn.1.2.1 occurring at the solid – solution interface. The exponential relationship between the shift of the electrode potential from its equilibrium value or overpotential $\eta$ and the rate of reaction

as manifested by the electrode current density $i$ may be described by the following formula:

$$\eta = a + b \log i \tag{1.2.11}$$

where $a$ is a temperature depended constant and can be obtained from the intercept of a Tafel slope, b, with the log $i$ axis at $\eta = 0$, yelling to a value of the exchange current density $i_o$ for the process characterised by that Tafel slope. The parameter $b$ is known as the Tafel slope and for the case of a simple step one-electrode transfer it can be defined as follows:

$$b = \frac{RT}{\beta F} \tag{1.2.12}$$

where β refers to the symmetry factor, which is a number smaller than the unity and most typically equal to 0.50. The symmetry factor accounts for the fashion in which the effect of the potential is divided between the free energies of activation of forwarding and reverse reactions. A detailed discussion on the nature of the symmetry factor β will be subject to further discussion later in this section.

Reaction 1.2.11 can be rewritten as:

$$i = A\, exp\left[\frac{-\beta\eta F}{RT}\right] \tag{1.2.13}$$

If the above equation is compared to the Arrhenius eqn. of chemical kinetics:

$$k = A'\, exp\left[\frac{-E_{act}}{RT}\right] \tag{1.2.14}$$

where k is the reaction rate constant and $E_{act}$ is the activation energy. Since the similitude between eqns. 1.2.13 and 1.2.14 results evident, the product $\beta\eta F$ must be related to the energy of activation of an electrode reaction. The theoretical Eyring eqn.

$$k = \kappa\left\{\frac{K_B T}{h}\right\}\sigma \exp\left[\frac{\Delta S^{0*}}{R}\right]\exp\left[\frac{-\Delta H^{0*}}{RT}\right] \tag{1.2.15}$$

is related to the *transition state theory*, TST to experimental in regular chemical kinetics. The parameter $\kappa$ is known as the transmission coefficient, $\sigma$ as the reaction length of the order of a molecular diameter and $\Delta S^{0*}$ and $\Delta H^{0*}$ represent the standard entropy and

enthalpy changes of the activation process, respectively. The term $\frac{K_B T}{h}$ is related to the upper limit set on a heterogeneous rete constant by the vibrations of the transition state. The first two terms in eqn. 1.2.15, the pre-exponential and the first exponential, may be associated with the experimentally measurable Arrhenius coefficient A' in eqn. 1.2.14 whereas the second exponential term can be linked to the activation energy, β, in eqn. 1.2.13, which can also be measurable experimentally. It is important to mention that the rate constant for a typical process is fixed for a specific temperature and pressure and does not depend on the concentration of reactants nor products. Since the parallelism between both eqns. 1.2.13 and 1.2.14 have been outlined and assuming that the only rate control present is such systems is the charge transfer, it becomes apparent that the modified version of the conventional transition state theory (TST)[102] can account for the study of single-step transfer reaction processes whose rate limiting factor is controlled by the height of the activation energy barrier. Hence, these modifications must account for the effect of the electric field on the height of the activation energy barrier. Such modifications derive to the well-established current-potential characteristic known as the Butler-Volmer eqn.[87b], which was first developed by Butler[89] and Volmer[90] and it is presented below as:

$$i = i_0 \left\{ exp\left(\frac{-\beta F\eta}{RT}\right) - \left(\frac{(1-\beta)F\eta}{RT}\right)\right\} \tag{1.2.16}$$

where $i$ refers to the current density, associated with an overpotential $\eta$ and $\beta$ is the symmetry factor. The quantity $i_o$ is the exchange current density and is given by:

$$i_0 = Fk'^0 a_R^{\infty(1-\beta)} a_O^{\infty\beta} \tag{1.2.17}$$

which shows that the exchange current density is direct proportional to the standard electrochemical rate constant $k'^0$. The parameters $a_R^\infty$ and $a_O^\infty$ represent the bulk activities of oxidant and reductant species, respectively.

The thermodynamic equilibrium potential for the reaction type eqn. 1.2.1 is characterised by the Nernst eqn. which links together the bulk concentration of both the oxidant and the reductant species and the electrode potential. In this case, it may be written as:

$$E = E^0 - \frac{RT}{nF}\ln\left(\frac{C_0^*}{C_R^*}\right) \tag{1.2.18}$$

where $C_0^*$ and $C_R^*$ are the bulk activities of the species O and R, respectively. The parameter $E^{0'}$ is the standard potential, n is the number of electrons transferred in the balanced eqn. and E is the thermodynamic Nernst potential. It is clear for eqn. 1.2.18 that the Nernst potential is dependent on the ratio of activities $\frac{C_0^*}{C_R^*}$. Under equilibrium conditions, thus the electrode potential is $E^{0'}$, the forward and reverse free energies of activation are $\Delta G_{Of}^*$ and $\Delta G_{Or}^*$ respctively as seen in fig. 1.2.1.

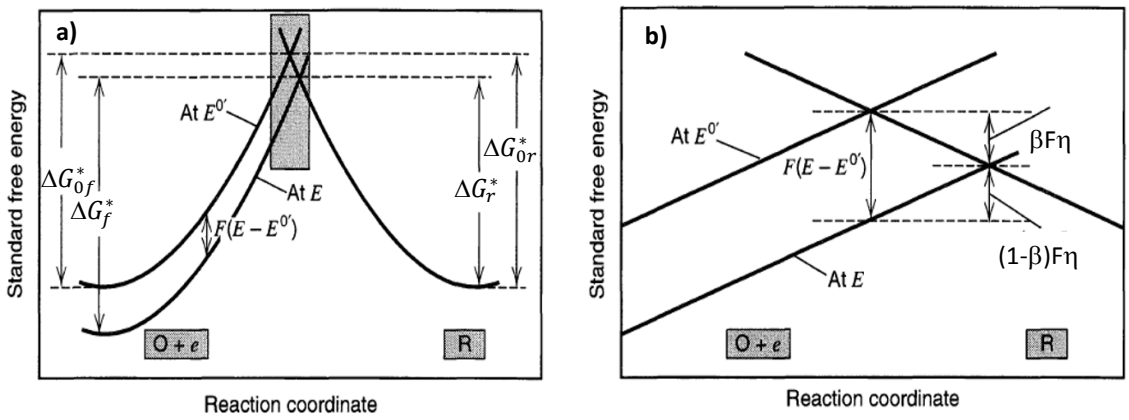



Figure 1.2.1 Schematic representation of the effects of a potential change on the free energies of activation for oxidation and reduction reactions. Adapted from Ref. [2]

A typical O + e curve shape can be observed in fig. 1.2.1a. If the potential is changed from its equilibrium value to a new value, the relative energy of an electron of the electrode surface changes by an amount of $-F\,\Delta E = -\mathrm{F}\left(E - E^{0'}\right)$ and thus the O + e curve moves up or down according to that amount. In the specific case that the potential is displaced from the equilibrium to more positive values, the free energy curve is lowered by the amount of $-\mathrm{F}\left(E - E^{0'}\right)$ which causes the potential barrier for the reverse reaction, $\Delta G_r^*$, to become smaller than its equilibrium value $\Delta G_{Or}^*$, by a magnitude of $\beta\mathrm{F}\left(E - E^{0'}\right)$, as seen in fig. 1.2.1b. Despite the symmetry factor parameter β was already introduced briefly earlier in this section, in order to facilitate a better understanding of future concepts it becomes necessary to further describe it in more detail.

The symmetry factor is also assumed to be the transfer coefficient only for single-step reaction and is a measure for the symmetry of the energy barrier between products and reactants. Its value depends on the relative shapes of the standard free energy functions, as noted in fig. 1.2.1a, at the point of intersection between the forward and reverse reactions. The following considerations assume that the intersection region between the reverse and the forward processes are linear, as it shown in fig. 1.2.2.

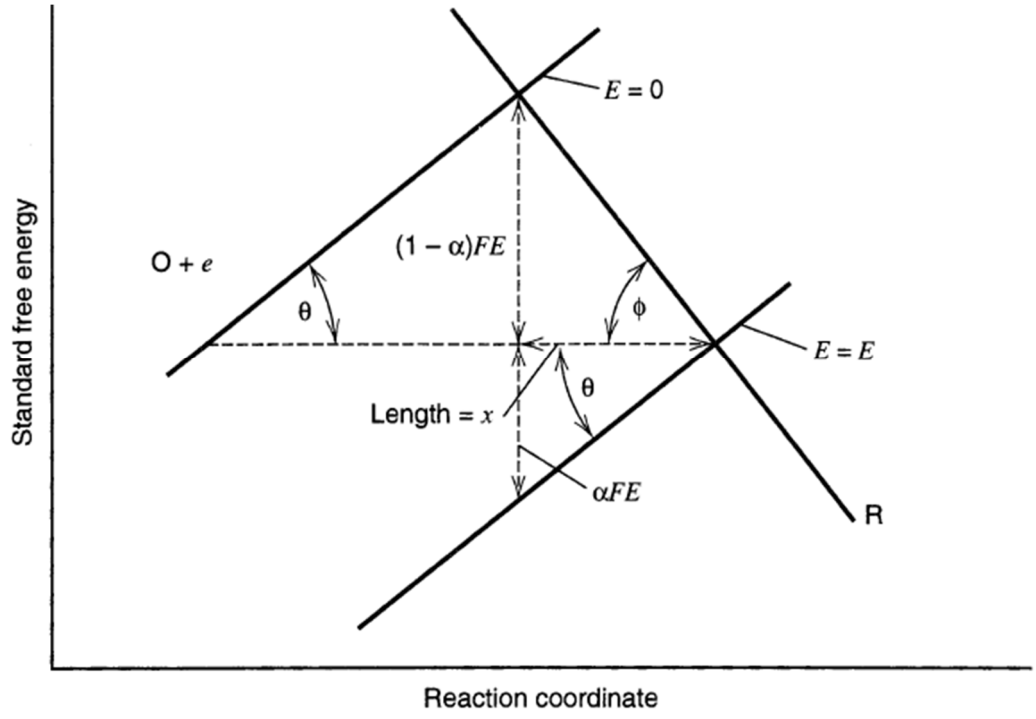



Figure 1.2.2 Schematic representation of the relationship between the symmetry factor and the angles of intersection of the free energy curves. Adapted from Ref.[2]

Under these circumstances, it is possible to represent the symmetry factor in geometrical terms where the angles θ and φ are defined as follows:

$$\tan\theta = \frac{\beta FE}{x} \tag{1.2.19}$$

$$\tan\phi = \frac{(1-\beta)FE}{x} \tag{1.2.20}$$

Rewriting eqn. 1.2.19 and 1.2.20, it may be found that:

$$\alpha = \frac{\tan\theta}{\tan\phi + \tan\theta} \tag{1.2.21}$$

On the one hand, when the interception of the activation energies of the forward and reverse processes is symmetrical, then $\phi = \theta$ and:

$$\alpha = \frac{\tan\theta}{\tan\phi + \tan\theta} = 0.5 \tag{1.2.22}$$

On the other hand, for a non-symmetrical situation, the symmetrical factor is comprised between either $0 \leq \beta < 0.5$ or $0.5 < \beta \leq 1$. Since the symmetry factor can also represent how symmetrical the transition state (TS) energy barrier is, it is agreed that for symmetrical TS values of $\beta = 0.5$ are expected, whereas for values $\beta < 0.5$ the TS is a product like and for values $\beta > 0.5$, the TS is reactant like.

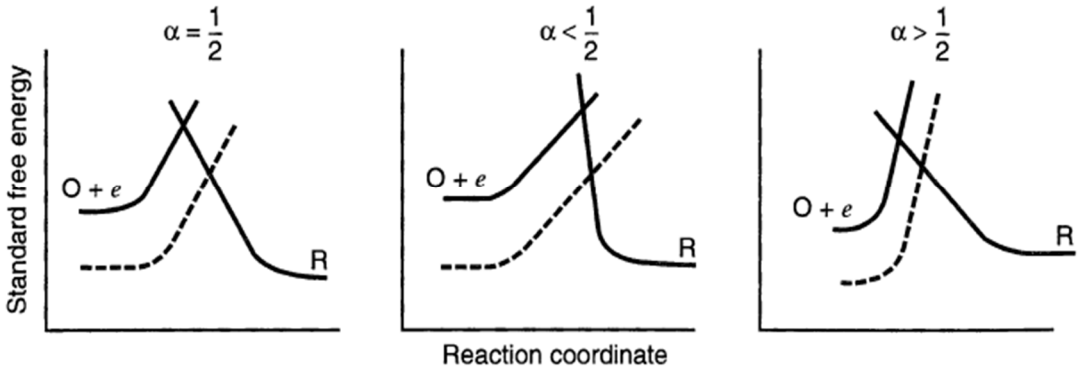



Figure 1.2.3 Schematic representation of the effect of various types symmetry factor coefficient. Note that the dash line represents the shift in the curve O + e as the potential is made more positive. Reproduced from Ref.[2]

Although this value can be found between $0 \leq \beta \leq 1$, it is generally assumed, in absence of actual measurements, to be 0.5.

Returning to the main plot of this section, the free energy of activation of the reverse reaction at a given potential E is therefore related to its value in equilibrium as follows:

$$\Delta G_r^* = \Delta G_{Or}^* - \beta F(E - E_N) \tag{1.2.23}$$

Contrarily, the application of a positive shift in the electrode potential causes the increase of the free energy of activation for the forward reaction, as it can be seen in fig.1.2.1, hence:

$$\Delta G_f^* = \Delta G_{Of}^* - (1-\beta)F(E - E_N) \tag{1.2.24}$$

Since $\Delta G^{0*} = \Delta H^{0*} - T\Delta S^{0*}$, the Eyring eqn. 1.2.15 can be written as:

$$k = \kappa \left\{\frac{K_B T}{h}\right\} \sigma \exp\left[\frac{-\Delta G^{0*}}{RT}\right] \tag{1.2.25}$$

and the rates *v* of the forward and reverse reactions are:

$$v_f = k_f' a_o^{\infty} = \frac{i_{cathodic}}{nFA} \tag{1.2.26}$$

$$v_r = k_r' a_r^{\infty} = \frac{i_{anodic}}{nFA} \tag{1.2.27}$$

where A is the active surface area of the electrode. Under thermodynamic Nernst potential for any $\frac{a_r^{\infty}}{a_o^{\infty}}$, the system stays in its equilibrium point, thus, $v_f = v_r$ holds. In the event that the ratio $\frac{a_r^{\infty}}{a_o^{\infty}} = 1$, then $E_N = E^0$ and so for this particular case $k_f' = k_r' = k'^0$ where $k'^0$ is the standard rate constant for the electrochemical system. It follows from eqn. 1.2.18 that in the case where $\frac{a_r^{\infty}}{a_o^{\infty}} = 1$ the equilibrium energy barrier must be symmetrical, since $\Delta G_f^* = \Delta G_{Or}^* = \Delta G^{o*}$. The rate constant for any potential different than the equilibrium one might be written in terms of $k'^0$:

$$k_f' = k'^0 \exp\left[-(1-\beta)\frac{F}{RT}(E - E_N)\right] \tag{1.2.28}$$

$$k_r' = k'^0 \exp\left[\beta\frac{F}{RT}(E - E_N)\right] \tag{1.2.29}$$

It is important to outline that these values apply regardless of the value of the ratio $\frac{a_r^{\infty}}{a_o^{\infty}}$ due to the fact that the symmetry factor considers the more general situation where $E_N \neq E^0$. The net current density *i* is the difference between the anodic and cathodic currents as represented by:

$$i = i_{anodic} - i_{cathodic} = nF[k_r' a_r(0,t) - k_f' a_o(0,t) \tag{1.2.30}$$

The insertion of the exertions for the rate constants $k_r'$ and $k_f'$ from eqns. 1.2.28 and 1.2.29 into eqn. 1.2.30 yields to the formation of eqn. 1.2.16, the Butler-Volmer eqn. presented earlier in this section. Three circumstances of the Butler-Volmer eqn. are of relevant

interest here: (i) $\eta = 0$; (ii) $\eta < 10$; and (iii) $\eta > 100$. In the first case, with $\eta = 0$ , the electrode potential is equal to equilibrium and thus $i_a = i_c$ and thus $i_T = 0$. Substitution of the condition $i_T = 0$ into the Butler – Volmer eqn. and its following simplification yields to the Nernst eqn. presented earlier in this chapter.

The second case, where $\eta < 10$ , corresponds to systems whose potential remains very close to the equilibrium potential. At low values of overpotential in the charge transfer controlled region, the exponential terms in eqn. 1.2.16 can be expanded in a Tailor series as follows:

$$e^x = \sum_{n=0}^{\infty} \frac{x^n}{n!} = 1 + x + \frac{x^2}{2!} + \frac{x^3}{3!} + \frac{x^4}{4!} + \frac{x^5}{5!} + \frac{x^6}{6!} \qquad (1.2.31)$$

Therefore, if the value of x is small, then eqn. 1.2.16 might be approximated to a single term and yield to:

$$i = \frac{i_0 F}{RT}\eta \qquad (1.2.32)$$

Under these conditions, eqn. 1.2.32 suggests that the relationship between the current and the overpotential is proportional. By analogy with the general form of Ohm's law, Vetter[87a] developed an eqn. where the slope of the η as a function of *i* was understood as the equivalent resistance per unit area of the charge transfer process at the electrode surface. This resistance is known as the Faradaic resistance, $R_F$, and might be represented as:

$$R_F = \left(\frac{\delta\eta}{\delta i}\right)_{i\to 0} = \frac{RT}{i_0 F} \qquad (1.2.33)$$

If the value of $R_F$ is large, the flow of small current results in a significant overpotential whereas if $R_F$ is small the potential does not alter from its equilibrium value. Therefore, the precise acquirement of the Faradaic resistance value is of a great interest for the analysis of electrochemical processes due to it provides a measure of the polarizability of the electrode. It is relevant to outline that the Faradaic resistance is inversely proportional to $i_o$ thus it follows that the larger the $i_o$ value, the less polarizable is the electrode. In addition, the relationship of both parameters, $R_F$ and $i_o$ is of a relevant importance in electrocatalysis analysis since the electrocatalytic activity is often related to the magnitude of $i_o$.

The third and last case, where $\eta > 100$, refers to systems where the electrode potential is very far from its equilibrium potential. Under these circumstances, either the first or the

second exponential term on eqn. 1.2.16 can be neglected, depending on whether the polarization is cathodic or anodic. Here, at high cathodic polarization, eqn. 1.2.34:

$$i = i_0 \exp\left(\frac{-\beta F \eta}{RT}\right) \tag{1.2.34}$$

might be rearranged to yield the so-called Tafel relationship:

$$\eta = \frac{2.303RT}{\beta F}\log i_0 - \frac{2.303RT}{\beta F}\log i \tag{1.2.35}$$

It is clear that eqn. 1.2.35 is a linear eqn. of the form $\eta = a - b\log i$ where:

$$a = \frac{2.303RT}{\beta F}\log i_0 \quad b = \frac{2.303RT}{\beta F} \tag{1.2.36}$$

It is relevant to mention now that the condition where the oxygen evolution reaction, which is of a high interest in this thesis, occurs is included in this last case, where the overpotential is large. Experimentally a linear relationship between the overpotential η and the current *i* is also often observed at high overpotentials. The graph $\eta$ *vs*. *i* is referred to as a Tafel plot. From the slope of the Tafel slope *e.g.* $\eta$ *vs*. ln $i_a$, a value for the symmetry factor $\beta$ is obtained since $b$ = RT/βF. Furthermore, from the extrapolation of the Tafel line to a point where $\eta = 0$, the exchange current density $i_o$ may be obtained. For the particular cases where the charge transfer step occurs very fast, the forward and reverse potential current densities are equal and thus the electrode potential can be described thermodynamically using the Nernst equation. This behaviour is observed, for example, in the hydrogen evolution reaction (HER) on platinum electrodes. In such systems, the rate determining is assumed to be at the step where the combination of hydrogen radicals takes place.

### 1.2.3 Surface Coverage Considerations and Adsorbed Isotherms

The previous discussions on electrode kinetics considered the effect of applied potential and electrolyte concentration on the rates of electrochemical reaction. Another factor, not hold into consideration yet, and that often has a significant impact on electrochemical kinetics, is the extent of the surface coverage during the electrochemical reaction by adsorbed reaction intermediates or products. In previous sections the effects on the electrode potential arising by surface adsorption species were outlined. It was also mentioned that the region where such species where found was the inner compact layer.

Thus, in the context of adsorption species onto the electrode surface, more detailed considerations about coverage and adsorbed isotherms are now to be presented.

The extent of the adsorption species onto the electrode surface is commonly expressed as a surface coverage θ. In other words, the surface coverage represents the fraction of the surface literarily covered by adsorbate. This might be interpreted from the point of view of a space competition of: (i) between all the atoms, molecules and ions in the system for sites on the electrode surface, and (ii) between the electrode surface and the solution medium for each of the species. The amount of a compound in a monolayer of adsorbate on the electrode surface is strongly related to both its molecular size and its orientation on the electrode surface. Atoms, molecules or ions may be adsorbed in various fashions, *e.g*. if the compound is adsorbed with equal regularity than the surface atoms, then this type of adsorption is known to be *commensurate.* Usually the size of the adsorbate compounds is much larger than the size for those in the surface, which causes the commensurate adsorption not to occur. At this point, the adsorbate molecules are widely spaced on the surface rather than packed together with the same regularity than the surface atoms. Generally, lower surface coverages are found when large molecules are present. Also, for low molecular weight elements, the surface coverage lies in the range between $10^{-9}$ to $10^{-10}$ mol $cm^{-2}$.[103] The surface coverage changes with the surface potential as it was introduced in previous sections, regarding the presence of adsorbed clusters of water molecules on the electrode surface. It was shown that shifts of electrode potential cause reorientation of the dipole of such adsorbed water molecules. It was also mentioned that for negative charged electrodes, the adsorption of cation occurs whereas for positive charged surfaces, it is the adsorption of anions that takes place. In the case of an uncharged surface, the adsorption of neutral molecules occurs.

As mentioned at the beginning of this section, all the standard equations regarding the current–potential characteristics consider the effect of the coverage to be neglected. This consideration assumes that the electrode surface is atomically a smooth surface and thus all the surface area is available for the adsorption of a given compound. However, the surfaces of essentially all solid electrodes, including single-crystal surfaces, do not present an ideal surface but a much rougher one.[3] Real electrode surfaces always exhibit a certain number of defects *e.g*. steps, plateaus and surface defects such as vacancies, kinks, etc. The different types of defects are presented in fig. 1.2.4.

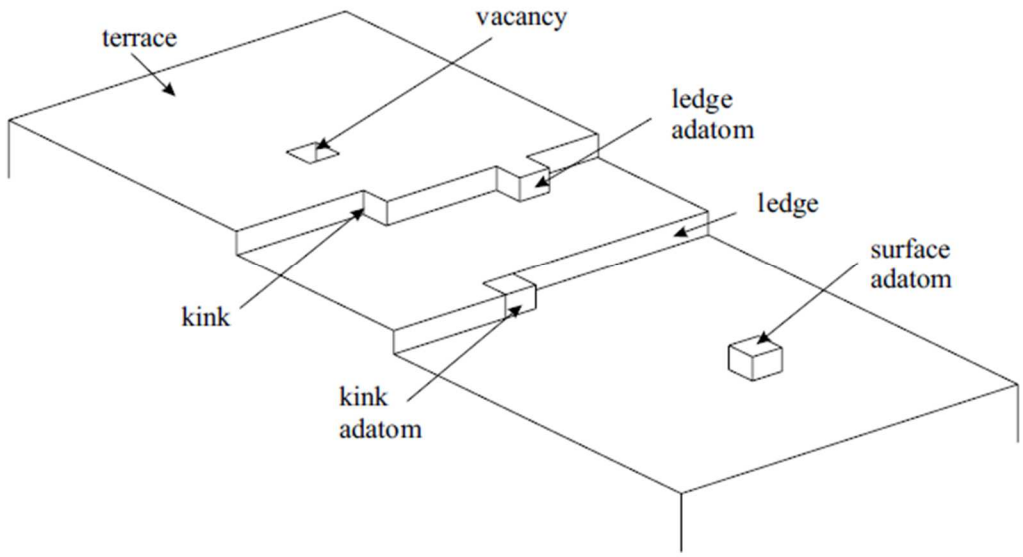



Figure 1.2.4 Schematic view of a real vicinal electrode surface with some surface defects. Reproduced from Ref.[3]

Such surface imperfections may increase the surface area and so they increase the coverage per unit area. The ratio between the real surface area of an electrode and the projected area, which is the area assumed to be perfectly smooth, is called the *roughness factor*. Even apparently smooth and polished solid electrodes have roughness factors of 1.5 to 2 or more.

Returning to the main topic of this section, the general form of the adsorption isotherm for species *i* might be obtained recalling that for systems in equilibrium. The electrochemical potential of species *i* is equal in the adsorbed and bulk solution states as:

$$\bar{\mu}_i^A = \bar{\mu}_i^B \tag{1.2.37}$$

The relation between both standard electrochemical potentials $\bar{\mu}_i^A$ and $\bar{\mu}_i^B$ is represented as follows:

$$\bar{\mu}_i^{O,A} + RT \ln a_i^A = \bar{\mu}_i^{O,B} + RT \ln a_i^B \tag{1.2.38}$$

where $a_i^A$ and $a_i^B$ denote the surface concentration of the adsorbate and the bulk, respectively. The electrochemical standard free energy of adsorption, $\Delta G_{ads}^0$ of species i must be the difference between the standard electrochemical potentials of such species in the adsorbed and bulk states as:

$$\Delta G_{ads}^{0} = \bar{\mu}_i^{O,A} - \bar{\mu}_i^{O,B} \tag{1.2.39}$$

Substituting eqn. 1.2.38 into 1.2.39 and rearranging, it yields to:

$$a_i^A = a_i^B \exp\left(\frac{-\Delta G_{ads}^{0}}{RT}\right) \tag{1.2.40}$$

Eqn. 1.2.40 is agreed to be the general form of the adsorption isotherm for species *i*. However, different models or assumptions might be formulated in order to fit those into a particular situation, *e.g*. Henry, Freundlich, Langmuir and Temkin.[3] The simplest model was proposed by Henry *et al*.[104] who assumed a linear relationship between the surface concentration and the bulk concentration. Another important model for the study of adsorption isotherms was presented by Freundlich[105], who assumed, for heterogeneous surfaces, the presence of favourable adsorption sites on the surface. These sites should exhibit high affinity to the adsorbate species whereas other sites show low affinity. This factor conditions the fashion of how the molecules are adsorbed onto the surface, as the sites with high affinity are occupied first. He also accounted for the existence of lateral repulsion between adsorbed molecules.

Finally, the most commonly used model for describing the adsorption processes is the one proposed by Langmuir[106]. The Langmuir isotherm assumes: (i) that there is no lateral interaction between the adsorbed molecules, (ii) that the surface is homogeneous, and (iii) that for large bulk concentrations, the surface is considered to be fully covered by adsorbate of amount $\Gamma_i$. Thus, the Langmuir isotherm may be represented as follows:

$$\frac{\Gamma_i}{\Gamma_s - \Gamma_i} = a_i^B \exp\left(\frac{-\Delta G_{ads}^{0}}{RT}\right) \tag{1.2.41}$$

This model can also be written in terms of the fractional coverage of the surface, θ, thus:

$$\frac{\theta}{1-\theta} = K \exp\left(\frac{F\Delta\phi}{RT}\right) \tag{1.2.42}$$

Where K refers to the adsorption equilibrium constant, $K = \exp\left(\frac{-\Delta G_{ads}^{0}}{RT}\right)$, related to the free energy of adsorption and $\Delta\phi$ denotes the metal-solution potential difference. Since the parameter *K* is assumed to be a constant, eqn. assumes that the $-\Delta G_{ads}^{0}$ is independent of the coverage, $\theta$. However, none of the Langmuir isotherm assumptions is likely to be realistic since, as it was demonstrated in previous sections and at the beginning of this one,

the lateral interactions between the adsorbed molecules and the presence of defects, which causes heterogeneity, do, in fact, exist on real electrode surfaces. Furthermore, the kinetic analysis based upon the Langmuir isotherm does accurately predict experimental operations in situations where intermediate coverage is either very small $\theta \approx 0$ or nearly complete $\theta \approx 1$. This occurs because an isotherm which assumes that $\Delta G_{ads}^{0}$ is dependent on the coverage reduces to Langmuir isotherm at extreme coverage conditions.

A more realistic adsorption isotherm would involve the apparent free energy of adsorption $\Delta G_{ads}^{0}$ at a given coverage, θ, being the former dependant on the value of θ. If the apparent free energy of adsorption is considered to decrease linearly with the surface coverage, it might be possible to write:

$$\Delta G_{ads}^{0} = \Delta G_{ads=0}^{0} - fRT\theta \tag{1.2.43}$$

where $\Delta G_{ads}^{0}$ and $\Delta G_{ads=0}^{0}$ represent the standard free energies of adsorption corresponding to a finite coverage and no surface coverage, respectively, and the parameter $f$ is a constant called the heterogeneity factor. A relation of the form of eqn. 1.2.41 was first used to conceive an electrochemical adsorption isotherm by Frumkin[107] in 1925. The Frumkin isotherm can be expressed as:

$$a_i^B K = \frac{\Gamma_i}{\Gamma_s - \Gamma_i} \exp\left(\frac{-2g\Gamma_i}{RT}\right) \tag{1.2.44}$$

where the parameter K represents $K = \exp\left(\frac{-\Delta G_{ads}^{0}}{RT}\right)$. The Frumkin isotherm assumes that the electrochemical free energy of adsorption defined as $\Delta G_{ads}^{0} = \bar{\mu}_i^{O,A} - \bar{\mu}_i^{O,B}$ is linearly related to $\Gamma_i$:

$$\Delta G_{ads}^{0}(Frumkin) = \Delta G_{ads}^{0}\ (Langmuir) - 2g\Gamma_i \tag{1.2.45}$$

The parameter *g,* with units of J mol$^{-1}$ or mol cm$^{-2}$, expresses the fashion in which changes in the coverage affect the adsorption energy of species *i*. For example, if $g > 0$ the interactions between the surrounding adsorbed molecules on the surface are attractive. However, if $g < 0$, the interactions are repulsive. For those cases where $g = 0$, the Frumkin isotherm approaches the Langmuir model.

Sixteen years after, in 1941, Temkin[108] proposed a modification to the Frumkin's model resulting in a more realistic physical model than the original one. This new model

assumed that the whole electrode surface might be decomposed into small patches of equal size where the adsorption of each one obeys the Langmuir isotherm. In addition, the value of the standard free energy of adsorption was assumed to decrease or increase by small equal decrements over successive patches, corresponding to the increase of the surface coverage. Substitution of eqn. 1.2.43 into the Langmuir isotherm yields to:

$$\frac{\theta}{1-\theta}\exp(f\theta) = a_i K \ \exp\left(\frac{F\Delta\phi}{RT}\right) \tag{1.2.46}$$

At intermediate values of the coverage, the term $\frac{\theta}{1-\theta}$ might be neglected. This assumption reduces eqn. 1.2.46 to:

$$\exp(f\theta) = a_i K \ \exp\left(\frac{F\Delta\phi}{RT}\right) \tag{1.2.47}$$

and the simplification of eqn. 1.2.47 yields one type of the Temkin isotherm eqn. as:

$$\theta = \frac{F}{fRT}\Delta\phi + \frac{1}{f}\ln K + \frac{1}{f}\ln a_i \tag{1.2.48}$$

Other form of the Temkin isotherm is also presented below:

$$\Gamma_i = \frac{RT}{2g}\ln(a_i^B K) \tag{1.2.49}$$

It is relevant to note that the previous approximation is only valid for an intermediate range of surface coverage values, *e.g.* $0.2 < \theta < 0.8$. It may be clear that eqn. 1.2.48 is characterized by a linear dependence of the surface coverage, θ, with the potential difference, $\Delta\phi$. The adsorption of an electroactive specie may affect the kinetics of a redox couple in solution, generally by reducing its rate. This inhibition effect arises for various reasons, for instance: (i) a reduction of the active surface area for the electron transfer in the electrode surface, or (ii) the electron transfer process, due to the formation of a monolayer of adsorbate species onto the electrode surface, which occurs over a greater distance. When the electroactive species are itself adsorbed, it provokes the electron transfer to take place with more difficulty, while adsorption of the products makes electron transfer easier. The adsorption of intermediates formed by electron transfer is of a relevant importance in electrocatalysis.

It is useful at this point to introduce the velocity of a general charge transfer reaction, taking into account the extent of surface coverage during the reaction:[109]

$$i = \tau \frac{kT}{h} \exp\left[\frac{\Delta G^0}{RT}\right] zF\Gamma_i(1-\theta) \tag{1.2.50}$$

where $\Delta G^0$ accounts for the electrochemical standard free energy, $\Gamma_i$ denotes the surface concentration of the reactant of ionic species *i* where surface and bulk concentrations are related *via* an adsorption isotherm. The quantity $(1-\theta)$ refers for the geometrical factor which expresses the specific fractional area available for discharge of further species on the surface. The parameter $\theta$ considers the steady-state coverage of intermediates or products adsorbed onto the surface at a given rate. The process of the electro-adsorption of intermediates gives rise to a general expression for the adsorption pseudo-capacitance:

$$C_{ps} = \frac{dq}{d\eta} = k' \frac{d\theta}{d\eta} \tag{1.2.51}$$

where q is the charge related to the fractional surface coverage by the expression $q = q_1\theta$. Hence, the parameter $k'$ denotes the total charge required for the deposition of a monolayer of the adsorbed intermediate by discharged of the appropriate ionic species. Differentiation of the expression $\theta = \frac{F}{fRT}\Delta\phi + \frac{1}{f}\ln K + \frac{1}{f}\ln a_i$ with respect to the potential difference yields to the following expression for the adsorption pseudo-capacitance C:[110]

$$C_{ps} = \frac{dq}{d\Delta\phi} = k' \frac{d\theta}{d\Delta\phi} = \frac{k'F}{fRT} \tag{1.2.52}$$

### 1.2.4 Multistep Kinetics

The discussion on electrochemical kinetics presented so far was limited to the case, as exemplified by the reaction (see eqn.1.2.1) of the electrode chemical reaction consisting on a single-electron transfer taking place in one step. However, in practise, most electrochemical reactions consist of a number of consecutive steps, *e.g.* hydrogen evolution reaction (HER)[111], oxygen evolution reaction (OER)[112], oxidation of hydrocarbons[113], etc.

In considering such reaction sequences, it is generally assumed[114] that charges cross the interface electrode-electrolyte one at a time, which meaning that only one electron might be transferred in any given step. In other words, if an overall process involves a change of n electrons, it must also involve n distinct electron transfer steps. However, charge transfer may occur in any of the consecutive steps of the overall reaction.

During the decades of the 50s and 60s, various different methods for the treatment of multistep electrode kinetic were published.[93, 107-108, 112, 115] All these methods share the assumption that the rate constant of one of such steps is significant smaller than that of any other step in the successive mechanism. The step of which the rate constant is much more sluggish than all the others is considered as rate determining, that is, it controls the rate of the overall reaction. Since a rate determining step (RDS) is always a one-electron-process, the considerations outlined in previous sections for the one-step, one electron process might be used to describe the RDS. It must be noted that when using single-step kinetics to describe the RDS, the concentrations should refer to the formation of intermediates rather than to the starting reactants or final products. A general multi-electron transfer process of the form:

$$A + ne^- \rightleftarrows Z \tag{1.2.53}$$

might be decomposed into the partial reactions such that:

$$A + e^- \rightleftarrows B \qquad step1 \tag{1.2.54}$$

$$B + e^- \rightleftarrows C \qquad step\ \vec{n} \tag{1.2.55}$$

$$\upsilon(C + re^- \rightleftarrows D)\ \ RDS\ repeated\ \upsilon\ times \tag{1.2.56}$$

$$\upsilon D + e^- \rightleftarrows E \qquad step\ n - \vec{n} - rv \equiv \overleftarrow{n} \tag{1.2.57}$$

. . . . .

$$Y + e^- \rightleftarrows Z \qquad step\ n \tag{1.2.58}$$

where the parameter $\vec{n}$ expresses the number of electrons transferred before the RDS, and the $r$ refers to the number of electrodes transferred during each occurrence of the RDS step for a given overall reaction. The number of times that the rate determining step occurs for one act of the overall reaction is known as the stoichiometric number $\upsilon$.[116] As outlined above, the number of electrons transferred after the RDS is given by:

$$\overleftarrow{n} = n - \vec{n} - rv \tag{1.2.59}$$

If all the steps proceeding and succeeding the RDS are in quasi-equilibrium, and also that each single-step in the multistep reaction may be described by the simple Butler-Volmer eqn. (see eqn.1.2.16), then this yields to a general form of the Butler-Volmer eqn. or a sequential multistep reaction. Hence, the overall rate is given by:

$$i = i_0 \left\{ \exp\left[ \left( \frac{\vec{n}}{v} + r\beta \right) \frac{F\eta}{RT} \right] - \exp\left[ -\left( \frac{n_\Sigma - \vec{n}}{v} - r\beta \right) \frac{F\eta}{RT} \right] \right\} \tag{1.2.60}$$

Where:

$$\frac{\vec{n}}{v} + r\beta = \vec{\alpha} \tag{1.2.61}$$

$$\frac{n_\Sigma - \vec{n}}{v} - r\beta = \overleftarrow{\alpha} \tag{1.2.62}$$

which rearranging eqn. 1.2.61 and 1.2.62 gives:

$$\vec{\alpha} + \overleftarrow{\alpha} = \frac{n}{v} \tag{1.2.63}$$

The quantities $\vec{\alpha}$ and $\overleftarrow{\alpha}$ are known as the transfer coefficients[117] for the forward and reverse directions of the overall reaction. In section 1.3, which introduced the kinetics for a single-step electron transfer processes, it was stated that transfer coefficients have equal fundamental meaning than the symmetry factor, $\beta$. However, for a multistep electron transfer reaction, the observation of eqns. 1.2.61 and 1.2.62 indicates that they are fundamentally different quantities and thus, the transfer coefficient from a multistep reaction should not be confused with the one defined for single-step electron transfer reactions. To clarify this, it is necessary to recall that while the symmetry factor is only associated with the activation of vibrational states and related to the presence of activation energy barriers, the transfer coefficients for a multistep reaction still incorporates these factors, since $\alpha$ is expresed in terms of $\beta$, it also integrates both the stoichiometry of the reaction, through the parameter $v$, and the succession of steps in the overall reaction,

through the parameters $n, \vec{n}$ and $n_{\Sigma}$. Substituting the parameters $\vec{\alpha}$ and $\overleftarrow{\alpha}$ into eqn. 1.2.16, the general form of the Butler-Volmer equation may be written as:

$$i = i_0 \left\{ \exp\left[\frac{\vec{\alpha} F\eta}{RT}\right] - \exp\left[-\frac{\overleftarrow{\alpha} F\eta}{RT}\right] \right\} \tag{1.2.64}$$

which describes the net current for a redox couple reaction. For the case that:

$$n = \vec{n} = r = 1 \tag{1.2.65}$$

then $v = 1$ and eqn. 1.2.64 reduces to the conventional form of the Bulmer Volmer eqn. presented in section 1.3. Accounting for eqn. 1.2.64, the plot of the $\log i \ \ vs. \eta$ yields to the expression of the Tafel slope for a multistep reaction, which is of a primary interest in mechanism determination since its value can generally determine the particular rate determining step in the overall reaction.

### 1.2.5 Tafel Slope

Taking into account eqn. 1.2.64, the relationship between the steady-state anodic current and the overpotential might be expressed as:

$$i = i_0 \exp\left(\frac{\alpha_a F\eta}{RT}\right) \tag{1.2.66}$$

where $i_0$ is the exchange current which represents the rate of the forward and reverses reactions at the equilibrium potential, $\alpha_a$ is the transfer coefficient for the anodic reaction, $\eta$ is the overpotential, and all the other parameters have their usual significance. In this formula, the reaction is assumed to take place under kinetic control since the expression does not consider mass transfer limitations, which would alter the concentrations of reactants at the electrode surface. If eqn. 1.2.66 is expressed in the logarithmic form, the Tafel expression for a multistep electron reaction is obtained as:

$$\log i = \log i_0 + \frac{\eta}{b} \tag{1.2.67}$$

Rearranging eqn. 1.2.67, it may be expressed in the original format proposed by Tafel back in 1904:

$$\eta = a + b \log i \tag{1.2.68}$$

where the parameter *a* is a constant and *b* refers to the Tafel slope given by:

$$b = \frac{d\eta}{d \log i} = \frac{2.303RT}{\alpha_a F} \tag{1.2.69}$$

It is clear from eqn. 1.2.67 that a linear relationship between the overpotential $\eta$ and the $\log i$ can be predicted. It is also noticeable from eqn. 1.2.69 that the transfer coefficient determines the Tafel slope value, which can be the diagnostic of a particular reaction mechanism, as mentioned in section 1.5. In addition, the Tafel slope, *b*, which is commonly expressed in millivolts (mV) per decade of applied current ($dec^{-1}$) might be directly extracted from experimental plots of log(*i*) *vs*. $\eta$. The latter is only possible when the experiment is recorded using Galvanostatic methods, that is, where the current is controlled by the potentiostat and the potential response is measured, as described by eqn. 1.2.68. The use of galvanostatic methods instead of potentiostatic methods arises from the difficulty, for period potentiostats, to precisely control the potential. However, due to the ease with which the potential can be controlled by modern potentiostats, Tafel plots are now normally recorded in the form of $\log i = \log i_0 + \frac{\eta}{b}$ and, thus, the Tafel slope is obtained from the inverse slope of the experimental plot. It is important to outline that the magnitude of the Tafel slope is strongly dependent on the value of the transfer coefficient, $\alpha_a$, which rearranging eqn. 1.2.69, yields to:

$$\alpha_a = \frac{1}{b}\left(\frac{2.303RT}{F}\right) \tag{1.2.70}$$

Eqn. 1.2.70 is strongly involved in the development of a mechanistic pathway of various multistep reactions such as the OER. This aspect will be further discussed throughout this section.

At its most basic level, Tafel plots, and especially, the Tafel slope, provides a measure of the rate of increase of electrode potential with the log of the current density. For that reason, it is considered an important sensitive parameter for the practical evaluation of the electrocatalytic materials' behaviour. Some authors[118] suggested that the utilisation of the catalytic evaluation of the Tafel slope parameter rather than the current density itself provides for a more realistic catalytic performance comparison. This concept is based on the idea that current density, $i_o$, only refers to the kinetics on the thermodynamic potential

and does not account for the kinetics of the electrode at higher potentials, that is, at potentials where some important reactions occur, *e.g.* HER or OER. Typical Tafel curves are illustrated in fig. 1.2.5. As it can be observed in fig. 1.2.5, the red line possesses a greater slope than that of the blue line. This provokes that for an equal overpotential value, the 30 / 70 M Ni/Co electrode displays larger current density than the other electrode. Consequently, the latter electrode could be considered less active. This catalytic behaviour is particularly important for systems such as water electrolysis, where high current densities -large rate of reaction- at minimum operational voltages are required for economic viability reasons. From an operational point of view, it is not just that the magnitude of the current density at a given overpotential that is important, but also the rate of change of the current density *vs*. the overpotential function. The latter refers to the inverse Tafel slope 1/*b* given by the slope of eqn. 1.2.70. Therefore, greater changes on the current density's response are observed for electrodes whose slope, in plots of log *i* *vs*. $\eta$, is large, which yields to small values of Tafel slope. It is also to be mentioned that low Tafel slopes are widely acknowledged as indicators of efficient electrocatalytic performance.[118-119]

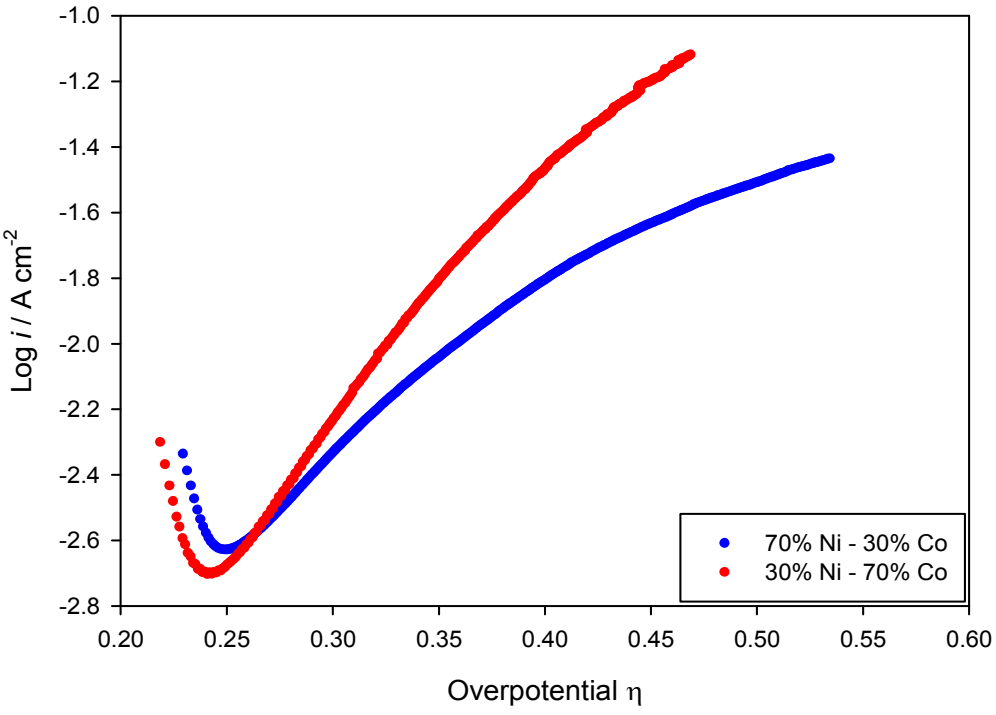



Figure 1.2.5 Schematic diagrams illustrating the significance of Tafel slopes for determining more favourable catalytic behaviour. These Tafel curves were recorded to analyse the anodic behaviour of two different electrodes in the OER. The blue line represents an electrode with a composition of 70 % M Ni and 30 % M Co whereas the red line refers to the opposite concentration. 30 % M Ni and 70 % M Co.

As early introduced, the Tafel slope yields insight into the mechanistic pathway of an electrode process. Considering that for a multistep reaction consisting in a sequence of one-electron transfer steps where one of those is a rate-determining step (RDS), the parameter $\alpha_a$ might be described as:[93, 120]

$$\alpha_a = \frac{n_f}{v} + \frac{n_n}{\beta} \tag{1.2.71}$$

in where all the parameters have already been defined throughout this section. It may be noted from eqns. 1.2.70 and 1.2.71 that the Tafel slope is a composite parameter, giving information on the stoichiometry and the succession of steps in the overall reaction. Different Tafel slopes can be predicted depending on the position of the RDS in the overall reaction. In this perspective, various scenarios are presented in order to explain the experimental values of the Tafel slope. For all these scenarios, four assumptions are to be considered: (i) the surface coverage is equal to 0.5, (ii) the number of electrons transferred in each step is equal to 1, (iii) the number of times that the RDS takes place in the reaction sequence of the multistep reaction is also equal to 1, and (iv) the existence of a single Tafel slope region in the graph $\log i \; vs. \eta$.

The first scenario assumes that the first electron transfer step in the sequence is considered to be rate determining, then the number of electrons before the RDS is zero, hence $n_f = 0$ and $n_n = 1$ , and $\alpha_a = \frac{1}{2}$ so the predicted Tafel slope is 120 mV dec$^{-1}$. The second scenario assumes that the second electron transfer step is now the RDS, then $n_f = n_n = 1$ and hence $\alpha_a = \frac{3}{2}$ giving a Tafel slope of 40 mV dec$^{-1}$. The third scenario assumes both that the rate determining step involves a chemical reaction rather than an electron transfer reaction and that the RDS occurs subsequent to an electron transfer step. Therefore, the number of electrons transferred in the RDS is equal to zero, and $n_f = 1$, and $\alpha_a = 1$ which predicts a Tafel slope of 60 mV dec$^{-1}$. An extended discussion about the different mechanistic pathways included here will be found present in future sections. It must be noted that the assumption (iv) - the existence of a single Tafel slope region in the graph $\log i \; vs. \eta$- cannot be always considered valid as two distinct linear regions are observed in the blue curve in fig. 1.2.5. The same observation has also been mentioned in other publications.[120a, 120c, 121] Note that the presence of two different linear Tafel regions might be directly attributed to either the effect of changing the potential on the adsorption species on the electrode surface, which has already been discussed in the section 1.2.3, or to a

change in the position of the RDS within a given pathway. However, increases in the Tafel slope do not necessarily have mechanistic significance. Taking as an example the oxygen evolution reaction, a raise of the electrode potential results of an increase of the oxygen reaction rate, which provokes the formation of oxygen gas. The formation of oxygen bubbles may reduce the active surface area available for the electron exchange and thus limit the reaction rate. In addition, the onset of mass transport limitations at high overpotentials also reduces the current response of the electrode resulting in an increasing Tafel slope.

The identification of mechanistically changes in the Tafel slope is best achieved using different techniques. Generally, the measurement of the Tafel slope is performed using steady-state polarisation measurements. However, due to the limitations previously mentioned arising from the utilisation of steady-state measurements, other techniques such as electrochemical impedance spectroscopy (EIS) and open circuit potential decay curves may be used to best accomplish the mechanistic pathway. Though a complete description of the determination of the equivalent Tafel slope using EIS is beyond the scope of this section, it can be said here that its measurement involves the experimentally analysis of the total Faradaic resistance, $R_{far}$, as a function of the applied potential according to:

$$\log\left(\frac{1}{R_{far}}\right) = \frac{V}{b} + \log\left(\frac{2.303 i_0}{b}\right) \qquad (1.2.72)$$

which implies that the inverse slope of a plot of $\log\left(\frac{1}{R_{far}}\right)$ against V is equal to the Tafel slope *b* (see section 3.7.5).

Some authors suggest that the interpretation of the mechanistic pathway using only a Tafel slope measured from electrochemical impedance spectroscopy may not provide for realistic nor accurate results.[122] This issue is based on the fact that the total Faradaic resistance accounts for the combination of the charge transfer resistance for each of the consecutive steps in the reaction, regardless of whether they are the RDS, a preceding step or a following step. However, it has also been mentioned that the effectiveness of this type of data treatment, when used in conjunction with steady-state polarisation techniques, is significantly useful.[121b, 123] A good example of the synergy of both techniques is presented in fig. 1.2.6. Both techniques provide similar values of Tafel slope which suggests that the Tafel behaviour of such system is closely related with the mechanistic pathway of the reaction. Similar Tafel behaviour has been published by Doyle and Lyons.[121b] It is

important to mention that if a lack of agreement between the steady-state Tafel polarisation and the Tafel from EIS is observed, effects such as mass transport limitation, a reduction of the active surface area or the presence of ohmic effects should be considered. Along with steady-state measurements and EIS, another technique that provides insight into the mechanistic pathway of the reaction is the decay of the open circuit potential (OCP). The use of the OCP decay is strongly recommended for systems where the steady-state polarisation analysis is complicated, that is, where there is not a defined linear Tafel slope region due to changes on the reaction mechanism. Those changes arise as a result of continuous alterations of the electrode surface with time.

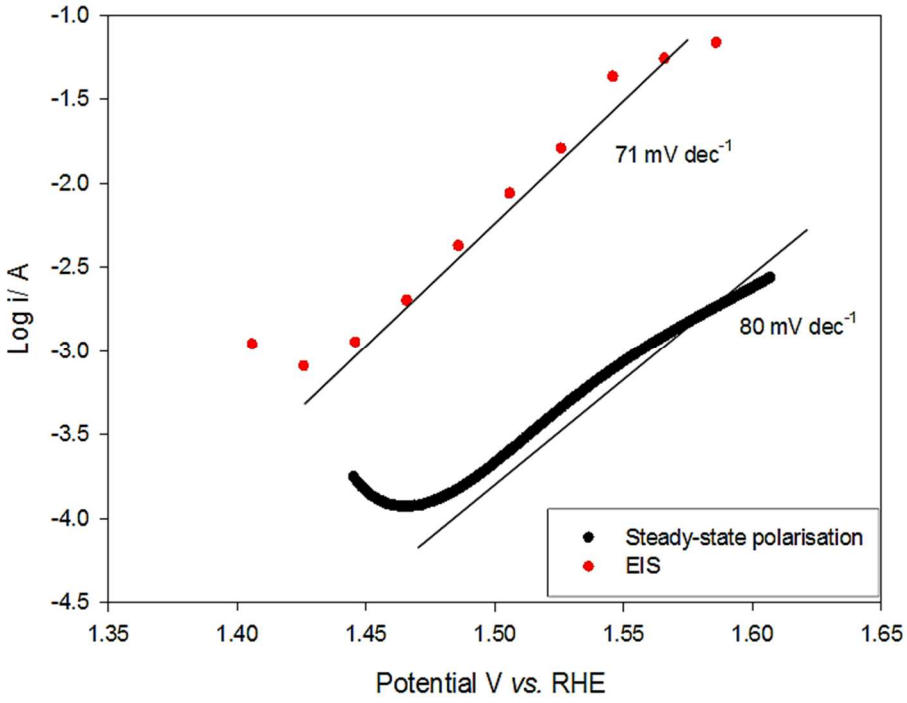



Figure 1.2.6 Comparison of the Tafel plots generated using EIS (red) and steady-state polarisation (black) data. These Tafel plots were recorded in the direction of increasing potential from a Manganese oxide electrode with 250 repetitive potential cycles, in 1.0 M NaOH at 25°C in a region where the oxygen evolution reaction occurs.

Before performing the OCP decay analysis, an initial polarisation at a potential in the region where the Tafel slope linearity occurs, is required. This step is conducted aiming the formation of a homogenous surface. Following the initial polarisation, the variation of the electrode potential at open circuit with time is given by:[124]

$$V_{OCP} = \frac{2.303RT}{\beta F}\log\left(\frac{RT}{\beta F i_0}\right) - \frac{2.303RT}{\beta F}\log(t) \quad (1.2.73)$$

Where the slope is given by:

$$b_{OCP} = \frac{-2.303RT}{\beta F} \quad (1.2.74)$$

According to Bockris[124] the slope $b_{OCP}$ of a plot of the measured potential during the decay as a function of $\log(t)$ is equal to the negative of the standard Tafel slope, $b$. The OCP decay analysis may be also useful to describe the potential dependence of the surface capacity and the fractional surface coverage of intermediate species. Note that eqn. 1.2.73 assumes that the electrode potential is independent of the surface coverage. In addition, according to some authors,[125] eqn. 1.2.73 only holds as long as the coverage is independent from the potential. Thus, the observation of numerical identity between the OCP decay slope and the Tafel slope from steady-state polarisation suggests that the surface capacity remains constant during the self-discharge measurement. Contrary, the scenario where surface coverage does change during the self-discharge with respect to the applied potential provokes a significantly difference between both slopes. The behaviour of both scenarios can be seen in fig. 1.2.7.

It is evident in fig. 1.2.7a, that the Tafel slope obtained from the OCP decay and that from steady-state polarisation are equal, whereas opposite behaviour is observed in fig. 1.2.7b where the slopes of the OCP decay vary with time.

The interpretation of this observation is discussed deeper in chapter 4 and 5. To conclude, the relationship between the decay slope and the steady-state Tafel slope may provide for a useful qualitative characterisation of the kinetics and mechanism of the basic processes involved in an electrocatalytic reaction.

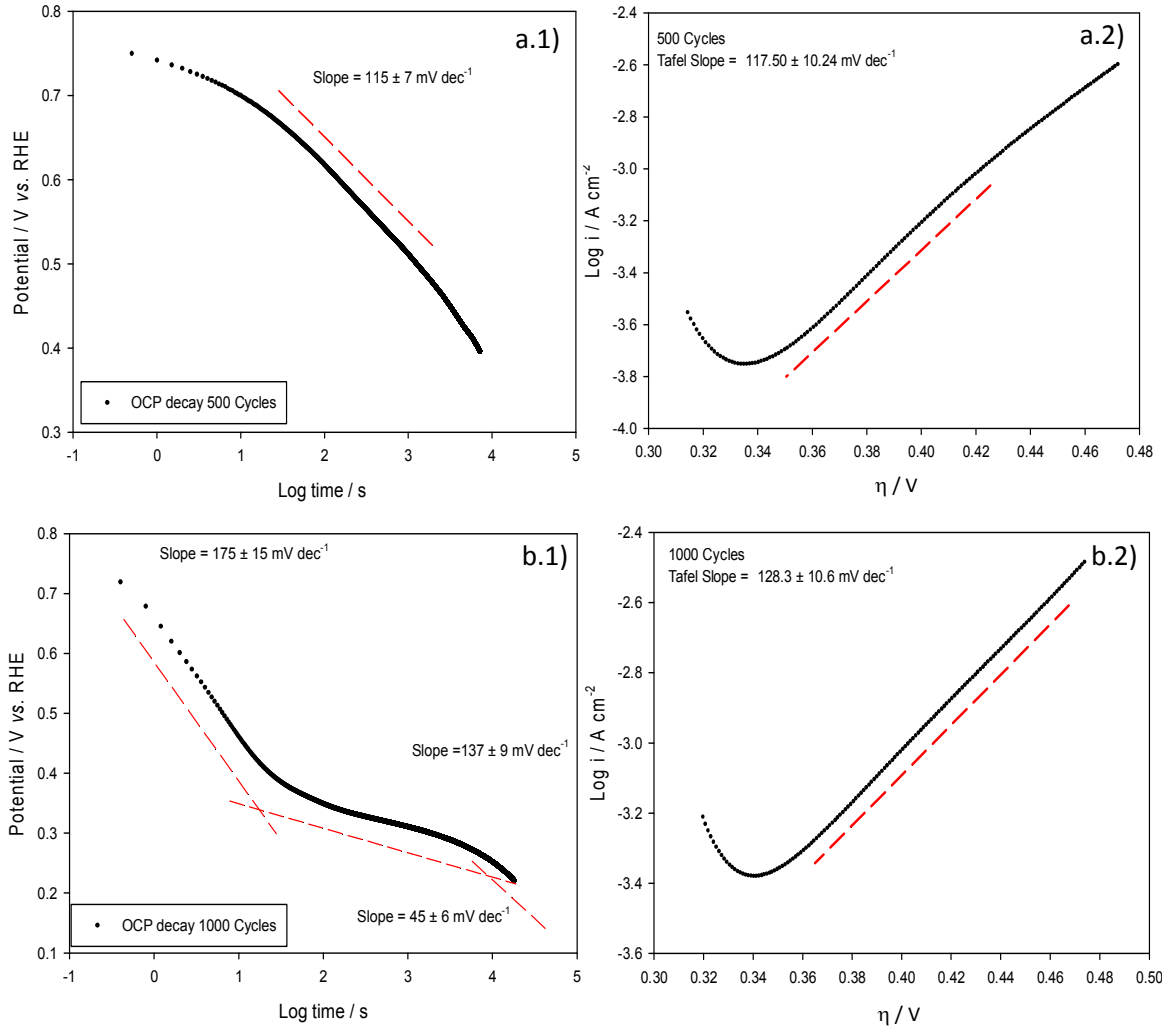



Figure 1.2.7 A comparison of the Tafel plots generated using the OCP decay (a.1, b.1) and steady-state polarisation (a.2, d.2) The curves a and b were obtained from a 500 and 1000 potential cycles Mn electrode, respectively, at 1.0 M NaOH at 25°C.

### 1.2.6 Electrochemical Reaction Order Determination

Following the context of multistep electron transfer kinetics, another useful piece of information regarding the elucidation of electrochemical reaction mechanisms may be obtained from the study of the reaction order. The reaction order is defined as the sensitivity of the reaction rate to the activity of particular reactant species. In electrochemical reactions, the reaction rate is expressed as current, so the electrochemical reaction order quantifies the sensitivity of the current to changes in reactant concentration. In addition, a realistic mechanism pathway should not only predict the Tafel slope over a range of overpotentials but should also match the predicted reaction order for such

mechanism when plots of $\log i \ vs. \log c$, or more precisely the $\log a$ (activity), at a given value of overpotential η are constructed. The reaction order was first investigated by Conway and Salomon[126] back in the early 60s. As mentioned by these authors: "the reaction orders depend on the isotherm for adsorption of the reactants at the electrode interface and the adsorption behaviour of intermediates involved in the reaction". In this way, they focused their studies on those cases where the electrode reaction involves the formation of intermediates adsorbed under Langmuir or Temkin conditions. That is where the apparent standard free energy of adsorption $\Delta G_{ads}^{0}$ of intermediates such as -H, -OH or -O may vary linearly with surface coverage. Following this criterion, they proposed an eqn. which relates the electrode potential at the outer Helmholtz plane and the current density at a steady-state coverage of adsorbed $H^+$ ions:

$$i = k_1(a_{H+})(1-\theta_H)\exp\left[-\left(\frac{\beta\eta F}{RT}\right)\right] \tag{1.2.75}$$

where $(a_{H+})$ is the activity of hydrogen ions within the double layer. The derivate of eqn. 1.2.75 can be written in three different fashions:

$$m_{x,i} = \left(\frac{d\,E}{d\log a_x}\right)_i \tag{1.2.76}$$

$$m_{x,\eta} = \left(\frac{d\log i}{d\log a_x}\right)_\eta \tag{1.2.77}$$

$$m_{x,E} = \left(\frac{d\log i}{d\log a_x}\right)_E \tag{1.2.78}$$

These three equations represent the electrochemical reaction order $m_x$ in terms of constant current, constant overpotential, and constant applied potential - which is relative to a pH independent reference electrode *e.g.* mercury-mercuric oxide Hg/HgO -, respectively. The determination of $m_x$ provides the relationship between the reaction rate and the concentration of a particular reactant. The derivative (iii) $m_{x,E}$ may be regarded as the "chemically" or "mechanistically" significant reaction order since it quantifies the dependence of log $(rate\ /\ i)$ on changes in the log $(reactant\ activity\ /\ a_x)$ in the absence of variations of double layer configuration, which implies constant interfacial potential conditions.

This manner of expressing the reaction order is very important since it provides direct information regarding the position of the RDS in the overall reaction. It is worth to mention that while the substitution between the overpotential or the potential in the process to obtain the Tafel slope was of no relevance, as the same result was obtained for the calculation of the reaction order it is no longer irrelevant and modifications in eqn. 1.2.77 will need to be carried out in order to be able to compare reaction order values obtained using constant potential or constant overpotential. The following correction factor accounts for this matter:[127]

$$m_{x,\eta} = m_{x,E} - \beta \tag{1.2.79}$$

where $\beta$ refers to the symmetry factor, which usually takes 0.5 value. In addition, the relationship between $m_{x,i}$ and $m_{x,E}$ offers a useful self-consistency check between the experimentally measured Tafel slope, $b$, and the mechanistically significant reaction order $m_{x,V}$ as follows:

$$m_{x,i} = -b\,(m_{x,E}) \tag{1.2.80}$$

Putting these concepts in line with the aim of this thesis, which is the study of the OER, in subsequent discussions all references to the parameter $m_x$ will refer to the mechanistically significant quantity $m_{x,E}$. Thus, in the case of OER in alkaline solution, where the reactant term is the activity of the hydroxide ion, $a_{OH^-}$, a plot of the $\log i$ with respect to the $\log a_{OH^-}$ should reflect a linear relationship with a slope equal to that of the corresponding electrochemical reaction order $m_{OH^-}$. Since some Tafel plots exhibit two different slopes, as previously mentioned in section 1.2.5, the generation of reaction order plots should consider this matter, as distinct reaction orders may be associated with each Tafel region. This issue may be solved by generating different reaction order at a range of potentials in the region of the OER. An important point that must be considered when interpreting such reaction order data is that, theoretically, reaction orders should be integer values. This may not always be the case, however, and fractional reaction orders may be observed. Further discussion is presented in significant detail in chapters 4 and 5.

Commonly, a reaction order $m_{OH^-} = 1$ suggests that only a single hydroxide ion reacts at each active site for all steps up to and including the RDS. Similarly, if $m_{OH^-} = 2$ then a total of two $OH^-$ equivalents may be assumed to be involved in the overall reaction prior to

and including the RDS. However, it can be more difficult to rationalise fractional reaction orders. Some authors suggested that the observation of fractional reaction orders may be related with the nature of the diffuse layer potential, $\phi$.[128] According to them, if reaction order experiments are not performed at a constant ionic strength, then the observed reaction order might not be obtained at a constant potential conditions. Other authors suggested that the observation of fractional reaction orders arises due to the existence of parallel reaction pathways. In such cases, the experimentally observed reaction order represents a combination of the parameters expected for the parallel pathways, the exact value of which depends on the fraction of catalytic sites following each individual pathway. Additionally, the existence of fractional reaction orders can also be due to the nature of the surface coverage of the intermediates, as mentioned by Lyons and Brandon[123], and by Bockris and Ottagawa[129]. In both publications, it was proposed that fractional reaction orders could be rationalised by admitting Temkin rather than Langmuir adsorption conditions.

### 1.2.7 Modified Nernst Equation for the Account of the pH

Some experimental results such as the redox peak potentials, the oxygen evolution onset potential or the Tafel slope, all of them with changing electrolyte concentration, are to be presented in chapters 4 and 5. Since the electrolyte is sodium hydroxide, NaOH, variations on its concertation may affect the pH of the electrolyte solution and therefore, change the electrochemical kinetics of the electrode reactions. It is, therefore, necessary to review the fashion that the pH provokes in these measurements. To begin with, a brief background may be presented on the basics of the Nernst eqn. and also on its modifications considering the pH. The Nernst eqn. is derived from the standard changes in the Gibbs free energy associated with an electrochemical reaction such as:

$$\Delta G = \Delta G^0 + RT \ln Q \tag{1.2.81}$$

where:

$$\Delta G^0 = -nFE^0 \tag{1.2.82}$$

$$\Delta G = -nFE \tag{1.2.83}$$

$$Q = \frac{C_R^*}{C_O^*} \tag{1.2.84}$$

The terms $\Delta G^0$and $\Delta G$ refer to the standard Gibbs free energy and the Gibbs free energy under non-standard conditions, respectively. The term $Q$ expresses the ratio between the bulk activities of the species products, $C_0^*$, and the reactants, $C_R^*$, respectively. Substituting eqns.1.2.82 and 1.2.83 into eqn. 1.2.81, gives:

$$-nFE = -nFE^0 + RT \ln Q \tag{1.2.85}$$

Rearranging eqn. 1.2.85 leads to the basic Nernst eqn. previously introduced in section 1.2:

$$E = E^0 - \frac{RT}{nF} \ln(Q) \tag{1.2.86}$$

A more common expression of the Nernst eqn. might be obtained by combining RT and F into one constant at 25°C and using the common logarithm instead of the natural logarithm:

$$E = E^0 - \frac{0.0591}{n} \log(Q) \tag{1.2.87}$$

Note that the Nernst eqn. is only valid in those cases where there is no applied potential onto the electrode. In other words, when the electrode is in its thermodynamic equilibrium *e.g*. no net flux of ions. In those cases, the electrode potential must be equal to the Nernst potential given by eqn. 1.2.87. It is also worth to mention that the sign of the second term of eqn. 1.2.87 is given by the $\log(Q)$. If $Q = \frac{C_0^*}{C_R^*}$ then the resulting sign is positive, whereas if $= \frac{C_R^*}{C_0^*}$, it is negative.

In many electron transfer reactions such as the OER, the electrochemical process involves both the transfer of hydrogen ions and the transfer of electrons. The standard potential for such reactions, therefore, should be dependent on the pH. This pH dependence yields to the existence of stable species at a given pH. Diagrams such as those proposed by Pourbaix[130] may serve as clarification. Taking the general eqn. for the OER half-cell reaction as:

$$O + mH^+ + ne^- \rightarrow R \tag{1.2.88}$$

From eqn. 1.2.88 it can be seen that the OER is a reaction involving both an electron transfer and a proton transfer. The Nernst equation for such systems may be written as:

$$E = E^0 + \frac{0.0591}{n}\log\left(\frac{a_O a_H}{a_R}\right) \tag{1.2.89}$$

If the activities of the oxidised and the reduced species are written in terms of the activity coefficient, then:

$$E = E^0 + \frac{0.0591}{n}\log\left(\frac{\gamma_O}{\gamma_R}\right) + \frac{0.0591}{n}\log\left(\frac{C_O}{C_R}\right) + \frac{0.0591\, m}{n}\log(a_H) \tag{1.2.90}$$

and considering that the $\mathrm{pH} = -\log(a_H)$, eqn. 1.2.90 simplifies to:

$$E = E^0 + A - 0.0591\left(\frac{m}{n}\right)pH \tag{1.2.91}$$

where $A = \frac{0.0591}{n}\log\left(\frac{\gamma_O}{\gamma_R}\right) + \frac{0.0591}{n}\log\left(\frac{C_O}{C_R}\right)$. Eqn. 1.2.91 can, therefore, predict that each increase or decrease in the magnitude of $OH^-$, or simply a change in the pH unit, induces a shift in the potential by 59 mV $pH^{-1}$. When the latter is observed, the system is known to be Nernstian.

It seems opportune to introduce the basics of the term *activity*, in this context. Commonly, in macroscopic chemistry, thermodynamic quantities and other general parameters refer to systems where all dissolved substances are measured in molarities, *e.g.* enthalpy, entropy, electrolyte concentration, standard cell potentials, etc. However, in systems where microscopic mechanisms are considered, the thermodynamic properties are typically defined in terms of activities. The term activity is a measure of the effective concentration of a mixture and refers to the ions in a solution that do not interact with the solvent nor with other molecules. Examples of these interactions are hydrogen bonding, ion-dipole interactions, and van der Waals forces. In addition, the activity is a way of defining deviations from the ideal behaviour of a mixture. Thus, the fashion to express the deviation from the ideal behaviour is *via* the molal activity coefficient $\gamma_i$. The activity of an isolated ion *e.g.* $OH^-$, in a solution of *e.g.* NaOH of molality *m* is expressed as the product of the molal concertation of a given ion and the molal activity coefficient by the following expression:

$$a_i = m_i\, \gamma_i \tag{1.2.92}$$

The molal activity coefficient depends on several factors such as the ionic strength of the solution, the charge of the ions on the solution, the density of the medium, etc. The activity coefficients have been experimentally obtained for many ionic solutions and are generally expressed in terms of molality. In this work, however, all solutions were prepared using molar rather than molal concentrations. The molality concentration of NaOH solutions was obtained by converting the molar concentrations into molal ones. Values of the molal activity coefficient for NaOH solutions of different molalities at 25°C were obtained from reference.[131] For the sake of convenience, a graph of the molal activity coefficient *vs*. molality is presented:

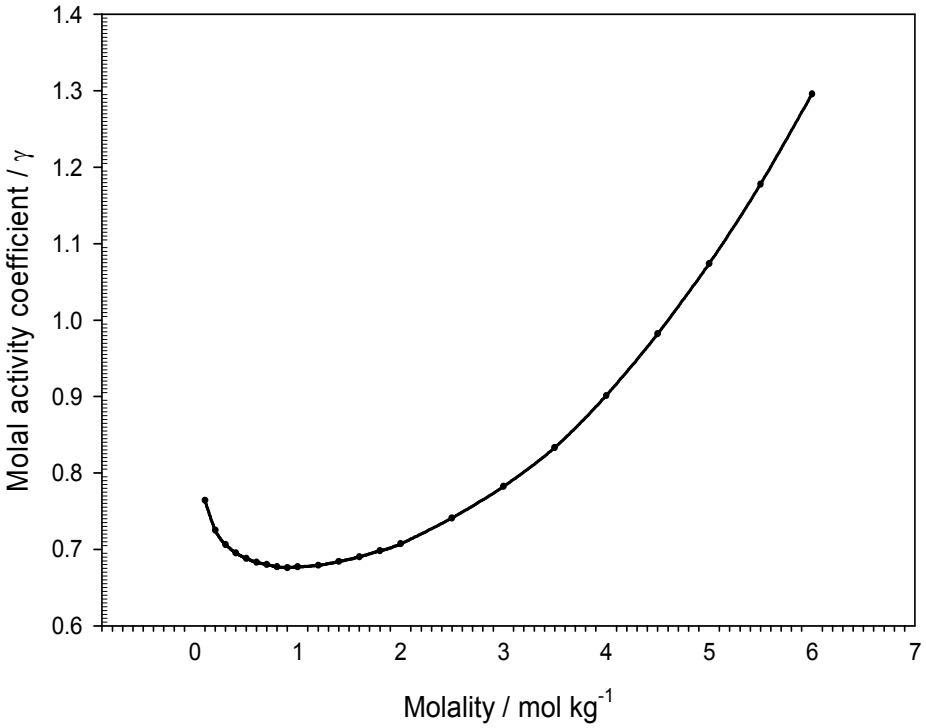



Figure 1.2.8 Representation of the relationship between the molal activity coefficient and molality of various NaOH solutions at 25°C. The solid line represents the line of best fit and the doted points the values obtained from Ref.[131]

From fig. 1.2.8, the appropriate values of the $a_{OH^-}$ for each solution were calculated. These values are summarised in Table 1.2.1 below.

| Molar / mol $dm^{-3}$ | Molal / mol $Kg^{-1}$ | Molal activity coef. | Activity / $a_{OH^-}$ | log ($a_{OH^-}$) | pH |
|---|---|---|---|---|---|
| 0.1 | 0.100 | 0.764 | 0.077 | -1.116 | 12.88 |
| 0.25 | 0.251 | 0.715 | 0.180 | -0.746 | 13.25 |
| 0.5 | 0.505 | 0.688 | 0.347 | -0.459 | 13.54 |
| 1.0 | 1.019 | 0.677 | 0.690 | -0.161 | 13.84 |
| 2.0 | 2.079 | 0.712 | 1.481 | 0.171 | 14.17 |
| 3.0 | 3.182 | 0.801 | 2.547 | 0.406 | 14.41 |
| 4.0 | 4.330 | 0.954 | 4.133 | 0.616 | 14.62 |
| 5.0 | 5.526 | 1.183 | 6.540 | 0.816 | 14.82 |
| 6.0 | 6.774 | 1.512 | 10.243 | 1.010 | 15.01 |

Table 1.2.1 Values of ionic activity $a_{OH^-}$ calculated for the various NaOH solutions utilised.

In the limit of an infinitely dilute solution, which is an analogy to an ideal mixture, the activity may be considered proportional to the concentration since the microscopic interactions between each pair of chemical species in solution are the same. Hence, $\gamma \rightarrow 1$ and $a_i = C_i$. This occurs because, in dilute solutions, all the ions lie at a greater distance to each other, which is mainly due to charge repulsion. Contrary, as the distances between ions are shortened as a result of a rise on the concentration, solvation occurs and thus the effective concentration decreases. Examples of these interactions were mentioned when discussing the Debye-Hunkel theory and the formation of the double layer in section 1.2.

### 1.2.8 Effects of the Double Layer and Mass Transport on the Electrode Kinetics

The effect of the double layer region on electrode kinetics was first introduced by Frumkin[92] in the 1930s. His investigations regarding the hydrogen reduction reaction yield to the discovery that the current produced due to the reduction of the hydrogen ion from dilute acid solutions using a mercury electrode as the working electrode was independent of the acid's concentration at constant overpotential. He attributed this observation to a change in the concentration of hydrogen ions at the reaction site in the double layer. Frumkin thereby developed a theory based on the assumption that the reaction sites within the double layer were situated at the outer Helmholtz plane with a

potential $\phi^d$. The expression for the potential dependence on the rate constant considering a simple electron transfer reaction:

$$O + e^- \rightarrow R \tag{1.2.93}$$

may be written as:

$$\ln k_f = \ln k_{f0} - z_A f \phi^d + \alpha f(\phi^d - \phi^m) \tag{1.2.94}$$

where $k_f$ is the forward rate constant, $k_{f0}$ is the rate constant when $\phi^m = 0$, $\phi^m$ is the electrode potential, $\alpha$ is the transfer coefficient and $f = \frac{F}{RT}$. The second term in eqn. 1.2.94 accounts for the concentration of compound A with charge $z_A$ within the outer Helmholtz region. The charge $z_A$ differs from the charge of compound A in the bulk. If the charge of compound A is known, the term on the left-hand side of eqn. 1.2.94 may be corrected for the change in concertation of reactant A on the OHP, which results:

$$\ln k_f + z_A f \phi^d = \alpha f(\phi^d - \phi^m) \tag{1.2.95}$$

This is known as the corrected Tafel plot which can be employed when the appropriate double layer data are available. Fig. 1.2.9 may be seen as an example of the effect on the Tafel slope arising from the change of the reactant A concentration situated on the OHP region.

Another topic of interest is the effect of mass transport in electrode kinetics. The kinetic equations introduced in the previous section assumed that there were no mass transport effects, thus the surface and bulk concentrations happen to be identical, their ratio is unity and the Butler-Volmer eqn. presented in eqn. 1.2.16 remains. Unfortunately, mass transport effects are commonly seen in electrochemical measurements[132], as observed in fig. 1.2.10.

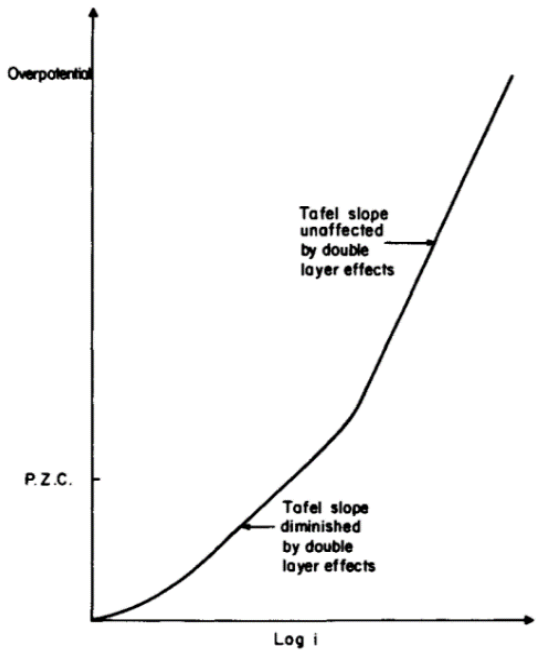



Figure 1.2.9 Schematic representation of mass transport effect on a typical Tafel plot. The existence of the region of diffuse charge in the electrified interface produces changes in the slope and deviates linearity. Reproduced from Ref.[133]

Under these circumstances, the above equations are no longer valid, and the addition of a modification is required to account for mass transport.

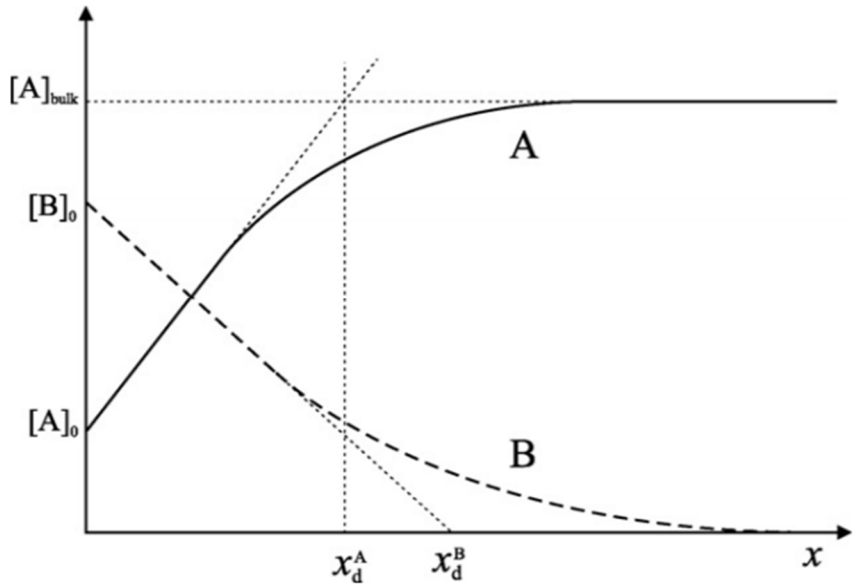



Figure 1.2.10 Schematic representation of the steady-state concentration profiles of compounds A and B at a polarized electrode. The parameters $x_d^A$ and $x_d^B$ are the steady-state diffusion layer thicknesses of species A and B, defined by an extrapolation of the concentration profiles at the electrode surface. Reproduced from Ref.[132]

If a simple electron transfer is considered, *e.g.* eqn. 1.2.93, a more complex $i\ vs.\ \eta$ function can be obtained when incorporating eqn. $\frac{C_s}{C^{\infty}} = 1 - \frac{i}{i_L}$ for the anodic and cathodic reactions into eqn. 1.2.16 to yield:

$$\frac{i}{i_0} = \left[\left[\left(1 - \frac{i}{i_{l,c}}\right) exp\left(\frac{-\beta F\eta}{RT}\right)\right] - \left(1 - \frac{i}{i_{l,a}}\right)\left(\frac{(1-\beta)F\eta}{RT}\right)\right] \tag{1.2.96}$$

The above eqn. represents the Butler-Volmer corrected eqn. for mass transfer effects. In the case of small overpotentials, eqn. 1.2.96 can be linearized by using Taylor expansion, yielding to:

$$\eta = \left(\frac{RTi}{F}\right)\left(\frac{1}{i_0} + \frac{1}{i_{l,c}} - \frac{1}{i_{l,a}}\right) \tag{1.2.97}$$

Where $i_{l,a}$ and $i_{l,c}$ are the limiting currents for the anode and cathode, respectively, while the parameter $\frac{RTi}{F}$ accounts for the mass transfer resistances. Since the fraction $\frac{1}{i_x}$ represents a resistance in parallel, eqn. 1.2.97 can be expressed as:

$$\eta = -i\left(R_{ct} + R_{mt,c} + R_{mt,a}\right) \tag{1.2.98}$$

where the $R_{ct}, R_{mt,c}, R_{mt,a}$ are the charge transfer resistance, the resistance produced by the mass transfer effect in the cathode and the anode, respectively.

Is it clear form eqn. 1.2.97 that for $i_o >> i_{l,c}$ and $i_{l,a}$ then the overpotential arises mainly due to mass transport effects and the kinetics for such system are very fast. Contrarily, if $i_o << i_{l,c}$ and $i_{l,a}$, the overpotential occurs due to poor charge transfer and the kinetics of the reaction sluggish.[103]

For cathodic branch at high overpotential values, the anodic contribution may be considered insignificant and eqn. 1.2.96 becomes:

$$\frac{i}{i_0} = \left(1 - \frac{i}{i_{l,c}}\right) exp\left(\frac{-\beta F\eta}{RT}\right) \tag{1.2.99}$$

The above eqn. might be rewritten to give:

$$\eta = \frac{RT}{\beta F}\ln\frac{i_0}{i_{l,c}} + \frac{RT}{\beta F}\ln\frac{i_{l,c} - i}{i} \tag{1.2.100}$$

It is important to outline that the above eqn. is only one form of the mass transport corrected Tafel eqn. such as:

$$\ln\left(\frac{i_l - i}{i}\right) = \ln\frac{k_l}{k^0} - \frac{\beta F\eta}{RT} \qquad (1.2.101)$$

where $k_l$ is the rate constant for the mass transfer process and $k^0$ is the standard rate constant. Since the plot resulting from $\ln\left(\frac{i_l - i}{i}\right)$ *vs.* $\eta$ is linear, the slope yields to $\frac{-\beta F}{RT}$ whereas the intercept with the y-axes yields to $\ln\frac{k_l}{k^0}$. Then, since $k_l$ may be readily evaluated, the standard rate constant may also be determined.

For multistep electrode reactions, the relationship between the overpotential and the current density is more complex and depends on precisely what path and mechanism apply.

## 1.3 Electrocatalysis

### 1.3.1 Basic Concepts of the Electrocatalysis

The term electrocatalysis was first mentioned by Grubb[134] in 1960s in relation to the anodic and cathodic reactions in fuel cells. It is now generally accepted that the term electrocatalysis refers to the catalytic influence of an electrode material upon an electrode reaction under standard conditions.

One of the first interpretations of electrocatalysis was provided by Houriuti and Polanyi[135] with regard to their study of the hydrogen evolution reaction. In this study, they observed that the energy required to move a proton towards the electrode exhibited a maximum at the intersection of the potential energy curve of the proton in solution and that of an $H^+$ ion adsorbed on the electrode surface. Consequently, they decided that a good catalyst for the HER would be the material with the smallest maximum energy value.

The electrocatalytic behaviour of different materials have been reviewed by many authors, most notably by Brokris[99], Srinivasan *et al.*[136] and, Trasatti[137]. Nowadays, it is well established that the catalytic behaviour or activity is mostly determined by both the electronic and the geometric properties of an electrode material, since there are normally several intermediate adsorption and desorption steps involved in an electrochemical reaction.

The transition metals, their alloys and their oxides have shown to be good materials for the technologically important oxygen electrode reactions and to the hydrogen evolution reaction.[138] The singular catalytic behaviour of transition metal oxides lies in the nature of the outer d-shell.[139] Due to the specific configuration of their last electronic shell (d-orbital) they can easily react with the electrolyte forming surface complexes such as MOH, $MO_2H$, $MO_2^-$ (here M represents the transition metal) which may decrease the energetic requirement for the reaction to take place. Singular electronic factors with regard to the transition metal are the work function Φ and the percentage d-band character or d-vacancy of the metal. Geometric factors not only include lattice structure and dimensions, but also surface heterogeneity, which is associated with the presence of various types of defects on the electrode surface, as introduced in section 1.2.3.

A brief comment regarding the term "work function" is pertinent at this stage. In solid-state physics or chemistry, the work function of a metal $\Phi^m$ is defined as the work required to move to infinity an electron from the Fermi level of a metal in contact with a vacuum.[140] Consequently, the expression for $\Phi^m$ may be written as:[141]

$$\Phi^m = -\mu_e^m + F\chi^m \qquad (1.3.1)$$

where $\mu_e^m$ is the chemical potential of an electron in the electrode and $\chi^m$ is known as the electron overlap potential difference. The former quantity takes into accont the nature of the electrode material bulk, whereas the latter is related to the nature of the crystal face concerned.

In the case where the electrode is in contact with an aqueous electrolyte, the definition of the work function may be expressed by the following expression:

$$\Phi^m = -\mu_e^m + Fg^m - Fg^s \qquad (1.3.2)$$

where *g* refers to the dipole potential difference caused by the electrified double layer formed in the vicinity of the electrode surface.

In the discussion on the effect of the electrode material on the behaviour of electrochemical reactions, it is useful to consider two general limiting cases: (i) the weak interaction between the reactants and the electrode surface, *e.g.* no adsorption occurs at the electrode

surface, and (ii) the strong interaction between the reactants and the electrode surface, *e.g.* when a single or several reactants or intermediates adsorb at the electrode surface.

Thus, in the former case, it has theoretically been shown[142] that no effect on the electrode material can be anticipated on the value of the rate constant for simple electron transfer. Experimental results[143] regarding single-electron transfer reactions confirmed that the activation energy was independent from the material nature, though they suggested the existence of a dependence of $\log i_0$ upon the work function, $\Phi$. This behaviour was predicted by Parsons[144] on the basis of double layer effects. In addition, the importance of the work function in double layer studies and in electrochemical kinetics has been reviewed by Trasatti.[145] Conversely, in cases of weak interaction between either the reactants or the intermediates with the electrode surface, it has long been considered that the nature of the electrode material has no impact upon the work function and, consequently, the electrode may be considered as an inert substrate which simply acts as a source or sink of electrons.[142]

In single-electron transfer catalysis at the electrode-solution interface, the catalytic activities of different substrates towards a particular reaction are typically compared by determining the standard rate constant $k^0$. Recall that $k^0$ is a measure of the kinetic facility of a redox couple. Hence, for large values of $k^0$, the system achieves equilibrium on a short time scale whereas for small $k^0$ values, the formation of the equilibrium is sluggish. Consequently, since $i = \left(\frac{n}{v}\right) F k'^0 a_i$, the exchange current density for an electrochemical reaction at an electrode of a particular material emerges as the primary criterion of electrocatalytic activity towards a particular reaction.

There are, however, several drawbacks with this practice. Bockris and Khan[146] mentioned that a comparison of $i_0$values takes no account of the influence of the transfer coeficient $\alpha$ which from the point of view of energy lost in overpotential has a significance comparable to that of $i_0$. Therefore, other parameters such as the overpotential, $\eta$, or the Tafel slope, $b$, are also used to effectively compare different electrocatalytic materials. Note that Tafel slope represents the relationship between the current density, $i$, and the overpotential $\eta$. This approach allows the comparison of electrocatalysis at typical operating current densities found in practical applications such as alkaline water splitting electrolysis reactors and fuel cells. Thus, in a nutshell, and from an electrical point of view,

an optimum electrocatalyst should show: (i) high values of $i_0$, (ii) low Tafel slopes, $b$, and (iii) low overpotential $\eta$ at a fixed operating current density (typically 10 - 100 mA $cm^{-2}$).

Earlier in this section, it was stated that the presence adsorbed species, either reactants or intermediates, on the electrode surface cause a significant impact on the electrocatalytic behaviour of an electrode. This impact is especially significant when dealing with multistep electrode reactions. Consider the following case: a general multistep electrode process must be written as:

$$R \rightarrow T + e^- \rightarrow O \tag{1.3.3}$$

where T is a reaction intermediate species with a formation step that is rate determining (RDS). If the process takes place at an electrode which catalyses the reaction and T is adsorbed on the electrode surface, then the formation of T occurs with lower Gibbs free energy of activation than it would otherwise. If potential energy curves are envisaged analogous to those in fig. 1.2.1, the adsorption of T brings about a vertical lowering of its Gibbs energy curve. The rate of reaction can then be represented as eqn. 1.3.4 if it is assumed that $\theta_T \rightarrow 0$:

$$i = FAk'^0 c_R \exp\left[\frac{\alpha F \eta}{RT}\right] \exp\left[-\frac{\alpha \Delta G'^0_{abs,T}}{RT}\right] \tag{1.3.4}$$

where A is the surface area in $cm^{-2}$, $c_R$ is the concentration of reactant species. All the other parameters keep their usual meaning. As previously mentioned, one of the approaches to compare the electrocatalytic properties of different electrodes consists in examining the current density, $i$, for each electrode at a given value of overpotential, $\eta$. As a result, and considering eqn. 1.3.4, the only free variable will be the Gibbs free energy of adsorbed species, T, $\Delta G'^0_{ads,T}$. Consequently, for different materials at constant $\eta$:

$$\ln i \propto -\Delta G'^0_{ads,T} \tag{1.3.5}$$

Eqn. 1.3.5 predicts that the rate of the electrode reaction increases proportionally as $\Delta G'^0_{ads,T}$ changes from positive values (non-bonding conditions or very weak adsorption) to negative values (very strong adsorption). However, since the fractional coverage $\theta_T$ of intermediate T increases as $\Delta G'^0_{ads,T}$, the assumption of $\theta_T \rightarrow 0$ is no longer valid when comparing different catalytic materials. From this view, eqn. 1.3.4 should be rewritten as:

$$i = FAk'^{0}(1-\theta_T)c_R \exp\left[\frac{\alpha F\eta}{RT}\right]\exp\left[-\frac{\alpha\Delta G'^{0}_{ads,T}}{RT}\right] \quad (1.3.6)$$

In the case where $\theta_T$ can be described by the Langmuir isotherm, the $(1-\theta_T)$ term, to a first approximation, decreases quicker, with decreasing $\Delta G'^{0}_{ads,T}$, than the equivalent rate of increase of the second exponential term. This implies that:

$$ln\, i \propto \Delta G'^{0}_{ads,T} \quad (1.3.7)$$

Since eqns. 1.3.5 and 1.3.7 predict opposing behaviour, the observed experimental behaviour can be understood as a combination of these two factors, and thus at a given value of $\Delta G'^{0}_{ads,T}$ which value depends on the electrode material, the current density will be determined by whichever factor produces the slowest rate.[147] Fig. 1.3.1 is commonly known as the volcano plot and it is based on Sabatier's principle[148] which states that the adsorption energy of intermediate species T should be neither too negative nor too positive. This is sometimes called the Goldilocks effect in catalysis. For example, if it is too positive, adsorption is slow and hence it limits the overall rate of the reaction. In contrast, if it is too negative, desorption is slow which also limits the overall rate of the reaction. Therefore, the maximum electrocatalytic effect occurs at the apex of the volcano curve, where $\Delta G'^{0}_{ads,T} = 0$.

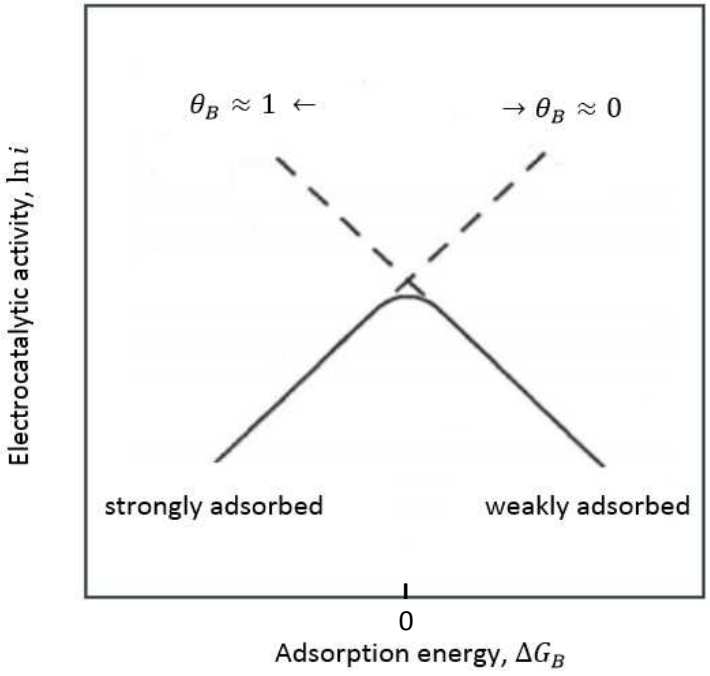



Figure 1.3.1 Schematic representation of an ideal volcano curve in electrocatalysis, where the adsorption of T is the RDS. Adapted from Ref.[147]

The formation of an apex suggests that the strenght of the bonds formed with the surface is equal to that of the bonds broken to form the intermediate T. Both dashed lines in fig. 1.3.1 represent the predicted behaviour of eqns. 1.3.5 and 1.3.7. Hence, optimal catalysis occurs when the binding of the critical reaction intermediate is just right as was the case with Goldilocks and the not too hot not to cold porridge.

### 1.3.2 Hydrogen Evolution Reaction

Although the present work is principally concerned about the anodic oxygen evolution reaction (OER), it seems opportune to devote some attention to the cathodic hydrogen evolution reaction (HER) as well, since, according to Bockris and Khan[146] this "acts as the archetype for the study of electrochemical reactions, for it involves simple versions of features which are met nearly all of them". The net water reduction reaction in acid and base are presented in eqns. 1.3.8 and 1.3.9, respectively.

$$\text{Anode: } 2H_2O \rightarrow 4e^- + 4H^+ + 2O_2 \quad (1.3.8a)$$

$$\text{Cathode: } 2H^+ + 2e^- \rightarrow H_2 \quad (1.3.8b)$$

and

$$\text{Anode: } 4OH^- \rightarrow 2H_2O + O_2 + 4e^- \quad (1.3.9a)$$

$$\text{Cathode: } 2H_2O + 2e^- \rightarrow H_2 + 2OH^- \quad (1.3.9b)$$

It is worth to point out that the HER is the cathodic reaction that occurs at the counter-electrode in aqueous solution, while the oxygen evolution reaction takes place at the working electrode. It is commonly agreed that the HER proceeds in two elementary steps, with only one intermediate reaction involved, following the discharge-electrochemical desorption mechanism (Volmer-Heyrovsky reaction).

The first step is known as the Volmer step, and involves the displacement of water molecules with the adsorption of hydrogen atoms on the electrode surface:

$$H_3O^+ + M + e^- \rightarrow MH_{ads} + H_2O \quad (1.3.10a)$$

$$H_2O + M + e^- \rightarrow MH_{ads} + OH^- \quad (1.3.10b)$$

where M is considered to be an active site on the electrode surface, which tipically is a metal. Eqn. 1.3.10a refers to the reaction in acid solution, while eqn. 1.3.10b refers to base media.

There are two different pathways for the second step, which brings about the detachment of molecular hydrogen from the surface. The first possible pathway is that the step occurs by chemical desorption *via* the following reaction, known as the Tafel step, which is identical in either acid or base media:

$$MH_{ads} + MH_{ads} \rightarrow H_2 + 2M \quad (1.3.11)$$

Alternatively, the desorption process may consist of a second discharge of $H_3O^+$ or $H_2O$, in case of acid or base media, respectively, which takes place on top of the adsorbed H produced by the Volmer step:

$$MH_{ads} + H_3O^+ + e^- \rightarrow M + H_2 \quad (1.3.12a)$$

$$MH_{ads} + H_2O + e^- \rightarrow M + H_2 + OH^- \quad (1.3.12b)$$

The reaction in eqn. 1.3.12 is known as the Heyrovsky step, where eqn. 1.3.12a refers to the reaction occurring in acid conditions and eqn. 1.3.12b in base condition. Note that either step in each pathway can be the RDS. Therefore, the alternative pathways may be described by the hydrogen evolution reaction: (i) Volmer–Tafel, (ii) Volmer–Heyrovsky, or (iii) Heyrovsky– Tafel.

If the reaction proceeds *via* the combination of the Volmer-Tafel, then the pathway will be known as the catalytic path.[21] In the catalytic path, if eqn. 1.3.10 is considered to be rate determining, the fractional surface coverage of adsorbed hydrogen $\theta_H$ will be small given that it will be rapidly consumed as it arrives to the electrode surface following eqn. 1.3.11; this situation is known as the Volmer mechanism. On the contrary, if the chemical recombination step is rate determining, the surface coverage of adsorbed hydrogen will be larger than that in the Volmer mechanism. This second scenario is known as Tafel mechanism. The combination of the Volmer-Heyrovsky steps is known as the electrochemical desorption path.[21]

The same scenario than that for the Volmer-Tafel exists in the Volmer–Heyrovsky steps, the Volmer step may again be the rate determining, or alternatively, the Heyrovsky step may limit the kinetics. The latter case is referred to as the Heyrovsky mechanism and if it is operative, it can be expected that $\theta_H \rightarrow 0$. The micro kinetic kinetic analysis, based upon a pseudo-equilibrium approximation, and with the assumption of a Langmuir adsorption isotherm, it can be shown that the mechanistic parameters listed in Table 1.3.1 are obtained.

| | | $\theta_H \rightarrow 0$ | | $\theta_H \rightarrow 1$ | |
|---|---|---|---|---|---|
| Path | RDS | $m$ $\left(d\ln i/d\ln c_{H_3O}\right)_\eta$ | $b$ $\left(d\eta/d\ln i\right)$ | $m$ $\left(d\ln i/d\ln c_{H_3O}\right)_\eta$ | $b$ $\left(d\eta/d\ln i\right)$ |
| Volmer- Tafel | 1.3.10 | 1 | $-2RT/F$ | – | – |
| Volmer-Tafel | 1.3.11 | 2 | $-RT/2F$ | 0 | $\infty$ |
| Volmer-Heyrovsky | 1.3.10 | 1 | $-2RT/F$ | – | – |
| Volmer-Heyrovsky | 1.3.12 | 2 | $-2RT/3F$ | 1 | $-2RT/F$ |

Table 1.3.1 Kinetic analysis of the various possible pathways for the HER. Tafel slopes, *b*, and reaction orders, *m*, predicted by a formal kinetic analysis under the assumption of a Langmuir adsorption isotherm and assuming a transfer coefficient $\beta = 0.5$.

At low overpotentials and low surface, coverage results in Tafel slope of ln RT / (1+β)F = 39.4 mV dec$^{-1}$ and ln RT / βF = 118.3 mV dec$^{-1}$ at 25°C. Regarding the Volmer-Tafel mechanism, under identical conditions than that for Volmer-Heyrovsky mechanism, and considering the Tafel step to be RDS, the resulting Tafel slope is ln RT/2F = 29.6 mV dec$^{-1}$ at 25°C. If, however, the overall reaction is considered to be limited by the Volmer step, the obtained Tafel slope is ln RT/βF = 118.3 mV dec$^{-1}$. At high overpotentials, when the process is limited by the rate of chemical reaction, the current becomes independent from the overpotential and the Tafel slope becomes infinite. This effect may be observed when a plateau region at high overpotentials on Tafel slope plots is formed.

As noticed in Table 1.3.1, the electrochemical oxide path for the OER presented in eqn. 1.3.12 is analogous to the anodic equivalent of the Heyrovsky mechanism, since both

mechanisms consist of an electrochemical step involving the adsorption of the intermediate species, followed by a rate-determining step involving the desorption of such intermediate specie. Therefore, the formal mathematical kinetic analysis of these two cases under pseudo-equilibrium is very similar.

If the strength of adsorption depends on surface electrical interactions between adsorbent and catalyst, a correlation of the reaction rate and d-band or d-vacancy of simple metals is to be expected. In 1946 Bockris[149] mentioned that there existed a linear relationship between the exchange current density, $i_0$, for the HER and the work function Φ of the electrode metal. He found that for the "soft" s-p metals in acid media, the $i_0$, was inversely proportional to Φ whereas $i_0$ of transition metals was direct proportional with the work function. This concept was further investigated by Conway and Bockris[150] in 1957. They observed opposite interaction between the $i_0$ and the metal-hydrogen bond strength. According to them, the s-p metals showed a catalytic effect on the rate for HER, increasing the metal-hydrogen bond strength, whereas the reaction rate decreases exponentially with this bond strength in the case of transition metals. Analogously to fig. 1.3.1, Trasatti[137] plotted the logarithm of the exchange current densities, log *i*, of different metals, against the metal–hydrogen, M-H, bond strength. This relation is presented in fig. 1.3.2.

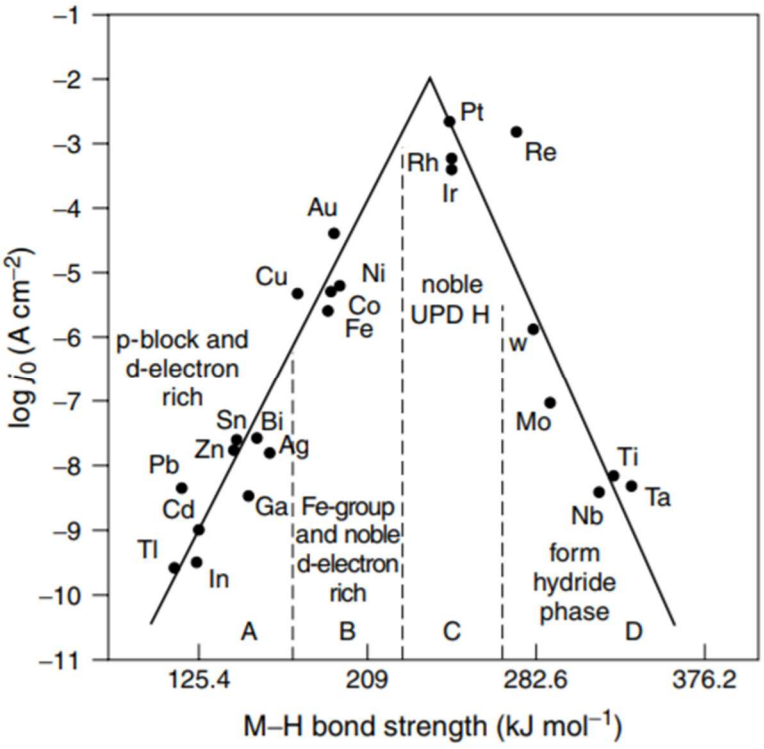



Figure 1.3.2 Experimental volcano plot of the standard exchange current density, log $i_0$, versus M–H bond energy on different metals. Reproduced from Ref.[151] based on Ref. [137]

Here, the catalyst's performance can be quantitatively evaluated by the position of its $i_0$ and M-H bond strength values relative to the volcano peak, *e.g.* the closer the position of these values to the peak, the better the catalyst is. Conway and Bockris[150] determined that the RDS of the HER in acid media, using metals with soft M-H bond strength (left hand side of the volcano plot), is often limited by the adsorption step (Volmer step) whereas if a metal with strong metal-hydrogen bond strength is used (right hand side of the volcano plot), the RDS is typically a desorption step (either Tafel or Heyrovsky step). This arises since on the left-hand side of the volcano plot the adsorption of hydrogen is difficult and is therefore RDS, while on the right-hand side the desorption of adsorbed hydrogen is difficult, since the stronger the M-H bond is, the more difficult is the desorption of the molecular hydrogen, and thus, the desorption becomes rate determining.

There are several problems with this approach: first, the volcano plot is only valid if the mechanism (as determined by the Tafel slope) is the same on each of the metals.[152] However, kinetic data used for the construction of fig. 1.3.2 were determined under different experimental conditions and even in solutions of widely varying pH. Furthermore, the nature of the electrode surface in contact with the solution is also different for different metals, since only some metals form stable oxides and/or hydrides. This is especially important given that two types of hydrogen can coexist together on certain metals, these being the under potential H (UPH) and the overpotential H (OPD), and only a weakly adsorbed OPD H will get involved in the HER. However, the adsorption energies used to create the volcano curve correspond to the under potential deposition (UPD) process. Finally, the M–H bond energies were taken from the gas phase reactions considering $\theta_H \rightarrow 0$. Despite all the caveats mentioned above, the volcano curve representation is a powerful and useful way to experimentally compare the catalytic activities of the metals. However, special care should be taken when comparing catalytic properties of metals for the HER using the volcano plot.

### 1.3.3 Further Observations on Electrocatalysis

As introduced in section 1.3.1, the variation of the standard Gibbs free energy of adsorption $\Delta G_{ads}^{\prime 0}$ of a given reaction intermediate on various metal electrodes leads to the formation of a volcano plot at a specific adsorption conditions. It has been also shown previously that approximate volcano relations do exist for the HER on metals[137] and for

the OER on transition metal oxides.[153] Similarly, to what was done for HER, Trasatti also correlated the catalytic activity towards the OER on various transition metal oxides in acid solutions. The results achieved by Trasatti are presented in fig. 1.3.3:

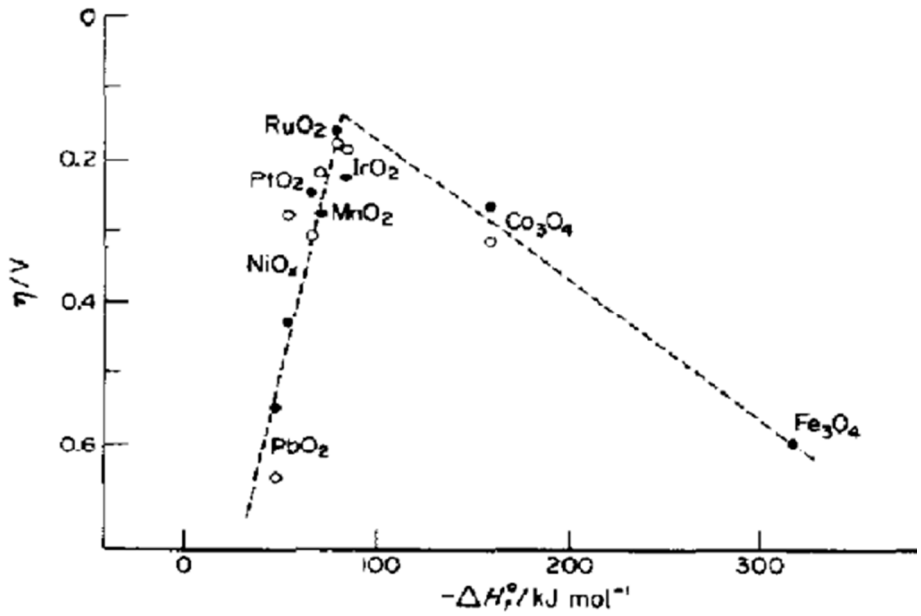



Figure 1.3.3 Volcano plot for the oxygen evolution overpotential on various oxides as a function of the enthalpy of lower to higher oxide transition. The black and the White dots represent acid and alkaline solution, respectively. Reproduced from Ref.[154]

Several discrepancies exist between the volcano plot for HER and OER. The most obvious one is that related to the symmetry of the curve: the volcano plot for the OER is strongly asymmetric whereas that for the HER is strongly symmetric. This asymmetry may arise from the formation of mixed oxides. For example, it has been pointed out that the catalytic activity of the Ni-Co mixed oxide electrodes exhibit a maximum when $NiCo_2O_4$ is the major phase in the electrode.[155] If the value on the x-axis is assumed to change linearly with composition, the strong asymmetry leads to expect that a lower amount of Ni added to Co would be sufficient to reach the apex. The synergetic electrocatalytic effect of the Ni-Co spinel for OER in alkaline solutions will be presented in chapter 5.

It has also been pointed out that while metals, alloys, metal oxides and complexes have all been shown to exhibit, to some extent, good catalytic properties, the greatest catalysis performance are those electrodes based on the transition metals.[87c] The most active metals for HER and OER are the noble metals Pt, Re, Rh and Ir. Amongst the most important of

these oxides are the thermally prepared $RuO_2$ and $IrO_2$, which exhibit high electrocatalytic activity for the chlorine and oxygen evolution reaction both in acid and base solutions. Nevertheless, on an industrial scale, their high cost and low stability in alkaline media make them impractical for hydrogen production.[156] Much deeper interest has been put into abundant transition metal oxides such as nickel, cobalt or manganese have been reported for OER. They have a competitive price, high electrical stability in alkaline media and an acceptable OER performance.[157]

A common approach in the optimisation of electrocatalysis is the empirical search for synergetic effects. This search is based upon the Brewer–Engel theory[158] which predicts that alloying metals of the left half of the volcano curve, which have empty or half-filled vacant d-orbitals, with metals of the right half of the volcano curve, which have internally paired d-electrons not available for bonding, a maximum in bond strength and stability is observed. In view of this, alloying the much cheaper and abundant transition metals with noble metals should lead to a synergetic effect on the activity towards the HER, with the activity dependant on the exact composition of the alloy, and the method and conditions of alloying.[159] Jakšić has applied this theory in predicting and explaining the enhanced activity towards the HER of several metal alloys.[160] Alloying transition metal oxides may also exhibit an enhancement on the catalytic activity of the material. It is widely believed that nickel along with cobalt generates a synergetic metal oxide, $NiCo_2O_4$, which has been reported as a stable catalyst in alkaline media for oxygen evolution reaction.[161] The electrocatalytic activity of a metal oxide material is proportional to its active surface area, which may be correlated to the crystal structure and the film morphology of the electrode surface. The $NiCo_2O_4$ possesses a high number of active sites and better conductivity than NiO and $Co_3O_4$ (this is of about two orders of magnitude higher), which exhibits not only large power density but also high energy density (up to 35 $W{\cdot}h{\cdot}kg^{-1}$). Most of the recently published work on the OER has focussed on the search for synergetic catalytic effects, as it will be further explained later in this thesis.

As mentioned earlier in section 1.3.1, the singular catalytic behaviour of transition metal oxides lies in the nature of the outer d-shell.[139] The specific configuration of their last electronic shell possesses unpaired d-electrons, and unfilled d-orbitals that may be available to form bonds with the adsorbed species. The enthalpy of adsorption depends on the number of unpaired d-electrons and on their energy levels. For example, in heterogeneous gas phase reactions[162] catalysed by transition metals, it has been found that

a correlation between d-band character and reaction rate exists. The more unpaired electrons that a transition metal has in its d-band, the lower the percentage of d-band character it is said to possess. The d-band character of a metal is defined as the easiness of its atoms in losing electrons. Therefore, for a reaction with a rate-determining adsorption step, the most suitable catalyst would be the one with a low-percentage d-band character. Contrary, for a desorption RDS the best catalysts would be the one with high d-band character.

The discussion so far has focused on the electronic behaviour of metals which may affect the catalytic behaviour of a given electrode material. However, the electronic configuration is not the only parameter defining a good catalyst. Geometric properties also play an important role in the catalytic activity of a metal. Properties such as grain size, concentration of surface defects, crystal structure, inter-atomic distance and defect type may have a significant impact on the electrocatalytic activity of a material. Also, the catalytic activity of a material may change with the preparation method used. In this view, Trasatti[154] noted that for the same electrode material, different preparation techniques displayed differences in the $\ln i_o$ values and Tafel slopes. Such behaviour was attributed to crystal particle size and surface defects. According to Appleby[163], the specific surface area and the surface distribution of catalytic active sites between crystal faces, edges and corners depends on the physical dimensions of crystallites or particles.

## 1.4 The Surface Electrochemistry of Nickel, Iron, Cobalt and Manganese

It is well known that, at potentials where the OER occurs in aqueous solution, metallic electrodes are typically covered by a hydrous oxide film. It is to be noted that any type of porous structure allowing intimate contact between the solid and aqueous phase is likely to yield to a hydrous phase. Therefore, to understand the principles that govern the OER, it is also essential to understand the nature of the substrate on which it occurs. In this sense, factors such as the oxidation state of the metal sites on the oxide film, the morphology and the degree of oxidation are to be considered. Various techniques were utilised in the determination of such factors, and as it will be stated below, among these the most important ones are the cyclic voltammetry and electrochemical impedance spectroscopy.

### 1.4.1 Nickel

Nickel is probably the most studied metal among all those used in electrochemistry. This section focuses on the redox switching behaviour of two forms of nickel: (i) hydroxides, and (ii) oxyhydroxides. Nickel hydroxides have been used as the main material in working electrodes for several alkaline batteries, *e.g*. the commercially important nickel-cadmium batteries (NiCad) and the pure nickel metal hydroxide battery (NiMH). In addition, its abundance and inexpensiveness (as compared to metals such as $RuO_2$ or $IrO_2$) make nickel and some of its alloys to be the preferred materials for use in alkaline electrolysis.[164]

Seghiouer *et al*.[165] observed that a bright polycrystalline Ni electrode had an OCP of -0.4 V *vs*. Hg/HgO in 1.0 M NaOH solution, which led to the conclusion that on immersion of metallic Ni into 1.0 M NaOH electrolyte an instantaneous layer of nickel hydroxide gets formed following the reaction.[166]

$$NiO + H_2O \rightarrow Ni(OH)_2 \qquad (1.4.1)$$

Further hydroxide growth is inhibited by applying negative potentials to the electrode. With the aim of reviewing the electrochemistry of polycrystalline nickel in aqueous alkaline media, the reproduction of a typical cyclic voltammogram is presented in fig. 1.4.1. A similar cyclic voltammogram (CV) is presented in several publications in the literature – random examples include publications of Burke *et al*.[167], Visscher and Barendrecht[168], de Souza *et al*.[169], and Šimpraga and Conway[170] to name but only a few.

Following literature precedents, the CV is normally split into three parts: regions (i) A, (ii) B, and (iii) C. Region A is known as the hydroxide region and is associated with the presence of nickel II. In this region a single anodic peak is observed at -0.8 to -0.6 V Hg/HgO in fig. 1.4.1. Note that the hydrogen evolution reaction is observed at lower negative potentials from region A, which is accompanied by hydrogen adsorption into the bulk Ni lattice. Some disagreement about the nature of the Ni (II) formed at these potentials exists. In this sense, some authors suggested that the oxide film in this region was a non-stoichiometric oxide consisting on NiO and $Ni_3O_4$.[171]

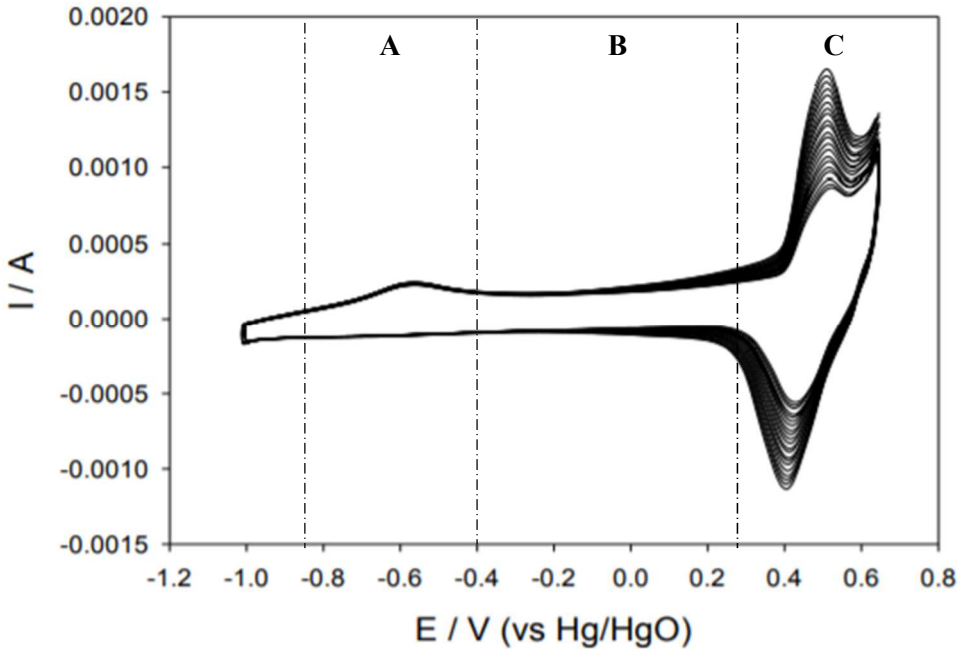



Figure 1.4.1 A typical CV of a polycrystalline Ni electrode in 1.0 M KOH at 25°C. The sweep rate was 350 mV $s^{-1}$. Reproduced form Ref.[172]

Others suggested the formation of α-$Ni(OH)_2$ along with the oxidation and expulsion of adsorbed hydrogen from the bulk, occurs at these potentials and, thus, the peak is to be associated with such processes.[173] In the latter case, the reaction may undergo as follows:

$$Ni + 2OH^- \rightarrow Ni(OH)_2 + 2e^- \qquad (1.4.2)$$

$$H_{ads} \rightarrow H^+ + e^- \qquad (1.4.3)$$

Burke and Twomey[167a] noted that the peak potential of this anodic peak varied with the pH in alkaline solutions. They proposed that both oxidation and hydrolysis processes take place in this potential region, yielding to the formation of a somewhat anodic species with formula $Ni(OH)_{2.4}^{-0.4}$. They also noted that if the anodic limit of the potential sweep was maintained just below -0.2 V *vs.* Hg/HgO, the formation of a cathodic peak, which was invariant to the pH, occurred. In view of this, they suggested that such cathodic peak may be the result of the initially produced anodic hydrous species, α-$Ni(OH)_2$, being reduced back to metallic Ni. Ellipsometry studies carried out by Souza *et al.*[169] found that the first layer of oxide formed in the vicinity of the anodic peak in the region A, consisted of NiO.

However, upon further increase of anodic potential, the NiO layer gets covered by a thick layer of $Ni(OH)_2$.

Burke and Twomey[167a] made an additional significant observation regarding the behaviour of the anodic peak upon repetitive potential cycling. They discovered that the peak potential remained approximately constant after numerous cycles, which lead to the relevant conclusion, in agreement with earlier works[173] that since it is the inner oxide layer the one that is reduced at significant cathodic potentials, the anodic potential on region A is associated with the oxidation of Ni metal to Ni (II) at the metal / porous metal hydroxide interface.

It is in the region B of fig. 1.4.1 where the irreversible transformation of $\alpha$-$Ni(OH)_2$ to $\beta$–$Ni(OH)_2$ occurs. It was found that further potential cycling from the upper limit of region B to negative potentials causes the diminution or even the disappearance of peaks in region A.[174] This has been attributed to the formation of $\beta$-$Ni(OH)_2$ which may not be reduced on the successive cathodic sweeps. McBreen found that further $\beta$-$Ni(OH)_2$ growth can be achieved by ageing the $\alpha$-$Ni(OH)_2$ by immersion in strong base for an extended period.

Region C is known as the oxyhydroxide region or the Ni (III) region. In this region a single anodic peak can be found at approximately 0.45 // 0.55 V, as shown in fig. 1.4.1. Since the potential in this region is enough to lead to the oxidation of most of the metals, the anodic peak is associated with the oxidation of $Ni(OH)_2$ to NiOOH. The relatively large anodic peak current is associated with further growth of NiOOH and is known to increase on repetitive potential cycling.[165, 167a] The Ni (II) to Ni (III) transitions are associated to the development of a charge storage film on nickel metal electrodes in alkaline solution. Therefore, it is the $Ni(OH)_2$ / NiOOH redox system that is of interest in the battery applications of nickel and nickel hydroxide electrodes. The oxidation of $Ni(OH)_2$ to NiOOH occurs *via* the reaction:

$$Ni(OH)_2 \rightarrow NiOOH + H^+ + e^- \qquad (1.4.4)$$

The above electrochemical reaction causes the expulsion of a proton from the Ni hydroxide layer, which is used to produce a water molecule under strong alkaline conditions.[175] If the potential is made more anodic, the surface bound oxy-nickel species increases its oxidation state from +3 to +4 according to eqn. 1.4.5:

$$\beta NiOOH + OH^- \rightarrow NiO_2 + H_2O + e^- \qquad (1.4.5)$$

Lu and Srinivasan[176] suggest that nickel (IV) oxide, $NiO_2$, may serve to inhibit the OER due to its poor conductivity. This is especially significant since the rising part of the profile arises due to the onset of active water oxidation. It is worth noting that the state of the electrode surface at potential values just below that at which the OER is the predominant process is largely influenced by the redox process occurring at the upper anodic peak.

A major advance in the understanding of the various nickel reactions in alkaline solutions was made by Bode *et al*.[177] in 1966. These authors rationalised the redox switching behaviour of nickel hydroxide films in terms of four phases, represented by the bode diagram in fig. 1.4.2. This bode scheme is presented in its traditional cyclical formation and also is a useful graphical format reproduced from a recent review paper.[177] According to fig. 1.4.2, the discharged or reduced $Ni(OH)_2$ material may exist in two different states: (i) the hydrous phase α-$Ni(OH)_2$, and (ii) the anhydrous phase β-$Ni(OH)_2$. Oxidation of the β-$Ni(OH)_2$ material is envisaged to produce a phase referred to as β-NiOOH, whereas the oxidation of the α-$Ni(OH)_2$ material produces γ-NiOOH. It can also be seen from fig. 1.4.3 that upon ageing, the α-$Ni(OH)_2$ can dehydrate and recrystallise as β-$Ni(OH)_2$.

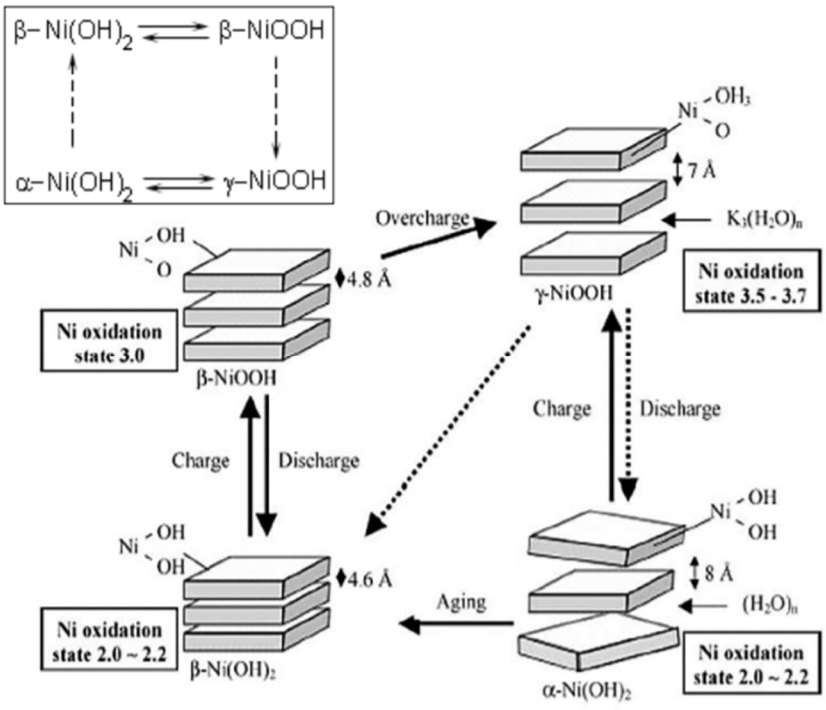



Figure 1.4.2 Graphical representation of the Bode scheme for the $Ni(OH)_2 \rightarrow NiOOH$ redox transformation in alkaline solution. Reproduced from Ref. [172] Inset – More traditional representation of the Bode scheme.

This transformation is favoured as the alkalinity of the contacting electrolyte solution increases. Furthermore, upon overcharge, β-NiOOH can convert into γ-NiOOH. Bode *et al*.[177] demonstrated another redox reaction between the α-$Ni(OH)_2$ and the γ-NiOOH. The α/γ transformation may involve more than one electron transfer per nickel atom, the number of electrons transferred being determined by the nature of the anions and the cations present in the solution.

Bode also envisaged and experimentally demonstrated that the oxidation of α-$Ni(OH)_2$ to γ-NiOOH would occur at a lower potential than the redox transition between the two β phases.[177] It is important to note that, while there is a general acceptance for the general features of the bode diagram, the four phases of bode scheme should be considered as limiting forms of divalent and trivalent materials. The actual composition of the oxide film at a given potential depends on a range of different factors, such as the method of preparation, the degree of hydration, the electrolyte's nature and concentration, the presence of defects etc. It should be noted, however, that in recent years there has been several proposed modifications to the Bode diagram. In this sense, Makrides[178] suggested the existence of additional phases to those described by the traditional Bode model. They argued that a third Ni (II) phase was formed from metallic nickel at low potentials and denoted it as compact α-$Ni(OH)_2$. Also, after a long period of oxygen evolution, an additional and more highly charged phase was said to be formed by γ-aged. Another phase was proposed by Yeo and co-workers.[179] Using Raman spectroscopy at the onset potential of the oxygen evolution, they suggested that the β-NiOOH phase would undergo to a phase called $\beta_{O2evolution}$, which shows differences to the previously mentioned γ-NiOOH. It should be noted that such phases may not be as defined as suggested by fig. 1.4.3.

Due to the slow transition behaviour from one phase to the other, the structure of the nickel oxyhydroxide phase analysed at a given time point may be, in fact, a transitional phase rather than a final phase. Bernard and co-workers[180] provided a good example of this when they were analysing the transformation from α-$Ni(OH)_2$ to β-$Ni(OH)_2$ and found a "badly crystallised β-$Ni(OH)_2$" corresponding to that transition phase.

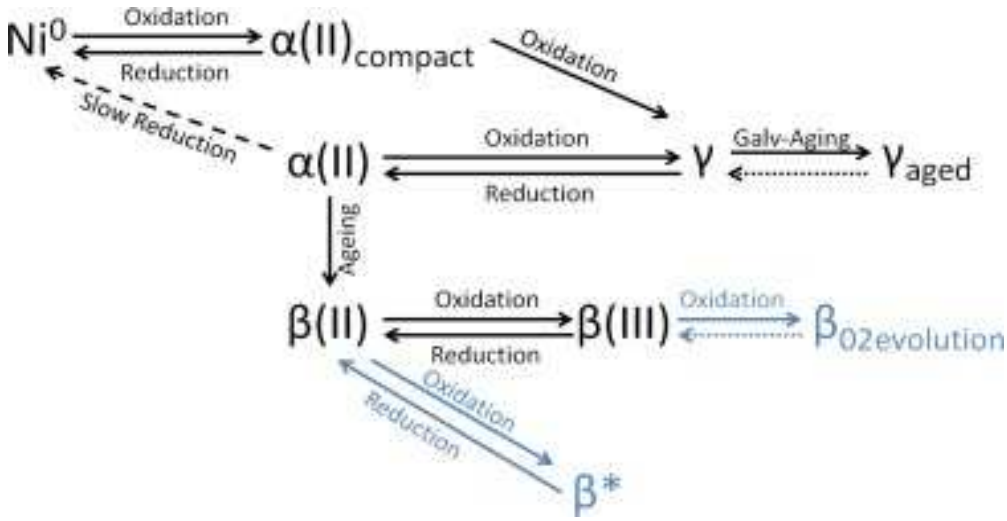



Figure 1.4.3 Updated model of nickel phases based on recent experimental data. Reproduced from Ref.[181]

In view of the singularities of the nature and the crystal structure of each of the four limiting model phases, a brief review of them is now considered. The definitive crystallographic review on β-$Ni(OH)_2$ was carried out by Greaves and Thomas.[182] Using powder neutron and X-ray diffraction studies they investigated the crystal properties of both a well crystallised deuterated $Ni(OD)_2$ sample pre-treated by a hydrothermal method, and a high surface area $Ni(OH)_2$ sample precipitated from a $NiSO_4$ solution upon the addition of KOH. These workers found that the structure of a high surface area precipitated β-$Ni(OH)_2$ is similar to that of the well crystallised material, though showing a larger number of defects related to a high concentration of surface $OH^-$ groups. Regarding the atomic disposition, the well crystallised β-$Ni(OD)_2$ sample adopts a brucite-type structure with layers of $Ni(OD)_2$ perfectly arranged along the c-axis, as seen in fig. 1.4.4. The cell arrangements for the $Ni(OD)_2$ layers consist of a hexagonal planar arrangement of $Ni^{2+}$-oxygen octahedral. McBreen[183] suggested that the nickel ions are all in the 001 plane configuration and are surrounded by six hydroxyl groups. The brucite structure of on β-$Ni(OH)_2$ is isomorphous with the divalent hydroxides of Ca, Fe and Co.[183] The unit cell parameter for the well crystallised $NiOD_2$ was found to be 3.126 Å while 0.973 Å was reported for the O-H bond length, whereas the high surface area sample had a unit cell parameter of 3.199 Å and a O-H bond length one of 1.08 Å. Based on these observations, Greaves and Thomas[182] concluded that the structure of the high surface area material, β-$Ni(OH)_2$ is similar to the well crystallised sample, but has a larger amount of defects

related to a high concentration of surface $OH^-$ groups. Typical XRD spectra[184] for both α-$Ni(OH)_2$ and β-$Ni(OH)_2$ are presented in fig. 1.4.5.

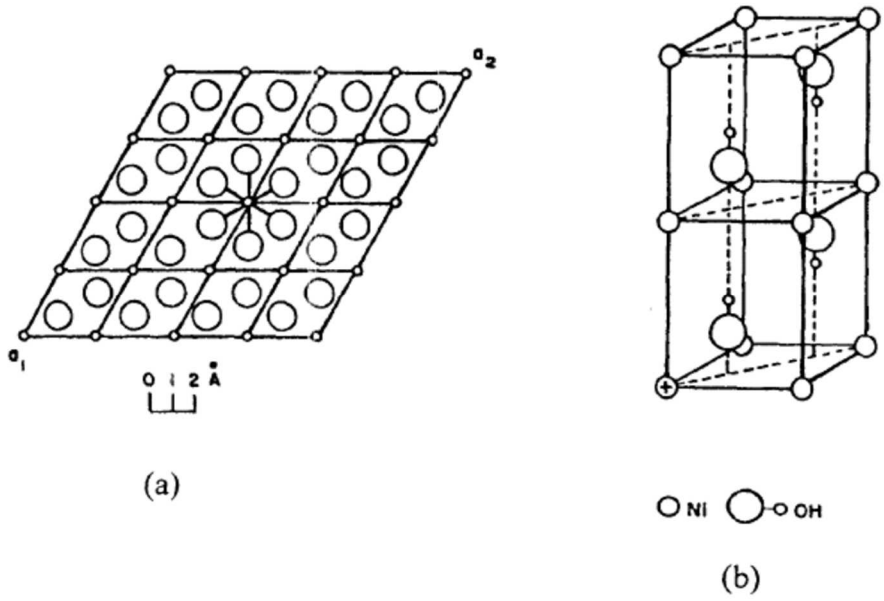



Figure 1.4.4 The brucite structure of β-$Ni(OH)_2$. (a) The hexagonal brucite layer-alternate O atoms are above and below the plane of the Ni atoms. (b) The stacking of the planes showing the orientation of the O-H bonds. Modified from Ref.[183]

Similar results are observed using more modern XRD instrumentation.[185] Comparison of the diffraction patterns in fig. 1.4.5 suggests that the A phase is notoriously more amorphous that the B phase since the latter displays more defined and intense peaks. According to Le Bihan and Figkarz[186] the main difference between α-$Ni(OH)_2$ and β-$Ni(OH)_2$ phases arises from the differences in the c-axis spacing, which are mainly due to the presence of water molecules and anionic species in the van der Waals gap which leads to the formation of a turbostratic phase. These water molecules should not be confused with the adsorbed water molecules on the electrode surface. Thermal gravimetric measurements carried out by Mani and deNeufville[187] showed that the adsorbed water molecules on the surface are removed at temperatures between 50°C and 90°C, while the intercalated water molecules are removed at higher temperatures up to 180°C.

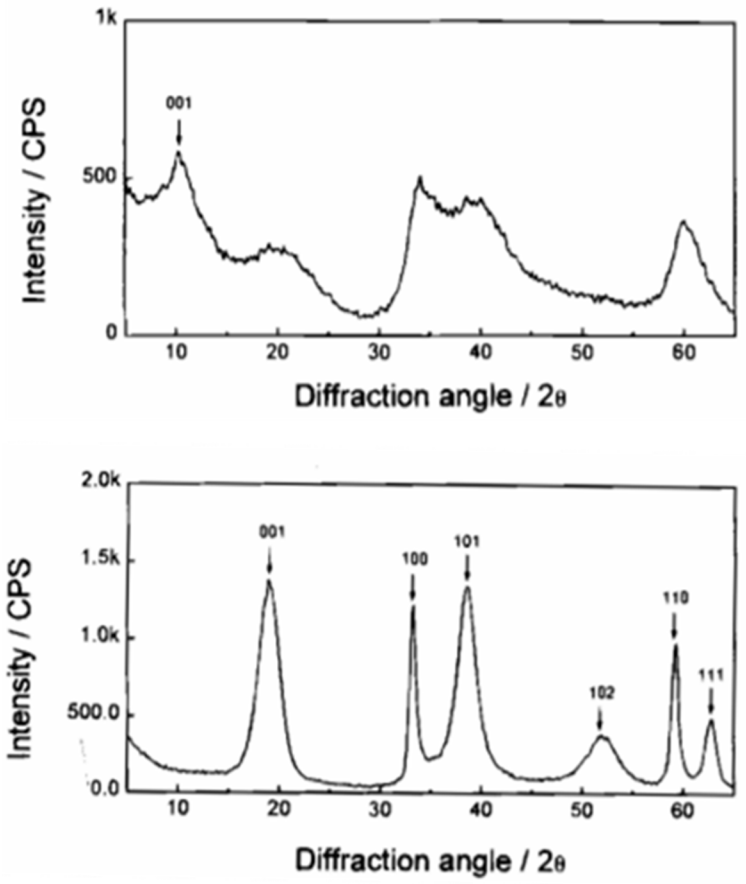



Figure 1.4.5 XRD patterns of a) α-$Ni(OH)_2$ and b) of β-$Ni(OH)_2$. Reproduced from Ref.[184]

Accurate determinations on the crystal structure of β-NiOOH and γ-$Ni(OH)_2$ are limited since these compounds are amorphous materials.[183] However, it is generally accepted that they do display a greater structural organisation than the α-$Ni(OH)_2$.[188] Upon oxidation, the unit cell parameters change from $a_0$ = 3.126 Å and $c_0$ = 4.605 Å for β-$Ni(OH)_2$ to $a_0$ = 2.82 Å and $c_0$ = 4.85 Å for β-NiOOH.[183] This suggests an expansion along the c-axis and a contraction in the in-plane Ni distance during the oxidation of β-$Ni(OH)_2$ to β-NiOOH.

Carpenter *et al*.[189] and Madou *et al*.[190] investigated the electronic conductivity of various Ni (II/III) structures. They found that the electronic conductivity of $Ni(OH)_2$ was a rather poor one, which is mainly due to its p-type conductivity nature with a band-gap of ca. 3.7eV.[189] On the contrary, they observed that β-NiOOH showed greater conductivity than its reduced form, that being mainly due to it displays n-type conductivity with an estimated band-gap of ca. 1.75 eV.[189] The enhanced conductivity of β-NiOOH compared to that of β-$Ni(OH)_2$ or γ-NiOOH (which has been found to have the lowest conductivity among all

the different nickel phases) is probably one of the reasons why the of β-NiOOH is referred to as "the right type of oxide" for OER catalysis.[176]

As previously noted in the discussion regarding the lower anodic/cathodic peak couple in the CV of polycrystalline nickel in alkaline solution (see fig. 1.4.1), it was postulated[167a], based on the variation of the anodic peak potential with pH, that the initially α-$Ni(OH)_2$ species in this potential range is anionic in nature. It has been observed[183] that the peak potential decreased linearly from 0.35 V *vs.* RHE at pH 9 to ca. 0.3V *vs.* RHE at pH 13 resulting into a potential/pH shift of approx. 13 mV $pH^{-1}$ unit. This behaviour is an example of the so-called super-Nernstian shift, a phenomenon that is often detected in peak potential/pH studies on electrochemically generated hydrous oxide films as reviewed by Burke and Lyons.[191]

According to eqn. 1.2.89, the potential shift of an ideal oxide electrode in aqueous solution at 25°C should decrease with increasing pH by 59 mV $pH^{-1}$ unit, with respect to a pH-independent reference electrode such as NHE. Note that if a pH-dependent reference electrode is used *e.g.* RHE or Hg/HgO, a potential shift of zero should be expected, since the potential of this type of reference electrodes also alters by 59 mV $pH^{-1}$ unit.

Burke and Lyons have also observed the super-Nernstian behaviour of anodic peaks for various hydrous oxide systems.[191] Although the mathematical treatment of the super-Nernstian shift of various hydroxides is beyond the scope of the present review, it is convenient to briefly summarize Burke and Lyons observations regarding the potential/pH shift behaviour. According to them, a positive potential shift on pH is indicative of an oxidised state that is more positive than the reduced state, whereas the opposite is true in the case of an observed negative potential / pH shift. They mentioned that from a thermodynamic point of view, potential / pH values greater than zero, in the RHE scale, are of thermodynamic significance since they imply that both the reactants and the products possess equal net charge. In accordance to the latter, Burke and Twomey[167b] observed a decrease in peak potential of ca. ½(2.303RT/F) V $pH^{-1}$ unit for an upper cathodic peak in the CVs of a multicycled Ni anode. They attributed the formation of this peak to the reduction of the γ phase to α-$Ni(OH)_2$. The authors hypostatised that the latter process was rationalised in term of the following equations:

$$[Ni(OH)_{3.5} * nH_2O]^{-0.5} * (Na^+)_{0.5} + e^- \leftrightarrow Ni(OH)_2 * nH_2O + 0.5Na^+ + 1.5OH^- \quad (1.4.6)$$

### 1.4.2 Iron

Typical cyclic voltammograms, reproduced from the literature, recorded for hydrous oxide layers and prepared using different numbers of growth cycles appear in fig. 1.3.9. The electrochemistry of iron, especially in acidic and neutral electrolyte solutions, has received much attention due to its fundamental relevance in understanding the mechanism of steel corrosion and the formation of corrosion resistant passive films.[192]

In corrosion processes, it is common to observe passivation of the film. Passivation describes the phenomenon of a given metal to substantially resist corrosion in an environment where thermodynamically there is a large free energy decrease associated with the passage from the metallic state to corrosion products. A notorious review of the corrosion dissolution and passivation of iron in various aqueous media has been presented by Bockris and Khan.[146] Special mention to the work carried out by Lyons *et al*.[123, 193] in the contribution of the electrocatalytic activity of iron electrodes in alkaline media is also due.

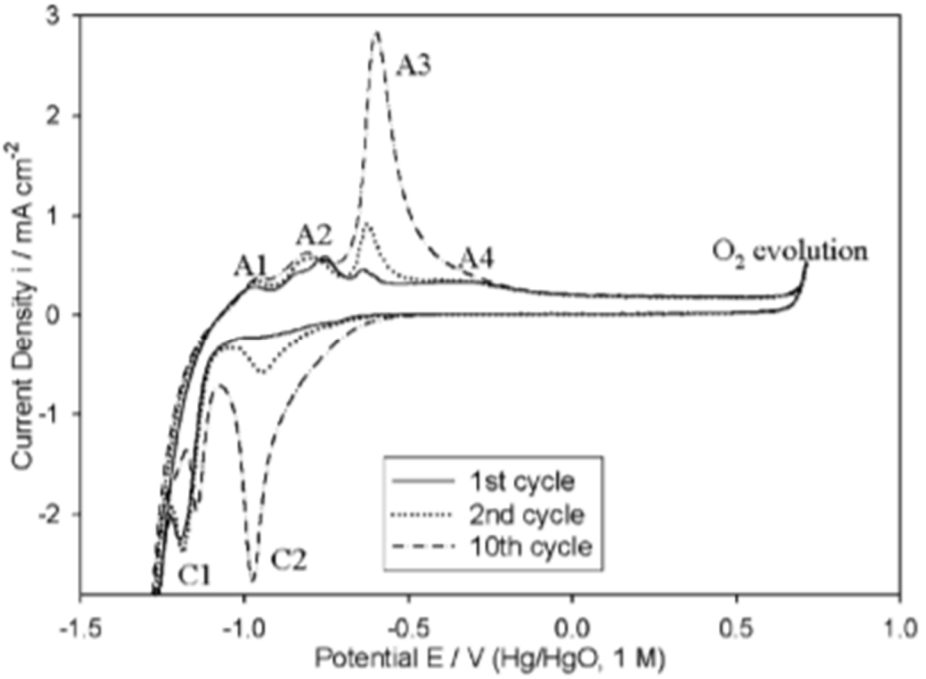



Figure 1.4.6 Typical CV representing the growth of hydrous iron oxide thin film on Fe support electrode recorded *via* analysis of the evolution of the real time voltammograms in 1.0 M NaOH. Reproduced from Ref.[123]

Upon repetitive potential cycling between the onset potentials for the HER and the OER, the formation of a hydrous oxide film occurs. At the first stages of oxidation (1 cycle), where the electrode has been previously polished to a bright finish, four well-defined anodic peaks (A1–A4) and two cathodic peaks (C1, C2) are typically observed (see fig. 1.4.6). These redox peaks reflect surface redox processes involving bound oxy-iron species.[194] There have been numerous proposals on the mechanism of the formation of the passive oxide film on Fe in alkaline solutions. There is general agreement[195] regarding the fact that peak A2 is due to the formation of ferrous ($Fe^{2+}$) species, whereas peak A3 and A4 have been attributed to the formation of ferric ($F^{3+}$) species.[191, 195c, 195d] It has been pointed out that the profile of the cyclic voltammogram for Fe electrodes depends on the nature of the potential perturbation applied.[195c] Following, a possible mechanism pathway proposed by Burke and Lyons[191] which has been shown to accurately correlate experimental data, is presented. Their scheme assumes that peak A1 is most likely due to the formation of a layer of adsorbed hydroxyl species:

$$Fe + OH^- \rightarrow FeOH_{ads} + 2e^- \qquad (1.4.7)$$

in combination with the electrochemical displacement of adsorbed hydrogen:

$$FeH_{ads} \rightarrow Fe + H^+ + e^- \qquad (1.4.8)$$

The peak denoted as A2 represents the conversion of both Fe and $FeOH_{(ads)}$ to a thin film of Fe(II) hydroxide or oxide according to:

$$FeOH_{ads} + OH^- \rightarrow Fe(OH)_2 + e^- \qquad (1.4.9)$$

$$FeOH_{ads} + OH^- \rightarrow FeO + H_2O + e^- \qquad (1.4.10)$$

In agreement with other workers[195c-f, 196], Burke and Lyons[191] proposed that peak A3 is associated to the following Fe(II) / Fe(III) surface redox transformation:

$$Fe(OH)_2 + OH^- \rightarrow FeOOH + H_2O + e^- \qquad (1.4.11)$$

These authors noted the fact that all but the complementary peaks A3 and C2 display a zero shift in peak potentials with respect to a pH dependence reference electrode over a

range of basic solution pH (7-14). It was found that A3 and C2 display a super-Nernstian shift of the order of ½ (2.303RT/F) V $pH^{-1}$ units.[191]

The formation of the A3 peak along with its cathodic counterpart, peak C2, based upon the aforementioned super-Nernstian shift, suggests that the operative reaction is not the formation of species such as $Fe_2O_3$ or FeOOH in a compact well-defined phase, but rather a Fe(II/III) redox transition in a polymeric micro-dispersed hydrous oxide layer. Such a phase is conceived to result from the hydration of the outer regions of the $Fe(OH)_2$ or FeO film. Hence, by analogy with a scheme proposed by Burke and Whelan[197] for redox switching of iridium oxide films, Burke and Lyons proposed that the main redox switching reaction may be given by:

$$[Fe_2(OH)_6(OH_2)_3]^{-2} + 3OH^- \rightarrow [Fe_2O_3(OH)_3(OH_2)_3]^{-3} + 3H_2O + 2e^- \quad (1.4.12)$$

Or, alternatively, by analogy to the Ni (II) to Ni (III) hydrous oxide transition of eqn. 1.4.4, as:

$$[Fe(OH)_{3.5} \cdot nH_2O]^{-0.5} \cdot (Na^+)_{0.5} + e^- \leftrightarrow Fe(OH)_2 \cdot nH_2O + 0.5Na^+ + 1.5OH^- \quad (1.4.13)$$

Peak A4 is also related to an Fe(II) / Fe(III) redox transition. However, at this potential, it is the inner more amorphous region of the Fe (II) species that is oxidised in the region of the film close to the metal surface. Possibly, oxidation products are largely anhydrous phases of $Fe_2O_3$, $Fe_3O_4$ or FeOOH.

The cathodic peak C2 shows a similar super-Nernstian shift to that of peak A3, which the authors have attributed it to the reduction of the Fe (III) species in the outer hydrous region of the film. As for the C1 peak, its formation has been attributed to the reduction of the compact, anhydrous inner layer according to the following reaction:

$$FeO \cdot FeOOH + H_2O + 3e^- \rightarrow Fe + {FeO_2}^{-2} + H_2O + OH^- \quad (1.4.14)$$

Due to the changing nature of the cyclic voltammogram profile with repetitive cycling, it is reasonable to assume that there will exist differences between the oxide layer formed during the first anodic cycles and those formed in successive sweeps. As similar behaviour of Mn electrodes, the repetitive potential cycling in Fe electrodes results in the formation

of a thick yellowish brown hydrous oxide layer. This arises since more oxide is formed on the anodic sweep than that reduced on the following cathodic sweep. Hence, over several cycles, the excess of oxide will tend to accumulate on the electrode surface yielding to thickening of the hydrous oxide structure.

Burke and co-workers[198] have proposed a dual layer structure for the passive oxide films formed only at certain metals such as Ni and Ir. This mode, illustrated in fig. 1.4.7, proposes the presence of an inner amorphous compact anhydrous layer of general $MO_x$ formula where M are the metallic species. Behind the inner compact layer, the oxide becomes dispersed, polymeric, hydrous and gel-like in nature, and is assigned to the general $Mo_a(OH)_B(OH_2)_C$ formula.

From a structural point of view, ions in the inner compact amorphous layer form a rigid structure held by strong polar covalent bonds, while the outer oxide layer consists of a much more open crystalline structure through which ionic species can easily diffuse to the bulk solution. The dual layer model may be used to explain the structure of the oxyhydroxide film formed by repetitive potential cycling on Fe electrodes in alkaline media, presented by Burke and Lyons.[191] In this view, it is proposed that the passivating species is the anhydrous material of the compact inner layer, whereas the outer layer is formed by a hydrous oxide layer.

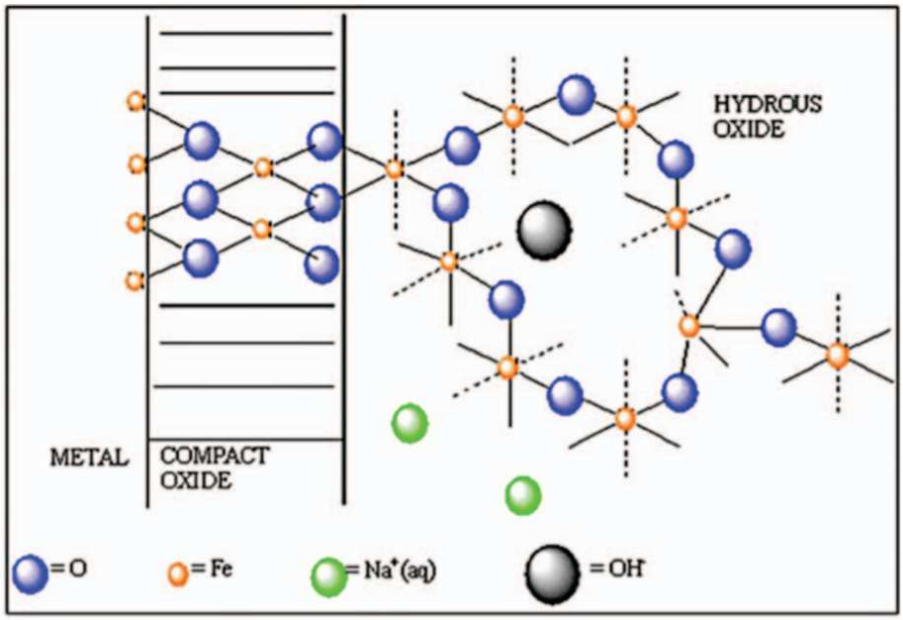



Figure 1.4.7 Schematic representation of the dual layer structure proposed for the hydrous oxyhydroxide, formed on Ni and Fe electrodes under potential cycling in aqueous alkaline solutions. Reproduced from Ref.[199]

The latter is supported by the fact that Fe oxyhydroxide films of various thickness exhibit a charge capacitance dependence on sweep rate, that is in line with Laviron's well known theory regarding redox polymer electrodes.[191, 200] This concept was further reinforced by spectroscopy studies carried out by Mossbauer.[201] Such studies revealed the presence of Fe in a hydrous, polymeric, gel-like form in the inner region.

Another observation made by Burke and Lyons[191], which may be applied to Mn oxide electrodes, is the fact that a repetitive anodising cycle near or in the OER may provoke the dissolution of the hydrous oxide film, since species such as $FeO_4^{-2}$ and $MnO_2$ may be prone to corrode under these extreme conditions.

### 1.4.3 Cobalt

Cobalt has been widely used as an additive to nickel electrodes. Among many of its advantages, the most important are: (i) the enhancement of the nickel electrode conductivity[202], and (ii) the reduction of the OER overpotential and the OER onset potential.[203] These two factors arise due to the fact that the addition of cobalt onto nickel electrodes yields to a minimisation of the amorphous phase γ-NiOOH growth which, as previously mentioned, shows the lowest conductivity among the other Nickel phases in fig. 1.4.2. Thus, if the conductivity of the electrode increases, then the catalytic activity of the electrode is expected to increase as well. According to Oshitani *et al*.[202] when either cobalt hydroxide $Co(OH)_2$ or cobalt oxide $Co_3O_4$ are added to a nickel electrode, the resulting enhanced catalytic activity is considered to be due to the presence of a highly conducting phase. This conducting phase arises from the precipitation of CoOOH around nickel hydroxide sites yielding to a good electrical pathway between them. A more detailed review of the properties of Ni-Co alloys will be presented later in this section.

As for Ni, a brief review is presented on the electrochemistry of polycrystalline Co in aqueous alkaline solutions with the intention of gaining a conceptual understanding of the oxide surface involved in the OER enhancement observed experimentally at high anodic potentials. Studies of Cobalt hydroxides were also covered by Bode *et al*.[177] as part of their seminal work. Analogously to the situation for divalent nickel hydroxides, cobalt oxides may exist in both the hydrous phase, α-$Co(OH)_2$ and the anhydrous phase β-$Co(OH)_2$.[177, 204] Also, the crystal structure of cobalt is similar to that of nickel, thus the α-Co(II) phase has a turbostratic structure, with a mean inter-lamellar distance of 8.4 Å[204b],

whereas the β-Co(II) has a brucite-like lamellar structure with the basal plane consisting of edge sharing $CoO_6$ octahedral.[204] In total, six species of cobalt oxide have been identified so far: (i) $CoO_2$, (ii) $Co_2O_3$, (iii) $Co_3O_4$, (iv) CoO, (v) $Co(OH)_2$ and (vi) CoOOH.[205] Shu-Hua Chien[206] observed that cobalt ions with an oxidation state of +3 [CoO(OH)], +8/3 [$Co_3O_4$] or +2 [CoO] may be obtained from $CoO_x$ by thermal decomposition at various temperatures. Thus, CoOOH, $Co_3O_4$ and CoO would be formed at temperatures around 280°C, 450°C and 950°C, respectively. Using XRD, he observed that the diffraction profile of CoOOH revealed a hexagonal structure with a divalent cobalt cation located at an octahedral site and coordinated by six hydroxyl oxygen. The average particle size of this phase was ca. 10 nm; $Co_3O_4$ profile revealed a spinel structure with an average particle size of ca. 11 nm whereas the CoO phase was found to be a face-centred cubic (FCC) arrangement with an average particle size of ca. 16 nm. Typical XPS patterns of the above phases are presented in fig. 1.4.8.

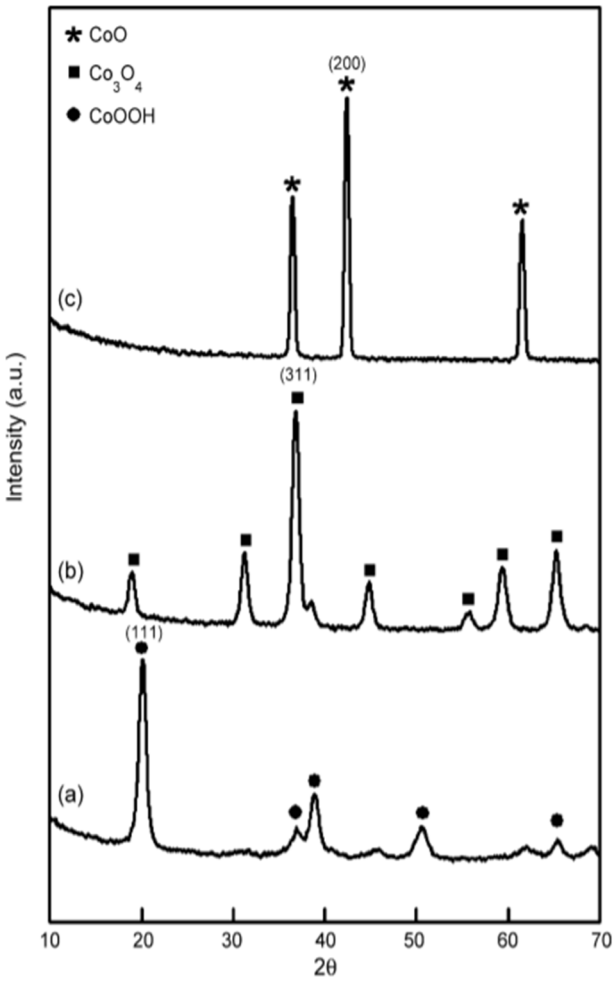



Figure 1.4.8 XRD profiles of (a) CoOOH (b) $Co_3O_4$ (c) CoO obtained from $CoO_x$ thermally decomposed in air at: 280°C, 450°C and 950°C, respectively. Reproduced from Ref. [206]

The spinel tricobalt tetroxide, $Co_3O_4$, has an energy band-gap of 1.4 – 1.8 eV that can be used as a p-type semiconductor. The distribution of cations on $Co_3O_4$ is assumed to be $Co^{2+}[Co_2{}^{3+}]O_4{}^{2-}$. The $Co_2{}^{3+}$ cations show an octahedral arrangement with the oxygen ions whereas $Co^{2+}$ shows a tetrahedral arrangement.

Cyclic voltammogram of polycrystalline Co in 1.0 M NaOH, is presented in fig. 1.4.9.

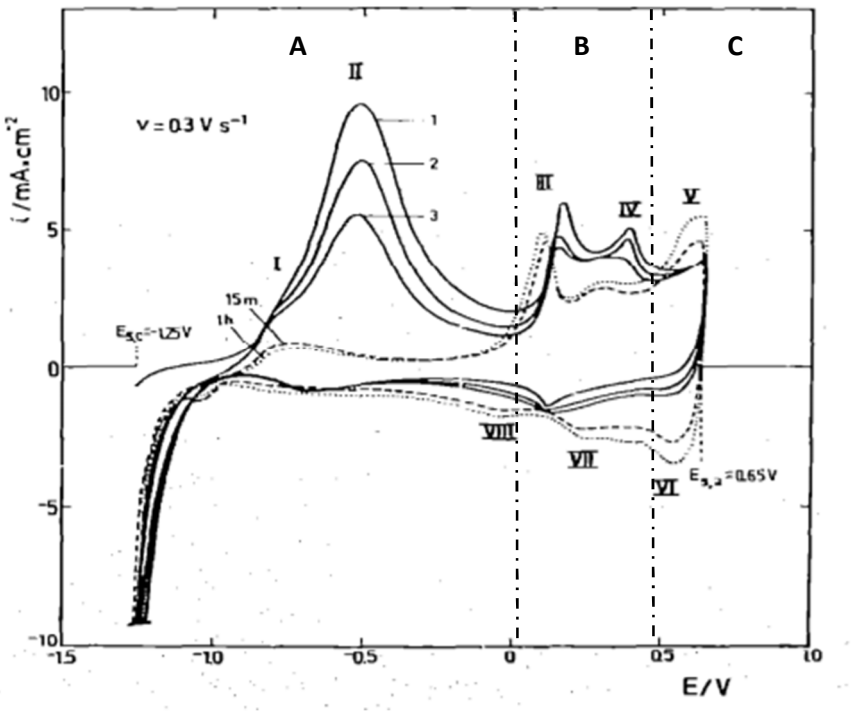



Figure 1.4.9 Cyclic voltammogram for a polycrystalline Co electrode in 1.0 M KOH at 25°C *vs.* Hg/HgO 1.0 M KOH. The sweep rate was 300 mV $s^{-1}$. The first there sweeps and those recorded after both 15 min and 1hr of cycling are shown. Relevant for this work is the dotted voltammogram corresponding to the first sweep. Adapted from Ref.[207]

A similar approach than that carried out on Ni to analyse its cyclic voltammogram was also adopted on Cobalt. Here, the CV can be divided into three regions. The analysis presented, regarding the nature of the peak potentials in fig. 1.4.9, is based upon the work of Behl and Toni[208], who compared the peak potentials with thermodynamic data. Thus, in the A region, a single anodic peak with the presence of a small shoulder peak is observed at -0.7 V (*vs.* Hg/HgO). This shoulder peak is attributed to the formation of adsorbed $OH^-$ species on the electrode surface:

$$Co + OH^- \leftrightarrow Co(OH)_{ads} + e^- \quad (1.4.15)$$

The major peak is attributed to a combination of the formation of a passivating film of $Co(OH)_2$ and/or CoO:

$$Co + 2OH^- \leftrightarrow Co(OH)_2 + 2e^- \quad (1.4.16)$$

$$Co + 2OH^- \leftrightarrow CoO_{inner} + H_2O + 2e^- \quad (1.4.17)$$

In region B, the observed peak is attributed to the oxidation of Co(II) species to Co(III) species. In agreement with Gomez Meier *et al*.[207] this process may be represented by the oxidation of the inner layer of CoO to $Co_3O_4$ according to:

$$3CoO_{inner} + H_2O \leftrightarrow Co_3O_4 + 2H^+ + 2e^- \quad (1.4.18)$$

Contrary to Gomez Maier *et al*., Burke *et al*.[209] suggested that such process could be represented by the reaction:

$$3Co(OH)_2 + 2OH^- \leftrightarrow Co_3O_4 + 4H_2O + 2e^- \quad (1.4.19)$$

Regarding the large background currents in the anodic sweep, in the region above 0.4 V *vs*. Hg/HgO, Bruke and co-workers[209] defended that a hydrous Co(II) films may be gradually converted into Co(II) containing species such as $Co_3O_4$, $Co_2O_3$ and CoOOH. They remarked that this situation is further complicated by various factors such as the existence, according to Benson *et al*.[210], of three different forms of CoOOH: (i) CoO(OH), (ii) CoOOH, and (iii) $CoHO_2$.

The peak observed in region C is widely attributed to the oxidation of Co(III) to Co(IV). This process can be represented as:

$$CoOOH + OH^- \leftrightarrow CoO_2 + H_2O + e^- \quad (1.4.20)$$

The reduction peak, (VI) at 0.5 V (*vs.* Hg/HgO) in fig. 1.4.9, corresponds to the reduction of the Co(IV) oxide back to cobalt oxyhydroxide.[211] The broad ill-defined cathodic peak at potentials between ca. –0.4 and –0.8 V (*vs*. Hg/HgO) is typically attributed to the reduction of Co(III) species. Although in fig. 1.4.9 this is not apparent at first sight,

probably due to the relatively fast scan rate at which this CV was recorded, most workers[138a, 212] have observed a reasonably well-defined peak at ca. –1.0 V (*vs.* Hg/HgO) which is associated with the reduction of Co (II) species. Further, ellipsometry measurements have been performed on electrochemically generated passive films on Co in alkaline solutions.[213] These studies led to the conclusion that cobalt can form two different types of passive layers in alkaline solutions. The formation of the first layer is observed at lower potentials where the thickness of the film is pH dependent. This layer consists of a mixture between $Co(OH)_2$ and CoO. A second layer is formed on top of the first layer at potentials above ca. 0 V *vs*. Hg/HgO. This second layer is mainly formed by Co (III) species, and to a lesser extent by Co (IV) species as well. These observations were further studied by XPS measurements. In this sense, Foelske *et al*.[214] when analysing the polycrystalline Co in 0.1 M NaOH also emphasised the idea of a twin-layer type passive film. The peak located in region A was described to be $Co(OH)_2$ film, whose thickness can grow to 40 nm depending on the potential and time. In region C in fig. 1.4.9, the outer layers of the film were said to be composed mainly by Co (III) species with the XPS measurements identified $Co_3O_4$ and CoOOH. A more recent publication on the topic also pointed out the possible coexistence of Co (II) and Co (III) species in this potential region. [215]

### 1.4.4 Manganese

As with Ni and Co, a brief review is to be presented here on the electrochemical behaviour of polycrystalline metallic Mn in aqueous alkaline solutions in order to understand the oxide surface that enhances the catalytic activity of this electrode for the OER. Analogous to nickel, the electrochemical behaviour of manganese in strongly alkaline aqueous solutions essentially concerns the manganese dioxide, $MnO_2$, which is typically used as a cathode material in alkaline batteries.[216] Its popularity arises from its material properties, such as its abundance of raw materials, low cost, low toxicity, etc. Manganese dioxide electrodes are also used in electrochemical water electrolysis. Suib *et al*.[217] studied the catalytic activity for the OER of three different phases of $MnO_2$, (α, β and γ) in a carbon support fabricated using three similar hydrothermal routes. The catalytic activities of manganese oxides rely, basically, on the following three factors: (i) their chemical compositions, (ii) their crystallographic structure, and (iii) their morphology and pore

structure.[218] One of the more relevant observations made by Suib, was the significant differences present in the OER overpotential for the three different phases. He found that the overpotential at 10 mA $cm^{-2}$, which is the most common value used to compare the catalytic activity on metal oxides, for the α, β and γ phases were 0.49 V, 0.60 V and 0.74 V, respectively.[217] This observations were further investigated by Bergmann *et al*.[219] who established a structure-activity relationship through studies of δ-$MnO_2$-like, and β-$MnO_2$-like which have a layered disposition and a tunnelled disposition, respectively. In agreement with Suib's results, and regarding the overpotential differences, Bergmann attribute these to the crystalline structure and to the presence of structure defects *e.g*. tunnel structures were proven to have higher intrinsic activities over layered materials, due to the easy accessibility of water molecules into the electrode and the defects offered by these two systems.[219] Therefore, manganese oxides can have very diverse structures depending on the connectivity between the [$MnO_6$] units *via* sharing corners or edges. According to Cao *et al*.[220] the catalytic activity towards the OER for the different phases of $MnO_2$ may be expressed by the type of $MnO_2$ phase:

$$\alpha \sim \delta > \gamma \gg \beta \qquad (1.4.21)$$

A brief introduction on the physical properties of the above phases is now presented. The three major $MnO_2$ phases showing tunnel structures are: (i) the cryptomelane α-$MnO_2$ phase, (ii) the pyrolusite, β-$MnO_2$ phase, and (iii) the ramsdellite γ-$MnO_2$ phase. In addition, a fourth phase showing layered disposition, δ-$MnO_2$, will be presented.

Among the three major polymorphs of $MnO_2$, the α-$MnO_2$ phase shows the presence of the largest tunnels, 2x2 tunnels, formed by double chains of $MnO_6$ octahedral. Due to its large channel size, the diameter of ca. ~ 4.6 Å, it exhibits significant advantages to accommodate cations or protons in its structure compared to other $MnO_2$ polymorphs.[221] It has been pointed out[222] that the accommodation of cations or protons within the crystallographic structure increases the specific capacitance of such materials. In addition, the presence of cations within the crystalline structure may favour both the ionic and electronic conductivity of the film. The disposition of the various channels results in a tetragonal structure with $a_0$ = 9.82 Å, $c_0$ = 2.86 Å.

The β-$MnO_2$ phase may be described as chains of edge-sharing $MnO_6$ octahedral which, in conjunction with the neighbouring chains, forms a framework structure of 1x1 octahedral

with a diameter size of ~ 1.89 Å. The result is a tetragonal structure with $a_0$ = 4.398 Å and $c_0$ = 2.873 Å.[223] Due to its small tunnel size, cations such as $Na^+$ and $K^+$ cannot be accommodated in the structure and as a result $Mn^{4+}$ is the predominant component of the crystal structure.

The γ-$MnO_2$ phase has similar crystal structure than the β-$MnO_2$ phase, except that in the direction there are alternating doubly occupied and unoccupied octahedral sites. The tunnels are 2x1 octahedral in size with a diameter size of ca. 2.3 Å.[218b] The resulting unit cell has an orthorhombic configuration with $a_0$ = 4.533 Å, $b_0$ = 9.27 Å, and $c_0$ = 2.866 Å dimensions.

The δ-$MnO_2$ phase is build form layers of disordered $MnO_6$ octahedral. Its random structure yields to the creation of unbalanced local charge regions, which in order to compensate such charge, are occupied by cations and protons.[224]

To clarify the different $MnO_2$ crystal structures, a typical polyhedral representation of different crystal structures of $MnO_2$ polymorphs along with a table with their crystallographic characteristics is presented in fig. 1.4.10 and Table 1.4.1, respectively.

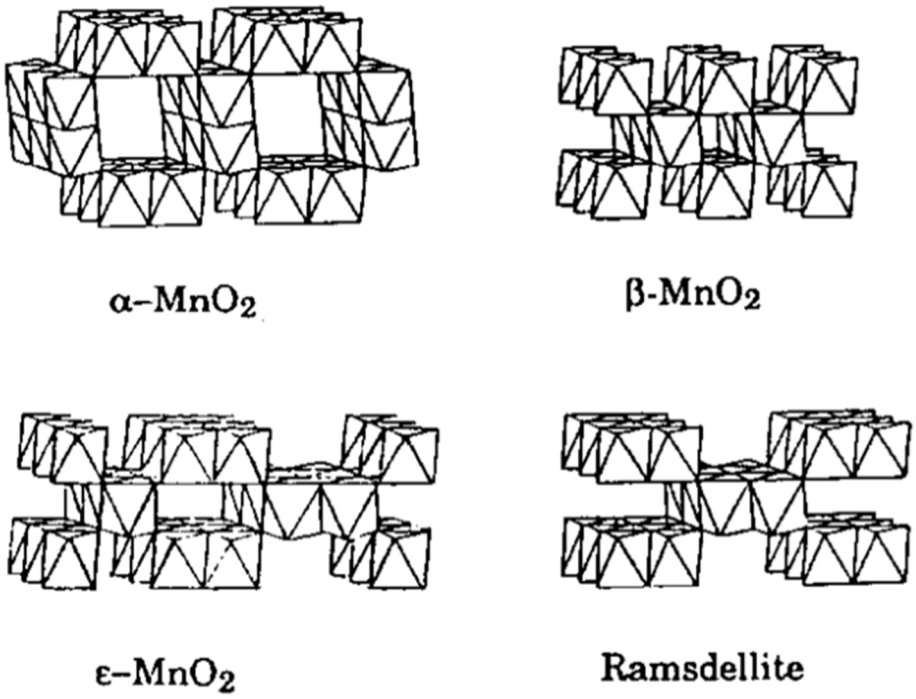



Figure 1.4.10 Various crystal structures of $MnO_2$, polymorphs showing the connection of the $MnO_2$, octahedral and tunnels shape. Reproduced from Ref.[225]

| $MnO_2$ type | Structure-type | Symmetry | Description |
|---|---|---|---|
| α-$MnO_2$ | Cryptomelane | Tetragonal | Double chains of [$MnO_6$] octahedral form a tunnel structure with a tunnel size of 2 × 2 |
| β-$MnO_2$ | Pyrolusite | Tetragonal | [$MnO_6$] octahedral share edges; a tunnel structure with a tunnel size of 1 × 1 |
| γ-$MnO_2$ | Ramsdellite | Octahedral | A tunnel structure with a tunnel size of 1 × 2 |
| δ-$MnO_2$ | Birnessite | Laminar | A random layered structure built of two-dimensional networks of corner-sharing [$MnO_6$] octahedral |

Table 1.4.1 Crystallographic characteristics of different forms of $MnO_2$.

It should be stated, as already mentioned above, that in any crystal, the ideal lattice is found only in the bulk whereas the surface always exhibits defects. All atoms present in $MO_6$ octahedral bulk are binding (M-O-M) species. However, at the surface of the lattice there are several terminal oxygen species because of the coordinative and unsaturated surface of metal ions, such as -$OH_2$, -$OH^-$ or -$O^-$. These oxygen species might have an important role in the conversion of anhydrous to hydrous forms of oxides, *e.g*. $MnO_6$ could be transformed to $(-O-)2Mn(OH)_4^{-2}$ at the solid/solution interface. Thus, structures which allow intimate contact between the solid and the liquid phase are likely to produce hydrous oxide layers. These types of hydrous oxides are not strictly confined in the oxide surface but can also exist on an open surface or porous regions of the oxide.

There are different preparation techniques for electrodepositing manganese oxide and hydroxides. Electrochemical properties of Mn have been observed for manganese oxide films prepared by chemical precipitation, electrodeposition and potential cycling growing both for base and acid solutions.[226] However, since this thesis deals only with manganese hydroxide synthetized by repetitive potential cycling in alkaline solution, the following discussion especially focuses on such method.

Typical cyclic voltammograms recorded for hydrous oxide layers prepared using different growth cycles in the alkaline electrolyte are presented in fig. 1.4.11.

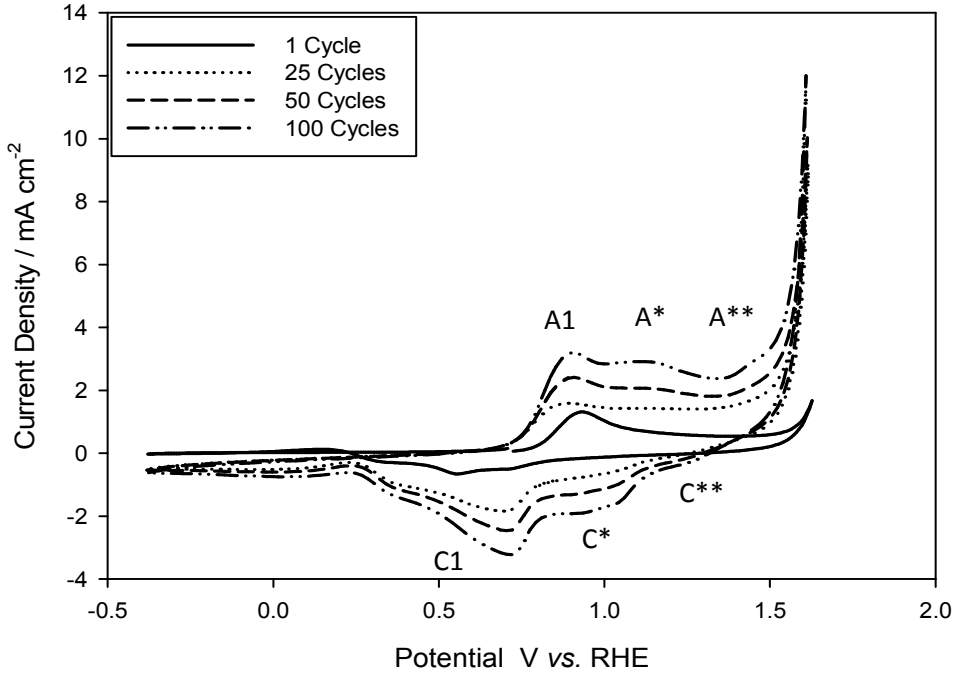



Figure 1.4.11 Cyclic voltammograms characterising the surface electrochemistry of an initial bright Mn electrode at various potential cycles. All the above CVs were recorded in 1.0 M NaOH with an sweep rate of 40 mV $s^{-1}$.

The redox peaks observed in fig. 1.4.11 are in excellent agreement with earlier works reported by Burke and Ahern[227], and by Yano *et al*.[228] Clearly, as the film gets thicker the voltammetric response becomes more complex. The formation of two additional potential peaks, a shoulder at ca. 0.93 V *vs.* RHE, and a main peak at 1.25 V *vs.* RHE, can be observed. With a further increase of deposition cycle *e.g.* n° potential cycles > 750 applied to the Mn wire, a third anodic peak is observed at potentials 1.45 V *vs*. RHE. Many authors agreed with the nature of the single peak observed in the initial stages of Mn metal (1 potential cycle) at 0.9 V *vs.* RHE, which may be assigned to the oxidation of manganese metal to $Mn(OH)_2$ according to the reaction:

$$Mn + 2OH^- \rightarrow Mn(OH)_2 + 2e^- \qquad (1.4.22)$$

It has been pointed out that eqn. 1.4.22 probably follows along a similar path to that of Ni. As a result of the above reaction and taking into account that the $Mn(OH)_2$ film formed on the electrode surface is not reduced as its reduction occurs at more negative potentials than -0.5 V *vs.* RHE according to Pourbaix diagram[130], the following reactions must be

considered to arise from the $Mn(OH)_2$ phase. There exists some disagreement with the nature of the double anodic peak in the region 1 V - 1.7 V *vs.* RHE especially with the one corresponding to the formation of $MnO_2$.

Liu You-Qin *et al*.[229] suggested that the observation of a doublet may be attributed to two distinct oxidation mechanisms: the ECE (electron transfer - chemical – electron transfer step) and the disproportionation mechanism. These mechanisms are represented in eqns. below:

ECE mechanism:

$$Mn^{2+} \rightarrow Mn^{3+} + e^- \quad (1.4.23)$$

$$Mn^{3+} + 2H_2O \rightarrow MnOOH + 3H^+ \quad (1.4.24)$$

$$MnOOH \rightarrow MnO_2 + H^+ + e^- \quad (1.4.25)$$

Disproportionation mechanism:

$$Mn^{2+} \rightarrow Mn^{3+} + e^- \quad (1.4.26)$$

$$2Mn^{3+} \rightarrow Mn^{2+} + Mn^{4+} \quad (1.4.27)$$

$$Mn^{4+} + 2H_2O \rightarrow MnO_2 + 4H^+ \quad (1.4.28)$$

Su-Moon[230] mentioned that the shoulder peak, at about 0.93 V *vs.* RHE, corresponds to the direct oxidation of $Mn^{2+}$ to $Mn^{3+}$ according to eqn. 1.4.26. In addition, further oxidation of the oxide film may involve the Mn(III/IV) redox transition following:

$$Mn(OH)_2 + OH^- \rightarrow MnOOH + H_2O + e^- \quad (1.4.29)$$

$$MnOOH + OH^- \rightarrow MnO_2 + 2H_2O + e^- \quad (1.4.30)$$

Special mentioned should be done to a recent work published by Daniel G. Nocera.[231] These authors, by using X-ray absorption spectroscopy techniques, observed that $M^{3+}$ may be introduced into $MnO_2$ lattice by an electrochemically induced comproportionation

reaction with $Mn^{2+}$ being the former kinetically trapped in tetrahedral interstitial sites. According to the authors, the presence of $Mn^{3+}$ species into the $MnO_2$ lattice would result in an OER enhancement in alkaline solutions, since $Mn^{3+}$ species (either MnOOH or $Mn_2O_3$) are only stable in high pH solutions.

Kao *et al*.[232] argued that MnOOH was an intermediate specie in the $Mn^{2+}$ oxidation to form $MnO_2$ according to eqn. 1.4.31:

$$2MnOOH \rightarrow MnO_2 + Mn(OH)_2 \qquad (1.4.31)$$

In relation to the observations pointed out by Sugimori, Kao *et al*.[232] mentioning that this pathway leaves a small amount of not oxidized MnOOH intermediate species on the surface, a similar argument was used by Su-Moon Park, who, based on his XPS measurements, suggested the possibility that the formation of $MnO_2$ is produced from the direct oxidation of $Mn(OH)_2$ rather than *via* MnOOH supported by his voltammograms, in which a very small amount of current was measured during the oxidation of $Mn(OH)_2$ to MnOOH.

Paul and Cartwright[233] though that the possible pathway for the formation of $MnO_2$ involved the formation of porous solid intermediates like MnOOH, $Mn_2O_3$ and $Mn(OH)_4$ during oxidation of $Mn^{2+}$ to give $MnO_2$.

Zaretskii *et al*.[234] proposed a pathway similar to that argued by Su-Moon Park. According to Zaretskii, a direct oxidation of $Mn^{2+}$ to $Mn^{3+}$ or $Mn^{4+}$ existed. In this case, the $Mn^{3+}$ might undergo disproportionation to produce $Mn^{2+}$ and $Mn^{4+,}$ following reaction 1.4.32, which then it hydrolyses to form $MnO_2$:

$$Mn_2O_3 + 2OH^- \rightarrow 2MnO_2 + H_2O + 2e^- \qquad (1.4.32)$$

Regarding the cathodic sweep, it was established that the reaction that takes place during the reduction process in sodium hydroxide solutions corresponds to the transition Mn(IV) / Mn(III) and Mn(III) / Mn(II). As observed in the anodic sweep, Gosztola and Weaver[235] identified intermediates of MnOOH and Mn(IV)-O-Mn(III) species during reduction of several equivalent monolayers of $MnO_2$ to $Mn(OH)_2$.

It is also important to mention the observation made by Burke and Murphy[236], who noted that the redox transition reactions for thin films were accompanied by a reversible

electrochromic transition in which the oxide layer changed from pale yellow at low potentials to reddish brown on the oxidized state. This effect was no further observed for thicker layers, and especially on those present after 250 cycles the oxide layer remained black throughout the cycle. It is also important to mention that the electrocatalytic redox behaviour of Mn electrodes is highly affected by the pH of the solution in which the $MnO_2$ growth occurs. In this perspective, it was pointed out that, for very strong alkaline solutions, the possible formation of complexes such as $Mn(OH)^{4-}$ and $Mn(OH)_4^{2-}$ may be observed. However, they seem to be highly unstable and tend to decompose to $MnO_2$ species.[237]

## 1.5 The Oxygen Evolution Reaction

### 1.5.1 Introduction to the Oxygen Evolution Reaction

The interest in using hydrogen as a fuel has majorly increased along the last few decades, which is mainly due to its non-polluting nature and its large energy storage ability.[238] That is because hydrogen can react with oxygen in an electrochemical fuel cell and produce electrical current. This type of process is known as cold combustion reaction. In obtaining that hydrogen, water splitting using renewable energies accounts for: (i) a "clean" hydrogen product, since it only involves hydrogen and oxygen molecules, (ii) prevents the formation of secondary products such as $CO_2$, and (iii) an environmentally friendly hydrogen production, given that the energy needed to split the water molecule comes from renewable sources. [239]

Hydrogen electrolysis is carried out in a cell which usually contains (i) two electrodes, an anode and a cathode, along with (ii) a high conductivity electrolyte, either acid or basic solution, allowing the generation of both hydrogen and oxygen gas. The process can be described by the following two half-cell redox reaction in alkaline solution:

$$\text{Cathode: } 2H_2O + 2e^- \rightarrow H_2 + 2OH^- \qquad E = -0.83\ \text{V} \qquad (1.5.1)$$

$$\text{Anode: } 4OH^- \rightarrow 2H_2O + O_2 + 4e^- \qquad E = +0.40\ \text{V} \qquad (1.5.2)$$

$$\text{Overall: } 2H_2O \rightarrow 2H_2 + O_2 \qquad E = -1.23\ \text{V} \qquad (1.5.3)$$

The total potential required to drive the electrolysis reaction has both cathode and anode overpotentials and ohmic resistance contributions, as seen in eqn. 1.5.4 below.

$$E(i) = E_{e,cell} + |\eta_c| + \eta_A + iR \quad (1.5.4)$$

Where *E(i)* is the energy input (potential applied), $E_{e,cell}$ represents the equilibrium potential, $\eta_C$ and $\eta_A$ are the cathode and anode overpotential, respectively, and *iR* represents the ohmic drop arising from the electrolyte resistance. Please note that iR has already been presented in detail in section 1.2.1. The cathode, where the $H_2$ evolution takes place, has overpotentials of around 0.1 V, while the anode, where the $O_2$ evolution takes place, has overpotentials typically of around 0.33 V - 0.5 V.[240] The high potential associated with water oxidation to generate molecular oxygen represents the most energy intensive step and is a major factor in limiting device operational efficiency.[241]

This high value, coupled with the instability of the anode materials in alkaline solution have limited the scope for electrolytic hydrogen production to date. In this view, the electrochemical evolution of oxygen from water have received great research attention owing to the importance of this reaction in industrial applications and to its intrinsic complexity.

### 1.5.2 Difficulties of the Anodic Oxygen Evolution Reaction

The oxygen evolution reaction is of special importance in water oxidation, in view of the large overpotential associated with the process. The overall reaction may be written, in acid solutions, as:

$$2H_2O \rightarrow O_2 + 4H^+ + 4e^- \quad E^o = 1.229\,V \quad (1.5.5)$$

And, when referring to the alkaline solution, it shall be presented as:

$$4OH^- \rightarrow O_2 + 2H_2O + 4e^- \quad E^o = 0.401\,V \quad (1.5.6)$$

However, the OER has not yet been fully understood by scholars. Some of the difficulties which appear to be responsible for this lack of understanding are:

(1) The fact that the OER only takes place on most electrode materials at rather high positive potentials (typically greater than 1.5 V at 25°C), which is of relevance since only few electrode materials are corrosion resistant at those potentials where the OER occurs and, consequently, most of the electrodes would undergo dissolution. As a result, most studies of the process have been confined to the noble metals and their alloys. However, in recent years, the usage of transition metals oxides has attracted considerable attention. These metal oxides and their alloys possess metallic or semi-conductive properties and have been found to exhibit high electrocatalytic performance for OER in terms of: (i) low onset potential, (ii) high stability of the oxide film in alkaline media, and (iii) low overpotential at a standard current density (10 mA $cm^{-2}$). Notwithstanding, at the present time, detailed information on the dependence of the OER processes on the nature of the substrate is still insufficient.

(2) It is rather difficult to investigate the kinetics of the OER on bright noble metals substrates where dissolution may be assumed negligible, as oxide film formation occurs in the potential region of interest. Some authors[242] have suggested that the formation of this film affects the rate of the OER since it may act as a barrier to the electron transfer, causing the exchange current density in the OER region at constant potential to decrease as the thickness increases. The specific features of electron transfer at the electrode-oxide and oxide-electrolyte interfaces are still being investigated.

(3) The toughness of the analysis of the electrochemical data. In some cases[243], polarization curves revealed the presence of a discontinuity electrical response, a behaviour typically associated with an alternation of the stoichiometric on the anodic film, possibly accompanied by a charge in the rate determining step in the electrode process, which make it hard to provide for general assumptions of the topic.

(4) A large number of reaction pathways come up as conceivable if all potential intermediates in the OER are considered to be valid.[244] In this sense, Damjanovic *et al*.[120c] have summarized fourteen possible pathways for the OER with accompanying Tafel parameters and stoichiometric numbers. However, these reaction pathways are not unique in their respective values of kinetic parameters.

Indeed, it is not strictly correct to deduce stoichiometric numbers from direct comparison of anodic and cathodic Tafel slopes, due to the anodic OER and cathodic ORR paths are quite different from one another since both reactions take place on metal surfaces of significant different degrees of oxidation. The determination of such parameters at low overpotentials using the low field approximation of the Butler-Volmer eqn.[112] has also not proved practical, which is understood to be due to the fact that: (i) the exceedingly low values of the exchange current density, typically 10 mA $cm^{-2}$, allow for the interference of minuscule amounts of impurities in the solution, and (ii) the oxide film formation provokes a continuous variation in the substrate catalytic activity.

### 1.5.3 General Comments on the Oxygen Evolution Reaction

Since the principal focus of the present work is on the OER at polycrystalline Ni, Co and Mn electrodes in aqueous alkaline solution, a detailed review of the literature in this area is now pertinent. Although the discussion of the nature of the reaction on the three transition metals will receive priority in this review, many significant experimentally observations have been made on these electrodes in acidic solution, and some of these will also be enounced in this section.

Amongst the large number of reviews on various aspects of the OER, the most relevant are those presented by Damjanovic[245], Trasatti and Lodi[246], Burke[247], Conway[248], Lyons[192], Bockris and Khan[21] and Gattrell and MacDougall[249].

Modern investigations on the OER are typically based on the work presented by Bockris and Hug[250] in 1956 in relation to the experimental observation of the oxygen electrode thermodynamic reversible potential at Pt electrodes in $H_2SO_4$ solution. Much effort has been focused on gaining understanding of the reaction mechanism and of the development of an appropriate anode material with both high catalytic activity towards the reaction and high catalytic behaviour stability. The driving forces behind this thesis include the requirement to improve the operational efficiency of alkaline water electrolysis as well as the intrinsic scientific interest in the OER from the point of view of developing a more precise understanding of electrocatalysis in general.

A notorious aspect to be considered in any study of oxygen evolution anodes is that oxide growth is a parallel electrochemical process that always accompanies the OER. Hence, the

possible impact of both the oxide growth and the nature of the oxide surface must always be contemplated when dealing with the OER. These points will be discussed in tandem with kinetic and electrocatalytic considerations throughout this chapter. It is well established that the OER on noble metals electrodes, *e.g*. Ir, Pt, Rh, Ru occurs at potentials where a relative thin film of oxide is formed.[176, 243b] Contrary, on base metals, especially in those of interest in the present thesis, the oxide layers are rather thicker. The work of Simpraga and Conway[170, 251], as discussed in section 1.4, deals with this fact. In general, it has been found that electrodes composed of bulk metal oxides such as $RuO_2$, $IrO_2$ and perovskites have superior electrocatalytic activity towards the OER than metallic electrodes. Significant work on the topic was carried out by Tseung and Jasem[138b], who review the electrocatalytic activity of twenty metal oxides in order to provide "guidelines for the choice of semiconducting oxides as oxygen evolution electrodes". They elaborated a table benchmarking heterogeneous electrocatalyst for the OER considering: (i) their conductivity, (ii) their corrosion resistance at pH 14, (iii) the equilibrium potential of the metal/metal oxide or lower metal oxide/higher metal oxide couple, and (iv) their oxygen reduction performance. Their conclusions revealed that none of the oxides studied fulfilled all the above criteria, though the most suitable candidate couples were found to be $Co_2O_3$ / $CoO_2$, $Ni_2O_3$ / $NiO_2$ and lower $NiCo_2O_4$ / $NiCo_2O_4$. The latter material, which shows a spinel type structure, was found to be preferable to the former two, mainly due to its superior electrical conductivity. While bulk $RuO_2$ exhibited good electrical and catalytic properties, its poor corrosion resistance in concentrated alkaline solutions limited their operational usage. These observations were first highlighted by Tseung and Jasem[138b] in 1977 although they did also note that when coated on Ti, $RuO_2$ and $IrO_2$ would prove more stable with respect to corrosion in alkaline media. Following the same research stream than that made by Tseung and Jasem, Miles *et al*.[252], one year later, observed the following trend in the electrocatalytic activity of metal oxides towards the OER in alkaline media: $Ru > Ir{\sim}Pt{\sim}Rh{\sim}Pd{\sim}Ni{\sim}Os \gg Co \gg Fe$. Poor activities were observed on V, Cr, Mo, W, Mn, and Re oxide electrodes. Indeed, it is accepted that the optimum oxygen evolution anode materials to date are both $RuO_2$ and $IrO_2$, especially in acidic solutions where these materials are less prone to corrode than in alkaline media.[138a, 246] One of the factors which contributes to the success of this type of electrode as an OER catalyst is its formidable electronic conductivity. Although being an oxide, $RuO_2$ displays a metallic-like conductivity[138a] between $2{\cdot}10^4$ to $3{\cdot}10^4$ $\Omega^{-1}$ $cm^{-1}$ at 25°C. It is important to recall that most of the metal oxides, as discussed previously, are generally semiconductors or insulators.

Further, $IrO_2$ may also be a suitable anode for OER since it exhibits low overpotential for the reaction at practical current densities.[243b, 253] However, their high cost, arising from the fact that none of them are earth abundant materials, and their relatively poor long-term stability in alkaline media casts doubts on the economic viability and practicality of their widespread commercial utilisation as suitable electrodes. Consequently, there has been a considerable research effort throughout recent years in finding inexpensive, earth abundant materials which exhibit excellent catalytic activity and material stability under prolonged electrolysis.[254] Understanding the mechanistic details, optimizing the performance of the OER at the surface of the electrode and developing anodes from earth abundant non-platinum group metals (Ni, Fe, Co and Mn) hydroxide which may serve as a stable and cathartically active electrode is seen as one of the remaining grand challenges for nowadays energy science.

### 1.5.4 Introduction to Synergy

As suggested in section 1.3.3, a common approach in OER catalyst enhancement is the empirical research of synergetic effects between multicomponent catalyst systems. In line with the latter, it has been outlined that amongst the most promising materials forwarded as OER anodes are: (i) various inter-metallic alloys often containing significant amounts of Ni, Co or Fe, (ii) mixed oxides including spinels such as nickelites, cobaltites and ferrites, and (iii) perovskites.

Several authors have attributed the catalytic enhancement to changes in the local electronic properties of the active sites in the metal surface. For example, Yeo and Bell[179] compared the OER activity of Ni and Co oxides prepared on a range of substrates. They observed that the OER activity of a sub-monolayer of cobalt oxide decreased with decreasing electronegativity of the substrate in the order $CoO_x$/Au > $CoO_x$/Pt > $CoO_x$/Pd > $CoO_x$/Cu > $CoO_x$/Co. They also noted that similar behaviour was to be found for a monolayer of nickel oxide deposited on Au substrate.

Of particular importance are the binary mixtures of Ni-Co and Ni-Fe.[255] Typically, these type of alloy oxide materials are prepared by thermal decomposition of the precursor salts, commonly nitrates and chlorides and therefore, the resulting oxide thin film consists of a compact anhydrous oxide in the form of perovskite or spinel structures. In such structures, oxygen atoms are presented only as a bridging species between two metal cations and ideal

crystals constitute tightly packed giant molecules.[256] It was observed by Lyons and co-workers[254a] that the choice of annealing temperature is probably the most important consideration when using a thermal preparation technique, having a demonstrated influence on the composition, morphology and electrocatalytic properties of the resulting oxide film.

The insertion of the Ni in the $Co_3O_4$ structure forms a mixed oxide called nickel cobaltite, $NiCo_2O_4$. This mixed oxide presents stability, high catalytic activity and is of low cost, being active in the oxygen evolution and reduction reactions in alkaline medium.[257]

An important feature of special interest in this work is the formation of different phases during the thermal decomposition process of $NiCo_2O_4$. Recent XRD studies[258] revealed that the ratio NiO / $NiCo_2O_4$ is strongly related with the calcination time. The results suggested that at first stages of calcination, at 140°C and for calcination times of around 4 hr, the XRD patterns reveal the presence of NiO along with $NiCo_2O_4$. With further increases in the calcination time, for instance, making it up to around 6 hr, the NiO gets converted into $NiCo_2O_4$. Further, an XRD pattern of 15 hr calcination time would exhibit an enhanced amount of NiO in $NiCo_2O_4$, which may be due to the decomposition of $NiCo_2O_4$ upon longer heating.[259]

Some authors have suggested that $NiCo_2O_4$ / NiO films may outperform commercial $RuO_2$, exhibiting overpotentials of ca. 40 mV at a current density of 10 mA $cm^{-2}$ and a small Tafel value of 61 mV $dec^{-1}$ during OER in 1.0 M NaOH.[258, 260]

In addition, Xiaobo Ji *et al*.[260] noted that $NiCo_2O_4$ possesses richer electroactive sites and at least two magnitudes higher electrical conductivity than that of NiO and $Co_3O_4$. In this view, the electrical conductivity of such oxides may be expressed in the following sequence: $NiCo_2O_4$ > NiO > $Co_3O_4$. Many publications have also demonstrated that nickel cobaltite has a much lower film resistance than nickel oxides and cobalt oxides.[261]

### 1.5.4.1 Nickel Cobalt Mixed Oxides

Many publications revealed that the oxygen evolution occurs preferentially on the Co (IV) sites in the octahedral site of spinel $NiCo_2O_4$ oxide surfaces.[262] The mechanism of the oxygen evolution on $NiCo_2O_4$ spinel films has been examined several times.[155, 263] However, controversial points still exist in some aspects of the reaction. Different

perspectives with respect to the OER mechanism in $NiCo_2O_4$ electrodes are presented below.

Gonzalez[264] studied the effect of electrolyte temperature, in the range of 25°C - 80°C, in the Tafel slope in 28 % KOH electrolyte. He noted that variations in the electrolyte temperature provoke changes in the Tafel slope in the order of ca. 10 mV $dec^{-1}$ and 30 mV $dec^{-1}$ for the lower and higher overpotential regions, respectively. Significant diminutions of three orders of magnitude were observed regarding the current density. He also observed the formation of two Tafel slope regions, *e.g.* Tafel slope changes from 51 mV $dec^{-1}$ to 91 mV $dec^{-1}$ at around 0.6 V in 25°C, being the latter observation of the two to possible changes in the OER mechanism. In this perspective, other authors noted the same Tafel slope behaviour when changing the electrolyte temperature. All the following authors also noted these two different Tafel slope regions.

Davidson *et al.*[155] reported that the most significant change in the Tafel slope was observed at 23°C changing from 48 mV $dec^{-1}$ to 80 mV $dec^{-1}$ at low and high overpotential, respectively. In this case, the authors explained this behaviour by the possible change in the valence state of the active site of the electrode material.

Jasem and Tseung[265] attributed the Tafel slope behaviour to the influence of the formation of a higher oxide at high overpotentials in the OER. Efremov and Tarasevich[266] argued that a possible explanation for the change of Tafel slope was the oxidation of $M^{2+}$ active sites to $M^{3+}$ active sites as the overpotential increases.

Relevant investigations on the OER mechanism in $NiCo_2O_4$ films were also carried out by Rasiyah and Tseung[263], who observed that the Tafel slope changed from 40 mV $dec^{-1}$ to 120 mV $dec^{-1}$ in the 1.0 - 5.0 M KOH concentration range whereas for more diluted solutions (conc.< 0.4 M) the slopes were unclear in the low overpotential region. Aiming to explain such Tafel behaviour, they proposed that the Tafel slope of 120 mV $dec^{-1}$ might be justified due to the fact that the OER occurs on divalent sites, whereas in the region where the Tafel slope is 40 mV$dec^{-1}$ the OER takes place on trivalent sites of $NiCo_2O_4$. Further, Tseung *et al.*[267] mentioned that the cation distribution of $NiCo_2O_4$ at may be conceived as:

$$Co_{0.9}{}^{+2} + Co_{0.1}{}^{+2}\left(Ni_{0.9}{}^{+2} + Ni_{0.1}{}^{+3} + Co^{3+}\right) O_{3.2}{}^{-2} - O_{0.8} \qquad (1.5.7)$$

In this structure, the cations inside the parenthesis are in an octahedral environment and those outside are in tetrahedral sites. According to these authors, a probable mechanism sequence for the OER on trivalent sites (T) is:

$$T + OH^- \rightarrow TOH + e^- \quad (1.5.8)$$

$$TOH + OH^- \rightarrow TO^- + OH^- \quad (1.5.9)$$

$$TO^- + M \rightarrow T - O - M + e^- \quad (1.5.10)$$

$$2T - O - M \rightarrow 2T + 2M + O \quad (1.5.11)$$

A Tafel slope of 0.04V per decade could be due to eqn. 1.5.10 being rate determining at low TOH coverage e.g. T-OH > 0. A low coverage condition, in this case, is justifiable since T sites are minority sites. On the other hand, the mechanisms on divalent sites may follow:

$$M + OH^- \rightarrow MOH + e^- \quad (1.5.12)$$

$$MOH + OH^- \rightarrow MO + H_2O + e^- \quad (1.5.13)$$

$$2MO \rightarrow 2M + O_2 \quad (1.5.14)$$

The slope of 0.12 V $dec^{-1}$ may be due to eqn. 1.5.12 being rate determining at low coverage of MOH, i.e., MOH > 0, or due to eqn. 1.5.13 being rate determining at high coverage of MOH, (MOH ~ 1). Eqn. 1.5.12 is the preferred rate-determining step. This study suggests that trivalent nickel and cobalt ions evolve oxygen at lower potentials than divalent nickel and cobalt ions.

Analogous to Ni-Co, the doping of Fe into NiO phases has also attracted considerable attention due to an enhancement in the catalytic activity of the electrode. The latter is mainly because of the two components contributing to different fundamental functionalities required for the OER, these are: (i) forming an active O radical, and (ii) catalysing the O-O coupling, respectively. Some authors associated the observed catalytic enhancement to the electronic nature of Fe-doped NiOOH. The high spin $d^4$ Fe (IV) leads

to the efficient formation of an active O radical intermediate, while the closed shell $d^6$ Ni (IV) catalyses the subsequent O-O coupling.

While there is consensus on the idea that the Fe-doping to NiOOH species shows an improvement in the catalytic activity towards the OER, a variety of views have been reported regarding the structure of the active phase and whether Fe or Ni constitute the active centre. It is not clear yet whether the substitution of Fe cations into NiOOH enhances the OER activity of Ni, of Fe, or of both, and whether the substitution of Ni into FeOOH can enhance the activity of this phase. A recent publication investigated the way that Fe-doping affects Ni oxide electrodes using in situ HERFD XAS.[268] They aimed to obtain a fundamental understanding of the interactions of Ni and Fe and how they contributed to the high OER activity of Ni−Fe catalysts. These authors found that small quantities of Fe-doped (< 25 % Fe) into γ-NiOOH yielded to an enhancement of the OER activity due to the substitution of $Fe^{3+}$ cations in the framework of γ-NiOOH (Fe substitutes for Ni in both α-$Ni(OH)_2$ and γ-NiOOH). Subsequent increases in $Fe^{3+}$ produce the formation of a mixture of FeOOH and $Fe_2O_3$ along with NiOOH. They proposed that two different $Fe^{3+}$ species were found present: (i) $Fe^{3+}$ dopants in α-$Ni(OH)_2$ / γ-NiOOH, and (ii) $Fe^{3+}$ sites within a separate γ-FeOOH phase. Regarding the OER catalytic enhancement, when $Fe^{3+}$ is doped into the lattice, the authors propose two possibilities: "(i) the substituted $Fe^{3+}$ sites become more active when hosted in the lattice of γ-NiOOH due to a change in their electronic environment, and (ii) the activity of $Ni^{3+}$ sites increases as a consequence of their electronic properties being altered by the substitution of $Fe^{3+}$ cations into the γ-NiOOH lattice".

The result of their study leads to the following oxidisation sequence: at lower potentials of the onset of the OER, Ni and Fe cations form a layered double hydroxide structure, $Ni(II)_{1-x}Fe(III)_x(OH)_2$. As the potential is raised, but still below that for the onset of the OER, the Ni cations undergo oxidation to $Ni^{3+}$ while Fe cations remain as $Fe^{3+}$. For Fe levels below approximately 25 %, the previous oxidations result in the formation of γ-$Ni_{1-x}Fe_xOOH$, which indicates the substitution of various Ni cations by Fe cations. Based on their findings, they noted that $Fe^{3+}$ cations in γ-$Ni_{1-x}Fe_xOOH$, exhibit a significantly lower overpotential than $Ni^{3+}$ cations do in either γ-$Ni_{1-x}Fe_xOOH$ or γ-NiOOH. Therefore, it may be suggested that Fe sites are the active sites for the OER.

### 1.5.5 Reaction Pathways for the Oxygen Evolution Reaction

In terms of a mechanistic analysis of the OER, the major difficulty lies in the fact that the OER is a complex process involving the transfer of four electrons. Since electrons are transferred one at a time, the process will be, by necessity, a multistep process in which distinct intermediates are generated on the electrode surface. Consequently, as outlined in section 1.5.2, many reaction pathways are conceivable if all potential intermediates in the OER are considered to be valid. In this sense, Hoare[269] and Kinoshita[138a], who making a number of assumptions, were able to reduce to approximately ten or eleven different pathways. Similar mechanistic studies for the OER were presented by Damjanovic *et al*.[120c] who summarized fourteen possible paths for the OER with accompanying Tafel parameters and stoichiometric numbers at both limiting low and high adsorbed intermediate coverage. A further probe inherent in attempt at kinetic mechanistic analysis lies in the fact that, even with this reduced number of possible mechanisms, the values of kinetic parameters such as Tafel slopes predicted for a given path are not unique. Hence, it is often very difficult to clearly identify the operative pathway for a particular system. In this perspective, other parameters will have to be used to account to this issue.

An early kinetic mechanism analysis of possible OER pathways was produced by Bockris[112] in 1956. In this work, the author applied the "Christiansen method" to calculate the expected values of the Tafel slope under Langmuir intermediate adsorption conditions. This analysis was further investigated by Conway and co-workers[110c, 270] who derived the predicted kinetic parameters for various pathways in the case of Temkin adsorption of intermediate species. Reproduced here as Table 1.5.1 is presented a summary of the diagnostic criteria of proposed paths for the OER which was originally provided by Bockris and Otagawa.[271]

In table 1.5.1, the authors describe the five-particular mechanism which are understood to be "the paths most often considered in oxygen evolution studies". Other notable early studies on the mechanistic pathway of OER include the works of Bockris and Otagawa[129, 272] (1983), Krasil'shchikov[245] (1963), Kobussen and Broers[273] (1981), Willems *et al.*[274] (1984) and O'Grady *et al.*[275] (1974).

| rate-determining step | $\nu$[b] | Langmuir $\partial V/\partial \ln i$ $\theta \to 0$ | Langmuir $\partial V/\partial \ln i$ $\theta \to 1$ | $(\partial \ln i/\partial \ln C_{OH^-})_{V,\zeta}$[c] $\theta \to 0$ | $(\partial \ln i/\partial \ln C_{OH^-})_{V,\zeta}$[c] $\theta \to 1$ | Temkin $\partial V/\partial \ln i$ NA[d] | Temkin $\partial V/\partial \ln i$ A[e] | NA[d] | A[e] | condition[f] |
|---|---|---|---|---|---|---|---|---|---|---|
| **(I) Bockris's Oxide Path** | | | | | | | | | | |
| 1. $M + OH^- \to MOH + e^-$ | 4 | $2RT/F$ | | 1 | | | | | | |
| 2. $2MOH \to MO + M + H_2O$ | 2 | $RT/2F$ | $\infty$ | 2 | 0 | $2RT/F$ | | 0.5 | | $r_{OH} \sim r_O$ |
| | | | | | | $RT/F$ | | 1 | | $r_{OH} >> r_O$ |
| 3. $2MO \to 2M + O_2$ | 1 | $RT/4F$ | $\infty$ | 4 | 0 | $RT/2F$ | $RT/F$ | 2 | 1 | $K_3 \sim 1$ |
| | | | | | | $RT/4F$ | $RT/3F$ | 2 | 1 | $K_3 << 1$ |
| **(II) Bockris's Electrochemical Path** | | | | | | | | | | |
| 1. $M + OH^- \to MOH + e^-$ | 2 | $2RT/F$ | | 1 | | | | | | |
| 2. $MOH + OH^- \to MO + H_2O + e^-$ | 2 | $2RT/3F$ | $2RT/F$ | 2 | 1 | $2RT/F$ | | 1 | | $r_{OH} \sim r_O$ |
| | | | | | | $RT/F$ | | 1.5 | | $r_{OH} >> r_O$ |
| 3. $2MO \to 2M + O_2$ | 1 | $RT/4F$ | $\infty$ | 4 | 0 | $RT/2F$ | $RT/F$ | 2 | 1 | $K_3 \sim 1$ |
| | | | | | | $RT/4F$ | $RT/3F$ | 4 | 3 | $K_3 << 1$ |
| **(III) Krasil'shchikov's Path** | | | | | | | | | | |
| 1. $M + OH^- \to MOH + e^-$ | 2 | $2RT/F$ | | 1 | | | | | | |
| 2. $MOH + OH^- \to MO + H_2O$ | 2 | $RT/F$ | $\infty$ | 2 | 1 | $\infty$ | | 1 | | $r_{OH} \sim r_{O^-}$ |
| | | | | | | $2RT/F$ | | 1.5 | | $r_{OH} >> r_{O^-}$ |
| 3. $Mo^- \to MO + e^-$ | 2 | $2RT/3F$ | $2RT/F$ | 2 | 0 | $2RT/F$ | | 0 | | $K_2 \sim 1$ |
| | | | | | | $2RT/F$ | | 1 | | $K_2 << 1$ |
| 4. $2MO \to 2M + O_2$ | 1 | $RT/4F$ | $\infty$ | 4 | 0 | $RT/2F$ | $RT/F$ | 2 | 1 | $K_3 \sim 1$ |
| | | | | | | $RT/4F$ | $RT/3F$ | 2 | 1 | $K_3 << 1$ |
| **(IV) O'Grady's Path** | | | | | | | | | | |
| 1. $M^z + OH^- \to M^zOH + e^-$ | 2 | $2RT/F$ | | 1 | | | | | | |
| 2. $M^zOH \to M^{z+1}OH + e^-$ | 2 | $2RT/3F$ | $2RT/F$ | 1 | 0 | $2RT/F$ | | 0 | | $r_1 \sim r_2$[g] |
| | | | | | | $RT/F$ | | 0.5 | | $r_1 >> r_2$ |
| 3. $2M^{z+1}OH + 2OH^- \to 2M^z + H_2O + O_2$ | 1 | $RT/4F$ | $\infty$ | 4 | 2 | $RT/2F$ | $RT/F$ | 4 | 3 | $K_2 \sim 1$ |
| | | | | | | $RT/4F$ | $RT/3F$ | 4 | 3 | $K_2 << 1$ |
| **(V) Kobussen's Path** | | | | | | | | | | |
| 1. $M + OH \to MOH + e$ | 1 | $2RT/F$ | | 1 | | | | | | |
| 2. $MOH + OH^- \to MO + H_2O + e^-$ | 1 | $2RT/3F$ | $2RT/3F$ | 2 | 1 | $2RT/F$ | | 1 | | $r_{OH} \sim r_O$ |
| | | | | | | $RT/F$ | | 1.5 | | $r_{OH} >> r_O$ |
| 3. $MO + OH^- \to MO_2H$ | 1 | $RT/2F$ | $\infty$ | 3 | 1 | $\infty$ | | 1 | | $K_2 \sim 1$ |
| | | | | | | $RT/F$ | | 2 | | $K_2 << 1$ |
| 4. $MO_2H^- + OH^- \to MO_2^- + H_2O + e^-$ | 1 | $2RT/5F$ | $2RT/F$ | 4 | 1 | $2RT/F$ | | 1 | | $K_3 \sim 1$ |
| | | | | | | $2RT/F$ | | 2 | | $K_3 << 1$ |
| 5. $MO_2^- \to M + O_2 + e^-$ | 1 | $2RT/7F$ | $\infty$ | 4 | 0 | $RT/F$ | $2RT/F$ | 1 | 0.5 | $K_4 \sim 1$ |
| | | | | | | $RT/2F$ | $2RT/3F$ | 1 | 1.5 | $K_4 << 1$ |

[a] Symmetry factors, i.e., $\beta$, $\gamma$, and $\delta$, in all steps, were taken as $^1/_2$. [b] Stoichiometric number. [c] $\zeta$ is the potential difference between the cHp (outer Helmholtz plane) and the bulk of the solution ($\zeta$ potential). [d] Nonactivated desorption of $O_2$. [e] Activated desorption of $O_2$. [f] $r$ is a coefficient determining the variation of heat of adsorption of a particular species with coverage. Unless stated, $r$ values for each species were taken as equal. $K_i$ is the equilibrium constant of the $i$th step. [g] $r_1$ and $r_2$ refer to $r$ for $M^zOH$ and $r$ for $M^{z+1}OH$, respectively.

Table 1.5.1 Diagnostic criteria of proposed paths for the oxygen evolution reaction. Reproduced from Ref.[271]

The pathway proposed by Krasil'shchikov[245] (mechanism III in Table 1.5.1) is widely the most proposed reaction mechanism for the OER on both anodic oxide films on metallic electrodes and thermally prepared metal oxide electrodes. Authors who rationalised their data based on Krasil'shchikov mechanism have been able to attribute changes in the slopes of steady-state polarisation curves with increasing overpotential to changes in the RDS within the pathway. The Krasil'shchikov pathway predicts that the O-O bond of the evolved oxygen molecule will be formed after the rate determining step, since steps 1, 2 or 3 are normally considered to be the RDS (depending on the value of the Tafel slope).

The relevant work of Damjanovic, Dey and Bockris[120c], concerning the OER on Pt electrodes in both alkaline and acidic electrolytes lead these authors to the general

conclusion that the following modified Krasil'schchikov scheme might explain the observed experimental kinetic parameters in the alkaline case:

$$M + OH^- \leftrightarrow MOH + e^- \quad (1.5.15)$$

$$MOH + OH^- \leftrightarrow MO - H - OH^- \quad (1.5.16)$$

$$MO - H - OH^- \leftrightarrow MO - H - OH + e^- \quad (1.5.17)$$

$$MO - H - OH \leftrightarrow MO + H_2O \quad (1.5.18)$$

$$2MO \leftrightarrow 2M + O_2 \quad (1.5.19)$$

where M represents a catalytic active site on the metal oxide surface. Experimentally, the aforementioned authors found that the anodic Tafel slope in 1.0 N KOH at 25°C was approximately 2.303RT/F, which is ca. 60 mV $dec^{-1}$ at lower values of overpotential. The value of Tafel slope changes at higher overpotentials to values of approximately 2.303 x 2RT/F which is ca. 120 mV $dec^{-1}$. The observed value of 60 mV $dec^{-1}$ was rationalised by admitting step 2 to be the RDS under low coverage Langmuir adsorption conditions, with step 1 becoming RDS under Temkin adsorption conditions at higher overpotentials. An important issue that was considered by Damjanovic, Dey and Bockris[120c] was the origin of the change in the Tafel slope observed from their steady-state measurement data of Pt in 1.0 M KOH. Such changes in the Tafel slope with increasing overpotentials are often observed in polarisation measurements that characterise the kinetics of the OER. So, the discussion of these authors may be applicable to several different systems than those they explicitly investigated. The authors considered four possible explanations for the change in the Tafel slope, those being: (i) a change in the reaction pathway, (ii) a change in the electrode substrate, (iii) a change in the RDS within a given pathway, and (iv) the influence of changing potentials on the adsorption of the reaction intermediate species. They concluded that the latter two reasons were the most likely to occur, and that it may be possible to discriminate between behaviours due to (iii) or (iv) by carefully studying the steady-state polarisation curves. It is relevant to mention that the surface coverage of the reaction intermediate may vary with the applied potential. To support this idea, Damjanovic, Dey and Bockris provided a rough calculation which showed that, if the heat

of adsorption of an intermediate species changes by a typical value of approximately 10 Kcal $mol^{-1}$ as it fractional coverage increases from $\theta = 0.1$ to $\theta = 0.9$, then the range of potential over which Temkin conditions might be expected to hold is limited to ca. 150 mV. Observation of the limitation of one of the straight line Tafel regions to such a potential range would point towards (iv) as opposed to (iii) being the reason behind the dual slope behaviour in such a case.

The OER mechanistic pathway for transition metals slightly differs from the one previously introduced for metals. In line with this section, possible mechanistic pathways for Ni and Co electrodes are presented. Lu and Srinivasan[276] found that the potential at which Ni electrodes were polarized on 1.0 M KOH affected the shape of the Tafel slope. They found that if the electrode was previously oxidised at ca. 575 mV, the steady-state polarisation measurement revealed a single Tafel slope region with b= ca. 40 mV $dec^{-1}$, whereas at higher oxidation potentials, ca. 0.8 - 1 V, yielded to the observation of two Tafel slope regions. In the latter case, at low current densities on the steady-state polarisation plot the slope was again ca. 40 mV $dec^{-1}$, while at higher current densities a less well-defined slope of ca. 170 mV $dec^{-1}$ was observed. The authors proposed that this kinetic data could be accounted for the following modified Krasil'shchikov mechanism with step 3 being the RDS in the low Tafel region of potential:

$$OH^-_{(ads)} \leftrightarrow OH_{(ads)} + e^-_{(latt)} \quad (1.5.20)$$

$$OH_{(ads)} + OH^- \leftrightarrow O^-_{(ads)} + H_2O \quad (1.5.21)$$

$$2\beta NiOOH_{(surf)} + O^-_{(ads)} \leftrightarrow 2NiO_{2(surf)} + H_2O + e^-_{(latt)} \quad (1.5.22)$$

$$2NiO_{2(surf)} + H_2O \leftrightarrow 2\beta NiOOH_{(surf)} + O_{(ads)} \quad (1.5.23)$$

$$O_{(ads)} + O_{(ads)} \leftrightarrow O_2 \quad (1.5.24)$$

As discussed in section 1.3.3, the β-NiOOH was mentioned to be the "right type of oxide" for the electrocatalysis of the OER. In this perspective, Lu and Srinivasan[276] have attributed the decrease in the electrocatalytic activity of β-NiOOH to the formation of $NiO_2$ on the surface of the oxide film. They proposed that the generation of each $Ni^{4+}$ ion on the

film surface creates and inert site for the oxygen evolution. The authors further proposed that the observance of a Tafel slope of 170 mV $dec^{-1}$ at high overpotentials arises from barrier layer effects associated with the poor conductivity of the oxide film germinated at these potentials, owing to their relatively higher $Ni^{4+}$ content.

Modified Krasil'shchikov mechanism has also been proposed in the rationalisation of OER kinetic data obtained on Co electrodes in alkaline solution. Burke *et al*.[277] performed steady-state polarisation measurements in 6.0 M KOH at 30°C on both a Co electrode on with a hydrous oxyhydroxide layer grown by a potential cycling method, and on an initially oxide free Co rod electrode. The potential cycling region was set between 0 V and 1.2 V (*vs.* RHE) at 33 mV $s^{-1}$ in 6.0 M KOH for 30 minutes. A Tafel slope of 60 mV $dec^{-1}$ was observed for the initially oxide free electrode, while a somewhat lower slope of 52 mV $dec^{-1}$ was recorded for the pre-cycled electrode. The polarisation curves for the two electrodes were coincident at lower current densities. However, owing to its smaller Tafel slope, the current density achieved at the pre-cycles electrode was higher than the other one by a factor of ca. 2.5 over a potential range between 1.6V - 1.7V. The two polarisation curves converged at higher overpotentials. These workers proposed the following modification of the Krasil'shchikov mechanism pathway to explain their experimental observations:

$$OH^- \leftrightarrow OH_{(ads)} + e^- \tag{1.5.25}$$

$$OH_{(ads)} + OH^- \leftrightarrow O^-{}_{(ads)} + H_2O \tag{1.5.26}$$

$$Co \cdot O_2 + O^-{}_{(ads)} \leftrightarrow CoO_2 \cdot O + e^- \tag{1.5.27}$$

$$2NiO_{2(surf)} + H_2O \leftrightarrow 2\beta NiOOH_{(surf)} + O_{(ads)} \tag{1.5.28}$$

$$O_{(ads)} + O_{(ads)} \leftrightarrow O_2 \tag{1.5.29}$$

It is noteworthy that the above reaction scheme is similar, in the first two steps, to that proposed by Lu and Srinivasan presented in eqns. 1.5.20 - 1.5.24, for the OER on Ni electrodes in alkaline solution. A notorious difference between these two schemes arises on the respective third steps. In eqn. 1.5.22 of the scheme of Lu and Srinivasan, the electrocatalytically active surfaces species is a Ni (III) entry, with these authors placing

particular emphasis on the importance of $\beta NiOOH$ in the course of the OER on a polarized Ni electrode. On the other hand, in eqn. 1.5.27 proposed by Burke *et al*., the active surface species in the third step is Co (IV) entry.

## 1.6 Motivations and Objectives

From the times of the industrial revolution, back in 1770, until recent days, energy has been the driving force of technological, economical and social development of countries. These developments provoked large improvements on the standard of living, to the extent that world's population has reached 6 billion, but also led to a high energy demand. Interestingly, now a days, the energy consumption has exceeded the stage of fundamental needs.

The current energy model, based on the combustion of fossil fuels such as coal, crude oil or natural gas, is no longer sustainable. According with the European Environment Agency (EEA), "fossil fuels continue to represent by far the main source of energy, although their weight has constantly decreased over the past decades, from 83% in 1990 to 73% in 2015". Fossil fuels are carbon-based and their combustion leads to the release of carbon into the Earth's atmosphere. This provokes two main consequences: (i) the depletion of non-renewable resources, and (ii) the emission of greenhouse gases and air pollutants, *e.g.* $NO_x$ and $SO_2$. The latter, in turn, has negative effects on public health and biodiversity. However, over the past 60 years, considerable research efforts have been focused on the realisation of economical, efficient, clean and renewable energy sources.

The preferred green energy source must involve a clean, non-polluting fuel which, preferably, must be made out of the one of the most abundant raw materials available on earth. In this sense, a potential raw material to create green energy from could be the water.

Combining the two most abundant resources available: (i) water, and (ii) solar energy, it is possible to generate a clean fuel, hydrogen gas, which when burned would not generate pollution. It is possible to extract hydrogen gas from the sea using energy from the sunlight to power our planet. If hydrogen is combined with oxygen, one can generate electricity in a suitable device such as the electrochemical fuel cell. The optimum scenario would be such

in which the energy required for the electrolysis reaction to be minimum and the energy obtained from the $H_2$ combustion to be maximum.

It can be seen in eqn. 1.3.9b (electrolysis reaction) that an energy input is required in order to split apart the water molecules to generate hydrogen and oxygen gas. The total energy, or potential, required to drive the electrolysis reaction involves: (i) the thermodynamic potential, (ii) both cathode and anode overpotentials, and (iii) ohmic resistance contributions, as seen in eqn. 1.5.4. Whereas the thermodynamic potential value will be given by the Gibbs free energy of the reaction, both the cathode and anode overpotentials along with the ohmic resistance can be modified by using different catalysis or by improving the cell design, respectively.

Unfortunately, global hydrogen production form water electrolysis is currently not economically viable due to large production costs. The latter arise because the $H_2$ production from water splitting is mainly limited by the kinetics of the $O_2$ production at the anodes, that is, limited by the oxygen evolution reaction (OER) kinetics, as seen in eqn. 1.3.9a. Note that such reaction involves $4e^-$ transfer. Therefore, in order to reduce the energy requirements for the reaction to occur, transition metal oxides (cobalt, nickel, manganese, iron, ruthenium and iridium) have already been proposed as a catalysts materials for OER. The singularity of the proprieties of transition metal oxide lies in the nature of the partly electron filled d-shell which produces an easy electron transfer back and forth between free oxygen and transition metal ions. More information on the same can be found in section 1.3.2.

The required proprieties of an ideal OER catalyst are: (i) high electrochemical efficiency, (ii) low material cost, (iii) industrial use feasibility, (iv) long-term stability, and (v) earth abundance. As seen in fig. 1.3.3, iridium and ruthenium oxides have the best OER activity, however due to their high economical cost, they are not economically viable for industrial applications. Interestingly, nickel, cobalt, and manganese oxides offer a great balance between their cost and OER activity.

According with all of the previously exposed, it is the purpose of this doctoral thesis to develop an efficient, stable and cheap electrocatalyst electrode, using transition metal oxide electrodes, for the enhancement of OER. This work will focus, primarily, on the electrochemical analysis, in alkaline solution, of three types of chemical elements: (i) nickel, (ii) cobalt, and (iii) manganese oxides electrodes. It is also the intention of the

present work to give an overview of various approaches to study both the surface and the bulk proprieties of such catalyst electrodes.

## 1.7 References Chapter 1


[1] A. C. Fisher, *Electrode Dynamics*, **1996**.

[2] A. Bard, L. Faulkner, *Electrochemical Methods: Fundamentals and Applications*, John Wiley & Sons, Inc, **2001**.

[3] K. G. a. M. K. Hans-Jürgen Butt, *Physics and Chemistry of Interfaces*, 2nd ed., **2003**.

[4] L. Bellarosa, R. García-Muelas, G. Revilla-López, N. López, *ACS Central Science* **2016**, *2*, 109-116.

[5] J. W. Gibbs, *The Scientific Papers of J. Willard Gibbs, Vol. 1*, Dover Publications, New York, **1961**; E. A. Guggenheim, *The Journal of Physical Chemistry* **1928**, *33*, 842-849.

[6] W. Schottky, H. Rothe, H. Simon, *Physik der Glühelektroden*, Akademische Verlagsgesellschaft m. b. h., Leipzig, **1928**.

[7] J. O. M. Bockris, *Energy Conversion* **1970**, *10*, 41-43; J. O. M. Bockris, *Journal of Electroanalytical Chemistry and Interfacial Electrochemistry* **1972**, *36*, 495-496.

[8] aG. Lippmann, *Annalen der Physik* **1873**, *225*, 546-561; bG. Lippmann, *Annalen der Physik* **1880**, *247*, 316-324.

[9] D. C. Grahame, *Chemical Reviews* **1947**, *41*, 441-501.

[10] J. O. M. Bockris, A. K. N. Reddy, *Modern electrochemistry : an introduction to an interdisciplinary area, ch.7*, Plenum Press, New York, NY, **1977**.

[11] H. Helmholtz, *Annalen der Physik* **1879**, *243*, 337-382; H. Helmholtz, *Annalen der Physik* **1853**, *165*, 353-377.

[12] M. Gouy, *J. Phys. Theor. Appl.* **1910**, *9*, 457-468.

[13] D. L. Chapman, *The London, Edinburgh, and Dublin Philosophical Magazine and Journal of Science* **1913**, *25*, 475-481.

[14] A. J. Bard, *Electrochemical methods : fundamentals and applications / Allen J. Bard, Larry R. Faulkner*, Wiley, New York, **1980**.

[15] O. Stern, *Zeitschrift für Elektrochemie und angewandte physikalische Chemie* **1924**, *30*, 508-516.

[16] D. C. Grahame, *Chem. Rev. (Washington, DC, U. S.)* **1947**, *41*, 441-501.

[17] A. Luzar, S. Svetina, B. Zeks, *J. Chem. Phys.* **1985**, *82*, 5146-5154.

[18] B. E. Conway, J. O. M. Bockris, *Modern Aspects of Electrochemistry, No. 9*, Plenum, **1974**; B. E. Conway, *Adv. Colloid Interface Sci.* **1977**, *8*, 91-211; A. Lasia, in *Modern Aspects of Electrochemistry* (Eds.: B. E. Conway, J. O. M. Bockris, R. E. White), Springer US, Boston, MA, **2002**, pp. 143-248.

[19] J. R. Macdonald, C. A. Barlow, Jr., *Proc. Australian Conf. Electrochem., 1st, Sydney, Hobart, Australia* **1965**, *1963*, 199-247.

[20] J. O. M. Bockris, M. A. Habib, *Electrochim. Acta* **1977**, *22*, 41-46; J. O. M. Bockris, M. A. Habib, *Journal of Electroanalytical Chemistry and Interfacial Electrochemistry* **1976**, *68*, 367-370.

[21] J. O. M. Bockris, S. U. M. Khan, *Surface electrochemistry : a molecular level approach*, Plenum, New York, **1993**.

[22] S. Engstrom, H. Wennerstrom, *The Journal of Physical Chemistry* **1978**, *82*, 2711-2714.

[23] S. Hocine, R. Hartkamp, B. Siboulet, M. Duvail, B. Coasne, P. Turq, J.-F. Dufrêche, *The Journal of Physical Chemistry C* **2016**, *120*, 963-973.

[24] *Proceedings of the Royal Society of London. Series A. Mathematical and Physical Sciences* **1963**, *274*, 55.

[25] N. F. Mott, R. J. Watts-Tobin, *Electrochimica Acta* **1961**, *4*, 79-107; R. J. Watts-tobin, *The Philosophical Magazine: A Journal of Theoretical Experimental and Applied Physics* **1961**, *6*, 133-153.

[26] J. O. M. Bockris, K. T. Jeng, *Advances in Colloid and Interface Science* **1990**, *33*, 1-54.

[27] W. N. Hansen, *J. Electroanal. Chem. Interfacial Electrochem.* **1983**, *150*, 133-140; J. O. M. Bockris, M. A. V. Devanathan, K. Mueller, *Proc. Phys. Soc. (London) Ser. A* **1963**, *274*, 55-79.
[28] J. O. M. Bockris, S. U. M. Khan, *Surface Electrochemistry: A Molecular Level Approach*, Plenum, **1993**; T. Nagy, D. Henderson, D. Boda, *The Journal of Physical Chemistry B* **2011**, *115*, 11409-11419.
[29] A. J. S. Bard, M., Ed., Gileadi, E., Urbakh, M.,Vol, Ed., in *Encyclopedia of Electrochemistry, Vol. 1* (Ed.: A. A. Kornyshev, Sohr, E., Vorotyntsev., M.A.,), Wiley-VCH, Weinheim, **2002**.
[30] M. F. Toney, J. N. Howard, J. Richer, G. L. Borges, J. G. Gordon, O. R. Melroy, D. G. Wiesler, D. Yee, L. B. Sorensen, *Nature* **1994**, *368*, 444.
[31] J. R. Macdonald, *J. Chem. Phys.* **1954**, *22*, 1857-1866; R. J. Macdonald, C. A. Barlow, Jr., *J. Chem. Phys.* **1962**, *36*, 3062-3080.
[32] W. Schimckler*, Vol. 1* (Ed.: A. J. Bard, and Stratmann, M., Gileadi E., and Urbakh M. ), Wiley-VCH, Weinheim, **2002**.
[33] B. B. Damaskin, A. N. Frumkin, *Electrochim. Acta* **1974**, *19*, 173-176.
[34] M. A. Habib, *Mod. Aspects Electrochem.* **1977**, *12*, 131-182.
[35] W. R. Fawcett, *J. Phys. Chem.* **1978**, *82*, 1385-1390; W. R. Fawcett, *Isr. J. Chem.* **1979**, *18*, 3-16.
[36] R. Parsons, *Journal of Electroanalytical Chemistry and Interfacial Electrochemistry* **1975**, *59*, 229-237.
[37] J. O. M. Bockris, M. A. Habib, *J. Electroanal. Chem. Interfacial Electrochem.* **1975**, *65*, 473-489.
[38] S. Trasatti, *Journal of Electroanalytical Chemistry and Interfacial Electrochemistry* **1981**, *123*, 121-139.
[39] S. Trasatti, *Electrochimica Acta* **1983**, *28*, 1083-1093.
[40] J. P. Badiali, J. Goodisman, *J. Electroanal. Chem. Interfacial Electrochem.* **1978**, *91*, 151-171; J. P. Badiali, M. L. Rosinberg, J. Goodisman, *J. Electroanal. Chem. Interfacial Electrochem.* **1981**, *130*, 31-45.
[41] J. R. Macdonald, *The Journal of Chemical Physics* **1954**, *22*, 1857-1866.
[42] D. Henderson, L. Blum, M. Lozada-Cassou, *Journal of Electroanalytical Chemistry and Interfacial Electrochemistry* **1983**, *150*, 291-303.
[43] U. Stimming, W. Schmickler, *J. Electroanal. Chem. Interfacial Electrochem.* **1983**, *150*, 125-131; L. D. Burke, L. M. Kinsella, A. M. O'Connell, *Russ. J. Electrochem.* **2004**, *40*, 1105-1114; M. Haruta, N. Yamada, T. Kobayashi, S. Iijima, *J. Catal.* **1989**, *115*, 301-309.
[44] N. D. Lang, W. Kohn, *Physical Review B* **1973**, *7*, 3541-3550.
[45] D. H. Everett, Ed.,, *Definitions, Terminology and Symbols in Colloid and Surface Science, Vol. Part 1*, **1972**.
[46] J. O. M. Bockris, in *Trends in Electrochemistry* (Eds.: J. O. M. Bockris, D. A. J. Rand, B. J. Welch), Springer US, Boston, MA, **1977**, pp. 1-23.
[47] E. Yeager, *Surf. Sci.* **1980**, *101*, 1-22.
[48] G. Blondeau, E. Yeager, *Progress in Solid State Chemistry* **1976**, *11*, 153-202.
[49] H. Gerischer, C. W. Tobias, Editors, *Advances in Electrochemistry and Electrochemical Engineering, Vol. 10*, Wiley, **1977**; B. E. Conway, J. O. M. Bockris, Editors, *Modern Aspects of Electrochemistry, No. 13*, Plenum Press, **1979**; S. Trasatti, *J. Electroanal. Chem. Interfacial Electrochem.* **1975**, *65*, 815-829.
[50] B. G. Baker, Plenum, **1977**, pp. 233-239.
[51] F. M. Propst, T. C. Piper, *J. Vac. Sci. Technol.* **1967**, *4*, 53-56; H. Ibach, *J. Vac. Sci. Technol.* **1972**, *9*, 713-719.
[52] W. Heiland, E. Taglauer, *J. Vac. Sci. Technol.* **1972**, *9*, 620-623.
[53] J. D. E. McIntyre, *Surface Science* **1973**, *37*, 658-682.
[54] B. D. Cahan, *Surface Science* **1976**, *56*, 354-372; B. D. Cahan, *Surf. Sci.* **1976**, *56*, 354-372.

[55] S. J. Atkinson, C. R. Brundle, M. W. Roberts, *J. Electron Spectrosc. Relat. Phenomena* **1973**, *2*, 105-109.
[56] N. Sato, Editor, *Electrochemistry at Metal and Semiconductor Electrodes, Vol. Chapter 2*, Elsevier, **1998**.
[57] W. H. Strehlow, E. L. Cook, *Journal of Physical and Chemical Reference Data* **1973**, *2*, 163-200.
[58] N. Sato, in *Electrochemistry at Metal and Semiconductor Electrodes* (Ed.: N. Sato), Elsevier Science, Amsterdam, **1998**, pp. 61-86.
[59] N. Sato, Editor, *Electrochemistry at Metal and Semiconductor Electrodes, Vol. Chapter 5*, Elsevier, **1998**.
[60] J. S. Choy, W. J. Moore, *J. Phys. Chem.* **1962**, *66*, 1308-1311.
[61] M. T. Shim, W. J. Moore, *J. Chem. Phys.* **1957**, *26*, 802-804; M. O'Keeffe, W. J. Moore, *J. Phys. Chem.* **1961**, *65*, 1438-1439.
[62] R. E. a. T. Cech, T. D. , *Composites* **1969**, *1*, 185.
[63] A. Z. Hed, *The Journal of Chemical Physics* **1969**, *50*, 2935-2937; E. Fryt, *Oxidation of Metals* **1976**, *10*, 311-327.
[64] R. Platzer, E. Karapetrova, M. O. Zacate, J. A. Gardner, J. A. Sommers, W. E. Evenson, *Materials Science Forum* **1997**, *239-241*, 57-60.
[65] G. Rogers, G. Simkovich, K. Osseo-Asare, *Hydrometallurgy* **1983**, *10*, 313-328.
[66] P. Liao, J. A. Keith, E. A. Carter, *J. Am. Chem. Soc.* **2012**, *134*, 13296-13309.
[67] P. Kofstad, *Defects and Transport Properties of Metal Oxides, Vol. 44*, **1995**.
[68] A. S.M, *Oxides and Oxide Films, Vol. 1*, Marcel Dekker, New York, **1977**.
[69] J. R. O. Wiese G.R., Yates D.E and Healy T.W., *International Review of Science, Electrochemistry. Physical Chemistry, Vol. 6*, Butterworths, London, **1976**; D. E. Y. a. T. W. H. D.N. Furlong, (Ed.: S.Trasatti), Elsevier, Amsterdam, **1981**, p. 367.
[70] G. A. Parks, P. L. d. Bruyn, *The Journal of Physical Chemistry* **1962**, *66*, 967-973.
[71] H. Tamura, A. Tanaka, K.-y. Mita, R. Furuichi, *Journal of Colloid and Interface Science* **1999**, *209*, 225-231; A. J. Nozik, R. Memming, *J. Phys. Chem.* **1996**, *100*, 13061-13078; H. P. Boehm, *Discussions of the Faraday Society* **1971**, *52*, 264-275.
[72] H. Tamura, Furuichi, R., Ryusaburo *Bunseki Kagaku* **1991**, *40*, 635-640.
[73] H. Gerisher*, Vol. IXA* (Ed.: H. a. J. Reyring), Academic Press, New York, **1970**.
[74] V. A. Myamlin, Y. V. Pleskov, *Electrochemistry of Semiconductors*, Consultants Bur., **1967**.
[75] Y. V. Pleskov, *Elektrokhimiya* **1981**, *17*, 3-31.
[76] R. K. Kalia, M. F. Weber, L. Schumacher, M. J. Dignam, *Surface Science* **1980**, *101*, 214-223; M. J. Dignam, *Canadian Journal of Chemistry* **1978**, *56*, 595-605.
[77] J. N. Chazalviel, *Journal of The Electrochemical Society* **1982**, *129*, 963-969.
[78] K. Rajeshwar, *Journal of The Electrochemical Society* **1982**, *129*, 1003-1008.
[79] K. E. Heusler, *Zeitschrift für Elektrochemie, Berichte der Bunsengesellschaft für physikalische Chemie* **1958**, *62*, 582-587.
[80] T. P. H. a. T. Hurlen, in *CITCE* (Ed.: Butterworths), Madrid, **1956**.
[81] M. Tomkiewicz, *Surface Science* **1980**, *101*, 286-294; S. R. Morrsion, Plenum Press, New York, **1977**.
[82] I. Tamm, *Zeitschrift für Physik* **1932**, *76*, 849-850.
[83] M. Green*, Vol. 2*, Butterworths, London, **1959**.
[84] J. P. Carr, N. A. Hampson, R. Taylor, *Journal of Electroanalytical Chemistry and Interfacial Electrochemistry* **1970**, *27*, 109-116.
[85] S. M. Ahmed, D. Maksimov, *Journal of Colloid and Interface Science* **1969**, *29*, 97-104.
[86] G. E. Brown, V. E. Henrich, W. H. Casey, D. L. Clark, C. Eggleston, A. Felmy, D. W. Goodman, M. Grätzel, G. Maciel, M. I. McCarthy, K. H. Nealson, D. A. Sverjensky, M. F. Toney, J. M. Zachara, *Chemical Reviews* **1999**, *99*, 77-174.

[87] K. J. Vetter, Academic Press, New York, **1967**; J. O. M. a. R. A. K. N. Bockris, *Modern Electrochemistry, Vol. 2*, Plenum Press, New York, **1970**; R. Greff, R. Peat, L. M. Peter, J. Robinson, in *Instrumental Methods in Electrochemistry*, Ellis, Chichester, **1985**.
[88] J. Tafel, *Z. Phys. Chem.* **1905**, *50*, 641-712.
[89] J. A. V. Butler, *Transactions of the Faraday Society* **1924**, *19*, 729-733.
[90] T. Erdey-Grúz, M. Volmer, in *Z. Phys. Chem., Vol. 150A*, **1930**, p. 203.
[91] R. W. Gurney, E. Rutherford, *Proceedings of the Royal Society of London. Series A, Containing Papers of a Mathematical and Physical Character* **1931**, *134*, 137-154.
[92] A. Frumkin, in *Z. Phys. Chem., Vol. 164A*, **1933**, p. 121.
[93] R. Parsons, *Transactions of the Faraday Society* **1951**, *47*, 1332-1344.
[94] P. Delahay, *The Journal of Physical Chemistry* **1966**, *70*, 2373-2379.
[95] H. Fischer, *Zeitschrift für Elektrochemie und angewandte physikalische Chemie* **1951**, *55*, 92-97.
[96] W. Lorenz, *Z. Naturforsch* **1954**, *9a*, 716.
[97] H. Brandes, *E. Physik. Chem.* **1929**, *142*, 97.
[98] A. Bewick, A. Bewick, M. Fleischmann, M. Liler, *Electrochimica Acta* **1959**, *1*, 83-105; M. C. Wiles, D. J. Schiffrin, T. J. VanderNoot, A. F. Silva, *Journal of Electroanalytical Chemistry and Interfacial Electrochemistry* **1990**, *278*, 151-159.
[99] J. O. M. Bockris*, Vol. 1*, London, **1954**.
[100] B. E. Conway, R. Greef, *Journal of The Electrochemical Society* **1966**, *113*, 325C-326C.
[101] P. Delahay, Wiley Interscience, New York, **1966**.
[102] K. J. L. a. H. E. S. Glasstone, *The Tehory of Rate Processes*, McGraw-Hill, New York, **1941**; H. Eyring, S. Glasstone, K. J. Laidler, *The Journal of Chemical Physics* **1939**, *7*, 1053-1065; H. Eyring, L. Marker, T.-C. Kwoh, *The Journal of Physical and Colloid Chemistry* **1949**, *53*, 1453-1464.
[103] A. Bard, L. Faulkner, John Wiley & Sons, Inc, **2001**.
[104] D. C. Henry, A. Lapworth, *Proceedings of the Royal Society of London. Series A, Containing Papers of a Mathematical and Physical Character* **1931**, *133*, 106-129.
[105] H. Freundlich, in *Kapillarchemie*, Akademische Verlagsgesellschaft, Leipzig, **1923**.
[106] I. Langmuir, *Journal of the American Chemical Society* **1918**, *40*, 1361-1403.
[107] A. Frumkin, in *Z. Phys. Chem., Vol. 116U*, **1925**, p. 466.
[108] M. I. Temkin, *Zhurnal Fiziche Khimii* **1941**, *15*, 296.
[109] B. E. Conway, *Theory and Principles of Electrode Processes*, Ronald Press, New York, **1965**.
[110] P. D. a. B. Ershler, *Acta Physicochimica URSS* **1940**, 747; J. O. M. Bockris, H. Kita, *Journal of The Electrochemical Society* **1961**, *108*, 676-685; B. E. Conway, E. Gileadi, *Transactions of the Faraday Society* **1962**, *58*, 2493-2509.
[111] J. O. M. Bockris, E. C. Potter, *Journal of The Electrochemical Society* **1952**, *99*, 169-186.
[112] J. O. M. Bockris, *The Journal of Chemical Physics* **1956**, *24*, 817-827.
[113] D. J. Hautman, F. L. Dryer, K. P. Schug, I. Glassman, *Combustion Science and Technology* **1981**, *25*, 219-235.
[114] E. K.-E. a. J. P. E. Gileadi, *Interfacial Electrochemistry, An experimental Approach* Addison-Wesley, London, **1975**.
[115] K. C. Pillai, J. O. M. Bockris, *Journal of The Electrochemical Society* **1984**, *131*, 568-579; B. E. Conway, (Ed.: J. W. Sons), Barsoukov, E., Macdonald, J.R, **2005**.
[116] J. Horiuti, M. Ikusima, *Proceedings of the Imperial Academy* **1939**, *15*, 39-44; A. C. Makrides, *Journal of The Electrochemical Society* **1957**, *104*, 677-681; A. C. Makrides, *Journal of The Electrochemical Society* **1962**, *109*, 256-260; E. M.*, Vol. 11* (Ed.: J. O. M. a. C. B. E. Bockris), Plenum Press, New York **1975**.
[117] M. D. B. a. B. J.O'M.*, Vol. 6* (Ed.: J. O. M. a. C. B. E. Bockris), Plenum Press, New York, **1971**, p. 242.

[118] B. E. Conway, L. Bai, M. A. Sattar, *International Journal of Hydrogen Energy* **1987**, *12*, 607-621.
[119] M. D. Merrill, R. C. Dougherty, *The Journal of Physical Chemistry C* **2008**, *112*, 3655-3666.
[120] A. Damjanovic, M. A. Genshaw, J. O. M. Bockris, *Journal of The Electrochemical Society* **1967**, *114*, 1107-1112; M. A. Genshaw, A. Damjanovic, J. O'M. Bockris, *Role of hydrogen peroxide in oxygen reduction at rhodium electrodes, Vol. 71*, **1967**; A. Damjanovic, A. Dey, J. O. M. Bockris, *Electrochimica Acta* **1966**, *11*, 791-814; R. Guidelli, G. Compton Richard, M. Feliu Juan, E. Gileadi, J. Lipkowski, W. Schmickler, S. Trasatti, in *Pure Appl. Chem., Vol. 86*, **2014**, p. 245.
[121] E. Fachinotti, E. Guerrini, A. C. Tavares, S. Trasatti, *Journal of Electroanalytical Chemistry* **2007**, *600*, 103-112; R. L. Doyle, M. E. G. Lyons, *Journal of The Electrochemical Society* **2013**, *160*, H142-H154; R. L. Doyle, M. E. G. Lyons, *Physical Chemistry Chemical Physics* **2013**, *15*, 5224-5237.
[122] D. A. Harrington, P. van den Driessche, *Electrochimica Acta* **2011**, *56*, 8005-8013.
[123] M. E. G. Lyons, M. P. Brandon, *Physical Chemistry Chemical Physics* **2009**, *11*, 2203-2217.
[124] J. O. M. Bockris, Reddy A.K.N. and Gamboa-Aldeco M., 2nd ed., Kluwer Academic Publishers, New York,, **2002**, p. 1412.
[125] B. Conway, E. Gileadi, *Transactions of the Faraday Society* **1962**, *58*, 2493-2509.
[126] B. E. Conway, M. Salomon, *Electrochemical reaction orders: Applications to the hydrogen- and oxygen-evolution reactions, Vol. 9*, **1964**.
[127] M. E. G. Lyons, R. L. Doyle, D. Fernandez, I. J. Godwin, M. P. Browne, A. Rovetta, *Electrochemistry Communications* **2014**, *45*, 56-59.
[128] R. Parsons, *Advances in Electrochemistry and Electrochemical Engineering*, Interscience, New York, **1961**; W. J. Albery, *Electrode kinetics*, Clarendon, Oxford, **1975**; M. E. G. Lyons, S. Floquet, *Physical Chemistry Chemical Physics* **2011**, *13*, 5314-5335.
[129] J. O. M. Bockris, T. Otagawa, *The Journal of Physical Chemistry* **1983**, *87*, 2960-2971.
[130] M. Pourbaix, *Atlas of Electrochemical Equilibria in Aqueous Solutions*, 2nd ed., National Association of Corrosion Engineers, Houston, TX, **1974**.
[131] R. A. Robinson, R. H. Stokes, *Electrolyte solutions*, Butterworths, London, **1959**.
[132] I. Streeter, R. G. Compton, *Electrochimica Acta* **2007**, *52*, 4305-4311.
[133] J. O. M. Bockris, A. K. N. Reddy, *Modern electrochemistry : an introduction to an interdisciplinary area, ch.8*, Plenum Press, New York, NY, **1977**.
[134] W. T. Grubb, *Nature* **1963**, *198*, 883.
[135] I. Horiuti, M. Polanyi, *Transactions of the Faraday Society* **1934**, *30*, 1164-1172.
[136] S. Srinivasan, H. Wroblowa, J. O. M. Bockris, in *Advances in Catalysis, Vol. 17* (Eds.: D. D. Eley, H. Pines, P. B. Weisz), Academic Press, **1967**, pp. 351-418.
[137] S. Trasatti, *Journal of Electroanalytical Chemistry and Interfacial Electrochemistry* **1972**, *39*, 163-184.
[138] K. Kinoshita, *Electrochemical Oxygen Technology, Vol. 30*, John Wiley & Sons, **1992**; A. C. C. Tseung, S. Jasem, *Electrochimica Acta* **1977**, *22*, 31-34.
[139] C. N. R. Rao, *Annual Review of Physical Chemistry* **1989**, *40*, 291-326.
[140] L. I. Krishtalik, in *Comprehensive Treatise of Electrochemistry: Volume 7 Kinetics and Mechanisms of Electrode Processes* (Eds.: B. E. Conway, J. O. M. Bockris, E. Yeager, S. U. M. Khan, R. E. White), Springer US, Boston, MA, **1983**, pp. 87-172.
[141] R. Parsons, in *Modern aspects of electrochemistry., Vol. 1* (Eds.: J. O. M. Bockris, B. E. Conway), Butterworths, London, **1954**.
[142] Gerisher H., (Ed.: A. D. Franklin), U.S. Dept. of Commerce, Washington D.C., **1975**.
[143] J. O. M. Bockris, A. Damjanovic, R. J. Mannan, *Journal of Electroanalytical Chemistry and Interfacial Electrochemistry* **1968**, *18*, 349-361.
[144] R. Parsons, *Surface Science* **1964**, *2*, 418-435.
[145] S. Trasatti*, Vol. 10*, Wiley Interscience, New York, **1977**.

[146] J. O. M. Bockris, S. U. M. Khan, Plenum, New York, **1993**.
[147] S. Trasatti, in *Handbook of Fuel Cells: Fundamentals, Technology, and Applications, Vol. 2*, Taylor & Francis, Chichester, **2003**.
[148] P. Sabatier, *La catalyse en chimie organique*, Librairie polytechnique, Paris et Liege, **1920**.
[149] J. O. M. Bockris, *Nature* **1946**, *158*, 584.
[150] B. E. Conway, J. O. M. Bockris, *The Journal of Chemical Physics* **1957**, *26*, 532-541.
[151] B. E. Conway, G. Jerkiewicz, *Electrochimica Acta* **2000**, *45*, 4075-4083.
[152] O. A. Petrii, G. A. Tsirlina, *Electrochimica Acta* **1994**, *39*, 1739-1747.
[153] S. Trasatti, *Journal of Electroanalytical Chemistry and Interfacial Electrochemistry* **1980**, *111*, 125-131.
[154] S. Trasatti, *Electrochimica Acta* **1984**, *29*, 1503-1512.
[155] C. Davidson, G. Kissel, S. Srinivasan, *Journal of Electroanalytical Chemistry and Interfacial Electrochemistry* **1982**, *132*, 129-135.
[156] T. Reier, M. Oezaslan, P. Strasser, *ACS Catalysis* **2012**, *2*, 1765-1772.
[157] V. Artero, M. Chavarot-Kerlidou, M. Fontecave, *Angewandte Chemie International Edition* **2011**, *50*, 7238-7266; C. Lupi, A. Dell'Era, M. Pasquali, *International Journal of Hydrogen Energy* **2009**, *34*, 2101-2106.
[158] W. Hume-Rothery, *Progress in Materials Science* **1968**, *13*, 229-265.
[159] A. Laisa, in *Handbook of Fuel Cells: Fundamentals, Technology, and Applications, Vol. 2*, John Wiley & Sons, Chichester, **2003**; M. P. Browne, H. Nolan, G. S. Duesberg, P. E. Colavita, M. E. G. Lyons, *ACS Catalysis* **2016**, *6*, 2408-2415.
[160] M. M. Jakšić, *International Journal of Hydrogen Energy* **1986**, *11*, 519-532.
[161] G. Wu, N. Li, D.-R. Zhou, K. Mitsuo, B.-Q. Xu, *Journal of Solid State Chemistry* **2004**, *177*, 3682-3692; H. Hu, B. Guan, B. Xia, X. W. Lou, *Journal of the American Chemical Society* **2015**, *137*, 5590-5595; Z. Z. SOOK-kENG C., KAR-BAN T, NOR A. Y, W. M. D. WAN YUSOFF, *Sains Malaysiana* **2012**, *41*, 465-470.
[162] G. C. Bond, *Catalysis by Metals by* Academic Press, New York, **1962**.
[163] A. J. Appleby, *Catalysis Reviews* **1971**, *4*, 221-244.
[164] D. E. Hall, *Journal of The Electrochemical Society* **1983**, *130*, 317-321; bL. Chen, X. Dong, Y. Wang, Y. Xia, *Nature Communications* **2016**, *7*, 11741.
[165] A. Seghiouer, J. Chevalet, A. Barhoun, F. Lantelme, *Journal of Electroanalytical Chemistry* **1998**, *442*, 113-123.
[166] I. J. Godwin, R. L. Doyle, M. E. G. Lyons, *Journal of The Electrochemical Society* **2014**, *161*, F906-F917.
[167] L. D. Burke, T. A. M. Twomey, *Journal of Electroanalytical Chemistry and Interfacial Electrochemistry* **1984**, *162*, 101-119; L. D. Burke, T. A. M. Twomey, *Journal of Electroanalytical Chemistry and Interfacial Electrochemistry* **1984**, *167*, 285-290.
[168] W. B. Visscher, E, *Journal of Applied Electrochemistry* **1980**, *10*, 269.
[169] L. M. M. de Souza, F. P. Kong, F. R. McLarnon, R. H. Muller, *Electrochimica Acta* **1997**, *42*, 1253-1267.
[170] R. Šimpraga, B. E. Conway, *Journal of Electroanalytical Chemistry and Interfacial Electrochemistry* **1990**, *280*, 341-357.
[171] M. Okuyama, S. Haruyama, *Corrosion Science* **1974**, *14*, 1-14.
[172] M. E. G. Lyons, Brandon, M.P, Godwin, I., Doyle,R.L., O'Brien, M. , *International Journal of Electrochemical Science* **2012**, 2710.
[173] M. Dmochowska, A. Czerwiński, *Journal of Solid State Electrochemistry* **1998**, *2*, 16-23; S.-L. Yau, F.-R. F. Fan, T. P. Moffat, A. J. Bard, *The Journal of Physical Chemistry* **1994**, *98*, 5493-5499.
[174] J. McBreen, White R.E, in *Modern Aspects of Electrochemistry, Vol. 21* (Eds.: J. O. M. Bockris, B. E. Conway), Plenum Press, New York, **1990**.

[175] H. M. French, M. J. Henderson, A. R. Hillman, E. Vieil, *Journal of Electroanalytical Chemistry* **2001**, *500*, 192-207; H. M. French, M. J. Henderson, A. R. Hillman, E. Vieil, *Solid State Ionics* **2002**, *150*, 27-37.
[176] P. W. T. Lu, S. Srinivasan, *Journal of The Electrochemical Society* **1978**, *125*, 1416-1422.
[177] H. Bode, K. Dehmelt, J. Witte, *Electrochimica Acta* **1966**, *11*, 1079-IN1071.
[178] A. C. Makrides, *Journal of The Electrochemical Society* **1966**, *113*, 1158-1165.
[179] B. S. Yeo, A. T. Bell, *Journal of the American Chemical Society* **2011**, *133*, 5587-5593.
[180] M. C. Bernard, P. Bernard, M. Keddam, S. Senyarich, H. Takenouti, *Electrochimica Acta* **1996**, *41*, 91-93.
[181] I. J. Godwin, Trinity College Dublin (Dublin), **2015**.
[182] C. Greaves, M. A. Thomas, *Acta Crystallogr. Sect. B* **1986**, *42*, 51-55.
[183] J. McBreen, (Ed.: J. O. Besenhard), Wiley-VCH, Weinhein, **1999**.
[184] M. S. Kim, T. S. Hwang, K. B. Kim, *Journal of The Electrochemical Society* **1997**, *144*, 1537-1543.
[185] D. S. Hall, D. J. Lockwood, C. Bock, B. R. MacDougall, *Proceedings of the Royal Society A: Mathematical, Physical and Engineering Sciences* **2015**, *471*, 20140792.
[186] S. Le Bihan, M. Figlarz, *J. Cryst. Growth* **1972**, *13-14*, 458-461.
[187] B. Mani, J. P. de Neufville, *Journal of The Electrochemical Society* **1988**, *135*, 800-803.
[188] M. Wehrens-Dijksma, P. H. L. Notten, *Electrochimica Acta* **2006**, *51*, 3609-3621.
[189] M. K. Carpenter, D. A. Corrigan, **1988**, 700.
[190] M. J. Madou, M. C. H. McKubre, *Journal of The Electrochemical Society* **1983**, *130*, 1056-1061.
[191] L. D. Burke, M. E. G. Lyons, in *Modern Aspects of Electrocehmistry, Vol. 18* (Eds.: W. R.E, J. O. M. Bockris, B. E. Conway), Plenum Press, New York, **1986**.
[192] M. E. G. Lyons, University Collage Crok (Cork), **1983**.
[193] M. E. G. Lyons, R. L. Doyle, *International Journal of Electrochemcal Science* **2011**, 5710-5730; M. E. G. Lyons, L. D. Burke, *Journal of Electroanalytical Chemistry and Interfacial Electrochemistry* **1984**, *170*, 377-381; M. E. G. Lyons, R. L. Doyle, M. P. Brandon, *Physical Chemistry Chemical Physics* **2011**, *13*, 21530-21551.
[194] L. Öjefors, *Journal of The Electrochemical Society* **1976**, *123*, 1691-1696; R. Simpraga, B. E. Conway, *Journal of Electroanalytical Chemistry and Interfacial Electrochemistry* **1991**, *313*, 161-179.
[195] L. D. Burke, M. E. G. Lyons, *Journal of Electroanalytical Chemistry and Interfacial Electrochemistry* **1986**, *198*, 347-368; S. Joiret, M. Keddam, X. R. Nóvoa, M. C. Pérez, C. Rangel, H. Takenouti, *Cem. Concr. Compos.* **2002**, *24*, 7-15; R. S. Schrebler Guzmán, J. R. Vilche, A. J. Arvía, *Electrochimica Acta* **1979**, *24*, 395-403; S. Juanto, R. S. Schrebler, J. O. Zerbino, J. R. Vilche, A. J. Arvia, *Electrochimica Acta* **1991**, *36*, 1143-1150; D. D. MacDonald, B. Roberts, *Electrochimica Acta* **1978**, *23*, 557-564; S. T. Amaral, E. M. A. Martini, I. L. Müller, *Corrosion Science* **2001**, *43*, 853-879.
[196] J. Flis, H. Oranowska, Z. Szklarska-Smialowska, *Corrosion Science* **1990**, *30*, 1085-1099.
[197] L. D. Burke, D. P. Whelan, *Journal of Electroanalytical Chemistry and Interfacial Electrochemistry* **1984**, *162*, 121-141.
[198] L. D. Burke, M. I. Casey, V. J. Cunnane, O. J. Murphy, T. A. M. Twomey, *Journal of Electroanalytical Chemistry and Interfacial Electrochemistry* **1985**, *189*, 353-362.
[199] L. D. Burke, E. J. M. O'Sullivan, *Journal of Electroanalytical Chemistry and Interfacial Electrochemistry* **1981**, *117*, 155-160.
[200] E. Laviron, *Journal of Electroanalytical Chemistry and Interfacial Electrochemistry* **1980**, *112*, 1-9.
[201] W. E. O'Grady, J. O. M. Bockris, *Surface Science* **1973**, *38*, 249-251.
[202] M. Oshitani, H. Yufu, K. Takashima, S. Tsuji, Y. Matsumaru, *Journal of The Electrochemical Society* **1989**, *136*, 1590-1593.

[203] B. B. Ezhov, O. G. Malandin, *Journal of The Electrochemical Society* **1991**, *138*, 885-889; R. D. Armstrong, E. A. Charles, *J. Power Sources* **1989**, *25*, 89-97; D. H. Fritts, *Journal of The Electrochemical Society* **1982**, *129*, 118-122.
[204] G. W. D. Briggs, in *Electrochemistry - Vol. 4, Specialist Periodical Reports*, The Chemical Society, London, **1974**; M. Butel, L. Gautier, C. Delmas, *Solid State Ionics* **1999**, *122*, 271-284.
[205] H. Yamaura, K. Moriya, N. Miura, N. Yamazoe, *Sensors and Actuators B: Chemical* **2000**, *65*, 39-41; R. J. Van Zee, Y. M. Hamrick, S. Li, W. Weltner, *The Journal of Physical Chemistry* **1992**, *96*, 7247-7251; M. M. Elsemongy, M. M. A. Gouda, Y. A. Elewady, *Journal of Electroanalytical Chemistry and Interfacial Electrochemistry* **1977**, *76*, 367-373; Y. W. D. Chen, R. N. Noufi, *Journal of The Electrochemical Society* **1984**, *131*, 731-735; C.-B. Wang, H.-K. Lin, C.-W. Tang, *Catal. Lett.* **2004**, *94*, 69-74.
[206] C.-W. Tang, C.-B. Wang, S.-H. Chien, *Thermochim. Acta* **2008**, *473*, 68-73.
[207] H. Gomez, J. R. Vilche, A. Arvia, *The electrochemical behaviour of cobalt in alkaline solutions part II. The potentiodynamic response of Co(OH)2 electrodes, Vol. 138*, **1982**.
[208] W. K. Behl, J. E. Toni, *Journal of Electroanalytical Chemistry and Interfacial Electrochemistry* **1971**, *31*, 63-75.
[209] L. D. Burke, M. M. Murphy, *Journal of The Electrochemical Society* **1991**, *138*, 88-94.
[210] P. Benson, G. W. D. Briggs, W. F. K. Wynne-Jones, *Electrochimica Acta* **1964**, *9*, 281-288.
[211] R. N. S. M. Hamdani , P. Chartier, *Int. J. Electrochem* **2010**, *5*, 556-577.
[212] A. Damjanovic, in *Electrochemistry in Transition* (Ed.: P. Press), Murphy O.J.Srinivasan S.Conway B.E., New York, **1992**, p. 107; G. M., in *Handbook of Fuel Cells: Fundamentals, Technology, and Applications, Vol. 2* (Eds.: Vielstich. W., Lamm. A., Gasteiger. H.A.), John Wiley & Sons, Chichester, **2003**; A. J. Appleby, *Journal of Electroanalytical Chemistry* **1993**, *357*, 117-179.
[213] T. Ohtsuka, N. Sato, *Journal of Electroanalytical Chemistry and Interfacial Electrochemistry* **1983**, *147*, 167-179; K. E. Heusler, in *Passivity of Metals* (Eds.: Frankenthal. R.P., J. Kruger), Inc. Princeton, New Jersey, **1978**.
[214] A. Foelske, H.-H. Strehblow, *Surf. Interface Anal.* **2002**, *34*, 125-129.
[215] X. Du, H. Pan, Z. Yang, *New J. Chem.* **2018**, *42*, 4215-4222.
[216] D. Boden, C. J. Venuto, D. Wisler, R. B. Wylie, *Journal of The Electrochemical Society* **1967**, *114*, 415-417; A. Kozawa, J. F. Yeager, *Journal of The Electrochemical Society* **1965**, *112*, 959-963.
[217] Y. Meng, W. Song, H. Huang, Z. Ren, S.-Y. Chen, S. L. Suib, *Journal of the American Chemical Society* **2014**, *136*, 11452-11464.
[218] S. L. Suib, *Acc. Chem. Res.* **2008**, *41*, 479-487; F. Cheng, Y. Su, J. Liang, Z. Tao, J. Chen, *Chem. Mater.* **2010**, *22*, 898-905.
[219] A. Bergmann, I. Zaharieva, H. Dau, P. Strasser, *Energy & Environmental Science* **2013**, *6*, 2745-2755.
[220] Y. L. Cao, H. X. Yang, X. P. Ai, L. F. Xiao, *Journal of Electroanalytical Chemistry* **2003**, *557*, 127-134.
[221] M. M. Thackeray, *Progress in Solid State Chemistry* **1997**, *25*, 1-71.
[222] S. Devaraj, N. Munichandraiah, *The Journal of Physical Chemistry C* **2008**, *112*, 4406-4417.
[223] R. G. Burns, V. M. Burns, in *Proceedings of the Manganese Dioxide Symposium, A, Vol. 1* (Eds.: A. Kozawa, R. J. Brodd), Cleveland, OH, **1975**, p. 306; R. G. Burns, V. M. Burns, in *Proceedings of the Manganese Dioxide Symposium, B, Vol. 2* (Eds.: M. H. Joseph, A. Kozawa), Schumm, Tokyo, **1980**, p. 97.
[224] J. Luo, Q. Zhang, S. L. Suib, *Inorg. Chem.* **2000**, *39*, 741-747.
[225] G. Pistoia, A. Antonini, D. Zane, M. Pasquali, *J. Power Sources* **1995**, *56*, 37-43.
[226] L. D. Burke, M. J. Ahem, in *Prec. Symp. on Manganese Dioxide Electrode Theory and Practice for Electrochemical Applications*, American Electrochemical Society, Pennington,

N J, **1985**, p. 403; Kirk-Othmer, *Encyclopedia of Chemical Technology, Vol. 3*, Wiley, New York, **1978**; S. B. Kanungo, K. M. Parida, B. R. Sant, *Electrochimica Acta* **1981**, *26*, 1157-1167.
[227] L. D. Burke, M. J. Ahern, *Journal of The Electrochemical Society* **1985**, *132*, 2662-2666.
[228] M. Yano, S. Suzuki, M. Miyayama, M. Ohgaki, *Nanomaterials* **2013**, *3*, 204.
[229] L. E. Wen-Zhi, L. I. U. You-Qin, H. U. Guang-Qi, *Preparation of manganese dioxide modified glassy carbon electrode by a novel film plating/cyclic voltammetry method for H2O2 detection, Vol. 54*, **2009**.
[230] I. B. Singh, S.-M. Park, **2015**.
[231] Z. Morgan Chan, D. A. Kitchaev, J. Nelson Weker, C. Schnedermann, K. Lim, G. Ceder, W. Tumas, M. F. Toney, D. G. Nocera, *Proc. Natl. Acad. Sci.* **2018**, *115*, E5261-E5268.
[232] W. H. Kao, V. J. Weibel, *Journal of Applied Electrochemistry* **1992**, *22*, 21-27.
[233] R. L. Paul, A. Cartwright, *Journal of Electroanalytical Chemistry and Interfacial Electrochemistry* **1986**, *201*, 113-122; R. L. Paul, A. Cartwright, *Journal of Electroanalytical Chemistry and Interfacial Electrochemistry* **1986**, *201*, 123-131.
[234] S. Zaretskii, Z. Antonovskaya, *Elektrokhimiya. Margantsa* **1957**, 232.
[235] D. Gosztola, M. J. Weaver, *Journal of Electroanalytical Chemistry and Interfacial Electrochemistry* **1989**, *271*, 141-154.
[236] L. D. Burke, O. J. Murphy, *Journal of Electroanalytical Chemistry and Interfacial Electrochemistry* **1980**, *109*, 373-377.
[237] A. J. Bard, *Encyclopedia of Electrochemistry of the Elements, Vol. 1*, Marcel Dekker, New York, **1973**.
[238] G. P. Dinga, *Journal of Chemical Education* **1988**, *65*, 688; G. D. Brewer, *International Journal of Hydrogen Energy* **1978**, *3*, 461-474; J. S. a. W. Wallace, C. A., *International Journal of Hydrogen Energy* **1983**, *8*, 255-268.
[239] M. Ni, M. K. H. Leung, D. Y. C. Leung, K. Sumathy, *Renewable and Sustainable Energy Reviews* **2007**, *11*, 401-425.
[240] C. C. L. McCrory, S. Jung, I. M. Ferrer, S. M. Chatman, J. C. Peters, T. F. Jaramillo, *Journal of the American Chemical Society* **2015**, *137*, 4347-4357.
[241] M. E. G. Lyons, R. L. Doyle, M. P. Browne, I. J. Godwin, A. A. S. Rovetta, *Current Opinion in Electrochemistry* **2017**, *1*, 40-45.
[242] A. Damjanovic, A. T. Ward, M. O'Jea, *Journal of The Electrochemical Society* **1974**, *121*, 1186-1190; S. Shibata, M. P. Sumino, *Electrochimica Acta* **1971**, *16*, 1089-1098.
[243] B. E. Conway, M. A. Sattar, D. Gilroy, *Electrochimica Acta* **1969**, *14*, 677-694; D. N. Buckley, L. D. Burke, *Journal of the Chemical Society, Faraday Transactions 1: Physical Chemistry in Condensed Phases* **1976**, *72*, 2431-2440.
[244] P. C. Milner, *Journal of The Electrochemical Society* **1964**, *111*, 228-232.
[245] A. Damjanovic, in *Modern Aspects of Electrochemistry, Vol. 5* (Eds.: J. O. M. Bockris, B. E. Conway), Plenum Press, New York, **1969**, p. 369.
[246] S. Trasatti, S. Lodi, (Ed.: S. Trasatti), Elsevier, New York, **1980**, p. 521.
[247] L. D. Burke, (Ed.: S. Trasatti), Elsevier, New York, **1980**, p. 141.
[248] B. E. Conway, E. M. Beatty, P. A. D. DeMaine, *Electrochimica Acta* **1962**, *7*, 39-54.
[249] Gattrell M., B. R. MAcDougall, in *Handbook of Fuel Cells: Fundamentals, Technology, and Applications, Vol. 2* (Eds.: Vielstich. W., Lamm. A., Gasteiger. H.A.), John Wiley & Sons, Chichester, **2003**.
[250] J. O. Bockris, S. Taylor Hugh, *Proceedings of the Royal Society of London. Series A. Mathematical and Physical Sciences* **1956**, *237*, 1733.
[251] R. P. Šimpraga, *Journal of Electroanalytical Chemistry* **1993**, *355*, 79-96.
[252] M. H. Miles, Y. H. Huang, S. Srinivasan, *Journal of The Electrochemical Society* **1978**, *125*, 1931-1934.

[253] H. Dau, C. Limberg, T. Reier, M. Risch, S. Roggan, P. Strasser, *ChemCatChem* **2010**, *2*, 724-761.
[254] R. L. Doyle, I. J. Godwin, M. P. Brandon, M. E. G. Lyons, *Physical Chemistry Chemical Physics* **2013**, *15*, 13737-13783; N.-T. Suen, S.-F. Hung, Q. Quan, N. Zhang, Y.-J. Xu, H. M. Chen, *Chem. Soc. Rev.* **2017**, *46*, 337-365; S. Chen, S. S. Thind, A. Chen, *Electrochemistry Communications* **2016**, *63*, 10-17; L. Trotochaud, S. W. Boettcher, *Scripta Mater.* **2014**, *74*, 25-32; A. R. Zeradjanin, A. A. Topalov, Q. Van Overmeere, S. Cherevko, X. Chen, E. Ventosa, W. Schuhmann, K. J. J. Mayrhofer, *RSC Advances* **2014**, *4*, 9579-9587; T. Reier, H. N. Nong, D. Teschner, R. Schlögl, P. Strasser, *Advanced Energy Materials* **2017**, *7*, 1601275; X. Li, X. Hao, A. Abudula, G. Guan, *Journal of Materials Chemistry A* **2016**, *4*, 11973-12000; E. Fabbri, A. Habereder, K. Waltar, R. Kötz, T. J. Schmidt, *Catalysis Science & Technology* **2014**, *4*, 3800-3821.
[255] I. A. Raj, *Journal of Materials Science* **1993**, *28*, 4375-4382.
[256] L. D. Burke, O. J. Murphy, J. F. O'Neill, S. Venkatesan, *Journal of the Chemical Society, Faraday Transactions 1: Physical Chemistry in Condensed Phases* **1977**, *73*, 1659-1671; M. E. G. Lyons, L. D. Burke, *Journal of the Chemical Society, Faraday Transactions 1: Physical Chemistry in Condensed Phases* **1987**, *83*, 299-321; D. Galizzioli, F. Tantardini, S. Trasatti, *Journal of Applied Electrochemistry* **1974**, *4*, 57-67.
[257] J. F. Marco, J. R. Gancedo, M. Gracia, J. L. Gautier, E. Ríos, F. J. Berry, *J. Solid State Chem.* **2000**, *153*, 74-81; L. Mendoza-Huizar, C. Hilda Rios-Reyes, M. Rivera, *Cobalt electrodeposition onto highly oriented pyrolytic graphite (HOPG) electrode from ammonium sulfate solutions, Vol. 33*, **2010**.
[258] C. Mahala, M. Basu, *ACS Omega* **2017**, *2*, 7559-7567.
[259] M. Cabo, E. Pellicer, E. Rossinyol, O. Castell, S. Suriñach, M. D. Baró, *Crystal Growth & Design* **2009**, *9*, 4814-4821.
[260] Z. Wu, Y. Zhu, X. Ji, *Journal of Materials Chemistry A* **2014**, *2*, 14759-14772.
[261] X. Wang, W. S. Liu, X. Lu, P. S. Lee, *J. Mater. Chem.* **2012**, *22*, 23114-23119; Y. Li, P. Hasin, Y. Wu, *Adv. Mater.* **2010**, *22*, 1926-1929; H. Chen, J. Jiang, L. Zhang, T. Qi, D. Xia, H. Wan, *J. Power Sources* **2014**, *248*, 28-36.
[262] R. N. Singh, M. Hamdani, J. F. Koenig, G. Poillerat, J. L. Gautier, P. Chartier, *Journal of Applied Electrochemistry* **1990**, *20*, 442-446; S. Chen, S.-Z. Qiao, *ACS Nano* **2013**, *7*, 10190-10196.
[263] P. Rasiyah, A. C. C. Tseung, *Journal of The Electrochemical Society* **1983**, *130*, 2384-2386.
[264] A. C. D. Angelo, E. R. Gonzalez, L. A. Avaca, *International Journal of Hydrogen Energy* **1991**, *16*, 1-7.
[265] S. M. Jasem, A. C. C. Tseung, *Journal of The Electrochemical Society* **1979**, *126*, 1353-1360.
[266] B. N. Efremov, M. R. Tarasevich, *Kinetics and mechanism of electrochemical reduction and oxygen evolution on cobalt spinels, Vol. 17*, **1981**.
[267] W. J. King, A. C. C. Tseung, *Electrochimica Acta* **1974**, *19*, 493-498.
[268] D. Friebel, M. W. Louie, M. Bajdich, K. E. Sanwald, Y. Cai, A. M. Wise, M.-J. Cheng, D. Sokaras, T.-C. Weng, R. Alonso-Mori, R. C. Davis, J. R. Bargar, J. K. Nørskov, A. Nilsson, A. T. Bell, *Journal of the American Chemical Society* **2015**, *137*, 1305-1313.
[269] J. P. Hoare, *The Electrochemistry of Oxygen, ch. 2* Interscience, New York, **1968**.
[270] B. E. Conway, E. Gileadi, *Canadian Journal of Chemistry* **1962**, *40*, 1933-1942; B. E. Conway, P. L. Bourgault, *Canadian Journal of Chemistry* **1962**, *40*, 1690-1707.
[271] J. C. K. Ho, D. L. Piron, *Journal of Applied Electrochemistry* **1996**, *26*, 515-521.
[272] J. O. M. Bockris, T. Otagawa, *Journal of The Electrochemical Society* **1984**, *131*, 290-302.
[273] A. G. C. Kobussen, G. H. J. Broers, *Journal of Electroanalytical Chemistry and Interfacial Electrochemistry* **1981**, *126*, 221-240.
[274] H. Willems, A. G. C. Kobussen, J. H. W. De Wit, G. H. J. Broers, *Journal of Electroanalytical Chemistry and Interfacial Electrochemistry* **1984**, *170*, 227-242.

[275] W. O´Grady, Iwakura, C.,Huang, J.,And,Yeager, E.,, in *Proceedings of the Symposium on Electrocatalysis* (Ed.: M. W. Breiter), The Electrochemical Society Inc., Pennington, NJ, **1974**, p. 286.
[276] P. W. T. Lu, S. Srinivasan, *J. Electrochem. Soc.* **1978**, *125*, 1416-1422.
[277] L. D. Burke, M. E. Lyons, O. J. Murphy, *Journal of Electroanalytical Chemistry and Interfacial Electrochemistry* **1982**, *132*, 247-261.

# CHAPTER 2

# CONCEPTS OF EXPERIMENTAL TECHNIQUES

## 2.1 Introduction

This chapter focuses on the theory underpinning various techniques utilized throughout this thesis. Firstly, the understanding behind the electrochemical techniques used to investigate and monitor the catalytic activity of the materials will be dealt with, and secondly, a brief introduction to the characterization techniques will be presented so as to provide an understanding of the results presented in chapters 4, 5 and 6.

In the background description of the experimental methodology preseneted in chpater 3, the emphasis is placed on more complex techniques, such as electrochemical impedance spectroscopy (EIS), and on the theory behind the less often used experimental approaches, such as the potential step method applied here to probe the uncompensated resistance and the double layer capacitance of the electrolyte and the electrode. Cyclic voltammetry (CV) is nowadays so universally utilized and well understood by virtually all electrochemists that a detailed discussion of this technique is considered as unnecessary in the present work. Instead, a short summary of its application to the systems under investigation will be presented in this section.

## 2.2 Steady-State Polarization Measurements

The principal technique by which kinetic data was experimentally obtained in the present work was the use of steady-state polarization measurements. In this type of measurement, the potential of the working electrode (relative to the reference electrode) is set at a constant potential and the current density response is observed as a function of time until a constant current density is observed. When such a constant current density is obtained it is assumed that the electrochemical system is at steady-state.

Experimentally, in the present work, a potential step function was applied to the working electrode within the Tafel slope potential region. Upon reaching a new potential value, $E$, the working electrode could remain at a constant potential until a consistent constant current density value, $i$, was obtained. The potentiostat control software adjusted a steady-state to be achieved when the variation of $i$ with time $t$ over a certain period fell below a user-defined limit. When a steady-state current density was achieved, this value was

recorded to disk by the digitally controlled potentiostat and the potential was stepped to its next defined value, where the procedure was repeated.

When steady-state current densities are recorded at several different potentials it is possible to plot the logarithm of $i$ *vs.* $\eta$. The slope, $b = \frac{dE}{d\,log\,i}$, measured form such plot is, of course, the Tafel slope that was discussed in section 1.2.5. Since the Tafel slope obtained by this method refers to a steady-state situation, the multistep kinetic analysis of section 1.2.4, based upon the principal of pseudo-equilibrium, can be applied to compare values of measured Tafel slope.

The method of potentiostat measurement of steady-state polarization data, as described above, became possible after the introduction, in 1941 by Hickling[1], of an electronic feedback technique for maintaining a given electrode potential. Prior to this development, steady-state curves had to be recorded by galvanostatic constant current techniques, thus recording the potential against time. Such an approach was adopted by Bowden and Rideal[2] in their early seminal work on the HER. A brief literature review revealed that it was not until 1980 that steady-state polarization curves started to be recorded potentiostatically, rather than galvanostatically. Theoretically, an identical data set should be obtained regardless of the approach adopted, although as commented by Bockris and Khan[3] "conceptually, the potential step method is the better of the two methods for obtaining steady-state data because the rate depends exponentially on the potential".

A significant issue that arises in the collection of steady-state polarization data is whether an apparent time-invariant constant current density constitutes a steady-state of the system. This issue was particularly significant in the case of steady-state measurements that attempt to characterize the kinetics of the OER. As a relevant example from the literature, Lu and Srinivasan[4] studied the effects of the growth of Ni oxide that occur parallel to the OER on Ni anode in alkaline solutions. Over the course of a 20 hr polarization, in 1.0 M KOH at 1.8 V (*vs.* RHE), the recorded current density on a pre-anodized Ni electrode dropped continuously from ca. 80 mA $cm^{-2}$ to 14 mA $cm^{-2}$. Therefore, a proper steady-state current density was never achieved over this period. These authors performed ellipsometry studies which revealed that the thickness of the oxide film increased from 190 Å to almost 700 Å over the same period at 1.8 V. The variation of measured optical constants indicated that the film became an increasingly poor electrical conductor with increasing polarization. The authors suggested that the continuously decreasing current density arose because of

the growth of an oxide film, owing the oxidation of $Ni^{3+}$ ions to $Ni^{4+}$ ions. Thus, the failure to obtain a constant current density was due to electrochemical processes in the oxide film rather than to the kinetics of the OER.

The experience from the literature indicates that kinetically significant steady-state current should be achieved within a time scale of minutes from stepping the potential to a new value, which depends, of course, on the system under investigation and on the size of the potential steps. In a publication reviewed in section 1.5.5, Burke *et al.*[5] performed steady-state polarization measurements on the OER at a Co electrode in 6.0 M NaOH. They increased the applied potential in steps of 50 mV and found that a satisfactorily steady current was obtained after 10 minutes. In the present work, potential steps of 1 mV have been utilized in steady-state polarization measurements and steady currents have been observed and recorded after periods of approximately 1-minute following perturbation of the system. The requirement of shorter times to observe a satisfactorily steady current in the present work relative to the work of Burke *et al.* is, presumably, related to the smaller magnitude of the potential steps utilized.

It is generally possible to distinguish between the relaxation of an electrochemical system to a kinetically significant steady-state and the effects of a process relating to oxide growth / transformation by examining a plot of current against time following the application of a potential step. The latter process usually occurs at much longer time scales than the former one. Another important factor that must be considered when conducting steady-state polarization measurements aiming the determination of kinetic parameters such as the Tafel slope is the uncompensated solution resistance, $R_\Omega$. As discussed in section 2.3 in relation with the Randles equivalent circuit representation of an electrochemical system, the $R_\Omega$ is always present in series with the so-called solution resistance, $R_s$, when a potential is applied to the working electrode. Therefore, if a potential $E_{app}$ applied to the working electrode causes a current $i$ to flow across the electrochemical interface, these parameters can be related by the following expression:

$$E_{app} = i(R_\Omega + R_S) \qquad (2.2.1)$$

Eqn. 2.2.1 indicates that a fraction of the applied potential, given by $R_\Omega$, is dissipated by the solution resistance, which causes that the effective potential $E_{eff}$ of the working electrode and the applied potential $E_{app}$ on the electrode to be different. In this case, the

effective potential $E_{eff}$ is given by $R_s$. Thus, the kinetically significant polarization data is $iE_{eff}$ as opposed to $iE_{app}$. The value of the effective potential $E_{eff}$ is given by:

$$E_{eff} = E_{app} - iR_{\Omega} \tag{2.2.2}$$

To obtain realistic kinetically steady-state polarization data it is necessary to perform the correction outlined in eqn. 2.2.2 for each value of $E_{app}$. Therefore, it is necessary to know the value of the solution resistance. A common method for measuring this parameter is the so-called current interruption technique.[6] In this work, however, two different approaches were followed to obtain the uncompensated resistance: (i) electrochemical impedance spectroscopy, and (ii) a potential step method followed by a current density decay curve analysis. Both techniques are detailed in section 1.2.5.

## 2.3 Cyclic Voltammetry

As mentioned at the start of the chapter, it is not the aim to undertake a thorough discussion of cyclic voltammetry in this work for two principal reasons. Firstly, because the technique is well understood in modern electrochemistry and its fundaments have therefore already been thoroughly discussed in most standard general electrochemistry texts.[7] And, secondly, because since cyclic voltammetry is a potentiodynamic technique, it has limited application to the determination of the steady-state kinetic behaviour of the oxygen evolution reaction. The technique is principally applied to the qualitative analysis of the surface electrochemistry of the polycrystalline Mn and Ni, Co oxygen evolution anodes, studied in the present work. Detailed discussions of the voltammetric profiles of these metals and their alloys in alkaline solutions have been presented in chapters 4 and 5, respectively. The CV technique has been used in this thesis to characterize the state of electrodes prior to steady-state polarization measurements with the purpose of ensuring that the data obtained in the latter experiments relates to a reproducible oxide surface. In addition, the characterization of these metal oxides through the CV yielded potentially valuable information on the relationship between the oxide surface and the activity of the anode towards the OER, as discussed in chapters 4 and 5. Further, CV is a dynamic technique which involves sweeping the cell potential linearly from a set-point to another and back again. The rate of change of potential with time is known as the scan rate, *v*. The

voltammetric data is presented on a voltammogram with the current response presented as a function of applied potential. The resulting current-potential responses can be used to infer in a largely qualitative manner information of the redox processes occurring on the surface of an oxidized metal or metal oxides.[7b] More generally, the shape and scan rate dependence of these voltammetric responses are characteristic of the reversibility of the redox process and whether the redox species are solution based or adsorbed on the electrode surface.

Specifically considering the case of a redox active moiety in solution at an inert electrode, for the oxidative peak, as the applied potential moves towards E°, more oxidised species O are formed at the electrode surface. The formation of a concentration gradient causes mass transport in the electrolyte near the electrode as O diffuses away from the electrode surface and R diffuses towards it. The current flow due to oxidation of R increases as the potential also increases. This Faradaic current reaches its maximum at the oxidation peak, while at potentials beyond this the diffusion of fresh R to the electrode limits the creation of O. This causes the current to reduce and to stabilise at a constant level dictated by the mass transport regime which replenishes analyte at the electrode. The opposite takes place during the reductive sweep, where fresh O diffuses to the electrode surface. At higher scan rates the species close to the electrode are consumed quickly, resulting in larger peak currents with increasing scan rates. For the sake of simplicity, the diffusion of the analyte to the electrode can be considered semi-infinite linear in nature, allowing the peak current $I_p$ of a system to be described by the Randles-Sevcik equation as:[7a]

$$I_p = 0.4463nFA\sqrt{\frac{nF}{RT}}c^{\infty}\sqrt{Dv} \qquad (2.3.1)$$

where $I_p$ is the peak current, n is the number of electrons involved in the redox process, F is Faraday's constant, A is the electrochemical surface area of the electrode, R is the universal gas constant, T is absolute temperature, $c^{\infty}$ is the bulk concentration of the analyte, D is the diffusion coefficient of the analyte and v is the scan rate.

Of particular interest is the dependence of peak current on the potential scan rate. For reversible systems, a linear relationship should exist between $I_p$ and $v^{1/2}$. Faradaic processes for redox active species adsorbed onto the electrode surface exhibit a linear relationship between $I_p$ and $v$. For ideal single electron processes, the peak separation $\Delta E_p$

should equal 59 mV and be independent from the scan rate. The Randles-Sevcik eqn. also pertains for redox processes involving bound sites in a surface confined film, especially when the thickness of the latter is significant.

While the electrochemical methods above presented provide for powerful and sensitive ways of studying modified electrodes, *e.g.* electron-transfer kinetics information, they cannot provide information about the structure or elemental composition. Thus, a complete characterization requires the application of non-electrochemical methods, such as the X-ray diffraction spectroscopy, the X-ray photoelectrons spectroscopy, scanning electron microscope (SEM), the energy dispersive X-ray (EDX), the thermogravimetric analysis (TGA), the UV-vis spectroscopy, or contact angles measurements, among others. In this perspective, information about the physical structure of the film may be obtained by using scanning electron microscopy. Two types of elemental electrode composition analysis can be performed depending on to whether (i) the analysis focuses on the electrode surface, where X-ray photoelectron spectroscopy would be recommended, or (ii) intends to investigate the bulk of the material, when EDX and/or XRD analysis would be appropriate. An analysis of the permeability of the electrode surface can be conducted by using contact angles measurements. Finally, TGA is a useful technique to gain information about the mass lost during calcination processes, and its data may be used to explain different material decomposition reactions taking place during calcination.

## 2.4 X-ray Powder Diffraction

The information in the following section draws from the X-ray diffraction textbook by Warren[8] and the fundamentals of powder diffraction and structural characterization of materials by Vitalij K. Pecharsky and Peter Y. Zavalij.[9]

X-Ray diffraction is a crystallography technique in which the pattern produced by the diffraction of X-rays through the closely spaced lattice of atoms in a crystal is recorded and then analysed, using specific software, to reveal the nature of that lattice. This yields to an understanding of the material and the molecular structure of the sample, which can be presented either as a single crystal or as a powder.

X-ray diffraction from crystalline solids is a phenomenon discovered by Max von Laue[8] in 1912, who was interested in the way light and crystals interacted with one another. He

demonstrated mathematically that X-rays were diffracted by crystalline materials and concluded that X-rays are electromagnetic in nature. Subsequent work was carried by the English physicists Sir W.H. Bragg and his son Sir W.L. Bragg[10] in 1913, who proposed an expression to determine the spacing in the crystal lattice based on the diffraction angle of X-ray beams at certain angles of incidence (see fig. 2.4.1). The expression, commonly known as Bragg's Law, may be written as follows:

$$\lambda n = 2dsin\theta \tag{2.4.1}$$

where the variable *d* is the distance between atomic layers in a crystal, also known as the interplanar spacing, the parameter λ is the wavelength of the incident X-ray beam and the value *n* is an integer.

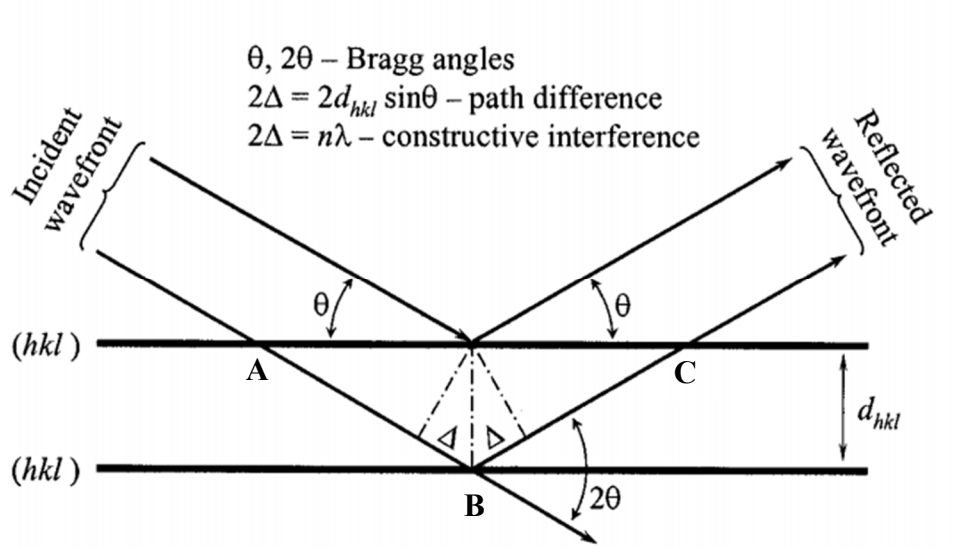



Figure 2.4.1 Schematic illustration of incoming X-rays satisfying the Braggs eqn. Reproduced from Ref.[9]

The Bragg model, as observed in fig. 2.4.1, can be visualized as the reflection of the incident radiation by parallel planes of atoms which are defined by Miller indices (hkl). If the second beam, which has travelled the extra distance of AB + BC, has a path length that is an integral, n, multiple of the wavelength, λ, the formation of a maxima in the X-ray spectrum is observed. These X-rays are scattered from the electron cloud surrounding an atom at the same frequency as the primary beam, known as Thomson scattering, and are collected on a detector. X-rays are produced when electrons decelerate as a result of a collision to metal anode target in an evacuated enclosure. In the case of a copper anode,

$CuK\alpha_{1,2}$, transitions produce a maximum at wavelengths equal to 1.54433 Å and 1.54051 Å, respectively. When an electron is drawn to the metal anode, part of the kinetic energy of the electron is converted into heat. However, a small portion of the kinetic energy causes an electron in core atomic orbital to be ejected. Under these circumstances, an electron from higher orbitals fills the core hole and the resulting drop in energy results in the emission of radiation of a definite wavelength. The wavelength of the X-ray is determined by the nature of the metal anode. Due to the importance of X-ray powder diffraction in this work, the general aspects of this technique will be presented below.

Prior to analysis, the sample is finely grounded, homogenized and placed on a zero-background holder (ZBH). Each microparticle is seen as a tiny crystal oriented at random with respect to the incident beam. The result is that every set of lattice planes will be capable of reflection. Fig. 2.4.2 below illustrates the powder diffraction setup.

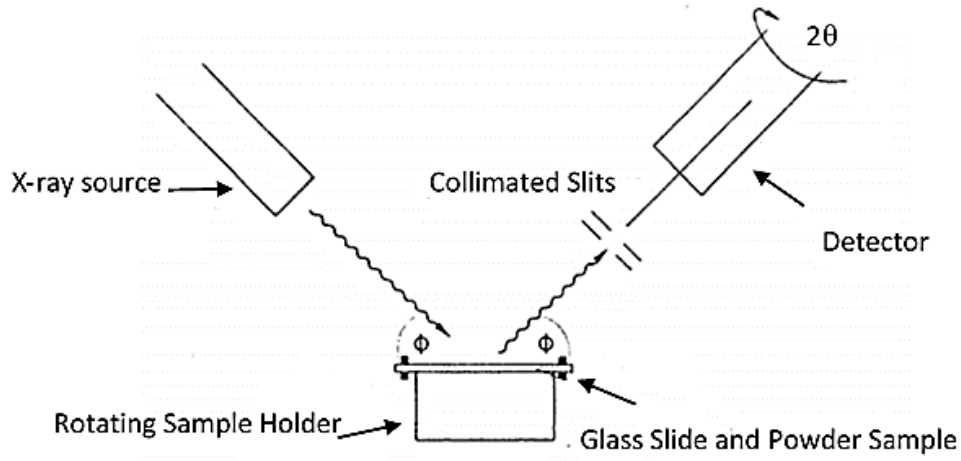



Figure 2.4.2 Schematic illustration of the operating setup of an X-ray powder diffractometer.

Powder patterns for pure phase of powders exhibit peaks at specific values of 2θ yielding a distinctive "fingerprint" that can be used to identify a crystalline phase. The values observed for the d-spacing are determined by the size and lattice centring of the crystal lattice. Further analysis requires the use of a database of known crystalline materials in order to identify the phase or phases present in the sample. In this work the PDF-2 database was used.

Full identification of crystal structures may be seen as a multistep process consisting on: (i) determination of the size and shape of the unit cell from the XRD peak positions, (ii) computation of the number of atoms/unit cell from the size and shape of the cell, their chemical composition and their measured density, and (iii) determination of atom positions from the relative intensities of the XRD peaks.

The shape and size of the unit cell can be deduced from the angular positions of the diffraction lines in a XRD pattern. However, a XRD pattern cannot be studied until it has been indexed using Millers indices to each peak in the diffraction pattern. To do so, the interplanar spacing in the cubic structure must be written in terms of lattice parameters using the plane spacing formula:

$$\frac{1}{d^2} = \frac{h^2 + k^2 + l^2}{a^2} \tag{2.4.2}$$

If the above equation is combined with Bragg's law ($\lambda = 2\ d\ \sin\theta$), the formula below can be obtained:

$$sin^2\theta = \left(\frac{\lambda^2}{4a^2}\right)(h^2 + k^2 + l^2) \tag{2.4.3}$$

Since the term in parenthesis is a constant, eqn. 2.4.3 can be rewritten leading to a relationship for any two different planes:

$$\frac{sin^2\theta_1}{sin^2\theta_2} = \frac{\left(\frac{\lambda^2}{4a^2}\right)(h^2 + k^2 + l^2)}{\left(\frac{\lambda^2}{4a^2}\right)(h_2^2 + k_2^2 + l_2^2)} \tag{2.4.4}$$

Considering that the plane with the lowest Miller indices corresponds to the first XRD diffraction peak, which represents the close packed plane, i.e. the primitive cubic (100) = $h^2 + k^2 + l^2 = 1$, body-centred cubic (110) = $h^2 + k^2 + l^2 = 2$, and face-centred cubic (111) = $h^2 + k^2 + l^2 = 3$), the Bravais lattice can be further calculated. If the different values of $\sin 2\theta$, corresponding to the XRD peaks, are divided by the first peak $\sin 2\theta$ and multiplied by the integer (either 1, 2 or 3), the Bravais lattice can be obtained by recognizing the sequence of allowed reflections for cubic lattices with the sequence of values previously calculated. The list of cubic lattices is shown in table 2.4.1.

| | |
|---|---|
| Primitive | h2+k2+l2 = 1,2,3,4,5,6,8,9,10,11,12,13,14,16… |
| Body-centred | h2+k2+l2 = 2, 4, 6,8,10,12,14,16… |
| Face-centred | h2+k2+l2= 3,4,8,11,12,16,19,20,24,27,32… |
| Diamond cubic | h2+k2+l2= 3, 8,11,16,19,24,27,32… |

Table 2.4.1 Sequence of cubic lattices as function of the crystal structure.

The lattice parameters can then be calculated using eqn. 2.4.4, which can be rewritten as:

$$a = \frac{\lambda}{2\,sin\,\theta}\sqrt{h^2 + k^2 + l^2} \tag{2.4.5}$$

Another attractive aspect of XRD is that it allows the determination of the mean size of nanocrystallites in nanocrystalline bulk materials. Note that the peak width increases with decreases in the crystalline size and increasing disorder within the crystal.[11] Paul Scherrer[8] in 1918 (Scherrer equation systematically show increased values of nanocrystalline size as *d* values decrease and 2θ values increase, since β cosθ cannot be maintained as constant) developed an expression to calculate the nano crystallite size (L) by XRD radiation of wavelength λ (nm) from measuring full width at half maximum of peaks ($\beta_L$) located at any 2θ in the pattern. Note that "crystallite size" is not synonymous with "particle size" and that the Scherrer equation predicts crystallite thickness only if the crystal size is smaller than 100nm. From the well-known Scherrer formula, the average crystallite size, L, can be calculated by:

$$L = \frac{K\,\lambda}{\beta_L\,cos\theta} \tag{2.4.6}$$

where λ is the X-ray wavelength in nanometres (nm), $\beta_L$ is the peak width of the diffraction peak profile at half maximum height resulting from small crystallite size in radians. The latter is also known as broadening size. K is a dimensionless shape constant related to crystallite shape, normally taken as 0.9. The value of β in 2θ axis of diffraction profile must be in radians, whereas θ can be written either in radians or in degrees, since the $\cos\theta$ corresponds to the same number. When different diffraction peaks are observed in an XRD spectrum, the average crystallite size measured must be identical for all the peaks in the spectrum. In other words, the determination of the crystallite size should be equal regarding the peak selected. However, Monshi *et al.*[12] during his extensive research

on different nano ceramic crystals observed that each peak in the spectrum yielded to a different size value and that there was a systematic error on the results obtained from each of the peaks. In order to overcome this problematic, he proposed a modified version of the Scherrer equation based on a method attributed to G.K.Williamson and his student, W.H.Hall.[13] This method relies on the assumption that the approximate equation for size broadening, βL, and strain broadening, βe , vary quite differently with respect to Bragg's angle, $\theta$. Note that lattice strain, $e$, is a local deviation of d-spacing from the average value, caused by local defects. While both size and strain broadening affect the width of diffraction peaks, they show a different angular dependence of the peak width given by:

$$\beta_L = \frac{K\,\lambda}{L\,cos\theta} \tag{2.4.7}$$

$$\beta_e = C_\varepsilon\,tan\,\theta \tag{2.4.8}$$

If both contributions, $\beta_L$ and $\beta_e$ are present in the sample measurement, then their combined effect should be determined by convolution. The Williamson and Hall model can be simplified assuming the convolution is either a simple sum or sum of squares of the former two equations. Performing the latter, it can be obtained the following expression:

$$\beta_{tot} = \beta_e + \beta_L = C_\varepsilon\,tan\,\theta + \frac{K\,\lambda}{L\,cos\theta} \tag{2.4.9}$$

If both sides of eqn. 2.4.9 are multiplied by cos θ yields to:

$$\beta_{tot}\,cos\,\theta = C_\varepsilon\ sin\,\theta + \frac{K\,\lambda}{L} \tag{2.4.10}$$

Note that equation 2.4.10 possesses the standard straight-line equation. Thus, if $\beta_{tot}\cos\theta$ is plotted against $\sin\theta$, the strain component is obtained from the slope ($C_\varepsilon$) and the size component from the intercept ($K\lambda/L$). Such a plot is known as a Williamson-Hall plot and is illustrated schematically in fig. 2.4.3. Recall that in this work the parameters K and λCukα used were 0.9 and 0.15405 nm, respectively.

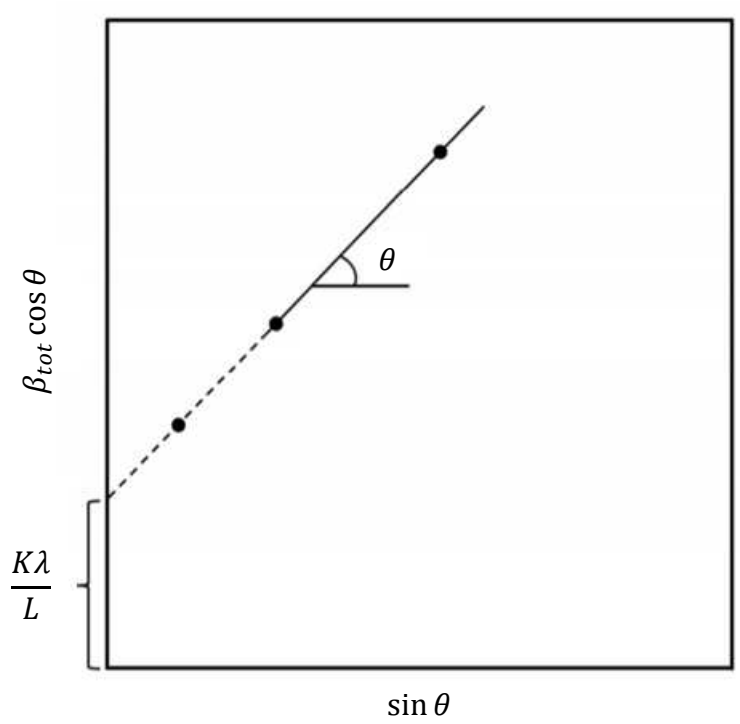



Figure 2.4.3 Modified Scherrer equation plot. Adapted from Ref.[12]

Another important aspect of XRD studies is the determination of the grade of crystallinity of the sample. This considers the degree of the amorphous phase in the sample. This value is typically expressed in percentage. The grade of crystallinity, expressed in crystallinity percentage, considers the ratio between the area under both the crystalline and the amorphous phase to arrive at crystallinity fraction. The formulas normally used to compute the crystallinity percentage are presented below:

$$\%\ Amorphous = \frac{Total\ area\ pattern - Peak\ area}{Total\ area\ pattern} \tag{2.4.11}$$

$$\%\ Crystallinity = 100 - \%\ Amorphous \tag{2.4.12}$$

We must recall that the values obtained using the above formulas do not express the absolute crystallinity of the sample but rather provides an indication of the nature of the sample that is if the sample is mostly crystalline or mostly amorphous.

## 2.5 X-ray Photoelectron Spectroscopy

The information in the following section draws from the introductory surface physics textbooks by Prutton[14], and Woodruff and Delchar[15]. Supporting information was obtained from the photoelectrochemical solar fuel production monograph edited by Giménez and Bisquert[16].

X-ray photoelectron spectroscopy (XPS) is a technique widely used to analyse the first few atomic layers of a sample aiming to quantitatively determine its chemical composition. Since the mean free path of electrons in solids is very small, the detected electrons originate from the few top atomic layers, typically 1-10 nm, making XPS to be a unique surface-sensitive technique.[17] This technique involves irradiating a solid sample in vacuum with X-rays and analysing, according with their energy, the emitted electrons. This analysis is based on the number of detected electrons per energy interval against their kinetic energy. This leads to the formation of a spectrum. Note that each element has a unique spectrum.

In addition, the XPS technique is based on the external photoelectric effect. The photoelectric effect was first reported by Hertz[18] in 1887 and was further described, in terms of quantum interactions, by Einstein[19] 22 years later. It refers to the phenomenon whereby photons of defined energy larger than the ionization energy cause the emission of electrons from the material. Various photon sources are available for lab-based photoemission setups, among the most important ones are the X-ray tubes, which typically utilize Mg or Al anodes providing photons of 1253.6 eV and 1486.6 eV energy with full widths at half-maximum (FWHM) of 0.7 eV and 0.85 eV, respectively. The kinetic energy of the emitted photoelectron, $E_K$, is described by the following expression:

$$E_K = hv - E_B - \phi \tag{2.5.1}$$

where $hv$ is the energy of the incident photon, $E_B$ is the binding energy of the atomic orbital from which the electron originates, and $\phi$ refers to the work function of the analyser. The parameter $\phi$ may be conceived as the energy required to remove an electron from the surface of the material. Since this parameter's value depends on each analyser, calibration against a standard, typically a silver film, is required.

The electrons that originate within tens of angstroms below the surface of the material and leave the surface without any energy loss are called primary electrons. These electrons contribute to the important chemical and electronic information. Other type of electrons which may also be emitted from the sample are the Auger electrons. These are emitted due to relaxation of the excited ions remaining after photoemission. In an Auger process, a higher energy level electron may fall into a lower energy level vacancy. When this occurs, a second electron is emitted carrying off the excess energy. Thus photoionization normally leads to two emitted electrons: (i) a photoelectron or primary electron, and (ii) an Auger electron.

### 2.5.1 Elemental Analysis of Peak Lines and Intensities

One of the most important aspects when dealing with XPS data is the understanding of the technique's limitations. Electrons with kinetic energy of 200-1500 eV have a mean free path of ca. 10 - 20 Å. Given that the attenuation is exponential, the sampling depth can be estimated to be equivalent to ca. 3 times the mean free path. The sampling depth may be defined as the depth from which 95% of all photoelectrons are scattered by the time they reach the surface. Fig. 2.5.1 shows the processes involved in X-ray photoemission.

The first step in evaluating XPS data is the analysis of the elements present at the surface of a sample. This step is normally called "survey" analysis and it is of quite a relevance since the presence of unexpected elements, *e.g.* contamination on the surface of the sample, may be observed. The elemental analysis is accomplished by the identification of all peaks in a survey spectrum, which spans the maximum possible energy range defined by the excitation source.

An example of a survey spectra is presented in fig. 2.5.2. Reference spectra for the different elements, as displayed for example in the Handbook of X-ray Photoelectron Spectroscopy[17], are indispensable tools for a correct peak assignment.

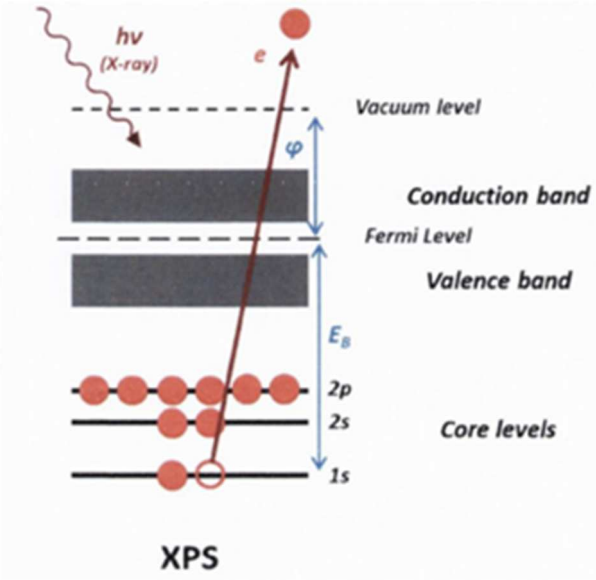



Figure 2.5.1 Photoemission process for X-ray irradiation (XPS) where $\phi$ is the work function of the analyser and $E_B$ is the binding energy of the emitted photoelectron. Reproduced from Ref.[14]

It is important to mention that cobalt, nickel and several other elements, may exhibit more than one emission line with a characteristic intensity pattern. If a notorious deviation from the intensity pattern is observed, it usually indicates the energy contribution of additional elements.

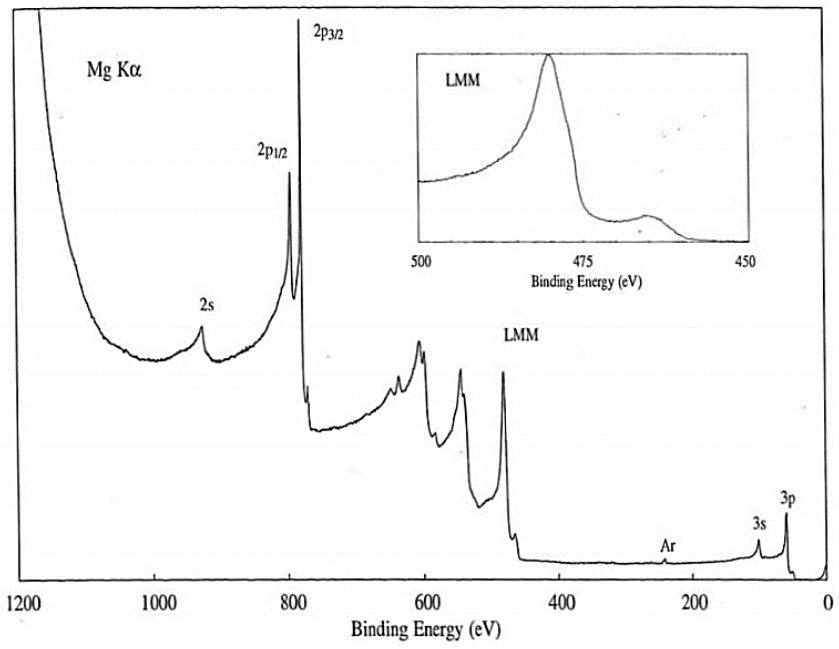



Figure 2.5.2 Represenrtation of a XPS surfvey. Reproduced from Ref.[17]

The second step for XPS analysis is the extraction of peak position and intensities for the survey analysis, prior to a background substation. Once all the previous steps are completed, a more detailed analysis of core level binding energies may be performed. A typical detailed analysis consists on the application of a high-intensity X-ray beam in the specific binding energy region of a given compound (previously detected in the survey spectra) followed by a curve fitting of the obtained spectrum. For non-metallic species, the lines are generally symmetric, whereas for metallic species, the lines exhibit an asymmetry towards higher binding energy due to interactions of the conduction electrons with the core hole.[20] Both metallic and non-metallic species are analysed by a convolution of Lorentzian and Gaussian curves.

A remarkable feature of XPS spectra is the "chemical shift" where a core peak is shifted up or down in energy in correspondence to the addition of a chemical bond. Note that as the electron density of an atom increases, its binding energy decreases due to the additional coulombic interaction between the photo-emitted electron and the ion core. Therefore, a chemical shift can reveal important information such as the oxidation states of metals by virtue of the magnitude of the observed chemical shift. Emitted electrons may lose their energy through a range of interactions which must be considered when interpreting the emission spectrum. These include, in order of increasing energy loss, phonon interactions, electron-electron or plasmon interactions, single or double particle excitations, and the generation of Auger electrons.

## 2.6 Scanning Electron Microscopy

Scanning electron microscopy was widely employed throughout this thesis to picture and characterize the surfaces of the various materials studied.

Scanning electron microscopy (SEM) is extensively used, particularly in material science. While optical microscopy is the simplest and least expensive small-scale material characterization technique, the lack of resolution at high amplifications limits its utilisation in material science. The visible light used in optical microscopes typically has wavelengths of the order of 600 nanometres.[8] With the presence of spherical aberration, these wavelengths translate into a resolution of one to two micrometres in most optical microscopes.[21] Contrary, SEM uses electrons rather than light to generate images and

therefore its resolution is limited by the wavelength of an electron rather than a photon. The latter translates into resolutions on the order of few nm.[21] In brief, a beam of electrons is emitted from an electron source, accelerated using high voltages and focused on a fine point of the material surface using magnetic lenses. This beam is scattered by the electron clouds and nuclei of atoms present in the sample, and scattered electrons may be detected on it. In SEM, the electron beam is scanned back and forth across the sample surface to generate an image of that surface. When the scanning electrons hit the material surface, different types of scattered electrons can be detected and different characteristic information about the sample determined. Typically, backscattered and secondary electrons are used to generate images. Fig. 2.6.1 displays a common setup of an SEM apparatus.

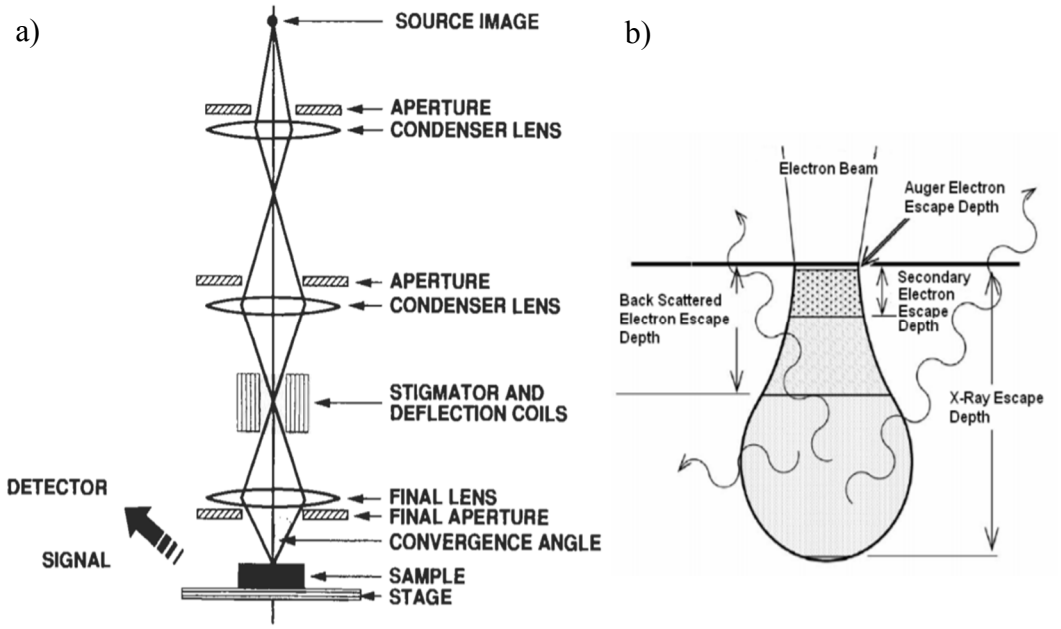



Figure 2.6.1 a) Schematic of the electron optics constituting a typical SEM apparatus and b) Various emissions upon interaction of the electron beam with the sample. Reproduced from Ref. [22]

However, there are some aspects to be considered when dealing with SEM in order to prevent the acquisition of potentially misleading images. For example, in SEM the brightness of an image is dependent on the number of secondary electrons reaching the detector from that specific area.[21] While this is the reason that allows SEMs to generate sharp, three-dimensional images, it can also lead to an "edge effect" in which sharp edges of a sample appear abnormally brighter than the rest of the sample. Another aspect to bear

in mind is that, in SEM analysis the interaction between the incident electron beam and the sample can often be destructive to the material being viewed.[23]

It is possible to perform an elemental composition evaluation using energy-dispersive X-ray spectroscopy (EDS) attached to the SEM. Briefly, EDS uses the emitted X-ray from the sample to obtain a localized chemical analysis. Qualitative analysis involves the separation of the characteristic X-rays of different elements into an energy spectrum and the subsequent analysis with a specific software. The result is a spectrum similar to that presented in fig. 2.6.2.

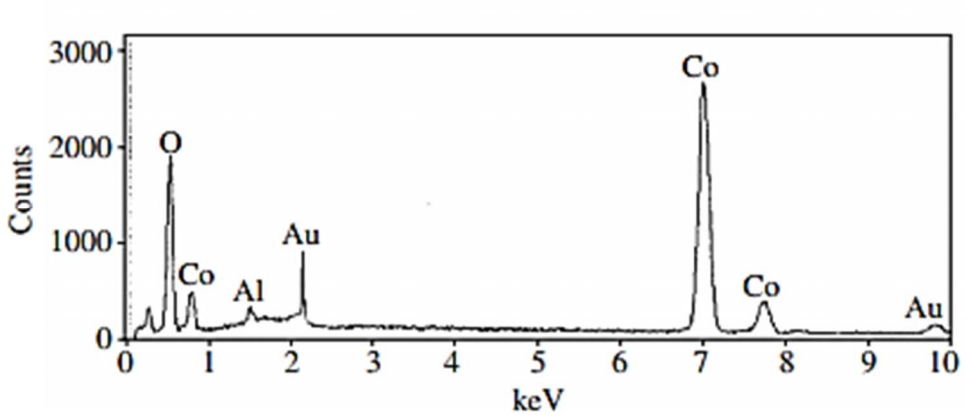



Figure 2.6.2 Example of an EDX spectra which corresponds to a Co nanowire. Reproduced from Ref.[24]

The determination of the concentrations of the elements present in a specific area of the sample entails, after the calibration of the analyser using standards of known composition, typically, either pure gold or pure titanium, the measure of line intensities for each element in the sample.

## 2.7 Miscellaneous Surface Characterisation

### 2.7.1 Contact Angle

This very simple technique gives valuable insight into the nature of the surface chemistry of samples. A drop of liquid placed on a smooth solid surface will form a particular shape depending on the wettability of the surface for a given liquid. Wettability, or the degree of wetting, is the tendency of a liquid to keep contact with a solid surface. The shape of the droplet is reflected on the contact angle with the surface, as shown in fig. 2.7.1. The

contact angle ranges from 0°, which means completely spreading, to 180°, that implying a completely non-spreading. In general, a small contact angle of less than 90° represents high wettability, while contact angles larger than 90° correspond to low wettability. This contact angle is a product of the liquid surface tension and the surface energies (solid, liquid-solid and liquid-surface tensions), which arises from various intermolecular forces such as Van der Walls, hydrogen bonding, polar interactions, etc. The contact angle at equilibrium may be defined according to Young's equation:[25]

$$\gamma_{LS} \cos \theta_e = \gamma_{LS} - \gamma_{LS} \tag{2.7.1}$$

where $\gamma_{LS}$ is the liquid-solid interfacial tensions in mN $m^{-1}$. The use of different liquids known to exhibit certain of these forces can give an indication of the nature of the interaction between the two materials at the interface. Highly polar liquids, such as water, exhibit a very clear distinction between hydrophobic and hydrophilic materials by the resulting contact angle.

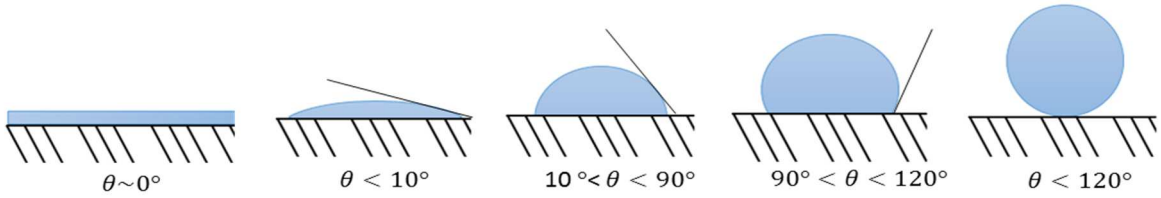



Figure 2.7.1 Schematic representation of different behaviours of water droplets on various surfaces, from left to right: perfect wetting, super-hydrophilic, hydrophilic, hydrophobic and super-hydrophobic.

### 2.7.2 Thermogravimetric Analysis

Thermogravimetric analysis (TGA) is a technique in which changes in the weight of a known amount of material are monitored as a function of temperature or time, while it is purged with an inert gas. TGA can provide quantitative information resulting from any process, causing an obvious weight variation during controlled heating. For example, it was previously used by Patil *et al.*[26] when investigating the stoichiometry and kinetics of thermal decompositions of the precursor for NiO films ($NiCl_2 \cdot 6H_2O$). TGA is also an extremely useful technique for studying polymer degradation since the decomposition temperature represents the upper limit of the processing temperature.[27] Typically, two types of phenomena are shown on a TGA plot, and these are illustrated in fig. 2.7.2.

Weight loss (a), the most frequent phenomenon, is generally represented by a downward shift in the plot, whereas weight gain (b) is represented by an upward shift in the plot.

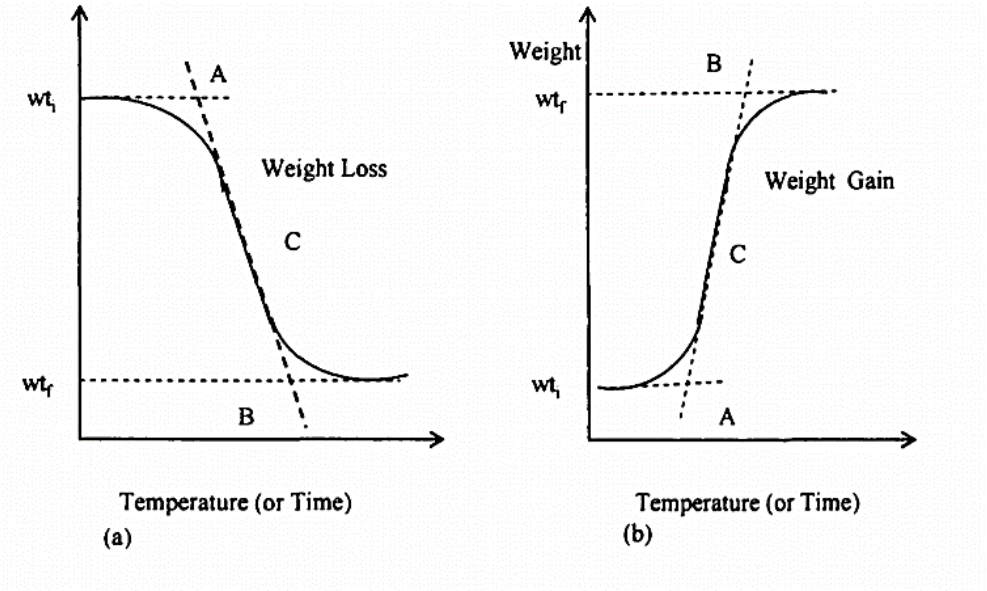



Figure 2.7.2 Schematic representation of a) weight loss and b) weight gain during thermogravimetric measurement. Point A is the start of weight variation, B is the end of weight variation, and C is the inflexion point, $wt_j$ is the initial while $wt_f$ is the final weight. Reproduced from the DTA / TGA Pyris manual.

A TGA measurement consists of a sample pan, typically ceramic, supported by a precision balance. That pan is inserted into the furnace for either heating or cooling and the mass of the sample is monitored along the process. During the decomposition, a gas, either inert or reactive, controls the sample environment flowing over the sample and exiting through an exhaust. Temperature scanning is an important factor when measuring decomposition temperature. For a better resolution of the transitions, it is recommended to use a slow scan rate of approximately 5°C $min^{-1}$. Contrary, if only aiming to calculate the remaining filler after all the decomposition transitions, then fast scan rate to be used is of approximately 40°C $min^{-1}$.

## 2.8 References Chapter 2


[1] A. Hickling, *Transactions of the Faraday Society* **1941**, *37*, 532-535.

[2] F. P. Bowden, E. K. Rideal, T. M. Lowry, *Proceedings of the Royal Society of London. Series A, Containing Papers of a Mathematical and Physical Character* **1928**, *120*, 59-79.

[3] J. O. M. Bockris, S. U. M. Khan, *Surface electrochemistry : a molecular level approach*, Plenum, New York, **1993**.

[4] P. W. T. Lu, S. Srinivasan, *J. Electrochem. Soc.* **1978**, *125*, 1416-1422.

[5] L. D. Burke, M. E. Lyons, O. J. Murphy, *Journal of Electroanalytical Chemistry and Interfacial Electrochemistry* **1982**, *132*, 247-261.

[6] A. Katsaounis, Brosada, S., VayenasC.G., in *Encyclopedia of Electrochemistry-Electrochemical Engineering, Vol. 5* (Ed.: A. J. Bard, Stratmann, M., MacDonald, D. D. Schmuki, P.), Wiley-VCH, Weinheim, **2007**.

[7] A. Bard, L. Faulkner, *Electrochemical Methods: Fundamentals and Applications*, John Wiley & Sons, Inc, **2001**; R. Greff, R. Peat, L. M. Peter, J. Robinson, in *Instrumental Methods in Electrochemistry*, Ellis, Chichester, **1985**; C. M. A. Brett, Brett, AM.O, *Electrochemistry- Principles, Methods and Applications*, Science Publications, Oxford, **1993**.

[8] B. E. Warren, *X-ray diffraction*, Dover Publications INC,, New Yorkz, **1990**.

[9] V. Pecharsky, P. Zavalij, *In Fundamentals of Powder Diffraction and Structural Characterization of Materials*, Business Media, Inc, New York, **2005**.

[10] W. H. Bragg, W. L. Bragg, *Proceedings of the Royal Society of London. Series A, Containing Papers of a Mathematical and Physical Character* **1913**, *88*, 428-438.

[11] B. Wunderlich, in *Macromolecular Physics* (Ed.: B. Wunderlich), Academic Press, **1973**, pp. 1-20.

[12] A. Monshi, M. R. Foroughi, M. R. Monshi, *World Journal of Nano Science and Engineering* **2012**, *2*, 7.

[13] G. K. Williamson, W. H. Hall, *Acta Metallurgica* **1953**, *1*, 22-31.

[14] M. Prutton, *Introduction to Surface Physics*, Clarendon Press, New York, **1994**.

[15] D. P. Woodruff, T. A. Delchar, *Modern Techniques of Surface Science*, Cambridge University Press, **1994**.

[16] S. Giménez, J. Bisquert, *Photoelectrochemical solar fuel production: From basic principles to advanced devices*, **2016**.

[17] J. F. Moulder, J. Chastain, *Handbook of x-ray photoelectron spectroscopy : a reference book of standard spectra for identification and interpretation of XPS data*, Physical Electronics, Eden Prairie Minnesota, **1995**.

[18] H. Hertz, *Annalen der Physik* **1887**, *267*, 983-1000.

[19] A. Einstein, *Annalen der Physik* **1905**, *322*, 132-148.

[20] S. Doniach, M. Sunjic, *Journal of Physics C: Solid State Physics* **1970**, *3*, 285.

[21] C. R. Brundle, C. A. Evans, S. Wilson, *Encyclopedia of materials characterization: surfaces, interfaces, thin films*, Gulf Professional Publishing, **1992**.

[22] C. R. Brundle, C. A. Evans, S. Wilson, Butterworth-Heinemann ; Manning, Boston; Greenwich, CT, **1992**.

[23] R. F. Egerton, P. Li, M. Malac, *Micron* **2004**, *35*, 399-409.

[24] V. d. R. Caffarena, J. L. Capitaneo, R. A. Simão, A. P. Guimarães, *Materials Research* **2006**, *9*, 205-208.

[25] T. Young, *Philosophical Transactions of the Royal Society of London* **1805**, *95*, 65-87.

[26] P. S. Patil, L. D. Kadam, *Applied Surface Science* **2002**, *199*, 211-221.
[27] C. A. Wilkie, *Polymer Degradation and Stability* **1999**, *66*, 301-306.

# CHAPTER 3

# EXPERIMENTAL METHODOLOGY AND PROCEDURE

## 3.1 Introduction

This chapter details the specifics of the various materials, methods and instruments used throughout this thesis. The theory and background behind the techniques was dealt with in chapter 2.

## 3.2 General Reagents and Solutions

Unless specified, all chemicals and solvents used in this work were purchased form Sigma-Aldrich (ACS reagent grit or higher) and used as-received. High purity nitrogen (99.998 %) and Argon (99.99 %) gases were supplied by BOC (BOC Gases Ireland Ltd). Any aqueous solutions were freshly prepared using purified water with resistivity > 15 MΩ cm. The purified water was obtained from a Millipore Elix 5 UV system. Also, unless otherwise stated, all electrochemical experiments were carried out in 1.0 M NaOH solution ( ≥ 98 % purity, pellets (anhydrous)).

Two acid solutions were utilised for cleaning purposes: 37 % HCl was used to clean all the glassware and Teflon® parts whereas 0.5 M $H_2SO_4$ was used to electrochemically clean the working electrodes.

## 3.3 Electrode Materials and Instrumentation

### 3.3.1 Electrochemical Cell

Electrochemical characterisation was carried out in 25 ml three electrode Pyrex water-jacketed cells connected to a temperature-controlled bath. All electrochemical measurements were done at 25°C. Fig. 3.3.1 shows a schematic of the typical electrochemical cell setup. This configuration consisted of a working electrode (WE) which depending on the experiment was: Ti foil (SEM analysis), Ti wire (electrochemical analysis), GC plate (XPS analysis and contact angle) or Mn rod (electrochemical analysis); a reference electrode (RE) and a counter electrode (CE). All the potentials are, unless otherwise stated, are reported with respect to mercury-mercury oxide reference electrode (Hg/HgO, 1.0 M NaOH).

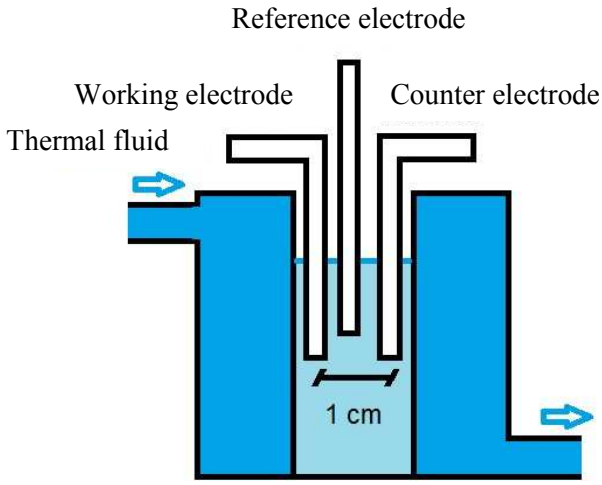



Figure 3.3.1 This schematic diagram shows the configuration adopted for all experiments.

The three types of electrodes were immersed in the electrolyte solution and connected to the potentiostat, which was controlled by an external computer unit. The distance between the electrodes was settled to be 1 cm. This was achieved using a Teflon® lid with openings for the electrodes and the gas inlet. Prior to each electrochemical characterisation, nitrogen or argon gas were injected into the solution for 15 min to ensure a consistent oxygen free environment. An oxygen free environment is essential in order not to have interactions between the oxygen produced and the oxygen dissolved. Since oxygen dissolved is electroactive, the $O_2$ dissolved produces a current arising from its reduction and affects the current response of the working electrode. Once a week, the glass cell and the Teflon® lid were cleaned with 37 % HCl acid and rinsed with Millipore water to ensure the full removal of possible contamination on the surface.

### 3.3.2 Electrodes

Throughout this work, all the materials characterised by electrochemical means are employed as a working electrode (WE). The WE, the electrode under analysis, is the electrode on which monitored electrochemical processes take place. The potential applied to the WE is referred to a stable reference electrode (RE), which in this work was typically a mercury-mercury oxide reference electrode. To complete the electrical circuit, a third electrode, the counter electrode (CE), is also used. Each type of electrodes used in this thesis are described with more detail in the following sections.

### 3.3.2.1 Working Electrode

In this work, we focused in the electrochemical reactions of the working electrode. The materials under investigation are Ni, Co and Mn. However, such electrodes are generally not commercially available for laboratory purposes and, therefore, it was necessary to construct suitable working electrodes in the laboratory. Following, various fashions to produce such electrodes are presented.

**a)** Metal Oxide Electrode Preparation *via* Potential Multicycling

The working electrodes used in chapter 4 and in the first section of chapter 6 were prepared from high purity manganese rod with 2.0 mm diameter and 99.5% purity (supplied by GoodFellow). The electrodes had an exposed surface length of 15 mm. This length was keep constant by sealing the rod electrode in glass. Prior to each experiment, the exposed area was manually polished with standard P1200 grit carbide paper (supplied by Buehler). After the polishing, the electrodes were rinsed with Millipore water.

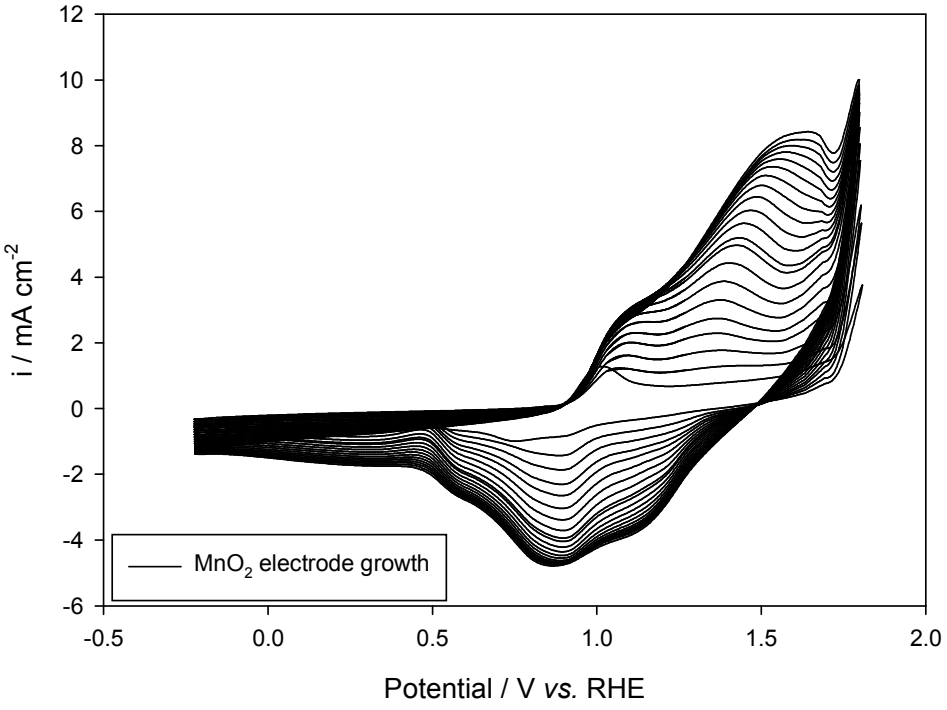



Figure 3.3.2 Example of Mn oxide film growth by cycling the potential in a potential window of -0.25 V to +1.75 V *vs.* RHE in 1.0 M NaOH at 25°C. Sweep rate was 40 mV $s^{-1}$.

The Mn electrode was further electrochemically pre-treated in $N_2$-saturated 1.0 M NaOH (≥98% purity, pellets (anhydrous)) solution by cycling the potential scan in the potential range of -0.25 V to +1.75 V (*vs.* RHE) at a sweep rate of 40 $mVs^{-1}$. Fig. 3.3.2 displays the voltammetric response of such procedure.

The redox charge capacity can be controlled by modifying the number of potential scans applied to the working electrode. Note that the redox charge capacity of the thin film is directly proportional to the layer thickness. A more detailed explanation of the latter will be presented in chapter 4. Under the former premises, different layer thicknesses of the metal oxide where fabricated by cycling the WE in 1.0 M NaOH in a range of 0 to 1000 cycles. Finally, the working electrode was rinsed with Millipore water in order to remove any remaining electrolyte from the film.

**b)** Metal Oxide Electrode Preparation *via* Thermal Decomposition

For the electrochemical characterisation of nickel cobalt mixed oxide electrodes in chapter 5, titanium wires of 99.99% purity and 1 mm diameter (supplied by Alfa Aesar- Johnson Matthey company) were encased in a custom-build glass holder insulator. The electrodes had an exposed surface length of 10 mm. Prior to each experiment, the wires were manually polished with standard P1200 grit carbide paper and rinsed with Millipore water. In addition, the working electrode was electrochemically cleaned in 0.5 M $H_2SO_4$ solution by applying +1.3 V (*vs.* Ag/AgCl) for 2 min and then cycling the potential scan between -0.2 V and +1.10 V (*vs.* Ag/AgCl) at 100 mV $s^{-1}$. This process anodically dissolves all metal traces remaining on the surface. Finally, the electrode was polished with 0.3 μm alumina powder (supplied by Buehler) until a "mirror bright" finish was achieved and sonicated for 5 min in Millipore water to ensure the full removal of alumina powder.

Different nickel cobalt mixed oxides with various % M Co content were prepared by thermal decomposition of the precursor metal solution coated either on Ti wire (for electrochemical analysis), Ti foil (for SEM analysis) or GC plates (for XPS analysis and contact angle) (99.9% purity, 1 mm thickness - supplied by HTW Hochtemperatur-Werkstoffe GmbH – IgradurG). Thermal decomposition was carried out using a hot wall quartz tube furnace with a tube diameter of 38 mm, cat no. MTF-10-25-130, manufactured by Carbolite Gero.

A mixed aqueous solution of 1 M $Ni(NO_3)_2 \cdot 6H_2O$ and 1 M $Co(NO_3)_2 \cdot 6H_2O$ (with different Ni/Co molar ratio) was dripped onto the working electrode surface using a brand-new glass pipette. The painted metal surface was treated with a heat gun (at ca. 200°C) for 1 min in order to remove the 2-butanol solvent. Subsequent, the sample was loaded into the furnace at 300°C annealing temperature for 5 min. This anneal procedure was repeated 20 times to deposit 20 ± 5 mg of metal oxide on the electrode surface. The final anneal was carried out for the duration of 4 hours at various constant temperatures in the range of 300°C and 550°C to ensure complete nitrate to oxide transformation. According to previous publications, 3 to 4 hours of annealing time is enough to remove all the solvent and to produce the corresponding transition metal oxide. Finally, the sample was cooled to room temperature in air. Fig. 3.3.3 shows the typical procedure setup used for the growth of the nickel cobalt oxide electrodes.

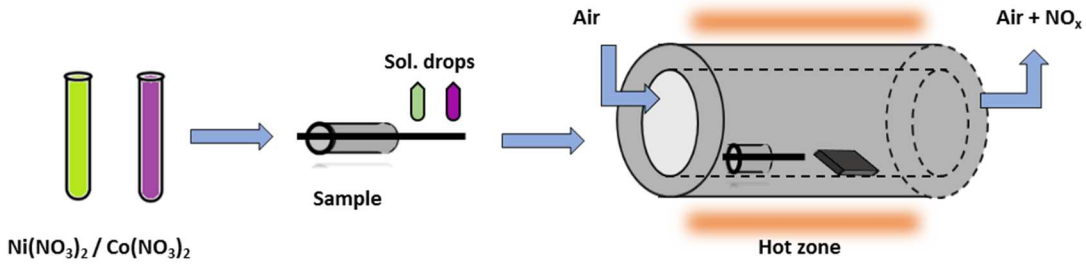



Figure 3.3.3 Typical procedure setup used for the grown of various Ni/Co oxides films.

### 3.3.2.2 Counter Electrode

The purpose of a counter electrode is to supply the current required by the working electrode, thereby preventing the polarization of the reference electrode due to passage of excessive current through it. A platinum wire electrode supplied by CH Instruments (cat. no. CHI 115) was employed as a counter electrode in this study. The use of a platinum wire as a counter electrode ensures a large electron transfer / surface area ratio within the cell while preventing the saturation of current density (overflow) in the working electrode. Moreover, it was found to be more suitable for electrochemical characterisation than other typical counter electrodes, such as graphite rod, due to the small number of compounds absorbed onto the surface. Prior of each experiment, the counter electrode was manually polished with standard P1000 grit carbide paper and rinsed with Millipore water. Then, it

was dropped into a 0.5 M $H_2SO_4$ solution for 5 seconds to ensure the full removal of any absorbed contamination. Finally, the counter electrode was rinsed with Millipore water.

### 3.3.2.3 Reference Electrode

Reference electrodes are typically used in electrochemistry as a potential benchmark against which potential changes of the working electrode can be monitored. The definition of an ideal reference electrode requires for such electrode to show two features: (i) time-invariant potential, and (ii) non-polarizable behaviour. On the one hand, to maintain a constant potential over time, full reversibility within the electrode is needed. During the electrochemical characterisation, the reference electrode must be charged and discharged in a reproducible manner, which implies the need for a reversible reaction. On the other hand, the non-polarizable aspect refers to the lack of net current flow through the electrode during the electrochemical measurements. Despite the latter is only possible under ideal conditions, the Butler-Volmer eqn. (see eqn. 1.2.16) shows that a reference electrode with high exchange current density or low overpotential best approximates the non-polarizable state. Normally, the potential of the reference electrode is related to a standard potential scale, *e.g.* to the normal hydrogen electrode (NHE) or to the standard hydrogen electrode (SHE). Sometimes, however, some scientific publications often use the NHE as a synonym for SHE and that is completely incorrect. The NHE refers to the historical standard reference electrode suggested by Nernst in the late 90s.[1] He defined it as "a metal in contact with a solution saturated with hydrogen gas at 1 atm partial pressure and containing 1.0 M sulphuric acid". In addition, at the time the NHE reference electrode was defined, the concept of activity was not yet developed and thus the potential of such reference is related to concentration. In contrast, the SHE is conceived as an ideal device and cannot be rigorously realized experimentally. In accordance with the IUPAC, the standard hydrogen electrode is conventionally taken as the universal (for solutions in protic solvents such as water) reference electrode for which, under standard conditions, $E^0\ (H^+/H_2) = 0$ at all temperatures. However, it is extremely difficult to achieve such standard conditions. Therefore, for experimental realization, only an electrode whose potential is not calculated at standard conditions but recalculated considering $H^+$ activity equal to unity and at $10^5$ Pa must be used. This electrode is known as the reversible hydrogen electrode (RHE) and is one of the references electrode utilised in the present work.

The fast oxidation of hydrogen molecules is described by the following reaction:

$$2H^+ + 2e^- \rightarrow H_2 \tag{3.3.1}$$

The electrode potential may therefore be calculated using the Nernst equation:

$$E = E^0 + \frac{0.0591}{2} log\left(\frac{(a_{H^+})^2}{\frac{p_{H_2}}{p^0}}\right) \tag{3.3.2}$$

Rearranging eqn. 3.3.2, it can be written as follows:

$$E_{RHE} = E_{SHE} + 0.059\, pH \tag{3.3.3}$$

As it is clear from eqns. 3.3.2 and 3.3.3, the equilibrium potential depends on the hydrogen ion activity and, therefore, on the pH of the electrolyte. Generally, it is very common to find in the literature potentials quoted against the RHE reference electrode. In view of this, it is necessary, in case the experimental data is measured against other reference electrodes such as Hg/HgO, to convert the potentials to the RHE scale. The conversion of potentials obtained using Hg/HgO to RHE scale is presented:

$$E_{RHE} = E_{meas} + 0.059\, pH + 0.098 \tag{3.3.4}$$

where $E_{meas}$ is the potential obtained against the Hg/HgO reference electrode. The value of 0.098 V refers to the standard potential of the Hg/HgO reference electrode. In the case of 1.0 M NaOH (pH=14) eqn. 3.3.4 simplifies to:

$$E_{RHE} = E_{meas} + 0.926\, V \tag{3.3.5}$$

More information regarding the Hg/HgO reference electrode will be presented later in this section.

Back on topic, the common design of a RHE uses a carbon supported platinum catalyst as a gas diffusion electrode. Through a small channel the *in situ* produced hydrogen gas is brought to an inert palladium containing sensor element. When the sensor electrode is immersed into the solution, the solution is separated from the electrode by a polymer membrane. These electrodes can be used either in strong acids or in strong alkali media. A

schematic diagram, of the RHE supplied by Gaskatel (cat no. HydroFlex), utilised in this thesis is presented in fig. 3.3.4.

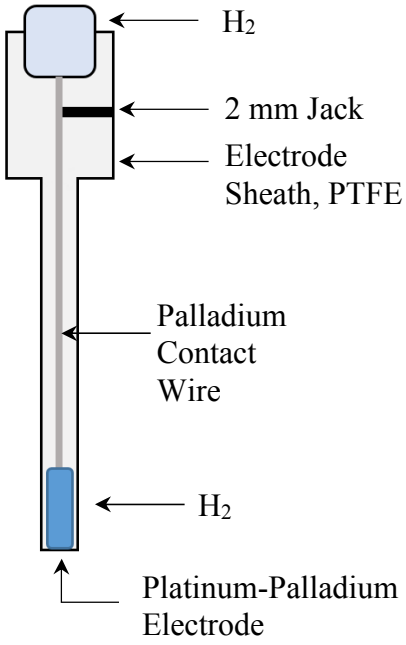



Figure 3.3.4 Schematic representation of the RHE reference electrode utilised in the present thesis.

In section 4.5, the RHE was specifically utilised to perform reaction order analysis. This type of reference electrode was utilised due to its direct calculation of the mechanistically significant reaction order, being the latter equal to the slope of the log ($i$) *vs.* log ($a_x$) plot. Prior to each analysis, the RHE was submerged into a NaOH solution of an equal concentration and temperature than that of the solution used for the electrochemical analysis. The electrode was left under this conditions for the duration of an hour. This was required to achieve a stable potential within the reference electrode. Fig. 3.3.5 shows the potential stabilisation of the RHE reference electrode used in this thesis in 1.0 M NaOH. Once the potential of the reference electrode was stable, it was rinsed with Millipore water and used for the analysis. It is noteworthy to highlight that any slight change on the concentration of NaOH within the electrode´s cell implies changes on the standard reference potential, as predicted by eqn. 1.2.89. For the sake of consistency, the potential of the reference electrode was measured before and after the experiment with a "master Hg/HgO electrode". In this work, none of the data obtained using the RHE with a potential shift greater than ± 5 mV is presented.

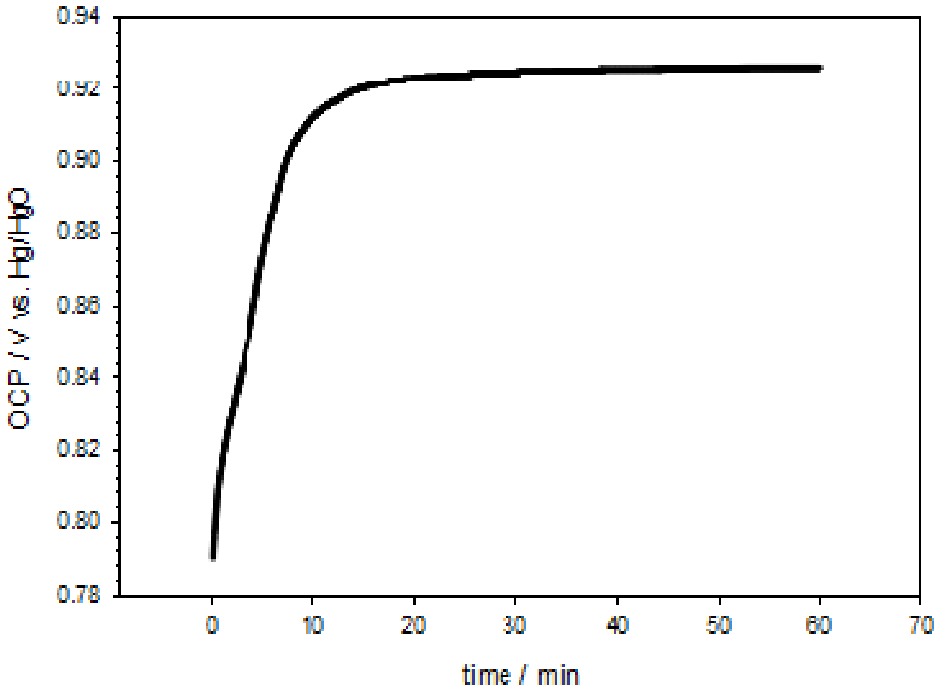



Figure 3.3.5 Potential stabilisation of the RHE reference electrode in 1.0 M NaOH quoted against Hg/HgO filled with 1.0 M NaOH. Electrolyte temperature was 25°C.

Another reference electrode utilised in this thesis was the mercury-mercury oxide (Hg/HgO) with an aqueous filling solution of 1.0 M NaOH, supplied by CH instruments (cat. no. CHI 152). A schematic diagram of this electrode is presented in fig. 3.3.6.

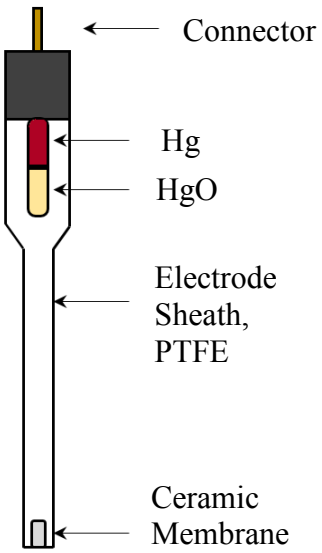



Figure 3.3.6 Schematic representation of the Hg/HgO reference electrode utilised in the present work.

According to the classic work of Ives and Hills[2] in 1961, the mercury-mercury oxide electrode is uniquely well behaved among metal-metal oxide electrodes in that it shows the expected Nernstian shift of 59 mV $pH^{-1}$ against a pH independent reference electrode. The Hg/HgO is the most commonly and stable reference electrode for use in alkaline solutions, since mercurous oxide do not exist in nature and, therefore, there is no disturbing effect due to a variable valence of the mercury oxide. In addition, the dissociation constant of mercury oxide in alkaline media has been estimated to be smaller than the one in acidic media.[2-3] The Hg/HgO was utilised as the reference standard for all the electrochemical characterisation carried out in this work including some reaction order analysis. The mercury-mercury oxide reaction can be represented by the following reaction:

$$HgO + H_2O + 2e^- \rightarrow Hg + 2OH^- \tag{3.3.6}$$

where HgO might be found in the following equilibrium:

$$HgO + H_2O \rightleftarrows Hg(OH)_2 \rightleftarrows Hg^{2+} + 2OH^- \tag{3.3.7}$$

Using the Nernst eqn., the potential of the Hg | $Hg^{2+}$ electrode may be written as:

$$E = E^0_{Hg/Hg^{2+}} + \frac{0.0591}{2} log\left(a_{Hg^{2+}}\right) \tag{3.3.8}$$

The standard potential for the $E^0_{\frac{Hg}{Hg^{2+}}}$ electrode *vs.* SHE, corrected to zero concentration, was found to be 0.0977 V at 25°C. Also, the equilibrium potential for such electrode in 1.0 M NaOH was found to be 0.92581 V (*vs.* RHE).[4] Now, since the equilibrium potential of the cell Hg/HgO is 0.926 V at 25°C and the equilibrium oxygen electrode potential is 1.229 V (*vs.* RHE), it follows that $E^0_{O_2}$ is 0.304 V (*vs.* Hg/HgO) in the same solution. It is common practise in the literature of the OER to express the potential in terms of the oxygen overpotential, $\eta$. When the reference electrode is a Hg/HgO electrode, the overpotential is related to the measured voltage, $E_{meas}$, as follows:

$$\eta = E_{meas} - 0.304V \ (at\ 25°C) \tag{3.3.9}$$

For the sake of consistency, a standard potential of the Hg/HgO reference electrode filled with 1.0 M NaOH was used in this work. When this type of reference electrode is used in NaOH solutions of different concentration that 1.0 M NaOH, a minor diffusion leakage

occurs in the electrode chamber, which causes a slight change on the equilibrium potential. In view of this, the potential of the reference electrode was checked both before and after the experiment against a "master" unused Hg/HgO reference electrode. The observation of a 0 ± 5 mV reading under open circuit potential (OCP) conditions in a 1.0 M NaOH solution, when the operational electrode and the "master" Hg/HgO were connected to the potentiostat, indicated that the operational Hg/HgO electrode system was functioning correctly. This implied that the NaOH concentration on the electrode chamber remained effectively constant for the duration of the experiment. In this work, none of the reference electrodes utilised for data acquisition had an error greater than ± 3 mV. In any case, the 1.0 M NaOH solution in the reference electrode was changed on a weekly basis to ensure experimental consistency.

### 3.3.3 Electrochemical Analysis

Unless otherwise stated, all electrochemical experiments were performed using a high performance PGSTAT302N potentiostat/galvanostat instrument (Metrohm, Utrecht, Netherlands). The potentiostat was controlled by a desktop computer unit. The measured data was primarily treated using the inbuilt analysis software, which in the case of Metrohm, was NOVA 1.0v package. The temperature of the cell was controlled using a F12-ED Refrigerated/Heating Circulator filled with deionized water and kept constant at 25ºC for all the experiments. The raw data was finally analysed using Sigma Plot 12.5v software package.

### 3.3.4 X-ray Powder Diffraction Spectroscopy

The crystallographic structure analysis was carried out using a Bruker D2 Phase diffractometer, Cu($K\alpha$) radiation ($\lambda$ = 1.5418 Å) and a graphite monochromator. The sample was loaded onto a quartz fibre cyanoacrylate and introduced in the XRD chamber. Patterns were collected in fluorescence-mode with 2θ range of ca. 5° to 55° at a rate of 1° $min^{-1}$. The raw data was analysed with the help of MDI Jade software, which enabled accurate background subtraction and enhanced peak resolution. The database used was the Cambridge Crystallography Database. The correct Bravais lattice and lattice

constants were obtained by recognizing the sequence of XRD peaks in terms of the quadratic form of the Miller indices.

Powder samples were prepared by grinding, in a granite grinder, different $Ni^{2+}/Co^{2+}$ molar ratio mixtures of $Co(NO_3)_2 \cdot 6H_2O(s)$ and $Ni(NO_3)_2 \cdot 6H_2O(s)$. The sample was then introduced into the furnace at room temperature and ramped to temperatures in the range of 300°C to 550°C. The samples were annealed at the desired temperature for 4 hours to ensure a complete nitrate to oxide transformation. After 4 hours, the furnace was switched off and the sample was cooled, inside the furnace, to room temperature. To conclude, the sample was grinded until a uniform powder sample was achieved.

### 3.3.5 Scanning Electron Microscope

SEM images were taken using a Zeiss Ultra field SEM with an acceleration voltage between 5 kV - 15 kV. All the images presented in this thesis were obtained using in-lens detector at a working distance between 3 and 8 mm.

For the morphological analysis of samples presented in chapter 5, Ti foil was used as a substrate electrode. The preparation of the metal oxide sample is explained with detail in section 3.2.2.1. For SEM imaging, the film of metal oxide was only deposited in one side of the sample. This procedure was found to achieve higher definition SEM images. The samples were attached to a simple holder using standard carbon tape. All SEM images were taken from the centre of the sample.

The SEM analysis of samples presented in chapter 4 were prepared by horizontally attaching the Mn rod (cylindrical shape) to the SEM holder using carbon tape. Since the electrode possesses a cylindrical shape, it is important to achieve a centred position of the electron detector in order to be able to consider the area under investigation to be flat. Therefore, all SEM images presented in this thesis are obtained from a cantered position of the sample.

### 3.3.6 Energy Dispersive X-ray

The elemental composition of the samples in both chapters was investigated using energy dispersive X-ray (EDX). The analysis was performed using an Oxford Instrument X-Max EDX detector in conjunction with a Zeiss Ultra SEM system. Due to the chemical proprieties of the different materials investigated in this thesis, all the analysis was carried out at an acceleration voltage of 15 kV. This acceleration voltage enabled accurate spectra with high defined peaks. The spectra was analysed with INCA software provided by Oxford instruments.

Identical SEM sample and identical area were chosen for the EDX analysis. See SEM sample preparation for more detailed information.

### 3.3.7 X-Ray Photoelectron Spectroscopy

Surface composition and oxidation metal state was investigated with X-ray photoelectron spectroscopy (XPS). The measurements were performed using a VG Scientific ESCAlab MKII system equipped with a polychromatic Al Kα source (1486.6 eV). Data acquisition was obtained by irradiating the X-ray beam within a spot size of ca. 3 millimetres, which was believed to be sufficient to represent the totality of the sample surface. For survey scans, an analyser pass energy of 200 eV was employed, whereas for high resolution peak scans 20 eV was used. For compositional analysis the raw data was fitted to the high-resolution peaks. The raw data fitting was processed using CASA XPS software. All the spectres were calibrated to the C 1s peak, which has a binding energy of 285eV. The fitting of Co 2p and Ni 2p levels in chapter 5 was performed using doublet peaks with 50% Gaussian and 50% Lorentzian character over a linear background function using CASA XPS software.

Identical SEM samples were chosen for the EDX analysis. See SEM sample preparation for detailed information.

### 3.3.8 Thermogravimetric Analysis

Thermogravimetric analysis was conducted using a Perkin Elmer Pyris 1 thermal analyser. The loss of sample weight during a linear increase in temperature was analysed

at a uniform scanning rate of 5°C $min^{-1}$. The scanning sequence was ramped between 30°C to 600°C. Samples of approximately 5 mg were put into a 500 µl ceramic crucible. The measurement was performed under air to provide both an oxidising atmosphere and a flowing gas for the removal of gases. A blank run was carried out with an empty ceramic crucible to set the base line, and this was subtracted from the subsequent recorded raw data.

Samples in chapter 5 were prepared from different $Ni^{2+}$ / $Co^{2+}$ molar ratio mixtures of $Co(NO_3)_2 \cdot 6H_2O(s)$ and $Ni(NO_3)_2 \cdot 6H_2O(s)$ of ca. 5 mg of the resulting mixture.

### 3.3.9 UV-Vis Spectroscopy

For the UV - Vis characterisation, in chapter 4, a Libra S22 UV - Visible spectrophotometer, supplied by Biochrom Ltd. and equipped with a xenon lamb as a source of light, was used. This technique was employed to assess the characterisation of the electrolyte composition under electrode corrosion conditions. Two different types of quartz cuvettes were utilized for UV-Vis measurements. An opened quartz cuvette was employed to analyse the effect of direct air contact with the sample, whereas a sealed quartz cuvette was used to analyse the sample under air free conditions. The closure was achieved by installing a Teflon® top and sealing it with paraffin film. Before the sealing, the air space left in the cuvette was filled with argon gas and the solution deoxygenated for the duration of 10 min using the same inherit gas. Sample's optical changes were analysed within a 7 hour from the production of the sample. Sequential spectres were collected every 20 min. Start and end wavelength were 250 nm and 750 nm, respectively. The scan was measured at 1.0 nm scan step and 750 nm $min^{-1}$ scan rate. All the spectra were obtained at room temperature.

Samples were obtained by polarizing the manganese working electrode in 1.0 M NaOH, previously deoxygenated, at 1.3 V *vs.* Hg/HgO for 2 min. This setup was sufficient to produce: (i) working electrode corrosion, and (ii) irreversible electrode damage. The pinky colored solution obtained was immediately transferred into the desired sample holder, which could be either an opened or sealed cuvette, and loaded into the UV-Vis chamber. The measurement was initialized after the loading.

### 3.3.10 Contact Angle

Static contact angle analysis was carried out on a CA analyser (FTA) under ambient conditions of temperature and humidity; samples were dried in oven at 50°C for the duration of 10 min in order to remove surface moisture. The contact angles were measured by propping a small droplet of Millipore water on top of the flat surface of the samples. A series of images were taken in order to study the droplets morphology. The contact angle was measured from the last image, which was recorded after 5s from the drop deposition.

Identical SEM sample preparation was carried out to fabricate samples for contact angle analysis. See SEM sample preparation for more detailed information.

## 3.4 Determination of iR Compensation

Commonly, when current flows through an electrochemical cell, a potential drop between the reference electrode and the working electrode occurs. This potential drop is caused by the electrolyte conductivity, the distance between the two electrodes and the magnitude of the current.

Electrolytic $O_2$ or $H_2$ production is typically limited by the large potential required to drive the electrolysis reaction. This occurs mainly due to the contributions of (i) an anode and cathode overpotentials, and (ii) an ohmic resistance, as seen in eqn. below:

$$E(i) = E_{e,cell} + |\eta_c| + \eta_A + iR \tag{3.4.1}$$

where E(i) refers to the energy input or applied potential, $E_{e,cell}$ represents the equilibrium potential of the overall reaction, $\eta_c$ and $\eta_A$ are the cathode and anode overpotentials, respectively, and iR is the ohmic drop. An observation is clear: the lower the contribution of both the anode and cathode overpotentials and the iR drop, the lower the potential required to drive the reaction. Following this rationalism, the lower the energy applied, the cheapest the process will be in economic terms. The ohmic drop, iR, considers the deviation between the real electrode potential or polarised potential, $E_p$, and the applied potential $E_a$. This phenomenon occurs due to the presence of an uncompensated resistance, $R_u$, between the working and the reference electrodes. It is relevant to mention that the

determination of the iR drop is of a fundamental importance in electrochemical measurements, especially in those which involve the determination of reaction rate constants and mechanistic parameters such as Tafel plot, since the iR drop contribution becomes more and more dominant with increasing current density. A detailed discussion regarding the various ways for the determination of this resistance is presented later in this section. This effect might also induce to a large deviation between $E_p$ and $E_a$. In addition, the iR drop determination is specially recommended for those systems where: (i) the solution of the cell is not very conductive, (ii) the currents measured are fairly high, and (iii) the cell design is far from the ideal one, that is when the distance between the working and the reference electrode is relatively far. Since these criteria may be subjective, a simple rule-of-thumb is often used to determine if iR correction is required; if the shape of the curve changes significantly when iR compensation is applied, then iR compensation is required. In view of this, fig. 3.4.1 may serve as an example of the iR compensation effect. It can be seen in fig. 3.4.1 that the effect of the iR correction is significant in terms of Tafel slope. As a result of the iR correction, the Tafel slope changed 12 mV $dec^{-1}$. Another observation that is extracted from the figure below is that the difference between both curves begin at ca. 0.25 mV and, form this point, it increases as the current raises.

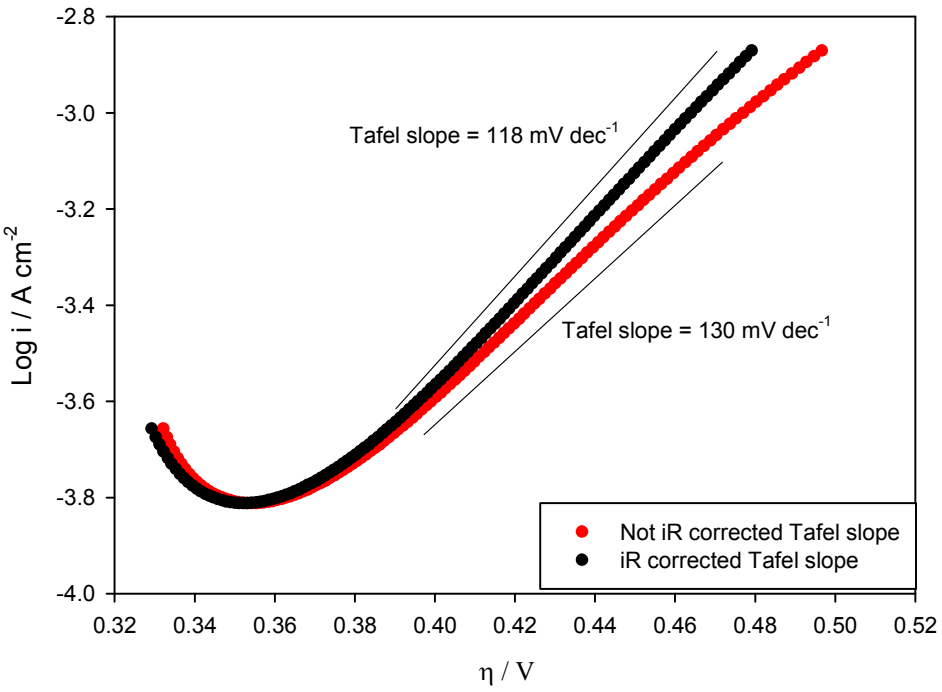



Figure 3.4.1 Difference between an iR corrected steady-state polarisation curve (black) and a steady-state polarisation curve without iR correction (red). Both curves were obtained from a 500 cycles manganese aged electrode and recorded in 1.0 M NaOH solution at 25°C recorded in the direction of increasing potential.

The most common fashion to depict the associated resistances is converting all the parameters involved in the cell to an electrical equivalent circuit. This equivalent circuit consists of a series of resistors and capacitors which accurately represent the chemistry involved in the cell. A standard three electrode cell may be represented as:

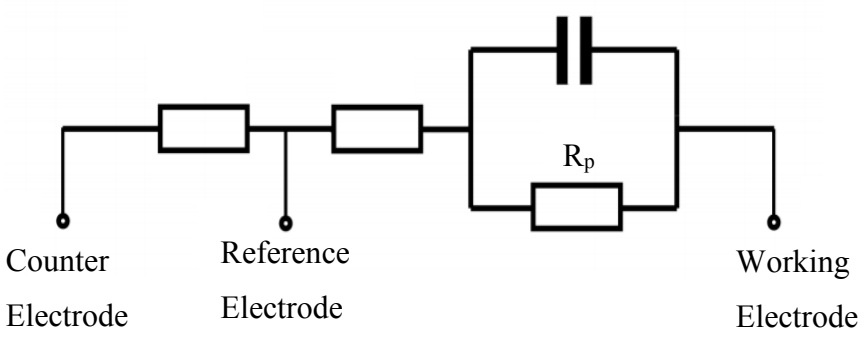



Figure 3.4.2 The electrical equivalent circuit of a standard three electrode cell used in this work. Reproduced from Ref. NOVA iR compensation tutorial.

In modern potentiostats, the resistance solution, $R_s$, which arises from the pass of current through the solution between the counter and the reference electrode, is compensated automatically by changing the applied potential, within the compliance voltage limits, of the counter electrode. As a result, the potential difference between the working and the reference electrode is maintained equal to the user-defined potential. For example, if the desired voltage in the working electrode is set at 0.5 V relative to the reference electrode, the potentiostat will set the counter electrode potential to - 0.6 V relative to the reference electrode to compensate the voltage drop caused by the $R_s$. While the resistance associated with the flowing of current between the counter and the reference electrode is compensated automatically by the potentiostat, the resistance attributed to the flowing of current between the working and the reference electrodes is not. This resistance is known as the uncompensated resistance, $R_u$. The potential drop associated with the uncompensated resistance is commonly called the iR drop. The iR drop is proportional both to the magnitude of current density flowing and to the electrical resistance of the solution. In view of this, the $R_u$ may be expressed as:

$$E_p = E_a - iR_u \tag{3.4.2}$$

where $E_p$ and $E_a$ are the polarisation or real electrode potential and the applied potential, respectively. Several methods have been developed to measure and correct the impact of

the uncompensated resistance on the real electrode potential. Some of these techniques include: (i) galvanostatic interrupter techniques,[5] (ii) impedance spectroscopy measurements,[6] which has the advantage that the iR drop does not affect the measurement adversely but in fact provides information concerning the solution's conductivity and its changes during the experiment, (iii) positive feedback circuits,[7] and (iv) voltammetry techniques such as potential step.[8] In the present work, iR compensation was calculated by both the potential step method and electrochemical impedance spectroscopy.

The potential step method was simultaneously developed by Gerischer and Vielstich[9] and by Fleischmann and Thirsk[10] in 1955. In general terms, this method consists in the application of a potential step function to the electrode, which causes an abrupt change in the electrode potential, and in further monitoring of the associated current-time response. In more detail, a constant potential $E_1$, typically in the double layer region (that being a potential region where no Faradaic current processes are taking place), is normally maintained during time until the current response reaches a stationary behaviour. Then, a sudden potential pulse such as $E_1 \rightarrow E_2 \rightarrow E_1$, being $E_1 < E_2$, is applied to the working electrode causing an abrupt raising of the current density followed by an exponential decay towards zero as represented in fig. 3.4.3.

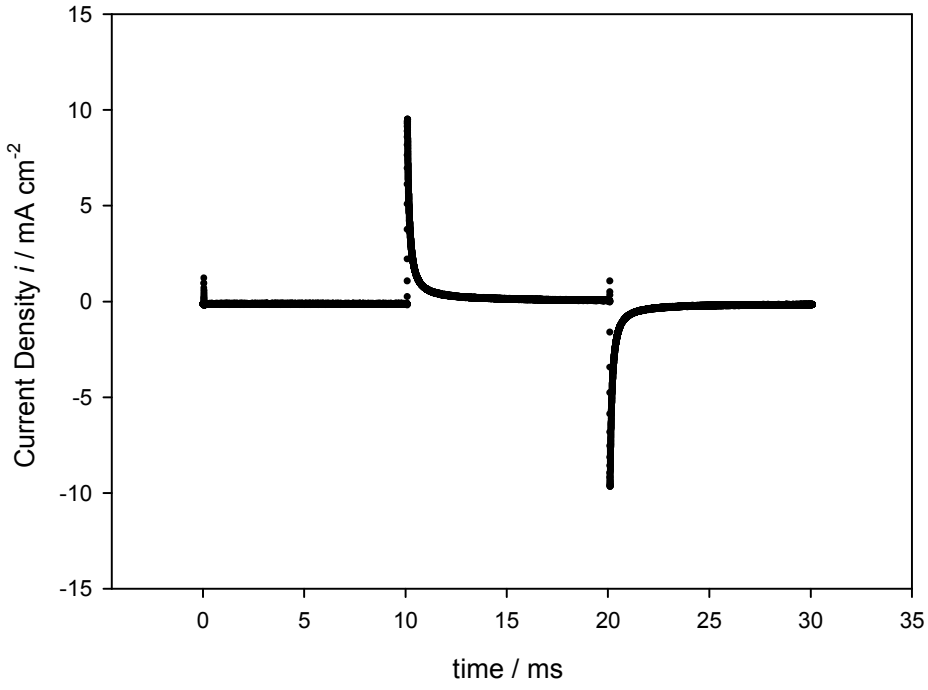



Figure 3.4.3 Transient current - time response profile for a potential pulse in the double layer region. The graph was obtained from a Mn electrode with 250 potential multicycles in 1.0 M NaOH at 25°C with a potential step of 50 mV.

Finally, the current flowing as a response to this potential step is measured. This technique is very attractive because of its simplicity, both with respect to performing the measurement and to its theoretical analysis. Furthermore, both the uncompensated resistance and the double layer capacitance can be obtained in a single experiment. It is worth mentioning now that the following model for the analysis of both the uncompensated resistance and the double layer capacitance only holds for reactions with fast kinetics in comparison with the time constant of the decay of charging currents. A similar model will be presented in section 3.5 for the study of uncompensated resistance and double layer capacitance in systems with slow kinetics. Since this experiment is performed in a potential region where the current response is invariant with the applied potential, that being the complete absence of Faradaic processes, it is assumed that the only current flow should be due to the charge of the double layer. Under these conditions, the current density response may be represented by:

$$i = \frac{\Delta E}{R_u} exp\left(\frac{-t}{R_u C_{dl}}\right) \tag{3.4.3}$$

Where ΔE represents the amplitude of the potential step, normally 50 mV, and $C_{dl}$ represents the double layer capacitance. For obtaining eqn. 3.4.3, the electric circuit presented in fig. 3.4.4 was considered.

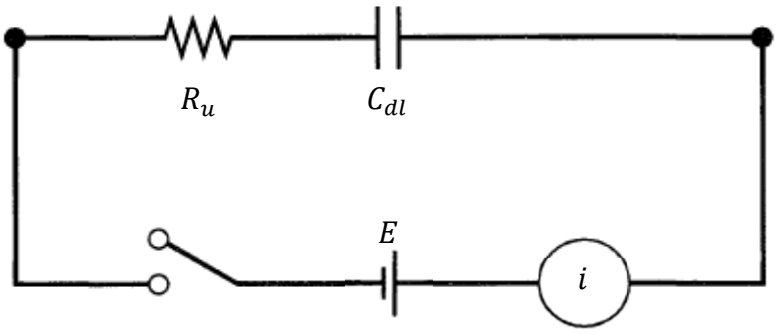



Figure 3.4.4 DC circuit used for the potential step experiment.

Eqn. 3.4.3 is derived from the general eqn. for the charge determination, introduced in section 1.1.4, on a capacitor as a function of voltage across it, $E_c$. Since the sum of the voltages across the resistor $E_R$ and the capacitor $E_c$ must be equal to the applied potential, hence:

$$E = E_R + E_c = iR_u + \frac{q}{C_{dl}} \tag{3.4.4}$$

Rearranging eqn. 3.4.4 and considering that $\mathrm{i} = \frac{\mathrm{dq}}{\mathrm{dt}}$ yields to:

$$\frac{dq}{dt} = \frac{E}{R_u} + \frac{-q}{R_u C_{dl}} \tag{3.4.5}$$

Now, if the capacitor is initially uncharged, that is $\mathrm{q} = 0$ and $\mathrm{t} = 0$, one can write:

$$q = EC_{dl}[1 - e^{-t/R_u C_{dl}}] \tag{3.4.6}$$

Differentiating eqn. 3.4.6 yields to the previous introduced eqn. 3.4.3.

If eqn. 3.4.3 is linearized using simple natural logarithm rules, it may be obtained that:

$$ln\, i = ln\left(\frac{\Delta E}{R_u}\right) - \left(\frac{t}{R_u C_{dl}}\right) \tag{3.4.7}$$

From eqn. 3.4.6, it can be noted that the current transient decay should have an exponential decay with a time constant $\tau = \mathrm{R_u C_{dl}}$. Since eqn. 3.4.7 has the same form than $\mathrm{y} = \mathrm{mx} + \mathrm{n}$, the intercept at $\mathrm{t} = 0$ of a $\ln \mathrm{i}\, vs.\, \mathrm{t}$ plot yields to the value of the uncompensated resistance $\mathrm{R_u}$.

An additional advantage of this method is that it allows for a direct estimation of the double layer capacitance from the slope of the graph $\ln \mathrm{i}\, vs.\, \mathrm{t}$. As an example, fig. 3.4.5 shows the $\ln \mathrm{i}\, vs.\, \mathrm{t}$ plot together with a regression line with the expression $\mathrm{y} = -10193\mathrm{x} - 4.2077,\ \mathrm{R^2} = 0.9996$ for the 250 cycles Mn electrode.

It is important to mention that the determination of the time constant value provides the idea of the charging nature of the capacitor. Taking as an example fig.3.4.5, the calculation of the time constant value gives $\tau = 98$ μs.

From fig. 3.4.6 it can be seen that at $\mathrm{t} = \tau$, the current for charging the double layer capacitance drops to 40% of its initial value, whereas a drop to 5 % occurs at $\mathrm{t} = 4\tau$. Therefore, it may be said that the double layer charging is 95% complete in ca. 400 μs. It is important to mention that for a period of about five times constant the capacitor is completely charged. Further, eqn. 3.4.7 is only valid for the period immediately after the step, usually around 20 μs. At later times, the electrode potential changes due to the charging of the double layer and eqn. 3.4.7 becomes invalid.[11]

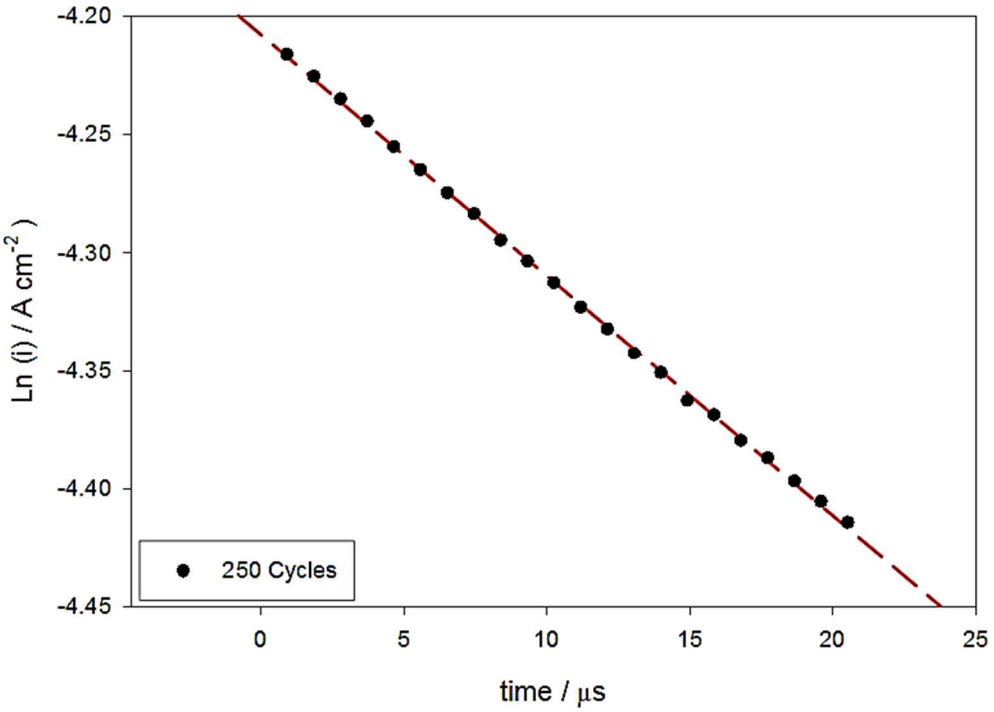



Figure 3.4.5 Linearized current -time response for a potential pulse in the double layer region. The time was corrected being 0 the beginning of the current decay. The graph was obtained from the 250 cycles Mn electrode in 1.0 M NaOH at 25°C with a potential step of 50 mV. The regression line had the expression $y = -10193x - 4.2077,\ with\ R^2 = 0.9996$ witch results in $R_u$=3.33 Ω and $C_{dl}$=29.43 µF $cm^{-2}$.

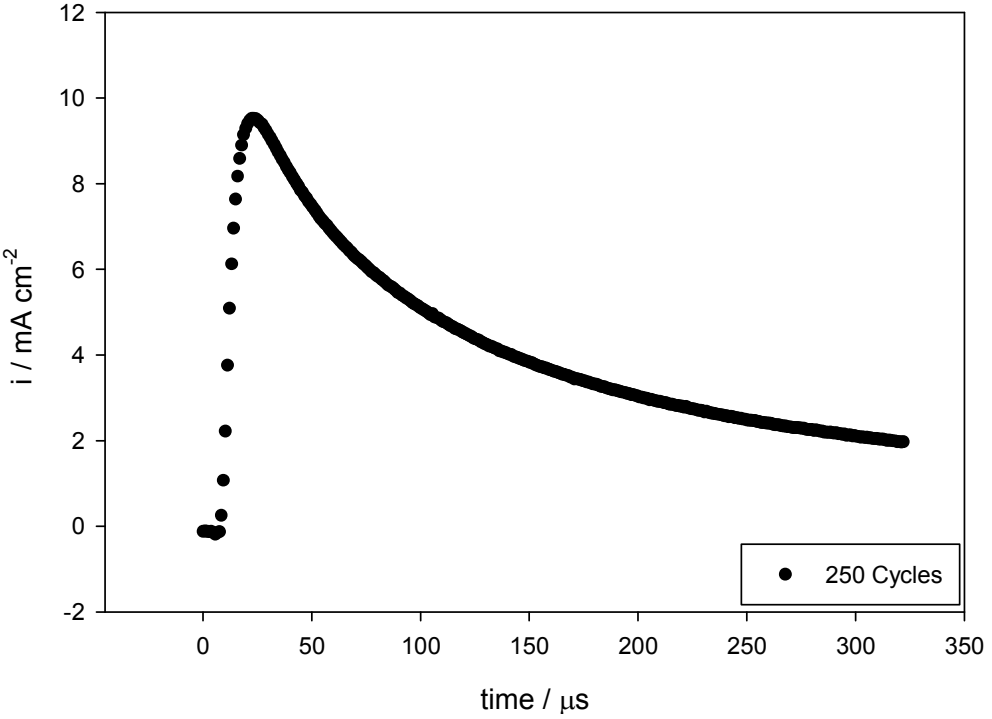



Figure 1.4.6 Typical potential pulse decay curve obtained from a pulse amplitude of 50 mV in a non-Faradaic region on a 250 potential cycles Mn electrode in 1.0 M NaOH at 25°C.

## 3.5 The Benefits of Potential Step Method

This section aims to introduce another application of the potential step technique with regards to the study of charge transfer resistances of reactions with slow kinetics. In previous sections this method was employed for the calculation of parameters such as uncompensated resistance, $R_u$, and the double layer capacitance, $C_{dl}$, for systems where the kinetics of the reaction were fast compared with the time constant of the current transient decay. It was also demonstrated that this technique provides both simplicity and accuracy in the fashion to obtain the values of the above-mentioned parameters.

The model discussed in this section was presented by S. Aberg[12] in 1997 as a part of a publication series with an special interest on the application of the potential step method. This model may be considered as an analogous to the model presented in section 3.4 for the calculation of the uncompensated resistance and the double layer capacitance with the distinction that the one presented here is designed for reactions with slow kinetics. However, its analysis, compared with the one in section 3.4, is considered more complex given that it involves a charge transfer reaction. In this view, the electric circuit used in this model may be represented as shown in fig. 3.5.1.

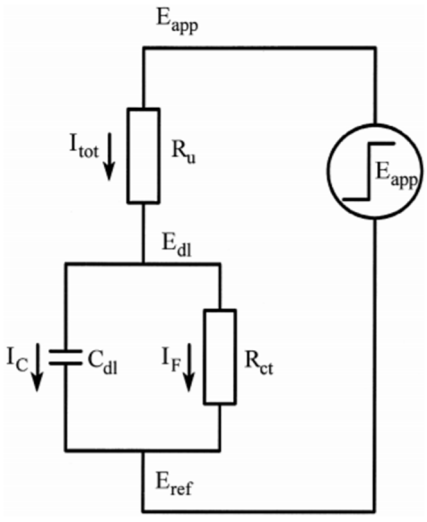



Figure 3.5.1 DC equivalent circuit to model the uncompensated resistance solution and double layer capacitance of a response to a small potential step. Reproduced from Ref.[12]

When a potential step is applied to the working electrode, which is initially at electrical equilibrium, both the iR drop and the potential drop across the double layer contribute to

the potential difference between the working and the reference electrode. Hence, the total current flow through the system shows both Faradaic and non-Faradaic contributions. If the surface concentration of active species does not show an appreciably change during the decay of the charging current, it is possible to define a charge transfer resistance, $R_\Sigma$, as:

$$R_\Sigma = \frac{R_u R_p}{R_u + R_p} \tag{3.5.1}$$

where $R_p$ is the polarization resistance and $R_u$ refers to is the uncompensated resistance. To model the current response under these circumstances, the Randles equivalent circuit is used. Therefore, the net current flowing through the circuit may be expressed as:

$$i(t) = \frac{\Delta E}{R_u + R_p}\left\{1 + \frac{R_p}{R_u} exp\left(\frac{-t}{R_\Sigma C_{dl}}\right)\right\} \tag{3.5.2}$$

At $t = \infty$, eqn. 3.6.2 may be rewritten as:

$$i(\infty) = \frac{\Delta E}{R_u + R_p} \tag{3.5.3}$$

and at $t = 0$:

$$i(0) = \frac{\Delta E}{R_u} \tag{3.5.4}$$

Rearranging eqns. 3.5.3 and 3.5.4 gives:

$$R_p = \frac{\Delta E}{i(\infty)} - R_u \tag{3.5.5}$$

$$R_u = \frac{\Delta E}{i(0)} \tag{3.5.6}$$

It is important to note that:

$$\frac{R_p}{R_u} = \frac{i(0)}{i(\infty)} - 1 \tag{3.5.7}$$

Substituting eqn. 3.5.5 into 3.5.7 yields to:

$$R_p = \Delta E\left\{\frac{i(0) - i(\infty)}{i(0)i(\infty)}\right\} \tag{3.5.8}$$

Finally, replacing 3.5.5 and 3.5.6 into eqn. 3.5.2 yields to:

$$\frac{\mathrm{i(t)}}{\mathrm{i}(\infty)} - 1 = \left\{\frac{\mathrm{i}(0)}{\mathrm{i}(\infty)} - 1\right\} \exp\left(\frac{-\mathrm{t}}{\mathrm{R_\Sigma C_{dl}}}\right) \tag{3.5.9}$$

Using simple logarithm rules on eqn. 3.5.9 gives:

$$ln\left\{\frac{i(t)}{i(\infty)} - 1\right\} = ln\left\{\frac{i(0)}{i(\infty)} - 1\right\} - \frac{1}{R_\Sigma C_{dl}} t \tag{3.5.10}$$

Since the potential step amplitude ΔE is known and both $\mathrm{i}(0)$ and $\mathrm{i}(\infty)$ can be measured from the current transient decay in a $\ln \mathrm{i}\ vs.\ \mathrm{t}$ plot, then the uncompensated resistance $\mathrm{R_u}$ and the polarization resistance $\mathrm{R_p}$ may be evaluated using eqn. 3.5.2. In addition, the time constant $\tau = \mathrm{R_u C_{dl}}$ may be obtained *via* graphical analysis of the $\mathrm{i(t)}$ data were a plot of $\ln\left\{\frac{\mathrm{i(t)}}{\mathrm{i}(\infty)} - 1\right\}\ vs.\ \mathrm{t}$ is linear with slope $\mathrm{S} = -\left(\frac{1}{\mathrm{R_\Sigma C_{dl}}}\right)$ and intercept $\mathrm{n} = \ln\left(\frac{\mathrm{R_p}}{\mathrm{R_u}}\right)$. Fig. 3.5.2 may serve as an example of the relation between the decaying and residual current transient after a potential step according to the equivalent circuit model in fig. 3.5.1.

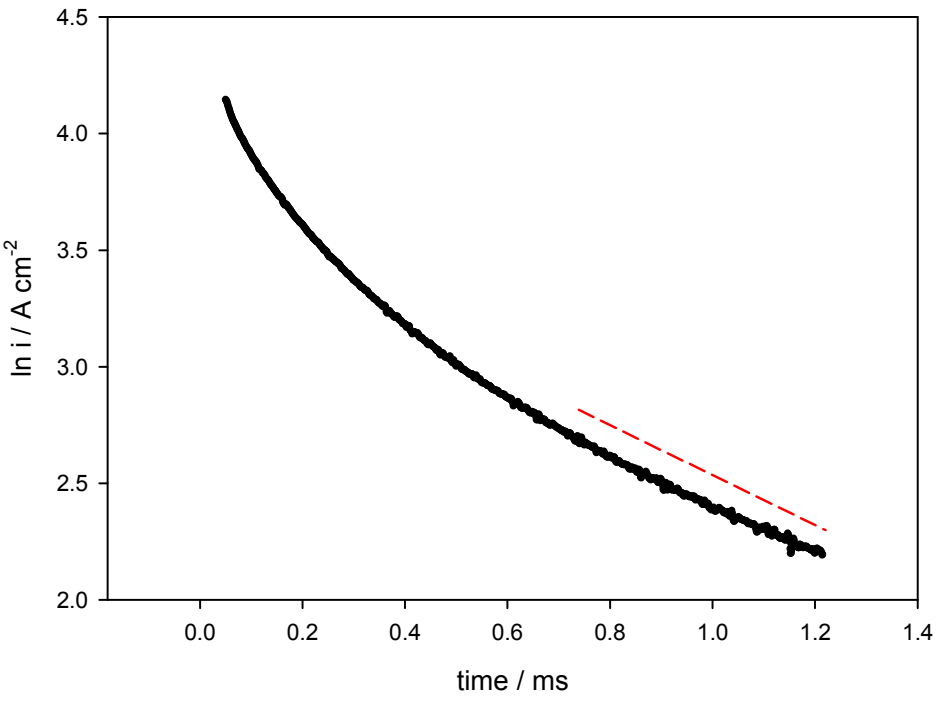



Figure 3.5.2 The current decay resulting from a 50mV potential step for the 500 cycles Mn electrode in 1.0 M NaOH at 25°C. The values of the regression line (red) are: y = -0.0011x + 3.4799, $R^2$ = 0.9941 which results in: $R_p = 105\ \Omega$, $R_u = 3.51\ \Omega$, $C_{dl} = 24$ mF

## 3.6 Electrochemical Impedance Spectroscopy

Traditional techniques of electrochemical measurement involving the usage of potential sweeps, potential steps, or current steps normally drive the working electrode to conditions far from equilibrium, where the current signal response is a combination of both Faradaic and non-Faradaic contributions. Although the contribution of the non-Faradaic current over the final current signal is small compared with the Faradaic one, the final current response cannot fully and precisely characterize the electrochemical reaction at an electrode-electrolyte interface.

While these techniques, however, are undoubtedly useful and relatively easy to perform, other techniques such as electrochemical impedance spectroscopy (EIS) can characterize the electrode properties by applying small perturbations, typically 5 mV amplitude, to the working electrode in a defined potential region. This is considered as a non-destructive technique, if used in equilibrium conditions, and particularly sensitive to small perturbations within the cell allowing the characterization of the electrode even in low conductive solutions. The simplest EIS analysis is performed under equilibrium conditions, where a simple Randles may be used as the equivalent circuit, whereas a more complex analysis is required for potentials far from the equilibrium, *e.g.* OER potential. For the latter case, a sophisticated equivalent circuit needs to be designed for a reliable and representative cell description to be achieved. A dedicated discussion about equivalent circuits will be presented in section 3.6.2.

Many advantages may arise from the implementation of this technique. Among the most important are: (i) its practical capability to perform high-precision measurements due to its ability to maintain steady-state conditions, and (ii) its ability to characterize systems in which the overall electrochemical reaction is determined by several steps, each proceeding at a different rate. The possibility to characterize single steps is of a special interest due to the opportunity to define the RDS of the overall reaction. In addition, EIS is a method that allows the calculation of the electrochemical parameters through the analysis of the measured impedance of an electrochemical cell as a function of frequency. It is important to mention that the electrode exhibit different electrochemical behaviour depending on the frequency of the applied voltage. A detailed discussion about this matter will be presented through this section.

The concept of electrical impedance was first introduced by O. Heaviside in 1880s and extended by Steinmetz[13] and Kennelly[14] in the 1900s. Impedance, Z, is defined as a measure of the ability of a circuit to resist the flow of electrical current. In recent years, there has been highly continued interest in applying EIS for the study of the electrochemical proprieties of electrodes.[15] As a general concept, when an electrochemical cell is electrically stimulated, various different processes may occur that contribute to the overall electrical response. They include, among others: (i) the transport of electrons through the electrode, (ii) the transport of electrons through the electrode-electrolyte interface to charged carriers situated in the boundaries of the electrode surface, and (iii) the flow of charged particles *via* favourable paths on the electrolyte. These processes are under the influence of the applied potential, and since distinctive electrode proprieties are observed at different potentials, it is possible to relate the physical and chemical proprieties of the electrode through the observation of the impedance as a function of frequency to a specific reaction step. Therefore, the main applications of EIS are, among others, the study of: (i) corrosion metals, (ii) adsorption and desorption on the electrode surface, (iii) electrochemical synthesis of material, (iv) catalytic reaction kinetics, and (v) energy storage devices such as batteries and supercapacitors, etc.

The technique consists on the application of a sinusoidal perturbation to the system using an alternating signal (AC) of small magnitude, typically 5 mV, to measure the fashion at which the system responds to the perturbation at steady-state.[10] In practice, the frequency of the ac potential is sweep over a large range of frequencies, usually $10^{-4}$ to $10^{-6}$ Hz, and the response of the system is monitored *via* its impedance spectrum. Generally, the parameters derived from such spectrum may be classified in two main groups: (i) those related only with the electrode material itself, such as its dielectric constant, resistance, capacitance and inductance, and (ii) those pertinent to the electrode-electrolyte interface, such as its adsorption reaction rate constants, capacitance of the interface region, etc.

Consideration is now given to the concept of electrical impedance and its particular implementation for the study of electrochemical systems.

### 3.6.1 AC Circuit Theory and Implementation

In order to understand the principles of EIS, the introduction of the fundamental alternating current ac theory is required. Impedance may be conceived as a complex resistance arising from the electrical current flow across an electrical circuit which consists of several resistors, capacitors and/or inductors. In addition, it may be defined as the ratio between the voltage (V) and the current (I) as:

$$Z = \frac{V}{I} \tag{3.6.1}$$

Where V and I are sinusoidal signals with equal angular frequency, $\omega$, but different magnitude and phase, $\phi$. On the one hand, the angular frequency is a scalar measure of the rotation speed and may be seen as the angular displacement of the signal per unit of time, typically seconds. Thus, $\omega$ is commonly measured either in radians (rad) or degrees ($^{o}$) per second. The relationship between the angular frequency and the regular frequency *f* by is given by:

$$\omega = 2\pi f \tag{3.6.2}$$

where *f* has units of Hertz. On the other hand, the phase refers to the instantaneous displacement of a sinusoidal wave. For the sake of convenience, it is more common to use the phase shift factor, which represents the time difference between an equal amplitude points of two different sinusoidal signals. The sinusoidal voltage may be represented as:

$$E = E_0 sin(\omega t) \tag{3.6.3}$$

where $E_0$ is the maximum amplitude of the signal. Since the current signal has equal frequency but different phase and amplitude than the voltage signal, it may be represented as:

$$I = I_0 sin(\omega t + \phi) \tag{3.6.4}$$

where $I_0$ is the maximum amplitude of the current. A convenient approach to study these parameters is to consider them as rotating vector quantities, $\dot{E}$ and $\dot{I}$, represented in a complex plane, following the so-called phasor concept of the sinusoidal altering current as presented in fig. 3.6.1.

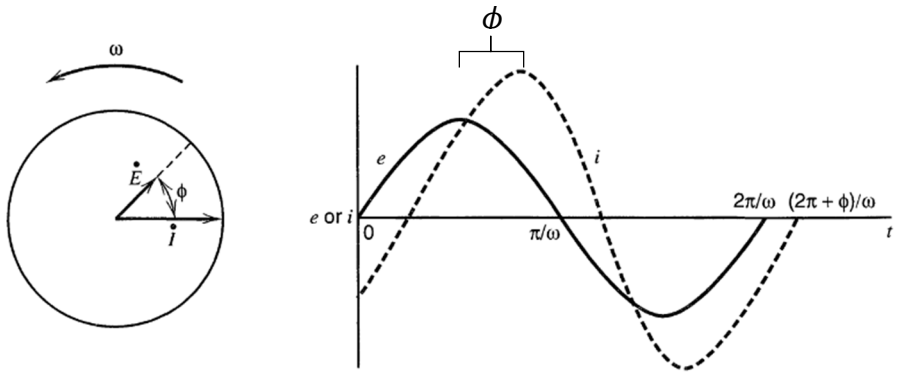



Figure 3.6.1 Composite phasor diagram showing current and voltage phasors separated by a phase angle $\phi$. Adapted from Ref.[10]

As seen in fig. 3.6.1, the maximum amplitude of a phasor is given by the length of that phasor, whereas the instantaneous value is given by the projection on the abscises in the diagram. The phase separation, ϕ, between the two signals can also be observed in fig. 3.6.1. Usually, one of the signals, either the voltage or the current, is taken as a reference signal and ϕ is measured with respect of it. For example, if the voltage is defined as the reference, then the current is said to lag the voltage by a phase angle of ϕ, which in this case will have a negative sign. Since the relationship between two phasors at the same frequency remains constant as they rotate, the phase angle may be considered to be constant. In this view, it is possible to simply study their relationship by plotting them as vectors having the same origin and separated by ϕ. These concepts may be applied to the analysis of simple electrical elements such as resistors, capacitors and inductors. In a pure resistor, when a pure sinusoidal voltage Ė is applied, Ohm's law holds and the resulting current İ is given by the expression:

$$\dot{I} = \frac{\dot{E}}{R} \tag{3.6.5}$$

Since the phase angle $\phi$ is zero in this case, the two signals are said to be in phase as seen in fig. 3.6.2.

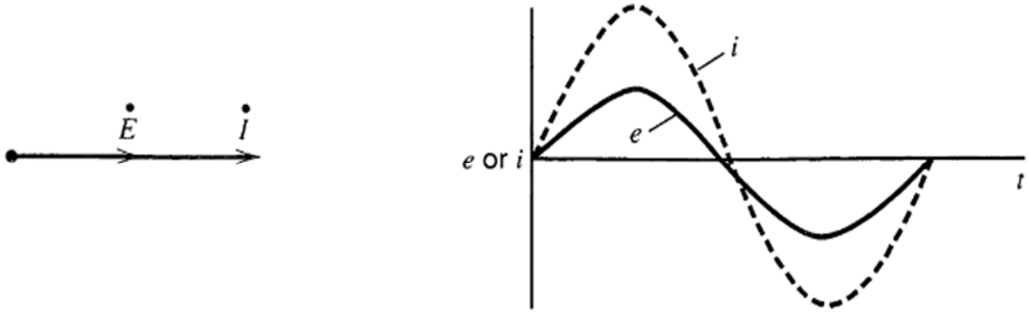



Figure 3.6.2 Relationship between the voltage and the current across a pure resistor. The phase angle in this case is zero. Adapted from Ref.[10]

A capacitance, C, across an ideal parallel plate capacitor is considered to be proportional to the product of the applied potential E and the charge $q$:

$$q = CE \tag{3.6.6}$$

An expression for the current i is obtained by differentiating of eqn. 3.6.6:

$$i = \frac{dq}{dt} = C\frac{dE}{dt} \tag{3.6.7}$$

From the definition of eqn. 3.6.4, yields to:

$$i = \omega C \Delta E cos(\omega t) \tag{3.6.8}$$

Eqn. 3.6.8 can also be expressed in terms of phasor notation as:

$$i = \frac{E}{X_C} sin\left(\omega t + \frac{\pi}{2}\right) \tag{3.6.9}$$

where $X_C$ is the so-called capacitive reactance defined as $X_C = \frac{1}{j\omega C}$. In this case, the phase angle is $\frac{\pi}{2}$ and the current is said to lead the voltage as shown in fig. 3.6.3.

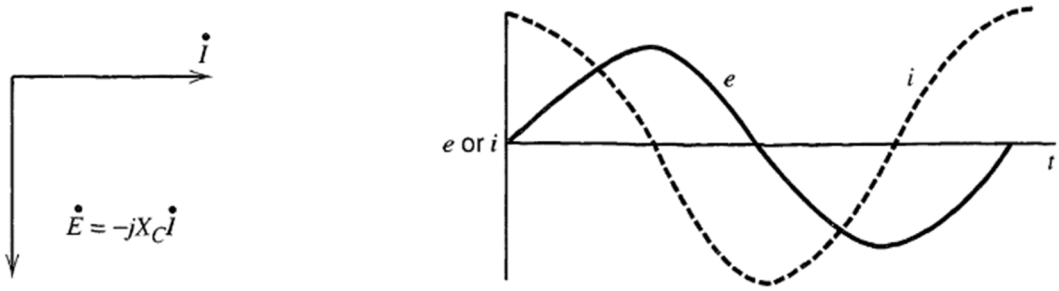



Figure 3.6.3 Relationship between the voltage and the current across a pure capacitor. The phase angle in this case is $\frac{\pi}{2}$. Adapted from Ref.[10]

In circuit analysis, it is advantageous to represent the phasors in terms of complex numbers. In complex notation, magnitudes along the ordinate axis are assigned as imaginary and are multiplied by $j = \sqrt{-1}$. Oppositely, components along the abscissa axis are said to be real. In this view, the current phasor is plotted along the abscissa, in which case the relationship in eqn. 3.6.5 may be expressed in complex notation as:

$$\dot{E} = -jX_C\dot{I} \tag{3.6.10}$$

The similarity between eqn. 3.6.9 and Ohm's law is clear with the complex quantity $X_C$ substituting the resistance R. The dimensional analysis suggests that $X_C$ must carry the dimensions of resistance, however, unlike R, its magnitude is frequent-dependent. For a resistance R and a capacitor C connected in series (RC series circuit), the sum of the individual voltage drops across the resistor and the capacitor must be equal to the total applied voltage Ė, so that:

$$\dot{E} = \dot{E}_R + \dot{E}_C \tag{3.6.11}$$

$$\dot{E} = \dot{I}(R - jX_C) \tag{3.6.12}$$

$$\dot{E} = \dot{I}Z \tag{3.6.13}$$

where the vector Z is called the impedance. It is evident from eqn. 3.6.12 that Z has two parts, one real, $Z' = R$, and another imaginary, $Z'' = -X_C = -\frac{1}{\omega C}$. In addition, the magnitude |Z| of the impedance may be expressed as:

$$|\mathrm{Z}| = \sqrt{(\mathrm{Z}')^2 + (\mathrm{Z}'')^2} = \sqrt{\mathrm{R}^2 + {\mathrm{X}_\mathrm{C}}^2} \tag{3.6.14}$$

and the phase angle, ϕ, is given by:

$$tan\,\phi = \frac{Z''}{Z'} = \frac{X_C}{R} = \frac{1}{\omega RC} \tag{3.6.15}$$

The relationship between the current and the voltage in an RC circuit might be graphically represented on an Argand plane, as presented in fig. 3.6.4.

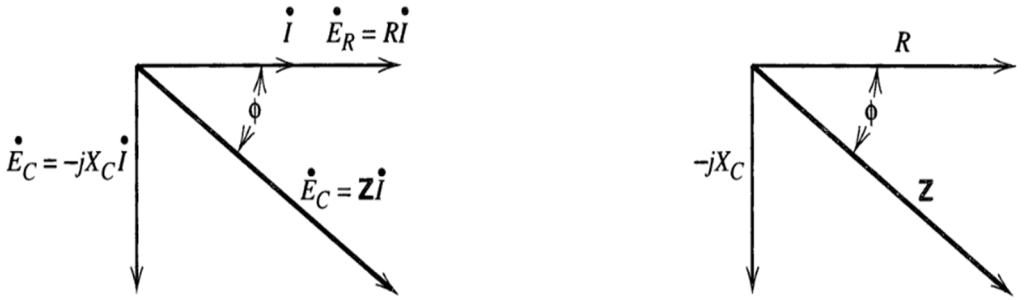



Figure 3.6.4 Phasor diagram or an RC series network, showing the relationship between the current and the voltage. The voltage *E* include both the resistive and capacitive resistance contributions. Adapted from Ref.[10]

From the Argand diagram in fig. 3.6.4 and from eqn. 3.6.15 it can be observed that the current is no longer either in phase or 90° out of phase with respect to the voltage.

The previous analysis may be extended to circuits of greater complexity by noting that impedances combine with rules analogous to those applicable to resistors in simple circuit analysis. For example, in the case of impedances in series, the overall impedance is the sum of the individual values expressed as complex vectors, whereas for impedances in a parallel arrangement, the inverse of the overall impedance is the sum of the reciprocals of the individual vectors. Fig. 3.6.5 presents a simple explanation of the latter.

It is important to mention another parameter in EIS analysis, the admittance Y. This may be seen as the inverse of the impedance, Z, following:

$$Y = \frac{1}{Z} \tag{3.6.16}$$

and represents a type of conductance. Therefore, eqn. 3.6.16 may be rewritten as a function of admittance, following the expression:

$$\dot{I} = \dot{E}Y \tag{3.6.17}$$

This parameter is significantly relevant in the analysis of parallel circuits since the overall admittance of elements in a parallel arrangement is directly the sum of the individual admittances.

Impedance results obtained from an EIS test can be graphically represented in various fashion, such as: (i) the Nyquist diagram, (ii) the Bode diagram, and (iii) the Phase diagram.

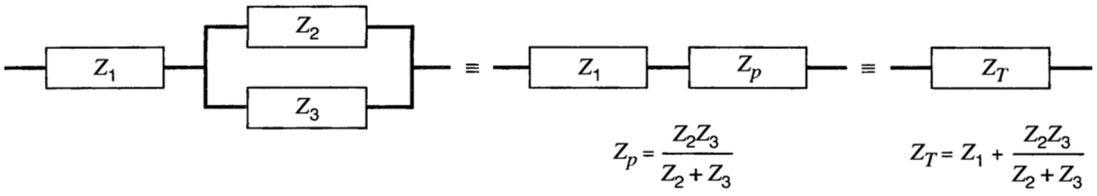



Figure 3.6.5 A schematic example for the calculation of a total impedance form impedances in series and parallel arrangement Adapted from Ref.[10]

### 3.6.2 The Nyquist Diagram

If the real part, $Z'$, and the negative form of the imaginary part, $-Z''$, of the impedance, at each frequency, are plotted on the abscissa and the ordinate, respectively, a Nyquist plot is generated. Several examples of the Nyquist plot for some simple RC circuits are presented in fig. 3.6.6. The Nyquist diagram is the most common representation for impedance data because it allows for both an easy prediction of the circuit elements and an easy relation to the equivalent electrical circuit. The analysis approach is based on the shape of the Nyquist diagram where each data point represents the value of the impedance for a particular frequency. The impedance data al low frequencies are found on the right-hand side of the diagram, while the data obtained at high frequencies are on the left-hand side.

Multiple observations may be extracted form fig. 3.6.6: (i) that the impedance for a pure resistance is independent from the frequency, (ii) that the impedance for a pure capacitor changes with frequency but only on its imaginary part, (iii) that the combination of a resistance in series with other/s elements produces a shift, in the abscissas axis of the

element/s initial impedance being the displacement the magnitude of the pure resistance impedance (cases c and f), (iv) that the combination of a RC in parallel yields to the formation of a semicircle (case d), (v) that the addition of a capacitor in series to a RC circuit in parallel arrangement adds an impedance signal of a pure capacitor to the Nyquist diagram (case e), and (vi) that the combination, in series arrangement, of two RC circuits in parallel results into the formation of two semicircles (case g).

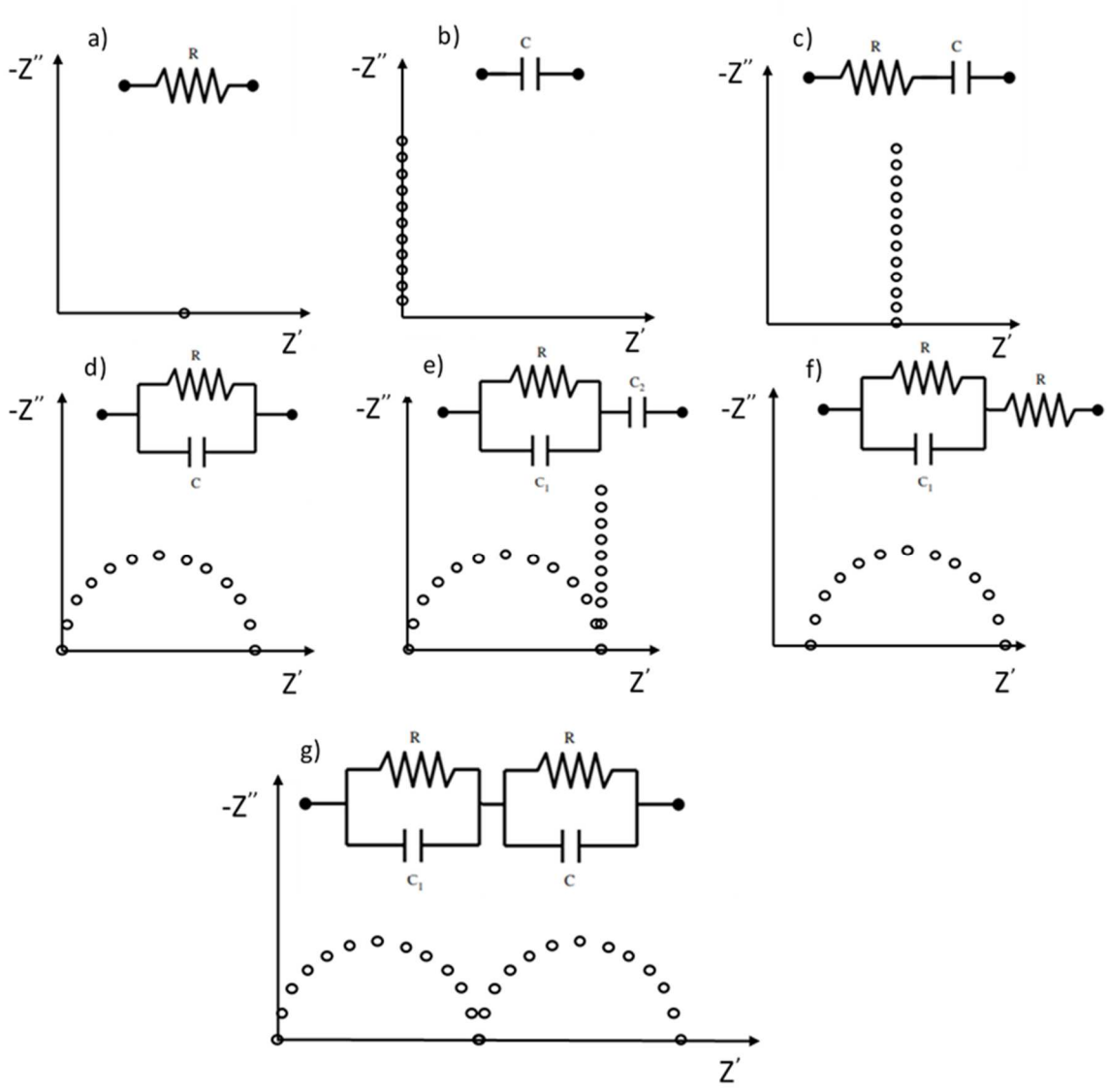



Figure 3.6.6 Some simple circuits and their associated Nyquist plots.

The formation of an individual semicircle is said to be characteristic of the presence of a single RC time constant. This representation allows the direct identification of various physical parameters of the electrode. For example, from the intersection of the semicircle

with the abscissas axis it is possible to obtain a value corresponding to the sum of the polarization resistance, $R_p$, and the uncompensated resistance $R_u$, whereas from the intersection with the origin, the value of the uncompensated resistance $R_u$ itself is obtained. In addition, from the value of the frequency at the maximum point, it may be possible to calculate the value of the electrochemical double layer capacity, $C_{dl}$. Fig. 3.7.7 may serve as clarification for the previous discussion.

The formation of a semicircle arises from the contributions of both the capacitance and resistance element behaviour at different frequencies. At high frequencies (left-hand side of the abscissa), the contribution of the capacitor to the impedance is zero, according to expression $X_C = \frac{1}{\omega C}$ . Hence, the only contribution to the impedance must arise from the pure resistance elements. As the frequency decreases, the contribution to the impedance of $C_{dl}$ along with the $R_p$ increases, which results in both a rise on the imaginary and real part of the impedance. At very low frequencies, since the capacitance $C_{dl}$ exhibits a large impedance, current flows through $R_p$ and $R_u$.

In relation to the number of semicircles in the Nyquist diagram, it is important to mention that the observation of multiple semicircles may suggest the presence of two time constants in the system and, thus, the presence of various R in parallel with C. Special attention should be taken when designing equivalent circuits from the Nyquist diagram since it may be difficult to distinguish correctly these semicircles and, thus, the presence of RC circuits. In this view, it is recommended to plot both the real and the imaginary parts of the logarithmic scale in order to assure the identification of the real number of semicircles present in each study. In addition, it is also common practice to plot the negative of $Z''$ on the ordinates, since this ensures, for graphical convenience, that semicircles characteristic of RC loops appear in the first quadrant.

Also, since the formation of a semicircle is due to the presence of an RC circuit, its absence in the Nyquist plot demonstrates the minimal distribution of charge in the electrode double layer interface.

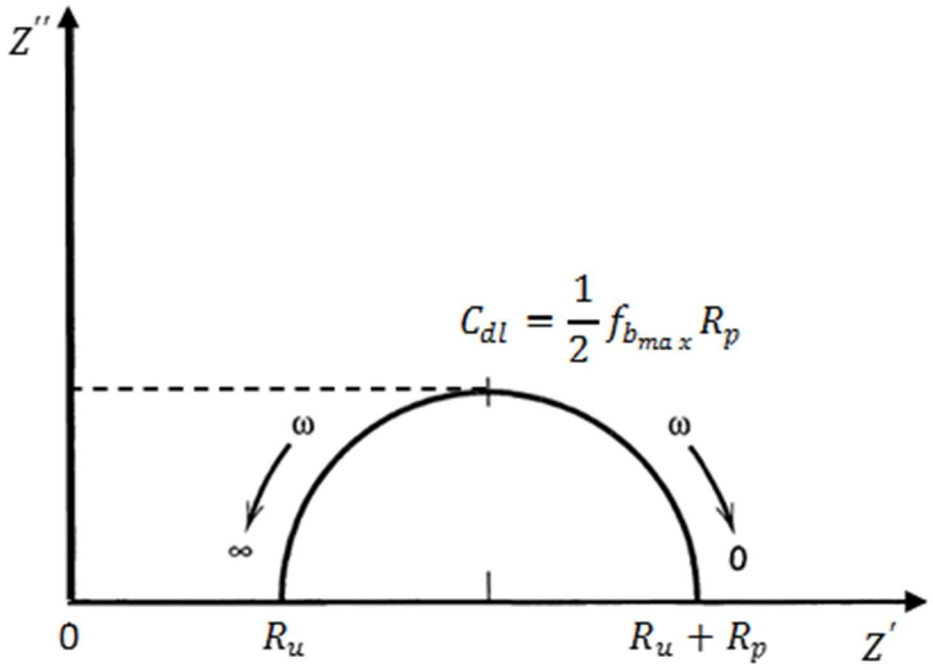



Figure 3.6.7 Impedance plane plot for a simple Randles equivalent circuit. Adapted from Ref.[6]

### 3.6.3 The Bode Diagram

Impedance data may also be presented in the form of Bode plot. In such a plot, both log |Z| and $\phi$ are plotted against log ω. Bode diagrams provide an immediately detection of the regions dominated by resistive and/or capacitance elements. According to eqn. 3.6.5, a pure resistance is frequency independent, yielding to a slope of zero on the log |Z| against log ω plot with a phase angle of 0°. For a pure capacitance, |Z| is inversely proportional to ω, since Z" = -Xc =-1/$\omega$C. Hence, the log |Z| against log $\omega$ plot has a slope of -1, while eqn. 3.6.9 predicts a phase angle of -90°. In fig. 3.6.8, a Bode plot for a simple parallel RC circuit with one-time constant is presented.

It is evident from fig. 3.6.8 that the resistance contribution dominates at lower frequencies, with the capacitive response becoming more important at high values of log $\omega$. For more complicated electrical circuits, it may not be so easy to analyse the impedance spectrum at a given frequency to a single circuit element.

In the present work, both Bode and Nyquist representations are used. While the Nyquist diagrams divides the impedance response into its resistive and capacitive components, it does have the shortcoming of not explicitly specifying the frequency of a given point. Furthermore, the high frequency data become bunched together towards $\omega \rightarrow \infty$ intercept on the Z-axis. Bode diagrams, while not splitting Z into its components, provide frequency information and plot the impedance data with equal weight at all frequencies along the length of the diagram.

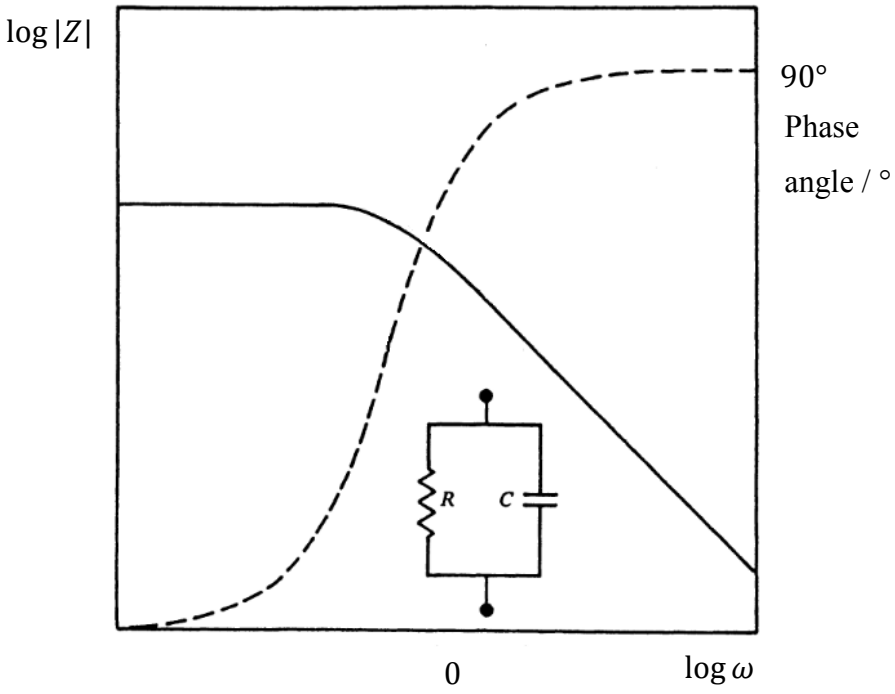



Figure 3.6.8 Bode representation of a single time constant, parallel RC circuit with $R = 100\,\Omega$ and C= 100 $\mu F$. Adapted from Ref.[6]

### 3.6.4 Practical Considerations

Special care must be taken in the cell design for EIS measurements. Since the amplitude of the ac applied signal must be very small to apply all the concepts explained in section 3.6.3, environmental electrical noise and the existence of mains hum can be issued. Another aspect to be noted is the electrode design, since poor conductivity through the connector to the electrode surface is critical for a good EIS data acquisition. Noise and mains hum contamination may be reduced by electrically isolating the cell using a Faraday cage properly connected to ground. It is also highly recommended to use shielded BNC cables of the shortest possible length to connect the electrodes to the control/measurement

equipment. The purpose of this is to minimize the real part of the impedance associated with the length of the conducting material.

### 3.6.5 Extracting Electrochemical Parameters from EIS Raw Data

In section 3.6.2, it was shown how simple graphical methods can, in principle, be used to extract resistive and/or capacitive parameters from the Nyquist diagram of a given electrochemical system, see fig. 3.6.7. Also mentioned in that section was the possible co-existence of two semicircles in a single Nyquist plot. In practise, however, various not ideal scenarios may be observed in impedance spectrums with two or more semicircles, those being: (i) the formation of arches instead of semicircles, and (ii) the overlap of various arches.[16] This yields to a difficult identification and subsequent graphical analysis of the Nyquist plots. In view of this, a more sophisticated analysis approach is required. The most common method to analyse impedance data is based upon modelling the electrochemical system in terms of an equivalent circuit. In the equivalent circuit approach, the experimental data is fitted to a theoretically proposed circuit using the complex nonlinear least-squares technique (CNLS) algorithms that automatically vary the values of the circuit elements until the best fit of the data to the model circuit is achieved. Fig. 3.6.9 serves as an example of the subsequent steps for a fitting to model process.

A remarkable feature of this model-fitting process is that it can be applied to a single measurement obtained at specific conditions, but also to a series of spectra obtained at various conditions. In the case a series of spectra are modelled, it may be advantageous to fit them using the series fitting technique which consists in the fit of all the spectra to a common model. This allows the analysis of electrical elements as a function of a distinct parameter of variation, such as time, potential, pH, etc.

Data interpretation is one of the most challenging aspects of impedance analysis. Typically, EIS data is analysed using models which should describe processes occurring within the electrochemical cell. The determination of the proper model may require both the knowledge of the chemical, physical and mechanical characteristics of the system and a good understanding of the measured values. There are two main approaches to system descriptive modelling: (i) formal or mathematical modelling, and (ii) physicochemical or structural modelling.[17] On the one hand, the former explains experimental impedances in terms of mathematical functions or equivalent electrical circuits. In view of this, it

conceives the electrochemical cell as a hypothetical electrical circuit consisting in a sequence of the electrical elements.

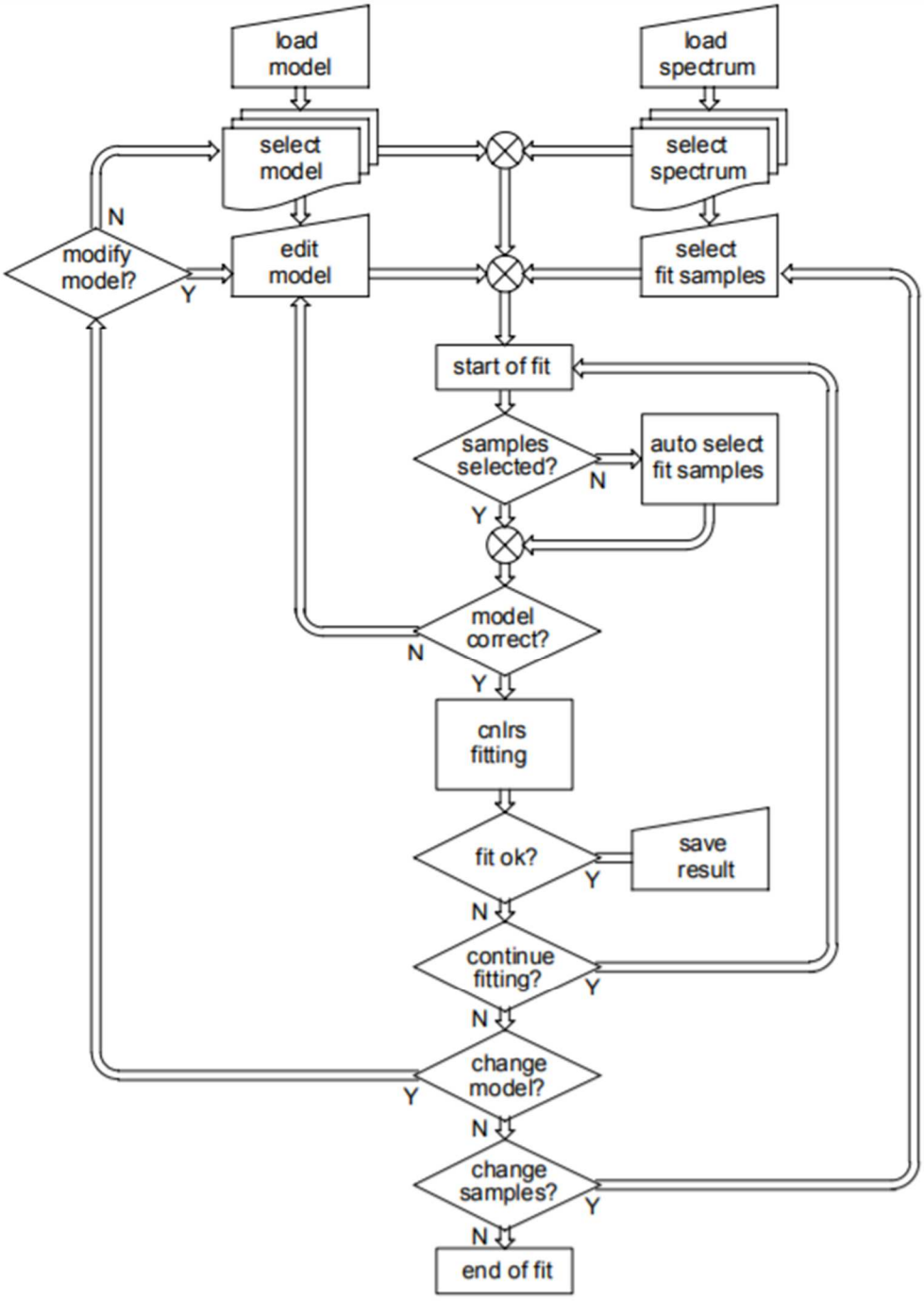



Figure 3.6.9 Flowchart illustrating the different steps when analysing raw data using CNLS modelling. Reproduced from Simulation & Fitting Zahner Manual.

Every electrical element is associated with a physical or electrochemical process occurring in the electrochemical cell. Equivalent circuit analysis is relatively simple for a circuit containing ideal elements R, C, and L but may become complex for processes where the electrical behaviour of the standard elements deviates from the ideality. This is especially notorious when measuring the impedance of solid electrodes. This type of analysis is convenient and graphically appealing, and the fit to the experimental data is performed using CNLS algorithms and commercially available impedance fitting software. The main problem with equivalent circuit modelling arises since a given impedance spectrum may often be represented by several equivalent circuits. This suggests that there may be more than one equivalent circuit that represents the system.[18] Therefore, it must be assumed that an equivalent circuit, which performs a good fit with the experimental data may not necessarily provide an accurate physical model of the electrochemical system. In view of this, special care must be taken when designing equivalent circuits, especially for largely unknown materials, since the expected values may be unknown. Another weakness of the use of equivalent circuits arises when ideal elements are used interconnected in different fashion and yet, with appropriate values, yield exactly to the same frequency response at all frequencies. Such scenario may result in an ambiguous system description.

On the other hand, physicochemical modelling is based upon the formation of equations which relate the measured impedance with physicochemical parameters of the process such as kinetic parameters, concentrations, sample geometry, or diffusion coefficients, among others. Typically, when modelling physicochemical parameters, the bulk of the electrodes and the sample material are presented as continuous media, and mass and charge transport processes can be represented by differential equations. Two main limitations arise from this method: (i) it requires a deep understanding of the relevant physical and chemical phenomena associated with the specific system under investigation, and (ii) complex reaction mechanisms produce equations containing too many free adjustable parameters, making the prediction of a model very difficult or even impossible to achieve.

A good approach, suggested by Zoltowski[19] to model an electrochemical system is presented below. Firstly, a measurement modelling must be used to determine the number and nature of the circuit elements and parameters required to describe the electrochemical system. Equivalent circuits containing ideal electrical elements, *e.g.* R, C, and L elements, or non-ideal elements, such as the CPE, may be employed. Secondly, the approach would consist on designing a physicochemical model. In the case of complex physicochemical

models, a simplification must be carried out. It is also suggested the precise determination of the nature of certain elements, for example, by changing the concentration, hydrodynamic conditions, adding poisons, or changing the temperature. Due to the interactive nature of the parameters, repetitions/corrections might be necessary to finally describe the electrochemical system. Note that in certain electrochemical processes, especially in multistep reactions such as OER or HER, it can be difficult to reconcile the experimental data with the theoretical impedance response predicted by a model derived from a kinetic analysis.[20] A possible approach to overpass this issue may be the use of non-ideal electrical elements such as CPE. An extended discussion about this topic will be presented later in this section.

A more detailed analysis will now be introduced regarding the nature of the impedance of solid electrodes, since these have been used in this thesis for the study of the stability and electrocatalytic activity of electrodes towards the oxygen evolution reaction (OER). Special attention will be given to the non-ideal element CPE.

Solid electrodes usually exhibit both: (i) a high level of roughness, caused by scratches, pits, etc., which causes coupling of the solution resistance with the surface capacitance (see section 1.2.3), and (ii) a capacitance dispersion of the electrode/solution interface along with slow adsorption of ions and chemical inhomogeneity of the surface.[21] As a result, deviation from the ideal behaviour of typical circuit elements such as R, L, and C is often observed and thus, measured impedances may not be represented by sequential connection of simple R-C-L elements. This issue may be overcome by using distributed elements such as the Warburg impedance or constant phase element (CPE). Since CPE has been widely utilised in this thesis for the analysis of impedance data, it has been considered opportune to introduce it in detail.

The impedance of an ideal polarizable electrode can be represented, in terms of equivalent circuit, as an RC in series, which typically produces a straight line, perpendicular to the real axis on a Nyquist diagram. However, on solid electrodes, the double layer capacitance is not purely capacitive and often displays a certain frequency dispersion. Under these circumstances, a straight line with an angle lower that $\frac{\pi}{2}$ is often observed in a Nyquist diagram. In order to describe such behaviour, a model of distributed time constants, similarly to that used by Cole and Cole[22], was proposed by Zoltowski[23], who introduced

the concept of constant phase element based on dielectric dispersion of capacitances on solid electrodes. The complex dielectric constant on a solid electrode may be described as:

$$\frac{\varepsilon(\omega)-\varepsilon_\infty}{\varepsilon_S-\varepsilon_\infty}=\int_0^\infty \frac{G(\tau)}{1+j\omega\tau}d\tau \tag{3.6.18}$$

where $\varepsilon_S$ and $\varepsilon_\infty$ are the dielectric constants at frequencies $\omega \longrightarrow 0$ and $\omega \longrightarrow \infty$, respectively, and $G(\tau)$ is the function describing the distribution of time constants on the electrode surface. Cole and Cole define the distribution function as:

$$G(\tau)=\frac{1}{2\pi\tau}\frac{sin[(1-\alpha)\pi]}{cosh[\alpha\, ln(\tau/\tau_0)]-cos[(1-\alpha)\pi]} \tag{3.6.19}$$

In the absence of time constant distribution, $G(\tau)$ approaches the Dirac's function, $\delta$, $G(\tau) = \delta(\tau-\tau_0)$. Thus, the integration of eqn. 3.6.19 yields to:

$$\frac{\varepsilon(\omega)-\varepsilon_\infty}{\varepsilon_S-\varepsilon_\infty}=\frac{1}{1+(j\omega\tau_0)^\alpha} \tag{3.6.20}$$

where $\alpha$ is a constant phase exponent ($0 \leq \alpha \leq 1$). By analogy, the dispersion of impedances may be described by:

$$\frac{\hat{Z}(\omega)-Z_\infty}{Z_0-Z_\infty}=\int_0^\infty \frac{G(\tau)}{1+j\omega\tau}\,d\ln\tau \tag{3.6.21}$$

When $\alpha = 1$, only one time constant exists in the system and eqn. 3.6.21 reduces to Dirac's function. Under these circumstances, a CPE element may be defined as:

$$\bar{Z}_{CPE}=\frac{R_p}{1+Q(j\omega)^\alpha R_p} \tag{3.6.22}$$

where Q is a constant related to the electrode capacitance[22] with units of in $F\, s^{\alpha-1}cm^{-2}$ and $R_p$ is the associated polarisation resistance. The units of $Q$ can also be expressed to $\Omega^{-1}s^\alpha cm^{-2}$.[23] However, as the impedance becomes purely capacitive $\alpha = 1$, it seems more logical to use farads instead of ohms. Note that depending on the value of $\alpha$, the CPE element can behave as a: (i) pure resistance when $\alpha = 0$, (ii) a pure capacitance when $\alpha = 1$, (iii) an inductance when $\alpha = -1$, or (iv) a Warburg impedance when $\alpha = 0.5$. Fig. 3.6.10 may serve as a graphical representation of the effect of $\alpha$ on the time constant distribution function.

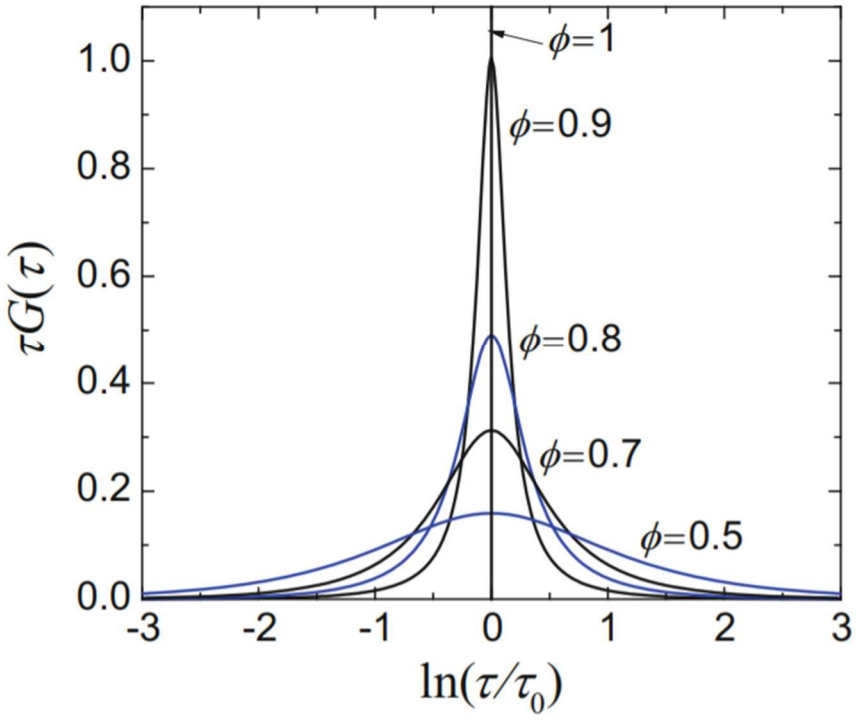



Figure 3.6.10 Schematic representation of the Dependence of time constant distribution function with the $ln\,\tau/\tau_0$. Reproduced from Ref.[24]

If the proprieties of the complex numbers are considered, eqn. 3.6.22 can be expressed as:

$$Z_{CPE} = \left[\frac{R_p \cos\left(\alpha\frac{\pi}{2}\right)}{1 + Q(\omega)^{\alpha}R_p}\right] - j\left[\frac{R_p \sin\left(\alpha\frac{\pi}{2}\right)}{1 + Q(\omega)^{\alpha}R_p}\right] \qquad (3.6.23)$$

The above equation suggests that the impedance of a CPE is no longer like pure imaginary, as it happened in the case of a pure capacitor but contains both real and imaginary components. Brug *et al.*[25] presented a simple method that allows estimation of the effective double layer capacitance, $C_{dl\,eff}$, from the values Q and α. It has been pointed out that the appearance of a CPE behaviour associated with a surface distribution of time constants requires the contribution of an Ohmic resistance, which in this case is the uncompensated resistance $R_u$.[26] Therefore, the model is presented as an uncompensated resistance, $R_u$ element and the CPE connected in series as observed in fig. 3.6.11. Note that the impedance of a CPE involves the polarisation resistance parameter, $R_p$.

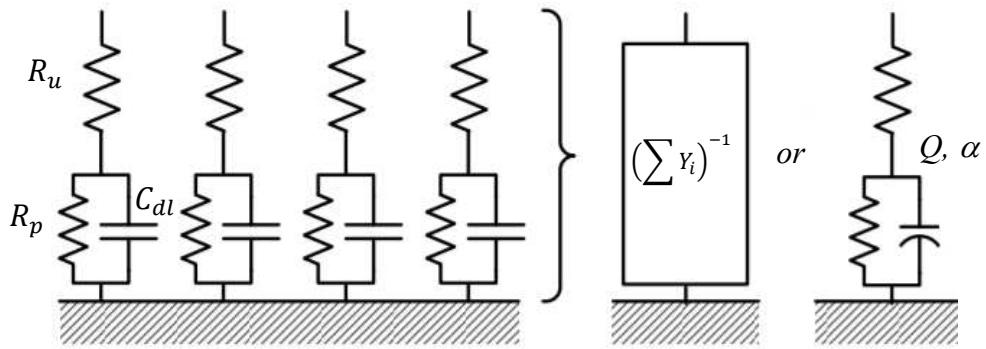



Figure 3.6.11 Schematic representation of a distribution of time constants in the presence of an Ohmic resistance in the electrode surface. Adapted from Ref.[27]

Taking into account the Cole-Cole expression for the distributed time constants (see eqn. 3.6.20), and following the development of Brug *et al.*[25] the relationship between CPE parameters and capacitance may be expressed in terms of admittance as:

$$Y = \sum_i Y_i = \left( R_{u,i} + \frac{R_{p,i}}{1 + jwR_{p,i}C_{dl,i}} \right)^{-1} \tag{3.6.24}$$

where $Y_i$ represents the local admittance for the solution resistance and a RC time constant involving the double layer capacitance,$C_{dl,i}$, and the polarisation resistance, $R_{p,i}$. The parameter $R_{u,i}$ refers to the local ohmic resistance. The total admittance of the electrode can also be expressed, in terms of the symmetric CPE represented by eqn. 3.6.22 as:

$$Y = \frac{1}{R_u}\left[ 1 - \frac{R_p}{R_u + R_p}\left( 1 + \frac{R_u R_p}{R_u + R_p} Q(jw)^{\alpha} \right)^{-1} \right] \tag{3.6.25}$$

where Q and α represent global properties of the CPE. Eqn. 3.6.25 can be rewritten in terms of a characteristic time constant associated with the admittance spectra Y as:

$$Y = \frac{1}{R_u}\left[ 1 - \frac{R_p}{R_u + R_p}(1 + (jw\tau_Y)^{\alpha})^{-1} \right] \tag{3.6.26}$$

where $\tau_Y = \frac{R_u R_p}{R_u + R_p} \bar{C}_{dl}$.

Comparison of eqns. 3.6.25 and 3.6.26 yields to:

$$\tau_Y{}^{\alpha} = \frac{R_u R_p}{R_u + R_p} Q = Q\left( \frac{1}{R_u} + \frac{1}{R_p} \right)^{-1} \tag{3.6.27}$$

The effective capacitance $C_{dl\,eff}$ associated with the CPE may therefore be expressed as:

$$C_{dl\,eff} = Q^{(1/\alpha)}\left[{R_u}^{-1} + {R_p}^{-1}\right]^{(1-\alpha)/\alpha} \tag{3.6.28}$$

Or:

$$C_{dl\,eff} = Q^{(1/\alpha)}\left[\frac{R_u R_p}{R_u + R_p}\right]^{(1-\alpha)/\alpha} \tag{3.6.29}$$

In the limit that $R_u \ll R_p$ , eqn. 3.6.29 becomes:

$$C_{dl\,eff} = Q^{(1/\alpha)}[R_u]^{(1-\alpha)/\alpha} \tag{3.6.30}$$

The eqn. 3.6.30 allows the evaluation of the average double layer capacitance in systems where the behaviour of electrical elements deviate from ideality.

A brief treatment is now given to the theory of CNLS fitting procedures. The nonlinear least-squares algorithm, which was introduced by Macdonald and Garber[28] in 1997, is based on the eqn. 3.6.31. In general, in CNLS, the weighted sum of squares is minimized by varying the values of the parameter *P*.

$$S = \sum_{i=1}^{N}\left\{w_i'\left[f_{ex}' - f_{i,calc}'(\omega_i, P)\right]^2 + w_i''\left[f_{ex}'' - f_{i,calc}''(\omega_i, P)\right]^2\right\} \tag{3.6.31}$$

where N is the number of data points, $P$ is a set of values for the various circuit elements, and $w_i'$ and $w_i''$ are the statistical weights coefficients associated with the $i^{th}$ data point. The experimental data, $f_{ex}'$ and $f_{ex}''$ consist of measurements made at a series of individual frequencies $\omega_i$. On the other hand, the function $f_{i,calc}(\omega, P)$ may be separated into a real part, $f_{i,calc}^{re}(\omega_i, P)$, and an imaginary part, $f_{i,calc}^{im}(\omega_i, P)$. Two fitting procedures may be distinguished depending on the EIS magnitude used for the fit. If the real and the imaginary part of the impedance are used for the fit, then $f_{ex}'$ and $f_{ex}''$ are the real and imaginary part of the experimental impedance data, respectively, at point i, while $f_{i,calc}'$ and $f_{i,calc}''$ are the real and imaginary part of the calculated impedance data, respectively, at a frequency $\omega_i$. On the other hand, if the phase $\phi$ and magnitude $|Z|$ are being used for the fit, then $f_{ex}'$ and $f_{ex}''$ are the magnitude and the phase part of the experimental measured impedance at point i, respectively, while $f_{i,calc}'$ and $f_{i,calc}''$ are the magnitude and the phase part of the calculated impedance data at a frequency $\omega_i$.

Since the value of the statistical weighting coefficients is a crucial factor to final fitting value, their estimation must be considered carefully. In this sense, Macdonald[16a] suggested two distinct approaches for defining weighting coefficients. The simplest of the two consists in defining all weights equal to unity, $w_i = 1$, which is also called unity weighting (UWT). However, when unit weighting is used ($w_i' = w_i'' = 1$) and the variation of the measured data is above one order of magnitude, the larger points of the measured data tend to dominate the fitting, resulting in both poor convergence and poor parameter fit. In addition, low time constants may be overlooked if $w_i' = w_i'' = 1$ .

The second approach for defining weighting coefficients is the so-called Proportional Weigh Ting (PWT), which is based upon considering weights inversely proportional to the square of the measured or estimated impedances at that point:[29]

$$w_i = \frac{1}{(Z_i)^2} \; or \; w_i = \frac{1}{(Z_{i\,calc})^2} \tag{3.6.32}$$

This approach is especially relevant because the ranges of the measured data can now be as large as six orders of magnitude. In addition, since it assumes a constant percentage error, small and large data values contribute equally to the final result. It is important to mention that several algorithms can be used to minimize CNLS fitting functions[30], *e.g.* the Levenberg-Marquardt algorithm, the Gauss-Newton algorithm, or Steepest Descent algorithm. While it is beyond the scope of this section to discuss in detail the various existing algorithms, it has been considered opportune to introduce the basics of Levenberg-Marquardt algorithm since it is the most commonly used algorithm in the software packages.[31] The Levenbert-Marquardt[32] method is an iterative technique that detects the minimum of a multivariable function and is expressed as the sum of the squares of non-linear real-value functions. In the late 1930s, most of the available methods to solve non-linear functions depended upon a reduction of the residuals to a linear form by first-order Taylor approximation taking about initial or trial solution for the parameter. However, if the procedure yields to calculated values which are not sufficiently close to the initial values, the neglect of second and higher order terms of the Taylor series may invalidate the process. In addition, this might result in a larger value of the sum of the squares obtained from the residuals than that obtained from the initial values.

Some of the standard methods which deal with this issue are the descent method and the Gauss-Newton method. The former is a general first order iterative method for finding the

minimum of a function. This method updates the parameter values in the opposite direction to the gradient of the function at a given point. Typically, it is used as the initial stage of the iterative process since, although it converges, it shows lack of precision in finding the minimum of the function.[33] The latter is a method for minimizing a sum-of-squares objective function and has as an advantage the fact that, since it always takes negative gradients, it is locally convergent on almost all nonlinear least-squares problems. However, the rate of convergence may still be slow on large residual functions and also in a very nonlinear function.[34]

The Levenberg-Marquardt algorithm adaptively builds a synergetic algorithm considering aspects from both Gauss-Newton and gradient descent theories. Consequently, if the calculated solution is far from the correct one, the algorithm behaves like a steepest descent method - slow but guaranteed to converge - whereas if the calculated solution is close to the correct solution, the Levenberg-Marquardt method approaches the Gauss-Newton method and the solution typically accelerates to the local minimum. Levenberg-Marquardt algorithm may be expressed as:[35]

$$[P^T P + \lambda(P^T P)]\delta = P^T(Y - f_0) \tag{3.6.33}$$

where $P^T$ and P are the Jacobian gradients. Note that the subscript t denotes matrix transposition. Y and $f_0$ are vectors and λ is the damping factor.

One of the limitations of the Levenberg-Marquardt algorithm is that it is only designed to find the closest local minimum with respect to the initial guess value, which may not necessarily be the global minimum of the function. Therefore, due to the iterative nature of the algorithm, the initial choice of the parameters is crucial. The seed value must lie relatively close to the real values, otherwise, the CNLS method may become divergent. Therefore, the determination of the initial estimates, or seed values, are critical to the quality of the CNLS fit.[30a] Several approaches for determining starting point values can be used: (i) by the graphically interpretation of the signal, (ii) by the reduction of the number of dimensions, *e.g.* substituting fix values for some parameters, (iii) by the evaluation of the signal at specific design values, and/or (iv) assuming conditional linearity.

Tafel slope values are normally measured using steady-state polarization techniques, however, they can also be determined using impedance spectroscopy measurements. The equivalent circuit employed for the determination of the Tafel slope is the so-called Armstrong-Henderson equivalent circuit[36], and it is presented in fig. 3.6.12.

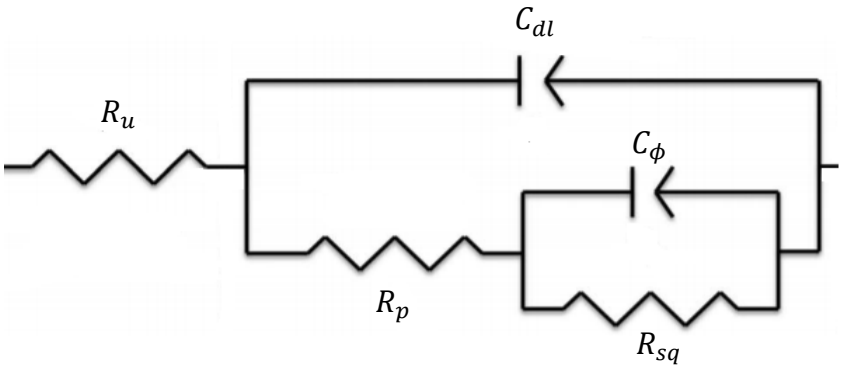



Figure 3.6.12 Schematic representation of the Armstrong-Henderson equivalent circuit used for the Tafel slope calculation in this thesis.

This equivalent circuit shows great agreement when fitting impedance experimental data of a multistep electrochemical reaction involving an adsorbed intermediate, such as the hydrogen evolution reaction or the oxygen evolution reaction. The significance of parameters $R_u$, $R_p$, and $C_{dl}$ has already been discussed previously. The pseudo capacitance $C_\phi$ is traditionally thought to account for the rate of either adsorption or desorption of intermediate species, while $R_{sq}$ is associated to the surface concentration of such intermediate specie. Both $C_\phi$ and $R_{sq}$, connected in parallel alignment, correctly model the relaxation of the charge associated with surface intermediates. A more contemporary view of this equivalent circuit is discussed in chapter 6.

Recall that at an overpotential, $\eta$, where simple Tafel behaviour prevails, the current density *i* is related to $\eta$ *via* the following expression:

$$i = i_0 \, exp\left(\frac{2.303\eta}{b}\right) \tag{3.6.34}$$

where $b$ is the Tafel slope ($\frac{d\eta}{d\log i}$). The differential Tafel slope, $b_{diff}$, conceived as an instantaneous Tafel slope at a given value of $\eta$ may be expressed as:

$$b_{diff} = \frac{d\eta}{d\log i} = 2.303\, i_{dc}\left(\frac{d\eta}{d\log i}\right) = 2.303 i_{dc} R_{far} \quad (3.6.35)$$

where $i_{dc}$ is the current density corresponding to the applied overpotential, $\eta$, and $R_{far}$ refers to the total Faradaic resistance of the working electrode and may be represented by:

$$R_{far} = R_{sq} + R_p \quad (3.6.36)$$

A Tafel slope can also be derived form $R_{far}$ values obtained over a range of potentials. The derivate of eqn. 3.6.34 with respect to η is given by:

$$\frac{di}{d\eta} = \frac{2.303 i_0}{b} exp\left(\frac{2.303\eta}{b}\right) \quad (3.6.37)$$

Performing the logarithm of eqn. 3.6.37 and noting that $\frac{di}{d\eta} = \frac{1}{R_{far}}$, the following expression may be obtained:

$$log\left(\frac{1}{R_{far}}\right) = \frac{\eta}{b} + log\left(\frac{2.303 i_0}{b}\right) \quad (3.6.38)$$

Eqn. 3.6.38 implies that the slope of a plot of $\log\left(\frac{1}{R_{far}}\right)$ against η is equal to the inverse of the Tafel slope.

### 3.6.6 Kramers-Kronig Transforms

In previous sections it was mentioned that the results of electrochemical impedance measurements are quite prone to be affected by several sources of errors such as environmental electrical noise and the mains hum. In addition, non-linearity in the measured system and instability owing to the long-time scale necessary for many EIS instruments also affects negatively the quality of the measured impedance data. Therefore, before starting the analysis and modelling of any experimental data, one should be certain that their impedances are valid. In this sense, it is relevant to mention the Kramers - Kronig transforms, introduced by Kramers[37] and Kronig[38] and further developed by Bode[39] which are a set of mathematical relations that allow for the verification of the impedance data. The calculation of the imaginary impedance from the real part is given by the following expression: [40]

$$Z''(\omega) = -\left(\frac{2\omega}{\pi}\right)\int_0^\infty \frac{Z'(x) - Z'(\omega)}{x^2 - \omega^2}dx \tag{3.6.39}$$

The real impedance from the imaginary part, if the high frequency asymptote for the real part is given by:

$$Z'(\omega) = Z'(\infty) + \left(\frac{2}{\pi}\right)\int_0^\infty \frac{xZ''(x) - \omega Z''(\omega)}{x^2 - \omega^2}dx \tag{3.6.40}$$

The real impedance from the imaginary part, if the zero-frequency asymptote of the real part is given by:

$$Z'(\omega) = Z'(0) + \left(\frac{2\omega}{\pi}\right)\int_0^\infty \frac{\frac{\omega}{x}Z''(x) - Z''(\omega)}{x^2 - \omega^2}dx \tag{3.6.41}$$

The polarization resistance, $R_p$, from the imaginary part is given by:

$$R_p = Z'(\infty) - Z'(0) = \left(\frac{2}{\pi}\right)\int_0^\infty \frac{Z''(\omega)}{x}dx \tag{3.6.42}$$

And finally, the phase-angle from the magnitude (modulus) can be calculated using:

$$\phi = \left(\frac{2\omega}{\pi}\right)\int_0^\infty \frac{ln\,|Z(x)|}{x^2 - \omega^2}dx \tag{3.6.43}$$

where ω and x are frequencies. The above equations suggest that the real component of the impedance may be calculated form the imaginary component and *vice versa*. In addition, the phase can be calculated form the magnitude of the impedance modulus. The main concern in applying the Kramers-Kronig transforms is that the integration must be performed over the whole frequency range, that is, from zero to infinity. It is obvious that, in practise, it is impossible to evaluate the integrals of eqns. 3.6.42 and 3.6.43 over an infinite range of frequencies. However, the error when performing the integration over a finite range of frequencies may be minimized if the limits of the frequency gap are separated by six or seven decades.[6] In order to be able to perform the Kramers-Kronig transforms, the physical system should hold the following four criteria:[41]

(1) Linearity: The relationship between the perturbation and the signal response must be linear. In other words, the response signal must be independent from the perturbation amplitude. To ensure this, the obtained impedance should be the same when the amplitude of the applied ac signal is halved. If so, the system is linear.

(2) Casualty: The measured response must be entirely determined by the applied perturbation and not contain contributions from other sources. To ensure this, when a perturbation is applied to a system in a rest at $t = 0$, the response must be zero for $t < 0$. The physical meaning of the previous criterion implies for the system not to generate noise independently of the applied signal.

(3) Stability: The system must remain stable unless excited by an external perturbation and it should return to its original state upon removal of such perturbation. In addition, the impedance measurements must be stationary, meaning that the measured impedance must not be time-dependent. This criterion can be easily checked by repetitive recording of the impedance spectra; then the obtained impedance plots (Nyquist and Bode) should be identical.

(4) Finiteness: The real and imaginary components of the impedance must be finite over the entire frequency range, including $\omega = 0$ and $\omega = \infty$.

### 3.6.7 Impedance Spectroscopy Uncompensated Resistance

In sections 3.4 and 3.5, it was shown that simple graphical methods were useful to extract parameters such the uncompensated resistance, $R_u$, the double layer capacitance $C_{dl}$, or the polarization resistance, $R_p$, from the transient current decay curve (see fig. 3.4.5). However, there are other more suitable methods that allow for the determination of these parameters in a more precise way. In this sense, electrochemical impedance spectroscopy (EIS) is another technique useable for the calculation of the above-mentioned parameters. Thus, $R_u$ may be determined using high frequency electrochemical impedance at a fixed potential, typically in potentials where no Faradaic process are occurring. Although the impedance response of the electrochemical cell, when taken over a range of frequencies, is prone to contain contributions from various diffusive, Faradaic and charging process, at high frequencies these contributions are negligible compared with $R_u$. Therefore, $R_u$ might be obtained from the high frequency intercept in a Nyquist plot as shown in fig. 3.6.7. Special care should be taken when analysing impedance data at high frequencies, since there is a danger that the measured spectrum may no longer be representative of the electrochemical cell but also of their electrical setup, including aspects such as wires, connections, etc. Therefore, it is recommended to perform an initial scan over an extended frequency range to determine the most appropriate frequencies for $R_u$ determination.

Subsequent measurements may then be performed over a reduced frequency range or even at a single frequency.

The two methods of iR compensation, pulse decay and EIS, typically agree within ± 0.5 Ω. The obtained values of the uncompensated resistances for various concentrations of NaOH solutions for manganese electrodes (chapter 4) and nickel/cobalt electrodes (chapter 5) are presented in Tables 3.6.1 and 3.6.2, respectively.

| | Mn electrode / n° cycles | | | | | |
|---|---|---|---|---|---|---|
| NaOH / M | 0 | 25 | 250 | 500 | 750 | 1000 |
| 0.1 | 23.2 Ω | 22.1 Ω | 24.2 Ω | 22.3 Ω | 21.4 Ω | 23.3 Ω |
| 0.25 | 13.3 Ω | 9.4 Ω | 10.3 Ω | 12.8 Ω | 11.1 Ω | 11.2 Ω |
| 0.5 | 5.0 Ω | 5.4 Ω | 4.5 Ω | 4.0 Ω | 5.0 Ω | 6.0 Ω |
| 1 | 2.5 Ω | 3.2 Ω | 3.5 Ω | 2.5 Ω | 2.9 Ω | 2.6 Ω |
| 2 | 1.6 Ω | 1.5 Ω | 1.8 Ω | 2.4 Ω | 2.1 Ω | 2.1 Ω |
| 3 | 1.4 Ω | 1.3 Ω | 1.6 Ω | 1.7 Ω | 1.6 Ω | 1.3 Ω |
| 4 | 1.5 Ω | 1.4 Ω | 1.5 Ω | 1.5 Ω | 1.7 Ω | 1.6 Ω |
| 5 | 1.2 Ω | 1.1 Ω | 1.0 Ω | 1.0 Ω | 1.4 Ω | 1.0 Ω |

Table 3.6.1 Uncompensated solution resistance values determined for manganese oxide electrodes at various NaOH concentrations at 25°C. This table shows the average calculated resistance values determined by EIS and pulse decay.

| | Ni-Co mixed oxide electrodes / % M Co content | | | | | | |
|---|---|---|---|---|---|---|---|
| NaOH / M | 100% | 80% | 60% | 50% | 40% | 20% | 0% |
| 0.1 | 25.1 Ω | 25.3 Ω | 23.2 Ω | 26.3 Ω | 22.2 Ω | 27.1 Ω | 24.3 |
| 0.25 | 11.0 Ω | 10.1 Ω | 9.5 Ω | 11.4 Ω | 9.7 Ω | 12.1 Ω | 11.0 Ω |
| 0.5 | 5.0 Ω | 5.4 Ω | 4.5 Ω | 5.3 Ω | 4.8 Ω | 7.0 Ω | 5.4 Ω |
| 1 | 3.2 Ω | 3.2 Ω | 2.5 Ω | 3.0 Ω | 2.6 Ω | 3.7 Ω | 3.1 Ω |
| 2 | 1.8 Ω | 2.1 Ω | 1.5 Ω | 1.8 Ω | 1.7 Ω | 2.2 Ω | 1.9 Ω |
| 3 | 1.4 Ω | 1.5 Ω | 1.3 Ω | 1.4 Ω | 1.2 Ω | 1.7 Ω | 1.4 Ω |
| 4 | 1.3 Ω | 1.5 Ω | 1.2 Ω | 1.3 Ω | 1.1 Ω | 1.6 Ω | 1.3 Ω |
| 5 | 1.2 Ω | 1.3 Ω | 1.0 Ω | 1.2 Ω | 0.9 Ω | 1.4 Ω | 1.2 Ω |

Table 3.6.2 Uncompensated solution resistance values determined for nickel/cobalt oxide electrodes at various NaOH concentrations at 25°C. This table shows the average calculated resistance values determined by EIS and pulse decay.

## 3.7 References Chapter 3


[1] W. Nernst, W. Wild, *Z. Electrochem* **1900**, 373.

[2] G. J. Hills, D. J. G. Ives, in *References Electrodes* (Ed.: D. J. G. Ives, Janz, G.J.), Accademic Press, New York, **1961**.

[3] J. Newman, K. E. Thomas-Alyea, *Electrochemical Systems*, John Wiley & Sons, **2004**; W. J. Hamer, D. N. Craig, *Journal of The Electrochemical Society* **1957**, *104*, 206-211.

[4] J. Balej, in *Standard potentials in aqueous solution, Vol. 3* (Eds.: A. J. Bard, R. Parsons, J. Jordan), Dekker, New York, **1985**; T. T. Kam, *Journal of Chemical Education* **1983**, *60*, 133.

[5] J. Garche, G. Schädlich, K. Wiesener, W. Oelssner, H. Kaden, *Journal of Electroanalytical Chemistry and Interfacial Electrochemistry* **1984**, *180*, 587-597.

[6] R. Greff, R. Peat, L. M. Peter, J. Robinson, in *Instrumental Methods in Electrochemistry*, Ellis, Chichester, **1985**.

[7] J. McIntyre, W. Peck, *Journal of the Electrochemical Society* **1970**, *117*, 747-751.

[8] K. Oldham, *Journal of Electroanalytical Chemistry (1959)* **1966**, *11*, 171-187.

[9] H. Gerischer, *Zeitschrift für Elektrochemie, Berichte der Bunsengesellschaft für physikalische Chemie* **1954**, *58*, 9-24.

[10] A. J. Bard, *Encyclopedia of Electrochemistry of the Elements, Vol. 1*, Marcel Dekker, New York, **1973**.

[11] S. Aberg, *Journal of Electroanalytical Chemistry* **1996**, *419*, 99-103.

[12] S. Åberg, *Journal of Electroanalytical Chemistry* **1997**, *439*, 63-71.

[13] C. P. Steinmetz, E. J. Berg, *Theory and Calculation of Alternating Current Phenomena*, Electrical world and engineer, incorporated, **1900**.

[14] A. E. Kennelly, *Proceedings of the IEEE* **1984**, *72*, 463-492.

[15] A. Lasia*, Vol. 32*, **1999**, pp. 143-248.

[16] D. D. Macdonald, in *Impedance Spectroscopy - Theory, Experiment, and Applications*, 2nd ed. (Ed.: M. E., J.R, Barsoukov, E.), J. Wiley & Sons, **2005**; D. V. Ribeiro, C. A. C. Souza, J. C. C. Abrantes, *Revista Ibracon de Estruturas e Materiais* **2015**, *8*, 529-546.

[17] V. F. Lvovich, *Impedance Spectroscopy: Applications to Electrochemical and Dielectric Phenomena*, Wiley, **2012**.

[18] B. E. Conway, in *Impedance Spectroscopy - Theory, Experiment, and Applications*, 2nd ed. (Ed.: M. E., J.R, Barsoukov, E.), J. Wiley & Sons, **2005**; *Electrochemical Impedance Spectroscopy Primer*, Gamry Instruments, **2005**; D. A. Harrington, B. E. Conway, *Electrochimica Acta* **1987**, *32*, 1703-1712.

[19] P. Zoltowski, *Journal of Electroanalytical Chemistry* **1994**, *375*, 45-57.

[20] A. G. C. Kobussen, G. H. J. Broers, *Journal of Electroanalytical Chemistry and Interfacial Electrochemistry* **1981**, *126*, 221-240; A. G. C. Kobussen, *Journal of Electroanalytical Chemistry and Interfacial Electrochemistry* **1981**, *126*, 199-220.

[21] K. Jüttner, *Electrochimica Acta* **1990**, *35*, 1501-1508; M. A. Igual, A. J. García, J. L. Guiñón, H. V. Pérez, *Corrosion Science* **2006**, *48*, 4127-4151; A. Norlin, J. Pan, C. Leygraf, *Biomolecular Engineering* **2002**, *19*, 67-71.

[22] K. S. Cole, R. H. Cole, *The Journal of Chemical Physics* **1941**, *9*, 341-351.

[23] P. Zoltowski, *Journal of Electroanalytical Chemistry* **1998**, *443*, 149-154.

[24] A. Lasia, **2014**, pp. 177-201.

[25] G. J. Brug, A. L. G. van den Eeden, M. Sluyters-Rehbach, J. H. Sluyters, *Journal of Electroanalytical Chemistry and Interfacial Electrochemistry* **1984**, *176*, 275-295.

[26] E. Chassaing, B. Sapoval, G. Daccord, R. Lenormand, *Journal of Electroanalytical Chemistry and Interfacial Electrochemistry* **1990**, *279*, 67-78; E. D. Bidóia, L. O. S. Bulhões, R. C. Rocha-Filho, *Electrochimica Acta* **1994**, *39*, 763-769.
[27] B. Hirschorn, M. E. Orazem, B. Tribollet, V. Vivier, I. Frateur, M. Musiani, *Electrochimica Acta* **2010**, *55*, 6218-6227.
[28] J. Macdonald, J. A. Garber, *Analysis of Impedance and Admittance Data for Solids and Liquids, Vol. 124*, **1977**.
[29] J. R. Macdonald, *Annals of biomedical engineering* **1992**, *20*, 289-305; J. R. Macdonald, *Journal of electroanalytical chemistry and interfacial electrochemistry* **1987**, *223*, 25-50.
[30] D. Bates, D. G. Watts, in *Nonlinear Regression Analysis and Its Applications*, Wiley Interscience **2008**, pp. 32-66; J. E. Dennis, *Proceedings of the IEEE* **1984**, *72*, 1765-1776.
[31] B. A. Boukamp, *Solid State Ionics* **1986**, *20*, 31-44; J. R. Macdonald, J. Schoonman, A. P. Lehnen, *Journal of Electroanalytical Chemistry and Interfacial Electrochemistry* **1982**, *131*, 77-95.
[32] K. Levenberg, *Quarterly Journal of Applied Mathmatics* **1944**, *2*, 164-168.
[33] K. Madsen, Nielsen, H.B., Tinglef, O., *Methods for Non-Linear Least Squares Problems (2nd ed.)*, Informatics and Mathematical Modelling, Technical University of Denmark, **2004**.
[34] Å. Björck, *Numerical Methods for Least Squares Problems*.
[35] D. W. Marquardt, *Journal of the Society for Industrial and Applied Mathematics* **1963**, *11*, 431-441.
[36] R. D. Armstrong, M. Henderson, *Journal of Electroanalytical Chemistry and Interfacial Electrochemistry* **1972**, *39*, 81-90.
[37] H. Kramers, *Physik. Z* **1929**, *30*, 52.
[38] R. d. L. Kronig, *Josa* **1926**, *12*, 547-557.
[39] H. W. Bode, *Network Analysis and Feedback Amplifier Design*, Van Nostrand, New York, **1945**.
[40] M. C. H. McKrube, Macdonald, D.D.,, in *Impedance Spectroscopy - Theory, Experiment, and Applications*, 2nd ed. (Ed.: M. E., J.R, Barsoukov, E.), J. Wiley & Sons, **2005**.
[41] J. J. DiStefano, Stubberud, A.R., Williams, I.J., *Theory and Problems of Feedback and Control Systems*, 2 ed., McGraw-Hill, New York, **1990**; M. Urquidi-Macdonald, S. Real, D. D. Macdonald, *Electrochimica Acta* **1990**, *35*, 1559-1566.

# CHAPTER 4

# THE REDOX AND ELECTROCATALYTIC BEHAVIOUR OF HYDROUS MANGANESE OXYHYDROXIDE FILMS

## 4.1 Introduction

The present chapter focuses on the presentation of the electrochemical redox and charge transfer proprieties of the hydrous oxyhydroxide films grown on polycrystalline manganese metal prepared by potential multicycling in alkaline solution. The state of the art presented in chapter 1 will now be used and leveraged to explain the results of a series of investigations on the charge storage proprieties, redox activity, growth characteristics and electrocatalytic activity of multilayered hydrous oxyhydroxide manganese films. The growth of hydrous oxyhydroxide manganese oxide will be examined by monitoring the voltammetric response as function of potential cycles and with the growth mechanism being explained using a place exchange mechanism. The potential-pH response of the major hydrous oxyhydroxide manganese redox voltammetric peaks will also be examined and used to assign a more accurate stoichiometry to represent the redox switching reaction exhibited by the surface bound oxy-manganese species in the oxide thin film. The response of this type of oxide will be examined both for an aged electrode and a fresh electrode. Aged in this sense refers to an electrode that had undergone several polarisation experiments prior to being subjected to a multicycling procedure to produce the hydrous oxide, whereas fresh refers to a newly prepared electrode, *e.g.* a previously unused one. Also included are relevant steady-state polarisation measurements that yield information on the nature of the catalytic surfaces on which the OER proceeds in these systems.

## 4.2 Oxide Growth and Surface Redox Chemistry

In view of the widely reported complexity (see section 1.4.4) of the surface electrochemistry of manganese in alkaline media, especially in connection to the pathway for the formation of $MnO_2$, the possible generation of various different phases in the oxyhydroxide manganese film, and the observation of a anodic doublet peak at large potential cycling scans, it was decided to begin the investigation of the oxygen evolution on manganese electrodes by characterising the redox behaviour of the metal in alkaline media and determining whether a stable, reproducible anode surface on which to study the reaction could be obtained. To this end, two different polycrystalline Mn rod electrodes, one aged and one fresh, were subjected to series of potential cycling experiments at a various number of potential cycles,

ranging between 0 to 1000 cycles. These experiments involved placing the rod electrode, which was previously polished to a "bright" mirror as described in chapter 3, in 1.0 M NaOH solution, and cycling its potential between the - 0.25 to 1.75 V (*vs.* RHE) at a sweep rate of 40 mV $s^{-1}$. For the sake of structure, the results of the newly electrode will be presented first, followed by those for the aged electrode.

The growth of a hydrous oxide film on an initially "bright" Mn substrate in 1.0 M NaOH is presented in fig. 4.2.1. The redox peak located in the potential region 0.70 - 1.10 V (*vs.* RHE) becomes increasingly more developed with increasing the number of potential cycles. It is worth noting that during film growth, a new set of peaks in the potential range of 1.2 – 1.6 V (*vs.* RHE) are formed. The integrated charge developed under either the anodic or the cathodic peak can be used as a measure of oxide film thickness, being the latter directly proportional to the redox capacity. The variation of oxide charge capacity $Q$ with several oxide growth cycles N is presented in fig. 4.2.2. The charge storage capacity, $Q$, was determined following the growth of each film by integration of the peaks in a voltammetric profile recorded at a slow sweep rate.

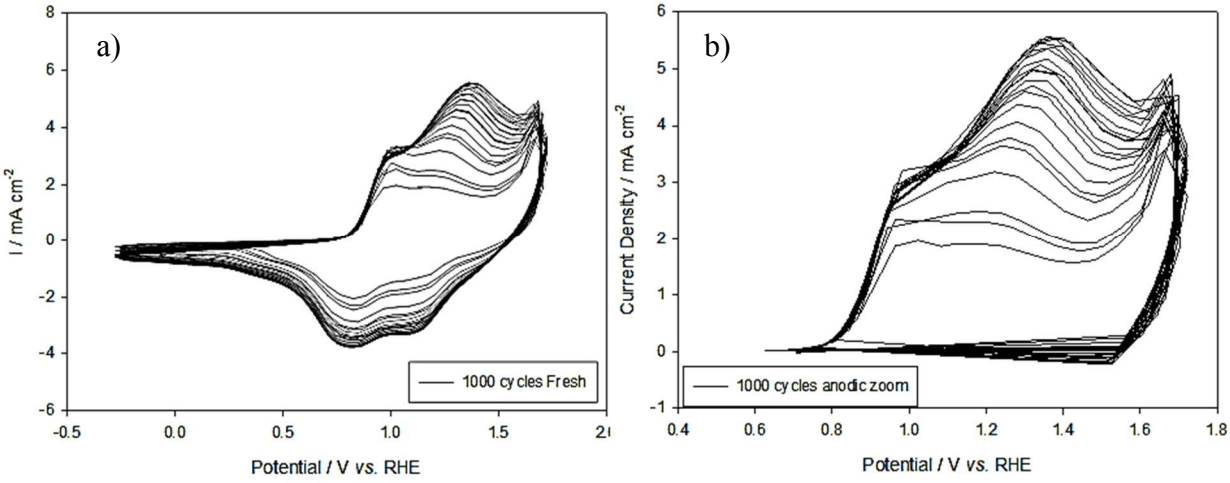



Figure 4.2.1 a) Growth of fresh hydrous oxyhydroxide manganese thin film on Mn support electrode monitored *via* analysis of the evolution of the real time voltammogram in 1.0 M NaOH. Growth potential limits: - 0.25 to 1.75 V (*vs.* RHE), sweep rate 40 mV $s^{-1}$; b) Voltammetric response zoom of the 0.6 - 1.7 V potential region.

The oxide growth kinetics can be fit into the following empirical expression:

$$Q = a(1 - \exp[-bN]) \qquad (4.2.1)$$

where $a$ and $b$ are empirical constants with numerical values determined *via* CNLS fitting predicted as $\mathrm{a} = 0.00178 \pm 4.11 \times 10^{-5}$ and $\mathrm{b} = 0.00341 \pm 2.98 \times 10^{-4}$. It is clear from fig. 4.2.2 that the oxide growth rate gradually decreases with increasing number of growth cycles and the charge capacity $Q$ approaches a constant limiting value as N gets larger, *e.g.* $Q \rightarrow \mathrm{a}$ as $\mathrm{N} \rightarrow \infty$.

The plot of redox charge capacity versus time is presented in fig. 4.2.3. Time was computed directly from the number of cycles by noting that the time corresponding to 1 cycle is equivalent to $\mathrm{t} = \Delta\mathrm{E}/\nu$ where $\Delta\mathrm{E}$ represents the voltage span for a single voltammetric cycle and $\nu$ denotes the potential sweep rate. The voltage span for a single voltammetric cycle is given by $\Delta\mathrm{E} = 2(\mathrm{E_{UL}} - \mathrm{E_{LL}})$ where $\mathrm{E_{UL}}$and $\mathrm{E_{LL}}$ represent the upper and lower limits of the potential sweep, respectively. Hence, N cycles correspond to a time of $\mathrm{t} = \mathrm{N}\Delta\mathrm{E}/\nu$. As previously mentioned, the charge capacity can be regarded as proportional to the amount of redox active Mn sites in the oxide film provided that both the electron hopping between the immobilized redox sites and the counterion diffusion through the solution filled pores of the oxide matrix are rapid.

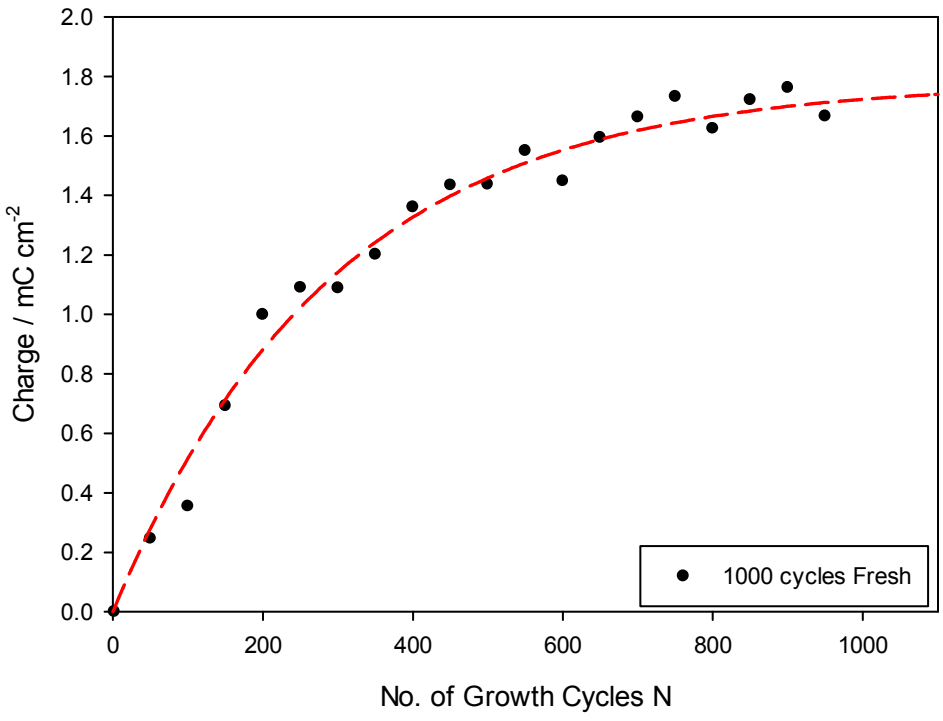



Figure 4.2.2 Growth of hydrous oxyhydroxide manganese thin film on Mn electrode monitored *via* analysis of the evolution of the real time voltammogram in 1.0 M NaOH. Plot of integrated voltammetric charge $Q$ (measured at 40 mV $s^{-1}$) as a function of number of oxide growth cycles N.

It is generally accepted that hydrated metal oxyhydroxide films should be regarded as a gel-like material containing chains of oxygen bridged hydroxyl aquo complexes of Mn. This feature has a huge influence on both the acid/base and redox behaviour of the hydrous oxide film as it will be noted later. In the present work, the scan rate employed during the integration of the voltammetric charge capacity was 40 mV $s^{-1}$ and 1 cycle corresponds to a potential interval of 2 V, so the time associated with 1 cycle coincide with 100 s.

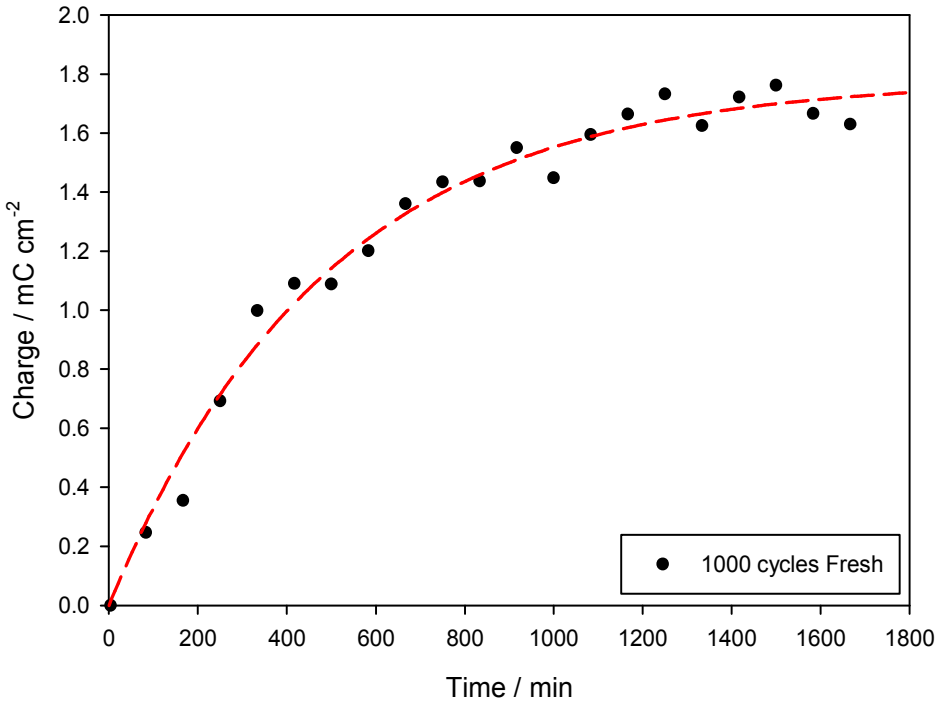



Figure 4.2.3 Growth of hydrous oxyhydroxide manganese thin film on Mn electrode monitored *via* analysis of the evolution of the real time voltammogram in 1.0 M NaOH. Plot of integrated voltammetric charge $Q$ (measured at 40 mV $s^{-1}$) as a function of time.

It is noted from fig. 4.2.2 that the quantity of redox sites, which are closely related with the charge capacity, increase with time. The redox process associated with the main charge storage reaction involving Mn (IV)/Mn(III) species in the hydrous oxide layer can be expressed as:

$$2[MnO_2(OH)_2(OH_2)_2]^{-2} + 2e^- \rightarrow [Mn_2O_3(OH)_3(OH_2)_3]^{-3} + 3OH^- \qquad (4.2.2)$$

or, alternatively, as:

$$2[Mn(OH)_6]^{-2} + 2e^- \rightarrow [Mn_2(OH)_9]^{-3} + 3OH^- \qquad (4.2.3)$$

It is proposed by analogy with iron growth, that under conditions of Mn thick film growth, the interfacial region may be represented by: $\mathrm{M/MO_x/MO_a(OH)_b(OH_2)_c}$ /aqueous phase as outlined in section 1.4.2. This is the duplex layer model of the oxide/solution interphase region where $\mathrm{MO_x}$ represents the inner compact layer and $\mathrm{MO_a(OH)_b(OH_2)_c}$ denotes the outer hydrous layer. This model was first suggested by Burke and O'Sullivan.[1] This discussion will be taken up later in this section when discussing the effect of potential limits on the oxide film growth.

Due to the micro-dispersed nature of the hydrous oxide layer charge compensating counter ions such as $Na^+$ or $K^+$ are usually present in the aqueous regions of the hydrous oxide films. These materials can be seen as analogous to redox conducting polymer films and exhibit both ionic and electronic conductivity. The reaction outlined in eqn. 4.2.2 suggests that the charge storage peaks might display a super-Nernstian shift in potential with changes in solution's pH. Quantitatively the shift should be given by $\mathrm{dE/dpH} = -2.303\ (\mathrm{mRT}/nF) = -2.303(3\mathrm{RT}/2F) = -0.088\ \mathrm{V\ pH^{-1}}$ since the hydroxyl ion/electron ratio is 3/2. This quasi-thermodynamic analysis was recently described in detail by Lyons *et al.*[2] The main charge storage reaction associated with hydrous oxide growth at Fe, Ni, Ir, and Rh metal electrodes follows a stoichiometry suggested by eqn. 4.2.2. All the mentioned metals show super-Nernstian shifts in redox potential with respect to changes in solution pH. Manganese is unusual in that the anodic and cathodic charge storage peaks shift negatively in potential with increasing solution pH to different extents over the range $9 < \mathrm{pH} < 14$ . Burke and Ahern[3] have shown that the anodic peak potential (obtained by recording the voltammograms at low sweep rate to ensure thermodynamic reversibility) exhibits a cathodic shift of ca. 137 mV per unit of change in pH at 298 K, whereas, in contrast, the cathodic peak potential shifts by the expected 90 mV per decade of change in hydrogen ion activity. Therefore, the average potential varies as 114 mV $dec^{-1}$. The redox activity associated with the cathodic peak is well described by eqn. 4.2.2. However, the redox behaviour associated with the main anodic peak is best described by the following expression:

$$[Mn_2(OH)_9]^{-3} + 4.6OH^- \rightarrow [Mn_2O_{4.6}(OH)_{4.4}]^{-5.6} + 4.6H_2O + 2e^- \qquad (4.2.4)$$

This is followed by a post electrochemical decomposition step:

$$2[Mn_2O_{4.6}(OH)_{4.4}]^{-5.6} + 4.6H_2O \rightarrow 2[Mn(OH)_6]^{-2} + 1.6OH^- \quad (4.2.5)$$

The very large super-Nernstian shift observed for the main anodic charge storage peak (as opposed to the 90 mV dec$^{-1}$ shift observed for iridium oxide redox peak described as ($[Ir_2(OH)_9]^{-3} + 3H_2O \rightarrow 2[Ir(OH)_6]^{-2} + 3H^+ + 2e^-$)) may arise as a result of the high acidity of the manganese oxy-cation. This is not an unreasonable assumption in view of the much smaller size and greater charge density for the same oxidation state of the first-row transition metal cation. Burke and Ahern[3] mentioned that the non-integral values in the unstable species formed initially during the anodic sweep, represented by eqn. 4.2.4, could be regarded to a mixture of anionic species with negative charge values of -5 and -6, *e.g.* $[Mn_2O_4(OH)_5]^{-5}$and $[Mn_2O_5(OH)_4]^{-6}$ joined together in a polymer chain structure with counterions present in the aqueous regions of the porous material. This arrangement reduces the degree of electrostatic repulsion between the highly anionic centres in the hydrous material. The hysteresis observed in the voltammograms between the main anodic and cathodic peaks can be attributed to the fact that the anodic and cathodic redox processes representing the Mn(III)/Mn(IV) redox transition differ. The 118 mV dec$^{-1}$ shift of the mean redox potential value calculated by Burke and Ahern [4] corresponds to the following type of redox process:

$$[Mn_2(OH)_9]^{-3} + 4OH^- \rightarrow [Mn_2O_3(OH)_7]^{-5} + 3H_2O + 2e^- \quad (4.2.6)$$

As observed in fig. 4.2.4, the first stages of the oxide growth (1 and 25 cycles) only reflect a single anodic peak. This peak, which is labelled as A1, shifts from the potential ca. 0.90 V to 0.85 V *vs.* RHE whereas the C1 cathodic peak shifts from the 0.54 V to 0.7 V. The peaks labelled A/C are located at potentials in excellent agreement with earlier work reported by Burke and Ahern.[3] These redox peaks can also be seen in a study by Yano *et al.*, for a mixed manganese oxide.[5] The A/C peaks can be assigned to either of the two following reactions involving a Mn(III)/Mn(IV) redox transition within the oxide film:[6]

$$Mn_2O_3 + 2OH^- \rightarrow 2MnO_2 + H_2O + e^- \quad (4.2.7)$$

$$MnOOH + OH^- \rightarrow MnO_2 + H_2O + e^- \quad (4.2.8)$$

The impact of the film growth on the OER onset potential is to be noted. The OER onset potential becomes thermodynamically more favourable as the film thickness increases, shifting from 0.52 V to 0.42 V (*vs.* RHE) for 1 cycle and 25 cycles, respectively. As it will be seen later, the value of the onset potential will remain stable at around 0.42 V (*vs.* RHE) for thick layers.

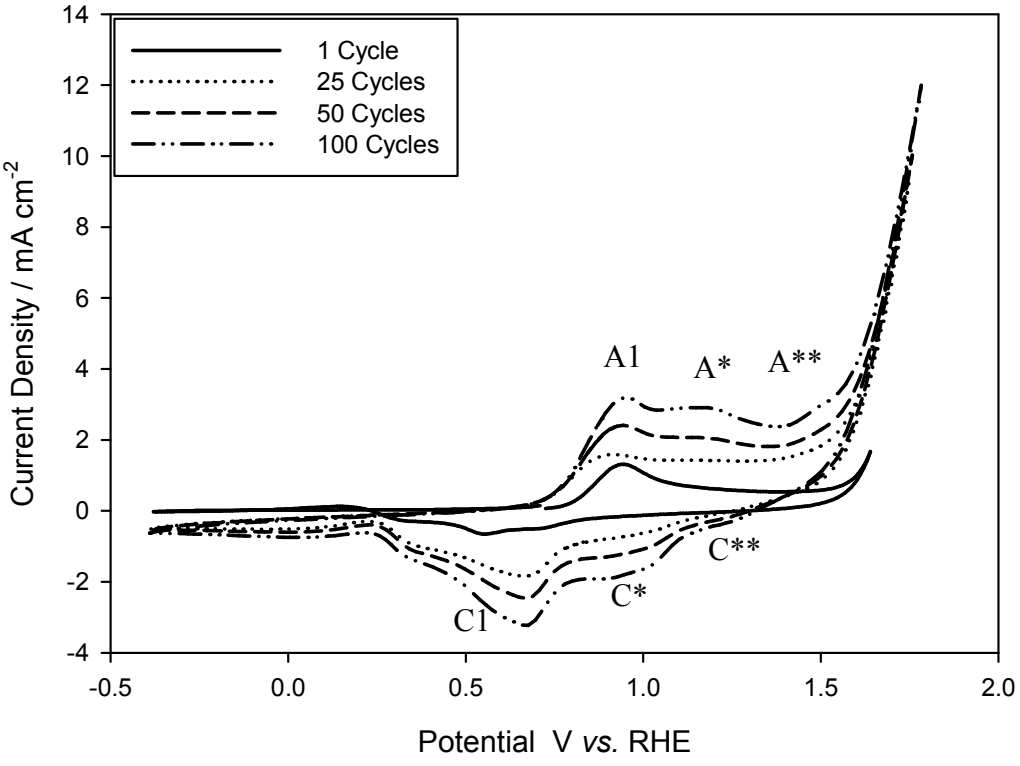



Figure 4.2.4 Analytical CVs (cycle number as indicates in the legend) recorded at 40 mV $s^{-1}$ , of an initially bright polycrystalline Mn electrode in 1.0 M NaOH. All CVs recorded between -0.4 and 1.75 V (*vs.* RHE) at 25°C.

As the thickness of the film increases, that is for cycles > 25, the voltammetric behaviour becomes more complex. For potential cycles in the range of 50 - 100 cycles (see fig. 4.2.4) the formation of two new redox pairs of peaks can be observed at 1.2/1.1 V and 1.45/1.35 V (*vs.* RHE), denoted by A*/C* and A**/C**, respectively:

$$MnO_2 + H_2O + e^- \rightarrow Mn(OH)_3 + OH^- \qquad (4.2.9)$$

$$2Mn(OH)_3 \rightarrow Mn_2O_3 + 3H_2O \qquad (4.2.10)$$

and

$$3MnO_2 + 2H_2O + 4e^- \rightarrow Mn_3O_4 + 4OH^- \quad (4.2.11)$$

$$2Mn_3O_4 + 2OH^- \rightarrow 3Mn_2O_3 + H_2O + 2e^- \quad (4.2.12)$$

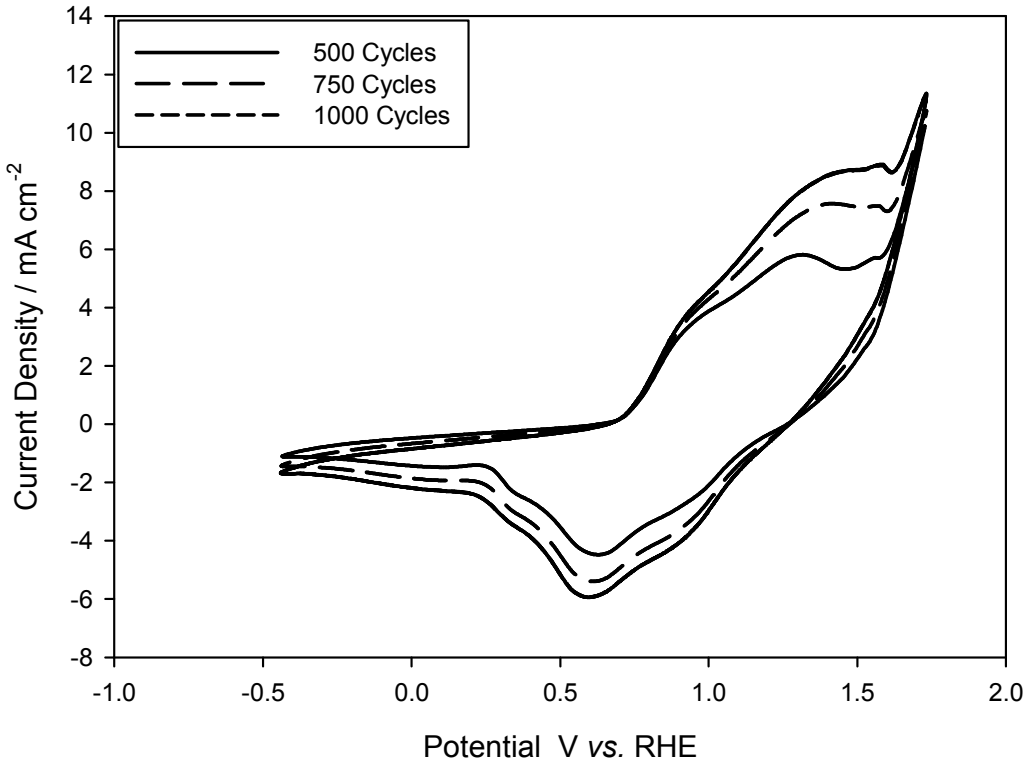



Figure 4.2.5 Analytical CVs (cycle number as indicates in the legend) recorded at 40 mV $s^{-1}$ , of an initially bright polycrystalline Mn electrode in 1.0 M NaOH. All CVs recorded between -0.4 and 1.75 V (*vs.* RHE) at 25°C.

At initial stages, the oxidation of Mn metal most probably is described, by analogy with Fe and Ni, by the following reactions:

$$Mn + 2OH^- \rightarrow Mn(OH)_2 + 2e^- \quad (4.2.13)$$

$$Mn + 2OH^- \rightarrow MnO + H_2O + 2e^- \quad (4.2.14)$$

The voltammetric profile presented in fig. 4.2.5 exhibits the feature that both the anodic and cathodic redox peaks are superimposed in a broad current background, which is

characteristic of a material with a rather large pseudo-capacitance. This observation is especially significant for those surfaces which have been extensively roughened *via* repetitive potential cycling. The large current background may be well ascribed to the formation of a porous film structure similar to that mentioned by Ivey.[7] It is well established that significantly enhanced capacitance is observed in structures with both high porosity and interconnectivity. These types of structures supply sufficient penetration space for ions while maintaining sufficient conductivity for solid-state electronic transfer. Moreover, they can provide short diffusion path lengths to both ions and electrons giving rise to high charge/discharge rates.[8]

Further, Mn (III) / Mn (IV) conversion in less hydroxylated, and therefore less active regions, of the film are observed in the region between the main redox oxidation and the increase in current associated with active oxygen gas evolution above ca. 1.7 V (*vs*. RHE). Furthermore, the potential of the main anodic oxidation peak shifts to more positive values with increasing number of potential cycling. The peak position of the cathodic counterpart appears to be independent of the degree of potential cycling. It is interesting to note that negative currents were observed over the lower region of the anodic sweep. This possibly arises from the reduction of some Mn (IV) centres trapped in the surface layer even at potentials below the main reduction peak C. In agreement with the earlier work of Burke and Murphy[6] the A/C redox transition observed for thin films is accompanied by a reversible electrochromic transition of the oxide layer changing from pale yellow, at low potentials, to reddish brown in the oxidized state. With thicker layers, especially those present after 250 cycles, the oxide layer was black throughout the cycle.

The A*/C* and A**/C** redox processes, present in surface layers generated at higher cycle numbers may arise to the formation of a different phase of $MnO_2$. The structural chemistry of $MnO_2$ has been extensively discussed in section 1.4.4. That analysis, along with other studies done elsewhere[9] revealed a high complex film structure with numerous phases of $MnO_2$ described with slightly different oxidation states. It was shown that the various $MnO_2$ phases, ($\alpha, \beta, \gamma$ and $\varepsilon -$ phases), which possess oxidation states from 3.7 to 3.9, exhibit different OER performance in alkaline media (unpublished work by M.P. Browne - group member). The additional redox peaks may also arise due to surface redox transitions involving manganite and permanganate species. During OER the $MnO_2$ layer may interact with the hydroxide ions in the solution to produce manganate ions or permanganate ions

either surface bound or present in the interface region. The reactions can be described as presented below:

$$MnO_2 + 4OH^- \rightarrow {MnO_4}^{-2} + 2H_2O + 2e^- \quad (4.2.15)$$

$${MnO_4}^{-2} \rightarrow {MnO_4}^{-} + e^- \quad (4.2.16)$$

and:

$$MnO_2 + 4OH^- \rightarrow {MnO_4}^{-} + H_2O + 3e^- \quad (4.2.17)$$

It was noted that the hexavalent manganate Mn (VI) ion forms a green colour and the heptavalent permanganate Mn (VII) ion is purple in aqueous alkaline solution. The production of manganite (blue/green solution) and permanganate (purple solution) ions in solution has been visually observed. The UV-Vis analysis of the electrolyte solution after extended oxygen evolution reaction is presented in fig. 4.2.6. The peak C at 530 nm corresponds to permanganate species.[10] As observed, the intensity of the absorbance of peak C deceases with time while peaks A, B and P increases. The latter suggest decomposition of the permanganate into manganate and oxygen. Peak P has been assigned to manganate species. The observation of two additional absorption peaks at 356 nm and 439 nm might to arise due to the electrolyte solution contains impure manganate species, which usually give rise to relatively higher results for the absorption wavelength. Such peaks are therefore ascribed to the formation of colloidal manganese dioxide. The curves presented in papers by Zimmermann[11] and Symons[12] for the permanganate spectrum and by Boef [13] for manganate are in fair agreement with our result presented in fig. 4.2.6. It has been suggested by Ferguson, Lerch, and Day[14] and by Duke[15] that the decomposition of permanganate is mainly due to the interaction of permanganate with $OH^-$ and, in a lesser extent, with water molecules following:

$$4MnO_4^- + 4OH^- \rightarrow 4MnO_4^{2-} + 2H_2O + O_2 \quad (4.2.18)$$

and

$$MnO_4^- + H_2O \rightarrow MnO_4^{2-} + H^+ + \cdot OH \quad (4.2.19)$$

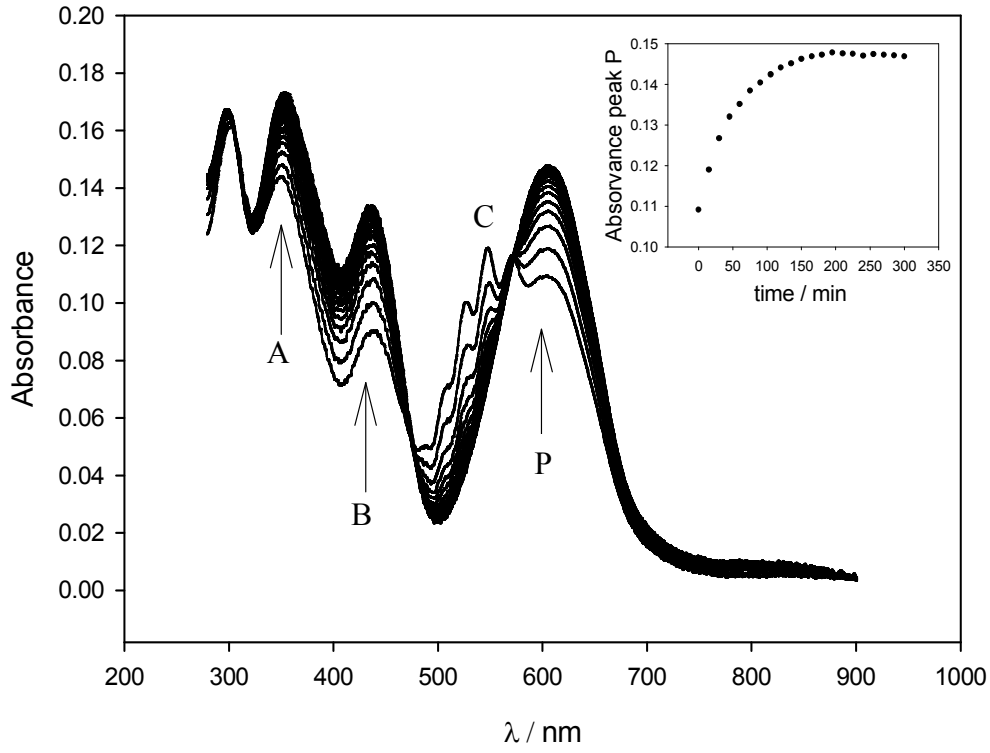



Figure. 4.2.6 UV-Vis spectrum of the electrolyte after extended oxygen evolution reaction using a Mn electrode in 1.0 M NaOH solution. The solution was deoxygenated before UV-Vis analysis.

Thus, we conclude that the observation of manganite and permanganate species at high anodic potentials suggests that corrosion of Mn oxide film competes with oxygen evolution in alkaline media. This mechanism for oxidized Mn metal electrodes is similar to that observed for Ru metal electrodes in an aqueous base. Here, Ru metal during potential cycling shows a main charge storage peak located between 0.4 - 0.5 V (*vs.* RHE) and is assigned to the Ru (III) / Ru (IV) transition with a stoichiometry similar to that presented in eqn. 4.2.7 and eqn. 4.2.8. Higher Ru oxidation states can be readily generated under conditions of high pH. According to Lam *et al.*[16] the $RuO_2$ species generated can hydroxylate to form a hydrous species $Ru(OH)_6^{-2}$ which then oxidizes over the potential range 0.9 -1.15 V (*vs.* RHE) to form $RuO_4^{-2}$ according to the following reaction:

$$RuO_2 + 2OH^- + 2H_2O \rightarrow Ru(OH)_6^{-2} \quad (4.2.20)$$

$$Ru(OH)_6^{-2} + 2OH^- \rightarrow RuO_4^{-2} + 4H_2O + 2e^- \quad (4.2.21)$$

Ru (VI) species can undergo subsequent oxidation at potentials close to oxygen evolution 1.35 V - 1.45 V (*vs.* RHE) to form:

$$RuO_4^{-2} \rightarrow RuO_4^{-} + e^{-} \qquad (4.2.22)$$

Indeed in the case of Ru metal in base it is very difficult to obtain a well-defined Tafel plot for OER because of the extensive active corrosion to form $RuO_4^{-2}$ and $RuO_4^{-}$ species as discussed by Burke and Whelan.[17] These authors proposed that under anodizing conditions the Ru metal surface is coated with strongly adherent, weakly adherent and dissolved oxide species. These contribute to oxygen gas evolution according to:

$$4RuO_4^{-} + 4OH^{-} \rightarrow 4RuO_4^{-2} + 2H_2O + O_2 \qquad (4.2.23)$$

However, the voltammetry results obtained in this thesis for the Mn electrodes in aqueous base solutions suggest that the Mn film is much more stable than that obtained for the Ru metal since corrosion was only observed when the electrode was submitted to potentials in the OER region. The latter implies that the manganite and permanganate (either surface bound or in the interfacial region) are formed at potential regions close to the onset potential for the OER, and that the peaks observed for extensively multicycled metal surfaces may well correspond to Mn (IV) / Mn (V) and Mn (V) / Mn (VII) redox transitions within the oxide surface layer. These species may actively participate in the OER according to the following homogeneous reaction:[12]

$$4MnO_4^{-} + 4OH^{-} \rightarrow 4MnO_4^{-2} + 2H_2O + O_2 \qquad (4.2.24)$$

These surface bounded groups with high oxidation states, also known as surfaquo groups, will be well accounted when dealing with both impedance analysis and mechanistic analysis. It has been proposed here that such species are bounded to the largely anhydrous bulk Mn oxide lattice. A possible explanation for the poor redox peak definition may be given by the fact that the surface coverage of surfaquo groups is low. These surface groups are highly energetic however and are located at defect centres such as step or kink sites. They are less strongly oxygen coordinated to the lattice and are likely to be partially hydrated.[18]

SEM and EDX were used to study the surface morphology of a series of hydrous oxyhydroxide manganese films as a function of number of potential cycles. Results are presented in figs. 4.2.7 and 4.2.8.

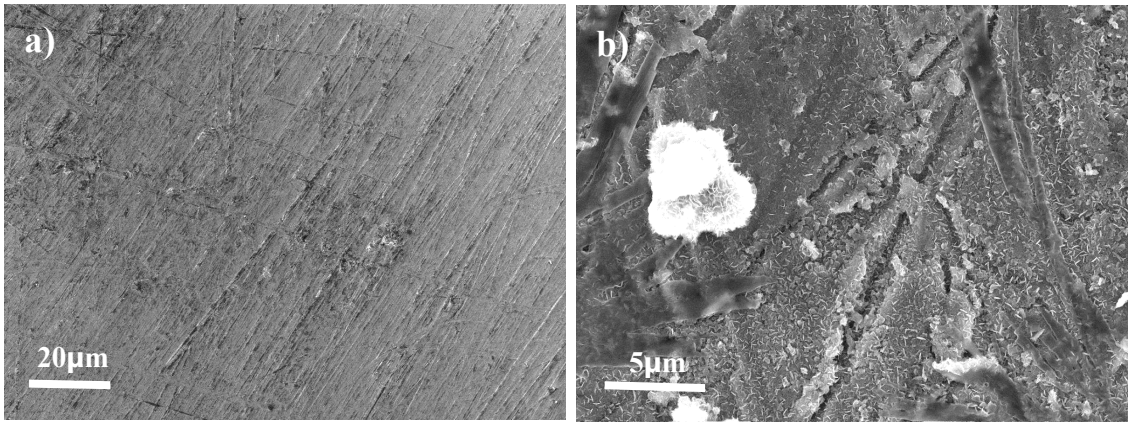



Figure 4.2.7 SEM images of a) Bright Mn electrode, b) Mn oxide 25 cycles.

Surface morphology was found to vary significantly with the number of potential cycles. As the number of cycles increase from 0 to 25, individual nanostructures are formed with a spongy like surface. Commonly, these nanostructures grow from one another, although also individual ones are observed. Further, as the number of cycles increases, the surface of these nanostructures changes in sense that becomes more structured (see fig. 4.2.8). The formation of micro rods begins at approx. 250 cycles (see fig. 4.2.8 a.2). SEM images of 500 and 1000 potential cycles, show further development of the micro- and nanostructures (see 4.2.8 d and d.2). At this stage, microstructures show larger heights if compared with those for 250 cycles. The height of these structures was observed to increase as the number of cycles increases whereas the average diameter seems to remain constant at ca. 18 µm. Importantly, the coexistence of both types of microstructures and nanostructures takes place. The presence of these type of structures will play an important role in the catalytic activity of the electrodes since they increase the active sites for the OER.

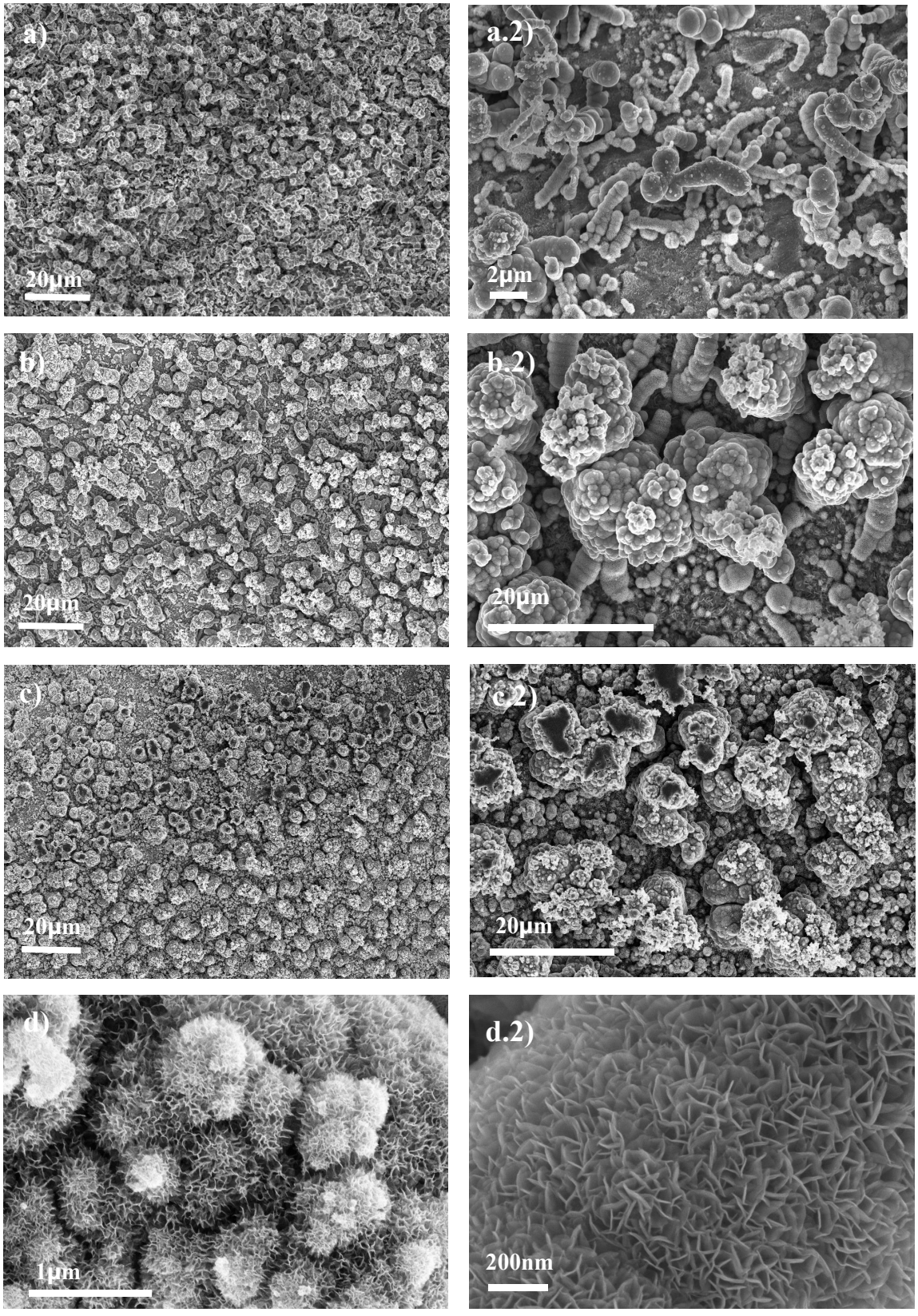
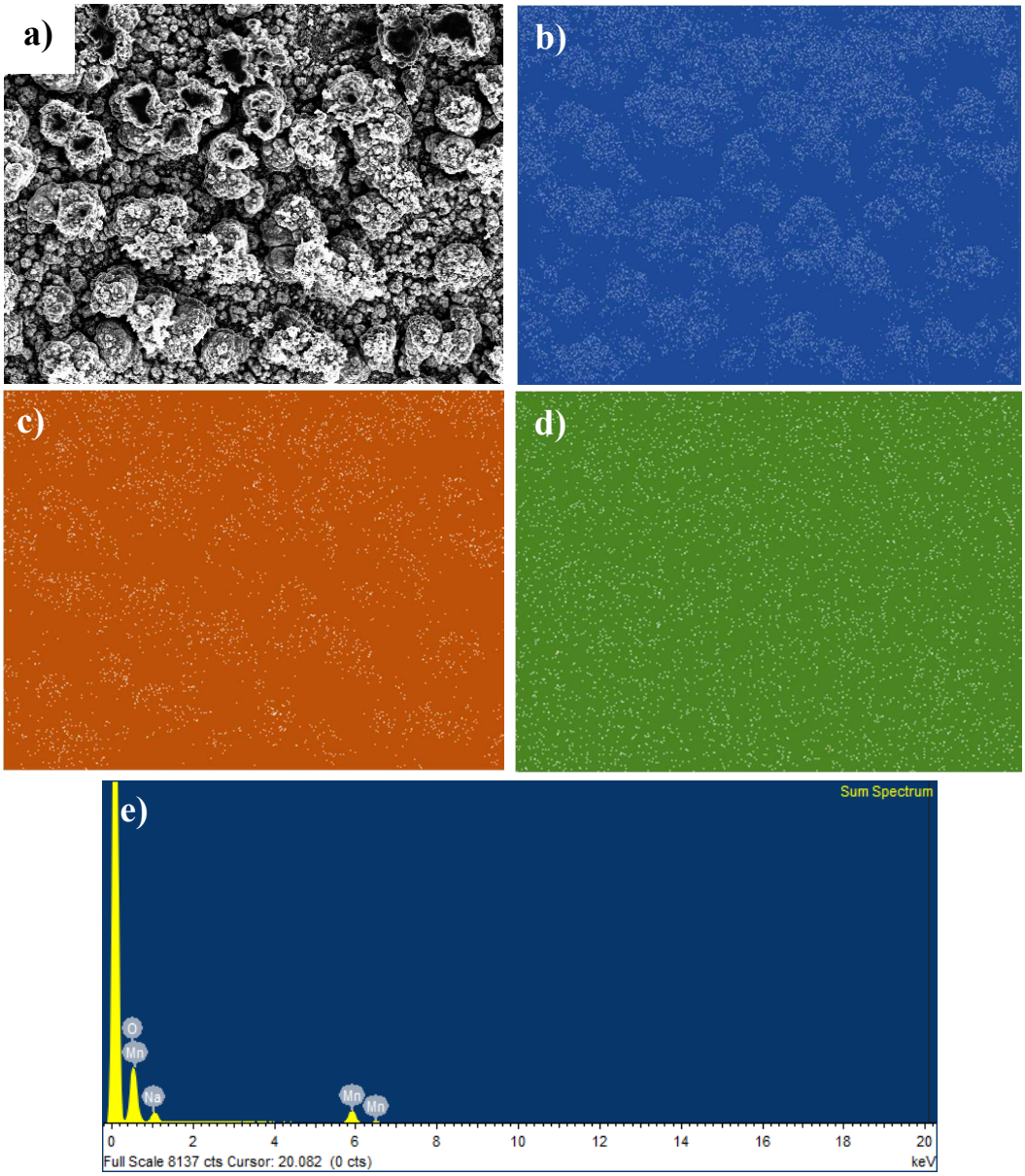



Figure 4.2.8 SEM images of: a) 250 cycles, b) 500 cycles, c) 1000 cycles and d) sponge-like structure of $MnO_2$ species. The images on the right-hand side represent a zoom-in version of the corresponding image on the left.

The EDX for the 1000 potential cycle electrode is presented in fig. 4.2.9.




| Spectrum | O | Na | Mn | Total |
|---|---|---|---|---|
| Sum spectrum | 63.05 | 7.26 | 29.69 | 100 |

Figure 4.2.9 SEM-EDX analysis of a 1000 potential cycles Mn electrode: a) SEM image, b) EDX oxygen map, c) EDX sodium map, d) EDX manganese map with the spots corresponding to the relative element underneath the image. e) EDX spectrum of image a) with quantitative table showing relative atomic % of each element present on the sample.

As observed in fig. 4.2.9, the EDX analysis revealed the presence of sodium species on the bulk of the electrode. Note that large sodium species were not observed on the surface leading to the conclusion that the detected sodium species are, in fact, inside the manganese oxide structure. This was previously mentioned in section 1.4.4 when introducing the various structures of the $MnO_2$ species. It was also mentioned in such section that $\alpha - MnO_2$ possess large tunnelled structures with large channel size (diameter of ca. ~ 4.6 Å), which may accommodate in its structure cations such as $Na^+$ or $K^+$. Therefore, based on these concepts, we suggest that the manganese oxide present on the surface of the film may correspond to $\alpha - MnO_2$.

## 4.3 Factors Affecting the Development of Charge Storage Capacity

Earlier in this section, it was suggested that hydrous oxide films deposited on metal surfaces *via* potential cycling were duplex in nature[2, 19] and could be represented schematically as: $M/MO_x/MO_a(OH)_b(OH_2)_c$ /aqueous phase. It was also mentioned that the extent of hydrous oxide film growth, and therefore, the extent of the charge storage capacity, was strongly dependent on the value chosen for the lower and upper limits of the potential sweep as well as on the sweep rate, the solution temperature and the solution pH.[20] The marked dependence of oxide growth rate on the lower limit of the potential sweep (found for a wide number of noble and non-noble transition metals [6, 20b, 21] is indicative of the essential role that partial reduction of the anhydrous oxide plays in the production of a thick deposit. In a previous work published by Lyons *et al.*[22] on the redox analysis at hydrous nickel oxide films in aqueous alkaline solution, it was suggested that partial reduction of the compact oxide layer may facilitate the rearrangement of oxidation species at the metal surface leaving it in a disrupted state. The authors mentioned that the subsequent reoxidation of the partially reduced metal surface yields to a restoration of the compact layer, while on the contrary, the outer region of the compact film remains in a more dispersed form. On further reductions, the latter material becomes incorporated into the hydrated outer layer. The authors also cast doubt on whether this rearrangement process involves detachment of oxidations or a certain weakening with a partial detachment of oxidation binding in the compact oxide layer. If a partial detachment of oxidation takes place, the partially reduced cations may be assumed to be displaced from normal lattice sites, which can make them more susceptible to oxidation

in the subsequent anodic sweep. Hence, a critical balance exists between the extent of oxide reduction needed to cause rearrangement at the metal/compact oxide interface and the loss of growth efficiency that arises if the reduction is too intense and extends into the thicker hydrous charge storage layer.

The importance of the upper sweep limit lies in the fact that high positive potentials extend oxygen penetration into the outer regions of the metal lattice and help generate a slight expansion and stress associated disruption at the metal/oxide interface. It may also facilitate uptake of a slight excess of oxygen by the oxide phase. If the upper limit is too anodic, the oxide becomes extensively passivated, which mitigates against hydrous oxide growth. Hydrous oxides are more stable than compact oxides and are more difficult to reduce as well. Therefore, for the compact layer to attain a reasonable thickness, an optimum upper limit should be found. The appropriate upper limit should correspond to the potential which exhibits the best compromise between two opposing cases: a high anodic potential which is required for a film growth, but not too high which would lead to the formation of a very unreactive layer (difficult to reduce readily at the lower potential limit).

Note that the study of the optimum lower and upper limits of the potentials for the growth of Mn oxide films was previously done in our lab (unpublished work by Shelly Stafford) Such study consisted on the analysis of charge storage capacity of a selected redox peak after a fixed number of cycles at a constant sweep rate. A relatively small number of cycles was used to maintain reasonably small current values (and hence, minimize potential errors associated with iR drop) and to ensure acceptable high level of reactivity throughout the surface layer. For the optimum lower limit determination, the high limit remained constant at 1.9 V *vs.* RHE while the lower limit varied in the range of -1 V. Opposite procedure was carried out for the determination of the upper potential limit. The observed optimum values, -0.4 V (*vs.* RHE) for the cathodic limit and 1.75 V (*vs.* RHE) for the anodic limit, were adopted throughout the present investigation for the growth of Mn oxide film. Furthermore, it is not only the magnitude of the potential range applied to the electrode which affects the growth of the Mn electrodes, the time on in the critical regions of the lower and upper limits of the sweep is also important.

The redox switching behaviour of the hydrated manganese oxide electrode in aqueous base to a potential sweep perturbation is now to be presented. Although it has already been noted at the beginning of this section and in previous chapters that the redox switching on Mn

electrodes is somewhat complex, the attempt to apply a simple first-order finite diffusion model to obtain quantitative transport information pertaining to the proton diffusion coefficient through the hydrous oxide layer occurred. Hence, it has been estimated to use the mathematical formalism presented by Aoki and co-workers[23] and more recently extended by Zivorad and Tomovski[24] to develop an expression for the inverse diffusive time constant $\tau_D = D\,L^{-2}$. These authors explained the finite diffusion problem under conditions of a linear potential sweep.

Diffusion transport parameters might be readily extracted from an analysis of the shape of the cyclic voltammogram as a function of sweep rate. Lyons' research group has previously reported the utilisation of the aforementioned analysis to investigate the redox switching behaviour for multicycled iron and nickel electrodes in aqueous alkaline solutions yielding to very interesting results. In line with the latter, the simplest variant of the Aoki model will be applied to Mn electrodes considering the situation where the charge percolation along the oxide layer and the proton diffusion in the pores can be treated to be irreversible. The conditions under which the latter holds may be recognised by examining the variation of the voltammetric peak potential with sweep rate. Thus, the cyclic voltammetric peak potential response as a function of the scan rate is examined for various hydrated manganese oxide films of varying thickness in fig. 4.3.1. Note that the thickness of the film is related with the number of cycles employed during the layer growth process. Briefly, when the relation between the voltammetric peak potentials and the sweep rate is linear, the diffusive charge percolation is considered to be reversible. In this view, it is defined the time window in which the latter holds. Two main observations can be extracted from fig. 4.3.1. Firstly, peak potentials for the anodic and cathodic for the whole series of cycles differ significantly between them and the cathodic peak seems to vary in a lower degree than the anodic peak when sweep rate changes. Secondly, the anodic peak potential begins to change significantly with increasing the sweep rate for values greater than 50 mV $s^{-1}$ whereas the cathodic peak shows constant shifting towards more negative potentials. However, the rate of change of the cathodic peak should be considered to remain constant for sweep rates below 100 mV $s^{-1}$ as the change between 10 mV $s^{-1}$ and 100 mV $s^{-1}$ is very low, of around ca. 4 % on average for all the thicknesses. Below 50 mV $s^{-1}$, the anodic peak potential remains stable with the sweep rate. Therefore, the redox switching reaction is regarded to be kinetically reversible at sweep rates below 50 mV $s^{-1}$. Note that the experimental data presented in this thesis for

the Nernstian peak shift as a function of pH analysis was taken from cyclic voltammograms recorded at a sweep rate of 40 mV $s^{-1}$.

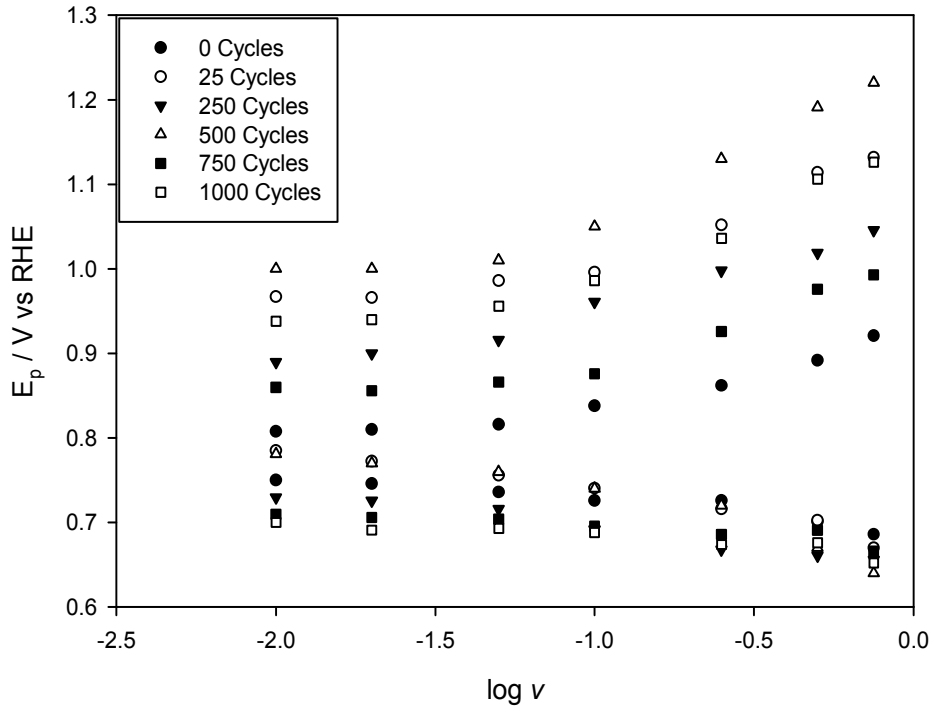



Figure 4.3.1 Variation of voltammetric peak potential with the log sweep rate for a series of multicycled Mn electrodes in 1.0 M NaOH at 25°C. Attention is focused on the main anodic and cathodic charge storage peaks corresponding to the Mn (III) / Mn (IV) redox transition.

Murray *et al.*[25] proposed that the charge capacity C of an electroactive polymer film can be treated to be directly proportional to the hydrous oxide charge capacity $Q$. Therefore, the variation of hydrous oxide charge capacity $Q$ as a function of the sweep rate is presented in fig. 4.3.2. It is noticeable that the film thickness plays a significant role in the charge capacity behaviour, *e.g.* for thick films (more than 25 cycles growth) the charge capacity exhibits a pronounced decrease in its values as the sweep rate increases for the whole range of sweep range. Indeed, the charge capacity decreases by ca. 90 % when the sweep rate is increased from 0.2 V $s^{-1}$ to 0.8 V $s^{-1}$. On the other hand, for thin oxide films (1 to 25 cycles), the charge capacitance values remain reasonably invariant with sweep rate between 0.8 V $s^{-1}$ to 0.2 V $s^{-1}$, and then a slight increase is observed for sweep rate values below 0.2 V $s^{-1}$.

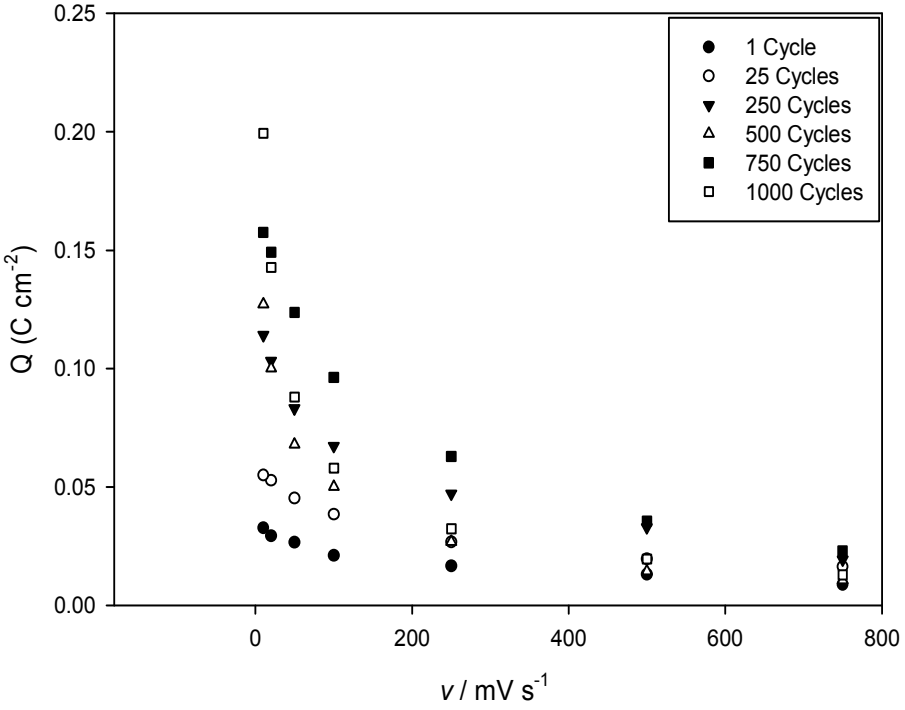



Figure 4.3.2 Comparison of the variation of voltammetric redox charge capacity *Q* as a function of sweep rate for a series of Mn oxide hydrous films grown under potential cycling conditions for a various number of cycles. Attention is focused on the main anodic and cathodic charge storage peaks corresponding to the Mn (III) / Mn (IV) redox transition.

The effect of sweep rate on the charge storage behaviour of hydrous oxides of multicycled films is in broad agreement with the theory of Laviron[26] for redox polymer electrodes. This theory states that with thinner films there is sufficient time at normal sweep rates for the redox reaction to extend to virtually all parts of the surface layer, *e.g.* the charge is virtually independent of the sweep rate (see fig. 4.3.2). However, as the film becomes thicker, there is not enough time (apart for very slow sweep rates) for the reaction to propagate throughout the hydrous layer. Hence, the charge capacity values drop dramatically as the sweep rate is increased. Similar results have been observed for hydrous iron oxide films in alkaline solutions as well as for hydrous nickel oxide films in the base.[22, 27] The hydrous Mn oxide films, presented in this work, are likely non-uniform (see fig. 4.2.9). Due to partially crystallisation (note that $MnO_2$ exhibit four defined crystal structures, see chapter 1.4.4) some parts of the film may be in poor contact with the electrode, which would explain the reason why even with thinner films there is a small steady decrease in the recorded charge capacity values with increasing sweep rate (see fig. 4.3.2). The increased charge capacity at

very slow sweep rates is possibly due to ion penetration into the more anhydrous compact material in the inner regions of the oxide film.

These observations may be justified using the simple diffusive model previously mentioned (Aoki's model). In this perspective, the potential applied at thinner oxide films (1 and 25 cycles) at normal sweep rates may have enough time to spread through all regions of the dispersed hydrous oxide layer. This is supported by the fact that redox charge capacity is effectively independent of the sweep rate. The extensive mathematical formulation of the Aoki model for the determination of diffusive time constant is beyond the scope of the present review and can be found in ref. 24-26. Therefore, only the final equations of the model will be highlighted in this section. The diffusion coefficient in a film in which the redox reaction is reversible takes the following form:

$$I_p = 0.4463nFA\Gamma\sqrt{\frac{nF}{RT}}\left(\frac{D}{L^2}\right)^{0.5}\upsilon^{0.5} \tag{4.3.1}$$

where $\Gamma$ and $L$ refers to the surface coverage and the layer thickness respectively and the parameter D accounts for the diffusion coefficient. Eqn. 4.3.1 is the well-known Randles-Sevcik expression characteristic of semi-infinite diffusion typically observed in very thick layers. The diffusive time constant or frequency $\tau_D = D\ L^{-2}$ can be extracted from the slope of a graph $I_p$ versus $\upsilon^{0.5}$. The variation of voltammetric peak current with the square root sweep rate for a series of multicycled Mn electrodes in 1.0 M NaOH at 25°C is presented in fig. 4.3.3. It is noted from fig. 4.3.3 the good Randles-Sevcik linearity for sweep rates between $0.01\ V\ s^{-1}$ to $0.5\ V\ s^{-1}$. However, the current response begins to rise from sweep rates higher than $0.5\ V\ s^{-1}$. It has been suggested by Aoki and co-workers that for intermediate thicknesses, that is $\sim 100 - 500$ cycles, the peak current $I_p$ may vary with the sweep rate according to:

$$I_p = 0.4463nFA\left(\frac{\Gamma D}{L^2}\right)W^{1/2}\,tanh[\Upsilon] \tag{4.3.2}$$

where:

$$\Upsilon = 0.56\sqrt{W} + 0.05W \tag{4.3.3}$$

The parameter W is given, according to Aoki, by:

$$W = \frac{nFL^2v}{DRT} \tag{4.3.4}$$

and it can be considered as the ratio of the layer thickness and the diffusion layer thickness in the film.

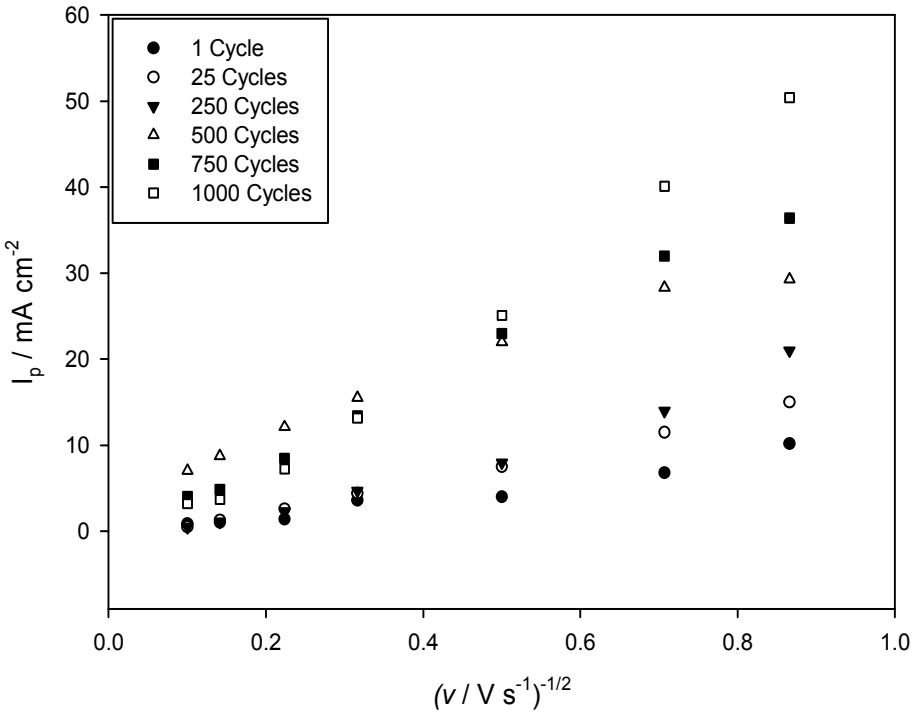



Figure 4.3.3 Typical Randles-Sevcik graphs recorded for a series of multicycled Mn electrodes in 1.0 M NaOH at 25°C as a function of several oxide growth cycles. Attention is focused on the main anodic and cathodic charge storage peaks corresponding to the Mn (III) / Mn (IV) redox transition.

Eqn. 4.3.3 may be rewritten in a non-dimensional format to produce a working curve as follows:

$$\Psi = \frac{I_p}{nFA\left(\Gamma/_L\right)}\left\{\frac{RT}{nFDv}\right\}^{1/2} = 0.446\, tanh[\Upsilon] \tag{4.3.5}$$

Therefore, the diffusive frequency $\tau_D = D\, L^{-2}$ might be evaluated *via* numerical analysis of expression 4.3.2:

$$G(\tau_D) = \alpha {\tau_D}^{0.5}\, tanh\left\{\beta {\tau_D}^{-0.5} + \frac{\gamma}{\tau_D}\right\} - I_p = 0 \tag{4.3.6}$$

where:

$$\alpha = 0.4463 \frac{(nF)^{3/2}}{(RT)^{1/2}} A\Gamma v^{0.5} \tag{4.3.7}$$

$$\beta = 0.56 \sqrt{\frac{nFv}{RT}} \tag{4.3.8}$$

$$\gamma = 0.05 \left(\frac{nFv}{RT}\right) \tag{4.3.9}$$

By using a standard numerical protocol, *e.g.* the Bisection algorithm[28], the roots of the $\tau_D$ can be extracted from eqn. 4.3.6. This equation allows the determination of the diffusive frequency $\tau_D = D\,L^{-2}$ if the peak current $I_p$ and surface coverage $\Gamma$ are known at a given sweep rate $v$. Furthermore, if the layer thickness L can be predicted then the diffusion coefficient D may be calculated.

In this work, eqn. 4.3.6 and the Randles-Sevcik equation have been used to calculate the diffusive frequency for relatively thin and thick layers, respectively. Fig. 4.3.4 shows the diffusive frequency results obtained for a multicycled Mn electrode in 1.0 M NaOH at 250°C as a function of several growth cycles.

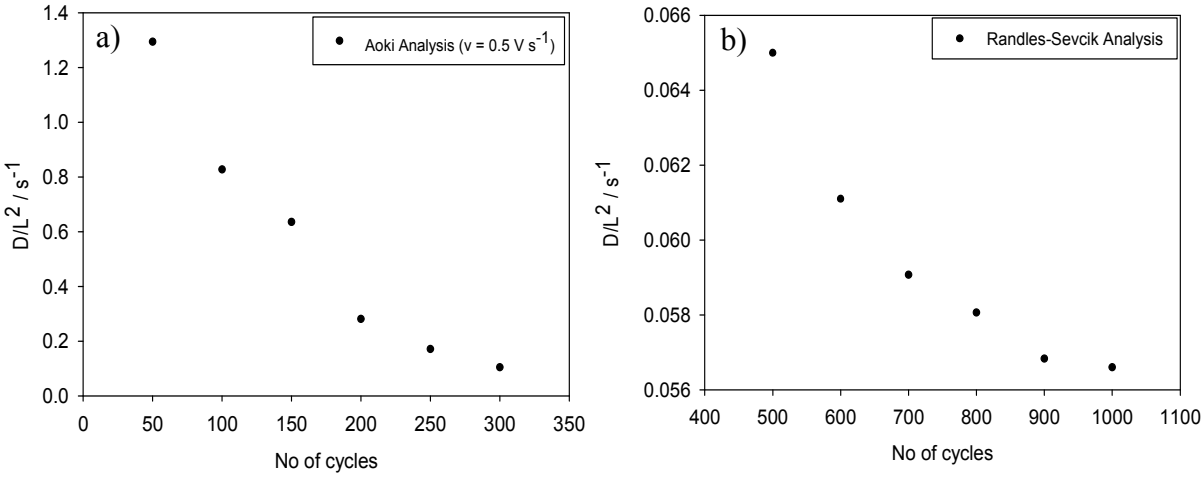



Figure 4.3.4 Variation of diffusive frequency characterising redox switching in multicycled hydrous oxide Mn electrodes in 1.0 M NaOH at 25°C with number of oxide growth cycles. a) Aoki analysis and b) Randles-Sevcik analysis. The results were calculated considering the surface coverage to be 0.8.

As observed in fig. 4.3.4 (a), the diffusive frequency decreases rapidly with increasing number of growth cycles N from a value of ca. $1.3\ s^{-1}$ for the thinnest manganese oxyhydroxide film to ca. $0.1\ s^{-1}$ for layers formed at 300 cycles. Similar behaviour, it is observed in fig. 4.3.4 (b). However, for very thick films, the diffusive frequency tends to decrease slower as the film becomes thicker, changing from ca. $0.066\ s^{-1}$ for electrodes with 500 growth cycles to ca. $0.56\ s^{-1}$ for the thickest oxide film. The percentage difference for intermediate thicknesses that is from 50 to 300 cycles is approximately 90% whereas, for thicker films, the percentage difference is ca. 15%.

In this work, ellipsometry analysis has not been done to estimate the absolute value of the layer thickness L, therefore it was not possible to determine the diffusion transfer coefficient from diffusive frequency values. Instead, it has been considered opportune to deal with the diffusive frequency $\tau_D = D\ L^{-2}$.

## 4.4 The Influence of the Solution pH on the Voltammetric Response

The influence of the solution pH on the voltammetric response as a function of number of potential cycles is now presented. Due to the large number of graphs required to discuss this effect in detail (note that six different number of growth cycles will be presented), a comparison is only given to voltammetric behaviour exhibit by a clean Mn electrode (1 cycle), a medium thick oxide layer electrode (500 cycles) and a very thick oxide layer (1000 cycles). Therefore, the voltammetric response of an electrode with 1 growth cycle will be presented and discussed first, followed by that for the 500 growth cycles and finally the one for 1000 cycles. The voltammetric behaviour of the Mn electrode with 1 growth potential cycle is outlined in fig. 4.4.1. Table 4.4.1 shows the regression lines of the fig. 4.4.1b and c. As it can be seen in fig. 4.4.1c, the peak A2 exhibit a positive slope which is very unusual, whereas fig. 4.4.1b exhibit a typical super-Nernstian shift. The voltammetric behaviour of the Mn electrode with 500 growth potential cycles is outlined in fig.4.4.2. Table 4.4.2 shows the regression lines of figs 4.4.2 b and c. Similar peak potential shift behaviour than that for the 1 cycle is observed in fig 4.4.2. Note that for a 500-growth oxide cycles the electrode peak labelled A2 exhibits a super-Nernstian shift. The voltammetric behaviour of the Mn electrode with 1000 growth potential cycles is outlined in fig. 4.4.3. Table 4.4.3 shows the regression lines of the fig. 4.4.3b and c. Potentials of the anodic and cathodic charge storage

peaks (A1, A2, C1 and C2) do not exhibit a regular Nernstian pH response of 0 mV $pH^{-1}$ unit with respect to a pH-dependent reference electrode (RHE). Instead, they display a super-Nernstian potential peak shift.

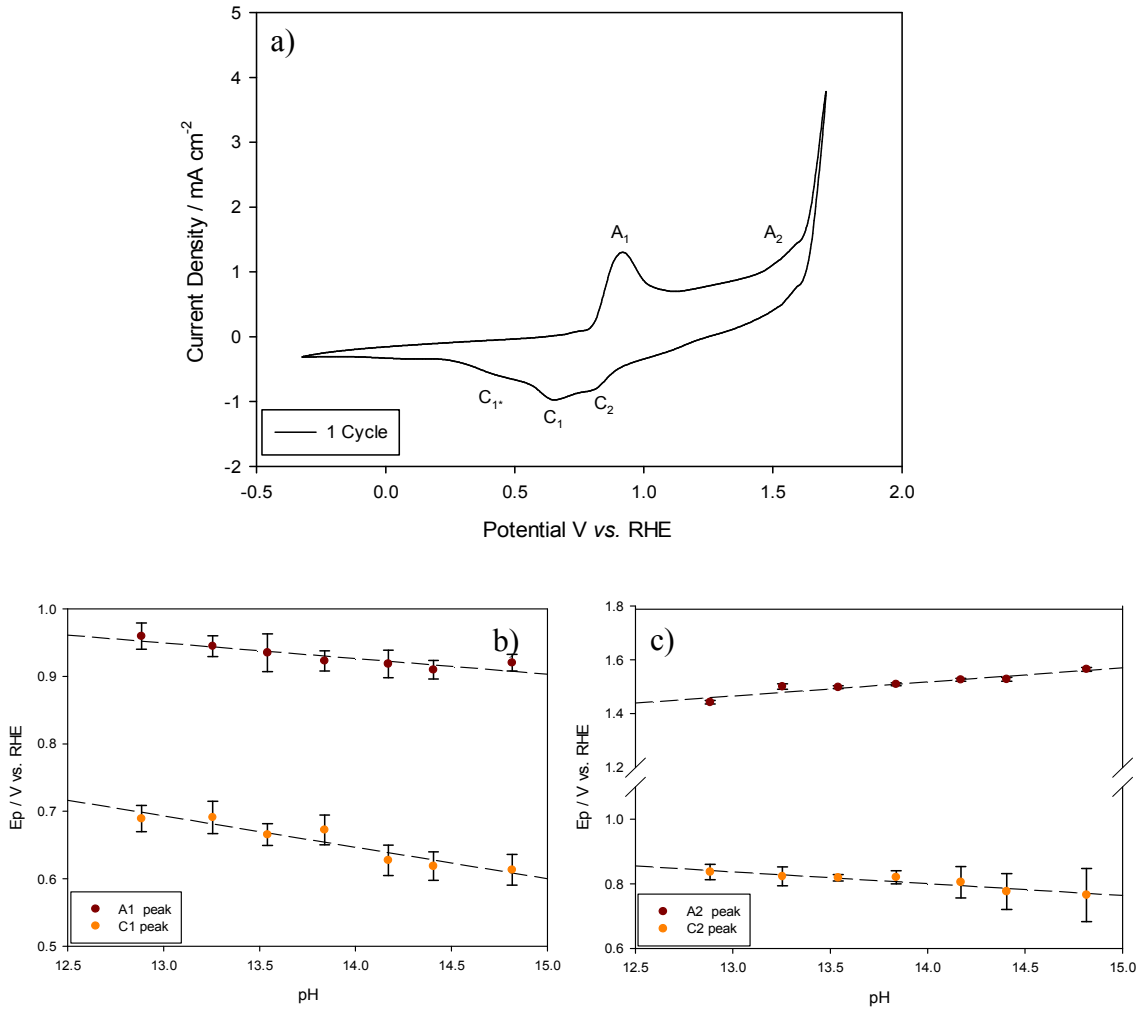



Figure 4.4.1 a) Cyclic voltammogram of an Mn electrode with 1 oxide growth cycle. The experimental conditions are: 1.0 M NaOH, 25°C and 0.4 V $s^{-1}$; b and c) Variation of the voltammetric peaks A1 and A2 as a function of pH.

| No Growth Cycles | Anodic slope / mV $pH^{-1}$ | | Cathodic slope / mV $pH^{-1}$ | |
|---|---|---|---|---|
| | A1 | A2 | C1 | C2 |
| 0 | $y = -0.023x + 1.251$<br>$R^2 = 0.8287$ | $y = 0.052x + 0.787$<br>$R^2 = 0.8979$ | $y = -0.046x + 1.298$<br>$R^2 = 0.8871$ | $y = -0.037x + 1.314$<br>$R^2 = 0.8858$ |

Table 4.4.1 Regression lines eqn. corresponding to the variation of the corresponding voltammetric peaks as a function of pH presented in fig. 4.4.1 b and c.

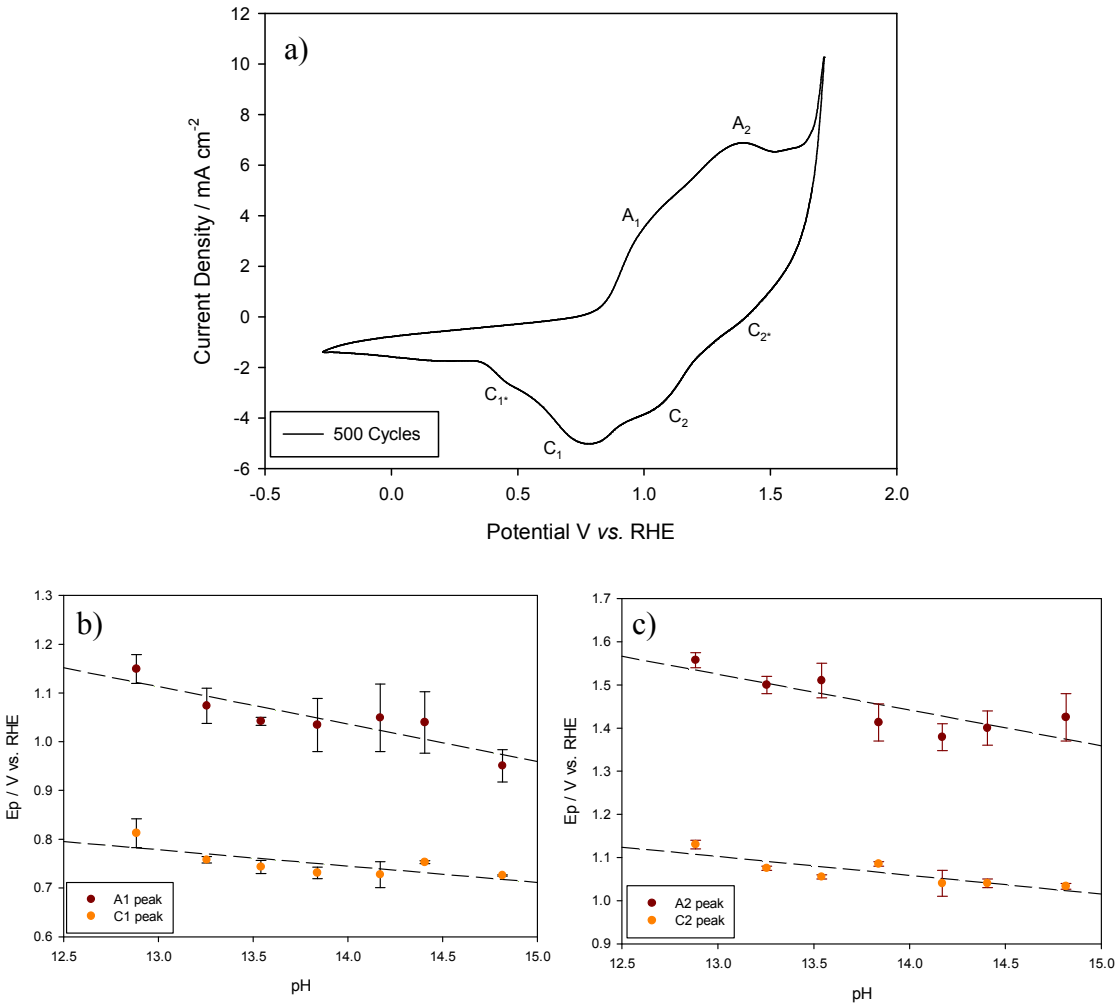



Figure 4.4.2 a) Cyclic voltammogram of a Mn electrode with 500 oxide growth cycles. The experimental conditions are: 1.0 M NaOH, 25°C and 0.4 V s-1; b and c) Variation of the voltammetric peaks A1 and A2 as a function of pH.

| No Growth Cycles | Anodic slope / mV pH $^{-1}$ | | Cathodic slope / mV pH $^{-1}$ | |
|---|---|---|---|---|
| | A1 | A2 | C1 | C2 |
| 500 | y = -0.077x + 2.111<br>$R^2$ = 0.8154 | y = -0.08x + 2.603<br>$R^2$ = 0.8819 | y = -0.044x + 1.215<br>$R^2$ = 0.9067 | y = -0.031x + 1.668<br>$R^2$ = 0.8961 |

Table 4.4.2 Regression lines eqn. corresponding to the variation of the corresponding voltammetric peaks as a function of pH presented in fig. 4.4.2 b and c.

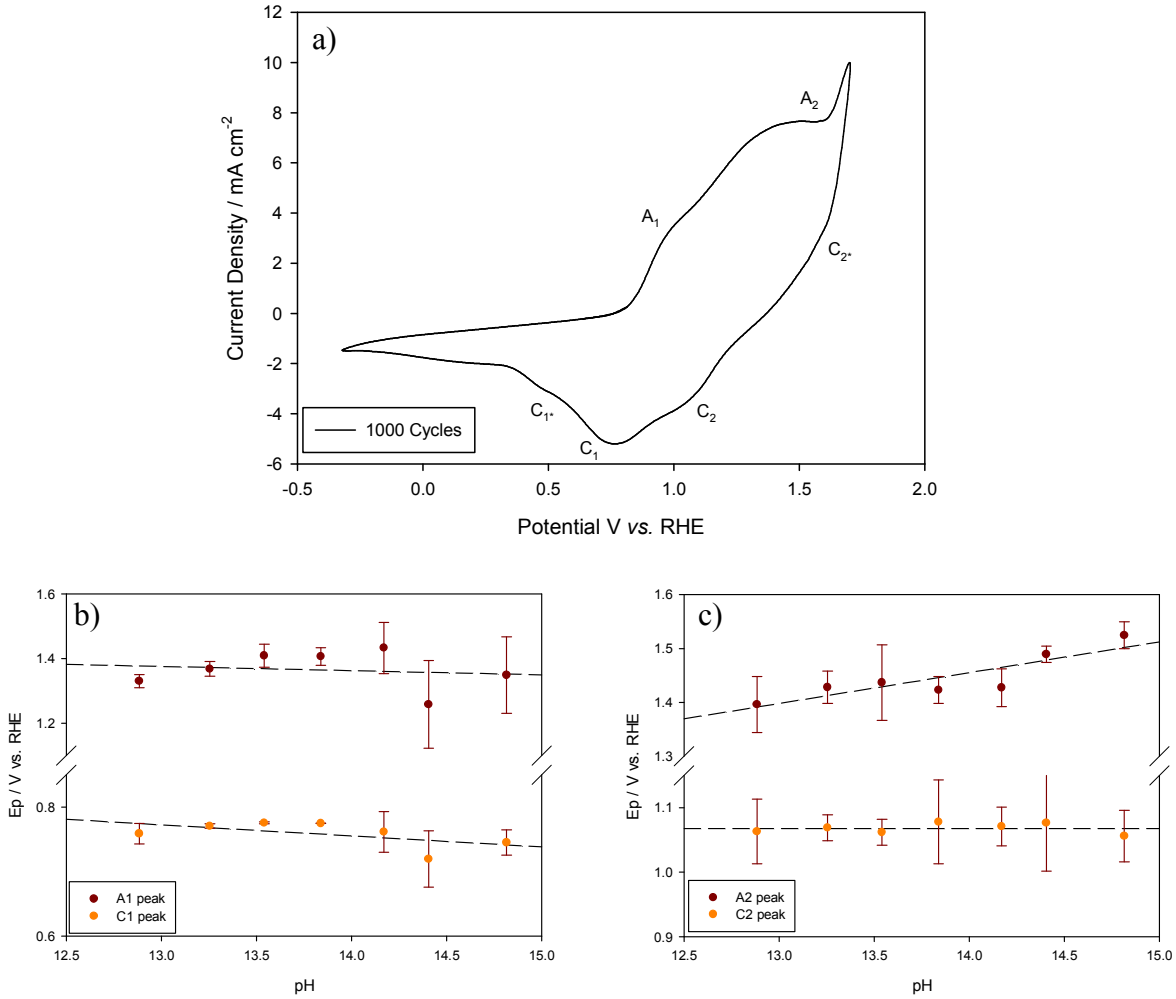



Figure 4.4.3 a) Cyclic voltammogram of a Mn electrode with 1000 oxide growth cycles. The experimental conditions are: 1.0 M NaOH, 25°C and 0.4 V s-1; b and c) Variation of the voltammetric peaks A1 and A2 as a function of pH.

| No Growth Cycles | Anodic slope / mV pH $^{-1}$ | | Cathodic slope / mV pH $^{-1}$ | |
|---|---|---|---|---|
| | A1 | A2 | C1 | C2 |
| 1000 | y = -0.013x + 1.546<br>$R^2$ = 0.8481 | y = 0.057x + 0.654<br>$R^2$ = 0.7556 | y = -0.017x + 0.995<br>$R^2$ = 0.8662 | y = 2E-05x + 1.068<br>$R^2$ = 0.9561 |

Table 4.4.3 Regression lines eqn. corresponding to the variation of the corresponding voltammetric peaks as a function of pH presented in fig. 4.4.3 b and c.

Some authors related this effect to the nature of the oxide layer. In this sense, Bode, Dehmelt and Witte suggested that the oxidised state of the oxide layer may be more negative than the reduced state and that causes the super-Nernstian shift.[27] Other authors, as mentioned in

section 1.4, suggested that the observation of a super-Nernstian potential shift was probably connected with the effect of specific adsorption of $OH^-$ ions onto the electrode surface, which may cause an increase in both the dielectric constant and the compact layer capacity and, therefore, it changed the hydroxide Mn film surface charge. In 1987 Lyons and Burke[29] added their bit proposing that the surfaquo groups were connected to the oxide surface by two bridging oxygen species $(-O\ -)$.

The influence of surfaquo groups in the electrochemical behaviour of oxide films has been extensively investigated on several thermal oxides[29-30], passive oxides[30b, 31], and hydrous oxide surfaces[32]. Further to their review, Lyons *et al.*[33] suggested that the surfaquo groups were located throughout the hydrous layer. Especially significant is the work carried out by Lyons and Floquet[30a] in 2011 regarding the effect of pH on the voltammetric behaviour of $MnO_2$ oxide layers. In such work, the authors observed peak potential shifts with pH (8.0 and 13.6) in the order of -50 mV $pH^{-1}$ (*vs.* RHE) for hydrous Mn oxide films with the exception of an observed peak shift of -113 mV $pH^{-1}$ (*vs.* RHE) for the A1 oxidation peak. To explain this shift, the authors assumed the formation of an acidic product *e.g.* a reaction involving a ratio of hydroxide ions (or protons) to electrons of 115/59 or ca. 2/1 resulting in the following reaction scheme:

$$MnOOH.nH_2O \rightarrow MnO(OH)_3^-.(n-2)H_2O + 2H^+ + e^- \qquad (4.4.1)$$

$$MnO(OH)_3^-.(n-2)H_2O + H^+ \rightarrow MnO_2 + nH_2O \qquad (4.4.2)$$

Eqn. 4.4.1 may also be represented as $MnO(OH)_3^-.H_f^-$, where $H_f^-$ is a proton lost from a co-ordinated water molecule. This thesis proposes a similar interaction of $OH^-$ ions with the hydrous Mn oxide surface (regardless the film thickness), since a similar super-Nernstian peak potential shift than that noted by Lyons and Floquet is observed for all the peaks (note that A2 in fig. 4.4.1c and 4.4.3c have a positive shift). It is also important to mention the difference in the peak shift with pH of the redox couple A2 and C2. As seen in Tables 4.4.1 - 4.4.3, the peak potential shift for the cathodic peak C2 is systematically lower than that for A2 for in the thickness studied, being the thickness (1000 cycles) invariant with respect to $OH^-$ solution concentration. This would be explained by the fact that the previous layer formation (A2 anodic peak) during OER creates a more compact and less hydrated oxide

film, hence the smaller potential shift. Note that the more hydrated and amorphous the film is, the more affected will be by the adsorption of $OH^-$ ions onto the film's surface. The latter implies that the final product at the anodic end of the sweep is not totally anhydrous but partially hydrous, since the previously super-Nernstian shift is observed. It is assumed that water molecules are present at both in the surface, including the internal surface, and in the defect centres. It is important to mention that the Nernstian analysis on electrode films only holds if the redox couple is reversible. Therefore, as it was mentioned in section 1.4, care should be taken when dealing with the analysis of peak potentials shift with pH, especially for very thick films where, according to fig. 4.3.1, at sweep rates higher than 40 mV $s^{-1}$ the redox couple becomes irreversible. The observation of the positive shift noted for peak A2 in figs. 4.4.1c and 4.4.3c are currently being investigated and thus, results are not presented yet.

## 4.5 Kinetic Analysis

This section focuses on the description of results of a comprehensive kinetic analysis performed on hydrous oxyhydroxide manganese films fabricated under different potential cycling regimes in aqueous alkaline solution. These studies were performed both as a function of hydrous oxide layer thickness, and as a function of base concertation using steady-state polarization techniques recorded at a sweep rate of 1 mV $s^{-1}$. The latter data was subsequently transformed into Tafel format, and the Tafel slope evaluated.

Tafel analysis is very useful to determine mechanistic information of the oxygen evolution reaction through calculating Tafel slopes, which may help to reveal if various kinetic steps in the reaction are determined by chemical or electron transfer steps. It can also provide information on possible rate-determining steps (RDS) for a multistep reaction. The results of a series of iR compensated OER steady-state polarisation curves recorded at a series of multicycled Mn electrodes in 1.0 M NaOH solutions are presented in fig. 4.5.1. In addition, the variation of Tafel slope values with respect to the film thickness in 1.0 M NaOH solutions is presented in fig. 4.5.2.

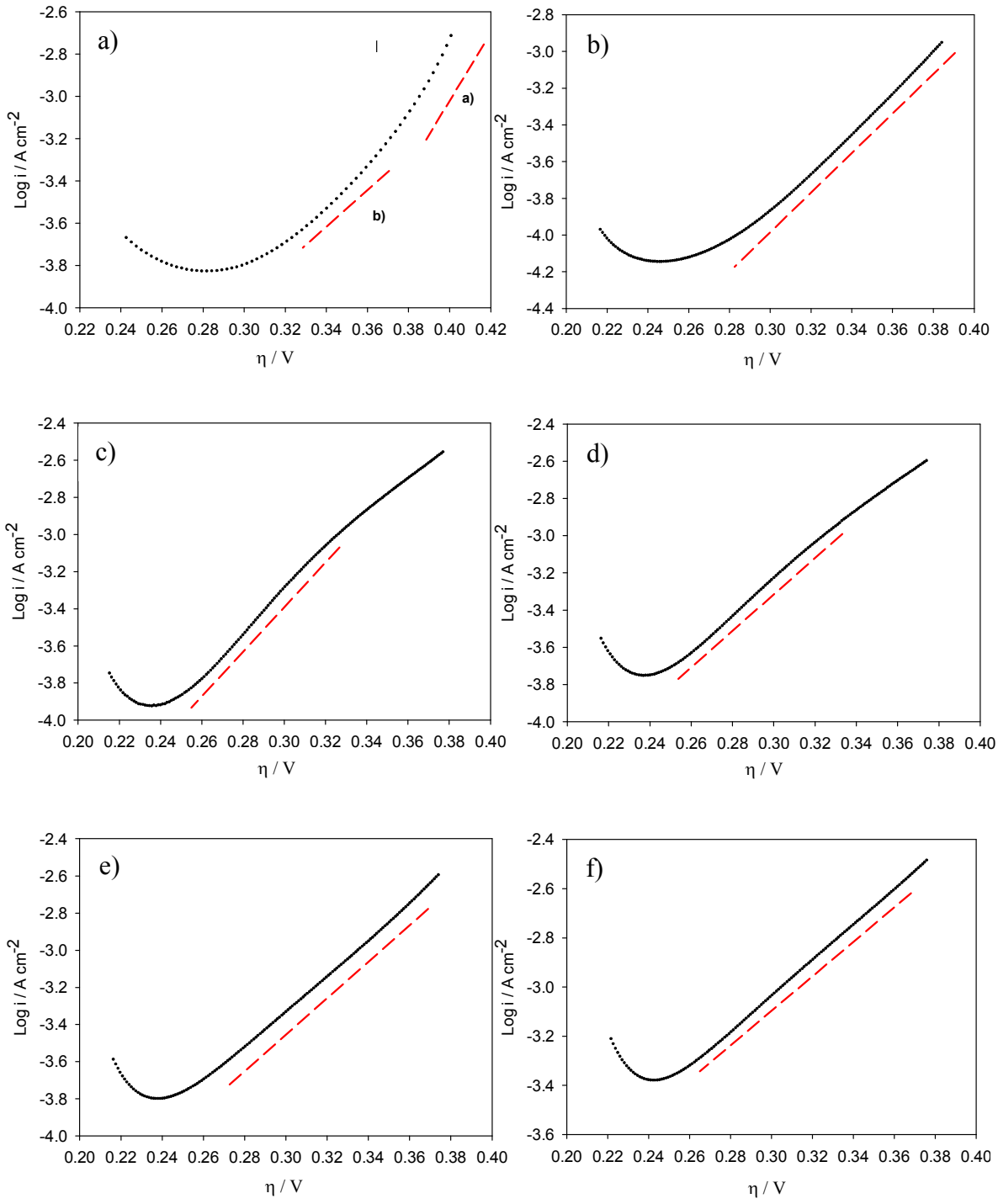



Figure 4.5.1 IR corrected steady-state polarisation curves recorded in the direction of increasing potential on a Mn electrode at sweep rate of 1 mV $s^{-1}$ in 1.0 M NaOH at 25°C. Fig a) 0 cycles. Tafel slope a) 41.06 ± 8.31mV $dec^{-1}$ and slope b) 120.3 ± 3.98 mV $dec^{-1}$; b) 25 cycles. Tafel slope 86.9 ± 3.71 mV $dec^{-1}$; c) 250 cycles. Tafel slope 76.38 ± 6.05 mV $dec^{-1}$; d) 500 cycles. Tafel slope 117.5 ± 10.24 mV $dec^{-1}$; e) 750 cycles. Tafel slope 110.2 ± 7.78 mV $dec^{-1}$; and f) 1000 cycles. Tafel slope 128.3 ± 10.6 mV $dec^{-1}$.

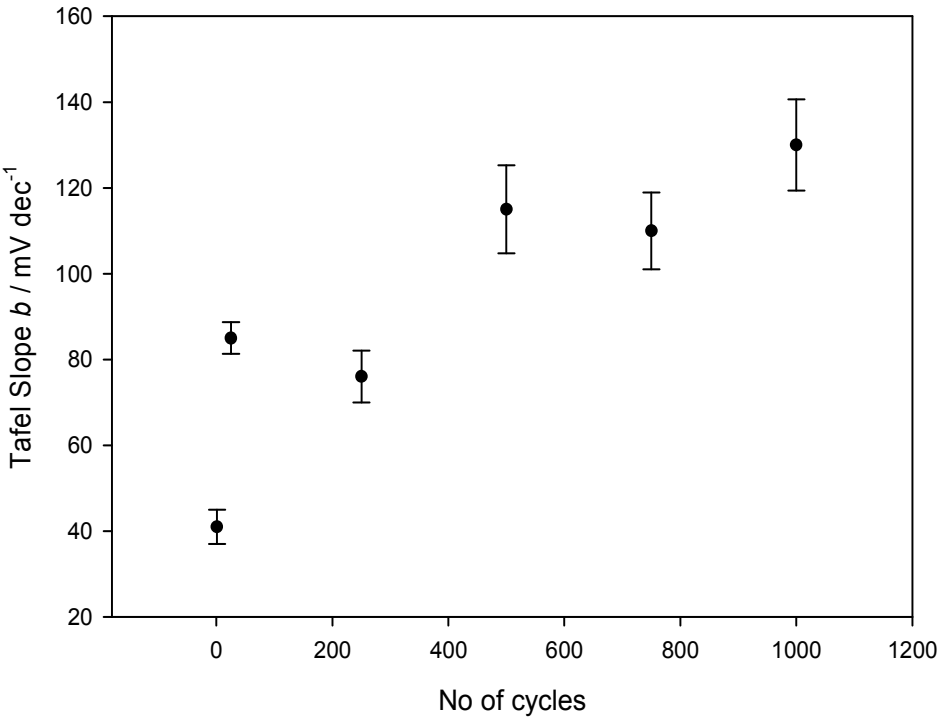



Figure 4.5.2 Tafel slope of Mn electrode as a function of number of potential cycles in 1.0 M NaOH at 25°C. These values were obtained from the steady-state polarisation curves presented in fig. 4.5.1.

It is evident from fig. 4.5.2 that the Tafel slope changes significantly with film thickness. It can be stated that the thicker the hydrous Mn oxide film, the greater the Tafel slope observed. The observed increase in Tafel slope values as the film becomes thicker is suggested to be related to the magnitude of the film resistance and the resistance contribution of surfaquo groups adsorbed on the electrode surface. These two parameters would increase in magnitude as the thickness increases. This assumption is supported by the fact that the oxyhydroxide outer layer of the electrode surface is a semiconductor, as mentioned in section 1.4.4. To better understand the effect of film thickness on the catalytic behaviour of the electrodes, the contributions of both the ohmic film resistance and the surfaquo resistance will be further investigated, in chapter 6, using electrochemical impedance spectroscopy (EIS).

As previously mentioned, Tafel slope provides important mechanistic information on the OER mechanism. The Tafel slope of ca. 120 mV $dec^{-1}$ observed for many oxides coated Mn electrodes can be associated with the first electron transfer step in the overall sequence describing oxygen evolution being slow and rate determining. This slow rate-determining

step involves the discharge of a $OH^-$ moiety at the oxymanganese surfaquo group, Mn (IV), to generate a Mn (V) surface group as follows:

$$(-O-)_2[MnOOH(OH_2)_2]^- + OH^- \rightarrow (-O-)_2[MnO(OH)_2(OH_2)]^- + H_2O + e^- \quad (4.5.1)$$

It is proposed here that the previous step may be followed by the following sequence of steps, which generate molecular oxygen *via* decomposition of highly active Mn (VI) intermediate and regenerate the Mn (IV) surfaquo group:

$$(-O-)_2[MnO(OH)_2(OH_2)]^- \rightarrow (-O-)_2MnO(OH)_2(OH_2) + e^- \quad (4.5.2)$$

$$(-O-)_2MnO(OH)_2(OH_2) + 3OH^- \rightarrow (-O-)_2[MnOOH(OH_2)_2]^- + O_2 + H_2O + 2\,e^- \quad (4.5.3)$$

If we add together the above equations and cancel out the common terms, we obtain the oxygen evolution reaction:

$$4OH^- \rightarrow O_2 + 2H_2O + 4e^- \quad (4.5.4)$$

Note that the Mn (VI) intermediate, $MnO(OH)_2(OH_2)$, should be stable at high pH and under conditions of active oxygen evolution. According with the above mechanism it can be shown that if the first electron transfer is rate determining, the predicted Tafel slope is 120 mV $dec^{-1}$, whereas if the second electron transfer is rate determining, the Tafel slope is presume to be 40 mV $dec^{-1}$. In fig 4.5.2, it is observed an increase on the Tafel slope from 40 mV $dec^{-1}$ for uncycled electrodes to a significantly larger values as the number of potential cycles increases, typically in the range of 80 to 120 mV $dec^{-1}$. It can be noted that the theoretical Tafel slope for a porous film can exhibit significantly higher numerical values as the layer thickness increases. Hence, the Tafel slope for a porous electrode is twice of that for a plane electrode. Recall from section 1.2.5 that: (i) the observation of a 80 mV $dec^{-1}$ Tafel slope indicates that the RDS involves a two electron transfer reactions, and (ii) that the RDS occurs after an electron transfer step. Therefore, the observation of a Tafel slope of ca. 80 mV $dec^{-1}$ indicates that the rate-determining step is mainly due to the second electron transfer step in tandem with a partially difficult electron transfer occurring at the first step of the above sequence.

The variations of the overpotential measured at 1 mA $cm^{-2}$ as a function of several growth cycles are presented in fig. 4.5.3. The overpotential values were measured in the linear Tafel region. An interesting observation can be seen in fig. 4.5.2 upon the error values associated with each growth cycle. The magnitude of the error associated with the measurement of the overpotential at a fixed current density slightly increases as the layer thickness increases. It is suggested that for longer growth time scale *e.g.* the formation of a thick layer *via* 1000 growth cycles takes ca. 28 hr, the uncertainty of data measurement increases due to possible alterations in the cell such as solution temperature change.

As mentioned in chapter 3, the cell in which the growth of the hydrous Mn oxide layer occurs is temperature controlled (jacked cell) with a Teflon® top covering the cell, used to ensure no contamination from possible particles, mainly dust. However, while the Teflon top does provide a protection against particles, it does not seal the cell perfectly and, therefore, the surface electrolyte layer may be exposed to direct contact with air at room temperature. Note that due to the long time scales required to produce a very thick layer, the process was left running overnight and, therefore, a drop in the room temperature is to be expected and that would change the "real" electrolyte solution affecting the growth of the hydrous Mn oxide film.

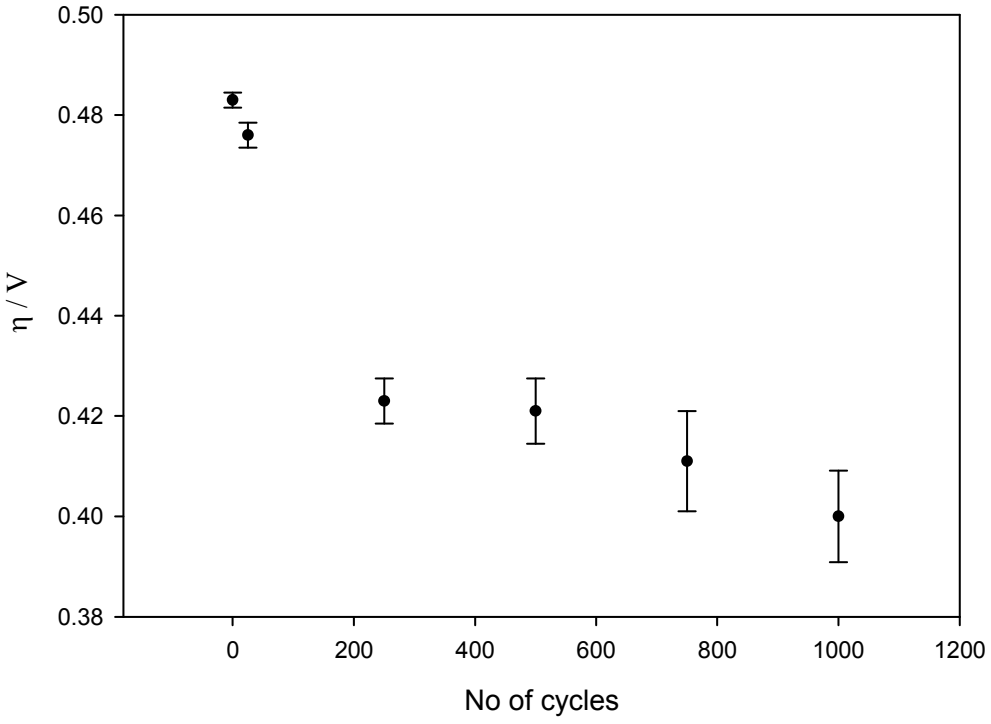



Figure 4.5.3 Oxygen evolution overpotential, measured at 1 mA $cm^{-2}$, of various multicycled Mn electrodes in 1.0 M NaOH at 25°C. These values were obtained from the steady-state polarisation curves presented in fig. 4.5.1. Error bars represent standard deviations of three different samples.

The impact of temperature in both the growth of an oxide film and the electrochemical behaviour of the electrode has been extensively investigated. It was highlighted that electrolyte temperature plays an important role in the growth of electrodes by potential multicycle. It seems that hydrous oxide films appear to be unstable under specific temperature conditions. Lyons[20a] mentioned the effect of electrolyte temperature on a hydrous iron oxide film generated under potential multicycling in 1.0 M NaOH at 25°C. He observed that there was a substantial increase in the rate of loss of oxide charge capacity with increases in the solution temperature above about 40°C. In view of the latter, it was decided that the impact of electrolyte temperature in the electrochemical behaviour of Mn electrodes would be investigated in a further analysis.

It is also clear from fig. 4.5.3 that the growth of the hydrous Mn film contributes to the decrease of the OER overpotential. An increase in electrocatalytic activity can be observed with the formation of the hydrous manganese oxide indicated by a lowering of the overpotential by ca. 90 mV from ca. 0.49 V to ca. 0.4 V corresponding to 0 cycles and 1000 cycles, respectively. As mentioned in section 1.4.4, tunnelled structures were proven to have high intrinsic activities towards the OER since they allow intimate contact between the solid and the liquid phases. At high potentials towards the OER, the film is mainly formed by Mn (IV) species ($MnO_2$) and to a less extent by Mn (III) species (either MnOOH or $Mn_2O_3$ species). Therefore, as the film becomes thicker, the surface of the hydrous oxide becomes more porous and thus favours the electron exchange in the oxide/electrolyte interphase. This is supported by SEM images presented in figs. 4.2.7 and 4.2.8. In line with the latter, the variation of the OER onset potential variation with film thickness is presented in fig. 4.5.4. The OER onset potential can be thought of as an activation barrier like in traditional chemical kinetics of a chemical reaction. As observed in fig. 4.5.4, the onset drops drastically by ca. 50 mV, from ca. 1.62 mV to ca. 1.57 mV (*vs.* RHE), as the film thickness increases. Another fashion to investigate the effect of layer thickness in the kinetic behaviour of hydrous Mn electrodes is the analysis of the current density recorded at a given potential as a function of n$^o$ of cycles. Fig. 4.5.5 shows the variation of the current density at a fixed overpotential of 0.44 V. The current density was found to increase as a function of oxide thickness. Similar increases in current density have been found for both hydrous iron oxide and hydrous nickel oxide when subjected to potential multicycling.[20a, 34] This increase, in tandem with the decrease in both the OER onset potential and the OER overpotential, suggests that, with the formation of the hydrous oxide, there is an intrinsic in catalytic activity due to: (i) the

lowering of the activation barrier for the OER, and (ii) the increase in surface active sites available to catalyse the OER.

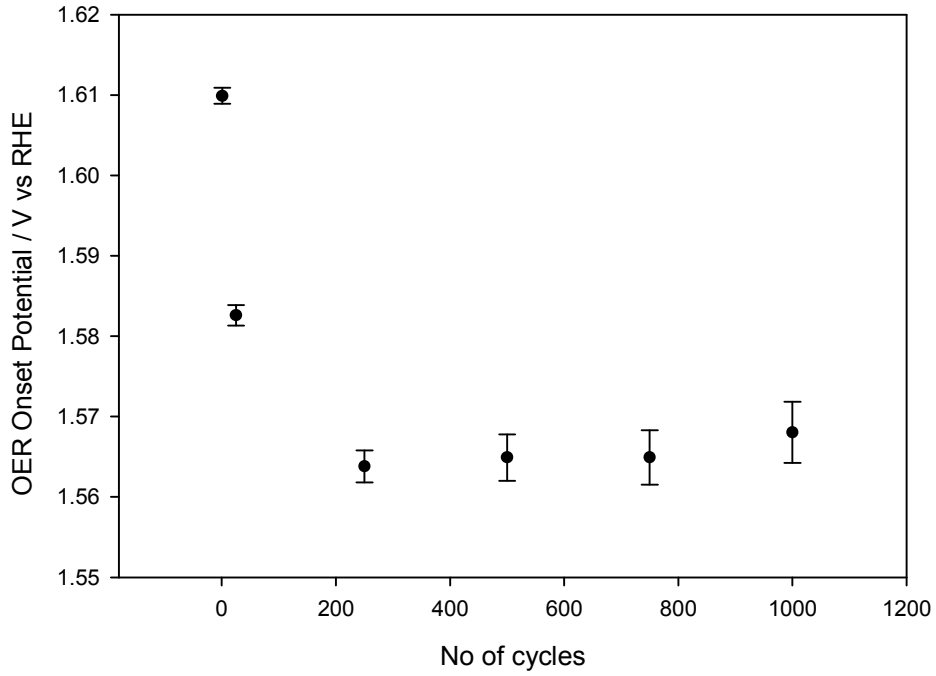



Figure 4.5.4 Oxygen evolution reaction onset potential of a Mn electrode as a function of number of potential cycles in 1.0 M NaOH at 25°C. These values were obtained from the steady-state polarisation curves presented in fig. 4.5.1. Error bars represent standard deviations of three different samples.

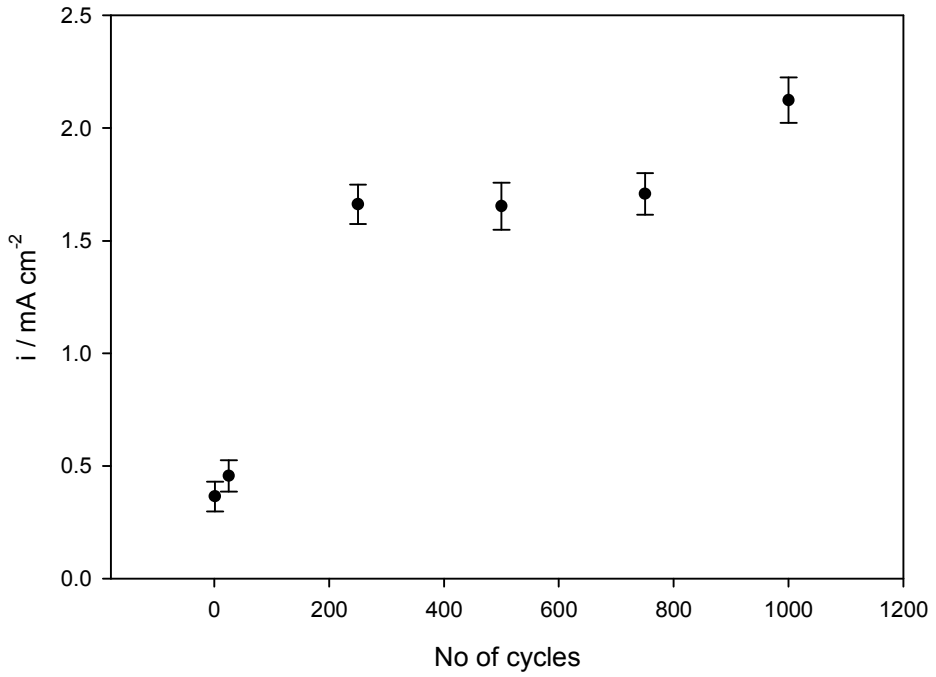



Figure 4.5.5 Current density (measured at $\eta = 0.44V$) of a Mn electrode as a function of nº of potential cycles in 1.0 M NaOH at 25°C. These values were obtained from the steady-state polarisation curves presented in fig.4.5.1. Error bars represent standard deviations of three different samples.

Typical steady-state Tafel plots were also recorded as a function of base concentration over an extended range of pH, from 0.1 M to 5.0 M NaOH. These types of plots are also known as reaction order plots. Recall that the reaction order is given by:

$$m_{OH^-,E} = \left(\frac{d\ log\ i}{d\ log\ a_{OH^-}}\right)_E \tag{4.5.5}$$

A series of Tafel plots and reaction order studies for a bare Mn electrode (N = 0 cycles), for a thin film (N = 250 cycles), for an intermediate thick film (N = 500 cycles) and for a very thick film (N = 1000 cycles) are illustrated in the below figs. 4.5.6(a) and (b), 4.5.7(a) and (b), 4.5.8(a) and (b), and 4.5.9(a) and (b), respectively.

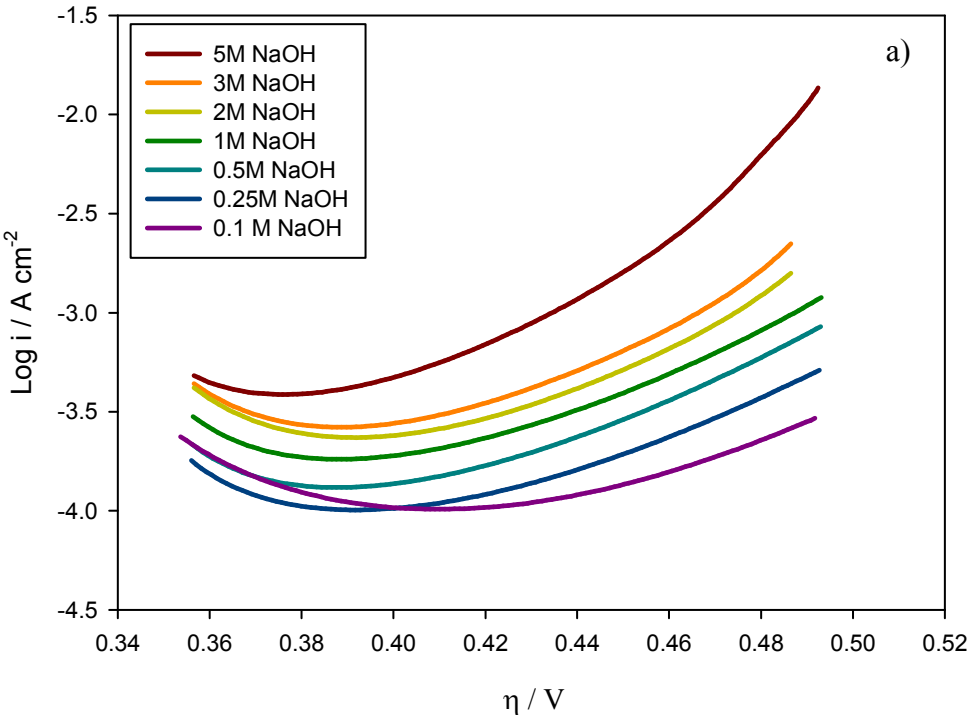



Figure 4.5.6 (a) IR corrected steady-state polarisation curves recorded in the direction of increasing potential on a Mn electrode with 0 potential cycles in NaOH solutions of various concentration at 25°C.

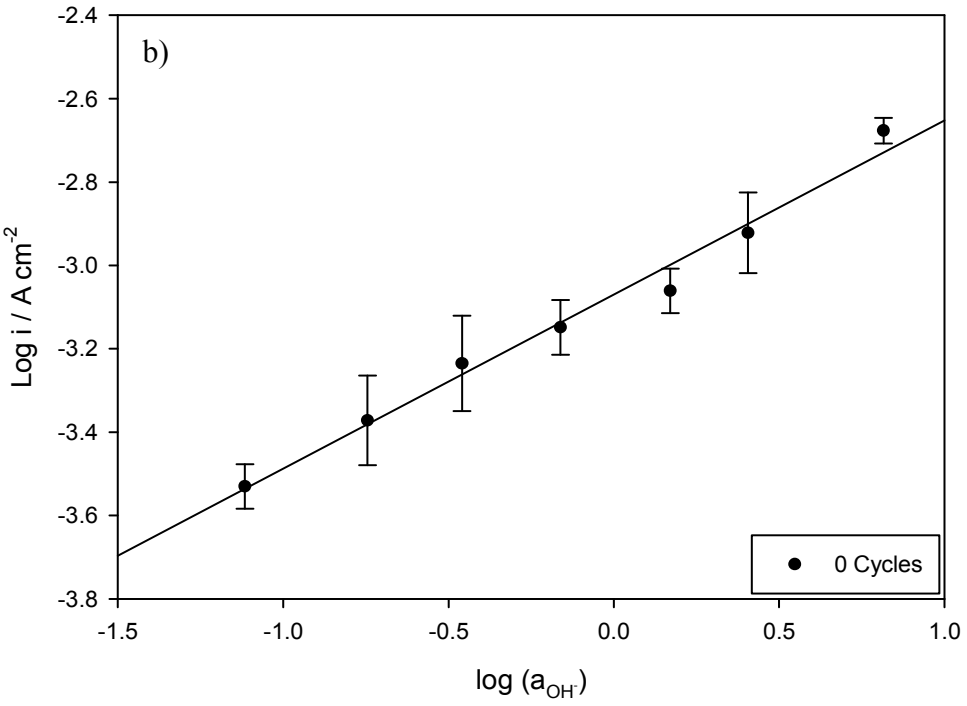



Figure 4.5.6 (b) Reaction order plots constructed from the polarisation data of fig. 4.5.6 (a) at an overpotential of 0.44V. Regression line equation: y = 0.4175 - 3.0699, $R^2$ = 0.9834. Error bars represent standard deviations of three different samples.

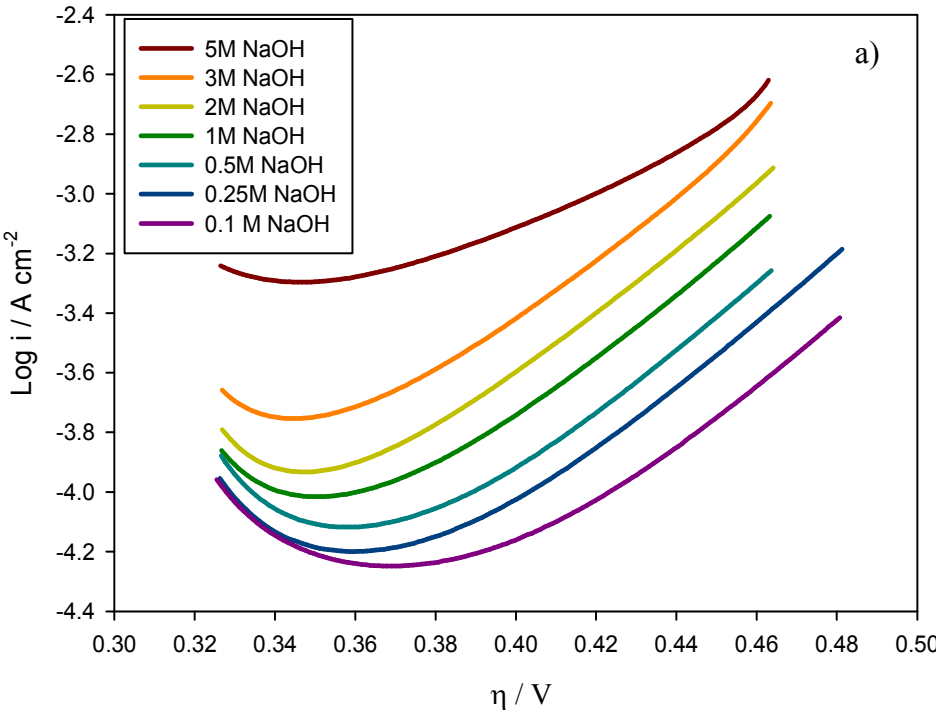



Figure 4.5.7 (a): IR corrected steady-state polarisation curves recorded in the direction of increasing potential on a Mn electrode with 25 potential cycles in NaOH solutions of various concentration at 25°C.

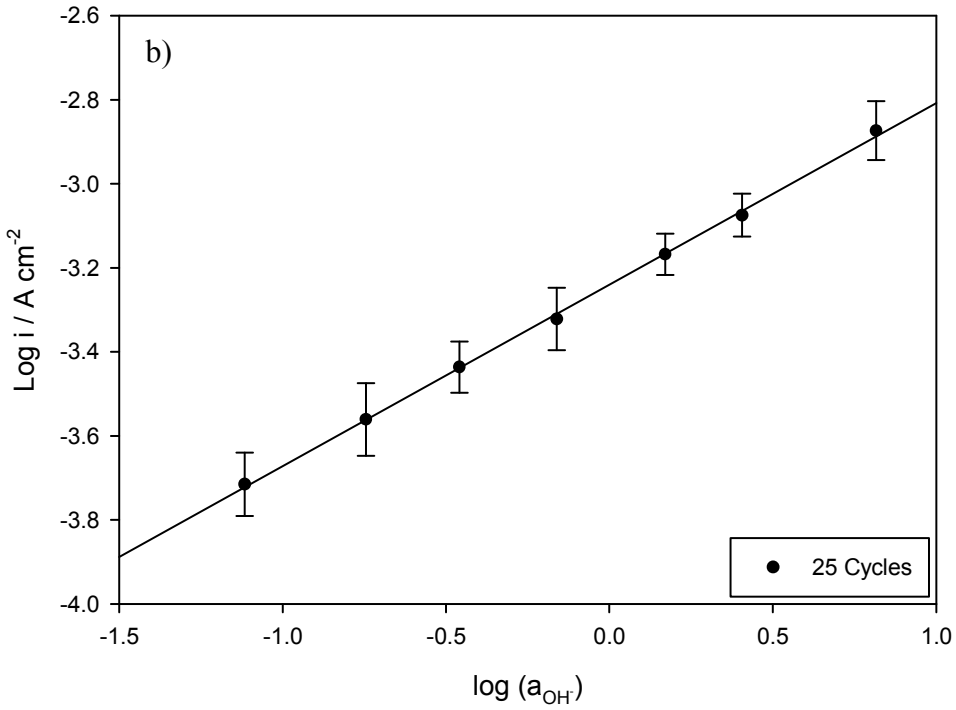



Figure 4.5.7 (b): Reaction order plots constructed from the polarisation data of fig. 4.5.7 (a) at an overpotential of 0.44V. Regression line equation: y = 0.432 - 3.399, $R^2$ = 0.9969. Error bars represent standard deviations of three different samples.

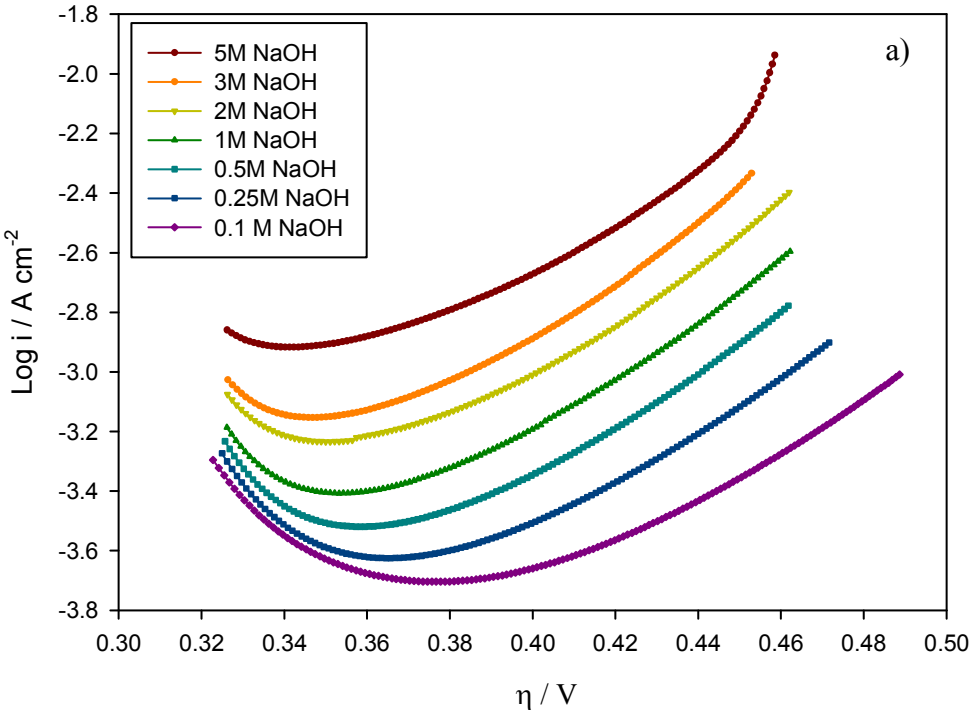



Figure 4.5.8 (a): IR corrected steady-state polarisation curves recorded in the direction of increasing potential on a Mn electrode with 500 potential cycles in NaOH solutions of various concentration at 25°C.

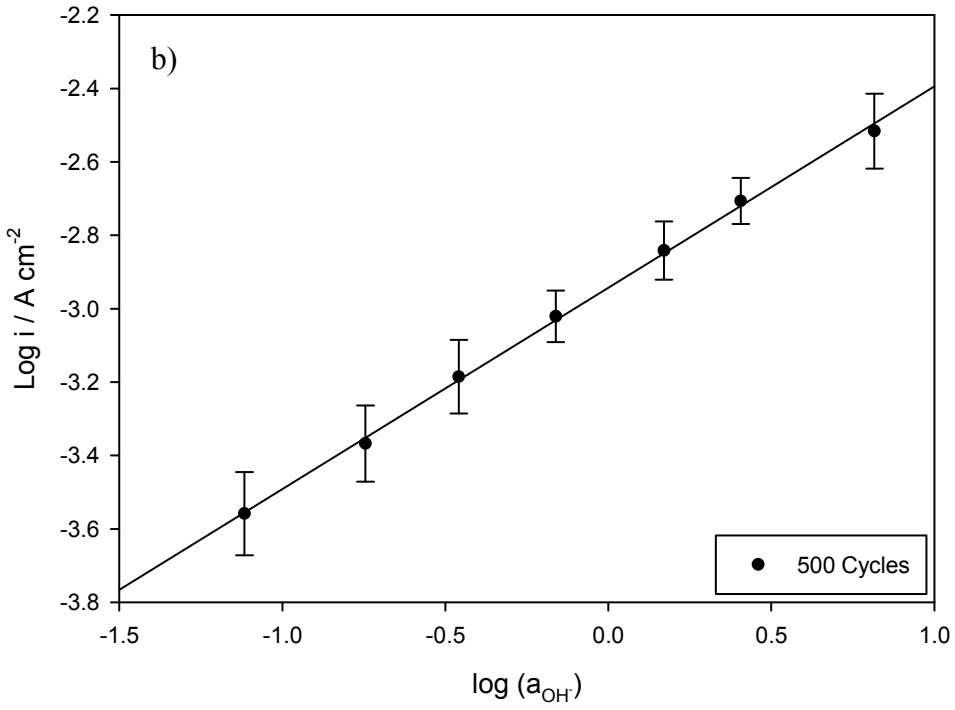



Figure 4.5.8 (b) Reaction order plots constructed from the polarisation data of fig. 4.5.8 (a) at an overpotential of 0.44V. Regression line equation: y = 0.5487 – 2.9426, $R^2$ = 0.9986. Error bars represent standard deviations of three different samples.

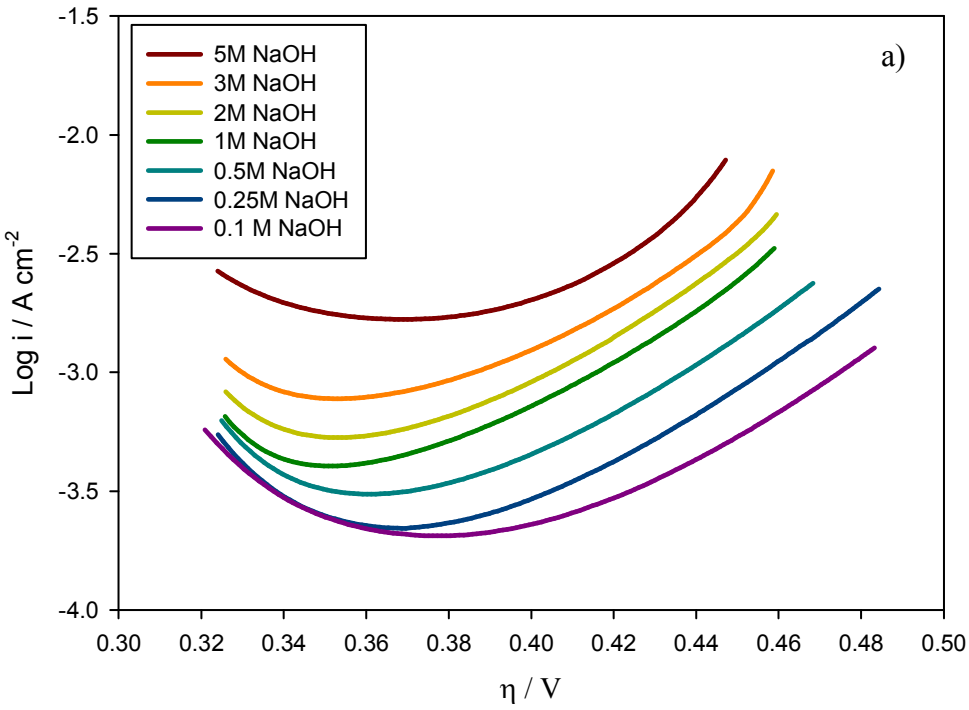



Figure 4.5.9 (a): IR corrected steady-state polarisation curves recorded in the direction of increasing potential on a Mn electrode with 1000 potential cycles in NaOH solutions of various concentration at 25°C.

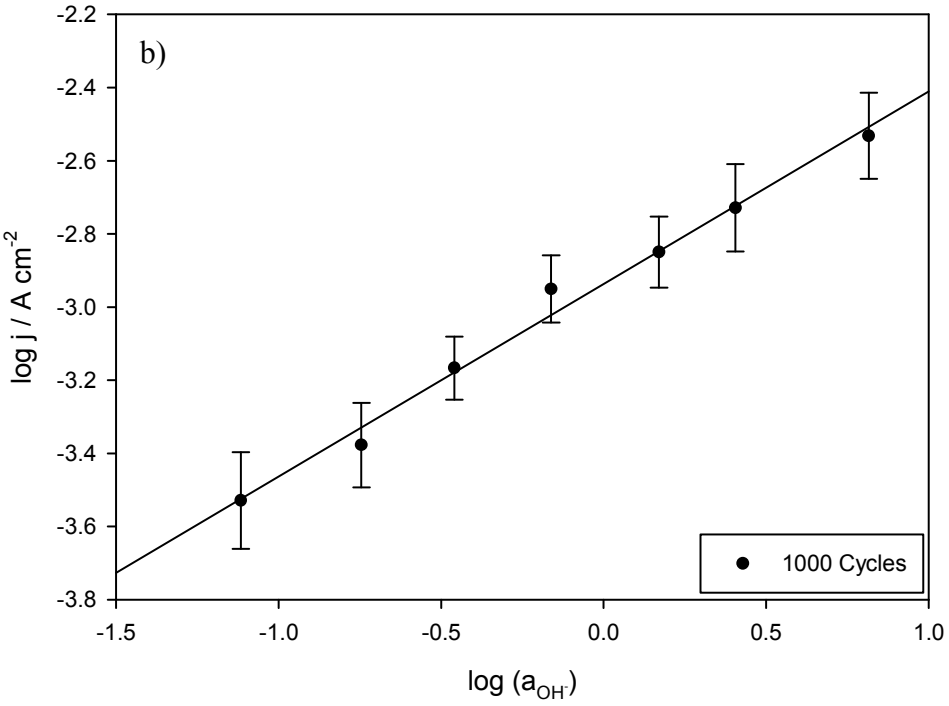



Figure 4.5.9 (b) Reaction order plots constructed from the polarisation data of fig. 4.5.9 (a) at an overpotential of 0.44V. Regression line equation: y = 0.5268 - 2.9369, $R^2$ = 0.9894. Error bars represent standard deviations of three different samples.

These reaction order studies were measured in terms of constant applied potential which is relative to a pH-independent reference electrode, *e.g.* mercury-mercuric oxide Hg/HgO. Recalling from section 1.2.6, in order to determine the mechanistically significant reaction order and considering the dependence of $\log(i)$ on $\log(a_x)$ in the absence of variations of double-layer configuration, the following correction factor needs to be applied:

$$m_{x,E} = m_{x,\eta} + \beta \qquad (4.5.6)$$

where $\beta$ refers to the symmetry factor, which usually takes 0.5 value. To clarify, $m_{x,\eta}$ refers to the slope of the regression line shown in figs. 4.5.6 - 4.5.9. The results for the reaction order values are presented in Table 4.5.1. Excellent linearity was found for all four logarithm reaction order plots for a range of overpotentials in the Tafel region.

Similar numerical values for the reaction orders were published for hydrous iron oxide layers prepared using a range of growth cycles.[35] Results observed in Table 5.4.1 indicate that the reaction order is independent of the hydrous oxide charge capacity. Also, it is clear from the

figs. 4.5.6 - 4.5.9 that the Tafel slopes remains constant with changing hydroxide ion concertation.

| **Nº of growth cycles** | **Reaction order** |
|---|---|
| 0 | 0.92 ± 0.02 |
| 25 | 0.94 ± 0.01 |
| 500 | 1.05 ± 0.03 |
| 1000 | 1.03 ± 0.05 |

Table 5.4.1 Mechanistically significant reaction order values obtained from figs. 4.5.6 - 4.5.9 at an overpotential of 0.44V for a series of Mn electrodes with different number of potential cycles.

This was noted for all the thicknesses analysed. Only Tafel slopes measured at 5.0 M NaOH exhibit different slopes. However, it is only in fig. 4.5.7 (a) where a significant change in Tafel slope was observed. A possible rationality to the latter is the indication of changes in rate-determining step in the OER mechanism. Fig. 4.5.10 shows the variation of the Tafel slope when the electrolyte concentration is increased from 3.0 M to 5.0 M NaOH. Note that the Tafel slope changes dramatically. The change from ca. 90 mV $dec^{-1}$ to ca. 120 mV $dec^{-1}$ indicates a change from a chemical step rate determining, affected by a slow electron transfer as mentioned above, to a pure electron transfer step being rate determining. Although a discussion about the corrosion effect is beyond the scope of this work, its mention is opportune since this effect was observed during reaction order measurements. The effect of corrosion processes in Tafel plots is presented in fig. 4.5.10. In general, a corrosion process was observed in all the electrodes studied, regardless of their thickness, though corrosion was specially significant under conditions of high pH and high potentials on the OER. As mentioned in section 1.4.2, corrosion may occur during OER, which typically develops a passivation layer in the electrode surface. The effect of corrosion in Tafel plots was investigated under different pH conditions for a bare Mn electrode and an intermediate thickness Mn oxide electrode. As noted in fig. 4.5.11, a sudden rise in the current density was observed at high overpotential values in the OER for 500 cycles Mn electrode at 5.0 M NaOH. The same measurement was performed on a bare electrode at 1.0 M NaOH conditions. The result is outlined in fig. 4.5.11 a and b. Since corrosion processes typically form a passivation layer, it is proposed here that such layer may exhibit high catalytic activity towards the OER. Further analysis will be undertaken to investigate this in detail.

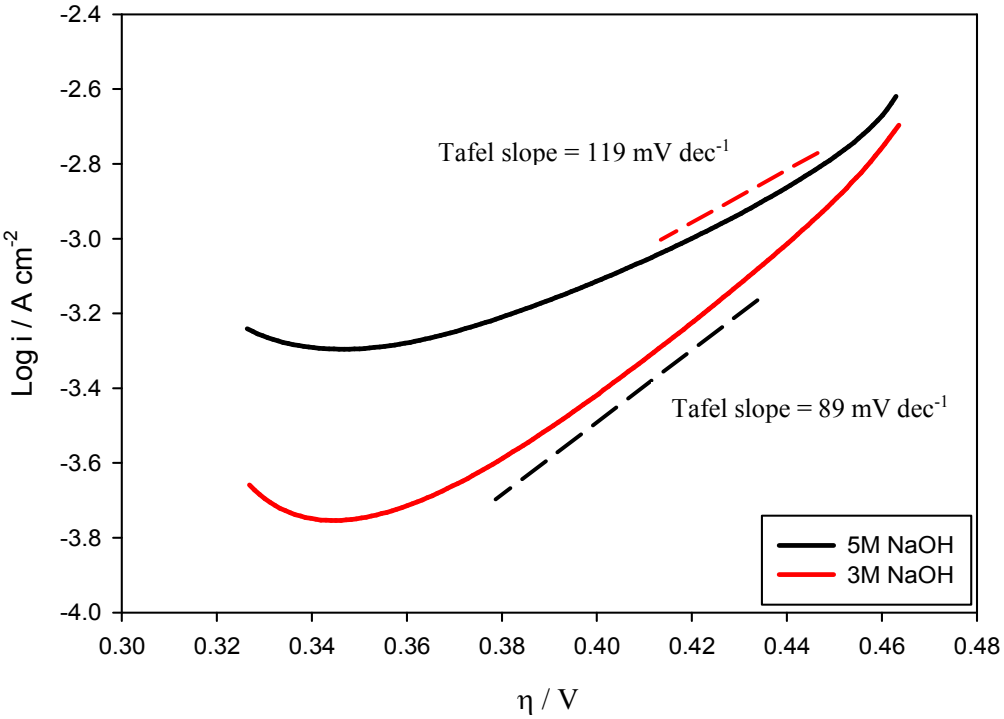



Figure 4.5.10 IR corrected steady-state polarisation curves recorded in the direction of increasing potential on an Mn electrode with 25 potential cycles in NaOH solutions of various concentration at 25°C.

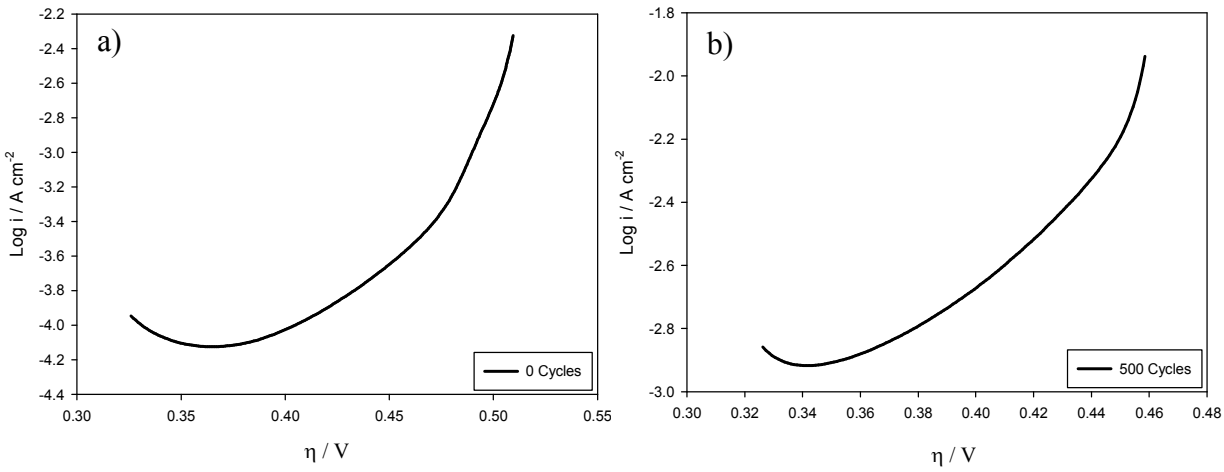



Figure 4.5.11 IR corrected steady-state polarisation curve recorded in the direction of increasing potential on a) Mn electrode with 0 potential cycles and b) Mn electrode with 500 potential cycles both in 1.0 M NaOH solution at 25°C.

## 4.6 Open Circuit Decay Measurements

Steady-state measurements of electrode processes are often complemented by studies of the decay of the Electro-Motive Force (EMF) on open circuits, which can also, in many cases, characterise the kinetics and mechanisms of processes involved in the electrode reactions.[36] The technique is frequently used in cases where elucidation of reaction mechanisms by steady-state polarisation techniques is complicated by continuous alterations of the electrode surface with time. The basics of EMF decay studies assume that the slope of $(-b)$ of the EMF decay curve is equal to the slope $b$ of the Tafel plot for steady-state polarisation.[37] A mathematical description of the latter is presented below. In general, the current density at the electrode can be written as the sum of the charging current ($I_c$) and the Faradaic current ($I_F$) as:

$$I = I_c + I_F \tag{4.6.1}$$

At time $t_o$, when the current is switched off, $I = 0$ and $\eta = \eta_0$, and thus:

$$I_c = -I_F \tag{4.6.2}$$

Noting that:

$$I_c dt = dq \tag{4.6.3}$$

and:

$$C = \frac{dq}{dE} = \frac{dq}{d\eta_t} \tag{4.6.4}$$

where $Q$ is charge and C is capacitance, it can be shown that:

$$-I_F dt = dt = C d\eta_t \tag{4.6.5}$$

Under anodic conditions with $\eta_t > RT/F$:

$$-I_o e^{\frac{\beta \eta_t F}{RT}} dt = C d\eta_t \tag{4.6.6}$$

Rearranging and integrating yields to:

$$\int_{t_o}^{t} I_o dt = \int_{\eta_o}^{\eta} C e^{-\frac{\beta \eta_t F}{RT}} d\eta_t \tag{4.6.7}$$

Now, for $t \gg t_o$ and $\eta_o \gg \eta$:

$$-I_o t = \frac{RT}{\beta F} e^{-\frac{\beta \eta_t F}{RT}} \tag{4.6.8}$$

And, taking the logarithm, this yields to:

$$\eta_t = \frac{2.303\ RT}{\beta F} log\left(\frac{RT}{\beta F I_o}\right) - \frac{2.303 RT}{\beta F} log(t) \tag{4.6.9}$$

Eqn. 4.6.9 suggests that an equivalent Tafel slope can be determined from the slope of a plot of the measured potential or overpotential, E or $\eta$, respectively, during the decay as a function of $\log(t)$. It is readily shown that the EMF, E, depends on the decay time $t$ as follows:

$$E = E_i - b\ log(t + \vartheta) \tag{4.6.10}$$

where $E_i$ refers to the initial potential. The parameter $\vartheta$ is the hypothetical time required for the electrode to decay from infinite potential to the potential at zero time.

In this view, open circuit potential (OCP) decay curves were used in this thesis, as well as steady-state measurements, to help determine the kinetics and mechanisms of the hydrous Mn oxide electrodes in alkaline solutions. OCP measurements were usually carried out after pre-polarizing the electrode at a potential in the oxygen evolution region typically at 1.72 V (*vs.* RHE). The time allowed for the system to reach steady current depends on the sample. All electrodes showed a steady-state current density after two minutes. Once a steady current was achieved, the polarization was switched off and the potential could decay with respect to time. Tafel slopes can be calculated for the decaying curve. A typical open circuit potential/time decay curve recorded for various Mn oxide film thicknesses in 1.0 M NaOH at 25°C is outlined in fig. 4.6.1.

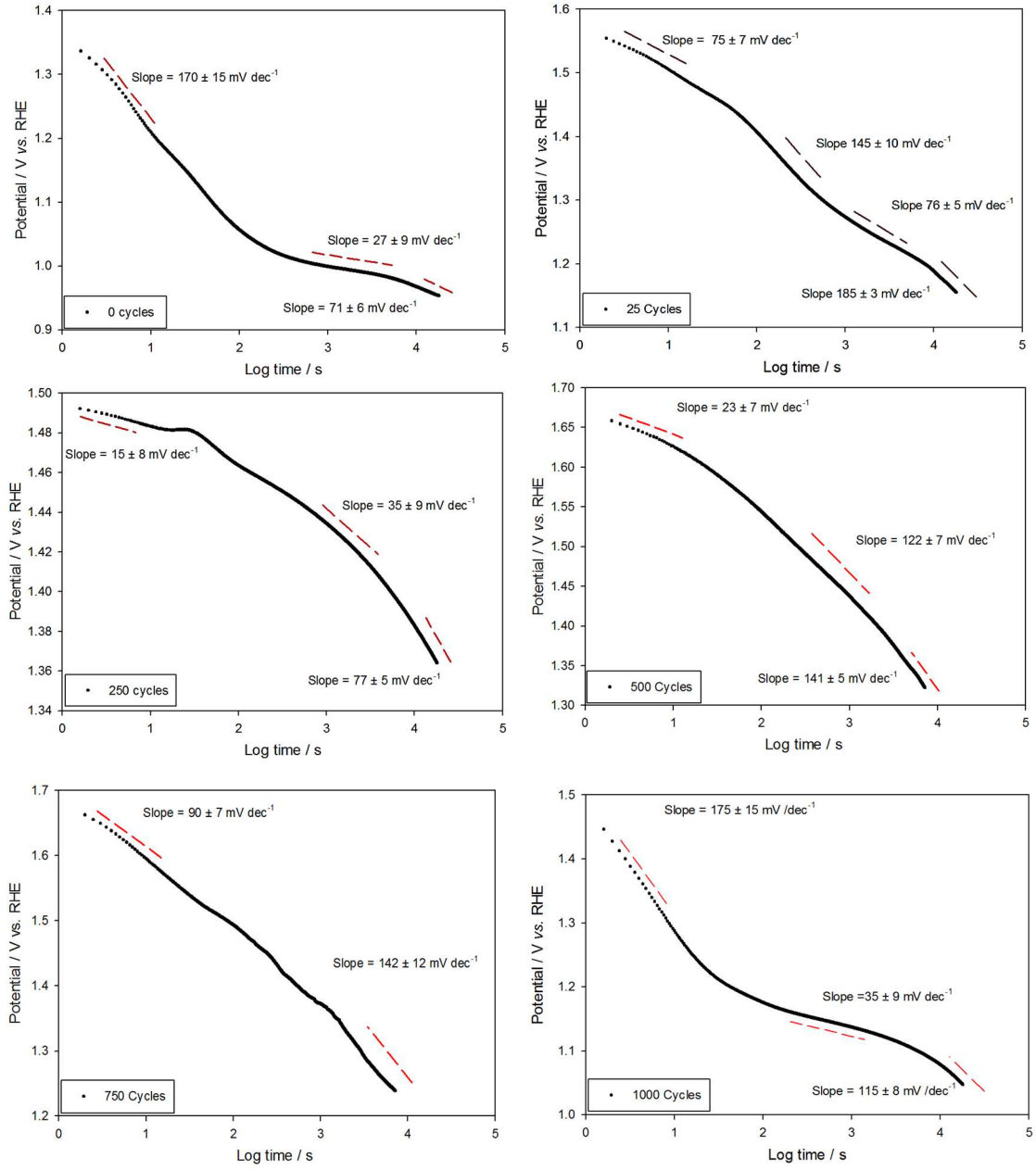



Figure 4.6.1 Typical open circuit decay curves for Mn electrode with different number of potential cycles in 1.0 M NaOH at 25°C.

The study of the OCP decay will be carried out by dividing in three-time regions the potential decay. The three-time regions are: (i) log 0 to 1, (ii) log 1 to 3, and (iii) log 3 to 5, which corresponds to the (i) short, (ii) intermediate, and (iii) long-time regions, respectively.

Table 4.6.1 shows the measured slope values of the three regions of the OCP along with the Tafel slope values measured from steady-state polarisation measurements.

| Nº of cycles | Short time (OCP) / mV dec$^{-1}$ | Intermediate time (OCP) / mV dec$^{-1}$ | Long-time (OCP) / mV dec$^{-1}$ | Tafel slope (SSP) / mV dec$^{-1}$ |
|---|---|---|---|---|
| 0 | -170 ± 15 | -27 ± 9 | -71 ± 6 | a) 40 ± 9<br>b) 120 ± 4 |
| 25 | -75 ± 7 | -145 ± 10 | -185 ± 3 | 86 ± 4 |
| 250 | -15 ± 8 | -35 ± 9 | -77 ± 5 | 76 ± 6 |
| 500 | -23 ± 7 | -122 ± 7 | -141 ± 5 | 117 ± 10 |
| 750 | -90 ± 7 | -90 ± 7 | -142 ± 12 | 110 ± 8 |
| 1000 | -175 ± 15 | -35 ± 9 | -115 ± 9 | 128 ± 11 |

Table 4.6.1 Comparison table showing the measured OCP decay slope values and the Tafel slope values from fig.4.5.1 and fig.4.6.1

Significant differences were observed when comparing the slopes form the OCP decay with the Tafel slopes. Such differences may arise from the decrease in the surfaquo group's concentration on the electrode surface as they become reduced as part of the accompanying cathodic process in self-discharges. Note that it has been pointed out that surfaquo groups are considered to be the active sites for oxygen evolution reaction (see section 2.5.4).[30b] This may be related to the work presented by Conway and Bourgault[38] in 1960. These authors have shown that only when the electrode capacitance is independent of the potential, which occurs during self-discharge, eqn. 4.6.9 holds. Therefore, the observation of equality between the decay slope and the Tafel slope suggests that the surface capacity remains constant during self-discharge. Contrary, in those systems where the surface capacity changes during self-discharge, the observed decay slope may differ quite significantly from the steady-state Tafel slope. This effect is evident in the first two-time regions of the 250 Mn electrode as shown in Table 4.6.1. At short and intermediate decay times, slopes of ca. 15 mV dec$^{-1}$ and ca. 35 mV dec$^{-1}$ are respectively observed. These slopes differ quite significantly from the slope measured from steady-state polarization, ca. 77 mV dec$^{-1}$. This may also be interpreted using the work of Conway and Bourgault[38] which leads to distinguish two possible scenarios. On the one hand, if the surface coverage of surfaquo groups during self-discharge is presumed to be low, the surface capacity decreases with decreasing potential giving the following relationship between the decay slope $b_{OCP}$ and the Tafel slope $b$:

$$b_{OCP} = \frac{b'b}{b - b'} \tag{4.6.11}$$

where $b'$ is a fraction of RT/F. Thus, the measured $b_{OCP}$ is predicted to be greater than the Tafel slope. On the other hand, if there is high but not full coverage of surfaquo groups, the surface capacity increases with decreasing potential and the decay slope follows:

$$b_{OCP} = -\frac{b'b}{b' - b} \tag{4.6.12}$$

Eqn. 4.6.12 points that $b_{OCP} < b$. Thus, it is suggested here, according to the values presented in Table 4.6.1, that the surface capacity does not remain constant during self-discharge. Doyle and Lyons[2] mentioned upon a study of hydrous iron oxide electrodes that: "At high potentials or short decay times a large proportion of the surfaquo groups are in the higher charged state implying significant surface coverage of intermediates and the observed decay slope is lower than the Tafel slope. On the other hand, for longer times the surface coverage becomes considerably reduced due to increased self-discharge of the surfaquo groups and the decay slope is found to be greater than the Tafel slope".

This agrees with the results presented in Table 4.6.1, as whereas the time scale increases, the values of the $b_{OCP}$ approach those for steady-state polarisation. Note that self-discharge is assumed to proceed by an electrochemical mechanism analogous to that of corrosion. That is the simultaneous occurrence of anodic and cathodic processes as a mixed potential *via* a local cell mechanism. In the present work, self-discharge refers of a cathodic oxide or surfaquo group reduction process and an anodic oxygen evolution process.

## 4.7 Double Layer Capacitance Study

The double layer capacitance contribution will be aprroached in this work by using both the potential step method and electrochemical impedance spectroscopy (EIS). In this section, however, only the results obtained from the potential step method will be presented, while those obtained from the EIS will be presented later in chapter 6.

Since this experiment is performed in a potential region where the current response is invariant with the applied potential, that being the complete absence of faradaic processes, it is assumed that the only current flow should be due to the charge of the double layer. Under these conditions, the current density response may be represented by:

$$i = \frac{\Delta E}{R_u} exp\left(\frac{-t}{R_u C_{dl}}\right) \tag{4.7.1}$$

If eqn. 4.7.1 is linearized using simple natural logarithm rules, it may be obtained that:

$$ln\, i = ln\left(\frac{\Delta E}{R_u}\right) - \left(\frac{t}{R_u C_{dl}}\right) \tag{4.7.2}$$

Therefore, the current response to a small potential step ΔE, of 50 mV was recorded in a potential region where no Faradaic processes were occurring to determine the $R_u$ and $C_{dl}$, respectively. Typical $\ln i \; vs. \; t$ plots are presented in fig. 4.7.1 as a function of number of repetitive potential cycles. In addition, the values for the uncompensated resistance and double layer capacitance are presented in Table 4.7.1.

A remarkable aspect that can be observed in Table 4.7.1 is the fashion in which the double layer capacitance varies with layer thickness. It was noted that for thin thicknesses the double layer is ca. 14 mF $cm^{-2}$. The intermediate thick film (250 cycles) may be considered as a transition point at which the $C_{dl}$ increases from ca. 24 mF $cm^{-2}$ to ca. 40 mF $cm^{-2}$ for thicker films. Opposite behaviour than that observed for $C_{dl}$ was noted for the uncompensated solution resistance. In this view, it was found that the uncompensated solution resistance decreased as the layer thickness increased. This suggests that the rate of capacitance discharge - that is how fast the current density tends to zero - is somewhat related with the type of oxide in the surface of the electrode.

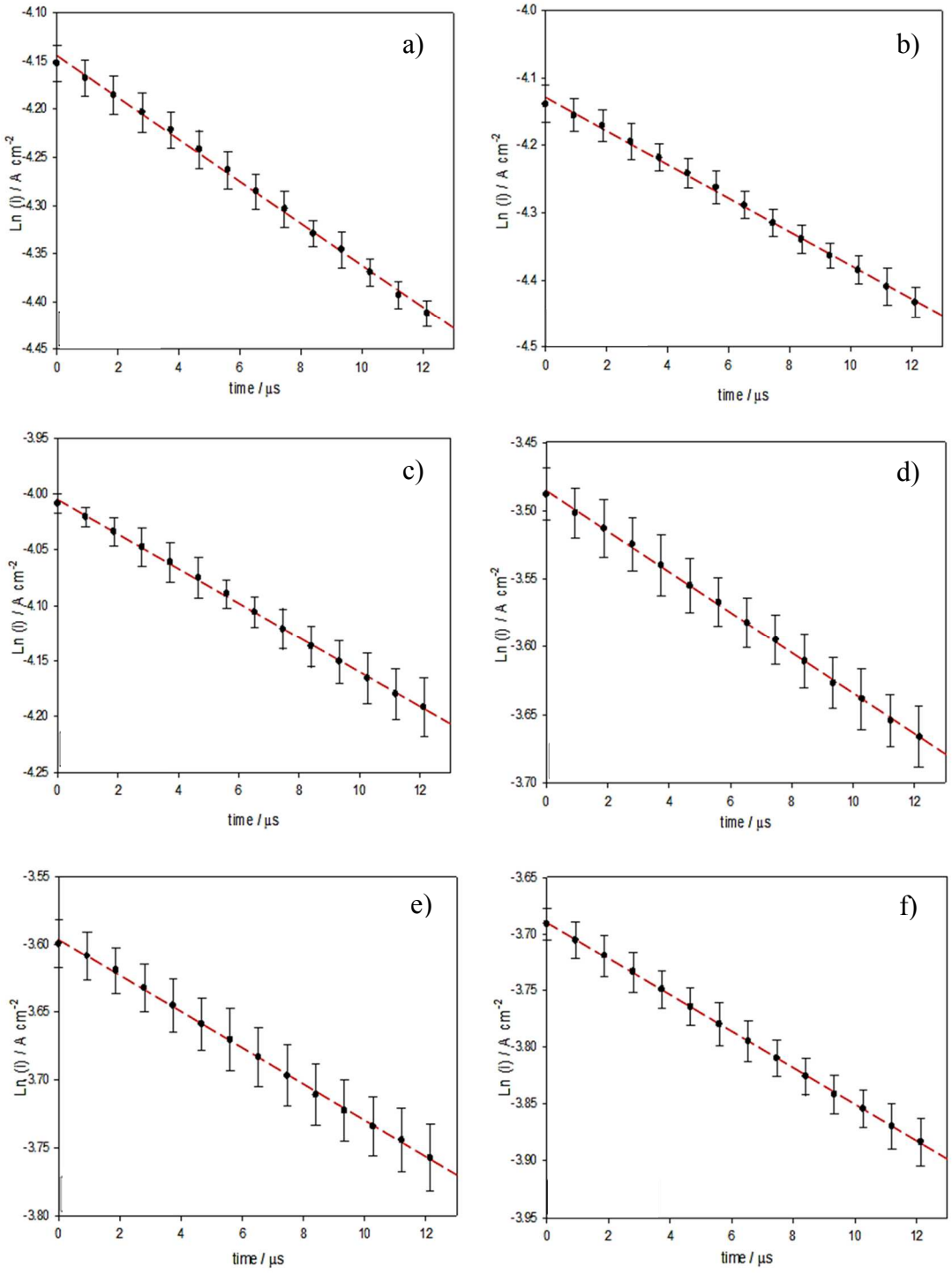



Figure 4.7.1 Logarithm of current decay curve following a 50 mV pulse applied to electrodes of different layer thickness: a) 0, b) 25, c) 250, d) 500, e) 750, and f) 1000 number of potential cycles. All the experiments were performed in 1.0 M NaOH at 25°C. Error bars represent standard deviations of three different samples.

| Nº of potential cycles | Regression eqn. | Double layer capacitance / mF $cm^{-2}$ | Uncompensated resistance / Ω |
|---|---|---|---|
| 0 | y = -0.0218x - 4.144 | 14.5 ± 1.5 | 3.2 ± 0.4 |
| 25 | y = -24909x – 4.128 | 13.1 ± 2 | 3.1 ± 0.3 |
| 250 | y = -15466x - 4.005 | 23.7 ± 1.3 | 2.7 ± 0.3 |
| 500 | y = -14912x - 3.485 | 40.5 ± 1.7 | 1.8 ± 0.6 |
| 750 | y = -13354x - 3.596 | 41 ± .1.1 | 1.9 ± 0.5 |
| 1000 | y = -13027x - 3.690 | 37.9 ± 2.4 | 2.0 ± 0.5 |

Table 4.7.1 Double layer and uncompensated resistance values obtained using eqn. 4.7.2 and data from fig. 4.7.1.

In section 4.2 it was outlined that, for thick layers, the surface of the electrode becomes porous as a result of the formation of an oxyhydrous Mn oxide layer. Such suggestion was then corroborated by analysing the SEM images in figs. 4.2.7 - 4.2.8. The latter would also explain the constant increase in the current density. Recall from section 1.1.4 that the charge storage behaviour of the double layer is strongly depended on the activities of electrolyte ions on the electrode surface. The greatest the concentration of charge carriers adjacent to the electrode surface (the inner compact plane), the larger the charge storage behaviour of the film. Certainly, if the surface of the electrode possesses a porous structure, it is expected that ions such as $OH^-$ would diffuse within the porous structure increasing the number of charge carriers on the inner compact plane and, consequently, increasing the double layer capacitance. This approach has been also proposed by other authors.[39]

Remarkable work was carried out by Lyklema[40] who stated: "It should also be noted that the number of counterions that can be accommodated in the surface layer depends primarily on penetration depth and only to a lesser extent on concentration and absorbability of the counterion. The reason for this is, of course, the high number of sites available in a voluminous surface layer compared to a two-dimensional surface array". This would explain the aforementioned suggestion that as the Mn oxide film becomes thicker, the penetration depth increases allowing more counter-ions to accommodate within the pore structure. Recent studies carried out by Lozano-Castello *et al.*[39a] confirm that capacitance not only depends on the surface area but also on two other parameters: (i) the pore size distribution, and (ii) the surface chemistry. These authors found that micro pores contribute to the double layer capacitance, *e.g.* if the mean pore size is very small, the penetration of electrolyte into

the pores is difficult. They suggested that if the latter occurs, such pores do not contribute to the total double-layer capacitance of the electrode. Regarding the surface chemistry, they found that the presence of oxygenated groups on the surface of the electrode influences the capacity storage in two fashions: (i) by increasing wettability of the electrode, which would increase the capacitance, and (ii) by producing pseudocapacitance effects, so that Faradaic charge transfer reactions occurs.

## 4.8 Electrocatalytic Behaviour of an Aged Manganese Electrode

In this section, the effect of using an aged Mn electrode on the OER will be discussed. Also, the redox and catalytic changes associated with using an aged electrode will be compared with those exhibit for a fresh electrode. Aged in this sense refers to an electrode that had undergone several polarisation experiments prior to being subjected to a multicycling procedure to produce the hydrous oxide whereas fresh refers to a newly prepared electrode, *e.g.* previously unused. Prior to investigating the catalytic behaviour of aged Mn electrodes towards the OER, and to understand the nature of such electrodes, the surface redox chemistry of an aged electrode ought to be presented. Thus, the growth of a hydrous oxide film on an initially bright aged Mn substrate in 1.0 M NaOH is presented in fig. 4.8.1. As referred at the beginning of this chapter regarding the charge storage capacity for a fresh electrode, the charge storage capacity, $Q$, was also determined for an aged Mn electrode. Fig. 4.8.2 shows the charge capacity variation as a function of several potential cycles.

The CNLS fitting predicted values of $\mathrm{a} = 0.00349 \pm 5.61 \times 10^{-5}$ and $\mathrm{b} = 0.00205 \pm 6.80 \times 10^{-5}$. The latter exhibited a less pronounced oxide growth rate decreases than that observed in a fresh Mn electrode. If comparing fig. 4.2.2 with fig. 4.8.2, it is rapidly noticeable that the aged Mn electrode shows a better distribution over the CNLS fitting curve. This suggests that the way the film grown is more stable in an aged surface than in a fresh one.

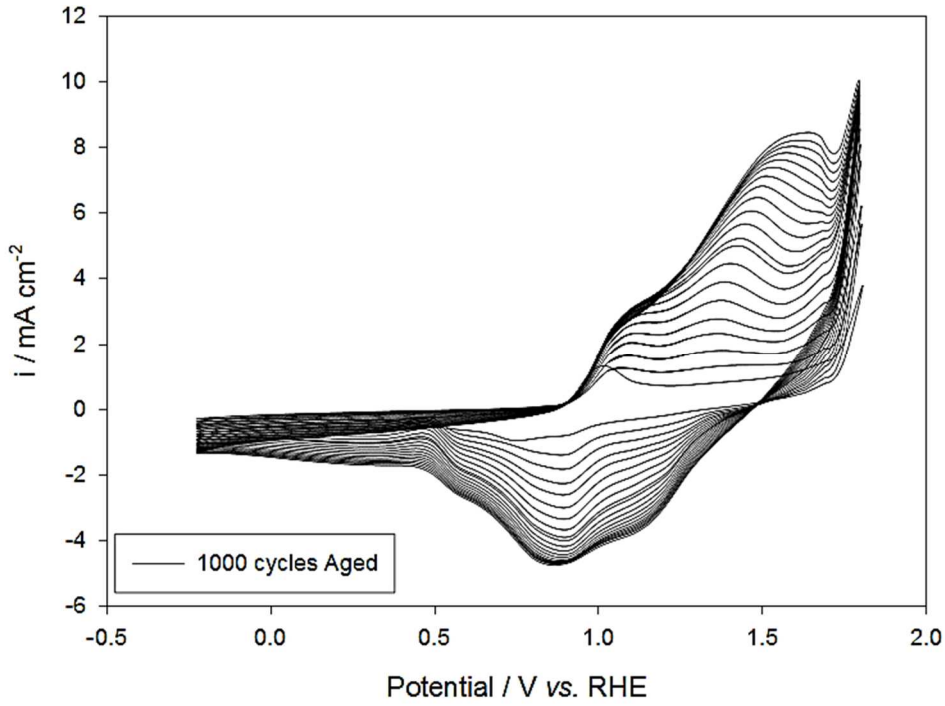



Figure 4.8.1 Growth of hydrous oxyhydroxide manganese thin film on aged Mn support electrode monitored *via* analysis of the evolution of the real time voltammogram in 1.0 M NaOH at 25°C. Growth potential limits: - 0.25 to 1.75 V (*vs.* RHE), sweep rate 40 mV $s^{-1}$.

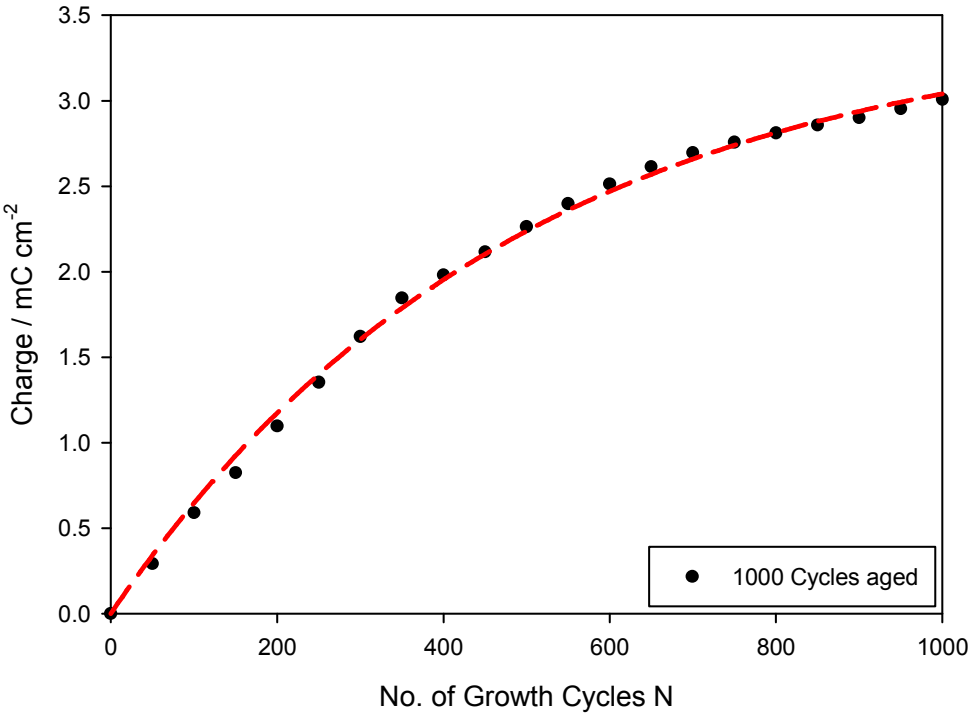



Figure 4.8.2 Growth of hydrous oxyhydroxide manganese thin film on aged Mn support electrode monitored *via* analysis of the evolution of the real time voltammogram in 1.0 M NaOH. Plot of integrated voltammetric charge *Q* (measured at 40 mV $s^{-1}$) as a function of oxide growth cycles N.

The growth stability seems to go in tandem with the amount of current density response observed. The aged electrode, after 1000 growth cycles, possess ca. 40 % more charge storage capacity than a fresh Mn electrode. Since the growth of the subsequent layers occur on top of the previous one, it is suggested that the nature of the Mn electrode affects the following Mn oxide layers.

To investigate possible differences in the surface of both electrodes, the SEM analysis was conducted. The result of such analysis is presented in fig. 4.8.3.

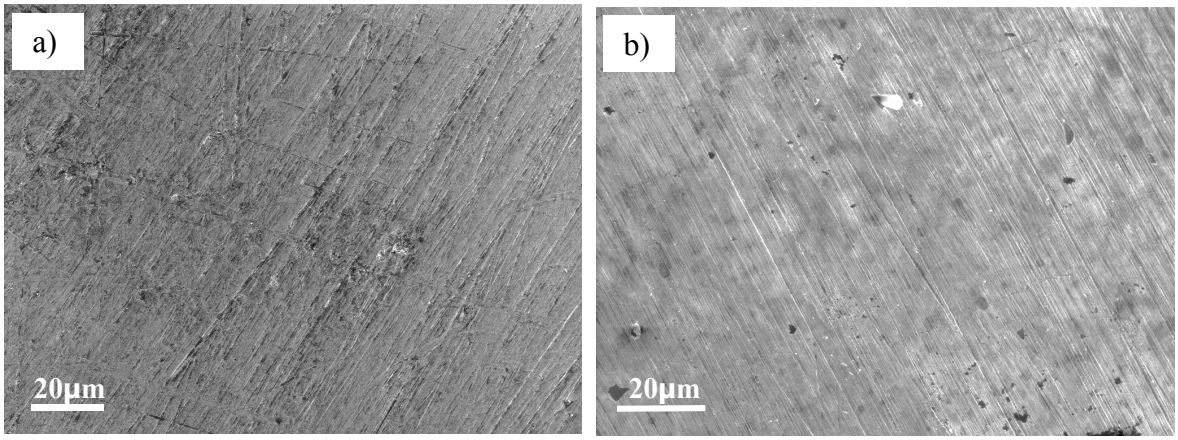



Figure 4.8.3 Typical SEM image of: a) fresh and b) aged Mn electrode. Images were obtained using inLens and EHT = 10 kV. Distance between the sample and the objective was 6.8 mm.

No apparent differences were observed between surfaces of an aged and fresh Mn electrode which suggests that differences may arise from the nature of the bulk Mn electrode. Future work will analyse such differences using EIS. The redox peak potentials of the aged Mn oxide film were found to coincide with those calculated for the fresh Mn electrode but exhibiting higher current densities. Due to the greater degree of current density shown in fig. 4.8.1 compared with that in fig. 4.2.1, one would indeed expect a larger relative increase in catalytic activity for the aged electrode towards the OER. The Tafel slope of an aged Mn electrode as a function of several growth cycles is presented in fig. 4.8.4.

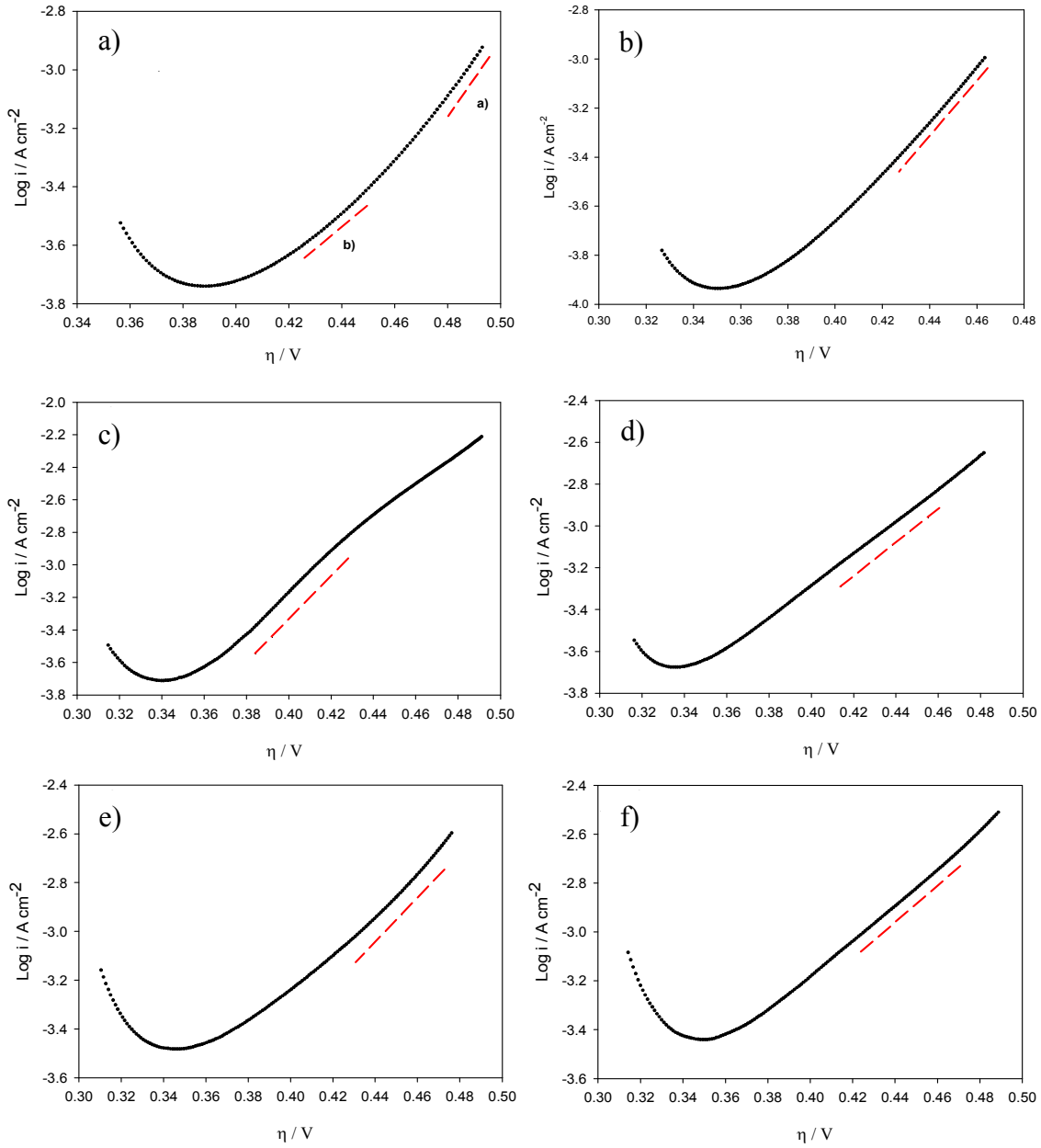



Figure 4.8.4 IR corrected steady-state polarisation curves recorded in the direction of increasing potential on an aged Mn electrode at sweep rate of 1 mV $s^{-1}$ in 1.0 M NaOH at 25°C. Fig a) 0 cycles. Tafel slope a) 82 ± 6.31 mV $dec^{-1}$ and slope b) 131 ± 4.62 mV $dec^{-1}$; b) 25 cycles. Tafel slope 82 ± 5.01 mV $dec^{-1}$; c) 250 cycles. Tafel slope 75 ± 4.43 mV $dec^{-1}$; d) 500 cycles. Tafel slope 118 ± 6.23 mV $dec^{-1}$; e) 750 cycles. Tafel slope 111 ± 5.48 mV $dec^{-1}$; and f) 1000 cycles. Tafel slope 131 ± 8.81 mV $dec^{-1}$.

Table 4.8.1 summarises the measured Tafel slope for various film thicknesses as a function of both fresh and aged Mn electrode. From Table 4.8.1 it can be noted that the values of the Tafel slope for both electrodes are equal, except for the uncycled electrode. Therefore, the latter also suggests that the OER mechanism holds equal in both types of electrodes.

| **Nº potential cycles** | **Fresh Mn electrode / mV dec$^{-1}$** | **Aged Mn electrode / mV dec$^{-1}$** |
|---|---|---|
| 0 | a) 41.1 ± 8.3<br>b) 120.3 ± 3.9 | a) 81.7 ± 6.3<br>b) 131.0 ± 4.6 |
| 25 | 86.9 ± 3.7 | 81.9 ± 5.0 |
| 250 | 76.4 ± 6.0 | 75.2 ±4.4 |
| 500 | 117.5 ± 10.2 | 117.7 ± 6.2 |
| 750 | 110.0 ± 7.8 | 111.0 ± 5.5 |
| 1000 | 128.3 ± 10.6 | 131.3 ± 8.8 |

Table 4.8.1 Comparison table with the measured Tafel slope values from fig. 4.8.3 and those from fig. 4.5.1.

Focusing on the electrode with 0 potential cycles, differences may arise due to imperfections on the surface of the electrode. The rationalisation for explaining equalities in the Tafel slope regardless of the type of Mn electrode is that, after a few growth cycles, the oxidation state of the electrode surface is similar in both cases. This was demonstrated from the observation of equal redox peak potentials from fig. 4.2.1 and fig. 4.8.1.

## 4.9 References Chapter 4


[1] L. D. Burke, E. J. M. O'Sullivan, *Journal of Electroanalytical Chemistry and Interfacial Electrochemistry* **1981**, *117*, 155-160.
[2] M. E. G. Lyons, R. L. Doyle, M. P. Brandon, *Physical Chemistry Chemical Physics* **2011**, *13*, 21530-21551.
[3] L. D. Burke, M. J. G. Ahern, *Journal of Electroanalytical Chemistry and Interfacial Electrochemistry* **1985**, *183*, 183-203.
[4] L. D. Burke, M. J. Ahern, *Journal of The Electrochemical Society* **1985**, *132*, 2662-2666.
[5] M. Yano, S. Suzuki, M. Miyayama, M. Ohgaki, *Nanomaterials* **2013**, *3*, 204.
[6] L. D. Burke, O. J. Murphy, *Journal of Electroanalytical Chemistry and Interfacial Electrochemistry* **1980**, *109*, 379-383.
[7] B. Babakhani, D. G. Ivey, *Journal of Power Sources* **2010**, *195*, 2110-2117.
[8] R. Liu, S. B. Lee, *Journal of the American Chemical Society* **2008**, *130*, 2942-2943; C.-C. Hu, K.-H. Chang, M.-C. Lin, Y.-T. Wu, *Nano Letters* **2006**, *6*, 2690-2695.
[9] in *Handbook of Battery Materials*.
[10] A. Mokhtari, *Chemiluminescence System of Permanganate-Sulfite for Simple Determination of Zolpidem, Vol. 12*, **2017**.
[11] G. Zimmerman, *The Journal of Chemical Physics* **1955**, *23*, 825-832.
[12] M. C. R. Symons, *Journal of the Chemical Society (Resumed)* **1953**, 3956-3961.
[13] G. Den Boef, H. J. van der Beek, T. Braaf, *Recueil des Travaux Chimiques des Pays-Bas* **1958**, *77*, 1064-1070.
[14] R. H. Ferguson, W. Lerch, J. E. Day, *Journal of the American Chemical Society* **1931**, *53*, 126-137.
[15] F. R. Duke, *Journal of the American Chemical Society* **1948**, *70*, 3975-3978.
[16] K. W. Lam, K. E. Johnson, D. G. Lee, *Journal of The Electrochemical Society* **1978**, *125*, 1069-1076.
[17] L. D. Burke, D. P. Whelan, *Journal of Electroanalytical Chemistry and Interfacial Electrochemistry* **1979**, *103*, 179-187.
[18] L. D. Burke, J. F. Healy, *Journal of Electroanalytical Chemistry and Interfacial Electrochemistry* **1981**, *124*, 327-332.
[19] P. G. Pickup, V. I. Birss, *Journal of Electroanalytical Chemistry and Interfacial Electrochemistry* **1987**, *220*, 83-100.
[20] M. E. G. Lyons, (University Collage Cork), **1983**; S. D. James, *Journal of The Electrochemical Society* **1969**, *116*, 1681-1688.
[21] J. W. Schultze, K. J. Vetter, *Electrochimica Acta* **1973**, *18*, 889-896.
[22] M. O'Brien, L. Russell, I. Godwin, R. L. Doyle, M. E. G. Lyons, *ECS Transactions* **2013**, *45*, 21-51.
[23] K. Aoki, K. Tokuda, H. Matsuda, *Journal of Electroanalytical Chemistry and Interfacial Electrochemistry* **1983**, *146*, 417-424; K. Aoki, K. Tokuda, H. Matsuda, *Journal of Electroanalytical Chemistry and Interfacial Electrochemistry* **1984**, *160*, 33-45.
[24] V. Mirčeski, Ž. Tomovski, *Journal of Solid State Electrochemistry* **2011**, *15*, 197-204.
[25] *Molecular design of electrode surfaces / edited by Royce Murray*, Wiley, New York, **1992**; J. C. Jernigan, C. E. D. Chidsey, R. W. Murray, *Journal of the American Chemical Society* **1985**, *107*, 2824-2826.

[26] E. Laviron, *Journal of Electroanalytical Chemistry and Interfacial Electrochemistry* **1979**, *100*, 263-270; E. Laviron, *Journal of Electroanalytical Chemistry and Interfacial Electrochemistry* **1980**, *112*, 1-9; E. Laviron, *Journal of Electroanalytical Chemistry and Interfacial Electrochemistry* **1979**, *101*, 19-28; dE. Laviron, *Journal of Electroanalytical Chemistry and Interfacial Electrochemistry* **1974**, *52*, 395-402.
[27] H. Bode, K. Dehmelt, J. Witte, *Electrochimica Acta* **1966**, *11*, 1079-IN1071.
[28] W. H. Press, S. A. Teukolsky, W. T. Vetterling, B. P. Flannery, *Numerical recipes in C (2nd ed.): the art of scientific computing*, Cambridge University Press, **1992**.
[29] M. E. G. Lyons, L. D. Burke, *Journal of the Chemical Society, Faraday Transactions 1: Physical Chemistry in Condensed Phases* **1987**, *83*, 299-321.
[30] M. E. G. Lyons, S. Floquet, *Physical Chemistry Chemical Physics* **2011**, *13*, 5314-5335; R. L. Doyle, I. J. Godwin, M. P. Brandon, M. E. G. Lyons, *Physical Chemistry Chemical Physics* **2013**, *15*, 13737-13783.
[31] M. E. G. Lyons, M. P. Brandon, *Journal of Electroanalytical Chemistry* **2010**, *641*, 119-130.
[32] M. E. G. Lyons, M. P. Brandon, *Journal of Electroanalytical Chemistry* **2009**, *631*, 62-70; L. D. Burke, E. J. M. O'Sullivan, *Journal of Electroanalytical Chemistry and Interfacial Electrochemistry* **1981**, *129*, 133-148; M. Lyons, L. Russell, M. O'Brien, R. Doyle, I. Godwin, M. Brandon, *Redox Switching and Oxygen Evolution at Hydrous Oxyhydroxide Modified Nickel Electrodes in Aqueous Alkaline Solution: Effect of Hydrous Oxide Thickness and Base Concentration, Vol. 7*, **2012**.
[33] R. L. Doyle, M. E. G. Lyons, in *Photoelectrochemical Solar Fuel Production: From Basic Principles to Advanced Devices* (Eds.: S. Giménez, J. Bisquert), Springer International Publishing, Cham, **2016**, pp. 41-104.
[34] I. Godwin, *PhD Thesis* **2015**.
[35] R. L. Doyle, M. E. G. Lyons, *Physical Chemistry Chemical Physics* **2013**, *15*, 5224-5237.
[36] B. E. Conway, E. Gileadi, *Transactions of the Faraday Society* **1962**, *58*, 2493-2509; P. C. Milner, *Journal of The Electrochemical Society* **1960**, *107*, 343-348; B. E. Conway, P. L. Bourgault, *Canadian Journal of Chemistry* **1959**, *37*, 292-307.
[37] R. A. Bockris JO'M, Gamboa-Aldeco M **2002**, 1412.
[38] B. E. Conway, P. L. Bourgault, *Transactions of the Faraday Society* **1962**, *58*, 593-607.
[39] D. Lozano-Castelló, D. Cazorla-Amorós, A. Linares-Solano, S. Shiraishi, H. Kurihara, A. Oya, *Carbon* **2003**, *41*, 1765-1775; M. J. Bleda-Martínez, J. A. Maciá-Agulló, D. Lozano-Castelló, E. Morallón, D. Cazorla-Amorós, A. Linares-Solano, *Carbon* **2005**, *43*, 2677-2684; R. Jurczakowski, C. Hitz, A. Lasia, *Journal of Electroanalytical Chemistry* **2004**, *572*, 355-366; A. Celzard, F. Collas, J. F. Marêché, G. Furdin, I. Rey, *Journal of Power Sources* **2002**, *108*, 153-162.
[40] J. Lyklema, *Journal of Electroanalytical Chemistry and Interfacial Electrochemistry* **1968**, *18*, 341-348.

# CHAPTER 5

# THE REDOX AND ELECTROCATALYTIC BEHAVIOUR OF THERMALLY PREPARED NICKEL COBALT MIXED OXIDE FILMS

## 5.1 Introduction

This chapter focuses on the presentation of the electrochemical redox and charge transfer proprieties on nickel cobalt mixed oxide electrodes in alkaline solutions. These electrodes were prepared by thermal decomposition of their precursor salts in air and coated on titanium wire. The state of the art presented in chapter 1 will now be used and leveraged to explain the results of a series of investigations on the charge storage proprieties, redox activity and the electrocatalytic activity of nickel cobalt mixed oxide films. The potential-pH response of the nickel cobalt mixed oxide redox activity will also be examined and used to assign a more accurate stoichiometry of the redox system. Also included are relevant steady-state polarisation measurements that yield information to the nature of the catalytic surfaces on which the OER proceeds in these systems. The electrochemical analysis for various nickel cobalt mixed oxide electrodes with different Ni/Co molar ratio content, was focused on electrodes annealed at 400°C for the duration of 4 hours in air. At such annealing temperature and time, nickel cobalt mixed electrodes were found to exhibit the highest catalytic performance. A short study of the electrocatalytic behaviour of nickel cobalt mixed oxide electrodes annealed at temperatures in the range of 300°C to 550°C is also presented in this chapter.

Important notice: the abbreviation "% M Co content" is used to express the molar ratio content percentage of cobalt utilised to prepare the electrode. This percentage value refers to the concentration of cobalt, from a cobalt nitrate hexahydrate stock solution, employed to prepare the mixed aqueous solution from which the working electrode was prepared, *e.g.* 50 % molar Co content electrode accounts for an electrode produced using a mixed aqueous solution with a Ni/Co molar ratio = 1.

## 5.2 Brief Electrochemical Study of Nickel Oxide and Cobalt Oxide for OER

It is considered opportune to first discuss the general aspects of the redox behaviour of the thermally prepared nickel oxide and the cobalt oxide electrode before the mixed oxide materials are considered. Recall that these metal oxides were prepared by annealing a mixed aqueous solution with different Ni/Co molar ratios, at 400°C for 4 hours.

### 5.2.1 Nickel Oxide

Typical voltammetric curve of nickel oxide recorded in 1.0 M NaOH at 25°C is presented in fig. 5.2.1

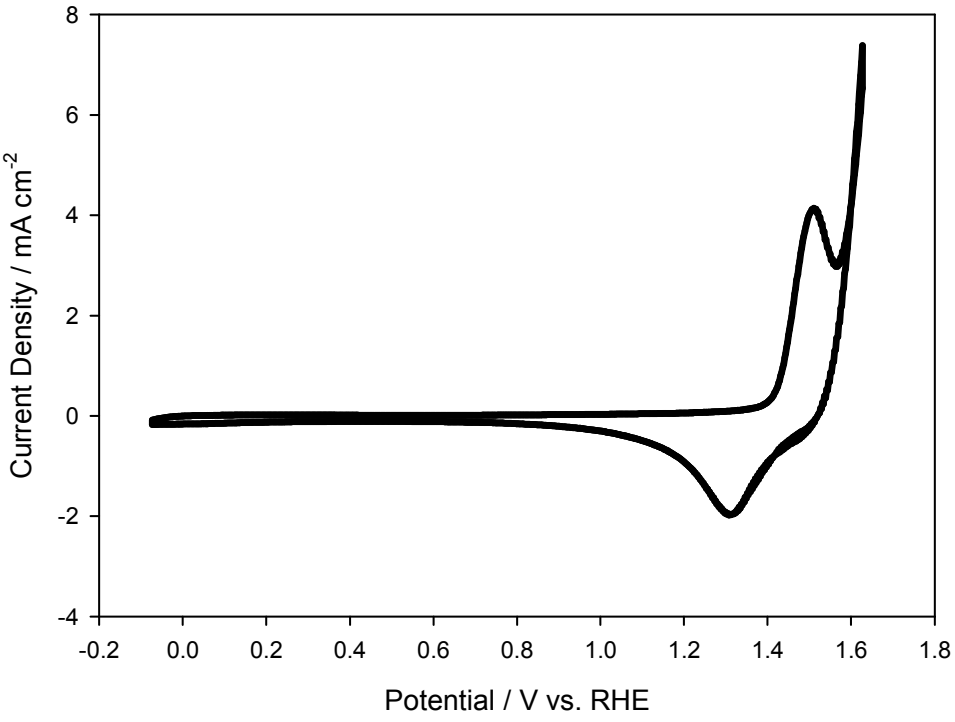



Figure 5.2.1 CV of a polycrystalline nickel oxide electrode in 1.0 M NaOH at 25°C. The sweep rate was 50 mV $s^{-1}$.

Redox peaks observed in fig. 5.2.1 are in good agreement with data published in literature.[1] For the nickel oxide film prepared by thermal decomposition, it can be assumed that it consists initially of a thick compact oxide layer, NiO according with the XRD results (see fig 5.3.5). In aqueous alkaline solution, however, the NiO undergoes the following reaction:

$$NiO + H_2O \rightarrow Ni(OH)_2 \qquad (5.2.1.1)$$

This was investigated by XPS analysis (see fig. 5.4.5) which proved the existence of $Ni(OH)_2$. The Ni (II/III) redox transformation can be though to be the same of the electroprecipitated nickel hydroxide shown in fig. 1.4.1. This oxidation reaction can be represented by the following reaction:[2]

$$Ni(OH)_2 \rightarrow \beta NiOOH + H^+ + e^- \qquad (5.2.1.2)$$

The NiO prepared by thermal decomposition can be seen to be analogous to the electroprecipitated nickel hydroxide electrode prepared by electrodeposition discussed in section 1.4.1, with the presence of a compact NiO inner layer. This inner layer has a significant impact on the electrocatalytic behaviour of the electrodes. In fig. 1.4.1 it can be observed that the onset potential for the OER in nickel oxide electrodes prepared *via* electrodeposition differs of ca. 30 mV more negative to those prepared by thermal decomposition. It is suggested that such difference in the OER onset potential can be attributed to the relatively thin insulating underlying thermally prepared NiO layer, with the smaller hydrous oxide layer. At high potentials in the OER region, the Ni (III/IV) redox transformation occurs according to eqn. 5.2.1.3:

$$\beta NiOOH + OH^- \rightarrow NiO_2 + H_2O + e^- \qquad (5.2.1.3)$$

Recall from section 1.4.1 that $NiO_2$ may exhibit an inhibitor behaviour for OER while the crystalline form of the nickel oxide hydroxide, the βNiOOH, is said to be "the right type of oxide" for the OER. The cathodic peak has been assigned to the reduction of βNiOOH back to $Ni(OH)_2$ according to the following expression:[3]

$$\beta NiOOH + H_2O + e^- \rightarrow Ni(OH)_2 + OH^- \qquad (5.2.1.4)$$

The Tafel plot obtained for NiO electrodes produced *via* thermal decomposition at 400°C in air in 1.0 M NaOH is presented in fig. 5.2.2.

As observed from fig. 5.2.2, the Tafel plot exhibits two different Tafel slopes, one at low overpotentials regions, 0.33 - 0.37 V, and another at high overpotentials regions 0.5 - 0.56 V. Tafel slope values for the first and second linear regions were found to be, 60 ± 5 mV $dec^{-1}$ and 230 ± 10 mV $dec^{-1}$, respectively. The latter may indicate changes in the position of RDS in the overall OER mechanism. A more detailed discussion of this observation will be given in section 5.4.

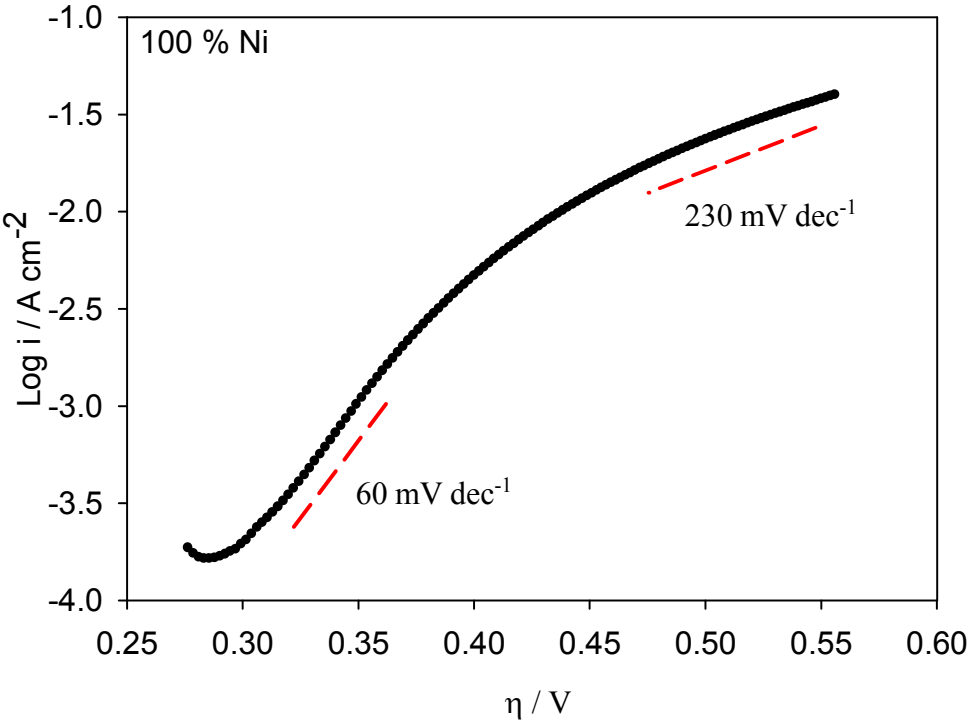



Figure 5.2.2 IR corrected steady-state polarisation curve recorded in the direction of increasing potential on a polycrystalline nickel oxide electrode in 1.0M NaOH solution at 25°C. The sweep rate was 1 mV $s^{-1}$.

### 5.2.2 Cobalt Oxide

Typical voltammetric curve of cobalt oxide recorded in 1.0 M NaOH at 25°C is presented in fig. 5.2.3. The cobalt oxide film prepared by thermal decomposition can be thought to consists of a thick compact oxide layer, $Co_3O_4$ according with the XRD results (see section 5.3.1). The cobalt oxide exhibits a spinel structure where the divalent, A, and trivalent, B, cations occupy the tetrahedral and octahedral sites, respectively (see section 5.4.2.2). Thus $Co_3O_4$ may be seen as $[Co^{2+}][Co^{3+}]_2O_4$. Analogous to the NiO film, cobalt oxide electrodes develop, in alkaline solutions, a thin outer oxide layer of cobalt (II) hydroxide, $Co(OH)_2$. Redox peak potential observed in fig. 5.2.3 are in good agreement with data published in literature.[4] The cyclic voltammogram of the film in 1.0 M NaOH revealed three oxidation peaks at ca. 0.5 V, ca. 1.1 V and ca. 1.5 V (*vs.* RHE), respectively, and a single reduction peak at ca. 1.45V that can be attributed to the conversion between four different cobalt oxidation states: (i) $CoO/Co(OH)_2$, (ii) $Co_3O_4$,(iii) CoOOH, and (vi) $CoO_2$.

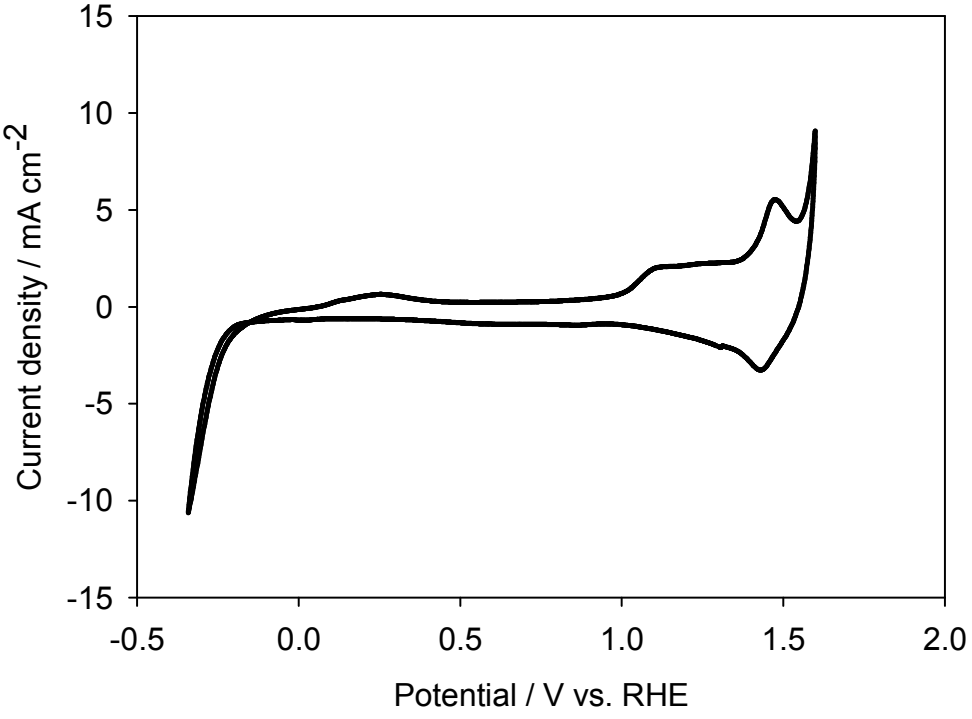



Figure 5.2.3 CV of a polycrystalline cobalt oxide electrode in 1.0 M NaOH at 25°C. The sweep rate was 50 mV $s^{-1}$.

According with previous publications, the first anodic peak may be assigned to the Co (II/III) transformation according to:

$$CoO_{inner} + 2H_2O \leftrightarrow Co_3O_4 + 2H^+ + 2e^- \quad (5.2.2.1)$$

or

$$3Co(OH)_2 + 2OH^- \leftrightarrow Co_3O_4 + 4H_2O + 2e^- \quad (5.2.2.2)$$

As mentioned in section 1.4.3, eqn. 5.2.2.2 may also form CoOOH species following:

$$Co(OH)_2 + OH^- \leftrightarrow CoOOH + H_2O + e^- \quad (5.2.2.3)$$

The formation of a second oxidation peak indicates the conversion of $Co(OH)_2$ to CoOOH. At higher positive potentials, the Co (III/IV) transformation takes place. This process can be represented as:

$$CoOOH + OH^- \leftrightarrow CoO_2 + H_2O + e^- \quad (5.2.2.4)$$

The very broad reduction peak, found at ca. 1.4 V, corresponds to the reduction of the Co (IV) oxide back to cobalt oxyhydroxide. The observation of a large charge under the cathodic peak may indicate that the Co (IV) reduces at the first instance to Co (III) followed by a final reduction to Co (II). The Tafel plot obtained for $Co_3O_4$ electrodes produced *via* thermal decomposition in 1.0 M NaOH is presented in fig. 5.2.4. As observed in fig 5.2.4, the Tafel plot revealed a single Tafel slope of 85.7 ± 4 mV $dec^{-1}$.

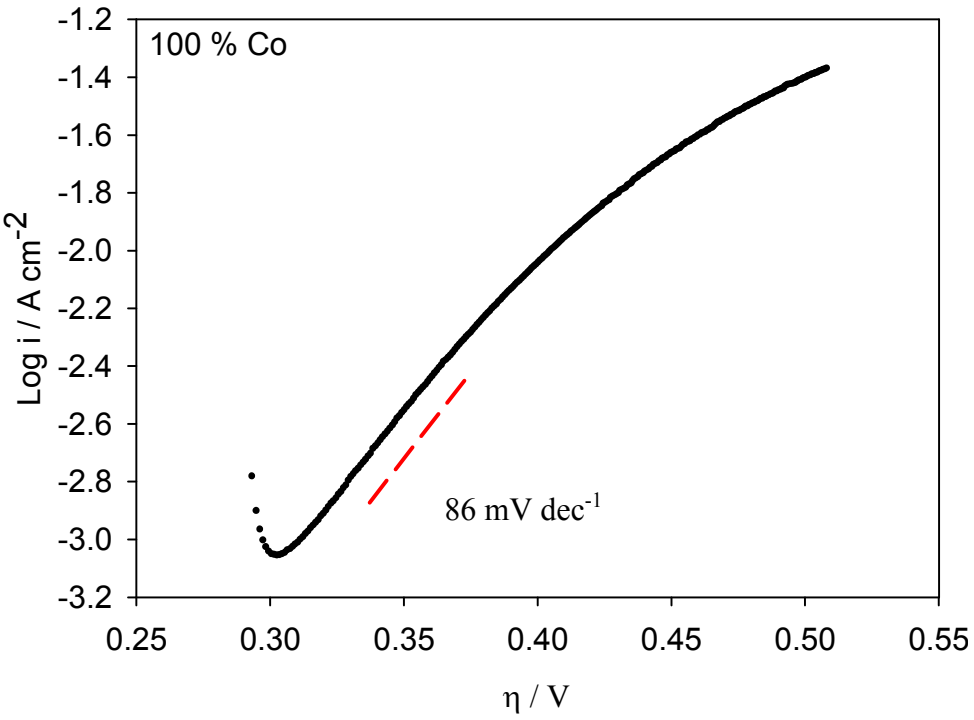



Figure 5.2.4 IR corrected steady-state polarisation curve recorded in the direction of increasing potential on a polycrystalline cobalt oxide electrode in 1.0 M NaOH solution at 25°C. The sweep rate was 1mV $s^{-1}$.

## 5.3 Annealing Temperature Effect on Nickel Cobalt Mixed Oxide Electrodes

In this section, the study of various physical parameters, such as: (i) phase composition and lattice constant, (ii) crystallite size, (iii) degree of crystallinity, and (iv) surface morphology as a function of annealing temperature, in a range of 300°C to 550°C are presented. We also include a brief electrocatalytic study on Ni/Co mixed oxide electrodes annealed at different temperatures aiming to determine the optimum annealing temperature to produce the most active catalytic film towards OER.

### 5.3.1 Structural Analysis

Since the aim of this chapter is to investigate the physical nature and electrocatalytic behaviour of nickel cobalt oxide prepared *via* thermal decomposition method, we found necessary to determinate the minimum annealing temperature at which the formation of the $NiCo_2O_4$ compound occurs. Previous publications suggested that the $NiCo_2O_4$ phase is observed, in XRD patterns, at minimum temperatures of around 300°C.[5] Therefore the absence of weight loss at such temperature should be observed since that would signify that the compound is completely formed. Fig. 5.3.1 depicts the typical thermogravimetric curves of pure nickel nitrate hexahydrate, pure cobalt nitrate hexahydrate and a 1:1 $Ni^{2+}/Co^{2+}$ molar ratio aqueous mixture.

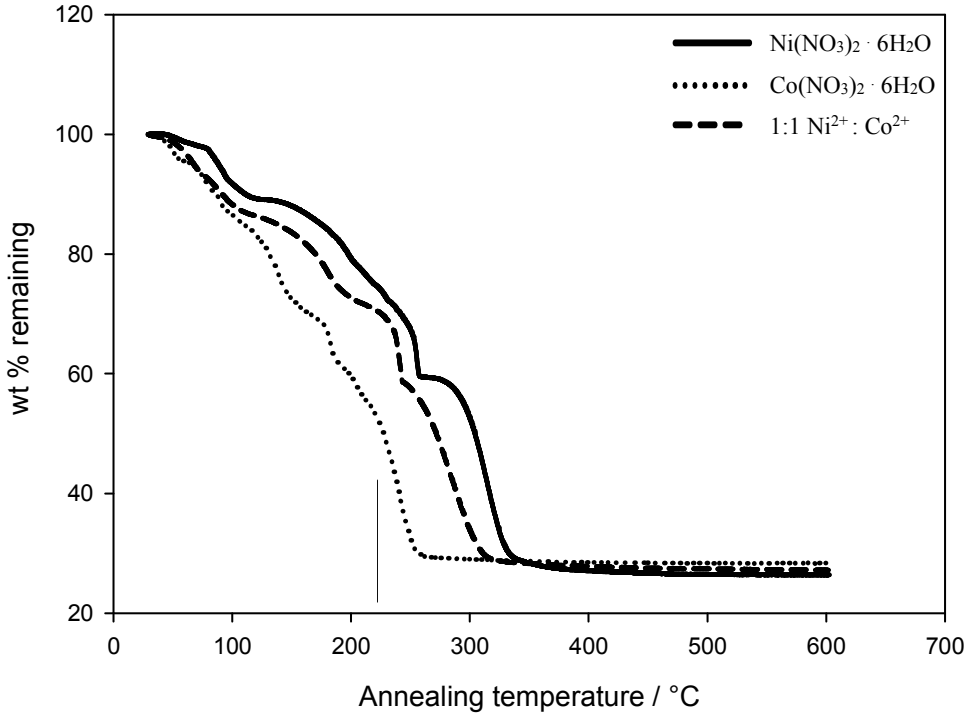



Figure 5.3.1 Thermogravimetric curves plotted as a fraction of the initial weight *vs.* temperature of: $Ni(NO_3)_2$ $6H_2O$ (solid line); $Co(NO_3)_2$ $6H_2O$ (dotted line); and a 1:1 molar ratio of $Ni^{2+}/Co^{2+}$ precursor solution (dashed line). The curves were recorded form 30°C to 600°C at a heating rate of 5°C $min^{-1}$.

It was observed from fig. 5.3.1 that the melting points of nickel and cobalt precursor salts were nearly the same at 57°C and 54°C, respectively. We suggest that the melting point do not play a crucial role in the formation of $NiCo_2O_4$ structures since both occur at similar temperatures. It can also be seen that the different steps, *e.g.* loss of adsorbed water, further decomposition of the nitrates and final oxide formation, take place at a lower temperature

for cobalt nitrate compared to that of nickel nitrate. On the other hand, decomposition and crystallization of mixed nitrates, from which the $NiCo_2O_4$ spinel species are formed, occurs at intermediate temperatures. For nickel nitrate, the TGA curve exhibits two sharp weight losses. The former corresponds to the evaporation of hydration water molecules, which is ca. 10 wt.% loss, and the latter is associated with the loss of water produced by dehydroxylation of the hydroxide layers, which is 30 wt.% loss.[6] The decomposition of the nitrate, with the evolution of $NO_x$, starts as soon as the dehydration is completed, which may occur at temperatures of ca. 260 °C. In the case of cobalt nitrate, the first peak, at ca. 120°C reflects the departure of physically adsorbed water molecules.[7] In addition, two endothermic decomposition events take place at 146°C and 185°C. Nitrogen dioxide and oxygen are the major gaseous products released in this range of temperatures. Note that all the statements regarding gas evolution do not arise from FTIR measurements and therefore, should be treated with care. Furthermore, oxygen decomposition is completed at 270°C. The weight at 270°C may not correspond exactly to that of $Co_3O_4$. J.Haenen *et al.*[8] mentioned that the presence of hydration water in excess over the nominal composition can disturb the calculations based on the TGA curve. The TGA curve of the nickel cobalt mixed oxide is initially similar to that obtained for cobalt nitrate: two distinct weight loss steps in the regions of 40° - 240°C, and 240° - 300°C, are observed, followed by a very small weight loss starting at 400°C. The first weight loss at 40° - 240°C corresponds to the exclusion of physically adsorbed water molecules and an endothermic decomposition peak related with nitrogen dioxide and oxygen removal. The second step at 240° - 300°C can be ascribed to the conversion of the anhydrous precursor into oxide, which would form either NiO, $Co_2O_3$ or $NiCo_2O_4$.[9]

From TGA results, it can be suggested that $NiCo_2O_4$ spinel oxide is already formed at temperatures about 300°C and remains stable up to about 400°C. The weight loss above 400°C can be interpreted as the start of the breakdown of the spinel oxide $NiCo_2O_4$. It was noted that the temperature at which the $NiCo_2O_4$ spinel structure is formed varies with the heating rate. Fig. 5.3.2 shows two TGA curves corresponding to 1:1 mixed $Ni^{2+}/Co^{2+}$ molar ratio obtained at different heating rates. It can be noted that the formation of a stable $NiCo_2O_4$ spinel structure occurs at different annealing temperatures, at 320°C and 350°C for heating rates of 5°C $min^{-1}$ and 10°C $min^{-1}$, respectively. Similar behaviour was observed for other spinel structures such as $Co_3O_4$. Pope *et al.*[10] observed that the decomposition of cobalt carbonate to form $Co_3O_4$ was completed at temperatures around 250°C in air, while

Garavaglia *et al.*[11] reported that at sufficiently long times $Co_3O_4$ can be formed at 150°C (48 hours). This author also mentioned that at temperatures around 400°C, cobalt nitrate hexahydrate decomposes to $Co_3O_4$ within 1 hour calcination time. Recall from chapter 3 that in this work, samples were calcined for the duration of 4 hours to ensure a complete nitrate to oxide transformation. Thermogravimetric analysis of the cobalt nitrate and the mixed cobalt nitrate is in agreement with the results obtained by other authors.[12]

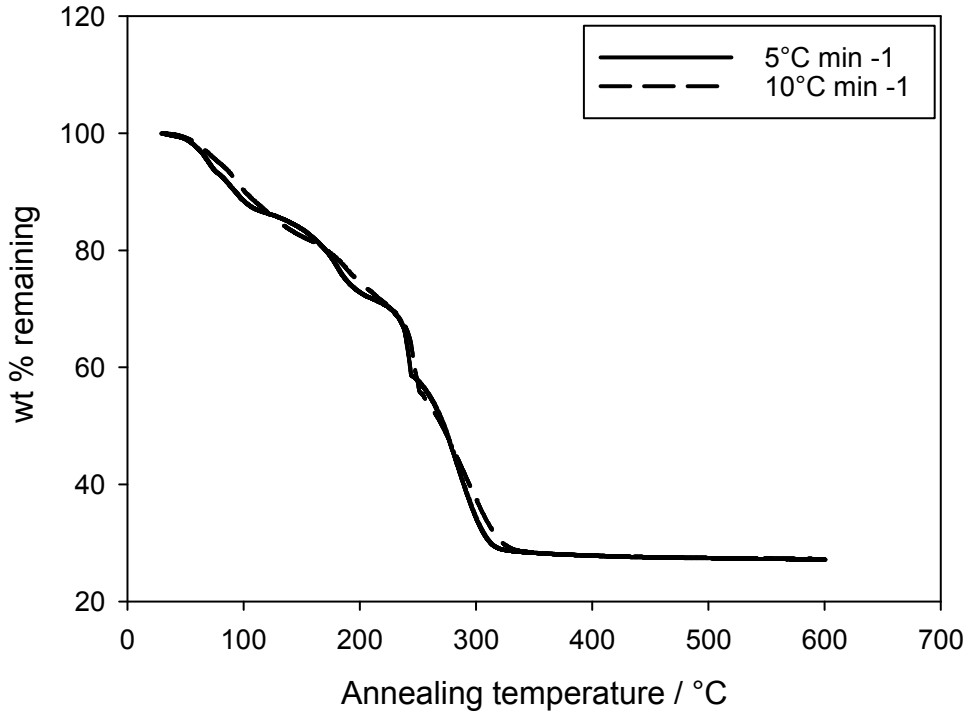



Figure 5.3.2 Thermogravimetric curves plotted as a fraction of the initial weight *vs.* temperature of 1:1 molar ratio of $Ni^{2+}/Co^{2+}$ precursor solution using different heating rates: 5°C $min^{-1}$ (solid line) and of 10°C $min^{-1}$ (dashed line). The curves were recorded form 30°C to 600°C.

The XRD diffraction patterns of the nickel cobalt mixed oxide electrodes with 50 % M Co content produced at different annealing temperatures are shown in fig. 5.3.3. The phase purity of all the samples was established by comparison of the X-ray diffraction pattern with the International Centre for Diffraction Data (ICDD) values. Note that the intensity of all peaks was normalized according to the maximum peak. It can be observed that all the diffraction patterns exhibit diffraction peaks at 2θ ca. 18.9°, ca. 31.1°, ca. 36.6°, ca. 38.3° and ca. 44.5° corresponding to (111), (220), (311), (222) and (400) planes, respectively. The latter calculated values were found to be in agreement with ICDD card number 20-0781 which corresponds to $NiCo_2O_4$ compound. Note that the intensity of the (311) $NiCo_2O_4$ peak

at 2θ = 36.6°, is significantly higher than the other peaks, indicating that the $NiCo_2O_4$ films grow preferentially textured along the (311) direction rather than along the (111), (220), (222) or (400). In addition, the positions of the peaks and the presence of more than one diffraction peak lead to the conclusion that these films are polycrystalline in nature with a face-centred cubic (FCC) lattice, which is in agreement with other reports.[13]

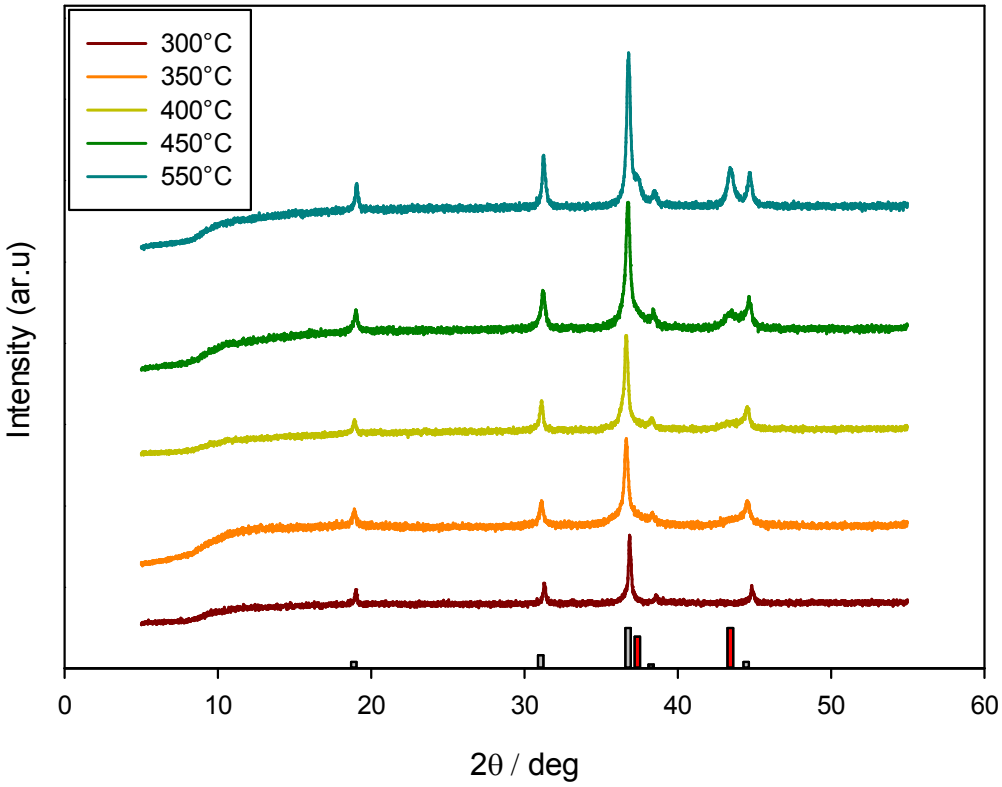



Figure 5.3.3 XRD powder patterns of 1:1 molar ratio $Ni^{2+}/Co^{2+}$ oxide powder evaluated at increasing annealing temperatures, from 300°C - 550°C. Grey and red vertical bars illustrate database's XRD reference patterns for nickel cobalt oxide, $NiCo_2O_4$ (PDF # 200781), and nickel oxide, NiO (PDF # 471049), respectively.

The calculated lattice constants for all the samples were in agreement with ICDD Card values. The lattice constant was found to be strongly influenced by annealing temperature. As it is clear from fig. 5.3.4, the lattice parameter of the $NiCo_2O_4$ phase changes quite slowly on heating between 300°C and 350°C but then dramatically decreases between 400 and 550°C, from 8.118 Å to 8.0991 Å, respectively. The significant reduction of the lattice parameter, observed in fig. 5.3.4, may suggest contraction of the crystals as the annealing temperature increases. Same lattice contraction behaviour was also noticed by other authors.[14]

Typically, the "expected" effect would be the opposite, that is, lattice expansion occurs as annealing temperature is increased. In other words, materials tend to expand at high temperatures. However, as mentioned in section 1.2.3, crystallite surfaces usually do not present an ideal surface. Real electrode surfaces always exhibit a certain number of defects. In this perspective, it has been pointed out that nickel cobalt oxide films exhibit several surface defects such as oxygen vacancies, lattice disorders, etc., and a large amount extent of impurities.[15] From our understanding of the defect kinetics in metals, we suggest that during annealing at high temperatures these defects and impurities are removed resulting in a lattice contraction. Another important observation from fig. 5.3.4 is the formation of a different crystal phase within the sample.

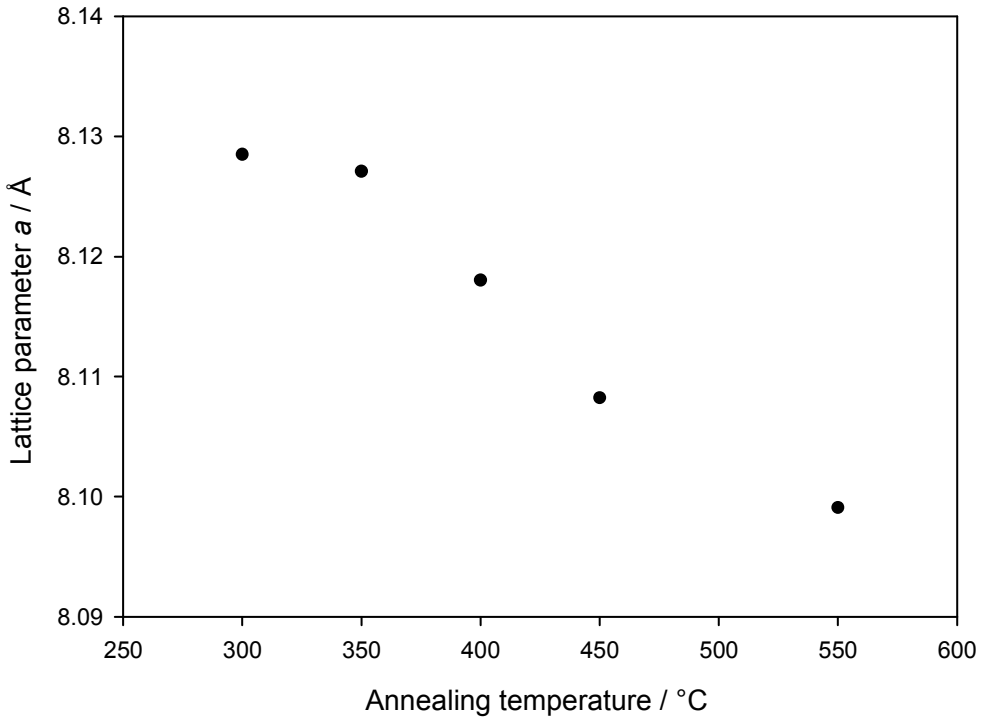



Figure 5.3.4 Lattice parameter *a* of 1:1 molar ratio of $Ni^{2+}/Co^{2+}$ oxide powder as a function of annealing temperature.

At temperatures above 400°C two diffraction peaks arise at 2θ ca. 37.5° and ca. 43.5° corresponding to (111) and (200) planes, respectively. These diffraction peak values were found to be in agreement with the ICDD card number 47-1049 which corresponds to NiO or Bunsenite compound. Such phase exhibit FCC lattice with a lattice constant of 4.1734 Å. The XRD diffraction pattern for pure nickel oxide is present in fig. 5.3.5. As observed from

fig. 5.3.5, both diffraction peaks match those found in fig. 5.3.3 at 2θ = 37.5° and ca. 43.5°. Therefore, the increase of such peaks may suggest that at annealing temperatures above 400°C, the NiO phase becomes more relevant within the sample by increasing its wt.% phase. It is therefore important to determine the origin of the nickel employed to form the NiO phase. Note that some NiO arises from the excess of nickel initially used to create the 1:1 $Ni^{2+}$:$Co^{2+}$ precursor solution. It has been pointed out that at annealing temperatures of about 400°C, the $NiCo_2O_4$ structure begins to decompose originating both the formation of $Co_3O_4$ phase and NiO phase (see Table 5.3.1).[16] This is in agreement with that observed in fig. 5.3.3 where, as the annealing temperature increases, the intensity of diffraction peaks corresponding to NiO increases.

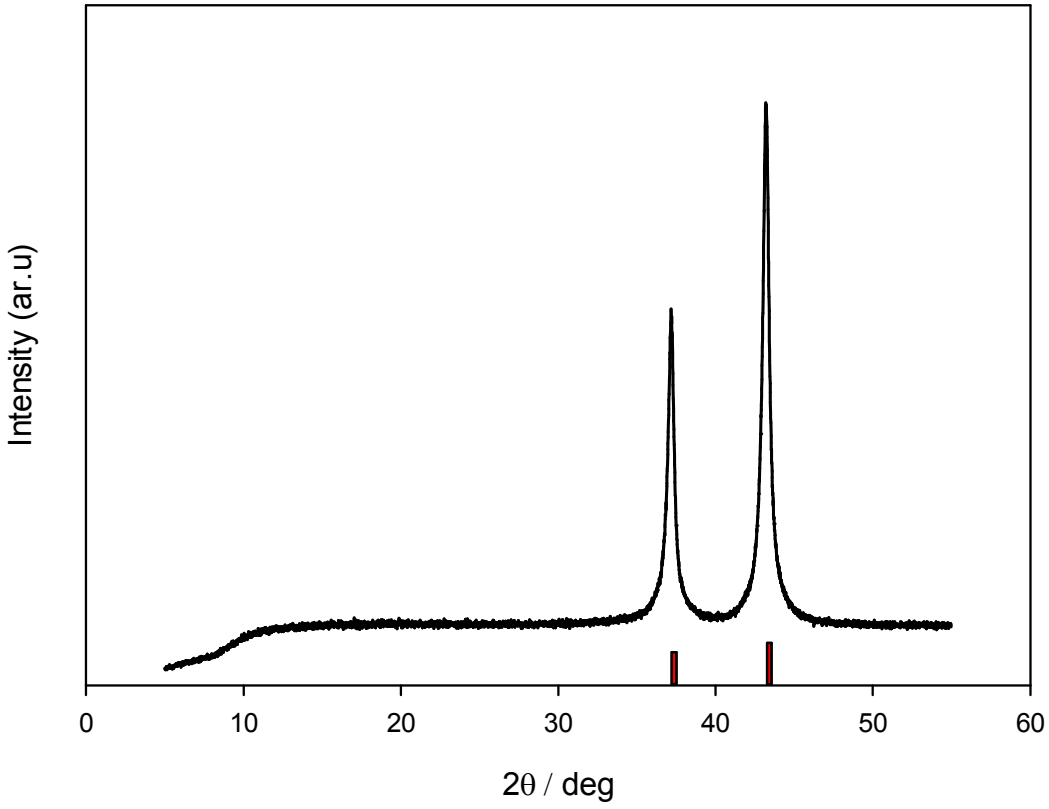



Figure 5.3.5 XRD powder pattern of $Ni(NO_3)_2$ $6H_2O$ annealed at 400°C compared to database's NiO reference pattern (PDF # 471049).

It must be mentioned that the determination of wt.% phase from XRD diffraction patterns should treated with care since, NiO and particularly $Co_3O_4$ reflection peaks can be masked in the XRD pattern. On the one hand, NiO peaks can be masked due to the concentration of NiO is lower with respect to that of $Co_3O_4$ or $NiCo_2O_4$, this results in lower peak intensities.

On the other hand, the $Co_3O_4$ peaks may be masked because of both phases, $Co_3O_4$ and $NiCo_2O_4$ possess same spinel structure with similar lattice parameters. The phase composition study as a function of annealing temperature for nickel cobalt oxide samples produced using 1:1 $Ni^{2+}$:$Co^{2+}$ ratio is presented in Table 5.3.1.

Considering both that the $NiCo_2O_4$ possesses a molar ratio of 1:2 $Ni^{2+}$:$Co^{2+}$ and the sample is produced from a 1:1 $Ni^{2+}$/$Co^{2+}$molar ratio precursor solution, it is suggested that powder samples can be composed theoretically of 60% NiO and 40% $NiCo_2O_4$. Thus, it should be expected to detect some extent of NiO phase in the XRD patterns.

| **Annealing Temperature / °C** | **NiO wt.%** | **$C_3O_4$ wt.%** | **$NiCo_2O_4$ wt.%** |
|---|---|---|---|
| 300 | 1.60 | - | 98.40 |
| 350 | 2.50 | - | 97.5 |
| 400 | 6.50 | - | 93.50 |
| 450 | 9.20 | 14.60 | 76.30 |
| 550 | 16.40 | 17.00 | 69.50 |

Table 5.3.1 Wt.% phase composition of nickel cobalt mixed oxides with 50 % M Co content annealed at different temperatures in air. These values are obtained from patterns in fig. 5.3.3 using MDI Jade software.

Opposite to theoretical calculations, NiO phase was not significantly observed until temperatures above 350°C were reached. Note that ca. 300°C is the minimum calcination temperature to form crystalline NiO films. At lower annealing temperatures, the presence of hydrated oxide forms (NiOOH) on the surface of NiO crystallites may be observed.[17] It has also been mentioned that NiOOH possesses amorphous structure which causes the impossibility to determine the NiOOH phase using XRD.[18] We would like to mention now that the presence of a NiO phase will affect, as it will be discussed in section 5.4, the electrochemical behaviour of Ni-Co electrodes since this phase is known to possess poor conductivity. We would like to mention that XRD results should be presented along with XPS and EDX analysis to precisely determinate the surface composition of the samples. Unfortunately, neither XPS nor EDX analysis was carried out to quantitative determine the effect of annealing temperature on phase composition of nickel cobalt mixed oxide samples.

### 5.3.2 Degree of Crystallinity

The calculation of crystallinity by XRD is based on the presumption that a broad peak arises from an amorphous phase whereas the sharp peak comes from a crystal phase. This parameter is unidimensional and normally, it is expressed as a percentage. Therefore, the absence of broad peaks indicate that the sample is completely crystalline. From this perspective, and taking into consideration eqn. 2.4.11, the degree of crystallinity as a function of annealing temperature is presented in fig. 5.3.6. Rapidly, from fig. 5.3.6, it may be deduced that the samples are not purely crystalline but very amorphous. It is also clear that as the temperature increases the crystallinity also increases. It has been pointed out that amorphous materials tend to obtain larger channels and more reaction sites; hence, ion diffusion enhancement occurs.[19] It has also been pointed out that crystallisation enhancement occurs as annealing temperature increases.[20] We understand this is also occurring in our samples.

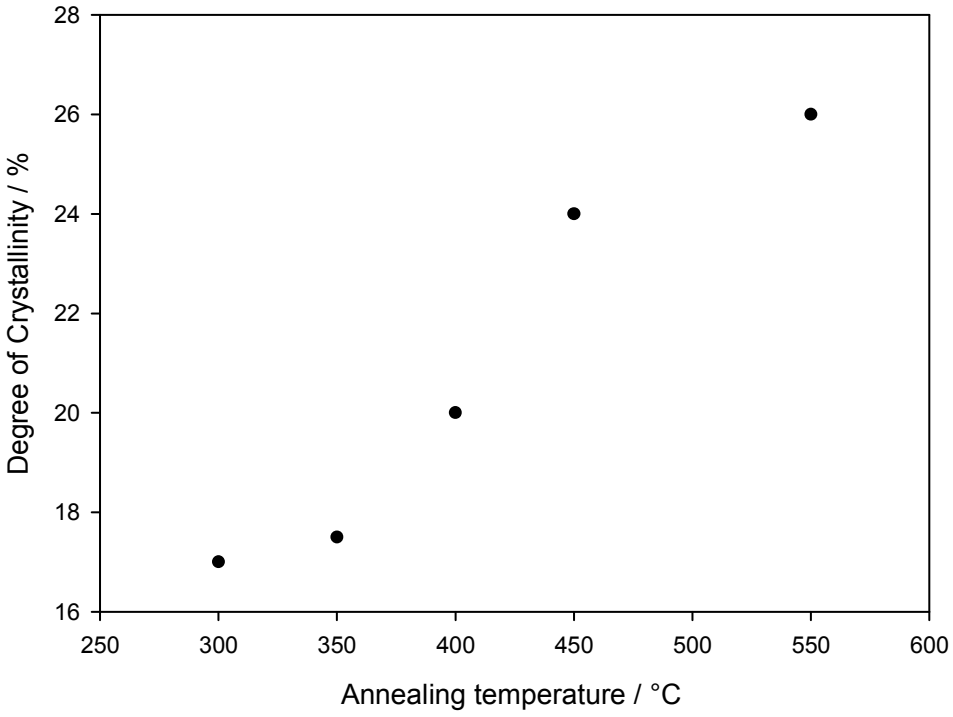



Figure 5.3.6 Degree of crystallinity of 1:1 molar ratio of $Ni^{2+}/Co^{2+}$ oxide powder as a function of annealing temperature.

### 5.3.3 Crystallite Size

Important: results presented in this section should be treated with care since the technique here utilised only holds for single phases. Note that linear regression lines in figs. 5.3.7 to 5.3.11 do not fit linearly with the data points. This suggests the existence of more than one phase in the samples.

Before introducing the discussion on the effect of annealing temperature on the electrocatalytic activity of Ni-Co electrodes, it is convenient to introduce first a crucial parameter which directly affects the nature of reactions on electrode surfaces, the crystallite size (see section 2.4). Lyons[21] observed that crystallite size is favoured by: (i) high annealing temperatures, (ii) slow heating rates, and (iii) a high oxidizing atmosphere. Work reported by Burke and Murphy[22] has indicated that the specific surface area, which is closely related to the crystallite size in porous electrodes, of an $RuO_2$ film can vary from ca. 70 $m^2g^{-1}$ to ca. 8 $m^2g^{-1}$ on increasing the annealing temperature from 300°C to 500°C. The decrease of the surface area with increasing annealing temperature is consistent with the operation of a sintering reaction. Among the available methods to estimate the crystallite size are the pseudo-Voigt function, Rietveld refinement, and Warren-Averbach analysis.[23] In the present study, Williamson-Hall (W-H) analysis is employed for determining crystallite size of 1:1 $Ni^{2+}/Co^{2+}$ molar ratio oxide electrodes annealed at different temperatures in the range of 300°C to 500°C. Recall that the Williamson-Hall method was discussed in section 2.4. In order to investigate the behaviour of crystallite size as a function of annealing temperature, Williamson-Hall plots are presented in figs. 5.3.7 – 5.3.11 along with their corresponding peak report table.

The determination of the crystallite size can be estimated from the y-intercept of the linear fit to the data lines in figs. 5.3.7 - 5.3.11 according to eqn. 2.4.10. The result of the crystalline size as a function of annealing temperature is presented in fig. 5.3.3.6. A marked decrease in the crystallite size, from ca. 38 nm to ca. 29 nm, was observed. In tandem with that previously mentioned in section 5.3.1, we suggest that during annealing at high temperatures impurities and defects are removed from the crystal structure resulting in both lattice contraction and crystallite size reduction. Normally, the crystallite size is expected to increase when the calcination temperature increases, however this was not the case. Further analysts is been carried out to investigate this.

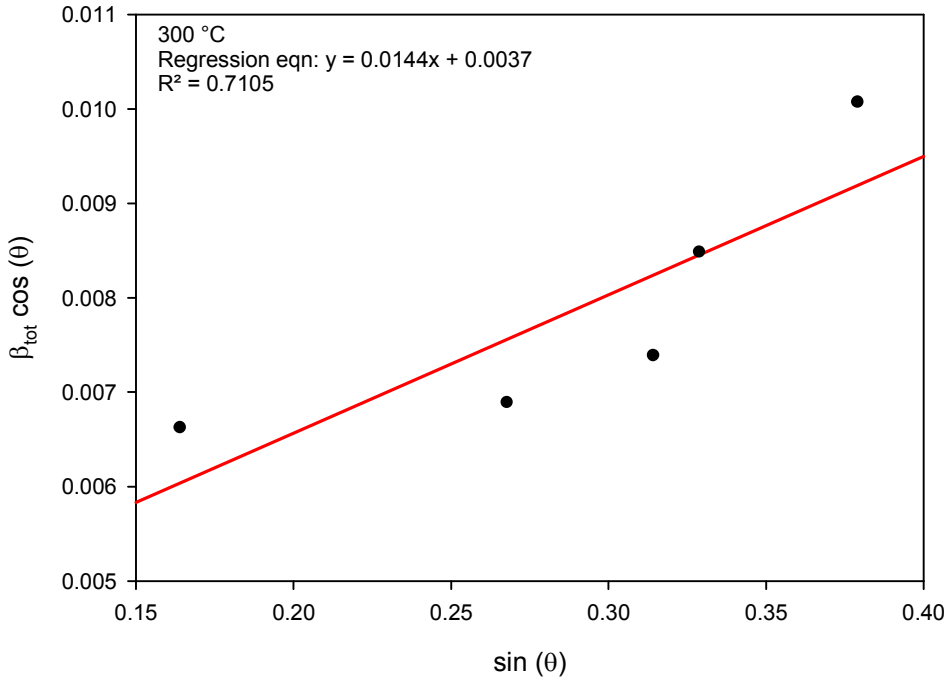



Figure 5.3.7 a) The Williamson-Hall analysis of 1:1 molar ratio of $Ni^{2+}/Co^{2+}$ oxide powder annealed at 300°C in air. The analysis revealed a particle size of 37.46 nm.

| 2-Theta / (°) | d / nm | BG | Height | I% | Area | I% | FWHM / (°) |
|---|---|---|---|---|---|---|---|
| 18.885 | 0.47001 | 30 | 210 | 17.8 | 81.6 | 15.9 | 0.385 |
| 31.048 | 0.28781 | 32 | 327 | 27.7 | 142.2 | 27.6 | 0.41 |
| 36.617 | 0.24521 | 150 | 1180 | 100 | 514.9 | 100 | 0.425 |
| 38.379 | 0.23435 | 46 | 166 | 14.1 | 72.7 | 14.1 | 0.515 |
| 44.536 | 0.20327 | 39 | 354 | 30 | 231.4 | 44.9 | 0.624 |

Table 5.3.7 b) The Williamson-Hall analysis of 1:1 molar ratio of $Ni^{2+}/Co^{2+}$ oxide powder annealed at 300°C in air. The analysis revealed a particle size of 37.46 nm.

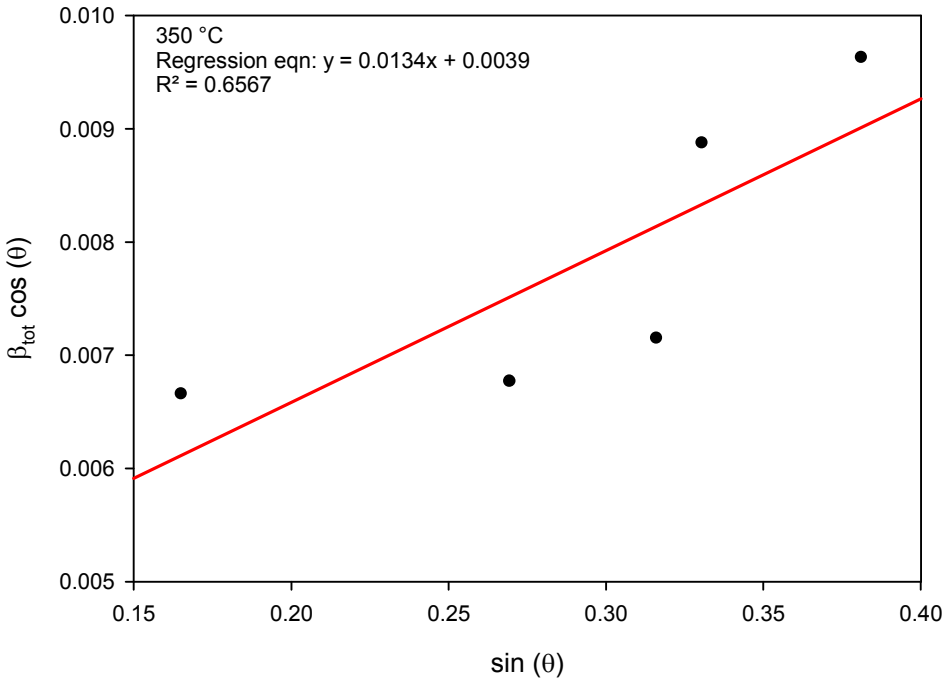



Figure 5.3.8 a) The Williamson-Hall analysis of 1:1 molar ratio of $Ni^{2+}/Co^{2+}$ oxide powder annealed at 350°C in air. The analysis revealed a particle size of 35.54 nm.

| 2-Theta / (°) | d / nm | BG | Height | I% | Area | I% | FWHM/ (°) |
|---|---|---|---|---|---|---|---|
| 18.987 | 0.46703 | 2 | 123 | 17.9 | 59.4 | 17.7 | 0.387 |
| 31.241 | 0.28608 | 9 | 205 | 29.8 | 93 | 27.7 | 0.403 |
| 36.832 | 0.24384 | 28 | 688 | 100 | 335.3 | 100 | 0.432 |
| 38.585 | 0.23316 | 3 | 69 | 13.3 | 73 | 20.1 | 0.539 |
| 44.790 | 0.20218 | 8 | 131 | 25.2 | 92 | 25.3 | 0.597 |

Table 5.3.8 b) The Williamson-Hall analysis of 1:1 molar ratio of $Ni^{2+}/Co^{2+}$ oxide powder annealed at 350°C in air. The analysis revealed a particle size of 35.54 nm.

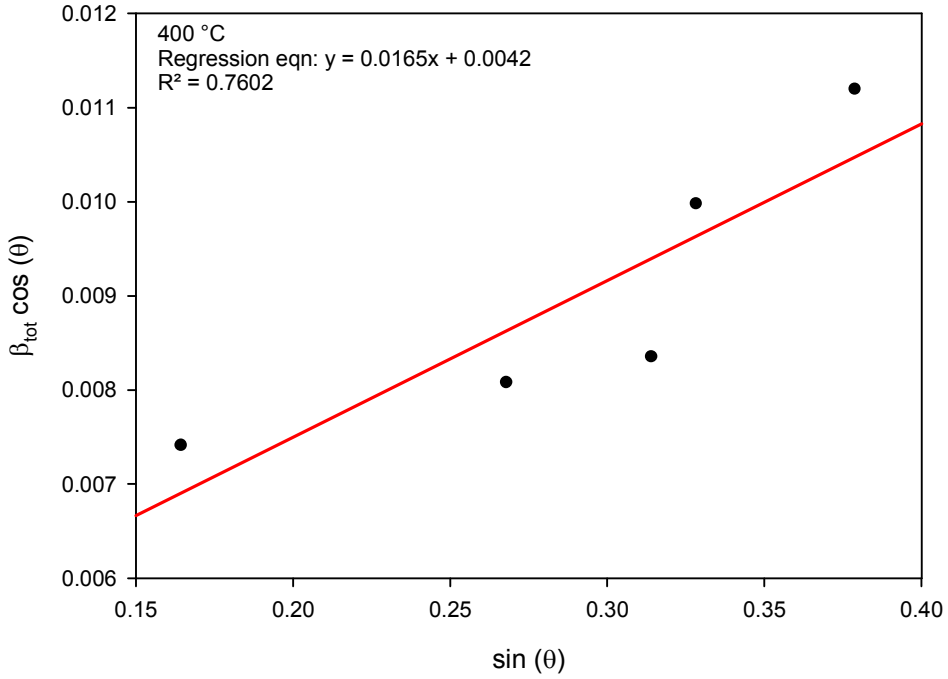



Figure 5.3.9 a) The Williamson-Hall analysis of 1:1 molar ratio of $Ni^{2+}/Co^{2+}$ oxide powder annealed at 400°C in air. The analysis revealed a particle size of 33.02 nm.

| 2-Theta / (°) | d / nm | BG | Height | I% | Area | I% | FWHM/ (°) |
|---|---|---|---|---|---|---|---|
| 18.905 | 0.46901 | 1 | 128 | 11.7 | 58.7 | 9.9 | 0.39 |
| 31.068 | 0.28762 | 24 | 320 | 29.2 | 165.4 | 27.8 | 0.439 |
| 36.597 | 0.24534 | 91 | 1095 | 100 | 595.5 | 100 | 0.462 |
| 38.318 | 0.2347 | 31 | 121 | 11.1 | 80.2 | 13.5 | 0.563 |
| 44.506 | 0.2034 | 22 | 281 | 25.7 | 214.7 | 36.1 | 0.65 |

Table 5.3.9 b) The Williamson-Hall analysis of 1:1 molar ratio of $Ni^{2+}/Co^{2+}$ oxide powder annealed at 400°C in air. The analysis revealed a particle size of 33.02 nm.

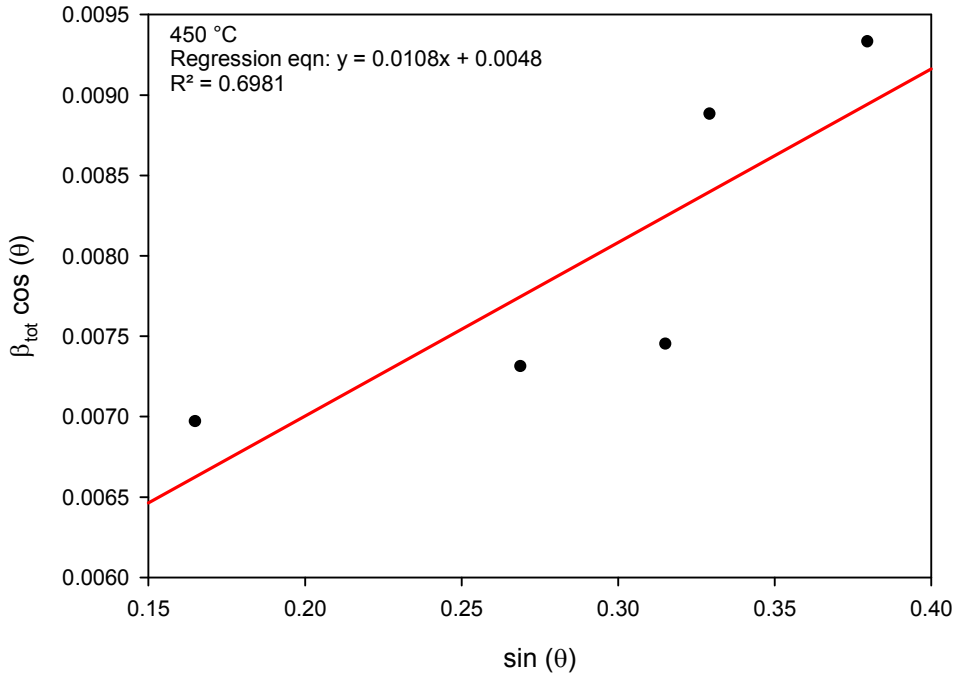



Figure 5.3.10 a) The Williamson-Hall analysis of 1:1 molar ratio of $Ni^{2+}/Co^{2+}$ oxide powder annealed at 450°C in air. The analysis revealed a particle size of 28.87 nm.

| 2-Theta / (°) | d / nm | BG | Height | I% | Area | I% | FWHM/ (°) |
|---|---|---|---|---|---|---|---|
| 18.976 | 0.46727 | 1 | 232 | 14.2 | 110.6 | 12.8 | 0.405 |
| 31.179 | 0.28662 | 35 | 500 | 30.6 | 255.7 | 29.5 | 0.435 |
| 36.729 | 0.24449 | 162 | 1635 | 100 | 866.5 | 100 | 0.45 |
| 38.440 | 0.23399 | 39 | 189 | 11.6 | 119.9 | 13.8 | 0.539 |
| 44.617 | 0.20292 | 27 | 420 | 25.7 | 285.4 | 32.9 | 0.578 |

Table 5.3.10 b) The Williamson-Hall analysis of 1:1 molar ratio of $Ni^{2+}/Co^{2+}$ oxide powder annealed at 450°C in air. The analysis revealed a particle size of 28.87 nm.

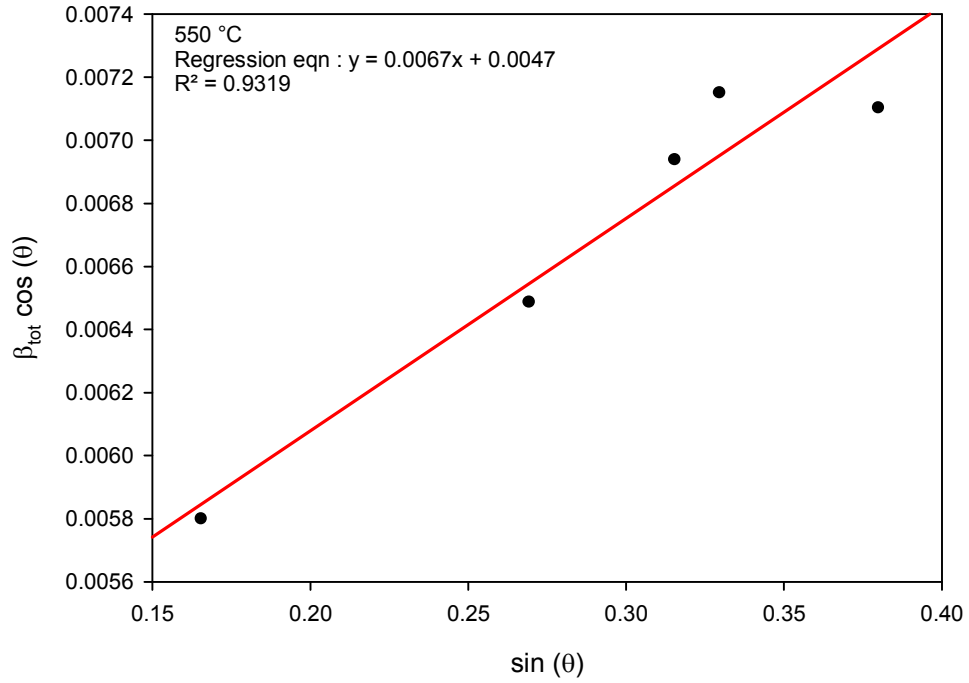



Figure 5.3.11 a) The Williamson-Hall analysis of 1:1 molar ratio of $Ni^{2+}/Co^{2+}$ oxide powder annealed at 550°C in air. The analysis revealed a particle size of 29.42 nm.

| 2-Theta / (°) | d / nm | BG | Height | I% | Area | I% | FWHM/ (°) |
|---|---|---|---|---|---|---|---|
| 19.027 | 0.46604 | 0 | 269 | 13.4 | 106.6 | 10.8 | 0.337 |
| 31.22 | 0.28626 | 26 | 611 | 30.4 | 277.3 | 28 | 0.386 |
| 36.759 | 0.24429 | 80 | 2007 | 100 | 988.7 | 100 | 0.419 |
| 38.471 | 0.23381 | 42 | 184 | 9.2 | 94 | 9.5 | 0.434 |
| 44.638 | 0.20283 | 30 | 450 | 22.4 | 217.2 | 22 | 0.44 |

Table 5.3.11 b) The Williamson-Hall analysis of 1:1 molar ratio of $Ni^{2+}/Co^{2+}$ oxide powder annealed at 550°C in air. The analysis revealed a particle size of 29.42 nm.

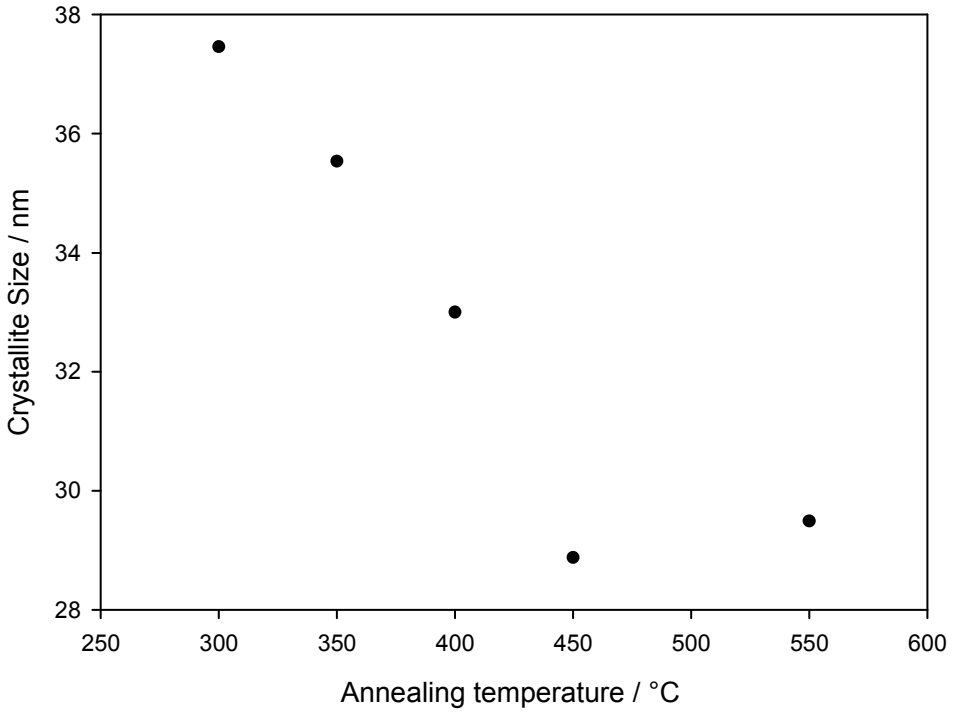



Figure 5.3.3.6 Size of the crystallites of 1:1 molar ratio of $Ni^{2+}/Co^{2+}$ oxide powder as a function of annealing temperature.

### 5.3.4 Surface Morphology

The different surface appearances for the 1:1 $Ni^{2+}/Co^{2+}$ molar ratio oxide electrode annealed at temperatures between 300°C and 550°C and coated on Ti foil are presented in fig. 5.3.12.All SEM images in fig. 5.3.12 were shown to display, on the microscale dimension, a mud cracked appearance, indicating poor dependence on annealing temperature. Interestingly, SEM images in Fig. 5.3.12 a) and b) show a widely spaced cracked layer morphology while c), d) and e) exhibit a compact mud-cracked morphology. Same cracked morphology has been observed for other metal oxides prepared *via* thermal decomposition.[24] Particularly, for $RuO_2$ electrodes it was mentioned that such morphology contributes to its low OER overpotential.[25] The latter may be attributed to the intimate interaction surface - electrolyte.

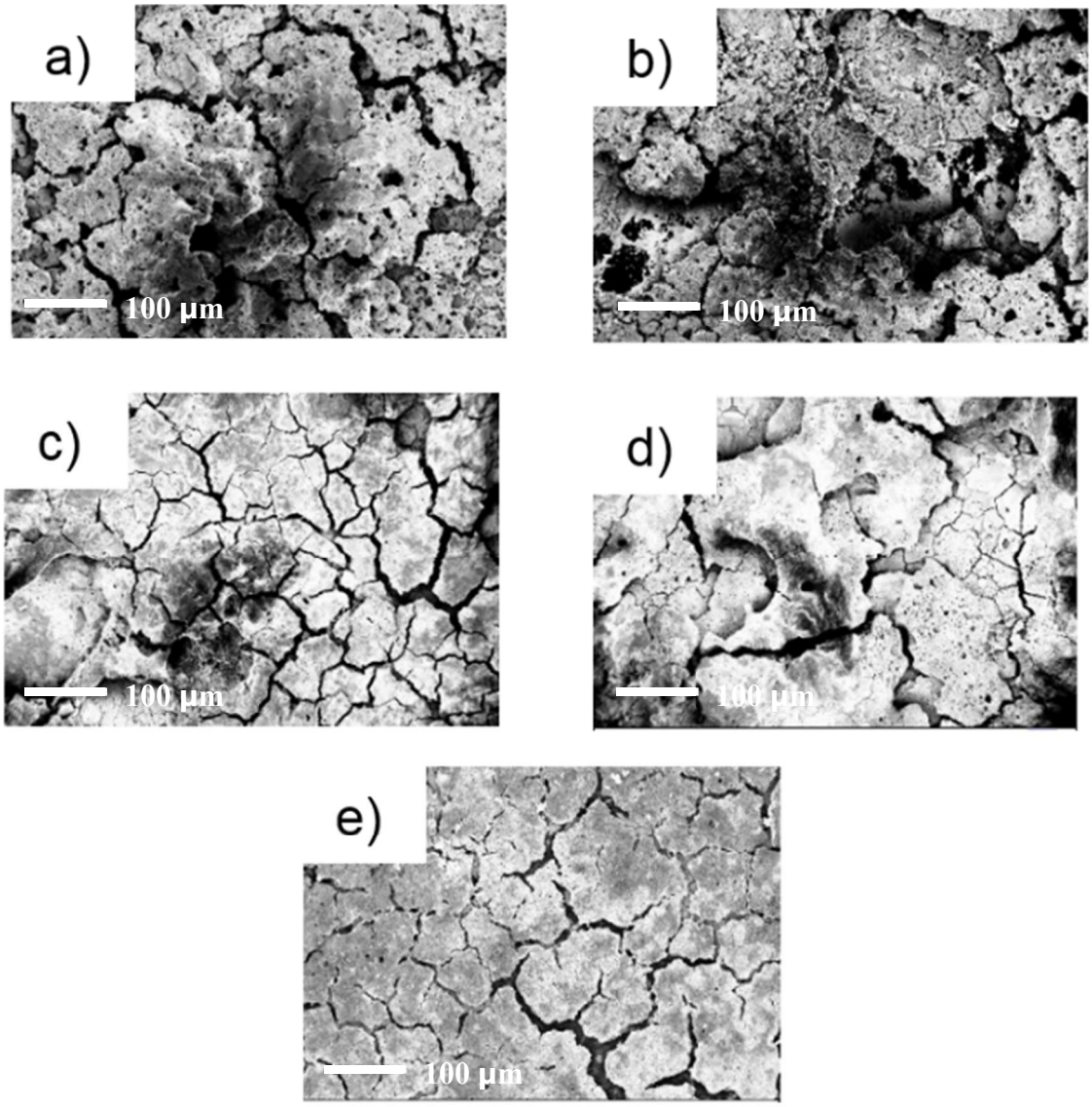



Figure 5.3.12 SEM images of 1:1 molar ratio of $Ni^{2+}/Co^{2+}$ oxide electrode annealed at different temperatures: a) 300°C; b) 350°C; c) 400°C; d) 450°C; e) 550°C. Images were obtained using inLens and EHT = 10 kV. Distance between the samples and the objective was ca. 7 mm.

### 5.3.5 Electrochemical Evaluation

The redox behaviour of the 1:1 $Ni^{2+}/Co^{2+}$ molar ratio oxide electrode film was investigated as a function of annealing temperature in alkaline media at 25°C.

The voltammetric curves are presented in fig. 5.3.13. The voltammetric behaviour was found to be in agreement with previous results reported by Junqing Hu *et al.*[26]

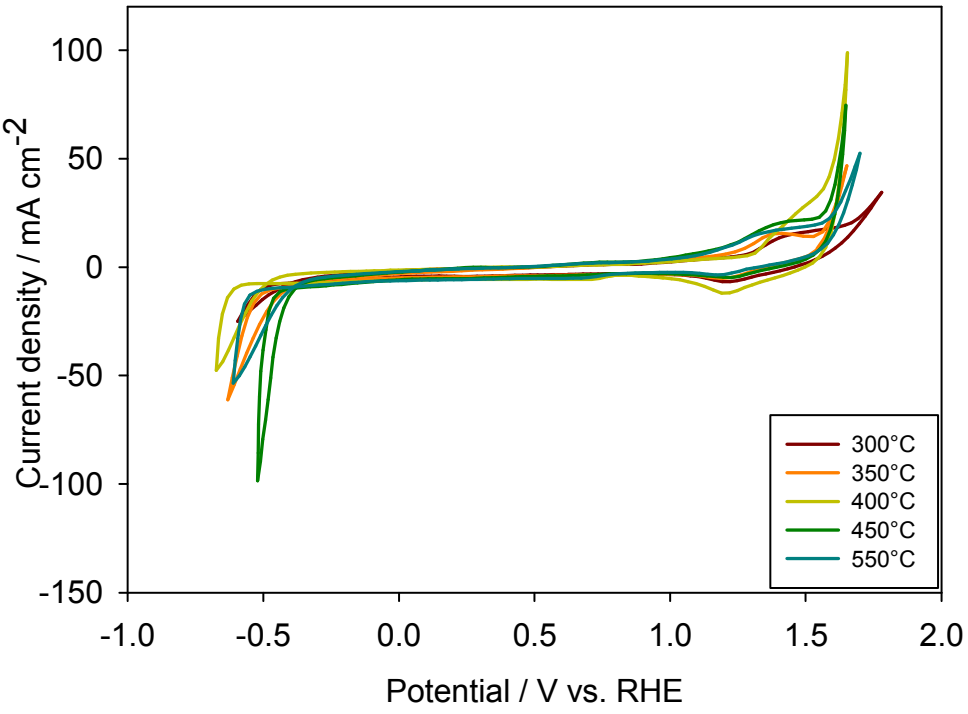



Figure 5.3.13 Cyclic voltammograms characterising the surface electrochemistry of the 1:1 molar ratio of $Ni^{2+}$:$Co^{2+}$ oxide electrode annealed at various temperatures in 1.0 M NaOH at 25°C. The sweep rate was 50 mV $s^{-1}$.

A redox couple can be observed in the CV curve at potentials ca. 1.15 - 1.55 V (*vs.* RHE), which is mainly associated with the Faradaic redox reactions corresponding to the reversible reactions of $Co^{3+}$ / $Co^{2+}$ and $Ni^{3+}$ / $Ni^{2+}$.[27] Minor differences are observed in the redox behaviour of curves 450°C and 550°C. This may be due to similarities in the degree of crystallinity, crystallite size and surface morphology, as outlined in figs. 5.3.6, 5.3.9 and 5.3.12, respectively. If the latter two curves are compared with the other three, it will be clear that the shape of the oxidation peak becomes wider than other temperatures below of 400ºC. This effect may be produced by an increase of the NiO phase, as a result of the decomposition of the $NiCo_2O_4$, when temperature was applied. Special mention should be made to the 400°C curve. It may be observed in fig. 5.3.13, that the voltammogram curve, corresponding to 400°C, displays the largest charge storage behaviour and highest current response if compared with the other annealing temperatures. We suggest that this arises due to a sum of various factors. The most relevant would be the phase composition. Recall from fig. 5.3.3

that at annealing temperatures higher than 400°C the decomposition of $NiCo_2O_4$ occurs, which produces a new phase, the NiO. As previously mentioned, not only the NiO phase possess poorer electrical conductivity than the $NiCo_2O_4$ phase but also a higher charge storage behaviour (see section 1.5.4). Differences between the electrode annealed at 400°C and those at 300°C and 350°C arise, mainly, from the fact that the former possess lower crystallite size, which may increase the active surface area. We may suggest now that electrodes annealed at 400°C enjoy the best proprieties than those annealed $T > 400°C$ and those annealed at $T < 400°C$, that is small crystallite size and large $NiCo_2O_4$ phase, respectively.

The electrocatalytic activity of the thermally prepared 1:1 molar ratio of $Ni^{2+}/Co^{2+}$ oxide electrode annealed at various temperatures was evaluated *via* Tafel plot analysis. The pertinent Tafel plot results are presented in figs. 5.3.14 - 5.3.16.

It is suggested that the notorious catalytic enhancement offered by electrodes annealed at high temperatures, $T > 400°C$, may be attributed to the decrease of crystallite size. Note that the smaller the crystallite size, the more catalytic active sites on the electrode surface. Tafel slopes vary from ca. 158 mV $dec^{-1}$ to ca. 86 mV $dec^{-1}$ which suggests variation of the RDS. It was previously mentioned (see section 1.5.4.1) that differences in Tafel slopes may be explained depending on what sites, on the $NiCo_2O_4$ octahedral structure, the OER takes place. There exist two possibilities either in trivalent sites or in divalent sites. According with Rasiyah and Tseung[28], the Tafel slope of ca. 120 mV $dec^{-1}$ might be justified due to the fact that the OER occurs on divalent sites. According to the aforementioned authors, the most probable rate determining steps is:

$$M + OH^- \rightarrow MOH + e^- \qquad (5.3.5.1)$$

It also observed that as the temperature increases, the Tafel slope reduces until ca. 86 mV $dec^{-1}$. We suggest that the OER may take place in both divalent and trivalent sites in the octahedral structure of the $NiCo_2O_4$, being the divalent sites the preferred, but not only, the sites for the OER.

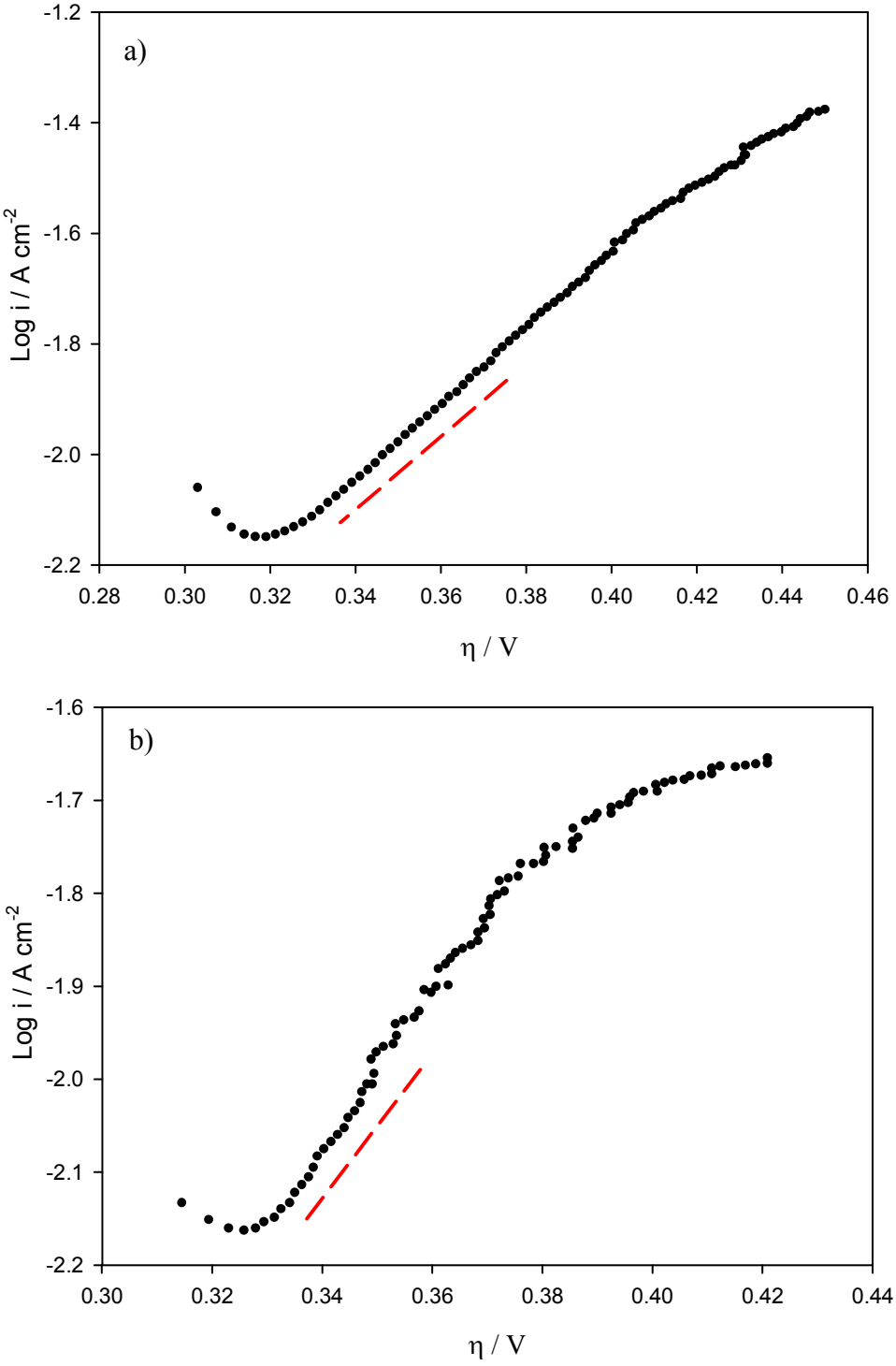



Figure 5.3.14 IR corrected steady-state polarisation curves recorded in the direction of increasing potential on a 1:1 molar ratio of $Ni^{2+}/Co^{2+}$ oxide electrode annealed in air at: a) 300°C and b) 350°C. The slope of the linear region revealed Tafel slopes of ca. 160 mV $dec^{-1}$ and ca. 130 mV $dec^{-1}$ for electrodes annealed at 300°C and 350°C, respectively. The polarisation was recorded in 1.0 M NaOH using a sweep rate of 1 mV $s^{-1}$.

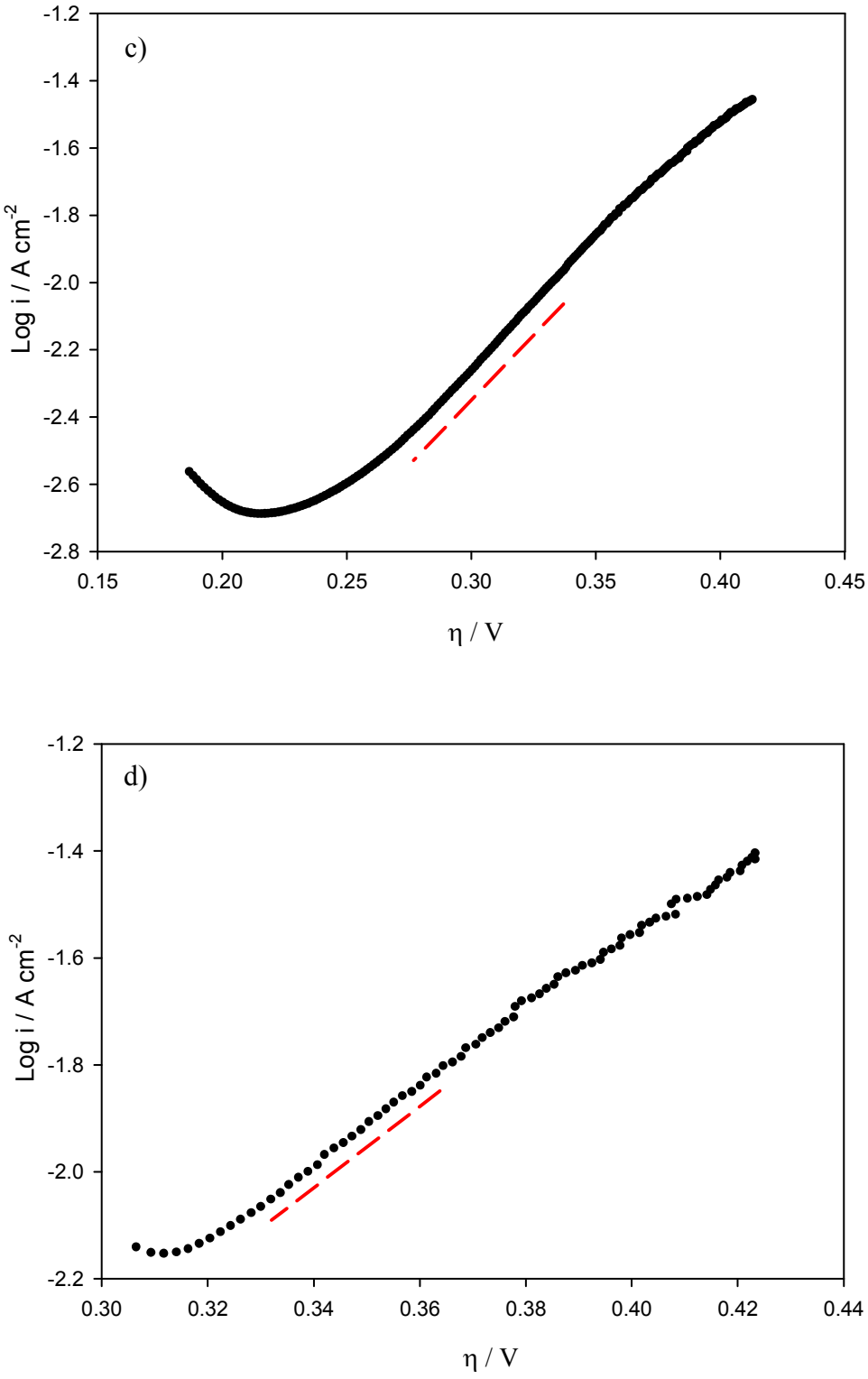



Figure 5.3.15 IR corrected steady-state polarisation curves recorded in the direction of increasing potential on a 1:1 molar ratio of $Ni^{2+}/Co^{2+}$ oxide electrode annealed in air at: c) 400°C and d) 450°C. The slope of the linear region revealed Tafel slopes of ca. 130 mV $dec^{-1}$ and ca. 115 mV $dec^{-1}$ for electrodes annealed at 400°C and 450°C, respectively. The polarisation was recorded in 1.0 M NaOH using a sweep rate of 1 mV $s^{-1}$.

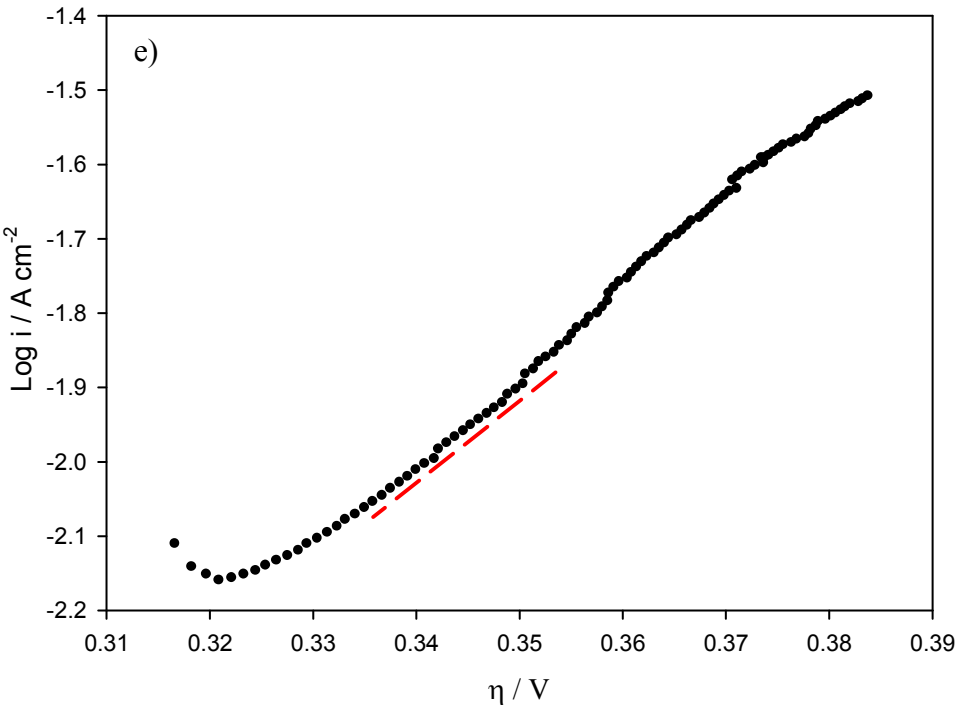



Figure 5.3.16 e) IR corrected steady-state polarisation curve recorded in the direction of increasing potential on a 1:1 molar ratio of $Ni^{2+}/Co^{2+}$ oxide electrode annealed in air at 550°C. The slope of the linear region revealed Tafel slopes of ca. 85 mV $dec^{-1}$. The polarisation was recorded in 1.0 M NaOH using a sweep rate of 1 mV $s^{-1}$.

Recall from section 1.5.4.1, that 40 mV $dec^{-1}$ slopes where associated with the OER occurring at trivalent sites. Another interesting fashion to determine the catalytic activity of electrodes is to plot the overpotential, typically at 10 mA $cm^{-1}$, against annealing temperature. In this perspective, fig. 5.3.17 shows the overpotential, at 10 mA $cm^{-1}$, for nickel cobalt mixed oxide films with 1:1 $Ni^{2+}/Co^{2+}$ molar ratio as a function of annealing temperature. It is clear form fig. 5.3.17, that the increase of annealing temperature plays a significant role in the overpotential behaviour of nickel cobalt mixed oxide materials. The increase of temperature, from 300°C up to 400°C results in a decrease in overpotential, from ca. 0.335 V to ca. 0.320 V, respectively. However, as the temperature is further increased, the overpotential increases sharply, from ca. 0.320 V to ca. 0.34 V. We may point out, however, that the differences between the overpotentials values are not large, but relatively significant. Note that in some cases there exists overpotentials with 20 mV difference. This significant variation is likely due to changes in the conductivity of the oxide film as a function of annealing temperatures attributed to changes in the film composition (recall the formation of NiO phase at $T > 400°C$). We conclude that the electrode prepared at 400°C

has the best electrocatalytic properties for the oxygen evolution reaction. When the temperature is low, incomplete crystallinity of $NiCo_2O_4$ electrode is obtained, which leads to low electrocatalytic properties. As the temperature increases, a low-surface area and a smoother electrode surface reduces the surface electrocatalytic properties. The appearance of NiO also decreases the electrocatalytic properties of electrode. Thus, 400°C was chosen to further investigate the effect of % M Co content on the OER of nickel cobalt mixed oxide materials.

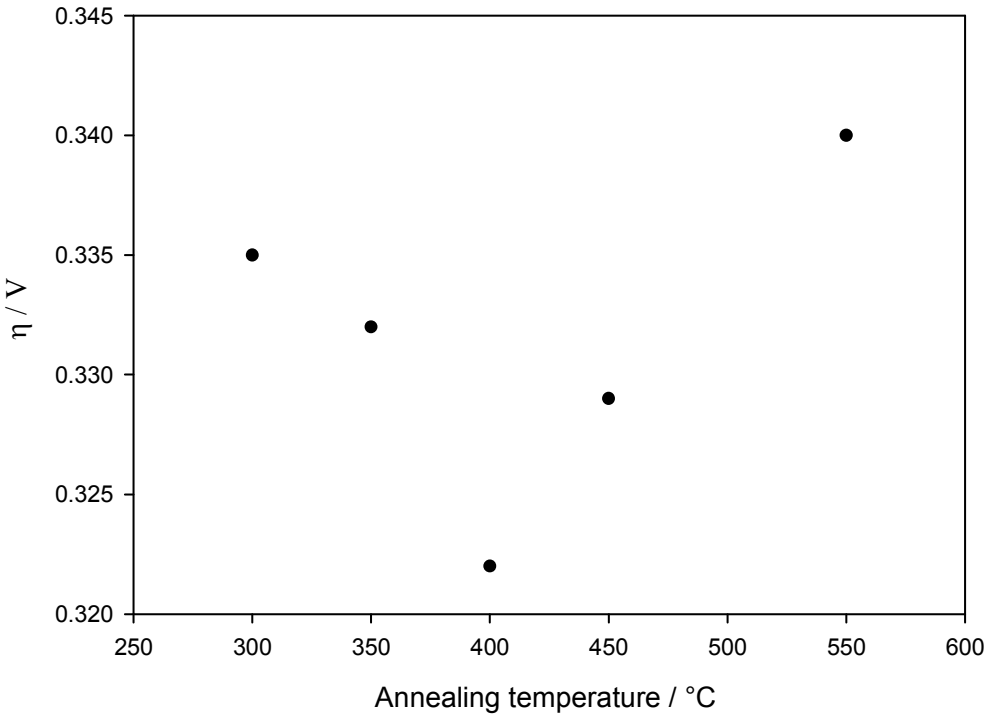



Figure 5.3.17 Oxygen evolution overpotential, measured at 10 mA $cm^{-2}$, for nickel cobalt mixed oxide films with 1:1 molar ratio of $Ni^{2+}/Co^{2+}$ in 1.0 M NaOH at 25°C.

## 5.4 The Effect of Cobalt Oxide on the OER of Nickel Cobalt Mixed Oxide Electrodes

### 5.4.1 Introduction

A series of nickel cobalt mixed oxides with different % M Co content, prepared by thermal decomposition method at 400°C in air, are investigated towards the oxygen evolution reaction in alkaline solutions. In this section, the physical characterisation of such electrodes using XRD, XPS and SEM-EDX techniques along with contact angle measurements is presented first, followed by the electrochemical characterisation and a kinetic study.

### 5.4.2 Physical Characterisation of Nickel Cobalt Mixed Oxide Electrodes

#### 5.4.2.1 X-ray Powder Diffraction Spectroscopy Analysis

X-ray powder diffraction spectroscopy (XRD) was employed in this work to analyse the bulk phases of various nickel cobalt mixed oxide electrodes with different % M Co content. Fig. 5.4.1 shows the XRD patterns of nickel cobalt mixed oxide samples as a function of increasing % M Co content. The peaks in the XRD patterns of nickel oxide and cobalt oxide samples are accurately ascribed to NiO phase with ICDD card number 47-1049 and $Co_3O_4$ phase with ICDD card number 43-1003, respectively. For the case of nickel cobalt mixed oxides (20% - 80 % M Co content), both $NiCo_2O_4$ phase with ICDD card number 20-0781 and NiO phase coexists. It was found difficult to distinguish between $NiCo_2O_4$ and $Co_3O_4$ phases due to they possess similar spinel structure. Note that reference lattice parameters for both $NiCo_2O_4$ and $Co_3O_4$ are ca. 8.110 Å and ca. 8.058 Å, respectively. Thus, a deeper investigation of the lattice parameter in XRD patterns in fig. 5.4.1 will be crucial to confirm the presence of $NiCo_2O_4$ phase. The lattice parameter and the phase wt.% were obtained from Rietveld refinement using an inbuilt software in the Jade MDI software. Note that the values of the wt.% are quantitatively estimated using relative peak intensity ratio.[29] All the samples can be classified into three different type of crystal structure, according to the major phase in the sample: (i) NiO, (ii) $NiCo_2O_4$, and (iii) $Co_3O_4$ type.

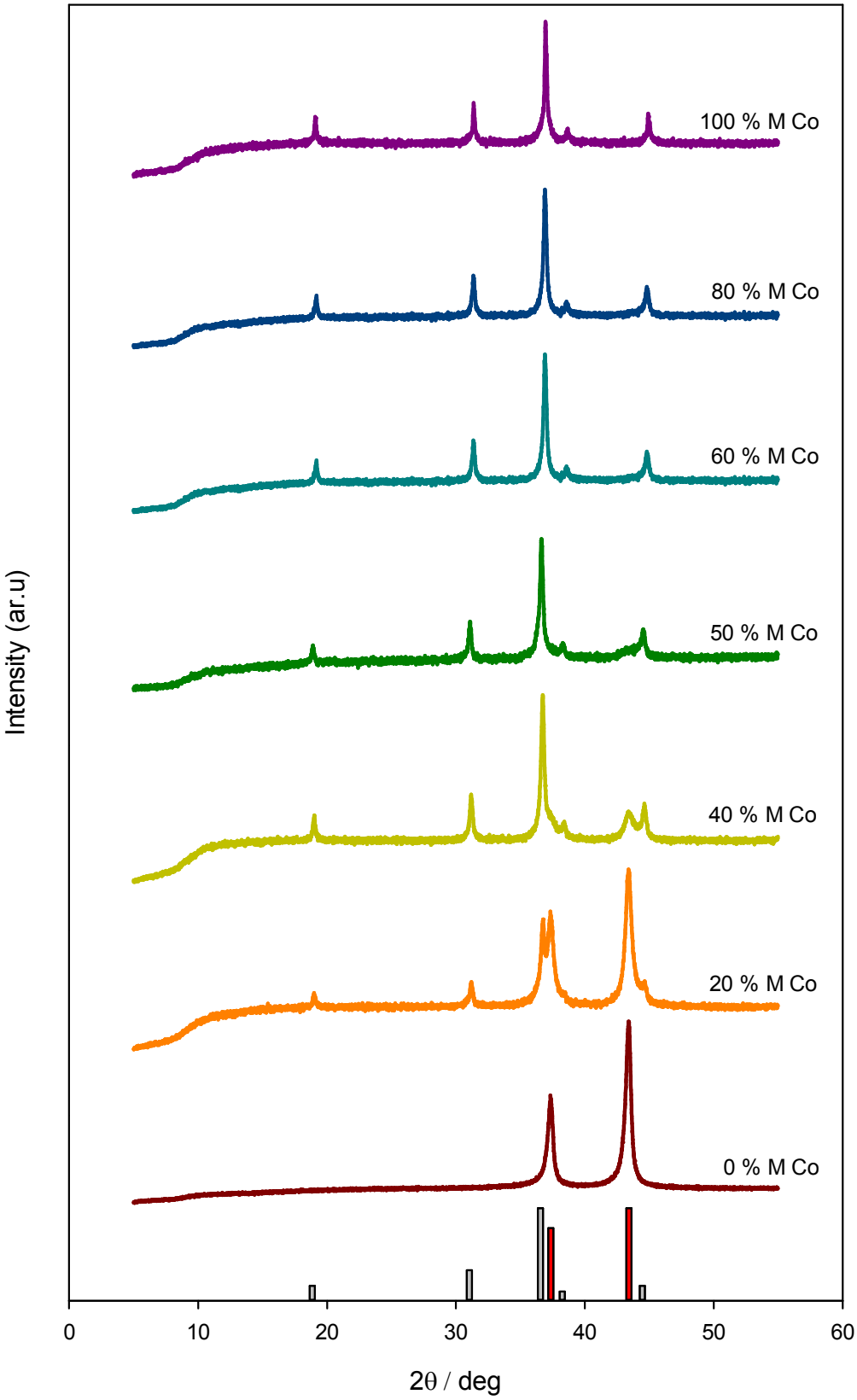



Figure 5.4.1 XRD powder patterns of nickel cobalt mixed oxide powders calculated at 400°C and evaluated at increasing % M Co content, from 0 % to 100% M Co content. Grey and red vertical bars illustrate database's XRD reference patterns for nickel cobalt oxide, $NiCo_2O_4$ (PDF # 200781), and nickel oxide, NiO (PDF # 471049), respectively.

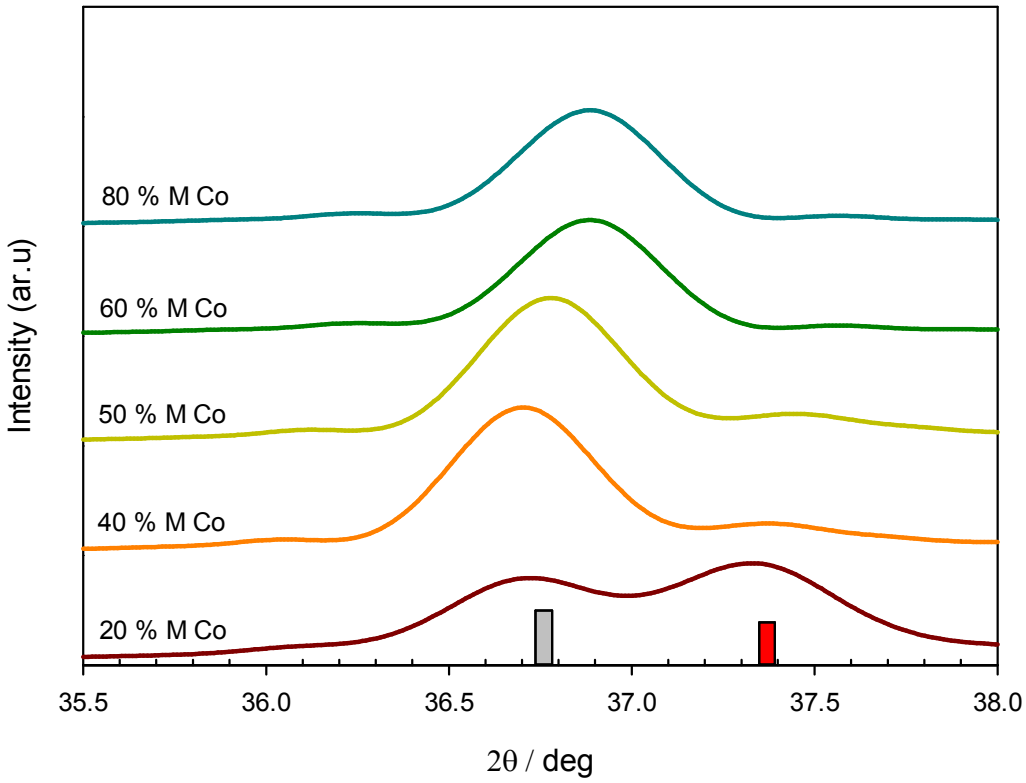



Figure 5.4.2 XRD pattern amplification of the region between 35.5° and 38° of fig. 5.4.1. Grey and red vertical bars illustrate database's XRD reference patterns for nickel cobalt oxide, $NiCo_2O_4$ (PDF # 200781), and nickel oxide, NiO (PDF # 471049), respectively.

The 0 % and 20 % M Co content samples are included in group type (i). Note that 0 % and 20 % M Co content refers to the 10/0 and 8/2 Ni/Co ratio, respectively; the 40 %, 50 % and 60 % M Co content samples are included in group type (ii). Note that 40 %, 50 % and 60 % M Co content refers to 6/4, 5/5 and 4/6 Ni/Co ratio, respectively; the 80 % and 100 % M Co content samples are included in group type (iii). Note that 80% and 100% M Co content refers to the 2/8 and 0/10 Ni/Co ratio, respectively. In order to analyse the detailed change in lattice parameter of the $NiCo_2O_4$ phase, a zoom in the region of 35.5° - 38° of the fig. 5.4.1 is shown in fig. 5.4.2. The shift of the diffraction peak (111) towards more positive angles is observed with increasing cobalt content from 40 % to 80 %. Especially significant is the peak shift in samples with 60 % and 80 % cobalt content with respect to the other samples. Such shift led to the reduction of the lattice parameter from the standard 8.11 Å to 8.0829 Å and 8.0744 Å, respectively.[30] When nickel ions are removed from the spinel $NiCo_2O_4$ structure, the unit cell decreases its size which causes the XRD peaks to shift towards larger diffraction angles (larger theta values). Thus, lattice reduction of the samples

can be ascribed to the increase of $Co_3O_4$ phase. Note that cobalt oxide and nickel cobalt mixed oxide have equal spinel structure but slightly different lattice parameter of 8.058 Å and 8.110 Å for $Co_3O_4$ and $NiCo_2O_4$, respectively. Therefore, we suggest that the main contribution to the peak angles shown in fig. 5.4.2 is due to an increase of $Co_3O_4$ phase rather than $NiCo_2O_4$ phase, being the latter enclosed in the diffraction reflection of the former. The results obtained for phase composition and lattice parameters of the various phases within the samples are summarized in Table 5.4.1. Lattice parameters of NiO and $NiCo_2O_4$ as a function of % M Co content are presented in fig. 5.4.3. Note that the value of phase wt.% is quantitatively estimated using relative peak intensity ratio.

| | **NiO** | | **$NiCo_2O_4$** | | **$Co_3O_4$** | |
|---|---|---|---|---|---|---|
| **% M Co content** | a (Å) | wt.% | a (Å) | wt.% | a (Å) | wt.% |
| 0 | 4.171 | 100 | - | - | - | - |
| 20 | 4.172 | 59.30 | 8.114 | 43.40 | - | - |
| 40 | 4.169 | 30.90 | 8.115 | 69.10 | - | - |
| 50 | 4.168 | 21.50 | 8.118 | 78.50 | - | - |
| 60 | 4.167 | 8.80 | 8.113 | 91.20 | - | - |
| 80 | - | - | 8.111 | 21.60 | 8.091 | 78.40 |
| 100 | - | - | - | - | 8.058 | 100 |

Table 5.4.1 Phase composition and lattice parameters calculated from XRD patterns presented in fig. 5.4.1.

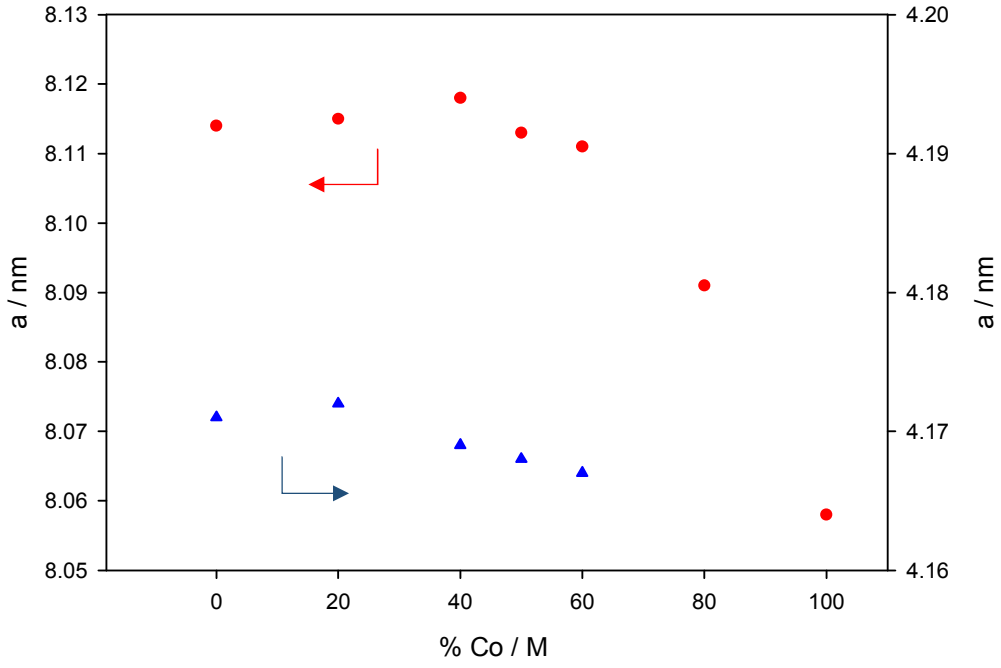



Figure 5.4.3 Lattice parameter values of NiO (▲) and $NiCo_2O_4$ (●) as a function of % M Co content. These values were obtained from XRD patterns presented in fig. 5.4.1.

As noted in Table 5.4.1, nickel oxide involved in films with $>$ 60 % M Co content was not observed in crystalline form since it was completely consumed in the reaction to produce $NiCo_2O_4$. The lattice parameter of $Co_3O_4$ against % M Co content plots exhibits an abrupt increase of $a$ as the content of % M Ni increases. This is probably attributed to inclusion of $Ni^{2+}$ ions from octahedral sites in $Co_3O_4$ spinel structure resulting in the formation of $NiCo_2O_4$ phase. Note that the ion radius (with coordination number 6) of $Ni^{2+}$ and $Co^{2+}$ differ significantly, 0.069 nm and 0.065nm, respectively.[31]

### 5.4.2.2 X-ray Photoelectron Spectroscopy Analysis

X-ray photoelectron spectroscopy (XPS) was used to probe the surface chemistry of a series of nickel cobalt mixed oxide films with different % M Co content in a quantitative manner. Survey scan X-ray photoelectron spectra, in the binding energy range 0-1200 eV, for all of the nickel cobalt mixed oxide samples investigated, are shown in fig. 5.4.4. The XPS and Auger lines from the constituent elements are easily identified and marked on the survey spectra. Before analysing with detail the atomic surface composition of the samples, it was convenient to define first the relevant emission peaks. From low to high binding energy one finds: (i) C 1s at 285 eV, (ii) O 1s at 529.7 eV, (iii) Co 2p doublet at 779.8 and 795.4 eV corresponding to $2p_{3/2}$ and $2p_{1/2}$, respectively, and (iv) Ni 2p doublet at 854.3 eV and 872.8 eV corresponding to $2p_{3/2}$ and $2p_{1/2}$, respectively. The presence of cobalt 2p was confirmed with the observation of the LMM auger peak at 713 eV. The high-resolution spectrum, taken in the binding energy range 274 - 300 eV, revealed a single C 1s peak which was again used as an energy reference at 285 eV.[32]

A primary surface composition analysis was carried out from the XPS survey spectrum outlined in fig. 5.4.4. The atomic percentage was calculated using CasaXPS in-built software which corrects the calculated area under the peaks with the relative sensitivity factor (RSF). The values of the RSF used for cobalt atoms and the nickel atoms are $Co_{RSF}$ = 19.16 and $Ni_{RSF}$ = 22.18, respectively. The results for the surface atomic composition of various nickel cobalt mixed oxide samples are summarized in Table 5.4.2.

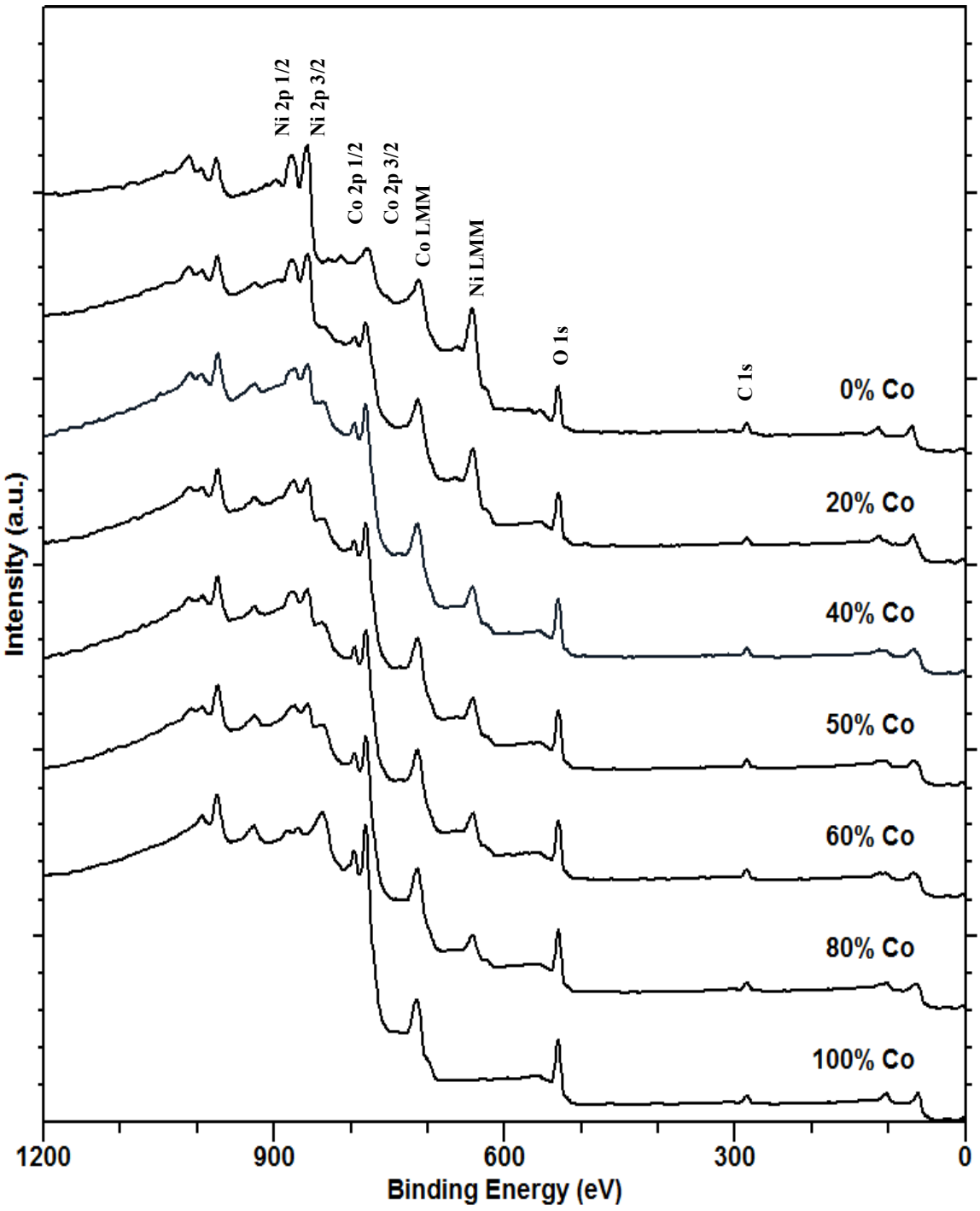



Figure 5.4.4 X-ray photoelectron spectroscopy (XPS) survey spectra of nickel cobalt mixed oxide electrodes as a function of % M Co content. All the samples were annealed at 400°C in air. Survey spectra have been corrected to the main line of the C 1s spectrum set to 285 eV. Survey spectra were recorded in a scan window of 0 – 1200 eV and 200 eV pass energy.

| % M Co content | Ni (% atomic) | Co (% atomic) | O (% atomic) | Ni/Co ratio | Ratio Ni/Co precursor sol. |
|---|---|---|---|---|---|
| 0 | 46.4 | 0 | 53.6 | - | - |
| 20 | 26.4 | 19.9 | 53.7 | 1.33 | 4 |
| 40 | 14.8 | 34.5 | 50.7 | 0.52 | 1.5 |
| 50 | 16.5 | 28.3 | 55.2 | 0.58 | 1 |
| 60 | 14.6 | 30.7 | 54.7 | 0.48 | 0.6 |
| 80 | 10.4 | 32.6 | 57.0 | 0.32 | 0.25 |
| 100 | 0 | 47.7 | 52.3 | - | - |

Table 5.4.2 Surface composition of a series of nickel cobalt mixed oxide electrodes as a function of % M Co content. These values were obtained from the analysis of XPS spectra presented in fig. 5.4.4.

Surface composition results presented in Table 5.4.2 show that surface composition differs significantly to that determined on the bulk, suggesting surface segregation of either Ni or Co species. Segregation phenomena may occur during thermal calcination and modify the elemental composition of the surface.[33] Several examples of cation segregation in oxide systems have been observed in the literature.[34] Segregation in the present study may arises from the increased size of $Co^{2+,3+}$ ions relative to the host $Ni^{2+}$ ion. Note that the calculated atomic radius for cobalt and nickel atoms are 152 pm and 149 pm, respectively.

Therefore, we suggest that the samples do not exhibit a uniform composition through the different depths of the oxide layer. High resolution XPS spectra are applied to obtain the information of the oxidation state of each element ion the surface. Ni 2p and Co 2p along with O 1s photoelectron spectra for nickel cobalt mixed oxide with various % M Co content are shown in fig. 5.4.5 and fig. 5.4.6, respectively. Fig. 5.4.5 show that Co 2p spectra are fitted to two main peaks of Co $2p_{3/2}$ and Co $2p_{1/2}$ with binding energy at 779.9 eV and 794.9 eV in addition to two satellite peaks.[32] To investigate the oxidation state of cobalt surface species, Co $2p_{3/2}$ spectra are de-convoluted into two spin-orbit doublets. [35]

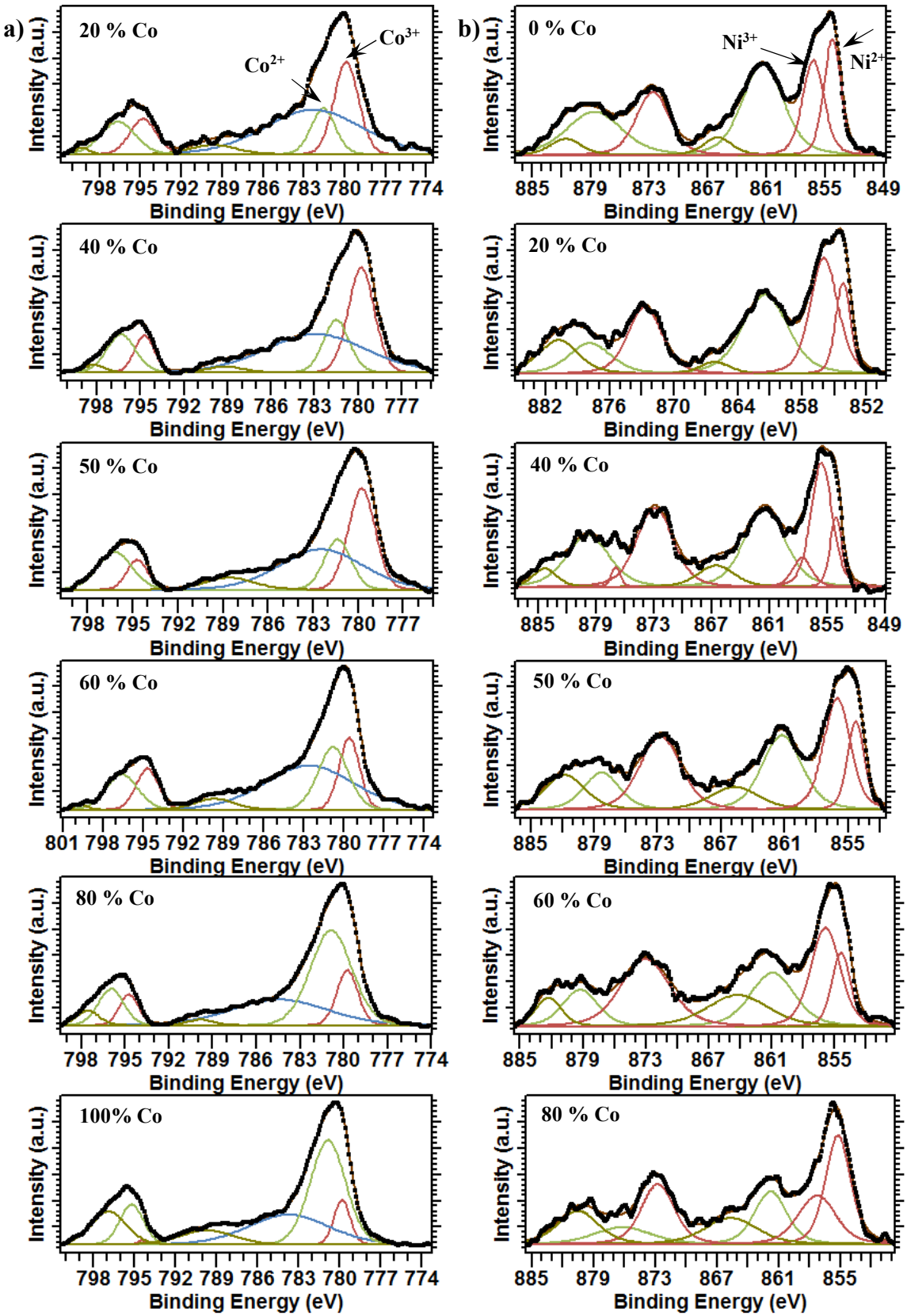



Figure 5.4.5 High resolution XPS spectra of a) Co 2p and b) Ni 2p of various nickel cobalt mixed oxide electrodes with different % Co content. High resolution spectra have been charged corrected to the main line of the carbon 1s spectrum set to 285 eV. The spectra were recorded at 20 eV pass energy.

Fitting peaks at binding energies at 779.6 eV and 794.3 eV (red), 780.8 and 796.7 eV (green) are assigned to $Co^{3+}$ and $Co^{2+}$, respectively.[36] At high binding energy side of Co $2p_{3/2}$ and Co $2p_{1/2}$, the fitting peaks at 782.4 eV (blue), 789.7 eV and 799.9 eV (dark green) are assigned as shake-up satellites. Likewise, Ni 2p spectrum (see fig. 5.4.5 b) can be deconvoluted into two spin-orbit doublets, and two shake-up satellites, which indicates the existence of $Ni^{2+}$ and $Ni^{3+}$. The fitting peaks of O 1s spectra (fig. 5.4.6) at 529.7 eV (red), 530.9 eV (green) and 531.7 eV (dark green) can be ascribed to metal-oxygen bond oxygen in cobalt hydroxyl group, and oxygen in nickel hydroxyl group, respectively.[35b]

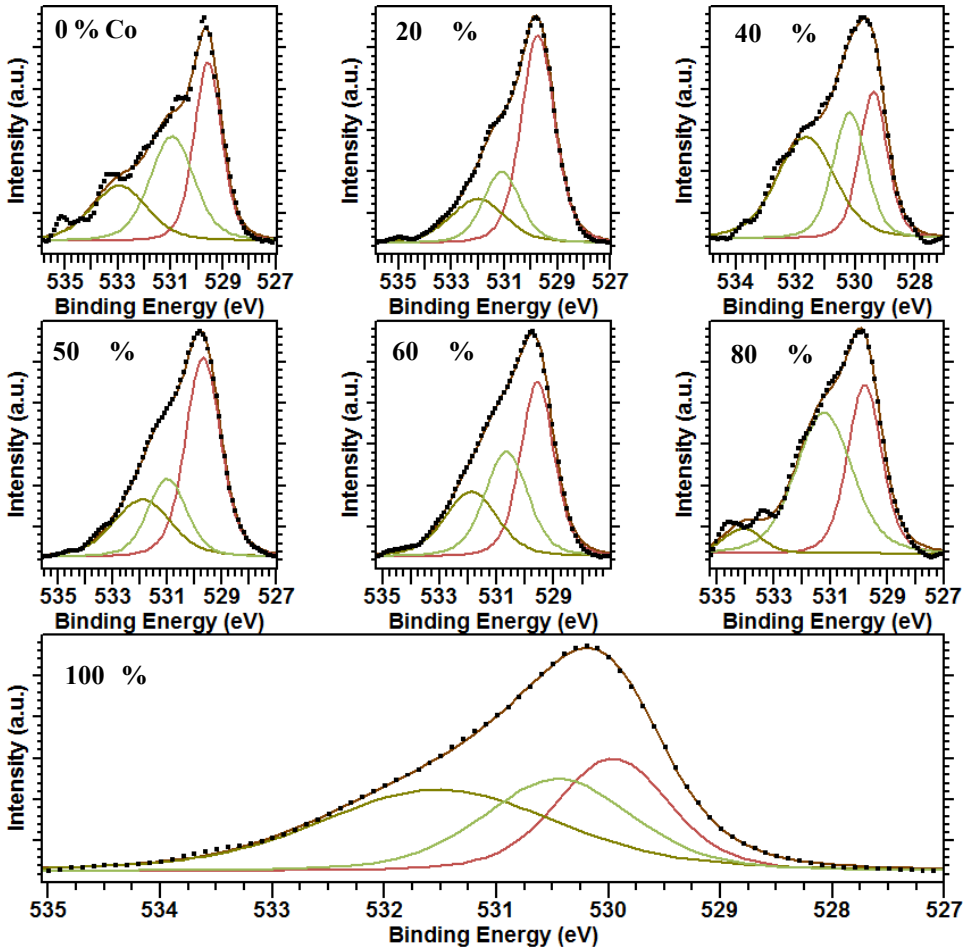



Figure 5.4.6 High resolution XPS O 1s spectra of various nickel cobalt mixed oxide electrodes with different % M Co content. High resolution spectra have been charged corrected to the main line of the carbon 1s spectrum set to 285 eV. The spectra were recorded at 20 eV pass energy.

According with King and Tsung[37], the ion distribution model of $NiCo_2O_4$ may be referred as:

$$Co_{0.9}{}^{+2} + Co_{0.1}{}^{+2}\left(Ni_{0.9}{}^{+2} + Ni_{0.1}{}^{+3} + Co^{3+}\right) O_{3.2}{}^{-2} \cdot O_{0.8} \qquad (5.4.2.2.1)$$

where the cations inside the parenthesis are in an octahedral environment and those outside are in tetrahedral sites. According to eqn. 5.4.2.2.1, 2/5 of the cations are trivalent and the rest divalent. Note that this model also involves a charged oxygen ion. The function of such charged oxygen ion is to balance the excess negative charge produced by the accommodation of divalent nickel ions into octahedral sites with decreasing the number of $Co^{3+}$ ions. According with the authors, these species might not be found in the bulk regions of the solid since the coordination shells are complete, but may exist at the surface of many transition metals as adsorbed oxygen.[37] Rasiyah and Tseung[28] pointed out that the extent of $Ni^{2+}$ ion in the octahedral sites of the $Co_3O_4$ spinel structure yields to important variation of the electrocatalytic activity of nickel cobalt mixed oxide electrodes. Thus, in order to investigate the extent of $Ni^{2+}$ ions onto the octahedral sites of $Co_3O_4$ spinel structure, the ratios of $Co^{2+}$ and $Co^{3+}$ are determined. The result of such calculations is presented in Table 5.4.3.

| % M Co content | $Co^{2+}$ (% atomic) | $Co^{3+}$ (% atomic) | $Co^{3+}/Co^{2+}$ |
|---|---|---|---|
| 0 | - | - | - |
| 20 | 33.3 | 66.7 | 2.00 |
| 40 | 34.2 | 65.8 | 1.92 |
| 50 | 34.5 | 65.5 | 1.89 |
| 60 | 51.6 | 48.4 | 0.94 |
| 80 | 77.2 | 22.8 | 0.30 |
| 100 | 83.5 | 16.5 | 0.20 |

Table 5.4.3 XPS results showing the fitting parameters of Co 2p of a series of nickel cobalt mixed oxides with various % M Co content. These values are extracted from XPS data presented in fig. 5.4.5.

As presented in Table 5.4.3, the ratio of $Co^{3+}$ / $Co^{2+}$ quickly increase with decreasing the percentage of cobalt on the electrode from 100 % to 60 %. Further reduction of % M Co content results in the stabilisation of $Co^{2+}$ and $Co^{3+}$ ions. This stabilisation may indicate saturation of $Ni^{2+}$ ions on octahedral sites on the spinel structure. Although the $Co^{3+}$ / $Co^{2+}$ ratio is similar for electrodes with 50 % and 20 % M Co content, the phases observed in the XRD patterns (see fig. 5.4.1) were found to possess different phase composition, being the

$NiCo_2O_4$ phase the major phase for the former and NiO for the latter concentration, respectively. We suggest that for % M Co content below 60 %, the excess $Ni^{2+}$ ions are not inserted into free octahedral sites anymore which results in a NiO phase surface enrichment. These assumptions are in agreement with the results presented in section 5.4.2.2.

### 5.4.3 Scanning Electron Microscope - Energy-Dispersive X-ray

SEM images of a series of nickel cobalt mixed oxide films with different % M Co content are presented in fig. 5.4.7 and 5.4.8.

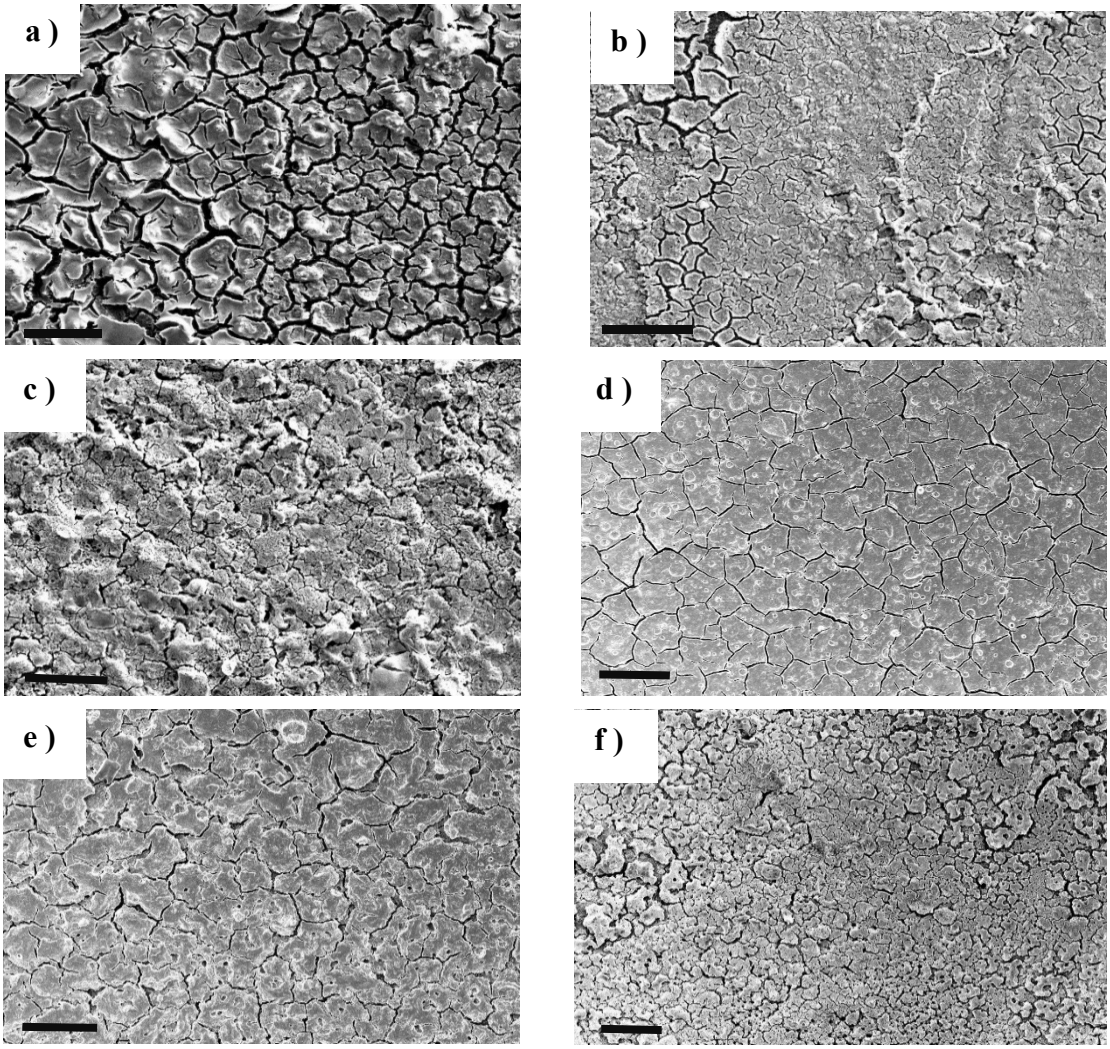



Figure 5.4.7 SEM images of nickel cobalt mixed oxides with various % Co content: a) 0 % M Co, b) 20 % M Co, c) 40 % M Co, d) 50 % M Co, e) 60 % M Co and f) 80 % M Co. The images are taken at 100 µm (black scale line) magnification using in-Lens detector and 5 kV EHT. Distance between the samples and the objective was ca. 7 mm.

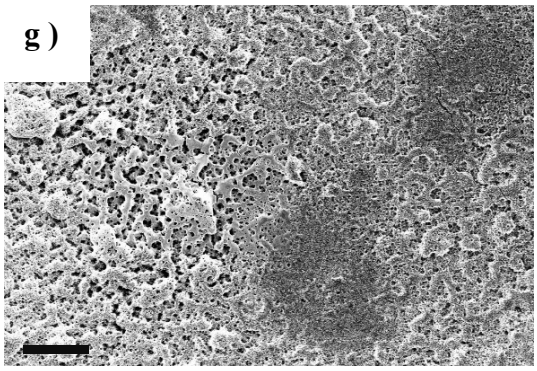



Figure 5.4.7 g) SEM image of nickel cobalt mixed oxide with 100 % Co content. The image is taken at 100 µm (black scale line) magnification using in-Lens detector and 5kV EHT. Distance between the samples and the objective was ca. 7 mm.

In fig. 5.4.7 a-f, oxide films prepared by thermal decomposition display the characteristic 'mud-cracked' appearance associated with other transition metal oxide prepared previously by other authors using the same preparation method.[16, 38] The oxide film interspacing, *e.g.* between the cracks and film thickness, are typically in the range of a micron in magnitude. Although electrodes with Co (M) > 40 % exhibit, in specific areas, a somewhat porous surface, sample with 100% M Co content exhibit porous surface morphology in almost the totally of the surface area, with a porous diameter of the order of 1 µm, as observed in fig. 5.4.8.

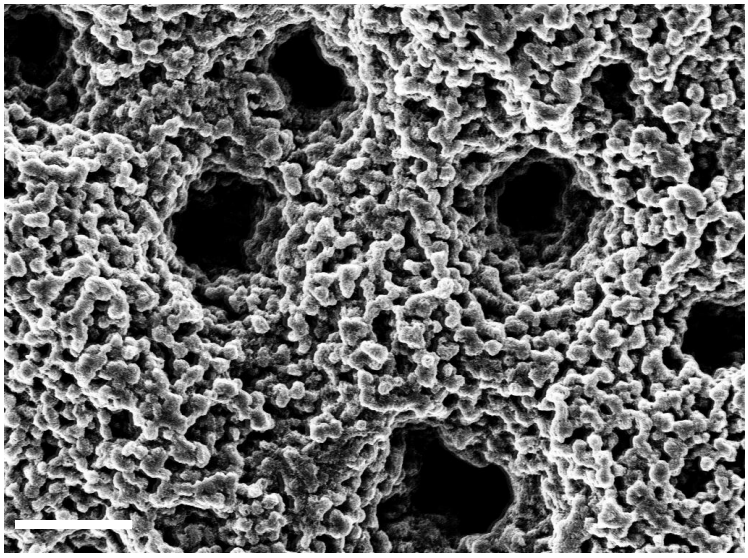


Figure 5.4.8 SEM image of nickel cobalt mixed oxide electrode with 100 % M Co content. The image is taken at 1 µm (white scale line) magnification using in-Lens detector and 5kV EHT. The image shows various pores with diameter of ca.1 µm. Distance between the sample and the objective was ca. 7 mm.

From fig. 5.4.7, it can be noted that further addition of nickel content dominates the resulting morphology of these mixed oxide film. It is not surprising that the observed morphology of the films exhibit a cracked surface given that they were prepared by a repeated sequence of coating and annealing application. Note that thermal stress induced by the mismatch in expansion coefficients of both oxide materials and the underlying titanium substrate results in the formation of surface cracks. In the nanoscale, see fig. 5.4.9, all oxide mixtures where shown to display surface nanoparticles of between 15 - 50 nm in diameter distributed uniformly across all faces of the oxide film. Such nanoparticles have been previously observed on $RuO_2$ and NiO films synthesised in this fashion.[39]

The presence of such nanoparticles would give rise to the highly active catalytic behaviour of these electrodes. Assuming a cubic shape for these nanoparticles, this would give a surface area of ca. 900 $nm^2$ for an individual nanoparticle which compares to an area of 0.34 $nm^2$ calculated for a surface active surfaquo group by Lyons and Burke[40], which we assume to be the active site for OER. Therefore, one may expect that there are > 2000 of these surfaquo groups on each nanoparticle site. We propose that these catalytically active surface nanoparticles account for the excellent OER activity displayed in samples especially in those with large $NiCo_2O_4$ phases, that is the 40, 50 and 60 % M Co content electrodes. Note from fig. 5.4.9 that the aforementioned electrodes possess larger and more compact nanoparticles distribution than the other samples.

It was also observed in electrodes with low % M Co content, the presence of NiO crystals, such as the one presented in fig. 5.4.10. The formation of such crystal structures arises, during annealing decomposition, due to imperfections or impurities on the surface of the electrode.[41] The presence of such crystals was found to decrease with increasing cobalt content. This may explained by the presence of free nickel on the surface which may be reduced, previous reaction with cobalt oxide, to form $NiCo_2O_4$ species.

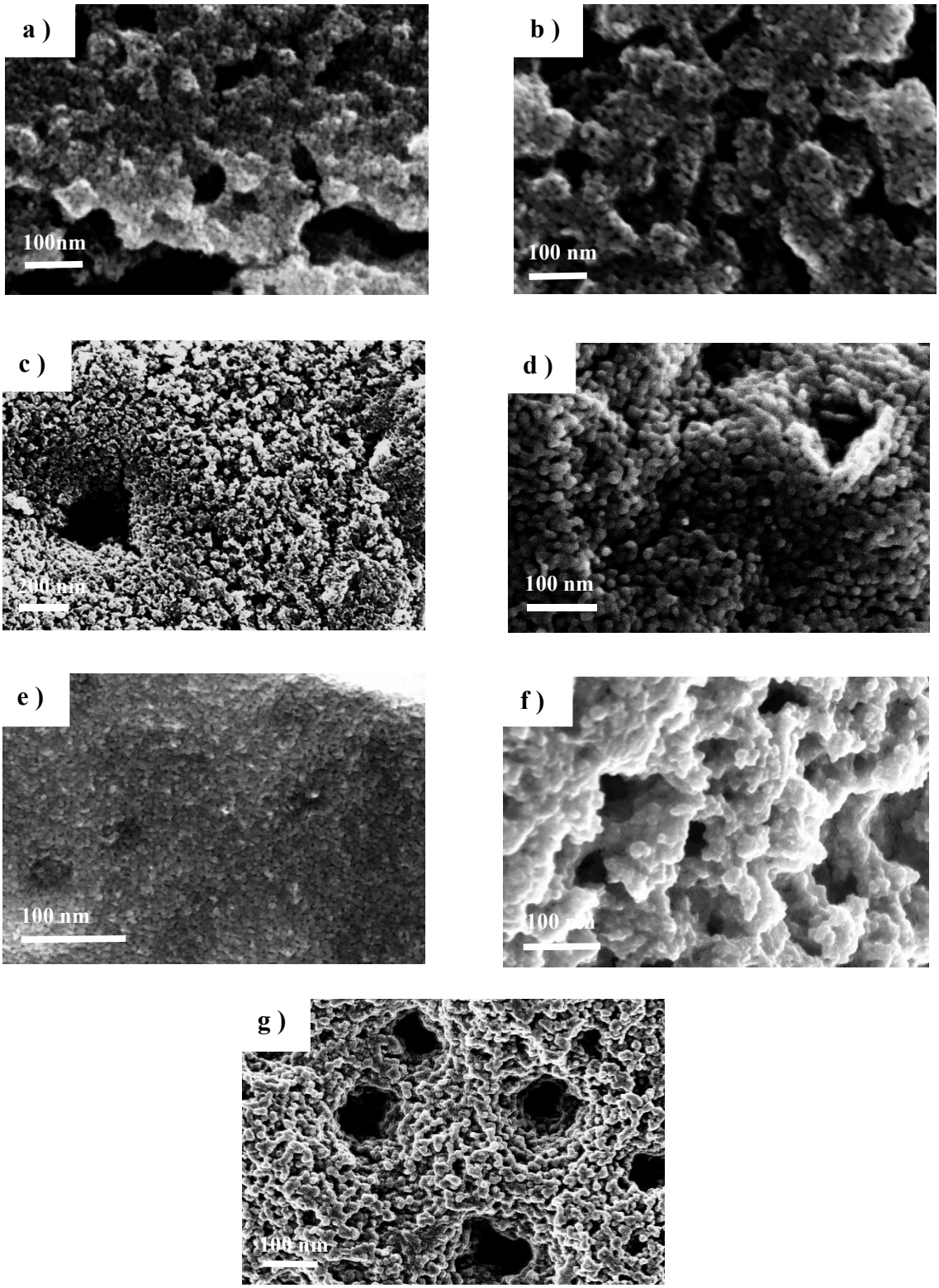



Figure 5.4.9 SEM images of nickel cobalt mixed oxides with various % M Co content: a) 0 % Co, b) 20 % Co, c) 40 % Co, d) 50 % Co, e) 60 % Co, f) 80 % Co and g) 100 % M Co. The images are taken at various magnifications (see white scale line) using in-Lens detector and 5kV EHT. Distance between samples and the objective was 7 mm.

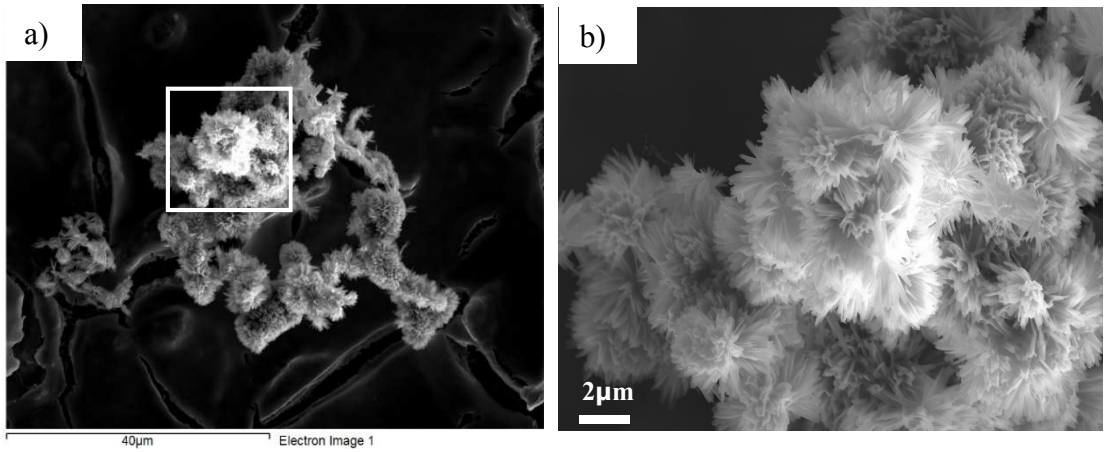
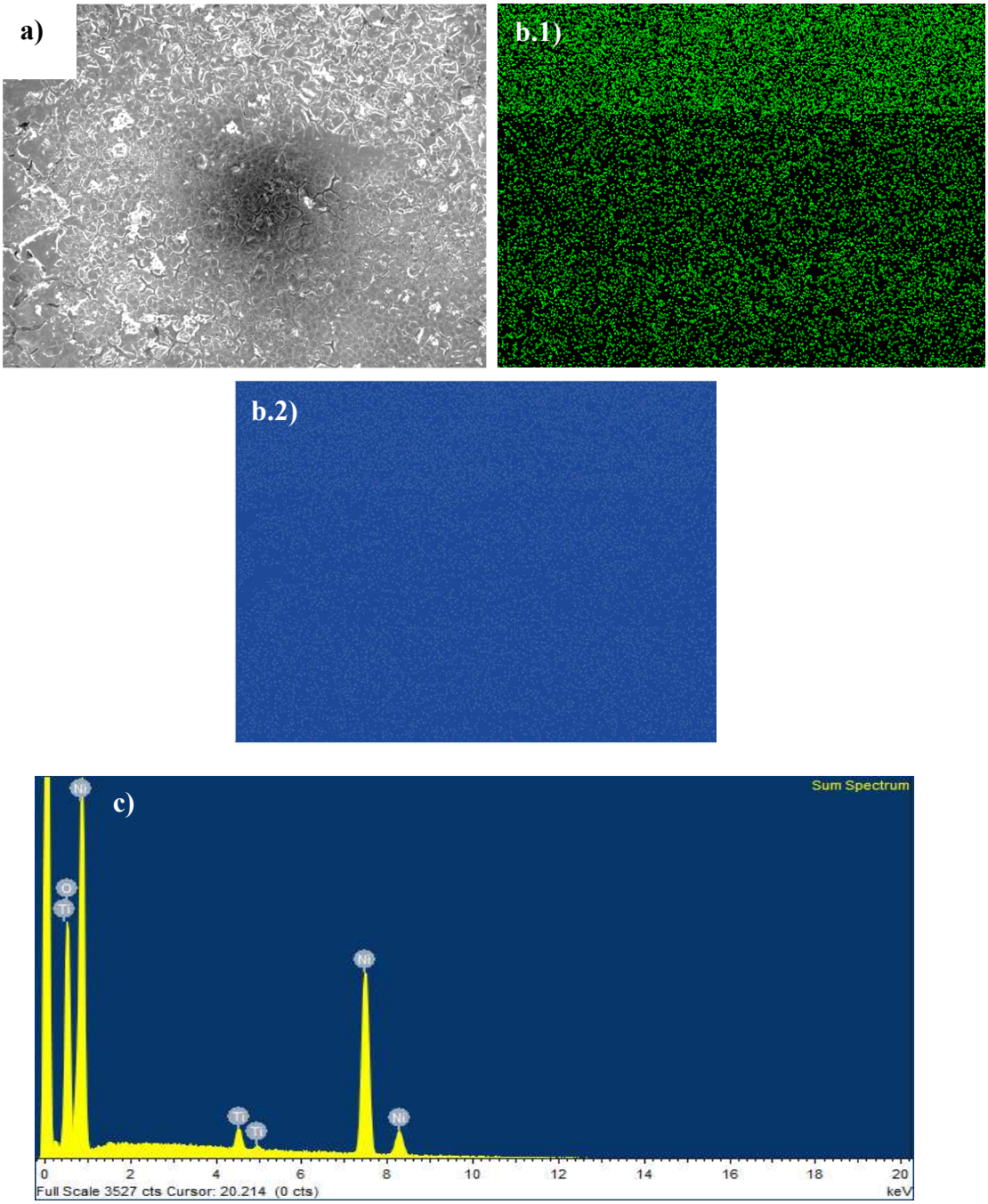



Figure 5.4.10 a) Nickel oxide self-oriented flowers; b) Zoom of square in figure "a". The presence of these crystalline structures was found to be indirect proportional to the % M Co content and dispersed randomly along the surface of the electrode. The images are taken at various magnifications (see scale line) using in-Lens detector and 5kV EHT. Distance between the samples and the objective was 7 mm.

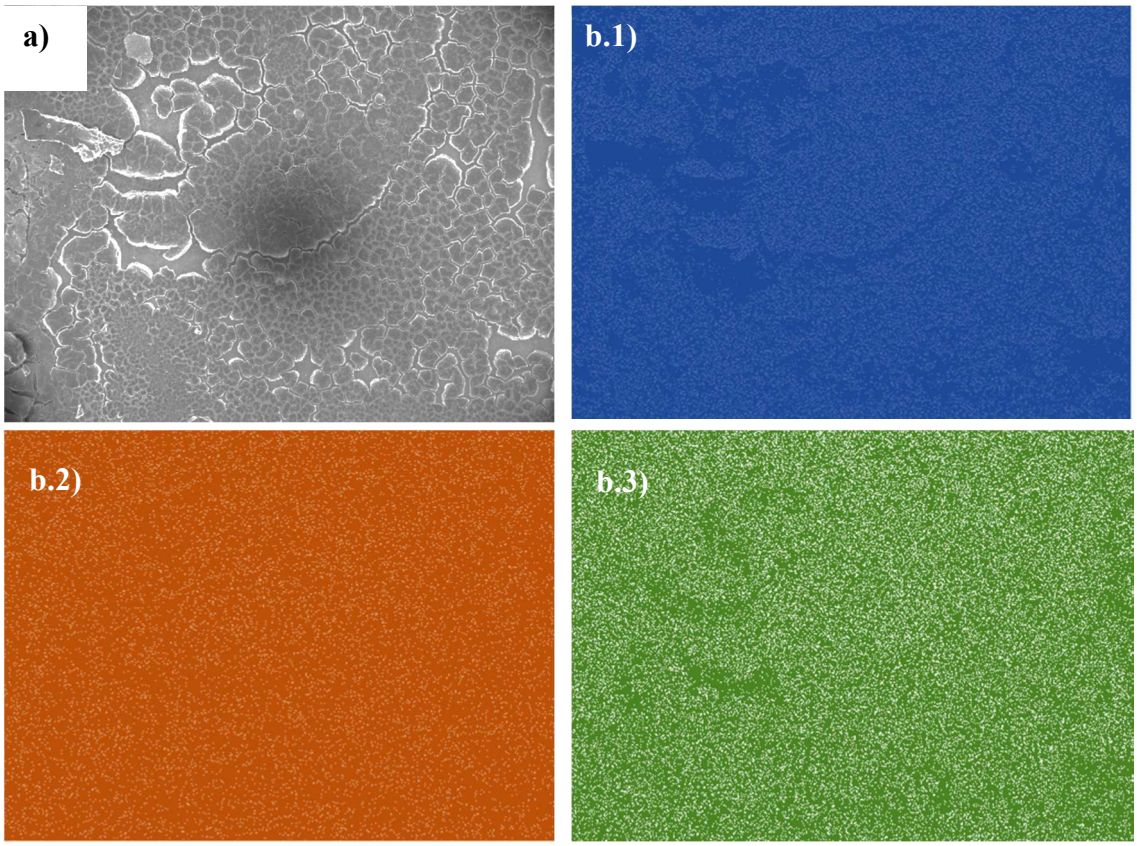
Energy dispersive X-ray spectroscopy (EDX) was used to chemically characterise the electrocatalyst oxide film. EDX, in this sense, provides a comprehensive analysis of the elements present in the sample bulk. To determine the total mixed oxide composition, several large EDX 'maps' were taken, and the average bulk composition value was obtained. These results are presented in fig. 5.4.11 to 5.4.17. The plots obtained in these experiments show the locations of nickel, cobalt and oxygen atoms on the film bulk. Also included in such figures are the EDX spectrum characteristic of each sample.

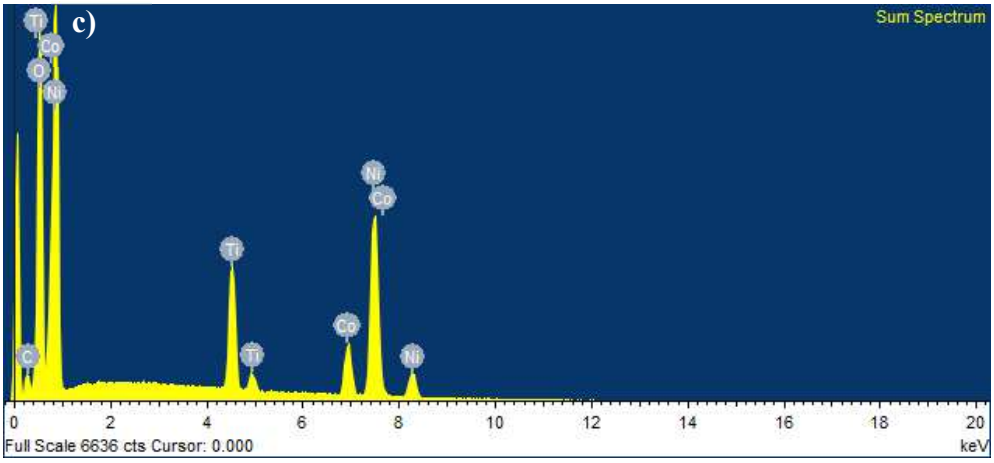
Before analysing the extent of both nickel and cobalt on the bulk, it is important to mention the presence of carbon detected. All samples were found to possess around 10 % carbon concentration. This experimental observation of carbon ions on the bulk of the films is in accordance with the work carried out by Dell and Stone[42] who observed that carbon monoxide, CO, and carbon dioxide, $CO_2$ may be adsorbed on both nickel oxide and cobalt oxide films. Also, carbon ions may arise from the support. Recall that carbon tape was used to put together the sample with the sample holder. Therefore, we may suggest that carbon ions arise partially from adsorbed CO and $CO_2$ and also from the carbon tape used as a support. EDX also provided the ratio of nickel and cobalt for each electrode. The maps in figs. 5.4.11 to 5.4.17 proved the uniform distribution of all the elements present in the sample. The atomic ratio of nickel and cobalt on each sample compared with that from the precursor salt are shown in Table 5.4.4.




| Spectrum | C (%) | O (%) | Ti (%) | Ni (%) | Total |
|---|---|---|---|---|---|
| Sum spectrum | 13.66 | 42.14 | 1.44 | 42.76 | 100 |

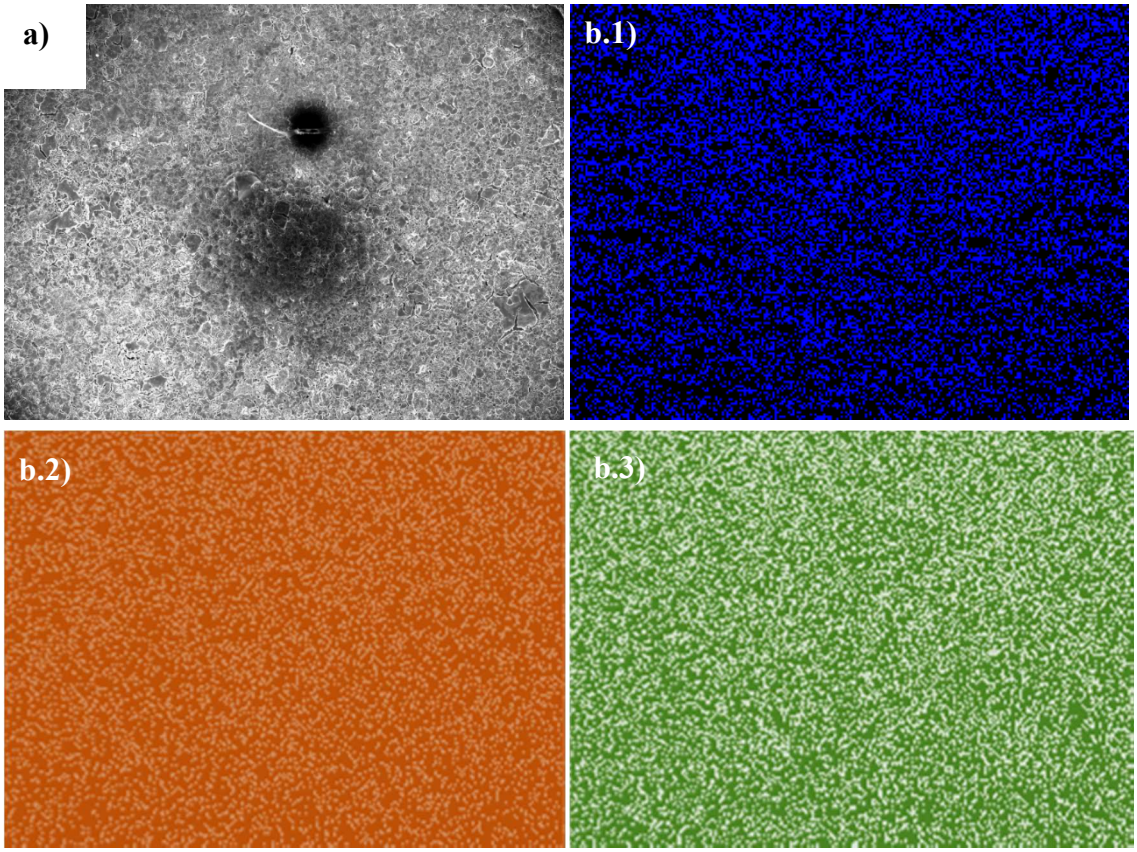
Figure 5.4.11 Shown are a) the SEM image of a sample with 0 % M Co content over which the EDX analysis was performed; b.1 and b.2) EDX map of image (a) displaying nickel and oxygen atoms, respectively. The coloured spots correspond to the relative element underneath the SEM image; c) EDX spectrum of image (a) with quantitative table showing relative mole % of each element present.

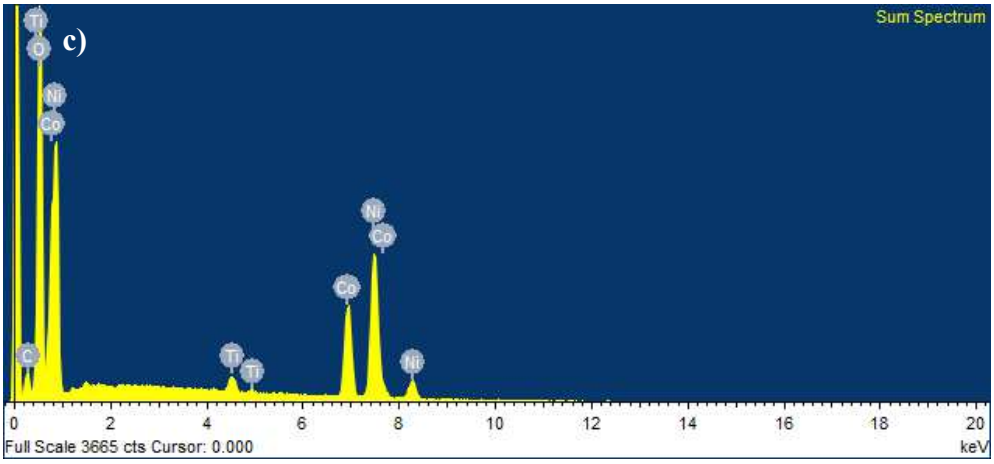



| Spectrum | C (%) | O (%) | Ti (%) | Co (%) | Ni (%) | Total |
|---|---|---|---|---|---|---|
| Sum spectrum | 10.65 | 46.77 | 6.35 | 6.29 | 29.94 | 100 |

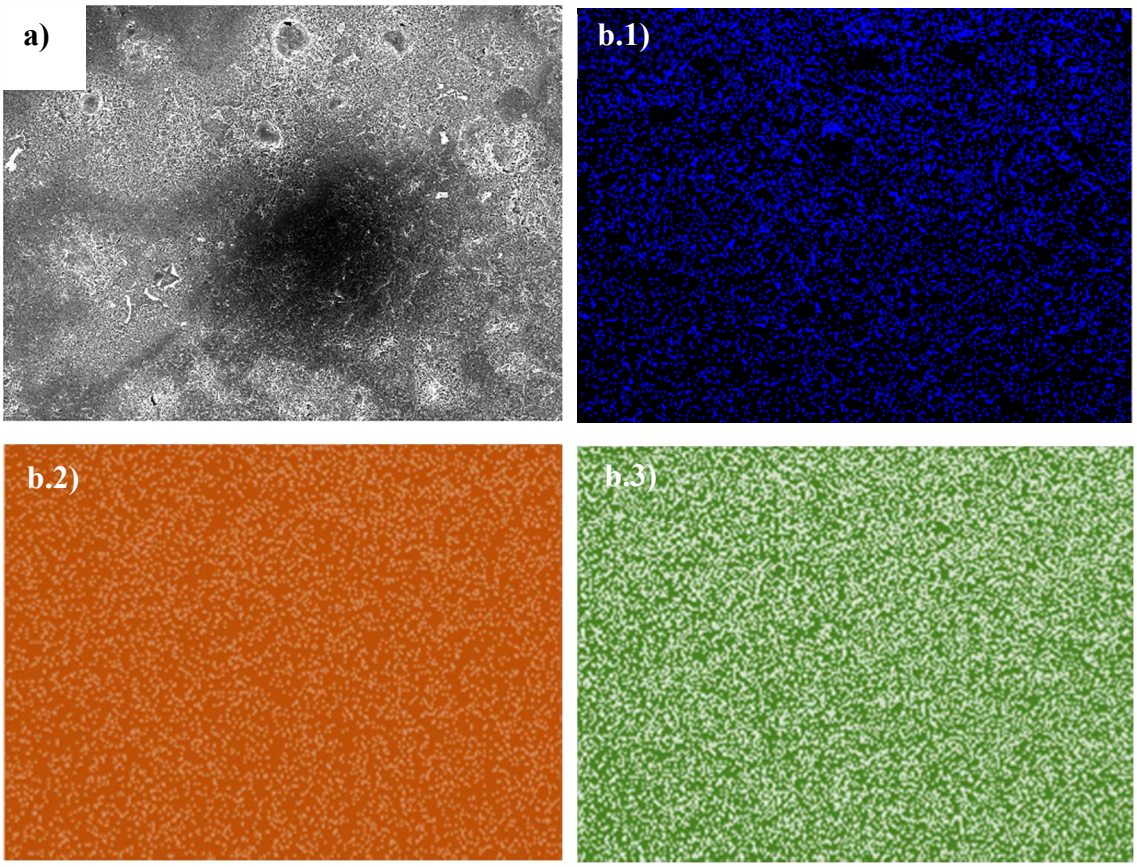
Figure 5.4.12 Shown are a) the SEM image of a sample with 20 % M Co content over which the EDX analysis was performed; b.1, b.2, b.3) EDX map of image (a) displaying oxygen, cobalt and nickel atoms, respectively. The coloured spots correspond to the relative element underneath the SEM image; c) EDX spectrum of image (a) with quantitative table showing relative mole % of each element present.

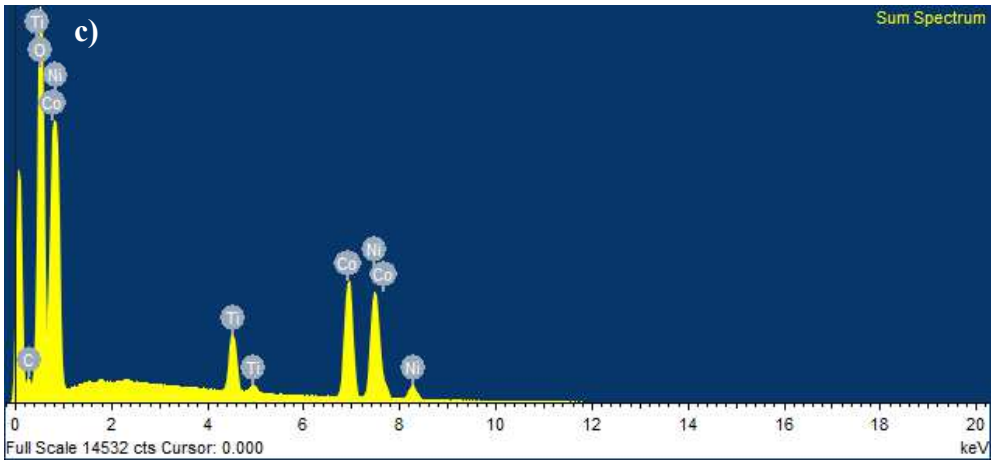



| Spectrum | C (%) | O (%) | Ti (%) | Co (%) | Ni (%) | Total |
|---|---|---|---|---|---|---|
| Sum spectrum | 12.67 | 45.46 | 0.91 | 14.08 | 26.88 | 100 |

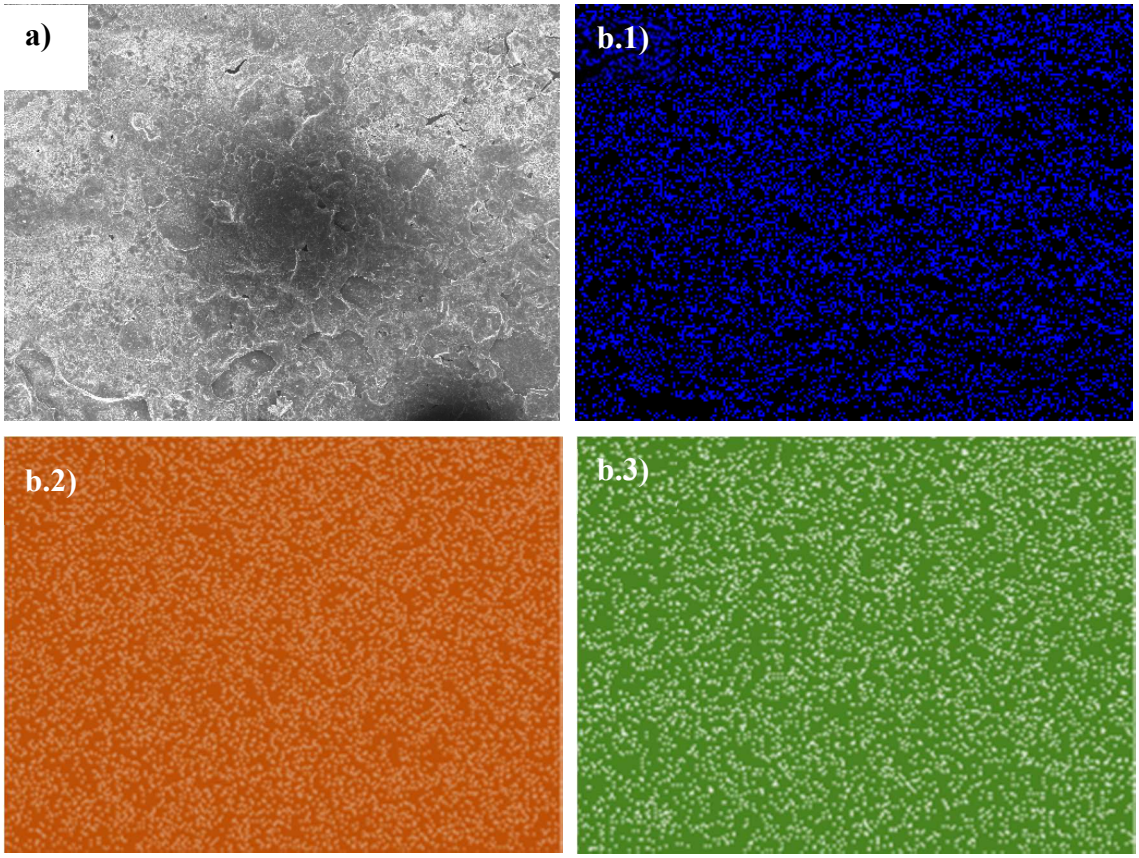
Figure 5.4.13 Shown are a) the SEM image of a sample with 40 % M Co content over which the EDX analysis was performed; b.1, b.2, b.3) EDX map of image (a) displaying oxygen, cobalt and nickel atoms, respectively. The coloured spots correspond to the relative element underneath the SEM image; c) EDX spectrum of image (a) with quantitative table showing relative mole % of each element present.

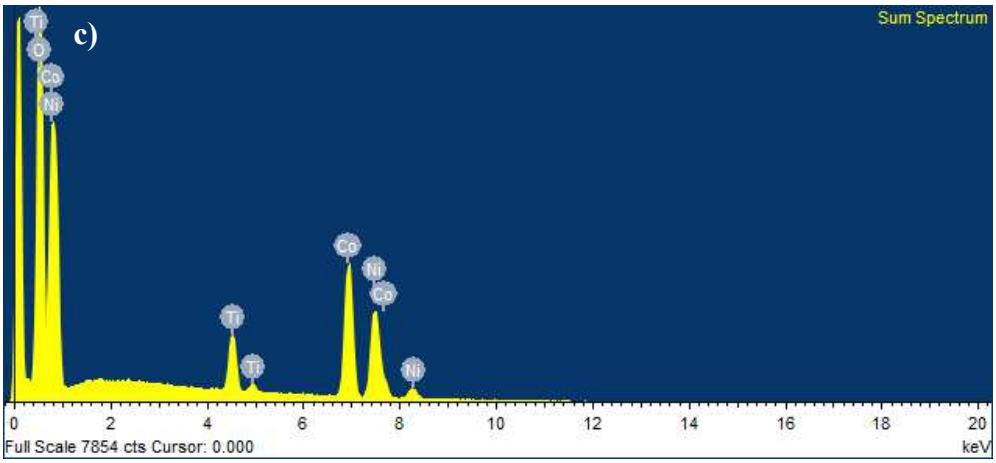



| Spectrum | C (%) | O (%) | Ti (%) | Co (%) | Ni (%) | Total |
|---|---|---|---|---|---|---|
| Sum spectrum | 13.09 | 52.92 | 1.66 | 15.19 | 17.14 | 100 |

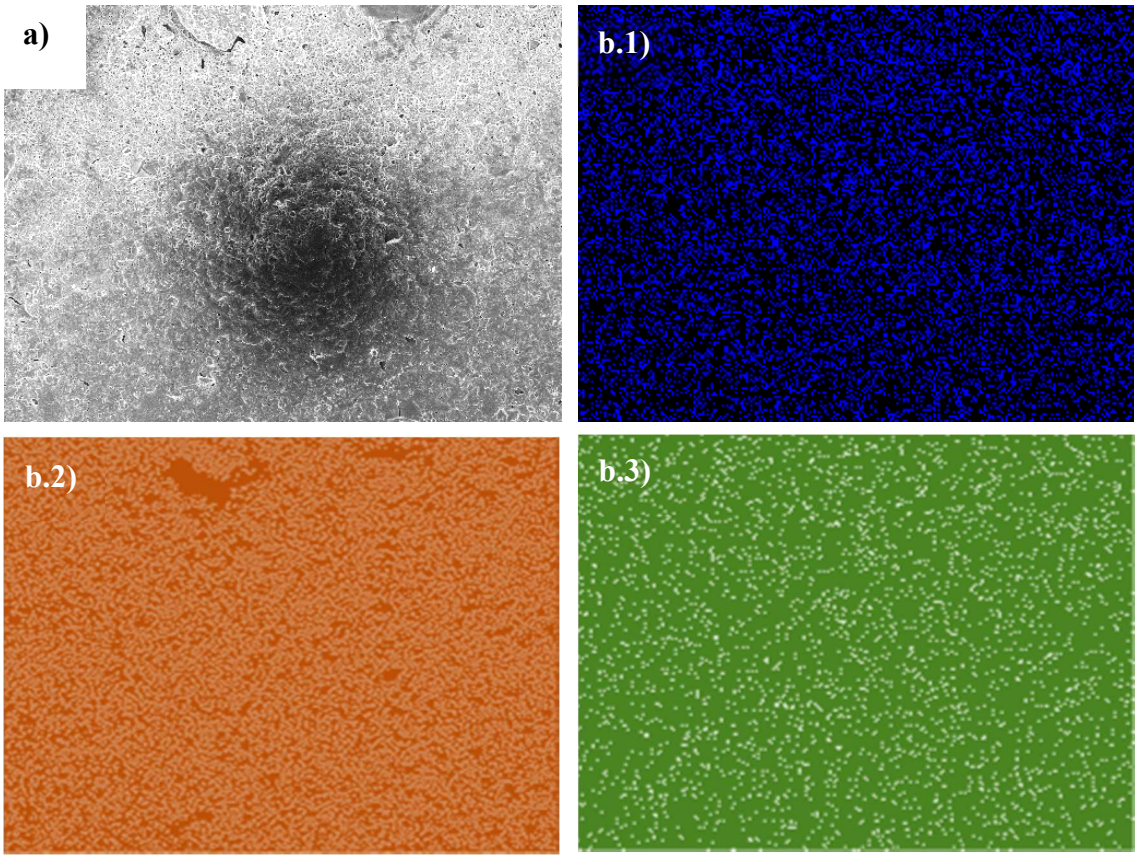
Figure 5.4.14 Shown are a) the SEM image of a sample with 50 % M Co content over which the EDX analysis was performed; b.1, b.2, b.3) EDX map of image (a) displaying oxygen, cobalt and nickel atoms, respectively. The coloured spots correspond to the relative element underneath the SEM image; c) EDX spectrum of image (a) with quantitative table showing relative mole % of each element present.

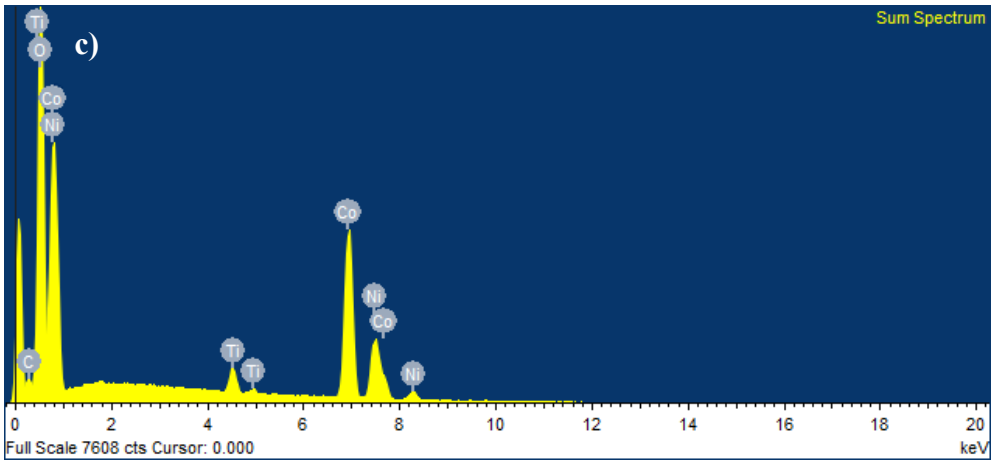



| Spectrum | C (%) | O (%) | Ti (%) | Co (%) | Ni (%) | Total |
|---|---|---|---|---|---|---|
| Sum spectrum | 10.47 | 51.46 | 1.52 | 20.50 | 16.05 | 100 |

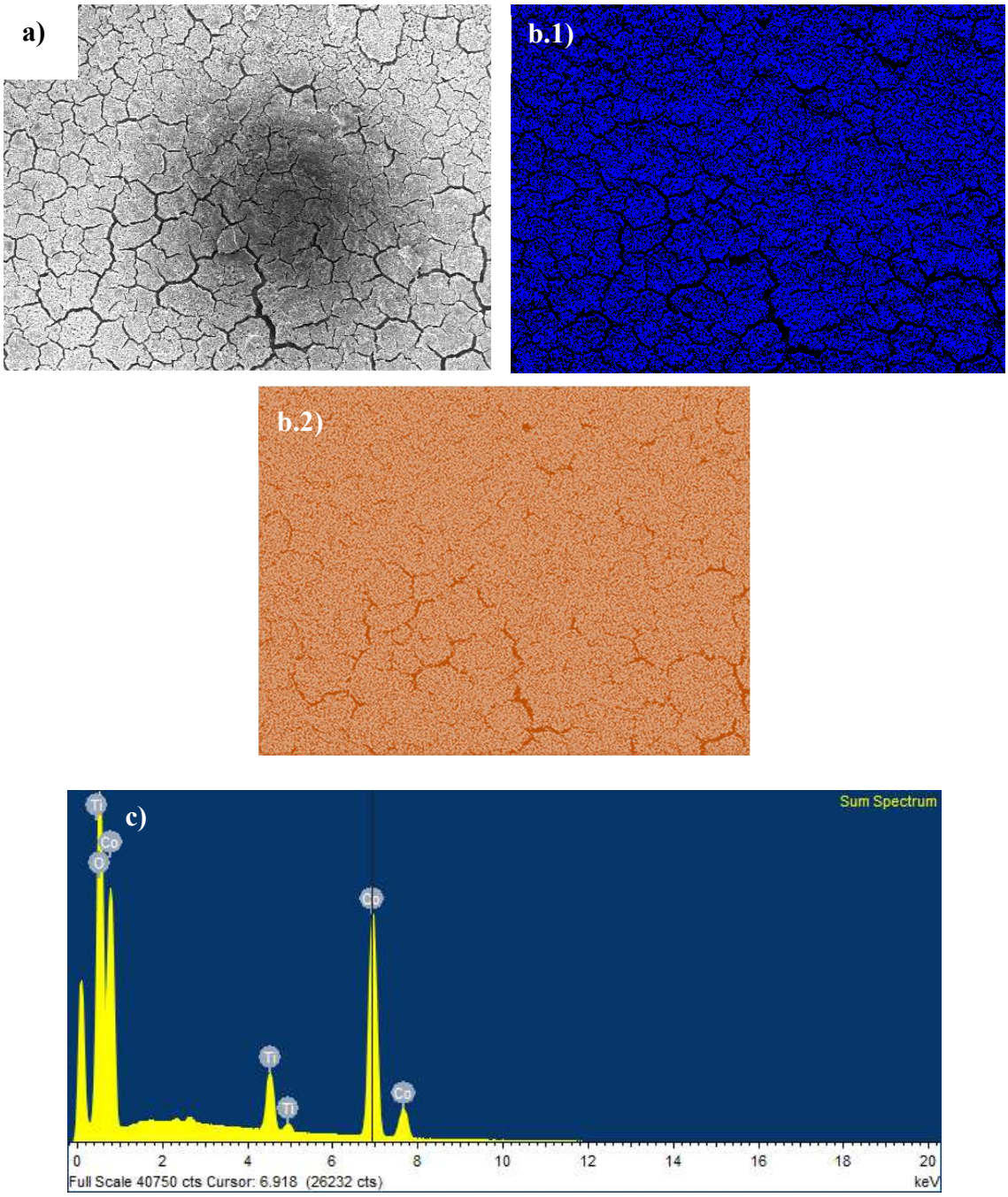
Figure 5.4.15 Shown are a) the SEM image of a sample with 60 % M Co content over which the EDX analysis was performed; b.1, b.2, b.3) EDX map of image (a) displaying oxygen, cobalt and nickel atoms, respectively. The coloured spots correspond to the relative element underneath the SEM image; c) EDX spectrum of image (a) with quantitative table showing relative mole % of each element present.




| Spectrum | C (%) | O (%) | Ti (%) | Co (%) | Ni (%) | Total |
|---|---|---|---|---|---|---|
| Sum spectrum | 13.37 | 52. 20 | 1.30 | 24.20 | 8.93 | 100 |

Figure 5.4.16 Shown are a) the SEM image of a sample with 80 % M Co content over which the EDX analysis was performed; b.1, b.2, b.3) EDX map of image (a) displaying oxygen, cobalt and nickel atoms, respectively. The coloured spots correspond to the relative element underneath the SEM image; c) EDX spectrum of image (a) with quantitative table showing relative mole % of each element present.




| Spectrum | C (%) | O (%) | Ti (%) | Co (%) | Total |
|---|---|---|---|---|---|
| Sum spectrum | 12.84 | 50. 48 | 1.84 | 34.84 | 100 |

Figure 5.4.17 Shown are a) the SEM image of a sample with 100 % M Co content over which the EDX analysis was performed; b.1, b.2) EDX map of image (a) displaying oxygen and cobalt atoms, respectively. The coloured spots correspond to the relative element underneath the SEM image; c) EDX spectrum of image (a) with quantitative table showing relative mole % of each element present

| % M Co content | Ratio Ni/Co precursor salt | Ratio Ni/Co EDX | Difference between ratios |
|---|---|---|---|
| 0 | - | - | - |
| 20 | 4.00 | 4.75 | 0.75 |
| 40 | 1.50 | 1.90 | 0.40 |
| 50 | 1.00 | 1.13 | 0.13 |
| 60 | 0.60 | 0.75 | 0.15 |
| 80 | 0.25 | 0.37 | 0.12 |
| 100 | - | - | - |

Table 5.4.4 Table of the EDX analysis results showing the different Ni/Co ratios of a series of nickel cobalt mixed oxides with various % M Co content. These values are extracted from Tables in fig. 5.4.11 to 5.4.17.

EDX analysis confirmed that the bulk composition follows close by the stoichiometry of the precursor solution mix. Interestingly, it was observed an indirectly behaviour between the % M Co content and the difference between ratios. The higher the extent of cobalt in the sample, the lower the difference between the Ni/Co molar ratios obtained from the precursor salt and from EDX analysis.

We suggest this may be due to two possibilities: (i) uneven deposition of the materials, and (ii) the presence of very concentrated nickel regions on the sample. Note, that the ratio of Ni/Co obtained from EDX analysis is larger than that obtained from the precursor salt, which suggests that the measured nickel concentration in the EDX is somewhat larger than the cobalt ion, or in other words, that the cobalt concentration measured by EDX is smaller than the expected one. Recall the observation of nickel crystal structures on the surface of samples with large amount of nickel content (see fig. 5.4.10). It was previously mentioned that the presence of such structures on the oxide surface decreased with increasing concentration of cobalt. Thus, the presence of singular points with large amount of nickel crystals may vary the % atomic concentration calculations yielding to variations on the Ni/Co molar ratio. Clearly, the difference would be more notorious in those cases where the amount of nickel atoms would be large, as observed in Table 5.4.4.

### 5.4.4 Contact Angle Analysis

Variation of the % M of Co content on samples brings about significant changes in the surface chemistry of films. Such changes were investigated by studying the water contact angle of each sample type. Calculations based on measured contact angle values yield to the determination of the solid surface tension, which quantifies the wetting characteristics of a solid material. Fig. 5.4.18 shows the water contact angles for each type of sample whereas fig. 5.4.19 outlines the contact angle as a function of % M Co content.

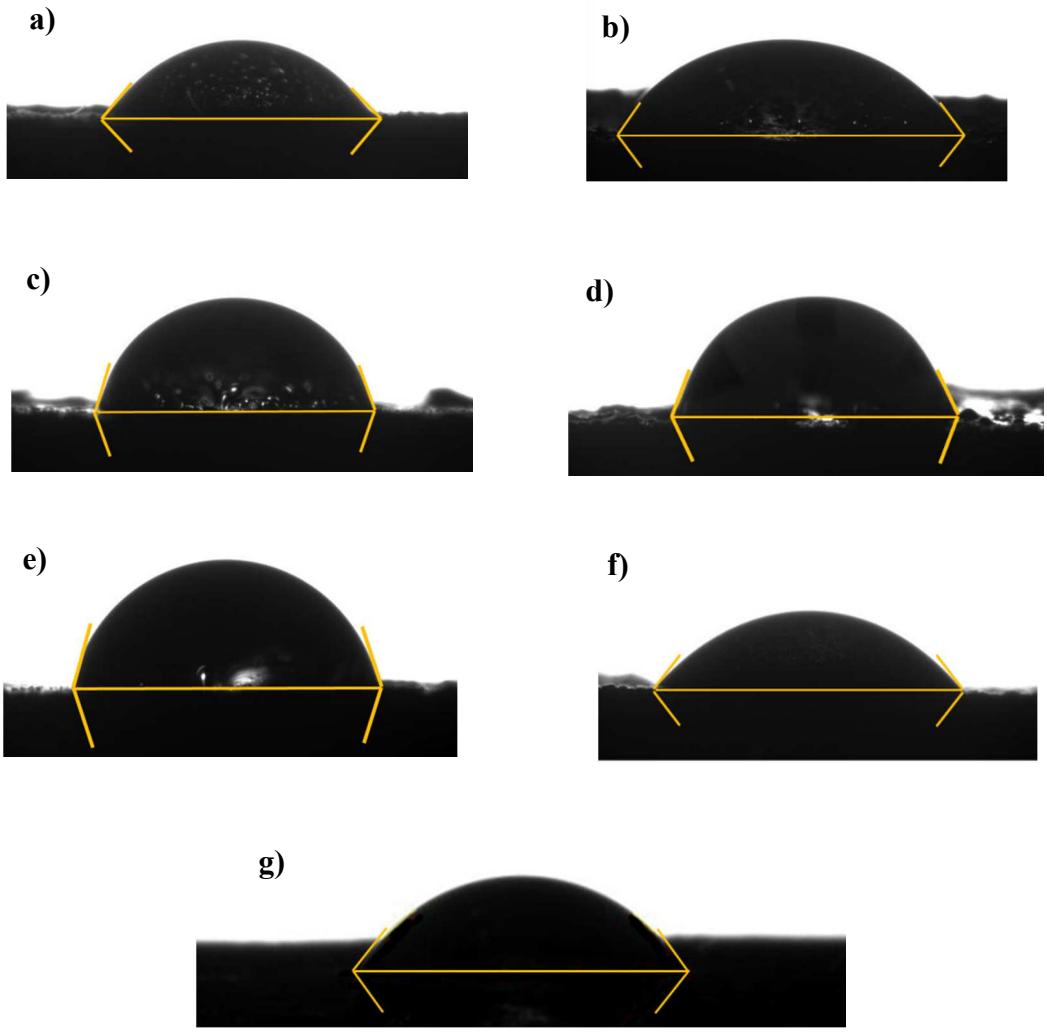



Figure 5.4.18 Various contact angle measurements on nickel cobalt mixed oxide electrodes with various % Co content: a) 0 %, b) 20 %, c) 40 %, d) 50 %, e) 60 %, f) 80 %, g) 100 % M Co content. The contact angle displayed in these images correspond to that formed between a water drop and the surface. All the images were obtained using the sessile drop method and captured after 5 s from the drop.

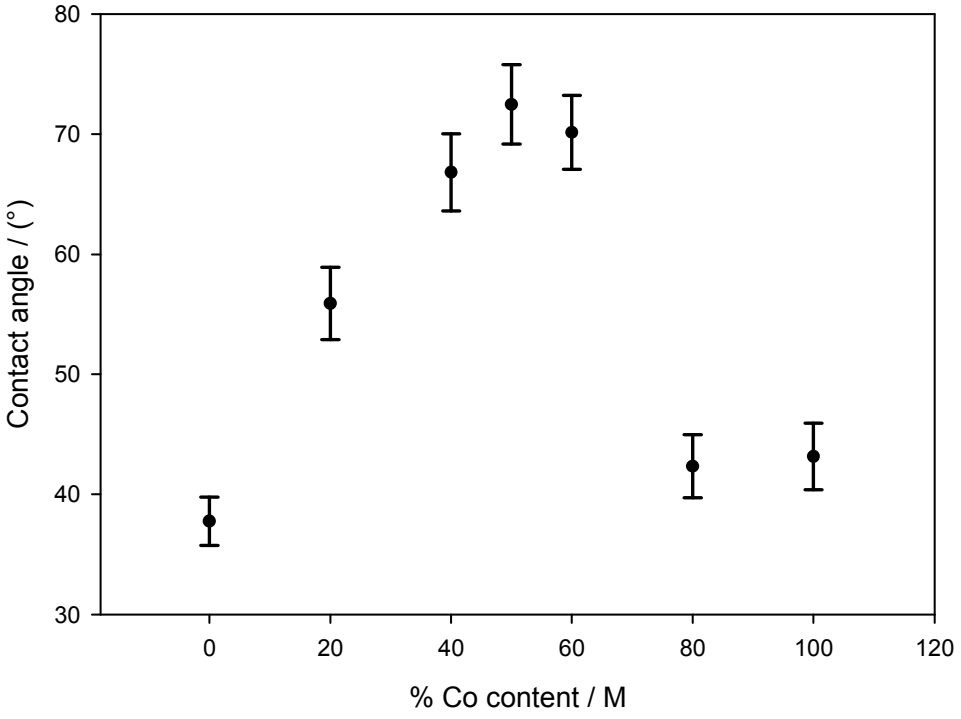



Figure 5.4.19 Contact angle values as a function of % M Co content on nickel cobalt mixed oxide electrodes. These contact angle values were determined from the images in fig. 5.4.18. Error bars represent standard deviations of three different samples.

As observed in fig. 5.4.19, the % M Co content present on the nickel cobalt mixed oxide electrodes produces significant changes in the wettability behaviour of the samples. It can also be noted that while all the samples were found to be hydrophilic in nature, not all the samples exhibit equal degree of wettability. It was found that those samples with a large wt.% of $NiCo_2O_4$ phase, those are 40 %, 50 % and 60 % M Co content, displayed the highest contact angles. The latter may indicate that $NiCo_2O_4$ phases possesses a relatively greater hydrophobic nature than those samples with larger NiO or $Co_3O_4$ phases. Similar observations were also found in the literature.[43] This hydrophobicity may be ascribed to the ease of the $NiCo_2O_4$ species to adsorb polar molecules, such as water or $OH^-$ onto its surface.

## 5.5 The Influence of Cobalt Oxide on the Electrochemical Behaviour of Nickel Cobalt Mixed Oxide Electrodes

The present section focuses on the presentation of the electrochemical redox and charge transfer proprieties of a series of nickel cobalt mixed oxides electrodes with different % M Co content prepared by thermal decomposition in air at 400°C. This study aims to investigate the effect of the extent of cobalt oxide on nickel cobalt mixed oxide electrodes on both the electrochemical proprieties and the catalytic activity of such electrodes towards the OER. The electrochemical redox proprieties of nickel cobalt oxide films will be examined by monitoring the voltammetric response as a function cobalt concentration. The potential-pH response will also be examined and used to assign a more accurate stoichiometry of the redox system. Also included are relevant steady-state polarisation measurements that yield information to the nature of the catalytic surfaces on which the OER proceeds in these systems.

### 5.5.1 The Surface Redox Chemistry

Typical cyclic voltammograms recorded for thermally prepared nickel cobalt mixed oxides with different % M Co content coated on titanium anodes in 1.0 M NaOH at 25°C are outlined in fig. 5.5.1. The voltammogram for the pure NiO (see fig. 5.5.1a) was found to possess a very sharp redox couple at potential range ca. 1.3 - 1.5 V (*vs.* RHE). Recall that the shape of the redox peaks is closely related with the nature of the crystal phase. Sharp peaks in cyclic voltammograms usually involve a high crystalline structure, whereas broad peaks involve the presence of an amorphous phase. It has also been pointed out that the boarding of the peaks arises in fig. 5.5.1 due to: (i) the formation of $NiCo_2O_4$ which, as previously mentioned in section 5.3.2, possesses a poor crystallite phase, and (ii) the redox peak may now involve more than one redox reaction. Note from fig. 5.5.1 that nickel and cobalt, 0 and 100 % M Co respectively, exhibit redox peaks in the same potential window ca. 1.3 -1.5 V and therefore, it would seem logical to assess the redox peaks associated with $NiCo_2O_4$ also takes place within this potential window.

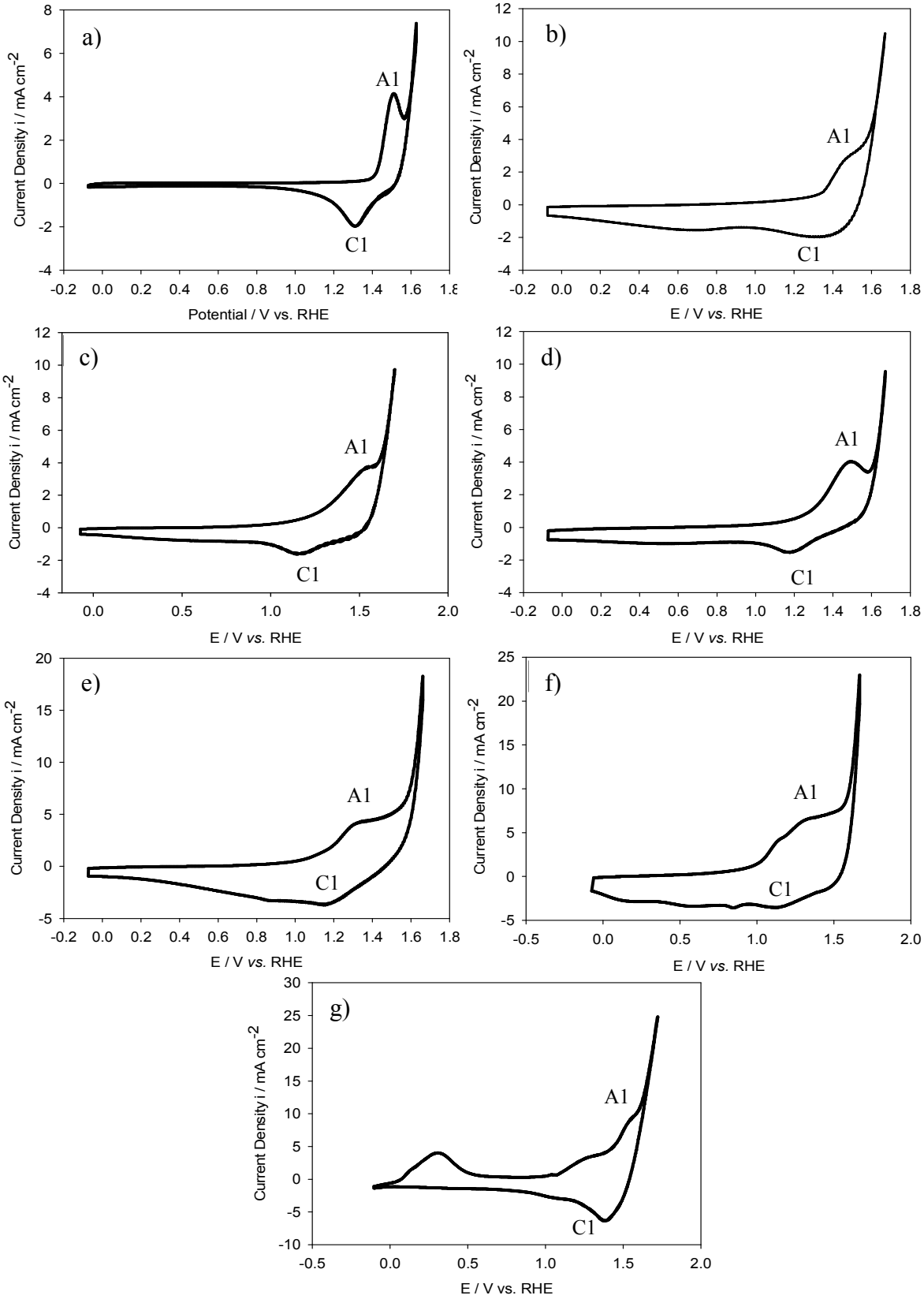



Figure 5.5.1 Cyclic voltammograms characterising the surface electrochemistry of a series of nickel cobalt mixed oxide electrodes annealed at 400°C: a) 0, b) 20, c) 40, d) 50, e) 60, f) 80, and g) 100 % M Co content. All the above CVs were recorded in 1.0 M NaOH between -0.3 and 1.7 V *vs.* RHE with a sweep rate of 50 mV $s^{-1}$ at 25°C.

Jiangping Tu *et al.*[27] have mentioned that the redox couple observed at ca. 1.3 - 1.5 V for electrodes with < 10 % M Co content involved both the Ni (II/III) and Co (III/IV) transitions based on the following two eqns.:

$$NiCo_2O_4 + OH^- + H_2O \leftrightarrow NiOOH + 2CoOOH + e^- \quad (5.5.1.1)$$

$$CoOOH + OH^- \leftrightarrow CoO_2 + H_2O + e^- \quad (5.5.1.2)$$

To validate the latter assumption and taking into consideration the fact that better defined redox peaks may be achieved by decreasing the sweep rate (only valid for slow rate reactions), a cyclic voltammogram for the nickel oxide with 50 % M Co content recorded at 5 mV $s^{-1}$ is presented in fig. 5.5.2.

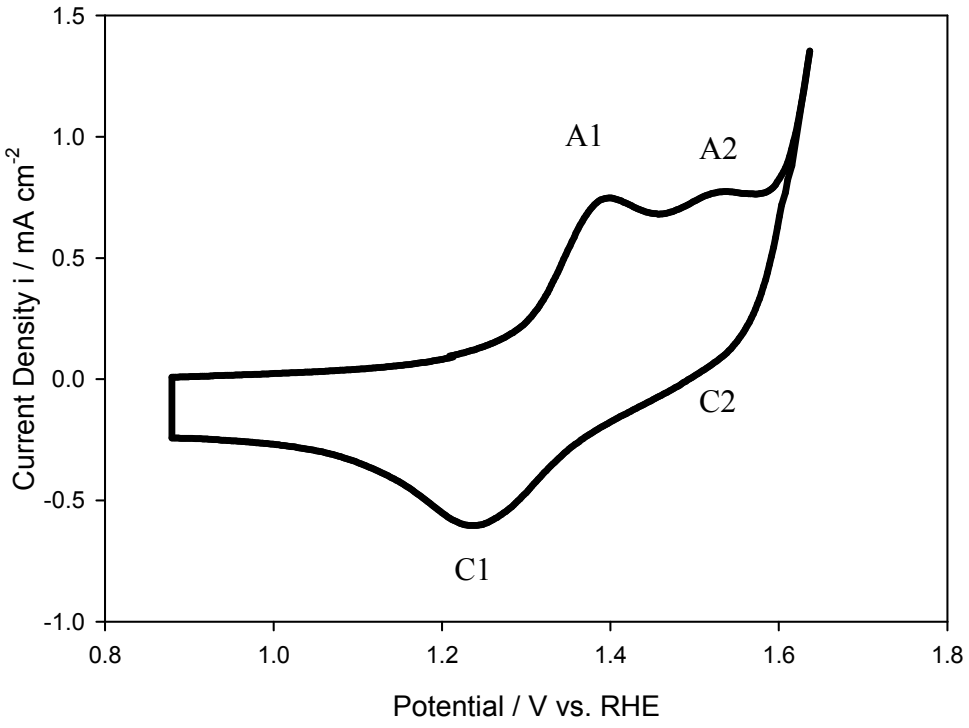



Figure 5.5.2 CV of a nickel cobalt oxide electrode with 50 % M Co content in 1.0 M NaOH at 25°C. The sweep rate was 5 mV $s^{-1}$.

It can be observed in fig. 5.5.2 two well defined anodic peaks A1 and A2, at ca. 1.4 V and ca. 1.5 V, respectively. Therefore, if peak potentials in fig. 5.5.2 are compared with those in fig. 5.5.1, 0 and 100 % M Co respectively, it is evident that peaks at ca. 1.3 V and ca. 1.5 V correspond to Ni (II/III) and Co (III/IV) transitions, respectively. The latter is supported by the fact that nickel increase its oxidation state at lower potentials than the cobalt.[27] It is

important to highlight that NiOOH and CoOOH have been identified as the active species to catalyse the OER.[44] As a consequence, the intensity of this characteristic anodic peak, or more precisely, the area enclosed by the peak, indicates the amount of NiOOH and CoOOH formed in the system and correlates positively with the OER efficiency of the electrocatalyst. Recall that the integrated voltammetric charge $Q^*$ determined between pre-defined limits has been shown to be a useful indicator of active surface area.[45] In this perspective, the plot of charge enclosed in the anodic redox peak as a function of % M Co content is presented in fig. 5.5.3. Note that 0 % and 100 % M Co content samples were omitted since these do not produce $NiCo_2O_4$ phase.

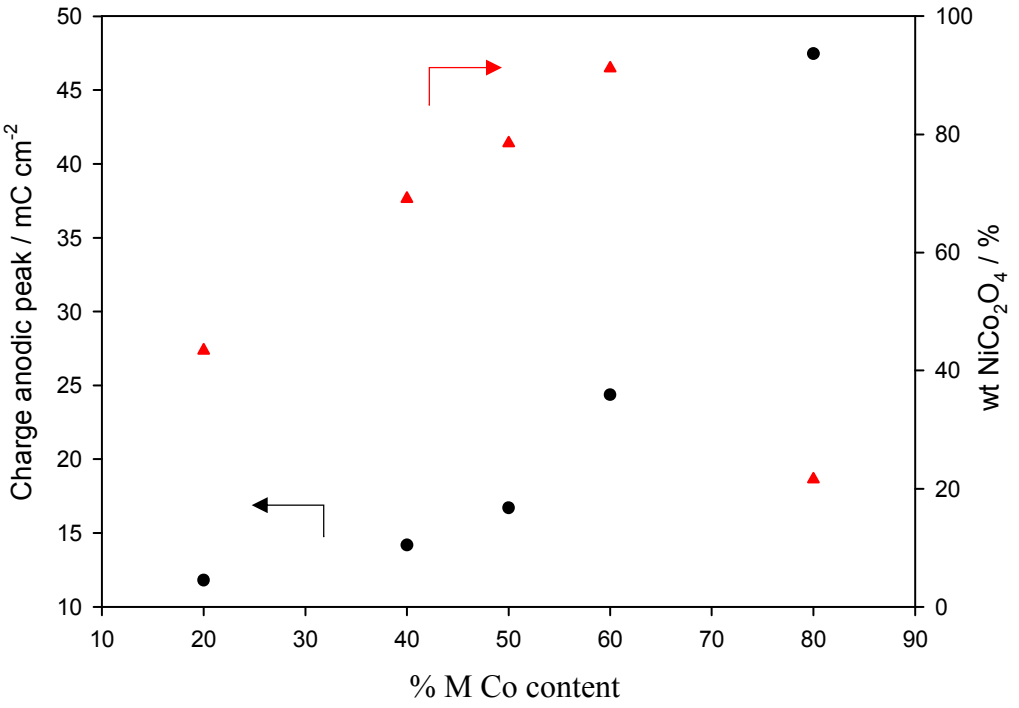



Figure 5.5.3 Left hand side: The charge associated with the anodic peak A1 of CVs in fig. 5.5.2 as a function of % M Co content (●). Right hand side: wt.% of $NiCo_2O_4$ phase as a function of % M Co content (▲). The $NiCo_2O_4$ wt.% are obtained from Table 5.4.1. The graph pretends illustrate the relationship between anodic charge and wt.% of $NiCo_2O_4$.

The increase in anodic charge seems to occur in tandem with the increase of $NiCo_2O_4$ wt.% content for samples with cobalt content between 20 % and 60 % being the latter the point with greater $NiCo_2O_4$ phase and peak charge. At 80 %, although there is a notorious increase in the peak charge, the wt.% of $NiCo_2O_4$ decreases drastically. This is due to $Co_3O_4$ phase is the predominant phase in the sample (see Table 5.4.1). The charge transfer kinetics

contributed by the redox reactions of Co (II/III) and Co (III/IV) in the redox couple are responsible for the high conductivity and capacitance of cobalt oxide electrode.

### 5.5.2 The Influence of the pH on the Voltammetric Response

The influence of the solution pH on the voltammetric response of a series of nickel cobalt mixed oxide with different % M Co content is now presented. The effect of alkaline concentration on the redox activity of the electrodes was tested at seven different pH concentrations, ranging from 0.1 M to 5.0 M NaOH. Alkaline concentration has two impacts on the electrode performance, firstly on the ionic conductivity between the electrolyte and the electrode, and secondly on the electrocatalyst activity since exchange current density typically increases as $OH^-$ ions increase. Figs. 5.5.4 to 5.5.10 show the peak potential dependence with the pH at 25°C of various electrodes. Table 5.4.2.1 summarizes regression line equations for the redox peak shift as a function of pH. It can be noted from the figures below that peak potentials *vs.* pH exhibit slopes ca. 0 mV per pH unit, for both anodic and cathodic peak potentials respectively. Also note that in the RHE scale, the observation of a zero shift is analogous to a potential shift of 59 mV $pH^{-1}$ in the Hg/HgO scale. These observations suggest the involvement of proton in the overall reaction as predicted by eqns. 5.5.1.1 and 5.5.1.2.

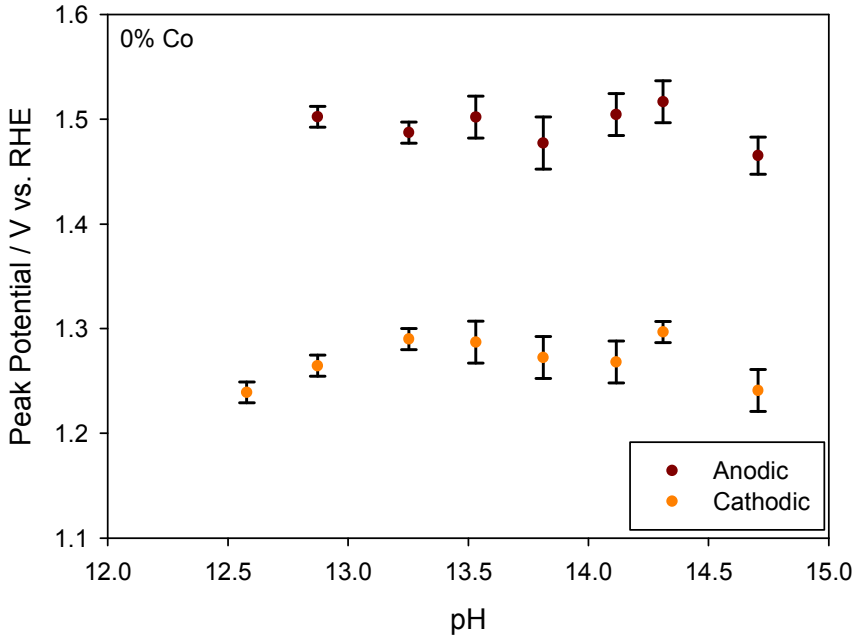



Figure 5.5.4 Potential-pH shift of nickel cobalt mixed oxide electrode with 0 % M Co content. The peak potential refers to A1 (brown dot) and C1 (orange dot) peaks in fig. 5.5.2. The peak potential was measured using a RHE reference electrode. Error bars represent standard deviations of three different samples.

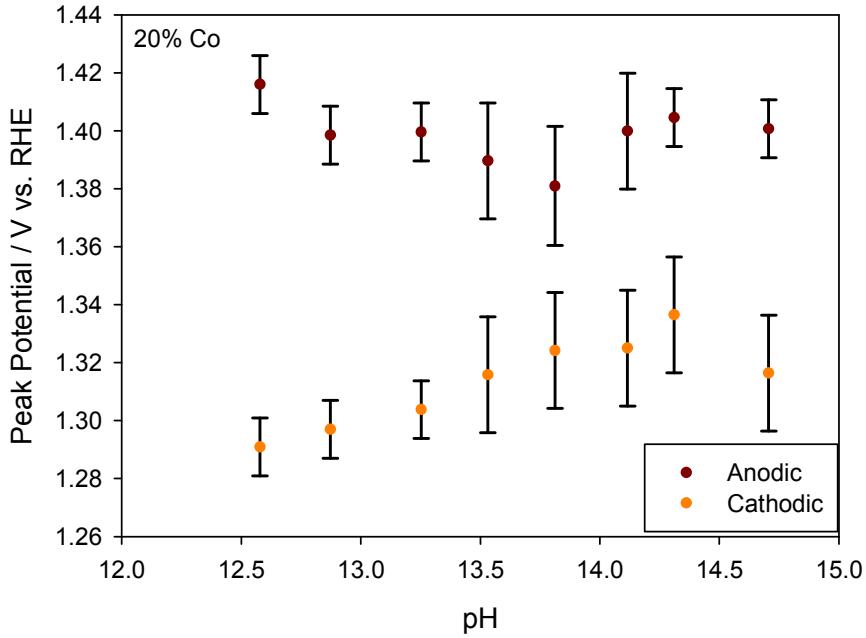



Figure 5.5.5 Potential-pH shift of nickel cobalt mixed oxide electrode with 20 % M Co content. The peak potential refers to A1 (brown dot) and C1 (orange dot) peaks in fig. 5.5.2. The peak potential was measured using a RHE reference electrode. Error bars represent standard deviations of three different samples.

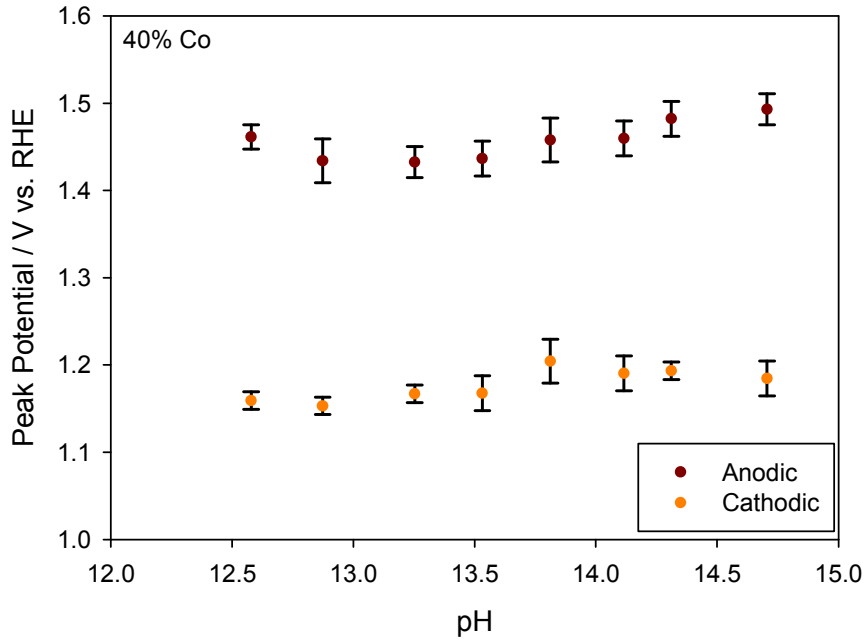



Figure 5.5.6 Potential-pH shift of nickel cobalt mixed oxide electrode with 40 % M Co content. The peak potential refers to A1 (brown dot) and C1 (orange dot) peaks in fig. 5.5.2. The peak potential was measured using a RHE reference electrode. Error bars represent standard deviations of three different samples.

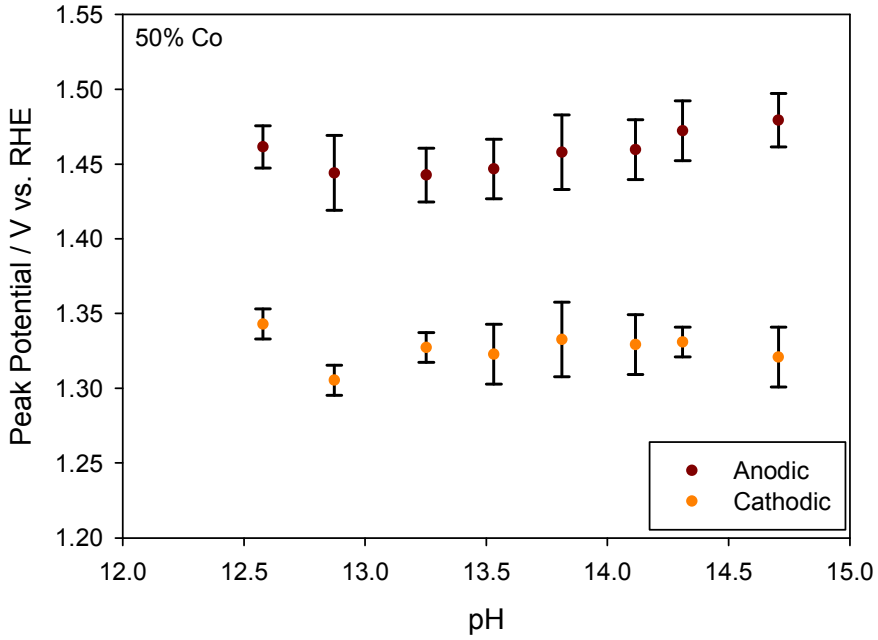



Figure 5.5.7 Potential-pH shift of nickel cobalt mixed oxide electrode with 50 % M Co content. The peak potential refers to A1 (brown dot) and C1 (orange dot) peaks in fig. 5.5.2. The peak potential was measured using a RHE reference electrode. Error bars represent standard deviations of three different samples.

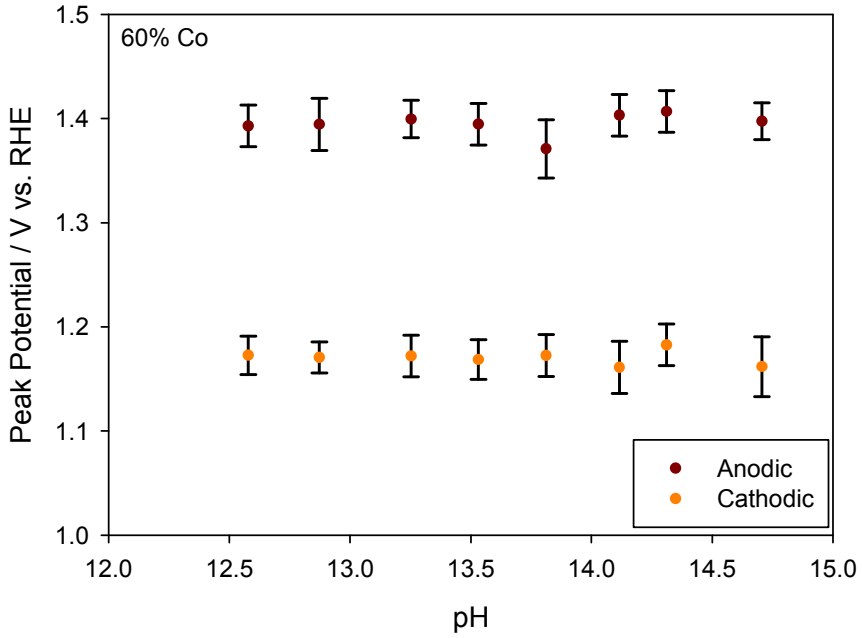



Figure 5.5.8 Potential-pH shift of nickel cobalt mixed oxide electrode with 60 % M Co content. The peak potential refers to A1 (brown dot) and C1 (orange dot) peaks in fig. 5.5.2. The peak potential was measured using a RHE reference electrode. Error bars represent standard deviations of three different samples.

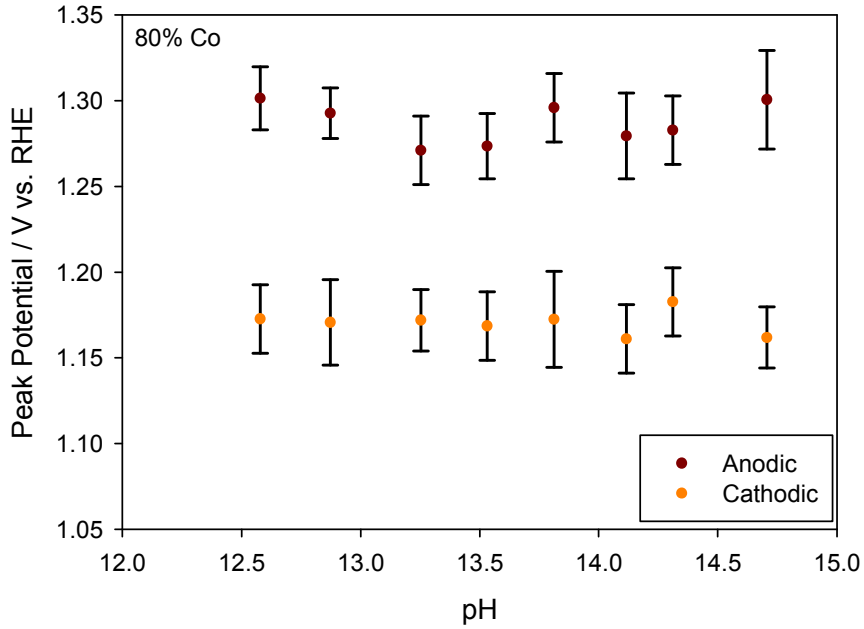



Figure 5.5.9 Potential-pH shift of nickel cobalt mixed oxide electrode with 80 % M Co content. The peak potential refers to A1 (brown dot) and C1 (orange dot) peaks in fig. 5.5.2. The peak potential was measured using a RHE reference electrode. Error bars represent standard deviations of three different samples.

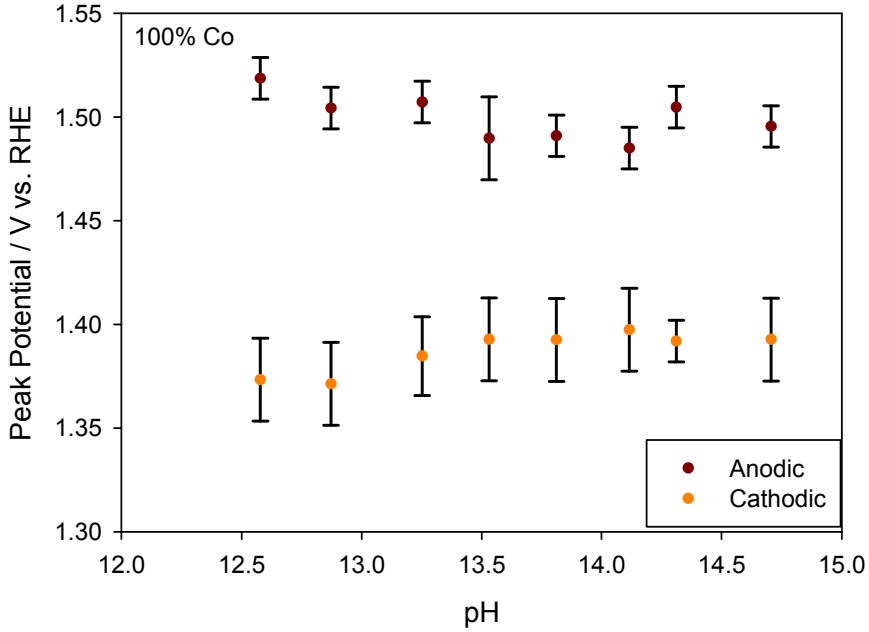



Figure 5.5.10 Potential-pH shift of nickel cobalt mixed oxide electrode with 100 % M Co content. The peak potential refers to A1 (brown dot) and C1 (orange dot) peaks in fig. 5.5.2. The peak potential was measured using a RHE reference electrode. Error bars represent standard deviations of three different samples.

| % M Co content | Anodic regression line eqn. of A1 peak | Cathodic regression line eqn. of C1 peak |
|---|---|---|
| 0 | y = -0.0073x + 1.59 | y = -0.0098x + 1.41 |
| 20 | y = -0.0038x + 1.45 | y = 0.0107x + 1.07 |
| 40 | y = 0.0104x + 1.25 | y = 0.0115x + 0.91 |
| 50 | y = 0.0052x + 1.38 | y = -0.0005x + 1.35 |
| 60 | y = 0.003x + 1.35 | y = -0.0022x + 1.25 |
| 80 | y = -0.0007x + 1.29 | y = -0.0022x + 1.24 |
| 100 | y = -0.0095x + 1.62 | y = 0.0103x + 1.25 |

Table 5.5.1 Calculated regression line eqns. of the potential-pH shift of figs. 5.5.4 - 5.5.10. The anodic and cathodic eqns. refer to A1 and C1 peaks in fig. 5.5.2.

### 5.5.3 The Kinetic Analysis

The mechanism of anodic oxygen evolution at the thermally prepared nickel cobalt mixed oxide electrode surfaces in contact with aqueous alkaline solution was examined using a variety of traditional electrochemical measurements such as steady-state Tafel plot analysis, reaction order studies and examination of open circuit potential decay transients. Such methods have been shown to be extremely effective in aiding the assignment of mechanism of complex multistep, multi-electron transfer surface electrochemical reactions such as the OER.[46]

This section presents the results of a comprehensive kinetic analysis performed on nickel cobalt mixed oxides electrodes in aqueous alkaline solution. These studies were performed as a function of % M Co content using steady-state polarization technique recorded at a sweep rate of 1 mV $s^{-1}$. The latter data was subsequently transformed into Tafel format, and the Tafel slope evaluated. The results of a series of iR compensated OER steady-state polarisation curves recorded at a series of nickel cobalt mixed oxides electrodes in 1.0 M NaOH as a function of % M cobalt content are presented in fig. 5.5.12. In addition, the variation of Tafel slope values with respect to the % M Co content in 1.0 M NaOH solutions is presented in fig. 5.5.11. It is evident from fig. 5.5.11 that the Tafel slope changes significantly with the % M Co content. Note that electrodes with a high content of $NiCo_2O_4$ phase, that is the, 50 % and 60 %, exhibit the lower Tafel slope values, $b$ = 40 mV $dec^{-1}$ , whereas for other % M Co content samples larger values of Tafel slopes were observed, $b \approx$ 80 mV $dec^{-1}$.

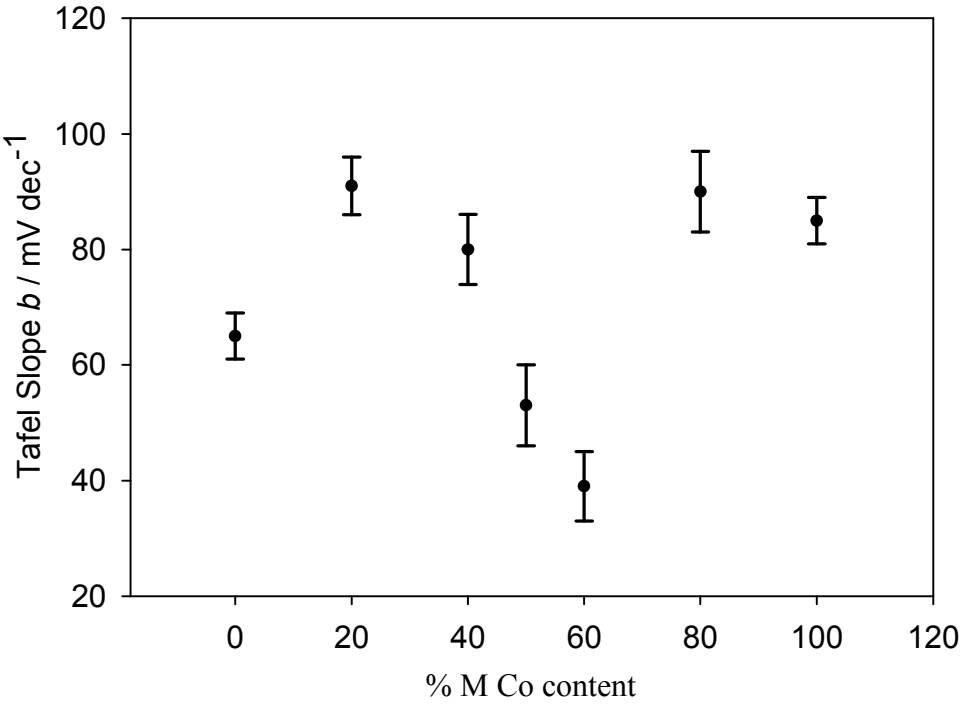



Figure 5.5.11 Tafel slope values of a series of nickel cobalt mixed oxide with different % M Co content in 1.0 M NaOH at 25°C. These values were calculated form the linear region (red dashed line) of the steady-state polarisation curves presented in fig. 5.5.12. Error bars represent standard deviations of three different samples.

This enhancement in the OER activity might be due to the distribution of $Ni^{2+}$ species in the octahedral sites of the spinel, which according with Yihua Zhu and Xiaoling[47], creates active sites for OER with much lower activation potential compared to that of the Co cation.[48] Particularly, for samples with 0 % and 20 % M Co content, where the NiO phase is the major phase, the resulting Tafel slopes are ca. 65 mV $dec^{-1}$ and ca. 91 mV $dec^{-1}$, respectively. On the other hand, for samples with 80 % and 100 % M Co content, where the $Co_3O_4$ phase is predominant, Tafel slope yielded values of ca. 90 mV $dec^{-1}$ and ca. 85 mV $dec^{-1}$, respectively. Although different Tafel slope values have been reported in the literature, depending on: (i) the nature of the substrate, (ii) the preparation method of the samples, and (iii) the experimental conditions, we exclude the possibility of the last two because experimental condition and preparation method are equal in this study.[47, 49]

As outlined in section 2.3.5, the Tafel slope variation can be explained based upon the different surface sites where the OER takes place in the $NiCo_2O_4$ octahedral structure. There exist two different active sites where the OER may occur: trivalent sites and divalent sites corresponding to $Ni^{2+}$ / $Co^{2+}$ and $Ni^{3+}$ / $Co^{3+}$, respectively. The coexistence of divalent and

trivalent states for Co and Ni implies that both Ni and Co species are partially oxidized and reduced, respectively, to balance the formation of oxygen vacancies.[50]

It has been pointed out that the average oxidation state of Ni or Co in the $NiCo_2O_4$ structure, is equal to $2.67^+$. As introduced in section 2.3.5, the slope of ca. 120 mV $dec^{-1}$ is related to oxygen evolution taking place at trivalent cation sites *via* a bridge formed species, whereas a slope of ca. 40 mV $dec^{-1}$ is attributed to divalent cations being the active sites, *via* the reaction sequence known as the electrochemical path. In addition, Efremov and Tarasevich[51] reported values of 50 mV $dec^{-1}$ and 120 mV $dec^{-1}$, respectively, in 0.1 M KOH solution at 60°C, and attributed it to the change in the RDS in the overall reaction due to the change of the $M^{2+}$ active sites to $M^{3+}$ active sites. In this perspective, Rasiyah and Tseung[28] proposed the formation of an intermediate T-O--M, where T is a trivalent site and M is either a trivalent or a divalent site.

According with these authors the most probable mechanism for the OER in $NiCo_2O_4$ electrodes would be given by:

$$M + OH^- \rightarrow MOH + e^- \quad (5.5.3.1)$$

$$M^z - OH \rightarrow M^{z+1} - OH + e^- \quad (5.5.3.2)$$

$$2M^{z+1} - OH + 2OH^- \rightarrow 2M + 2H_2O + e^- \quad (5.5.3.3)$$

with step (2), the formation of a higher oxide, being rate determining.

We suggest that the observation of a Tafel slope of ca. 80 mV $dec^{-1}$ indicates that the OER occurs indistinctively in divalent and trivalent sites on the $NiCo_2O_4$ structure, whereas if $b$ = ca. 40 mV $dec^{-1}$, the OER takes place only in divalent sites. It is important to mention that the above mechanism is strictly applicable to flat surfaces. Therefore, in the case of porous electrodes or very creaked surfaces, like those used in this chapter, the complexity of the kinetical analysis increases since different rate-determining steps may be operating in different parts of the electrode. The latter occurs as a result of different diffusion and ohmic control contributions along the pore or cracked surface.

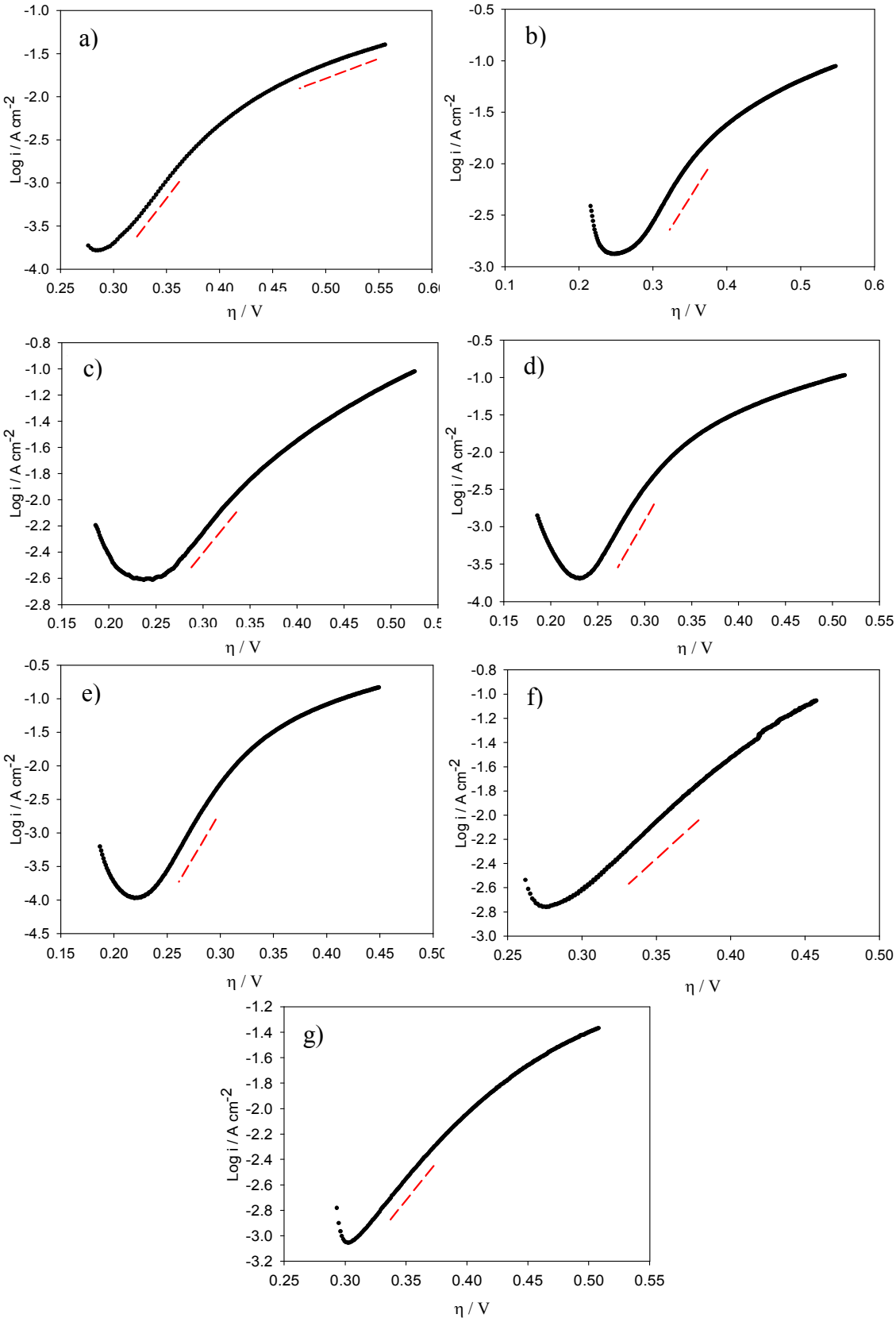



Figure 5.5.12 IR corrected steady-state polarisation curves recorded in the direction of increasing potential on a series of nickel cobalt mixed oxide electrodes: a) 0, b) 20, c) 40, d) 50, e) 60, f) 80, and g) 100 % M Co content. Sweep rate of 1 mV $s^{-1}$ in 1.0 M NaOH at 25°C.

This situation can be approached successfully using electrochemical impedance spectroscopy and establishing a valid model for the porous electrode. Besides the value of the Tafel slope, another common parameter to quantify the OER efficiency of a catalyst is the overpotential required to achieve a given current density, normally of 10 mA $cm^{-2}$, $\eta_{10}$, which is the smaller the better. The overpotential measured from the steady-state polarisation measurements in fig. 5.5.12 is summarized in fig. 5.5.13. The $\eta_{10}$ of both the 0 % and the 100 % M Co content electrodes is the largest and decreases by varying the % M Co content in the sample, as seen in the cases of the 20 % and the 80 % samples. The $\eta_{10}$ reaches the lowest level at the 60 % sample, in which both NiO and $NiCo_2O_4$ phases are present in the sample, being the latter the major phase with a ca. 90 wt.% of $NiCo_2O_4$. Its value, however, bounces back for samples of 50 % and 40 %, in which the amount of $NiCo_2O_4$ decreases and that of NiO increases. In summary, the $\eta$ values of the samples are in the decreasing order of $NiCo_2O_4$ phase content: $60\% > 50\% > 40\% > 20\%{\sim}80\% \gg 0\% \sim 100\%$.

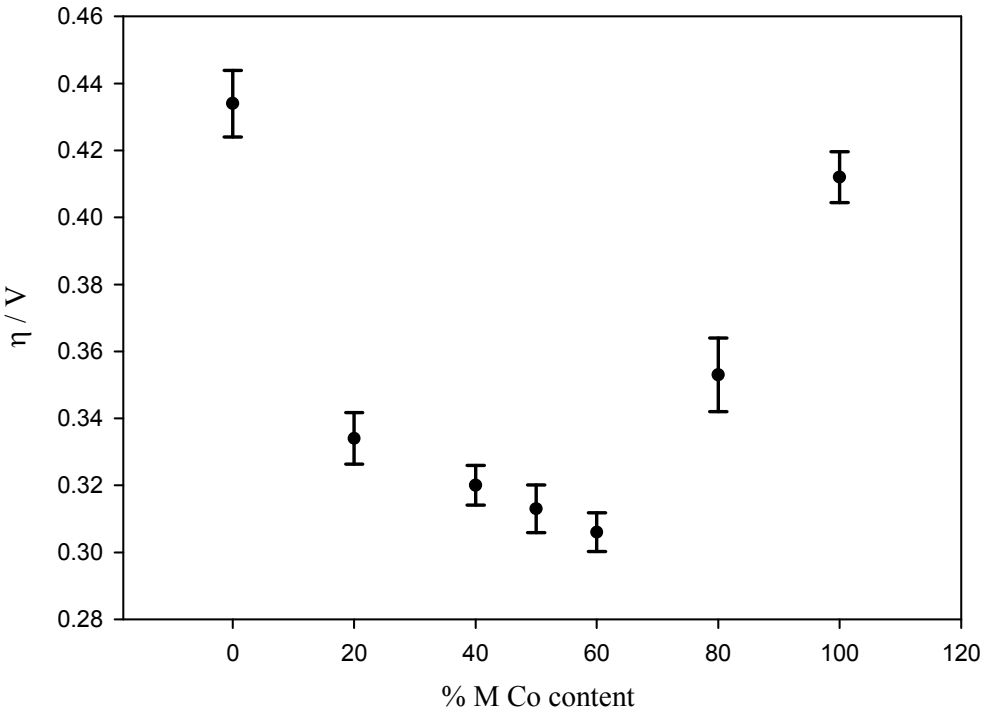



Figure 5.5.13 The oxygen evolution overpotential measured at 10 mA $cm^{-2}$ for a series of nickel cobalt mixed oxide electrodes in contact with 1.0 M NaOH at 25°C as a function of % M Co in the oxide film. These values were obtained from the steady-state polarisation curves presented in fig. 5.5.12. Error bars represent standard deviations of three different samples.

Although overpotential is a convenient performance index for the OER catalyst, it is usually accompanied by the value of the OER onset potential. The onset potential indicates the minimum applied potential at which the thermodynamic and kinetic barriers for OER become downhill. Fig. 5.5.14 summarizes the onset potential as a function of % M Co content for various nickel cobalt mixed oxide electrodes.

Correlation between the overpotential at 10 mA $cm^{-2}$, the oxygen evolution onset and current density at an overpotential of 0.32 V is evidently established for $NiCo_2O_4$ electrodes by combining fig. 5.5.13 and 5.5.14.

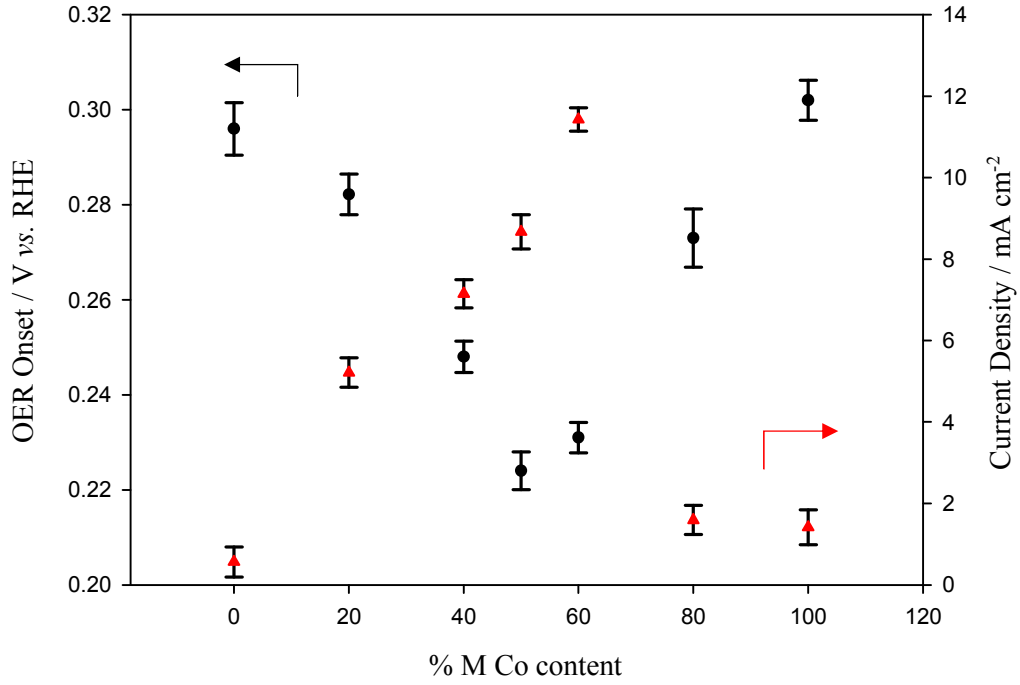



Figure 5.5.14 Left hand side: The oxygen evolution reaction onset potential for a series of nickel cobalt mixed oxide electrodes in contact with 1.0 M NaOH at 25°C as a function of mole % M Co in the oxide film (●). Right hand side: Current density at an overpotential of 0.32V phase as a function of % M Co content (▲). These values were obtained from the steady-state polarisation curves presented in fig. 5.5.12.

Typical steady-state Tafel plots were also recorded as a function of base concentration over an extended range of pH, from 0.1 M to 5.0 M NaOH. These types of plots are also known as reaction order plots. A series of Tafel plots and reaction order studies for a series of electrodes with different % M Co content are illustrated in the below figs. 5.5.15 – 5.5.17. The current density used for the reaction order analysis was obtained at an overpotential of

0.32 V *vs.* RHE for all the samples. Similar to the kinetic study in Mn oxide electrodes, the presented reaction order study was measured in terms of constant applied potential which is relative to a pH-independent reference electrode, *e.g.* mercury-mercury oxide, Hg/HgO. Consequently, a similar analysis than that performed for Mn oxide electrodes will be carried out for Ni/Co mixed electrodes. It is relevant to mention that equal Tafel slope values were found in each electrode measurement. Such behaviour may indicate that the rate determining step remains constant regardless the $OH^-$ ion concertation. In addition, higher current densities were observed at different $OH^-$ concentration which may suggest that the oxide formation at high potentials is pH-dependent.

The latter has also been observed in both redox peak potential *vs.* pH studies (see section 5.5.2) and in other studies of these mixed oxides.[52] The results for the reaction order values from figs. 5.5.15 – 5.5.17 are presented in Table 5.5.2. Excellent linearity was found for all logarithm reaction order plots for a range of overpotentials in the Tafel region.

| **% M Co content** | **Reaction order Ni/Co electrodes** |
|---|---|
| 0 | 0.82 ± 0.03 |
| 20 | 0.83 ± 0.02 |
| 40 | 0.99 ± 0.05 |
| 50 | 1.14 ± 0.02 |
| 60 | 1.18 ± 0.03 |
| 80 | 1.05 ± 0.02 |
| 100 | 0.93 ± 0.01 |

Table 5.5.2 Mechanistically significant reaction order values obtained from figs. 5.5.15 – 5.5.17 at an overpotential of 0.32V for a series of nickel cobalt mixed oxide electrodes with different % M Co content.

Results observed in Table 5.5.2 indicate that the reaction order is somewhat dependent of the phase composition. In this view, electrodes with large $NiCo_2O_4$ phase wt.%, 40 %, 50 % and 60 % exhibit reaction order values of ca. 1.15 whereas electrodes with large wt.% of NiO or $Co_3O_4$ phase exhibit reaction order of ca. 0.8 or ca. 0.95, respectively. To conclude this section, we would like to mention that the behaviour of the polarisation curves in fig. 5.5.12 along with the Tafel slope values presented in fig. 5.5.11 display good agreement with the mechanistic scheme proposed by Rasiyah and Tseung.[28]

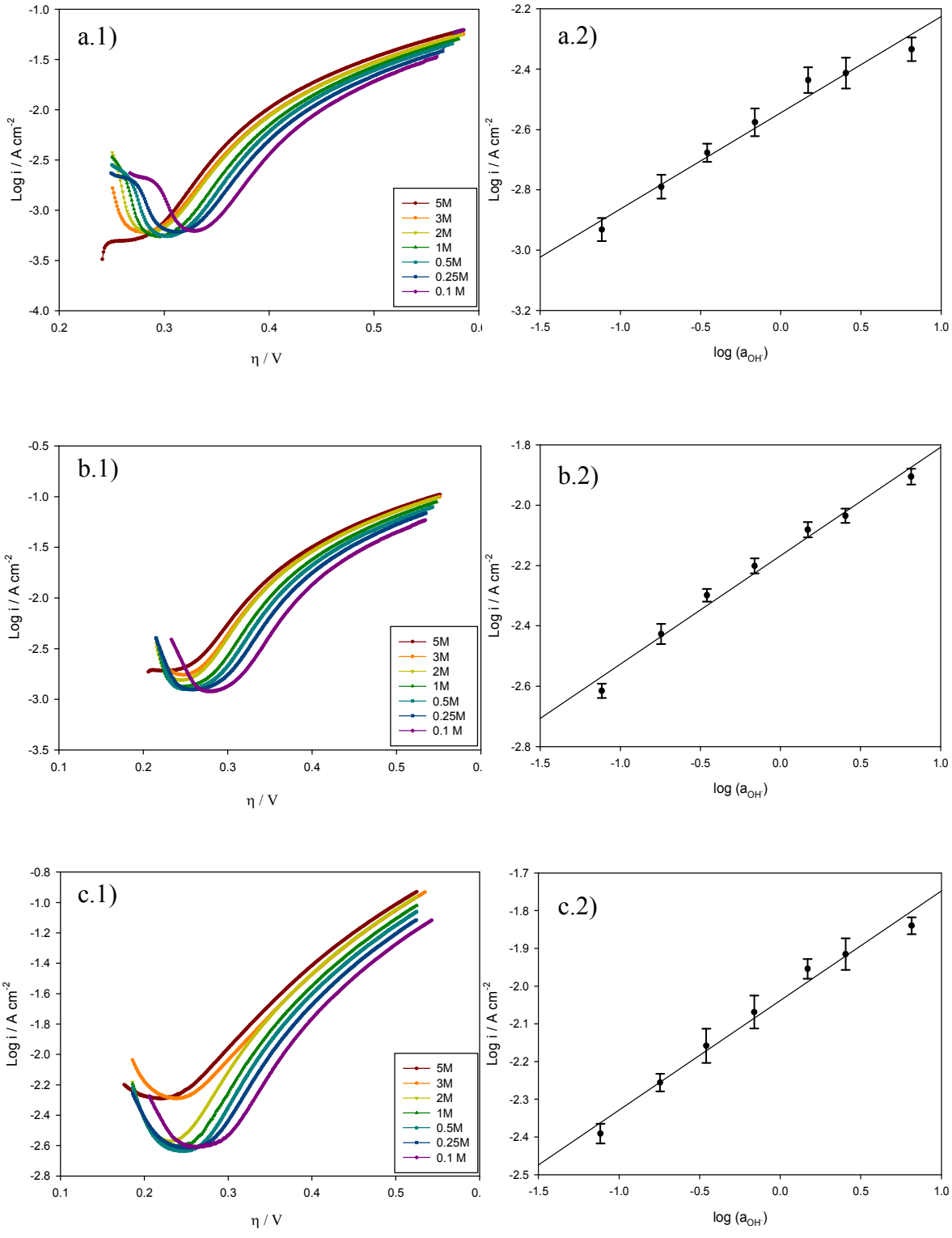



Figure 5.5.15 IR corrected steady-state polarisation curves recorded in the direction of increasing potential on an nickel cobalt mixed oxide with a.1) 0 % M Co, b.1) 20 % M Co and c.1) 40 % M Co in NaOH solutions of various concentration at 25°C. Fig. to the right hand side represent the reaction order plots constructed from the polarisation data (left hand side) at an overpotential of 0.32 V. The reaction order values are shown in Table 5.5.2. Error bars represent standard deviations of three different samples.

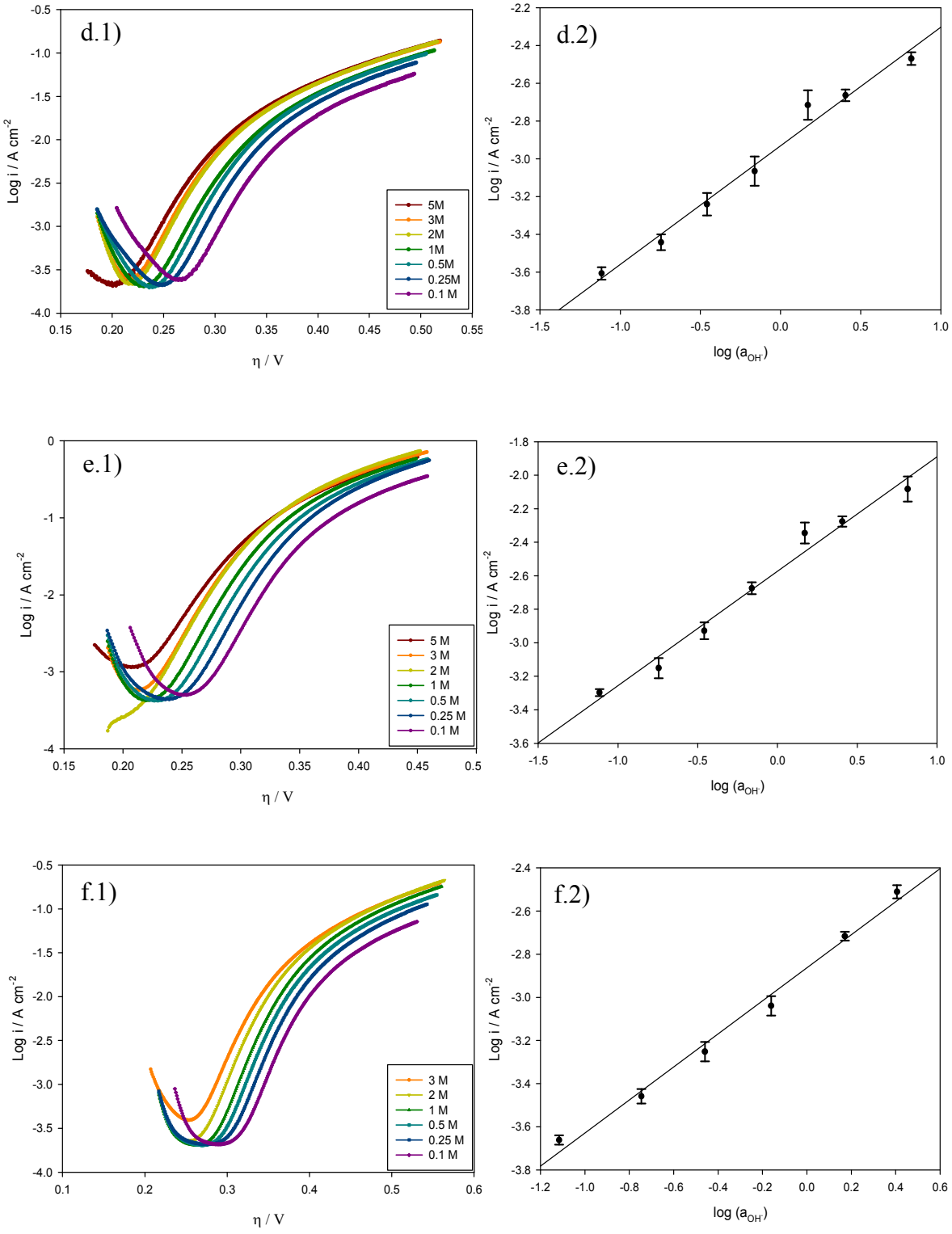



Figure 5.5.16 IR corrected steady-state polarisation curves recorded in the direction of increasing potential on a nickel cobalt mixed oxide with d.1) 50 % M Co, e.1) 60 % M Co and f.1) 80 % M Co in NaOH solutions of various concentration at 25°C. Fig. to the right-hand side represent the reaction order plots constructed from the polarisation data (left hand side) at an overpotential of 0.32 V. The reaction order values are shown in Table 5.5.2. Error bars represent standard deviations of three different samples.

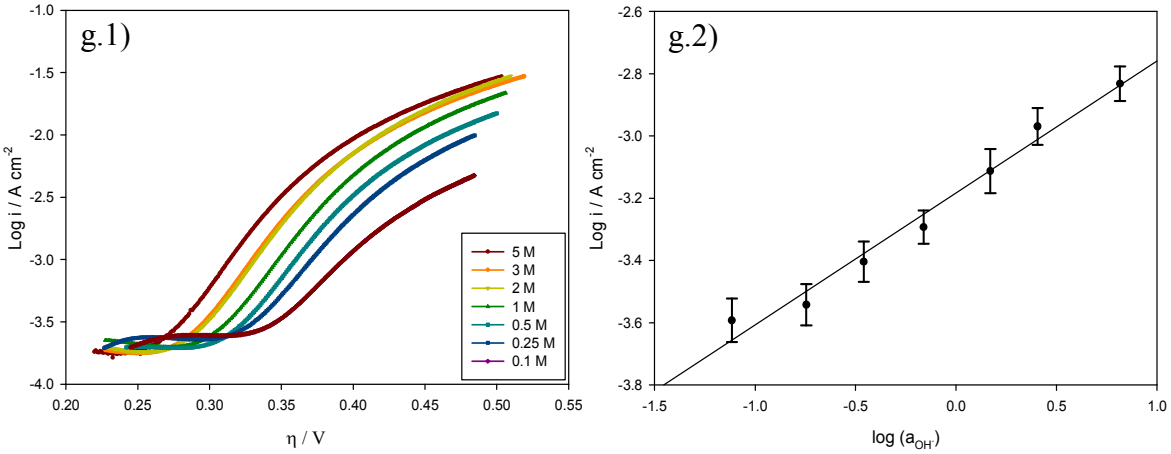



Figure 5.5.17 IR corrected steady-state polarisation curves recorded in the direction of increasing potential on a nickel cobalt mixed oxide with g.1) 100 % M Co in NaOH solutions of various concentration at 25°C. The figure to the right-hand side represents the reaction order plot constructed from the polarisation data (left-hand side) at an overpotential of 0.32 V. The reaction order value is shown in Table 5.5.2. Error bars represent standard deviations of three different samples.

## 5.6 Open Circuit Decay Measurements

As performed for Mn oxide electrodes in section 4.6, the analysis of open circuit potential (OCP) decay curves was carried out in this thesis, to help determine the kinetics and mechanisms of the nickel cobalt mixed oxide electrode with different % M Co content in alkaline solution. Typical open circuit potential/time decay curves recorded for a series of nickel cobalt mixed oxide electrode with different % M Co content in 1.0 M NaOH at 25°C are presented in fig. 5.6.1. The study of the OCP decay will be carried out by dividing in three-time regions the potential decay as it was done for Mn electrodes. The three-time regions are: (i) log 0 to 1, (ii) log 1 to 3, and (iii) log 3 to 5, which corresponds to the (i) short, (ii) intermediate, and (iii) long-time regions, respectively.

In addition, the Tafel slope obtained from steady-state polarisation measurements and that obtained by OCP decay *b* parameter are presented in Table 5.6.1 as a function of % M Co content.

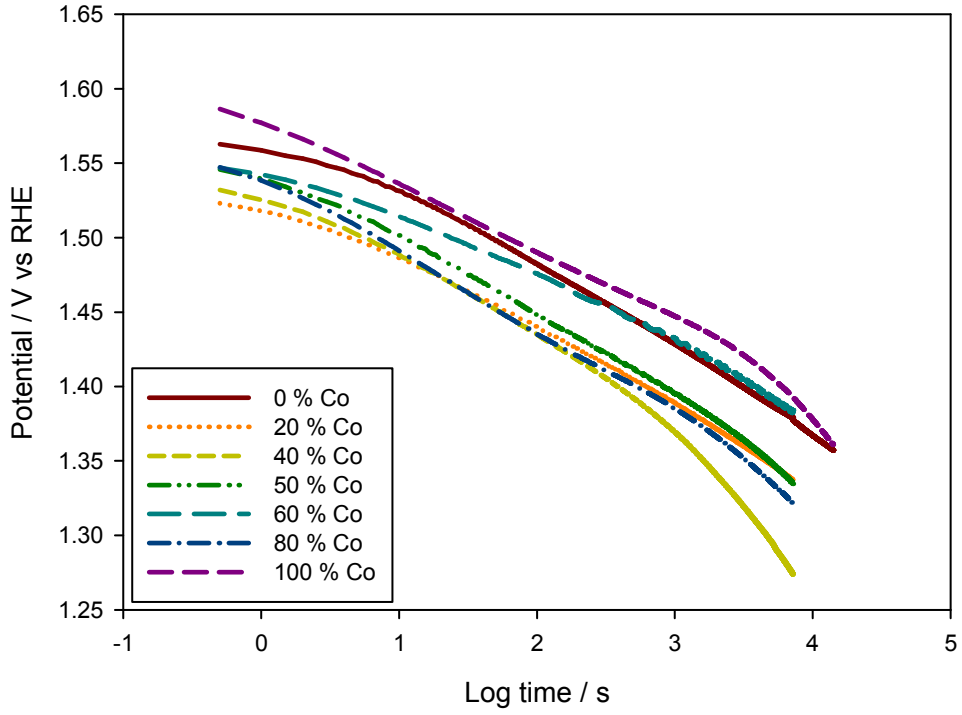



Figure 5.6.1 Typical open circuit decay curves for nickel cobalt mixed oxide electrodes with different % M Co content in 1.0 M NaOH at 25°C.

| % M Co content | Short time (OCP) / mV dec$^{-1}$ | Intermediate time (OCP) / mV dec$^{-1}$ | Long-time (OCP) / mV dec$^{-1}$ | Tafel slope (SSP) / mV dec$^{-1}$ |
|---|---|---|---|---|
| 0 | 45 ± 6 | 46 ± 4 | 66 ± 2 | 60 ± 4 |
| 20 | 37 ± 3 | 51 ± 4 | 86 ± 3 | 91 ± 5 |
| 40 | 34 ± 4 | 56 ± 3 | 94 ± 5 | 105 ± 5 |
| 50 | 32 ± 4 | 49 ± 6 | 64 ± 8 | 50 ± 7 |
| 60 | 32 ± 5 | 41 ± 5 | 65 ± 6 | 39 ± 6 |
| 80 | 45 ± 6 | 63 ± 4 | 110 ± 7 | 90 ± 7 |
| 100 | 40 ± 5 | 50 ± 6 | 95 ± 4 | 85 ± 4 |

Table 5.6.1 Comparison table showing the measured OCP decay slope values and the Tafel slope values from fig.5.6.1 and fig. 5.5.11, respectively.

For all the electrodes, the *b* factor derived from OCP decay curves is slightly larger than that derived from the analysis of steady-state Tafel plots. According to theoretical considerations,

see section 4.6, the slope of the open circuit potential decay curve will be identical to the Tafel slope only if the electrode capacitance (i.e. the surface capacitance) remains constant during the decay, i.e. under conditions where the coverage by intermediates in the rate determining step is independent of the potential. These results were also observed in the OCP decay curves for Mn oxide electrodes, see section 4.6. Therefore, following the same justification as that mentioned for OCP decay curves in Mn oxide electrodes, we suggest that the slight dissimilarity between the OPC decay curve slopes and the Tafel slopes observed in fig. 5.6.1 and 5.5.11 could possibly be due to a slight dependence of surfaquo group coverage on potential.[21, 53]

## 5.7 Double Layer Capacitance Study

The double layer capacitance contribution will be approached in this work by using both the potential step method and electrochemical impedance spectroscopy (EIS). In this section, however, only the results obtained from the potential step method will be presented, while those obtained from the EIS will be presented later in chapter 6. Same procedure than that employed in section 4.7.1 for Mn oxide electrodes, is used in this section for the determination of the double layer capacitance. Typical ln *i vs. t* plots are presented in fig. 5.7.1 and 5.7.1bis as a function of % M Co content. In addition, the values for the uncompensated resistance and double layer capacitance are presented in Table 5.7.1.

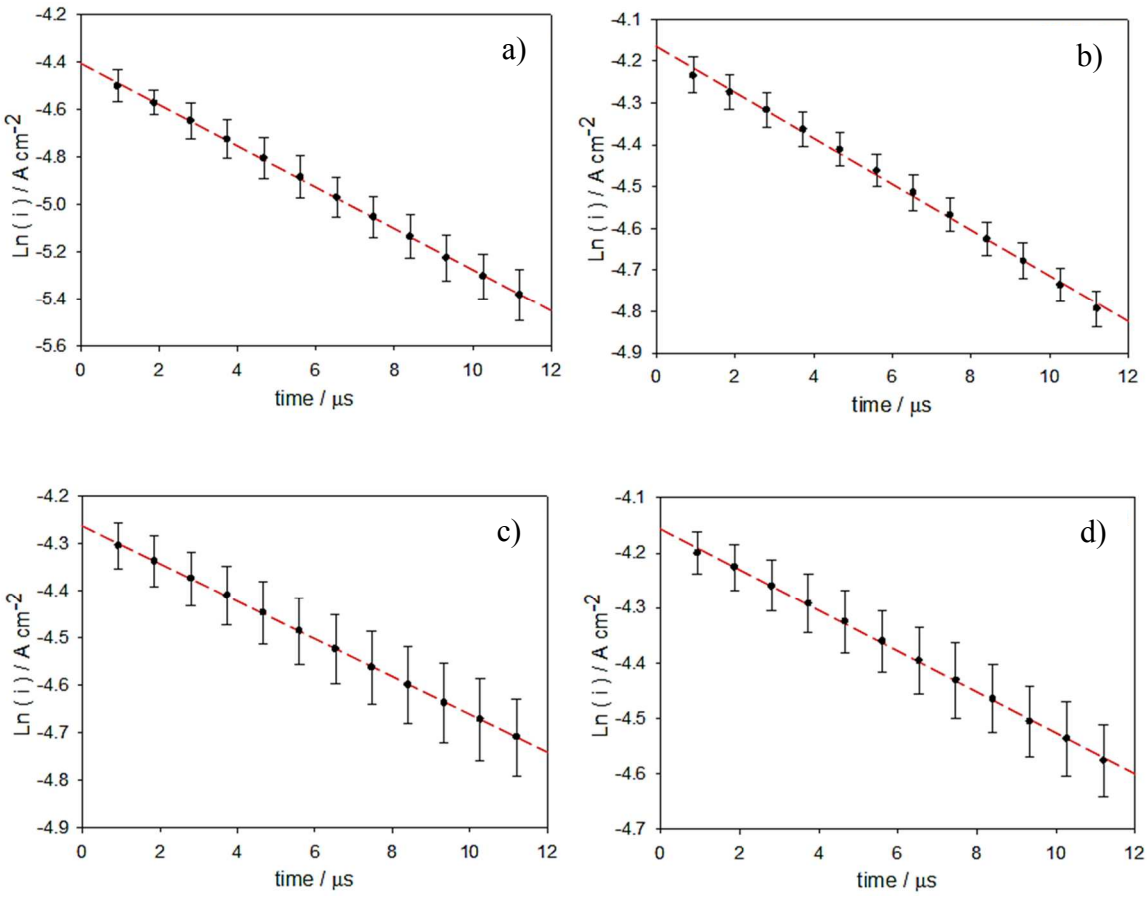



Figure 5.7.1 Logarithm of current decay curve following a 50 mV pulse applied to nickel cobalt mixed oxide electrodes: a) 0, b) 20, c) 40, and d) 50 % M Co content. The experiment was performed in 1.0 M NaOH at 25°C. Error bars represent standard deviations of three different samples.

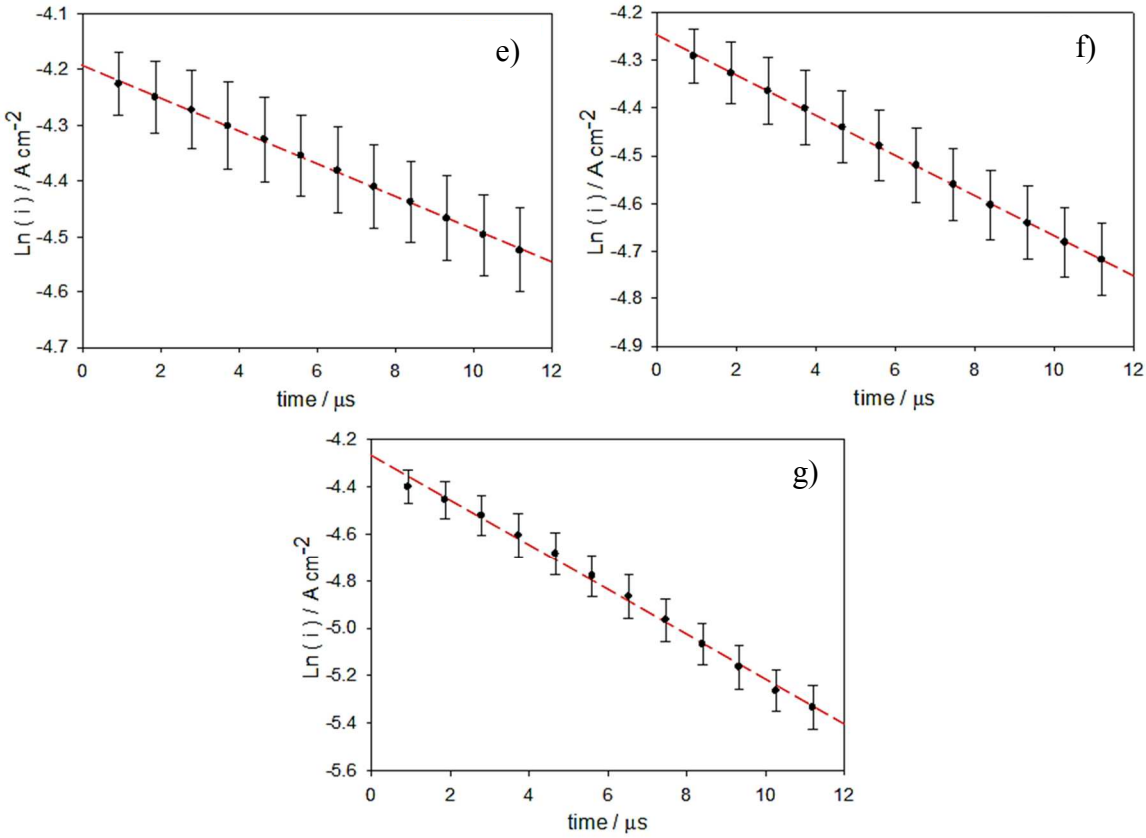



Figure 5.7.1bis Logarithm of current decay curve following a 50 mV pulse applied to nickel cobalt mixed oxide electrodes: e) 60, f) 80, and g) 100 % M Co content. The experiment was performed in 1.0 M NaOH at 25°C. Error bars represent standard deviations of three different samples.

| % M Co content | Regression eqn. | Double layer capacitance / mF cm$^{-2}$ | Uncompensated resistance / Ω |
|---|---|---|---|
| 0 | y = -86121x - 4.41 | 3.9 ± 1.1 | 3.7 ± 0.5 |
| 20 | y = -53893x - 4.17 | 5.9 ± 1.0 | 3.2 ± 0.2 |
| 40 | y = -39646x - 4.27 | 7.1 ± 1.5 | 3.4 ± 0.5 |
| 50 | y = -36478x - 4.16 | 8.5 ± 1.2 | 3.2 ± 0.3 |
| 60 | y = -28866x - 4.28 | 11.4 ± 1.9 | 3.3 ± 0.5 |
| 80 | y = -41478x - 4.25 | 6.9 ± 1.6 | 3.5 ± 0.2 |
| 100 | y = -91599x - 4.29 | 3.0 ± 0.9 | 3.6 ± 0.3 |

Table 5.7.1 Logarithm of current decay curve following a 50 mV pulse applied to nickel cobalt mixed oxide electrodes with different % M Co content. The experiment was performed in 1.0 M NaOH at 25°C

It can be observed from Table 5.7.1 that the double layer capacitance varies with % M Co content in a defined fashion. The double layer capacitance increases from 3.9 mF $cm^{-2}$ to 11.4 mF $cm^{-2}$ for an increase of % M Co content of 60 %. For higher concentrations than 60 % M Co content the double layer capacitance decreases from 7 mF $cm^{-2}$ to 3 mF $cm^{-2}$ which corresponds to 80 % and 100 % M Co content, respectively. Interestingly, the same behaviour for the double layer capacitance was also observed for the of $NiCo_2O_4$ phase wt.% as a function of % M Co content, which is presented in fig. 5.7.2. Note that 0 % and 100 % M Co content samples were omitted since these do not produce $NiCo_2O_4$ phase.

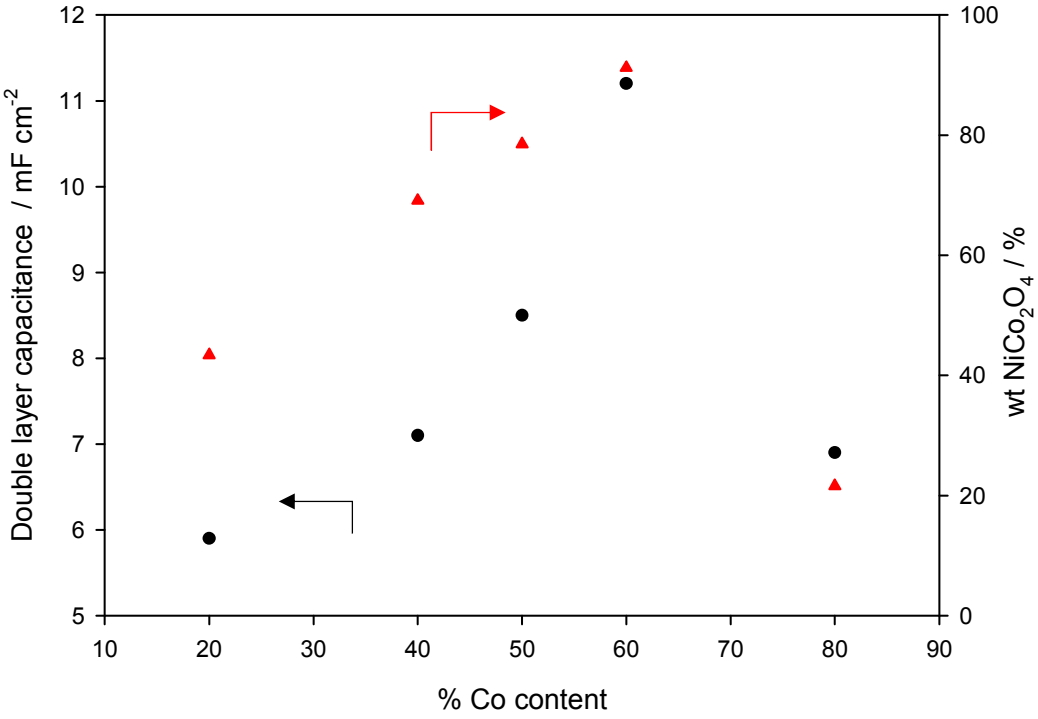



Figure 5.7.2 Left hand side: The double layer capacitance calculated from the current decay curves presented in fig.5.6.1 as a function of % M Co content ( ● ). Right hand side: wt.% of $NiCo_2O_4$ phase as a function of % M Co Content ( ▲ ).

The electrochemical performance, in terms of double layer capacitance, seems to follow the same trend as the wt.% $NiCo_2O_4$ phase on the electrode. It was observed relatively large double layer values if compared with those exhibited for NiO or $Co_3O_4$. Many authors have demonstrated that $NiCo_2O_4$ species exhibit higher capacitance behaviour than NiO and $Co_3O_4$ species.[54] Recall that: (i) the electrochemical double layer capacitance is believed to be proportional to the electrochemical active surface, and (ii) the $NiCo_2O_4$ phase possesses

richer electroactive sites and at least two magnitudes higher electrical conductivity than that of NiO and $Co_3O_4$. The high capacitance observed in $NiCo_2O_4$ electrodes may arise due to the fact that the incorporation of $Ni^{2+}$ into the octahedral sites of the $Co_3O_4$ spinel structure increases the electrical conductivity and creates new active sites where the $OH^-$ can be adsorbed resulting in an increase on the double layer capacitance.[55]

## 5.8 References Chapter 5


[1] M. R. Gennero de Chialvo, A. C. Chialvo, *Electrochimica Acta* **1988**, *33*, 825-830.

[2] C. Bocca, A. Barbucci, G. Cerisola, *International journal of hydrogen energy* **1998**, *23*, 247-252; Z.-H. Liang, Y.-J. Zhu, X.-L. Hu, *The Journal of Physical Chemistry B* **2004**, *108*, 3488-3491.

[3] X.-Y. Peng, X.-X. Liu, P.-J. Hua, D. Diamond, K.-T. Lau, *Journal of Solid State Electrochemistry* **2009**, *14*, 1-7.

[4] H. G. Meier, J. R. Vilche, A. J. Arvía, *Journal of Electroanalytical Chemistry and Interfacial Electrochemistry* **1982**, *138*, 367-379.

[5] W. Zhou, D. Kong, X. Jia, C. Ding, C. Cheng, G. Wen, *Journal of Materials Chemistry A* **2014**, *2*, 6310-6315; H. S. Jadhav, R. S. Kalubarme, J.-W. Roh, K.-N. Jung, K.-H. Shin, C.-N. Park, C.-J. Park, *Journal of The Electrochemical Society* **2014**, *161*, A2188-A2196.

[6] G.-R. Fu, Z.-A. Hu, L.-J. Xie, X.-Q. Jin, Y.-L. Xie, Y.-X. Wang, Z.-Y. Zhang, Y.-Y. Yang, H.-Y. Wu, *Electrodeposition of Nickel Hydroxide Films on Nickel Foil and Its Electrochemical Performances for Supercapacitor, Vol. 4*, **2009**.

[7] C.-W. Tang, C.-B. Wang, S.-H. Chien, *Thermochimica Acta* **2008**, *473*, 68-73.

[8] J. Haenen, W. Visscher, E. Barendrecht, *Journal of Electroanalytical Chemistry and Interfacial Electrochemistry* **1986**, *208*, 297-321.

[9] W. Brockner, C. Ehrhardt, M. Gjikaj, *Thermochimica Acta* **2007**, *456*, 64-68.

[10] D. Pope, D. S. Walker, R. L. Moss, *Journal of Colloid and Interface Science* **1977**, *60*, 216-217.

[11] R. Garavaglia, C. M. Mari, S. Trasatti, C. de Asmundis, *Surface Technology* **1983**, *19*, 197-215.

[12] O. Knop, K. I. G. Reid, Sutarno, Y. Nakagawa, *Canadian Journal of Chemistry* **1968**, *46*, 3463-3476; M. Cabo, E. Pellicer, E. Rossinyol, M. Estrader, A. López-Ortega, J. Nogués, O. Castell, S. Suriñach, M. D. Baró, *Journal of Materials Chemistry* **2010**, *20*, 7021-7028.

[13] R. R. Devadatha D, *J Material Sci Eng* **2013**, *S11*.

[14] L. Chen, P. Fleming, V. Morris, J. D. Holmes, M. A. Morris, *The Journal of Physical Chemistry C* **2010**, *114*, 12909-12919; A. J. Saldivar-Garcia, H. F. Lopez, *Metallurgical and Materials Transactions A* **2004**, *35*, 2517-2523.

[15] Y. E. Roginskaya, O. V. Morozova, E. N. Lubnin, Y. E. Ulitina, G. V. Lopukhova, S. Trasatti, *Langmuir* **1997**, *13*, 4621-4627; Y. M. Kolotyrkin, I. D. Belova, Y. E. Roginskaya, V. B. Kozhevnikov, D. S. Zakhar'in, Y. N. Venevtsev, *Materials Chemistry and Physics* **1984**, *11*, 29-48.

[16] B. Chi, J. Li, Y. Han, Y. Chen, *International Journal of Hydrogen Energy* **2004**, *29*, 605-610.

[17] U. Kwon, B.-G. Kim, D. C. Nguyen, J.-H. Park, N. Y. Ha, S.-J. Kim, S. H. Ko, S. Lee, D. Lee, H. J. Park, *Scientific Reports* **2016**, *6*, 30759.

[18] M. Sribalaji, P. Arunkumar, K. S. Babu, A. K. Keshri, *Applied Surface Science* **2015**, *355*, 112-120; M. W. Roberts, R. S. C. Smart, *Journal of the Chemical Society, Faraday Transactions 1: Physical Chemistry in Condensed Phases* **1984**, *80*, 2957-2968.

[19] Q. Lu, Z. J. Mellinger, W. Wang, W. Li, Y. Chen, J. G. Chen, J. Q. Xiao, *ChemSusChem* **2010**, *3*, 1367-1370; Y. Fu, J. Song, Y. Zhu, C. Cao, *Journal of Power Sources* **2014**, *262*, 344-348.

[20] M. Yin, X.-P. Zhang, H.-M. Liu, *Effect of Annealing Temperature on the Crystallization and Spectroscopic Response of a Small-Molecule Semiconductor Doped in Polymer Film, Vol. 32*, **2012**; J. Karamdel, F. Razaghian, A. Hadi, C. F. Dee, B. Majlis, *Effects of annealing temperature on morphology and Crystallinity of nitrogen doped zinc oxide (ZnO:N) nano films*, **2012**; V. Ghafouri, A. Ebrahimzad, M. Shariati, *Scientia Iranica* **2013**, *20*, 1039-1048.
[21] M. E. G. Lyons, (University Collage Cork), **1983**.
[22] L. D. Burke, O. J. Murphy, *Journal of Electroanalytical Chemistry and Interfacial Electrochemistry* **1979**, *96*, 19-27.
[23] H. Rietveld, *Australian Journal of Physics* **1988**, *41*, 113-116; D. Balzar, H. Ledbetter, *Journal of Applied Crystallography* **1993**, *26*, 97-103; B. E. Warren, B. L. Averbach, *Journal of Applied Physics* **1950**, *21*, 595-599.
[24] G. Lodi, C. de Asmundis, S. Ardizzone, E. Sivieri, S. Trasatti, *Surface Technology* **1981**, *14*, 335-343; M. P. Browne, H. Nolan, G. S. Duesberg, P. E. Colavita, M. E. G. Lyons, *ACS Catalysis* **2016**, *6*, 2408-2415.
[25] L. Trotochaud, J. K. Ranney, K. N. Williams, S. W. Boettcher, *Journal of the American Chemical Society* **2012**, *134*, 17253-17261.
[26] L. An, Q. Ren, W. Li, K. Xu, Y. Cao, T. Ji, R. Zou, Z. Chen, J. Hu, *Journal of Materials Chemistry A* **2015**, *3*, 11503-11510.
[27] X. Liu, S. Shi, Q. Xiong, L. Li, Y. Zhang, H. Tang, C. Gu, X. Wang, J. Tu, *ACS Applied Materials & Interfaces* **2013**, *5*, 8790-8795.
[28] P. Rasiyah, A. C. C. Tseung, *Journal of The Electrochemical Society* **1983**, *130*, 2384-2386.
[29] M. Cabo, E. Pellicer, E. Rossinyol, O. Castell, S. Suriñach, M. D. Baró, *Crystal Growth & Design* **2009**, *9*, 4814-4821.
[30] C. B. S. a. V. D. W. B. Pearson, *Structure Reports Metals and Inorganic Sections, Vol. 34A*, International Union of Crystallography, **1968**.
[31] W. M. Haynes, *CRC Handbook of Chemistry and Physics, 94th Edition*, CRC Press, **2016**.
[32] J. F. Moulder, J. Chastain, *Handbook of X-ray Photoelectron Spectroscopy: A Reference Book of Standard Spectra for Identification and Interpretation of XPS Data*, Physical Electronics Division, Perkin-Elmer Corporation, **1992**.
[33] P. G. Harrison, *Catalysis Today* **1993**, *17*, 483-491.
[34] M. Cotter, S. Campbell, L. L. Cao, R. G. Egdell, W. C. Mackrodt, *Surface Science* **1989**, *208*, 267-284; S. R. Leadley, J. F. Watts, C. J. Blomfield, C. Lowe, *Surface and Interface Analysis* **1998**, *26*, 444-454; G. C. Allen, S. J. Harris, J. A. Jutson, J. M. Dyke, *Applied Surface Science* **1989**, *37*, 111-134.
[35] G. Zhang, X. W. Lou, *Advanced Materials* **2013**, *25*, 976-979; S. V. Devaguptapu, S. Hwang, S. Karakalos, S. Zhao, S. Gupta, D. Su, H. Xu, G. Wu, *ACS Applied Materials & Interfaces* **2017**, *9*, 44567-44578.
[36] H. Li, G. Lu, D. Qiao, Y. Wang, Y. Guo, Y. Guo, *Catalysis Letters* **2011**, *141*, 452-458; J. F. Marco, J. R. Gancedo, M. Gracia, J. L. Gautier, E. Ríos, F. J. Berry, *Journal of Solid State Chemistry* **2000**, *153*, 74-81.
[37] W. J. King, A. C. C. Tseung, *Electrochimica Acta* **1974**, *19*, 493-498.
[38] C. S. Ferreira, R. R. Passos, L. A. Pocrifka, *Journal of Power Sources* **2014**, *271*, 104-107; M. Browne, R. J. Cullen, R. L. Doyle, P. E. Colavita, M. E. G. Lyons, *ECS Transactions* **2013**, *53*, 59-77.
[39] I. J. Godwin, R. L. Doyle, M. E. G. Lyons, *Journal of The Electrochemical Society* **2014**, *161*, F906-F917.

[40] M. E. G. Lyons, L. D. Burke, *Journal of the Chemical Society, Faraday Transactions 1: Physical Chemistry in Condensed Phases* **1987**, *83*, 299-321.
[41] C.-w. Lan, C. Hsu, K. Nakajima, in *Handbook of Crystal Growth (Second Edition)* (Ed.: P. Rudolph), Elsevier, Boston, **2015**, pp. 373-411.
[42] R. M. Dell, F. S. Stone, *Transactions of the Faraday Society* **1954**, *50*, 501-510.
[43] U. T. Nakate, S. N. Kale, *Materials Today: Proceedings* **2016**, *3*, 1992-1998; D. Pletcher, X. Li, S. W. T. Price, A. E. Russell, T. Sönmez, S. J. Thompson, *Electrochimica Acta* **2016**, *188*, 286-293.
[44] K. Juodkazis, J. Juodkazytė, R. Vilkauskaitė, V. Jasulaitienė, *Journal of Solid State Electrochemistry* **2008**, *12*, 1469-1479; N. Xu, G. Cao, Z. Chen, Q. Kang, H. Dai, P. Wang, *Journal of Materials Chemistry A* **2017**, *5*, 12379-12384; A. Rovetta, M. Browne, A. Harvey, I. Godwin, J. Coleman, M. Lyons, *Cobalt Hydroxide Nanoflakes and their Application as Supercapacitors and Oxygen Evolution Catalysts, Vol. 28*, **2017**; I. Godwin, M. Lyons, *Enhanced Oxygen Evolution At 'Aged' Hydrous Nickel Oxide Electrodes in Alkaline Solution: Kinetics and Mechanism*, **2013**.
[45] M. E. G. Lyons, S. Floquet, *Physical Chemistry Chemical Physics* **2011**, *13*, 5314-5335.
[46] W. Schmickler, *Berichte der Bunsengesellschaft für physikalische Chemie* **1994**, *98*, 1207-1207.
[47] X. Lv, Y. Zhu, H. Jiang, X. Yang, Y. Liu, Y. Su, J. Huang, Y. Yao, C. Li, *Dalton Transactions* **2015**, *44*, 4148-4154.
[48] D. U. Lee, B. J. Kim, Z. Chen, *Journal of Materials Chemistry A* **2013**, *1*, 4754-4762.
[49] B. Marsan, N. Fradette, G. Beaudoin, *Journal of The Electrochemical Society* **1992**, *139*, 1889-1896.
[50] D. Liu, C. Zhang, Y. Yu, Y. Shi, Y. Yu, Z. Niu, B. Zhang, *Nano Research* **2018**, *11*, 603-613.
[51] B. Efremov, M. Tarasevich, *Elektrokhimiya* **1981**, *17*, 1672-1679.
[52] E. Markina, M. Tarasevich, B. EFREMOV, *Soviet Electrochemistry* **1988**, *24*, 88-93; A. C. D. Angelo, E. R. Gonzalez, L. A. Avaca, *International Journal of Hydrogen Energy* **1991**, *16*, 1-7.
[53] B. E. Conway, P. L. Bourgault, *Canadian Journal of Chemistry* **1959**, *37*, 292-307; P. L. Bourgault, B. E. Conway, *Canadian Journal of Chemistry* **1960**, *38*, 1557-1575.
[54] C. Guan, X. Liu, W. Ren, X. Li, C. Cheng, J. Wang, *Advanced Energy Materials* **2017**, *7*, 1602391; Z. Wu, Y. Zhu, X. Ji, *Journal of Materials Chemistry A* **2014**, *2*, 14759-14772; Y. Hu, Y. V. Tolmachev, D. A. Scherson, *Journal of Electroanalytical Chemistry* **1999**, *468*, 64-69; J.-W. Lang, L.-B. Kong, W.-J. Wu, M. Liu, Y.-C. Luo, L. Kang, *Journal of Solid State Electrochemistry* **2008**, *13*, 333.
[55] M. Prabu, K. Ketpang, S. Shanmugam, *Nanoscale* **2014**, *6*, 3173-3181; L. Qian, L. Gu, L. Yang, H. Yuan, D. Xiao, *Nanoscale* **2013**, *5*, 7388-7396; cJ. Wang, T. Qiu, X. Chen, Y. Lu, W. Yang, *Journal of Power Sources* **2014**, *268*, 341-348.

# CHAPTER 6

# IMPEDANCE STUDIES ON HYDROUS MANGANESE OXYHYDROXIDE AND THERMALLY PREPARED NICKEL COBALT OXIDE ELECTRODES

## 6.1 Introduction

This chapter deals with the results of electrochemical impedance spectroscopy (EIS) studies on both polycrystalline Mn oxide electrodes and polycrystalline Ni-Co mixed oxide electrodes in 1.0 M NaOH solutions in the potential range associated with significant oxygen evolution current densities. The background theory behind this technique has already been presented in section 3.7. This chapter is divided into two main sections: (i) impedance study on hydrous Mn oxyhydroxide electrodes, and (ii) Ni-Co mixed oxide electrodes. In each section of this chapter, both the experimental and the fitting data are presented in the first place, followed by the analysis of the electrical parameters obtained by CNLS fitting.

## 6.2 Appropriate Equivalent Circuit Model Discussion

Electrochemical impedance spectroscopy (EIS) is a powerful *in situ* analytical technique to simultaneously extract kinetic and structural data about OER catalysts. In the present section, an examination of the OER kinetics along with some physical proprieties of hydrous Mn oxide electrodes will be presented first followed by a similar investigation on Ni-Co mixed oxide electrodes.

EIS was employed to obtain a better understanding of the different OER kinetic properties being exhibited by both the hydrous Mn oxide films and the Ni-Co mixed oxide films. In this perspective, the electrochemical impedance response of the aforementioned oxide electrodes was recorded, and examined, over a range of potentials associated with active oxygen evolution typically in the range 0.56 - 0.8 V (*vs.* Hg/HgO). The EIS response obtained for potentials greater than 0.8 V was discarded due to significant metal dissolution, which occurred simultaneously with active oxygen evolution. Therefore, such data was not considered in further analyses. The raw impedance data was fitted, using a CNLS fitting algorithm, to the equivalent circuit model developed by Lyons and Brandon[1] and depicted fig. 6.2.1.

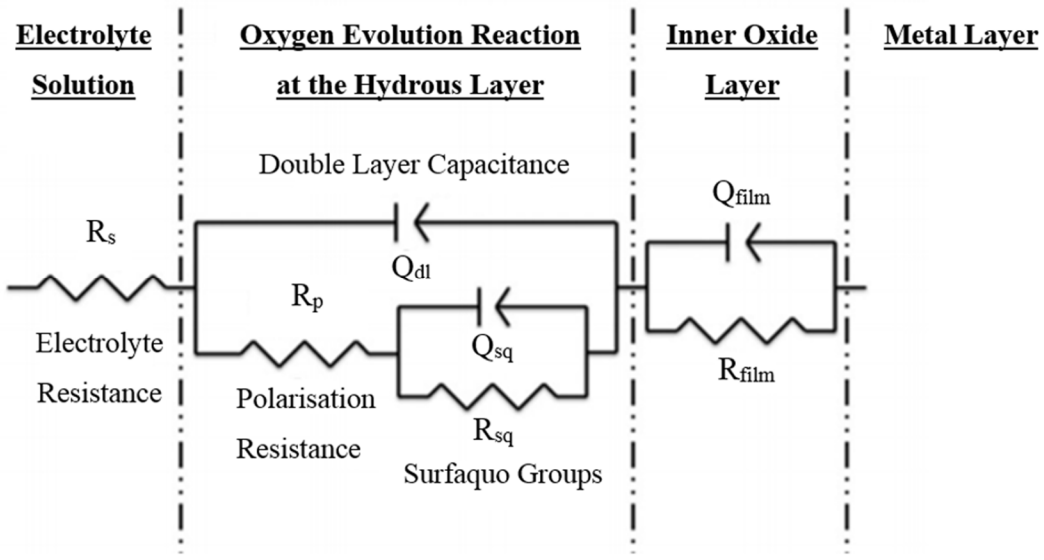



Figure 6.2.1 Equivalent circuit used in the CNLS fitting of the impedance data presented in section 6.3 and section 6.4. This equivalent circuit was proposed by Lyons and Brandon.[1]

In fig. 6.2.1 the $R_s$ refers to the uncompensated resistance, $Q_{dl}$ to the double layer capacitance, $R_p$ is the polarisation resistance, $Q_{sq}$ and $R_{sq}$ account for the capacitance contribution and resistance contribution of surfaquo groups, respectively. Finally, $Q_{film}$ and $R_{film}$ are the capacitance and the resistance of the oxide layer, respectively. This equivalent circuit has been proved to be a good general model for the OER at both passive and hydrous oxide coated electrodes of cobalt, iron, manganese and nickel in aqueous base solutions.[2] The equivalent circuit model proposed by Lyons and Brandon describes the OER catalysis by a resistive circuit element ($R_p$) in series with an RC loop ($R_s$ and $C\phi$). Typically, these circuit elements do not describe a single charge transfer process. Instead, each of them represents multiple steps within the overall catalytic reaction. The polarization resistance, $R_p$, relates to the reaction rate and handles the charge transfer resistance of the various steps within the OER up to and including the rate-determining step. The other resistance, $R_{sq}$, broadly incorporates the ease of forming surface intermediates on the catalyst, that is the surfaquo groups, and together with $R_p$, yields to the Faradaic resistance simply defined as:

$$R_{far} = R_{sq} + R_p \tag{6.2.1}$$

Charge relaxation associated with the formation of surface intermediates is described by the loop given by $R_{sq}$ and $C_\phi$. In this work, the model is extended with the inclusion of additional

elements in order to describe the catalyst double layer and the conductivity of the catalytic film. This equivalent circuit can be used to model both flat and porous surface electrodes at potentials where the oxygen evolution occurs. However, in order to achieve satisfactory fitting to the experimental data for both types of electrodes studied in this work, all the pure capacitive elements, C, in the model proposed by Lyons *et al.*[1a] were described by constant phase elements CPE, $Q^{\alpha}$. The CPE was discussed in detail in section 3.7.5. It shall be pointed out that the factionary exponent provides an additional and measurable degree of freedom in the parameter space of the relaxation function, whose value might indicate deviations from ideality. This feature was considered sufficient to achieve a more reliable fitting analysis on porous electrodes when using the model presented in fig. 6.2.1. There exist, however, some limitations in the use of this model, *e.g.* it cannot model the oxide film at Faradaic potentials, where redox processes occur. Therefore, if one aims to model impedance data recorded at potential ranges where Faradaic processes occur at porous surfaces, we suggests to take into account the models proposed by Bisquert[3] which describe the ionic and electric conductivity on porous electrodes. These models will be particularly important when we analyse the redox switching behaviour of Mn and Ni/Co oxide electrodes. Note that the latter analysis is still ongoing and will not be presented in this thesis.

A brief introduction of Bisquert's models is presented. These models, for the study of porous surfaces are based upon transmission lines. To introduce transmission lines from a general perspective, a comparison is presented between the homogeneous flat surface and the homogeneous porous surface in which two phases, liquid and solid, become mixed inside the film region. A homogeneous electrode with a macroscopically flat surface is shown schematically in fig. 6.2.2a. The equivalent circuit model to describe its cell impedance involves a series and/or parallel combination of resistive and capacitive components. This modelling assumes that the two phases, *e.g.* liquid and solid, are perfectly separated, as seen in fig. 6.2.2a. The latter implies that the flux of electrical charge is always normal to the plane of the surface and, thus, the impedance is essentially independent of the position on the electrode. Typically, this type of model is presented by dividing the system into three distinct parts: one at the bulk of the layer, another at the solid / liquid interface and, finally, a third one including the potential drop at bulk electrolyte.

A schematic representation of a homogeneous porous surface is presented in fig. 6.2.2b.

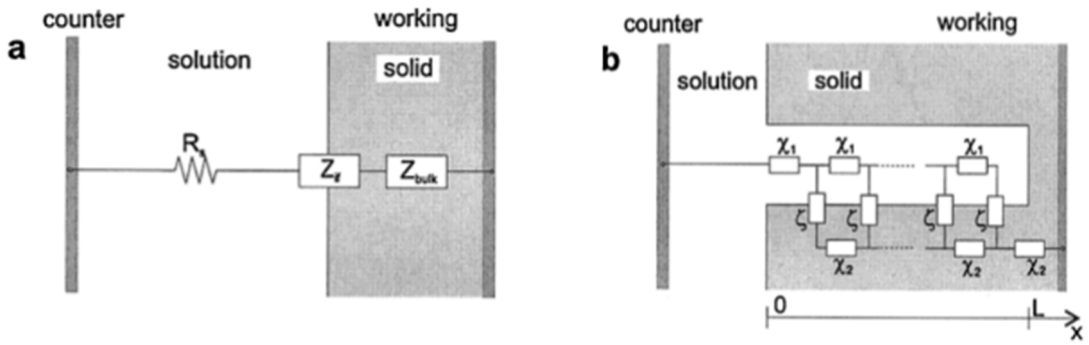



Figure 6.2.2: a) Scheme of a compact electrode with a macroscopically flat surface, and b) scheme of a porous electrode. Reproduced from Ref. [4]

In this type of systems, the two phases are closely mixed in space, *e.g.* the porosity allows the electrolyte to penetrate into the film. The typical standard equivalent circuit model for such systems involves: (i) the essential features of electrical transport along each phase, and (ii) the exchange of charge through the inner surface.[5] Note that each phase is conceived as a transmission line. This model assumes that the main contribution to the current response is electrical field driven rather than diffusive. In this situation, the electrical current is no longer normal to the surface but spread in various directions, *e.g.* electrical charge can flow parallel to the inner surface of the porous, which is in the abscissa's direction, as seen in fig. 6.2.3. Moreover, current can flow in the direction normal to the inner surface mainly due to electrochemical reactions and/or capacitive charging processes.

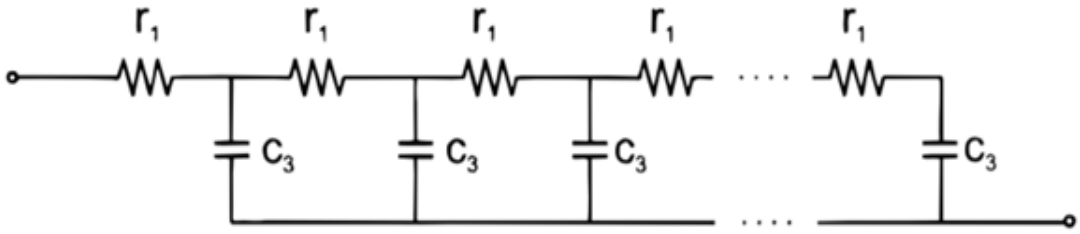



Figure 6.2.3 Transmission line simplification for the impedance of porous electrodes assuming either that the film, is much more conducting that the electrolyte or that the filed pores exhibit a distributed resistance. Reproduced from Ref.[3b]

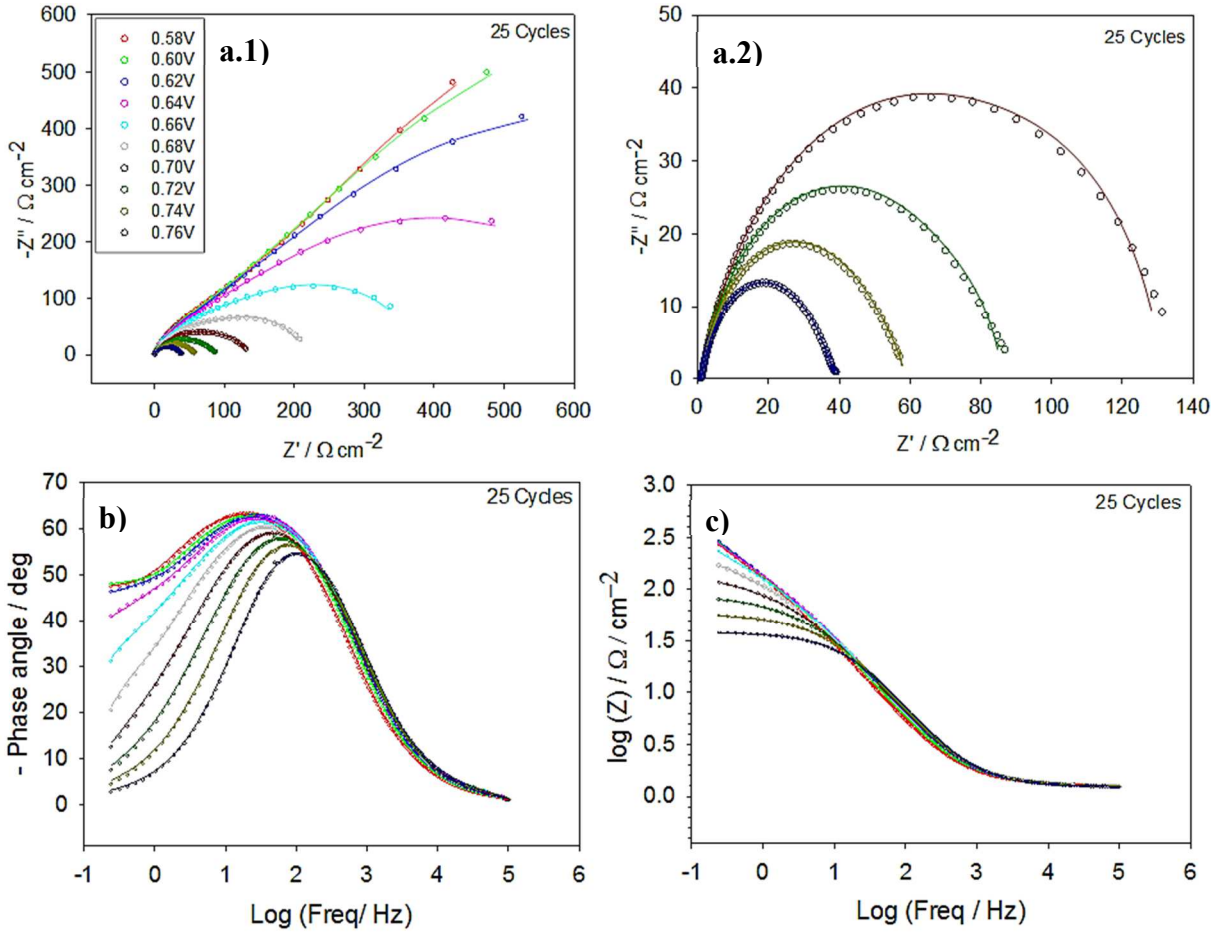
According to the latter description of electrical current distribution, the equivalent circuit branches at each point of the x-axes into an element that continues at the same phase, $\chi_1$ or $\chi_2$, and to another element $\xi$ that crosses the interface. Particularly, $\chi_1$ and $\chi_2$

represents the local ohmic drop at each point of the two phases whereas the element ξ describes the exchange of electrical charge at the interface as a result of Faradaic currents and polarization at the pore surface. Due to the high complexity to determine the impedance at a given distance, x, two assumptions may be taken. Firstly, that the solid phase, the film, is much more conducting that the liquid phase, the electrolyte, which causes the current flow through the liquid transmission line to be zero, $\chi_2 \approx 0$. In other words, the transmission line corresponding to the liquid phase is short-circuited at all points. The second assumption shall be that the filed pores exhibit a distributed resistance, $\chi_1 = r_1$, which depends on the conductivity of the electrolyte and causes some of the charge to be stored in the double layer at the pore's inner wall, $c_3$, and the formation of a charge transfer resistance in parallel to the capacitance $c_3$.

Returning to the oxygen evolution modelling discussion, we would like to point out that it is always useful to acquire a sense of the position, within the OER potential range, of the potential at which a given EIS spectrum has been recorded, by consulting the relevant polarisation curve. These impedance data were recorded continuously, starting at the lowest potential of 0.58 V (*vs.* Hg/HgO). The potential was then increased by steps of 20 mV in the direction of increasingly potential until the maximum potential value, 0.76 V (*vs.* Hg/HgO) or 0.8 V (*vs.* Hg/HgO) were reached for Mn electrodes or Ni/Co mixed electrodes, respectively. Each impedance measurement at a given potential lasted for approximately 10 minutes. For the present, we concentrate only on the raw impedance data points - the cycles in figs. 6.3.1- 6.3.5 and 6.4.1 – 6.4.7 and the plots that follow. As indicated in the captions of these figures, continuous lines represent the results of fitting the raw data into the appropriate equivalent circuit model, which are that presented in fig. 6.2.1.

## 6.3 Electrochemical Impedance Spectroscopy Studies of Oxygen Evolution on Manganese Oxide Electrodes

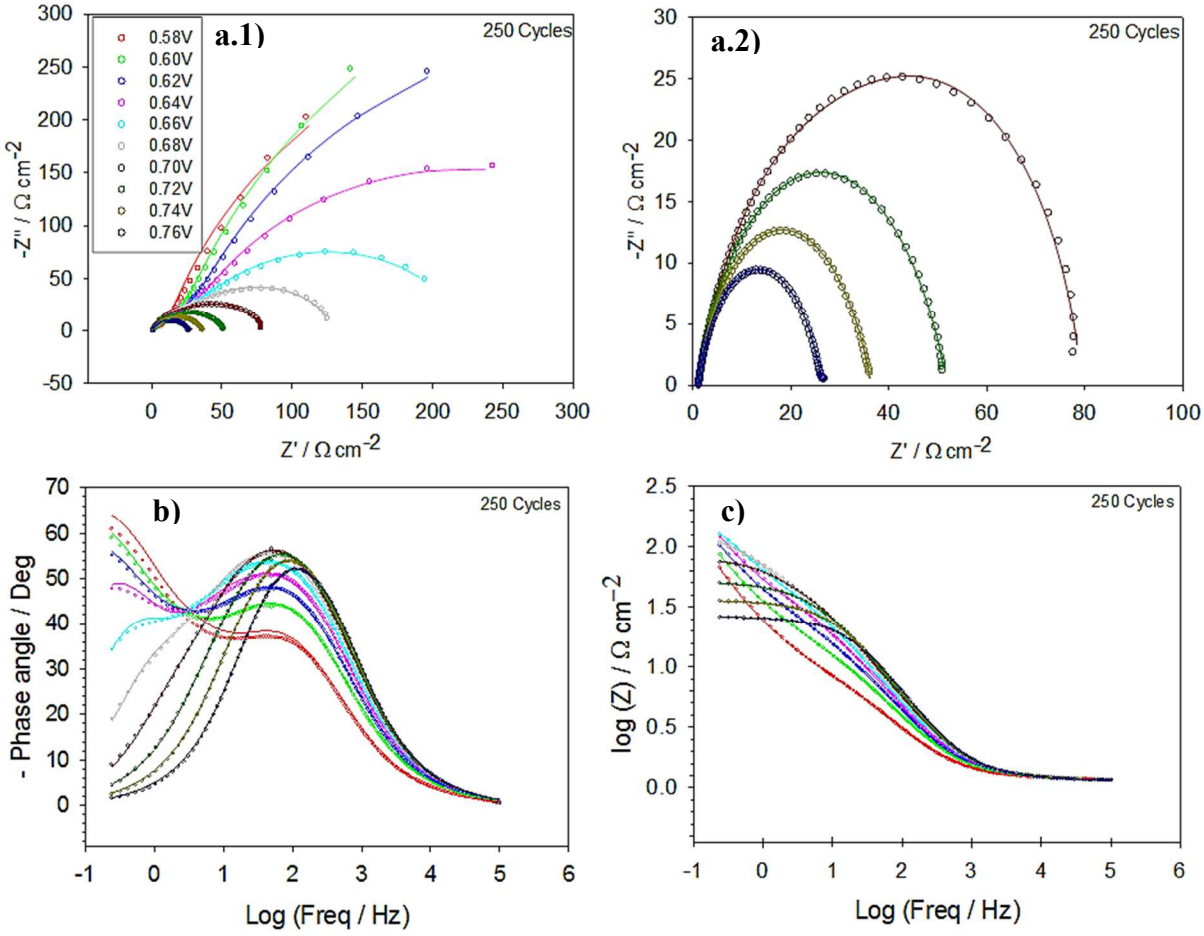
A series of impedance spectra, in the Nyquist and Bode format, recorded for a "fresh" manganese oxide films prepared *via* potential multicycling at N = 25, 250, 500, 750 and 1000 cycles are presented in figs. 6.3.1- 6.3.5. This is the type of electrode that was previously electrochemically characterised in chapter 4.




**d)**

| E / V | Qfilm / $\Omega^{-1}$ $cm^{-2}$ $s^{\alpha}$ | α film | R film / Ω | Qdl / $\Omega^{-1}$ $cm^{-2}$ $s^{\alpha}$ | α dl | Rp / Ω | Qsq / $\Omega^{-1}$ $cm^{-2}$ $s^{\alpha}$ | α sq | Rsq / Ω | Rs / Ω |
|---|---|---|---|---|---|---|---|---|---|---|
| 0.58 | 2.69E-03 ± 1.64E-04 | 0.72 | 201 ± 116 | 8.21E-04 ± 6.93E-05 | 0.97 | 823 ± 201 | 2.11E-03 ± 7.25E-04 | 0.94 | 2136 ± 541 | 2.81 ± 0.03 |
| 0.6 | 2.41E-03 ± 1.57E-04 | 0.72 | 176 ± 106 | 7.29E-04± 4.64E-05 | 0.97 | 810 ± 145 | 1.59E-03 ± 4.50E-04 | 0.94 | 2030 ± 434 | 2.79 ± 0.03 |
| 0.62 | 2.29E-03 ± 1.65E-04 | 0.72 | 163 ± 109 | 6.54E-04 ± 3.28E-05 | 0.97 | 728 ± 125 | 1.29E-03 ± 5.06E-04 | 0.94 | 1381 ± 250 | 2.78 ± 0.03 |
| 0.64 | 2.24E-03 ± 1.38E-04 | 0.72 | 153 ± 88 | 6.03E-04 ± 3.17E-05 | 0.97 | 560 ± 92 | 1.03E-03 ± 7.02E-04 | 0.94 | 670 ± 100 | 2.78 ± 0.03 |
| 0.66 | 2.20E-03 ± 9.69E-05 | 0.72 | 156 ± 73 | 5.62E-04 ± 3.87E-05 | 0.97 | 333 ± 70 | 9.82E-04 ± 1.04E-03 | 0.94 | 259 ± 33 | 2.78 ± 0.02 |
| 0.68 | 2.07E-03 ± 6.29E-05 | 0.72 | 262 ± 38 | 4.80E-04 ± 2.95E-05 | 0.97 | 118 ± 23 | 9.29E-04 ± 3.05E-03 | 0.94 | 67 ± 20 | 2.78 ± 0.02 |
| 0.7 | 2.12E-03 ± 6.32E-05 | 0.72 | 189 ± 23 | 4.43E-04 ± 7.26E-06 | 0.97 | 63 ± 14 | 1.73E-03 ± 8.18E-03 | 0.94 | 30 ± 14 | 2.78 ± 0.02 |
| 0.72 | 2.11E-03 ± 5.39E-05 | 0.72 | 127 ± 12 | 4.25E-04 ± 7.17E-06 | 0.97 | 50 ± 9 | 1.94E-03 ± 2.23E-02 | 0.94 | 12 ± 8 | 2.77 ± 0.01 |
| 0.74 | 2.13E-03 ± 4.31E-05 | 0.72 | 82 ± 6 | 4.11E-04 ± 7.97E-06 | 0.97 | 40 ± 6 | 2.77E-03 ± 6.03E-02 | 0.94 | 5 ± 4 | 2.76 ± 0.01 |
| 0.76 | 2.16E-03 ± 2.59E-05 | 0.72 | 50 ± 3 | 3.98E-04± 3.32E-05 | 0.97 | 32 ± 2 | 3.04E-03 ± 1.95E+02 | 0.94 | 2 ± 2 | 2.76 ± 0.01 |

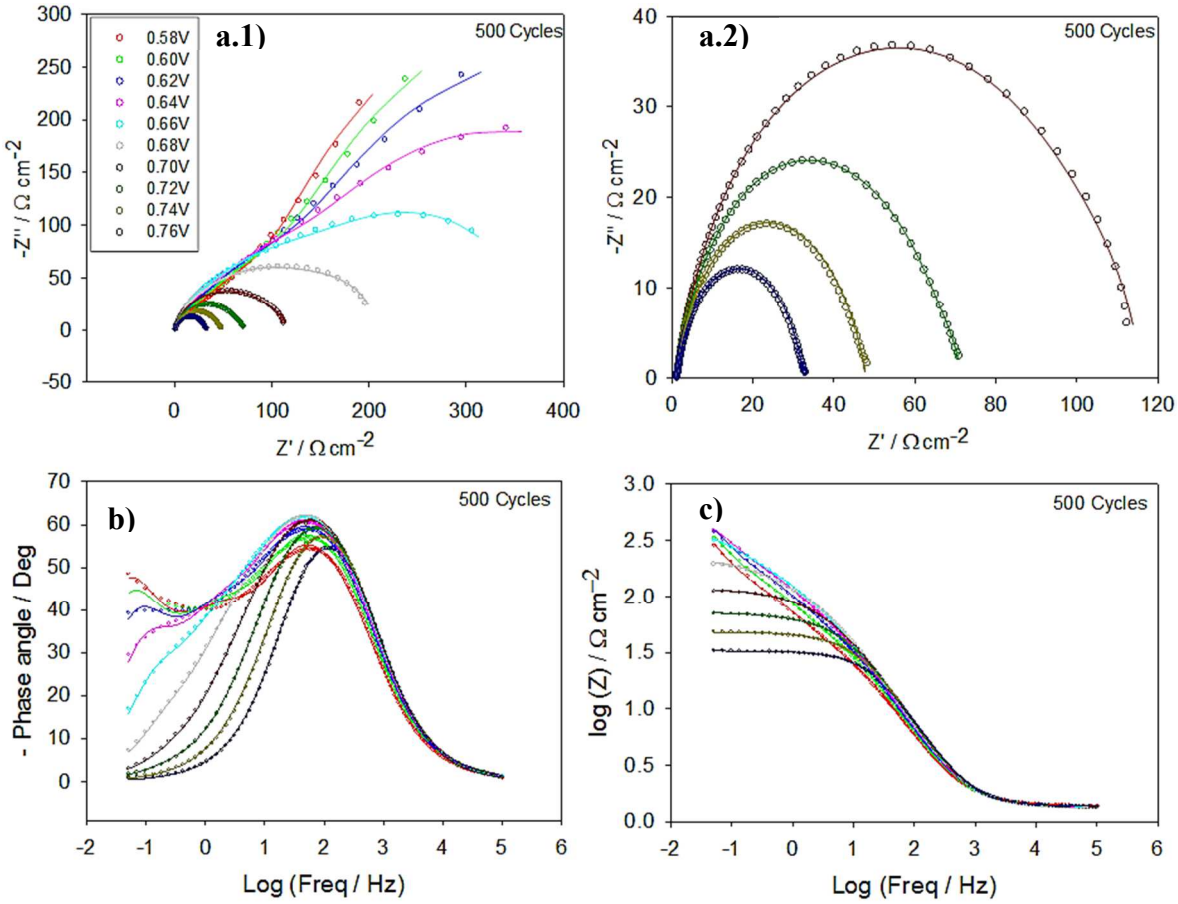
Figure 6.3.1 Electrochemical impedance spectra recorded in 1.0 M NaOH at a series of potentials associated with active oxygen evolution for a 25-cycled hydrous manganese oxide films in the Nyquist (a.1-a.2) and Bode (b-c) format. The experiment data is represented by discrete points and the simulated impedance response is represented by a continuous line. Image a.2 represent a zoomed in version of the Nyquist plot for potentials between 0.7 - 0.76 V. Table d) presents the optimum fit parameters for the CNLS fitting to circuit in fig. 6.2.1 of the raw impedance response.




**d)**

| E / V | Qfilm / $\Omega^{-1}$ cm$^{-2}$ s$^{\alpha}$ | α film | R film / Ω | Qdl / $\Omega^{-1}$ cm$^{-2}$ s$^{\alpha}$ | α dl | Rp / Ω | Qsq / $\Omega^{-1}$ cm$^{-2}$ s$^{\alpha}$ | α sq | Rsq / Ω | Rs / Ω |
|---|---|---|---|---|---|---|---|---|---|---|
| 0.58 | 4.43E-03 ± 1.39E-04 | 0.7 | 13 ± 3 | 2.41E-03 ± 5.56E-04 | 0.96 | 37 ± 27 | 4.31E-03 ± 1.28E-03 | 0.8 | 1433 ± 420 | 2.99 ± 0.03 |
| 0.6 | 3.40E-03 ± 4.11E-05 | 0.7 | 22 ± 2 | 1.80E-03 ± 3.39E-04 | 0.96 | 59 ± 17 | 4.15E-03 ± 4.43E-04 | 0.79 | 1929 ± 251 | 2.97 ± 0.01 |
| 0.62 | 3.09E-03 ± 3.69E-05 | 0.7 | 33 ± 4 | 1.51E-03 ± 3.03E-04 | 0.95 | 86 ± 27 | 4.23E-03 ± 3.54E-04 | 0.79 | 1343 ± 104 | 2.95 ± 0.01 |
| 0.64 | 2.95E-03 ± 1.57E-04 | 0.7 | 36 ± 11 | 1.35E-03 ± 2.56E-04 | 0.95 | 74 ± 43 | 6.59E-03 ± 4.66E-04 | 0.77 | 727 ± 91 | 2.94 ± 0.01 |
| 0.66 | 2.97E-03 ± 1.36E-04 | 0.7 | 36 ± 10 | 1.33E-03 ± 2.10E-04 | 0.95 | 58 ± 7 | 7.93E-03 ± 3.53E-04 | 0.77 | 321 ± 18 | 2.94 ± 0.01 |
| 0.68 | 2.85E-03 ± 9.40E-05 | 0.71 | 48 ± 6 | 1.49E-03 ± 1.98E-04 | 0.95 | 40 ± 7 | 8.28E-03 ± 2.05E-04 | 0.77 | 145 ± 7 | 2.95 ± 0.01 |
| 0.7 | 3.03E-03 ± 7.16E-05 | 0.7 | 47 ± 10 | 1.59E-03 ± 1.57E-04 | 0.95 | 40 ± 7 | 9.77E-03 ± 5.58E-04 | 0.77 | 61 ± 3 | 2.94 ± 0.01 |
| 0.72 | 2.99E-03 ± 3.14E-05 | 0.7 | 61 ± 7 | 1.34E-03 ± 1.02E-04 | 0.95 | 21 ± 3 | 1.18E-02 ± 1.20E-03 | 0.77 | 16 ± 4 | 2.94 ± 0.01 |
| 0.74 | 3.10E-03 ± 3.48E-05 | 0.7 | 40 ± 2 | 1.05E-03 ± 5.33E-05 | 0.95 | 21 ± 2 | 1.36E-02 ± 3.81E-03 | 0.77 | 8 ± 1 | 2.94 ± 0.01 |
| 0.76 | 3.25E-03 ± 4.78E-05 | 0.7 | 25 ± 2 | 8.45E-04 ± 2.13E-05 | 0.95 | 19 ± 2 | 1.53E-02 ± 1.03E-02 | 0.77 | 4 ± 1 | 2.93 ± 0.01 |

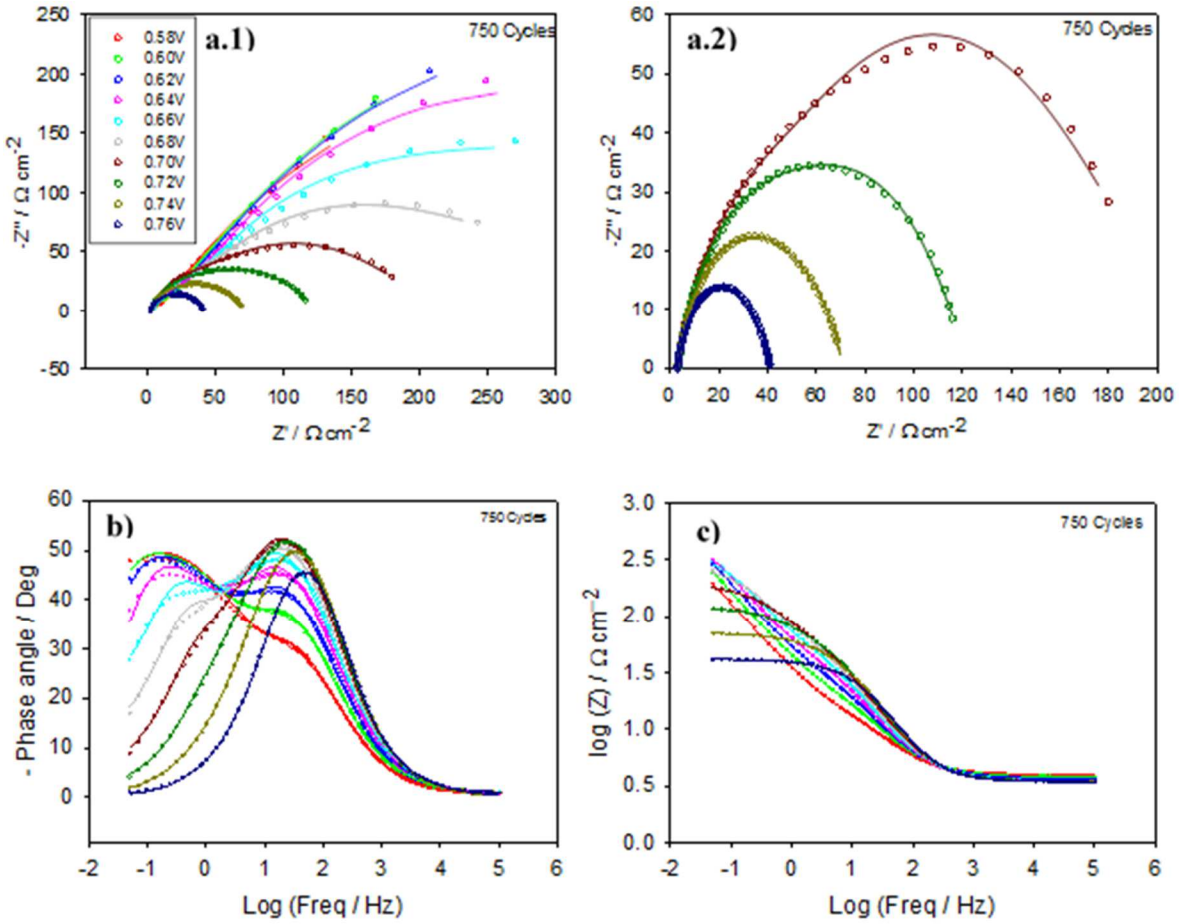
Figure 6.3.2 Electrochemical impedance spectra recorded in 1.0 M NaOH at a series of potentials associated with active oxygen evolution for a 250-cycled hydrous manganese oxide films in the Nyquist (a.1-a.2) and Bode (b-c) format. The experiment data is represented by discrete points and the simulated impedance response is represented by a continuous line. Image a.2 represent a zoomed in version of the Nyquist plot for potentials between 0.7 - 0.76 V. Table d) presents the optimum fit parameters for the CNLS fitting to circuit in fig. 6.2.1 of the raw impedance response.




**d)**

| E / V | Qfilm / $\Omega^{-1}$ cm$^{-2}$ s$^{\alpha}$ | α film | R film / Ω | Qdl / $\Omega^{-1}$ cm$^{-2}$ s$^{\alpha}$ | α dl | Rp / Ω | Qsq / $\Omega^{-1}$ cm$^{-2}$ s$^{\alpha}$ | α sq | Rsq / Ω | Rs / Ω |
|---|---|---|---|---|---|---|---|---|---|---|
| 0.58 | 8.31E-03 ± 6.15E-04 | 0.65 | 84 ± 10 | 3.89E-03 ± 3.54E-04 | 0.90 | 30 ± 4 | 6.60E-03 ± 1.22E-03 | 0.87 | 932 ± 259 | 2.92 ± 0.02 |
| 0.6 | 6.50E-03 ± 2.66E-04 | 0.65 | 117 ± 13 | 3.68E-03 ± 2.23E-04 | 0.90 | 50 ± 5 | 6.69E-03 ± 9.32E-04 | 0.87 | 1143 ± 258 | 2.87 ± 0.02 |
| 0.62 | 5.77E-03 ± 2.49E-04 | 0.66 | 151 ± 29 | 3.65E-03 ± 3.17E-04 | 0.90 | 71 ± 20 | 6.77E-03 ± 1.68E-03 | 0.87 | 830 ± 164 | 2.85 ± 0.02 |
| 0.64 | 5.61E-03 ± 4.62E-04 | 0.66 | 165 ± 30 | 2.95E-03 ± 7.09E-04 | 0.90 | 87 ± 18 | 6.85E-03 ± 4.74E-03 | 0.87 | 490 ± 104 | 2.84 ± 0.02 |
| 0.66 | 6.48E-03 ± 9.59E-04 | 0.67 | 167 ± 26 | 2.37E-03 ± 1.35E-04 | 0.90 | 37 ± 10 | 6.60E-03 ± 4.38E-03 | 0.87 | 329 ± 146 | 2.87 ± 0.02 |
| 0.68 | 7.88E-03 ± 1.12E-03 | 0.67 | 229 ± 67 | 2.25E-03 ± 1.24E-04 | 0.90 | 44 ± 5 | 7.50E-03 ± 4.12E-03 | 0.87 | 148 ± 34 | 2.88 ± 0.02 |
| 0.7 | 1.05E-02 ± 1.59E-03 | 0.67 | 167 ± 18 | 2.02E-03 ± 8.78E-05 | 0.90 | 52 ± 4 | 8.91E-03 ± 3.22E-02 | 0.87 | 56 ± 7 | 2.89 ± 0.01 |
| 0.72 | 1.55E-02 ± 1.73E-03 | 0.67 | 79 ± 4 | 1.89E-03 ± 1.87E-05 | 0.90 | 55 ± 1 | 1.20E-02 ± 2.93E-02 | 0.87 | 34 ± 2 | 2.90 ± 0.01 |
| 0.74 | 3.44E-02 ± 3.88E-03 | 0.67 | 37 ± 2 | 1.77E-03 ± 3.28E-05 | 0.90 | 49 ± 1 | 1.15E-02 ± 3.40E-02 | 0.87 | 15 ± 4 | 2.91 ± 0.01 |
| 0.76 | 2.74E-01 ± 3.11E-01 | 0.67 | 18 ± 4 | 1.69E-03 ± 1.73E-05 | 0.90 | 36 ± 1 | 1.38E-02 ± 8.15E-02 | 0.87 | 14 ± 2 | 2.91 ± 0.01 |

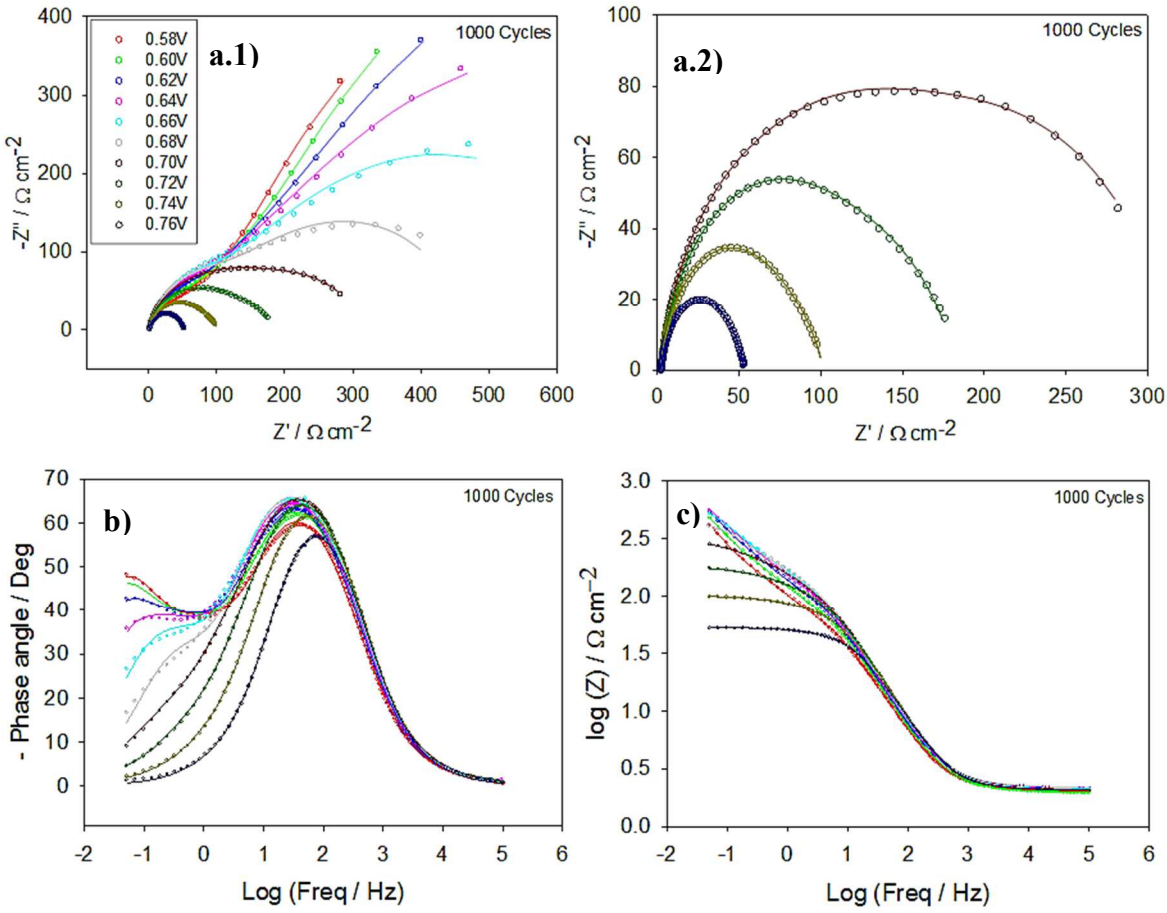
Figure 6.3.3 Electrochemical impedance spectra recorded in 1.0 M NaOH at a series of potentials associated with active oxygen evolution for a 500-cycled hydrous manganese oxide films in the Nyquist (a.1-a.2) and Bode (b-c) format. The experiment data is represented by discrete points and the simulated impedance response is represented by a continuous line. Image a.2 represent a zoomed in version of the Nyquist plot for potentials between 0.7 - 0.76 V. Table d) presents the optimum fit parameters for the CNLS fitting to circuit in fig. 6.2.1 of the raw impedance response.




**d)**

| E / V | Qfilm / $\Omega^{-1}$ $cm^{-2}$ $s^{\alpha}$ | α film | R film / Ω | Qdl / $\Omega^{-1}$ $cm^{-2}$ $s^{\alpha}$ | α dl | Rp / Ω | Qsq / $\Omega^{-1}$ $cm^{-2}$ $s^{\alpha}$ | α sq | Rsq / Ω | Rs / Ω |
|---|---|---|---|---|---|---|---|---|---|---|
| 0.58 | 6.69E-03 ± 9.67E-04 | 0.65 | 136 ± 278 | 7.61E-03 ± 3.52E-04 | 0.84 | 5 ± 1 | 4.32E-03 ± 1.03E-02 | 0.91 | 515 ± 242 | 3.41 ± 0.03 |
| 0.6 | 5.16E-03 ± 3.71E-04 | 0.65 | 77 ± 34 | 6.62E-03 ± 1.50E-04 | 0.84 | 9 ± 1 | 4.02E-03 ± 1.47E-03 | 0.91 | 709 ± 67 | 3.35 ± 0.02 |
| 0.62 | 4.54E-03 ± 3.43E-04 | 0.65 | 92 ± 75 | 6.13E-03 ± 1.59E-04 | 0.84 | 14 ± 2 | 4.36E-03 ± 1.85E-03 | 0.91 | 696 ± 66 | 3.30 ± 0.02 |
| 0.64 | 4.44E-03 ± 5.49E-04 | 0.65 | 105 ± 259 | 5.04E-03 ± 1.24E-05 | 0.84 | 23 ± 8 | 5.56E-03 ± 4.02E-03 | 0.91 | 549 ± 186 | 3.26 ± 0.02 |
| 0.66 | 4.99E-03 ± 1.04E-03 | 0.65 | 253 ± 353 | 4.82E-03 ± 1.77E-04 | 0.84 | 35 ± 7 | 5.66E-03 ± 4.36E-03 | 0.91 | 299 ± 109 | 3.27 ± 0.03 |
| 0.68 | 6.55E-03 ± 1.90E-03 | 0.65 | 176 ± 83 | 4.39E-03 ± 1.59E-04 | 0.84 | 50 ± 5 | 7.38E-03 ± 3.87E-03 | 0.91 | 141 ± 26 | 3.28 ± 0.03 |
| 0.7 | 1.01E-02 ± 3.20E-03 | 0.65 | 92 ± 21 | 4.01E-03 ± 1.04E-04 | 0.84 | 62 ± 4 | 8.45E-03 ± 9.80E-04 | 0.91 | 72 ± 9 | 3.30 ± 0.02 |
| 0.72 | 2.11E-02 ± 7.60E-03 | 0.65 | 37 ± 6 | 3.03E-03 ± 5.28E-05 | 0.84 | 65 ± 2 | 9.07E-03 ± 1.66E-03 | 0.91 | 34 ± 4 | 3.35 ± 0.01 |
| 0.74 | 5.60E-02 ± 1.08E-01 | 0.65 | 14 ± 3 | 2.84E-03 ± 2.58E-05 | 0.84 | 54 ± 2 | 1.08E-03 ± 2.98E-03 | 0.9 | 11 ± 3 | 3.36 ± 0.01 |
| 0.76 | 6.18E-02 ± 6.38E-02 | 0.68 | 5 ± 1 | 6.26E-03 ± 1.59E-05 | 0.85 | 37 ± 121 | 1.30E-02 ± 2.58E-02 | 0.9 | 7 ± 121 | 3.34 ± 0.01 |

Figure 6.3.4 Electrochemical impedance spectra recorded in 1.0 M NaOH at a series of potentials associated with active oxygen evolution for a 750-cycled hydrous manganese oxide films in the Nyquist (a.1-a.2) and Bode (b-c) format. The experiment data is represented by discrete points and the simulated impedance response is represented by a continuous line. Image a.2 represent a zoomed in version of the Nyquist plot for potentials between 0.7 - 0.76 V. Table d) presents the optimum fit parameters for the CNLS fitting to circuit in fig. 6.2.1 of the raw impedance response.




**d)**

| E / V | Qfilm / $\Omega^{-1}$ $cm^{-2}$ $s^{\alpha}$ | α film | R film / Ω | Qdl / $\Omega^{-1}$ $cm^{-2}$ $s^{\alpha}$ | α dl | Rp / Ω | Qsq / $\Omega^{-1}$ $cm^{-2}$ $s^{\alpha}$ | α sq | Rsq / Ω | Rs / Ω |
|---|---|---|---|---|---|---|---|---|---|---|
| 0.58 | 1.09E-02 ± 9.67E-04 | 0.65 | 221 ± 278 | 1.34E-02 ± 3.52E-04 | 0.81 | 8 ± 1 | 4.32E-03 ± 1.03E-02 | 0.91 | 317 ± 242 | 3.41 ± 0.03 |
| 0.6 | 8.39E-03 ± 3.71E-04 | 0.65 | 125 ± 34 | 1.10E-02 ± 1.50E-04 | 0.81 | 15 ± 1 | 4.02E-02 ± 1.47E-03 | 0.91 | 436 ± 67 | 3.35 ± 0.02 |
| 0.62 | 7.38E-03 ± 3.43E-04 | 0.65 | 150 ± 75 | 1.05E-02 ± 1.59E-04 | 0.81 | 23 ± 2 | 4.36E-03 ± 1.85E-03 | 0.91 | 428 ± 66 | 3.30 ± 0.02 |
| 0.64 | 7.22E-03 ± 5.49E-04 | 0.65 | 171 ± 259 | 7.87E-03 ± 1.77E-04 | 0.81 | 37 ± 8 | 3.83E-03 ± 4.02E-03 | 0.91 | 338 ± 186 | 3.26 ± 0.02 |
| 0.66 | 8.11E-03 ± 1.04E-03 | 0.65 | 411 ± 353 | 5.54E-03 ± 1.59E-04 | 0.81 | 57 ± 7 | 3.93E-03 ± 4.36E-03 | 0.91 | 184 ± 109 | 3.27 ± 0.03 |
| 0.68 | 1.06E-03 ± 1.90E-03 | 0.65 | 286 ± 83 | 5.40E-03 ± 1.04E-04 | 0.81 | 81 ± 5 | 6.03E-03 ± 3.87E-03 | 0.91 | 87 ± 26 | 3.28 ± 0.03 |
| 0.7 | 1.64E-02 ± 3.20E-03 | 0.65 | 150 ± 21 | 4.07E-03 ± 5.28E-05 | 0.81 | 101 ± 4 | 9.02E-03 ± 9.80E-04 | 0.91 | 44 ± 9 | 3.30 ± 0.02 |
| 0.72 | 3.11E-02 ± 7.60E-03 | 0.65 | 60 ± 6 | 3.80E-03 ± 2.58E-05 | 0.81 | 106 ± 2 | 1.06E-02 ± 1.66E-03 | 0.91 | 21 ± 4 | 3.35 ± 0.01 |
| 0.74 | 9.60E-02 ± 1.08E-01 | 0.65 | 23 ± 3 | 3.08E-03 ± 1.59E-05 | 0.81 | 88 ± 2 | 1.29E-02 ± 2.98E-03 | 0.9 | 7 ± 3 | 3.36 ± 0.01 |
| 0.76 | 9.18E-02 ± 6.38E-02 | 0.68 | 8 ± 1 | 2.34E-04 ± 1.24E-05 | 0.82 | 60 ± 121 | 1.27E-02 ± 2.58E-02 | 0.9 | 4 ± 121 | 3.34 ± 0.01 |

Figure 6.3.5 Electrochemical impedance spectra recorded in 1.0 M NaOH at a series of potentials associated with active oxygen evolution for a 1000-cycled hydrous manganese oxide films in the Nyquist (a.1-a.2) and Bode (b-c) format. The experiment data is represented by discrete points and the simulated impedance response is represented by a continuous line. Image a.2 represent a zoomed in version of the Nyquist plot for potentials between 0.7 - 0.76 V. Table d) presents the optimum fit parameters for the CNLS fitting to circuit in fig. 6.2.1 of the raw impedance response.

Although difficult to visualise from the Nyquist plot, it is evident from the phase angle plot *vs.* log frequency that there are two RC time constants involved in the impedance response for Mn oxide electrodes. The latter observation is only valid for potential regions where the OER is not intense, that is, between 0.58 V and 0.68 V (*vs.* Hg/HgO). As the potential shifts towards more positive regions, the presence of a dominant single RC time constant is observed. That there is only one RC time constant (one loop) for potentials above ca. 0.68 V is apparent from the graph a.2 in figs. 6.3.1 - 6.3.5. However, after a careful examination of this graph in the region below $10^2$ Hz, the presence of a rather semi-cycle which would indicate the possible superposition of two relaxation processes for these longer time scales was observed. The latter is clearer from fig. 6.3.4a.2. The model proposed by Lyons *et al.*[1a] foresees the observation of three RC time constants: (i) the $Q_{dl}$ / $R_p$, (ii) the $Q_{sq}$ / $R_{sq}$, and (iii) $Q_{film}$ / $R_{film}$.

It is important to mention that we could not observe more than two RC time constants for Mn electrodes' impedance data since, in figs. 6.3.1b - 6.3.5b, only two loops were observed. To discuss the latter, two scenarios are presented: (i) the relaxation processes in the cell takes place at different time scales and, thus, the slowest overlap the others; (ii) the values of RC time constants are similar and thus, they occur at the same time scale. This would result in the observation of a single loop. Another important aspect of the above plots is discussed now regarding the relatively poor fitting of some impedance plots. Examining the Nyquist plot for the 1000 cycles, the profile at potentials below 0.66 V show considerable worst fitting that those above 0.66 V. On this basis, the attempts to fit impedance data characteristic of two RC time constants (note that one RC time constant is overlapped) into the model in fig. 6.2.1, which is three clear RC loops, may be the reason for the anomalous fitting parameters. This is also reflected in the error values in tables presented in figs. 6.3.1 - 6.3.5 which for potentials below 0.66 V are quite significant compared with those for potentials above 0.66 V. It must be noted that such model was employed as a first approximation to linearize Mn electrodes and therefore, deviations from the ideality should be expected.

Having presented the results of the EIS studies on various Mn electrodes in 1.0 M NaOH at 25°C we turn our attention to the task of extracting useful information from this data regarding the nature of the OER and the physical nature on these surfaces. Immediately, it is apparent that all fitted parameters are affected by OER. An interesting aspect of the fitting parameters listed in tables in figs. 6.3.1 - 6.3.5 is the fact that the double layer capacitance

decreases with potential. It is also noteworthy that the modelled film capacitance is a more "pure" capacitance element than the simulated double layer capacitance, in that the α exponent for the former is closer to the ideal value of unity for a capacitor displaying no frequency dispersion. In order to determine the effective double layer capacitances, $C_{dl,eff}$, the method suggested by Brug *et al.*[6] was employed (see section 3.7.5 and specially eqn. 3.7.30). Fig. 6.3.6 shows the evolution of the double layer capacitance as a function of potential for various Mn films thickness.

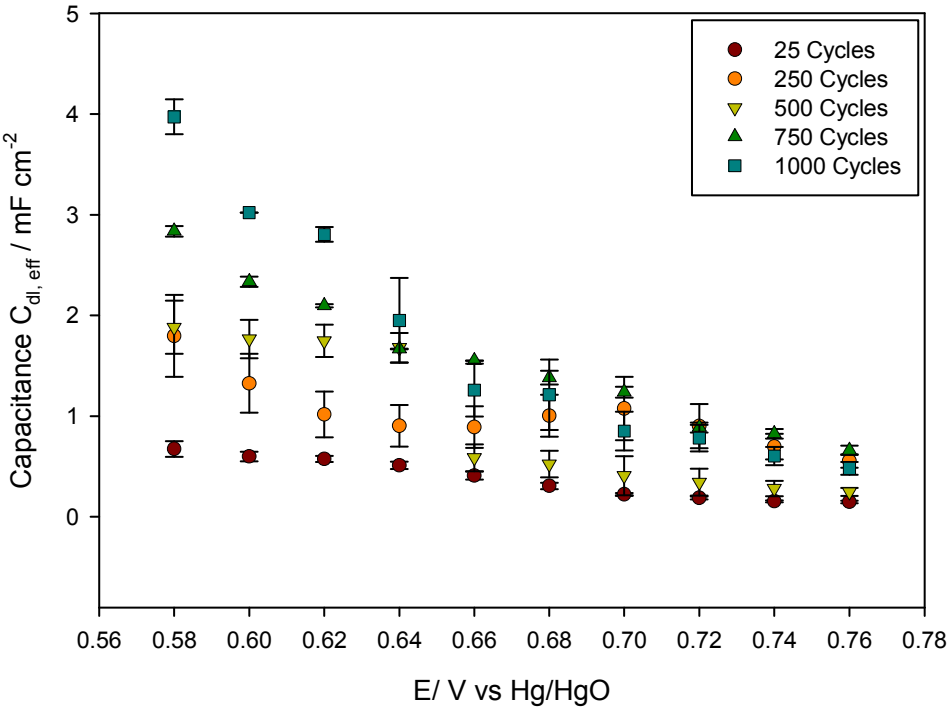



Figure 6.3.6 The optimum fitting values of $C_{dl,eff}$ plotted as a function of applied potential for various hydrous Mn oxide electrodes with different n° of potential cycles. These values were obtained from the fitting tables presented in figs. 6.3.1 - 6.3.5. Error bars represent standard deviations of three different samples.

As shown in fig. 6.3.6, the largest capacitance values are observed for very thick films. Note that thick layers possess very porous surfaces. This supports the suggestion that porous electrodes, due to their large surface area and their intimate contact with the electrolyte, exhibit excellent charge storage behaviour. The observation is in line with the capacitance nature for various Mn electrode thicknesses measured by potential pulse decay presented in section 4.7. However, these results differ by one order of magnitude with those presented in Table 4.7.1. We propose that the capacitance measured by pulse decay technique does not

only account for the double layer capacitance but for other capacitances such as film capacitance or surfaquo groups' capacitance. An interesting aspect of the behaviour of the double layer capacitance is its variation as the potential positively increases. For electrodes with 1000 growth cycles, the $C_{dl,eff}$ decreases from ca. 4 mF $cm^{-2}$ to ca. 0.4 mF $cm^{-2}$, which represents a decrease of 90 %, whereas for more thin films, *e.g.* 250 growth cycles, in the same potential range it shows a decrease of ca. 45%. We suggest that the effect of gas generation associated to the oxygen evolution causes the disruption of the double layer interface and thus limited charge can be stored within that region.

At first glance, the fitted $Q_{sq}$ parameter may seem to provide a route towards the construction of an experimental adsorption pseudo-capacitance *vs*. potential plot, and thus to make inferences regarding the nature of the adsorption isotherm required to account for the variation of the reaction intermediate coverage with potential (recall section 1.2.3). There are, however, problems with such an approach. The discussion that follows has been informed by a theoretical treatment, due to Harrington and Conway[7] of the significance of various experimental parameters that may be obtained from EIS measurements on Faradaic reactions involving electrosorbed intermediates (in particular in HER and OER). These authors mentioned that the quantity, typically referred to in the literature as "the pseudo-capacitance", is that presented in section 1.2.3, eqn. 1.2.51 and denoted in the present thesis as:

$$C_{ps} = \frac{dq}{d\eta} = k' \frac{d\theta}{d\eta} \tag{6.3.1}$$

The multiple symbols retain the significance earlier attributed to them in section 1.2.3. We would like to emphasise now that these are steady-state values of these parameters and thus, eqn. 1.2.51 should more properly be called the steady-state pseudo-capacitance. The pseudo-capacitance parameter determined by EIS is a complex, frequency-dependent quantity denoted by Harrington and Conway as $\bar{\bar{C}}_{ac}$, which refers to how the sinusoidal variation of charge sorted by the adsorbed intermediate depends on the sinusoidal changes of the potential. Thus, it is only at zero frequency that is, at steady-state in which the change in this adsorbate charge is in phase with the sinusoidal change in applied potential. Therefore, we may determine that:

$$C_{ps} = |\bar{\bar{C}}_{ac}| \tag{6.3.2}$$

The other pseudo-capacitive quantity that has been mentioned in the present work in chapter 3 and in this chapter is $C_\phi$ or $C_{sq}$. This parameter, which we understand to be in parallel with the resistance $R_{sq}$, in the equivalent circuit model in fig. 6.2.1, correctly models the relaxation of the charge associated with the adsorbed intermediate. Harrington and Conway pointed out that $C_{sq}$ will only be equal to $C_{sq}$ in cases where the net rate of consumption/production of electrons is equal to the net rate of production/desorption of the adsorbed species. An example where this condition holds is in the underpotential deposition (UPD) of hydrogen or other species. In this case, it can be shown that the $R_{sq}$ element of the Armstrong–Henderson[7] equivalent circuit and, in extension, of the model proposed by Lyons et al[1a], is infinite and thus this equivalent circuit reduces to the typical Randles circuit. Recall that $R_{sq}$ is typically used to model the adsorption of single species, and specifically in this work, of $OH^-$ species.

The aforementioned authors introduced the more general difference between $C_{sq}$ and $C_{ps}$ as arising from the fact that it is only in the UPD process that the Faradaic charge is all stored as the adsorbate. For Faradaic processes such as HER in which the adsorbed species are merely an intermediate that is consumed in steps (or a step) subsequent to its adsorption, these steps effectively facilitate charge leakage. In other words, the charge storage decreases and breaks the equality between the charge passed and stored, thus $C_{sq} \neq C_{ps}$. This situation becomes more complex for systems where reactions involve significant coverages of more than one intermediate species. The general conclusion from the foregoing discussion is that the values of $C_{sq}$, as obtained from the CNLS fitting of EIS data to the equivalent circuit model (see fig. 6.2.1), do not have a simple relationship to the steady-state pseudo-capacitance $C_{ps}$. It was considered opportune, therefore, not to attempt to draw a solid conclusion regarding the nature of the appropriate adsorption isotherm. Notwithstanding, it still seems interesting to compare the trend of the CNLS fitting data corresponding to $C_{sq}$ as a function of layer thickness during the OER. These results are presented in fig. 6.3.7.

We would like to remark again that the following discussion should be treated with caution since it considers that only one intermediate specie is adsorbed on the surface. It is clear from fig. 6.3.7 that $C_{sq,eff}$ increases with applied potential eventually reaching a maximum at ca. 7 mF $cm^{-2}$ for all the film thickness. A significant inflexion point in the capacitance behaviour of surfaquo groups is observed at 0.66 V. Such a trend may be expected for a capacitance arising from a Faradaic process. Coincidence in trends may indicate that the

$C_{sq,eff}$ element describes a similar charging process for each film thickness with the exception of 25 growth cycles electrode. The latter may also indicate that intermediate species, involved in the rate-determining process, are not the same for each film thickness in agreement with the contrasting Tafel behaviour observed for various hydrous oxide films presented in section 4.5.

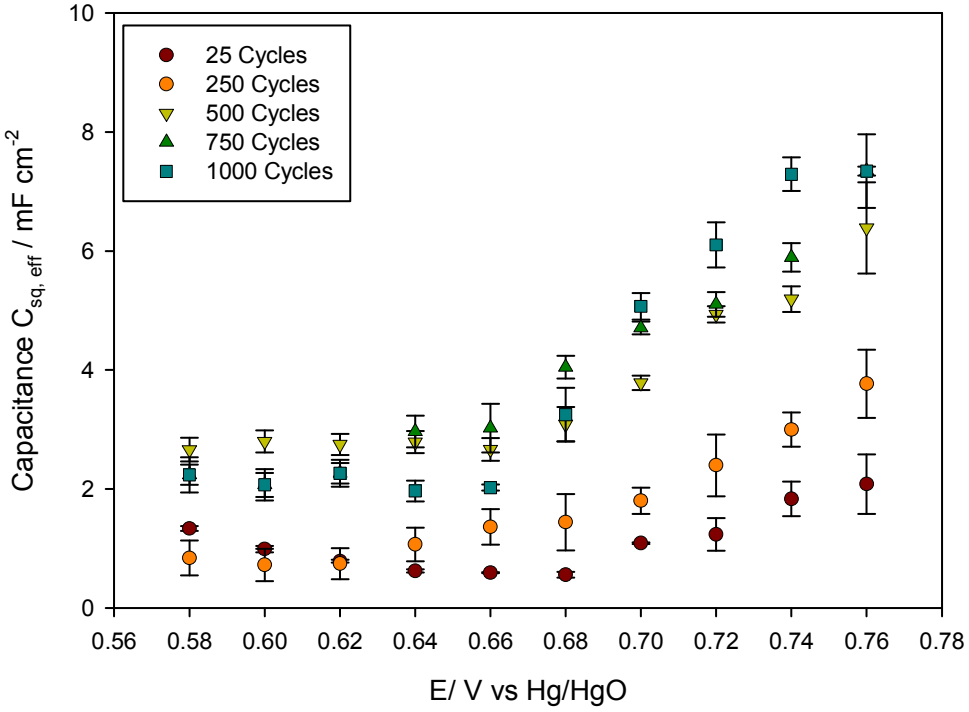



Figure 6.3.7 The optimum fitting values of $C_{sq,eff}$ plotted as a function of applied potential for various hydrous Mn oxide electrodes with different n° of potential cycles. These values were obtained from the fitting tables presented in figs. 6.3.1 - 6.3.5. Error bars represent standard deviations of three different samples.

Note that similarities between figs. 4.5.1 and 6.3.7 exist since both intermediate and very thick films exhibit similar surfaquo intermediate capacitances and also similar Tafel slope values. The discussion of the resistance $R_{sq}$ and $R_p$ is now presented. A common interpretation of these resistances is that $R_p$ refers to the charge transfer resistance of electrosorption step while $R_{sq}$ refers to the charge transfer of the electrodesorption process. Note that the reciprocal resistance $\frac{1}{Rp}$ was pointed out to be equal to the sum of similar reciprocal resistances for each of the individual charge transfer steps. Therefore, $R_p$ is related to the overall rate of the OER. In addition, $R_{sq}$ gives an indication of the ease with which these species can be formed. Following the analyses of Harrington and Conway[7], it would appear that the usefulness of the CNLS fitting parameters is restricted to the following

applications: (i) the roughness factor estimation of values (which we have not considered in this work), and (ii) the derivation of Tafel slopes *via* eqn. 3.7.38. The derivation of the Tafel slope form impedance data will be treated in a specific section in this chapter.

Now we present the evolution of both resistances, $R_{sq}$ and $R_p$ as a function of applied potential for various film thicknesses in figs. 6.3.8 and 6.3.9, respectively. It can be observed from fig. 6.3.8 that $R_{sq}$ values decrease significantly with applied potential. At a potential range of 0.7 to 0.76 V the surfaquo resistance reaches a plateau. The latter may be explained by the fact that as the potential is increased, the intermediate species are more readily formed and therefore, $R_{sq}$ decreases.

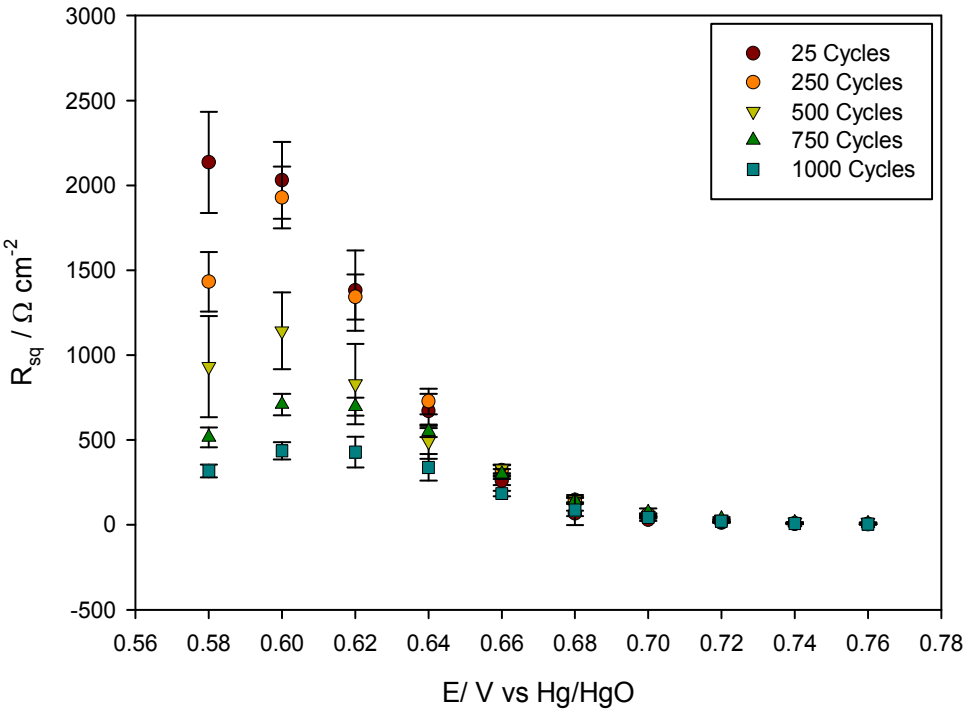



Figure 6.3.8 The optimum fitting values of $R_{sq}$ plotted as a function of applied potential for various hydrous Mn oxide electrodes with different n° of potential cycles. These values were obtained from the fitting tables presented in figs. 6.3.1 - 6.3.5. Error bars represent standard deviations of three different samples.

As expected for a Faradaic process, the polarisation resistance for each film thickness decreases with increasing potential indicating enhancement of electron transfer kinetics. This is especially notorious for electrodes with 25 growth cycles. However, the other electrodes exhibit relatively little difference in the $R_p$ values as the potential is increased.

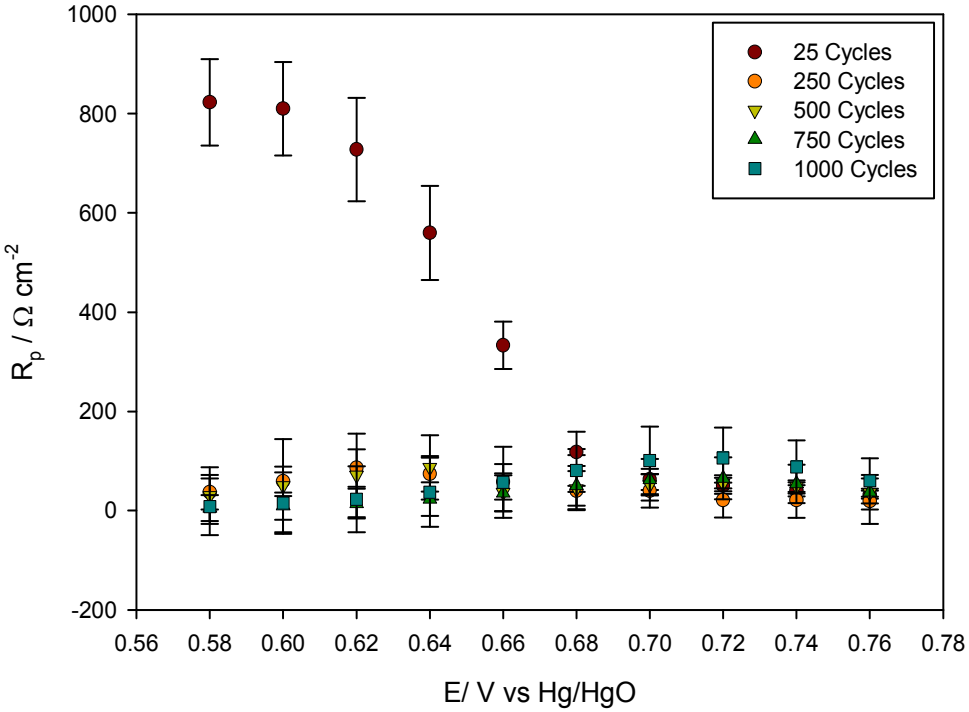



Figure 6.3.9 The optimum fitting values of $R_p$ plotted as a function of applied potential for various hydrous Mn oxide electrodes with different n° of potential cycles. These values were obtained from the fitting tables presented in figs.6.3.1 - 6.3.5. Error bars represent standard deviations of three different samples.

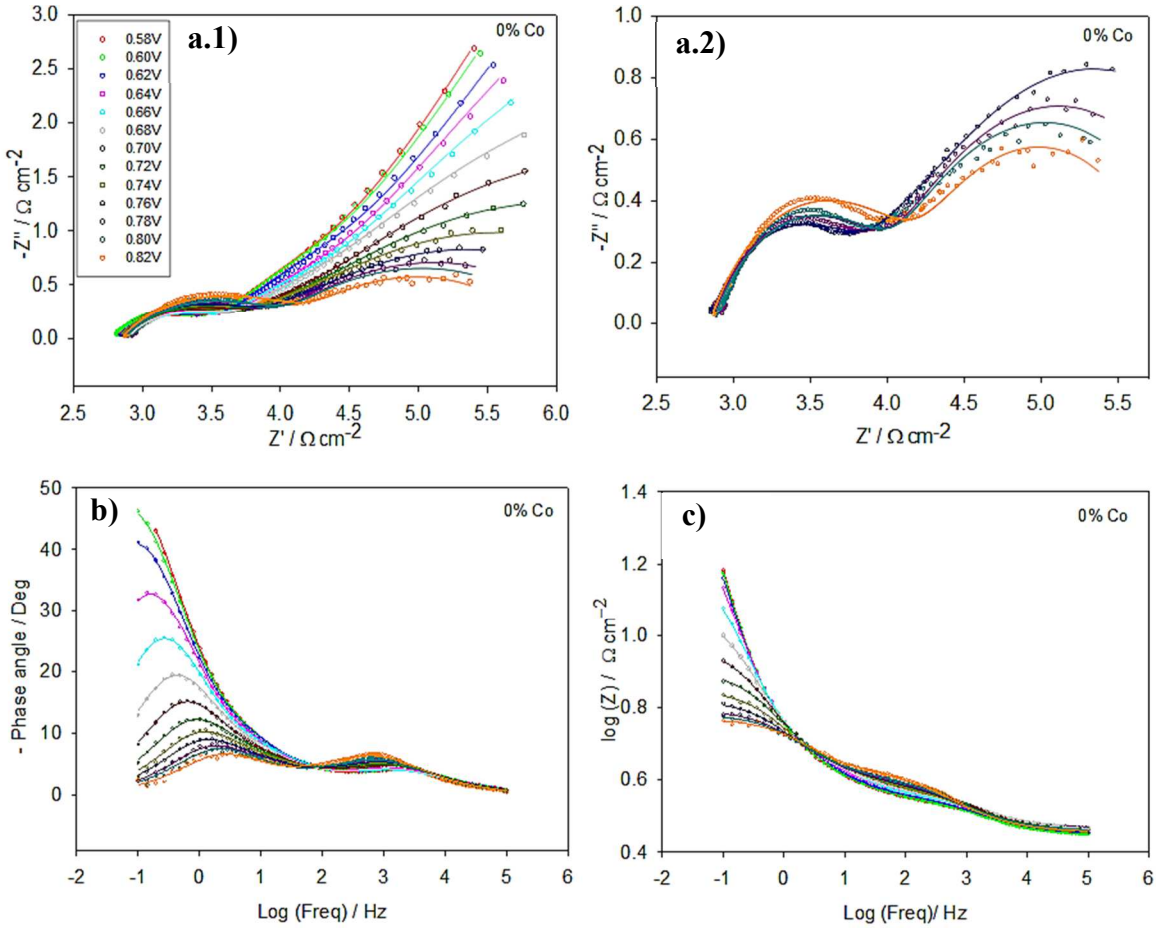
As mentioned previously, the $R_p$ is related to the overall rate of the OER, thus the observation of approximately constant $R_p$ values regardless the potential suggests that the overall rate remains constant in such potential range. This observation mirrors the Tafel characteristic illustrated in fig. 4.5.2. The behaviour of the $R_p$ values for 25 growth cycles is not in line with the latter discussion since we would expect to observe a double Tafel slope in its steady-state polarisation measurement (see fig. 4.5.2b), which is not the case here. We cannot provide an appropriate explanation for this observation. Future work will be carried to analyse the 25 cycles with more detail.

## 6.4 Electrochemical Impedance Spectroscopy Studies of Oxygen Evolution on Nickel Cobalt Oxide Electrodes

A series of impedance spectra, in the Nyquist and Bode format, recorded for a series of nickel cobalt mixed oxide electrodes prepared *via* thermal decomposition of precursor salts at 400°C, are presented in fig. 6.4.1 - 6.4.7. Recall that these type of electrodes were previously electrochemically characterised in chapter 5 where the relevant voltammetric curves and the steady-state polarisation curves were presented in figs. 5.5.1 and 5.5.12, respectively. As with the impedance measurements on the Mn electrodes outlined in section 6.3, all EIS data reported here were recorded continuously in the direction of increasing potential. Contrary to that observed for Mn electrodes, corrosion did not occur for nickel cobalt mixed oxide films at potentials below 0.82 V. This resulted in the possibility to extend the potential range at which the EIS was performed. Hence, we calculated the impedance at a maximum potential point of 0.82 V (*vs.* Hg/HgO).

Similar to that observed for Mn electrodes, it would appear from the phase angle *vs.* frequency plots and from the Nyquist plot of figures fig. 6.4.1 - 6.4.7 that the impedance response of all samples is characteristic of just two relaxation processes. Special mention to the sample with 100 % M Co content should be pointed out. The Nyquist plot in fig. 6.4.7a exhibit only a very large loop which suggests only a single relaxation process taking place. However, the phase angle *vs.* frequency plot in the same figure confront this idea. It can be noted in such plot that two relaxation processes occur at log -0.5 and log 2 Hz, respectively. Based on the equivalent circuit model employed to analyse these electrodes, one should expect to observe three relaxation time constants corresponding to: (i) the $Q_{dl}$ / $R_p$, (ii) the $Q_{sq}$ / $R_{sq}$, and (iii) $Q_{film}$ / $R_{film}$.

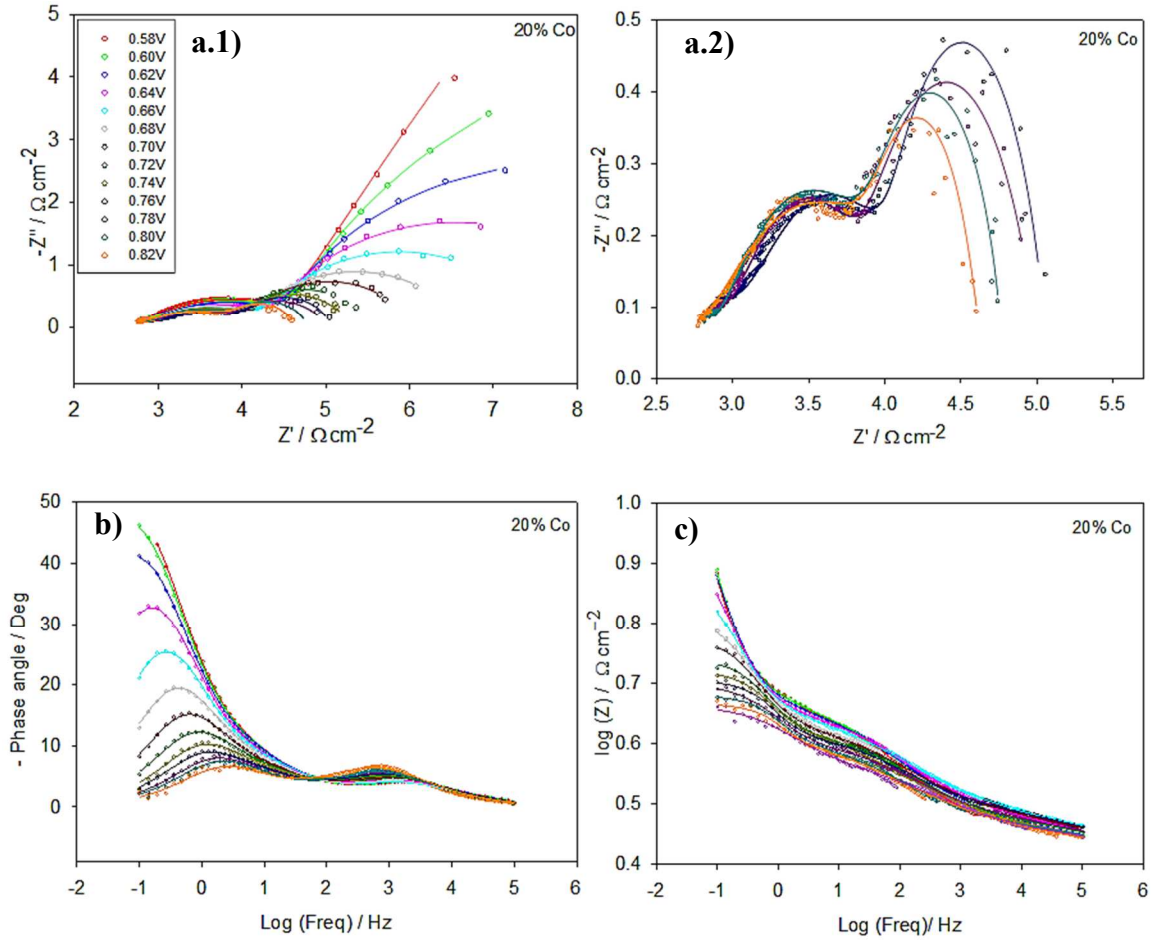
In the analysis of the Mn impedance data in section 6.3, it was observed superposition of various relaxation time constants due to: (i) the relaxation processes in the cell takes place at different time scales and thus, the slowest overlap the others, or (ii) the values of the RC time constants are similar and thus, they occur at the same time scale. Regarding the latter, we suggest that same effect takes place in nickel cobalt electrodes.




**d)**

| E/V | Qfilm / $\Omega^{-1}$ cm$^{-2}$ s$^{\alpha}$ | α | R film | Qdl / $\Omega^{-1}$ cm$^{-2}$ s$^{\alpha}$ | α dl | Rp | Qsq / $\Omega^{-1}$ cm$^{-2}$ s$^{\alpha}$ | α sq | Rsq | Rs |
|---|---|---|---|---|---|---|---|---|---|---|
| 0.58 | 4.31E-03 ± 8.26E-05 | 0.62 | 0.78 ± 6.81E-03 | 4.63E-02 ± 9.90E-04 | 0.74 | 2.43 ± 0.09 | 6.11E-02 ± 9.25E-04 | 0.76 | 151.4 ± 11.47 | 2.78±0.11 |
| 0.6 | 4.30E-03 ±7.88E-05 | 0.62 | 0.80 ± 6.72E-03 | 4.64E-02 ± 9.57E-04 | 0.74 | 2.52 ± 0.09 | 6.28E-02 ± 9.28E-04 | 0.76 | 89.1 ± 4.09 | 2.78±0.10 |
| 0.62 | 4.35E-03 ±6.57E-05 | 0.62 | 0.82 ± 5.68E-03 | 4.55E-02 ± 7.81E-04 | 0.74 | 2.5 9 ± 0.07 | 6.74E-02 ± 7.82E-04 | 0.76 | 48.7 ± 1.29 | 2.81±0.10 |
| 0.64 | 4.36E-03 ±7.01E-05 | 0.62 | 0.85 ± 6.28E-03 | 4.51E-02 ± 9.16E-04 | 0.74 | 2.13 ± 0.06 | 6.76E-02 ± 8.26E-04 | 0.76 | 22.7 ± 0.38 | 2.84±0.09 |
| 0.66 | 4.45E-03 ±1.11E-04 | 0.62 | 0.77 ± 9.85E-03 | 3.86E-02 ± 1.23E-03 | 0.74 | 1.70 ± 0.07 | 7.39E-02 ± 1.28E-04 | 0.76 | 11.9 ± 0.14 | 2.88±0.09 |
| 0.68 | 4.50E-03 ±8.77E-05 | 0.62 | 0.82 ± 8.86E-03 | 4.32E-02 ± 1.30E-03 | 0.74 | 1.71 ± 0.07 | 7.62E-02 ± 1.72E-04 | 0.76 | 6.6 ± 0.09 | 2.88±0.08 |
| 0.7 | 4.31E-03 ±6.85E-05 | 0.62 | 0.96 ± 8.91E-03 | 4.58E-02 ± 1.64E-03 | 0.74 | 1.54 ± 0.08 | 7.95E-02 ± 2.20E-04 | 0.76 | 4.1 ± 0.08 | 2.86±0.07 |
| 0.72 | 4.65E-03 ±8.01E-05 | 0.62 | 1.02 ± 1.13E-02 | 5.08E-02 ± 2.37E-03 | 0.74 | 1.57 ± 0.11 | 8.68E-02 ± 5.38E-04 | 0.76 | 2.7 ± 0.11 | 2.87±0.06 |
| 0.74 | 4.59E-03 ±1.10E-04 | 0.62 | 1.05 ± 1.85E-02 | 5.07E-02 ± 4.23E-03 | 0.74 | 1.32 ± 0.17 | 9.60E-02 ± 1.33E-04 | 0.76 | 1.9 ± 0.17 | 2.82±0.06 |
| 0.76 | 4.54E-03 ±9.00E-05 | 0.62 | 1.09 ± 1.46E-02 | 5.78E-02 ± 4.26E-03 | 0.74 | 1.23 ± 0.15 | 1.09E-01 ± 1.78E-04 | 0.76 | 1.5 ± 0.15 | 2.84±0.06 |
| 0.78 | 5.05E-03 ±1.26E-04 | 0.62 | 1.21 ± 2.34E-02 | 8.59E-02 ± 0.0116 | 0.74 | 1.69 ± 0.76 | 1.79E-01 ± 4.28E-04 | 0.76 | 0.5 ± 0.77 | 2.85±0.06 |
| 0.8 | 5.06E-03 ±1.20E-04 | 0.62 | 1.22 ± 2.02E-02 | 8.83E-02 ± 8.49E-03 | 0.74 | 1.82 ± 0.47 | 6.28E-01 ± 2.69E-04 | 0.76 | 0.2 ± 0.47 | 2.87±0.06 |

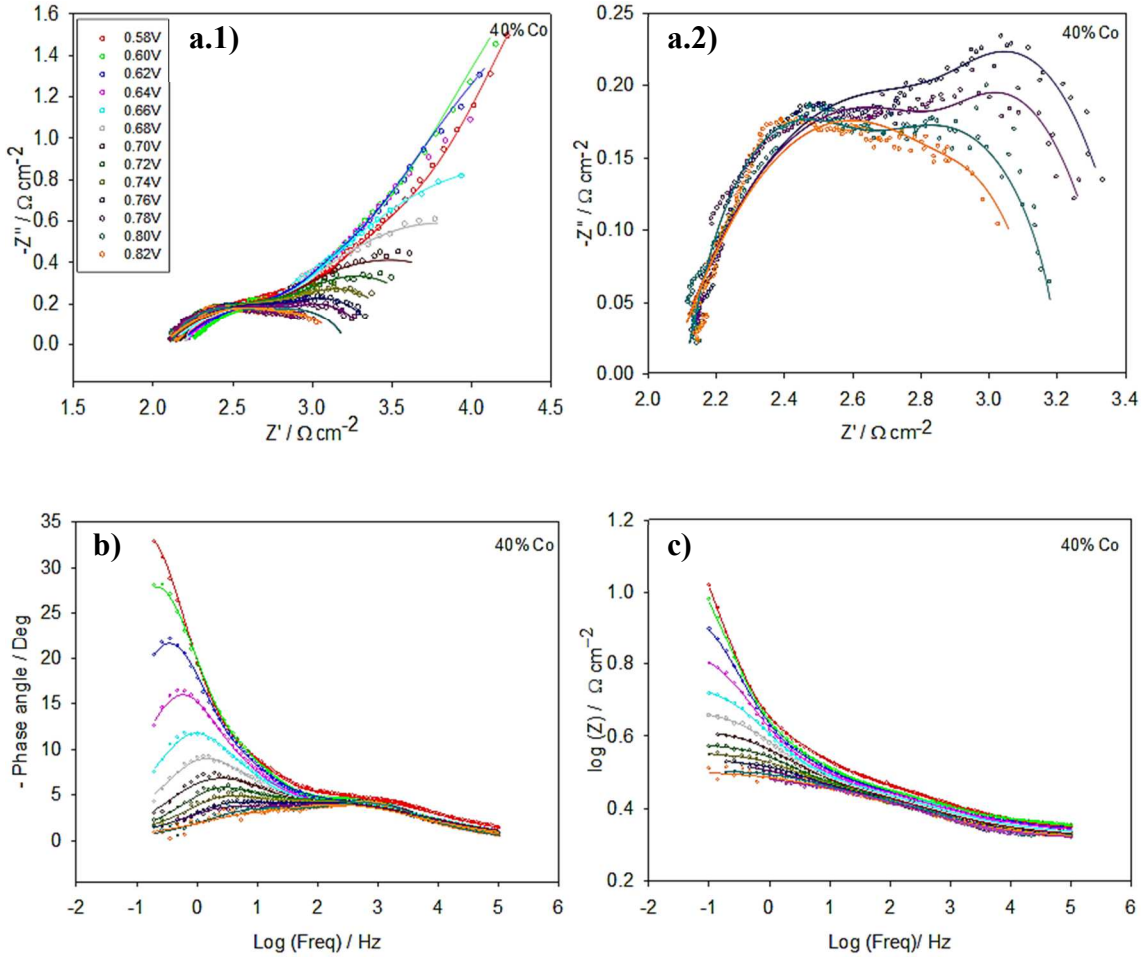
Figure 6.4.1 Electrochemical impedance spectra recorded in 1.0 M NaOH at 25°C for a series of potentials associated with active oxygen evolution for a nickel cobalt mixed oxide electrode with 0 % M Co content in the Nyquist (a.1-a.2) and Bode (b-c) format. The experiment data is represented by discrete points and the simulated impedance response is represented by a continuous line. Image a.2 represent a zoomed in version of the Nyquist plot for potentials between 0.76 - 0.82 V. Table d) presents the optimum fit parameters for the CNLS fitting to circuit in fig. 6.2.1 of the raw impedance response.




**d)**

| E/V | Qfilm / $\Omega^{-1}$ cm$^{-2}$ s$^{\alpha}$ | α film | R film /Ω | Qdl / $\Omega^{-1}$ cm$^{-2}$ s$^{\alpha}$ | α dl | Rp /Ω | Qsq / $\Omega^{-1}$ cm$^{-2}$ s$^{\alpha}$ | α sq | Rsq /Ω | Rs /Ω |
|---|---|---|---|---|---|---|---|---|---|---|
| 0.58 | 3.58E-02 ± 7.82E-04 | 0.57 | 1.80 ± 0.05 | 1.92E-02 ± 3.63E-03 | 0.87 | 1.82E-01 ± 2.95E-02 | 3.08E-02 ± 6.71E-04 | 0.81 | 29.20 ± 4.98 | 2.52 ± 0.23 |
| 0.6 | 3.01E-02 ± 8.64E-04 | 0.57 | 1.91 ± 0.02 | 3.36E-03 ± 1.64E-03 | 0.87 | 2.69E-02 ± 1.38E-02 | 3.19E-02 ± 4.58E-04 | 0.81 | 13.24 ± 0.59 | 2.38 ± 0.19 |
| 0.62 | 2.88E-02 ± 6.11E-04 | 0.57 | 1.84 ± 0.01 | 1.44E-03 ± 6.52E-04 | 0.87 | 2.40E-02 ± 8.76E-03 | 3.15E-02 ± 5.40E-04 | 0.81 | 7.30 ± 0.37 | 2.40 ± 0.26 |
| 0.64 | 2.87E-02 ± 4.87E-04 | 0.57 | 1.65 ± 0.01 | 2.90E-04 ± 2.30E-05 | 0.87 | 9.82E-02 ± 6.10E-03 | 3.16E-02 ± 3.77E-04 | 0.81 | 4.45 ± 0.06 | 1.99 ± 0.27 |
| 0.66 | 2.88E-02 ± 4.03E-04 | 0.57 | 1.49 ± 0.01 | 1.01E-04 ± 4.55E-06 | 0.87 | 1.51E-01 ± 4.37E-03 | 3.02E-02 ± 3.75E-04 | 0.81 | 3.09 ± 0.04 | 2.23 ± 0.22 |
| 0.68 | 3.00E-02 ± 6.55E-04 | 0.57 | 1.54 ± 0.01 | 7.69E-04 ± 1.53E-04 | 0.87 | 4.27E-02 ± 7.45E-03 | 3.00E-02 ± 7.47E-04 | 0.81 | 2.19 ± 0.03 | 2.68 ± 0.21 |
| 0.7 | 3.21E-02 ± 6.31E-04 | 0.57 | 1.38 ± 0.01 | 1.35E-04 ± 9.25E-06 | 0.87 | 1.23E-01 ± 5.70E-03 | 2.88E-02 ± 6.66E-04 | 0.81 | 1.77 ± 0.03 | 2.77 ± 0.20 |
| 0.72 | 3.08E-02 ± 1.04E-03 | 0.57 | 1.38 ± 0.02 | 5.49E-04 ± 1.37E-04 | 0.87 | 4.78E-02 ± 1.04E-02 | 2.88E-02 ± 1.47E-03 | 0.81 | 1.36 ± 0.04 | 2.78 ± 0.28 |
| 0.74 | 3.63E-02 ± 1.46E-03 | 0.57 | 1.34 ± 0.02 | 1.07E-03 ± 1.90E-04 | 0.87 | 7.05E-02 ± 1.31E-02 | 3.05E-02 ± 1.54E-03 | 0.81 | 1.13 ± 0.03 | 2.77 ± 0.25 |
| 0.76 | 3.64E-02 ± 1.39E-03 | 0.57 | 1.18 ± 0.02 | 9.89E-05 ± 8.20E-06 | 0.87 | 1.62E-01 ± 9.37E-03 | 2.92E-02 ± 1.98E-03 | 0.81 | 0.99 ± 0.03 | 2.68 ± 0.30 |
| 0.78 | 3.42E-02 ± 1.08E-03 | 0.57 | 1.19 ± 0.01 | 2.42E-04 ± 3.03E-05 | 0.87 | 8.61E-02 ± 8.37E-03 | 3.26E-02 ± 1.87E-03 | 0.81 | 0.95 ± 0.03 | 2.75 ± 0.19 |
| 0.8 | 4.17E-02 ± 2.35E-03 | 0.57 | 1.22 ± 0.02 | 1.34E-03 ± 4.20E-04 | 0.87 | 4.98E-02 ± 1.60E-02 | 3.24E-02 ± 3.05E-03 | 0.81 | 0.81 ± 0.03 | 2.80 ± 0.17 |

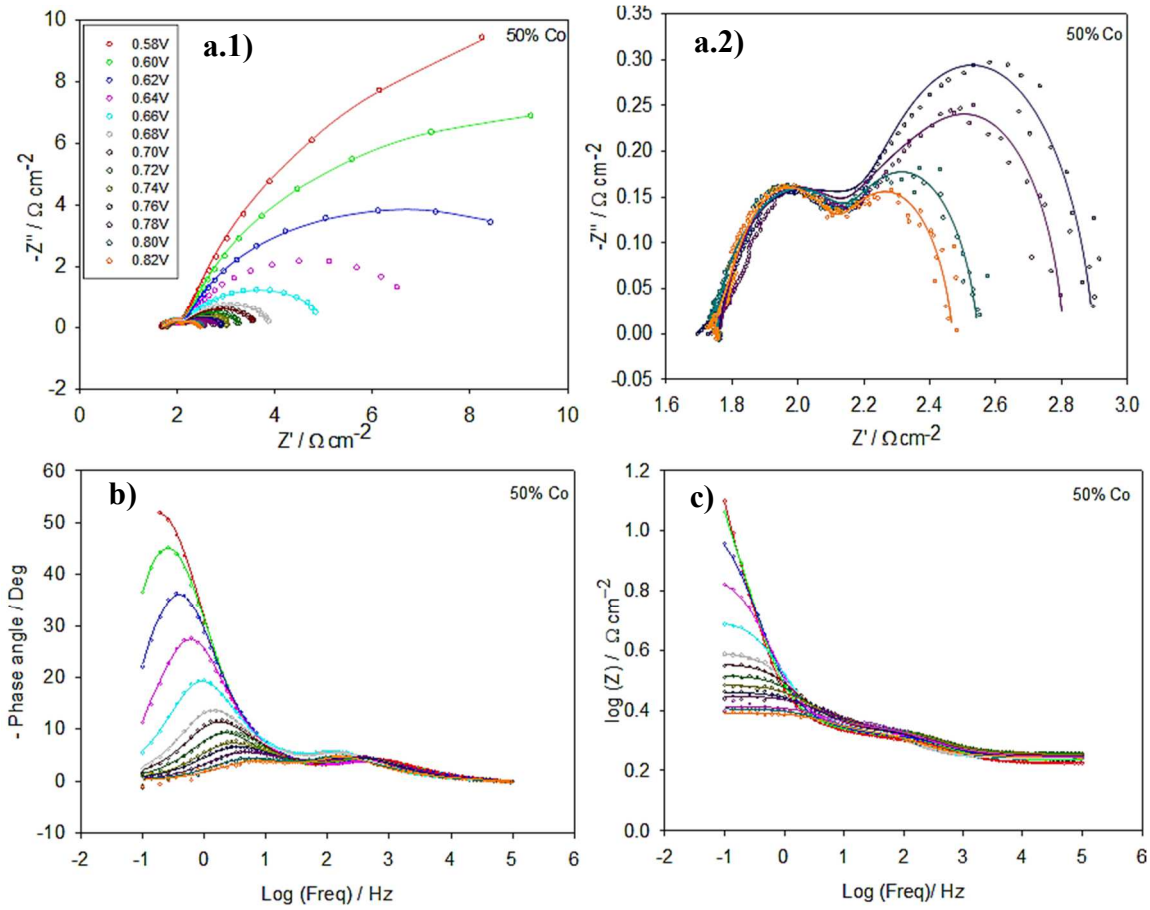
Figure 6.4.2 Electrochemical impedance spectra recorded in 1.0 M NaOH at 25°C for a series of potentials associated with active oxygen evolution for a nickel cobalt mixed oxide electrode with 20 % M Co content in the Nyquist (a.1-a.2) and Bode (b-c) format. The experiment data is represented by discrete points and the simulated impedance response is represented by a continuous line. Image a.2 represent a zoomed in version of the Nyquist plot for potentials between 0.76 - 0.82 V. Table d) presents the optimum fit parameters for the CNLS fitting to circuit in fig. 6.2.1 of the raw impedance response.




**d)**

| E/V | Qfilm / $\Omega^{-1}$ cm$^{-2}$ s$^{\alpha}$ | α | R film | Qdl / $\Omega^{-1}$ cm$^{-2}$ s$^{\alpha}$ | α dl | Rp | Qsq / $\Omega^{-1}$ cm$^{-2}$ s$^{\alpha}$ | α sq | Rsq | Rs |
|---|---|---|---|---|---|---|---|---|---|---|
| 0.58 | 0.17 ± 4.17E-02 | 0.7 | 1.28E-01 ± 1.64E-02 | 3.93E-05 ± 1.32E-03 | 0.9 | 3.44E-02 ±5.60E-01 | 8.74E-02 ± 1.39E-03 | 0.92 | 97.65 ± 6.34 | 2.68 ± 0.03 |
| 0.6 | 0.14 ± 3.72E-02 | 0.7 | 1.11E-01 ± 1.25E-02 | 6.81E-05 ± 1.39E-03 | 0.9 | 2.99E-02 ± 2.96E-01 | 8.39E-02 ± 1.46E-03 | 0.92 | 36.62 ± 1.91 | 2.70 ± 0.04 |
| 0.62 | 0.15 ± 3.94E-02 | 0.7 | 9.14E-02 ± 1.25E-02 | 1.86E-04 ± 1.59E-03 | 0.9 | 1.96E-02 ± 7.89E-02 | 8.22E-02 ± 1.64E-03 | 0.92 | 13.22 ± 0.14 | 2.72 ± 0.08 |
| 0.64 | 0.12 ± 1.92E-02 | 0.7 | 9.98E-02 ± 7.56E-03 | 9.14E-05 ± 1.00E-03 | 0.9 | 2.50E-02 ± 1.32E-01 | 8.17E-02 ± 1.10E-03 | 0.92 | 5.68 ± 0.03 | 2.72 ± 0.03 |
| 0.66 | 0.13 ± 1.15E-02 | 0.7 | 1.02E-01 ± 4.43E-03 | 8.18E-04 ± 8.91E-04 | 0.9 | 1.35E-02 ± 5.74E-03 | 8.15E-02 ± 9.86E-04 | 0.92 | 3.01 ± 0.01 | 2.74 ± 0.05 |
| 0.68 | 0.12 ± 5.83E-03 | 0.7 | 1.14E-01 ± 3.09E-03 | 4.33E-04 ± 8.91E-04 | 0.9 | 1.16E-02 ± 1.07E-02 | 8.32E-02 ± 9.52E-04 | 0.92 | 1.88 ± 0.01 | 2.74 ± 0.06 |
| 0.7 | 0.10 ± 4.08E-03 | 0.7 | 1.22E-01 ± 2.90E-03 | 1.26E-03 ± 1.03E-03 | 0.9 | 9.59E-03 ± 3.00E-03 | 8.40E-02 ± 1.12E- 03 | 0.92 | 1.32 ± 0.02 | 2.75 ± 0.08 |
| 0.72 | 0.09 ± 3.96E-03 | 0.7 | 1.43E-01 ± 4.45E-03 | 1.06E-03 ± 7.05E-04 | 0.9 | 1.19E-02 ± 3.03E-03 | 8.57E-02 ± 1.30E-03 | 0.92 | 1.02 ± 0.01 | 2.74 ± 0.09 |
| 0.74 | 0.10 ± 5.18E-03 | 0.7 | 1.14E-01 ± 3.43E-03 | 1.08E-03 ± 6.4 8E-04 | 0.9 | 1.26E-02 ± 2.91E-03 | 8.74E-02 ± 1.23E-03 | 0.92 | 0.81 ± 0.01 | 2.78 ± 0.05 |
| 0.76 | 0.09 ± 3.38E-03 | 0.7 | 1.55E-01 ± 5.18E-03 | 2.95E-04 ± 4.38E-04 | 0.9 | 1.58E-02 ± 1.05E-02 | 9.51E-02 ± 1.80E-03 | 0.92 | 0.66 ± 0.01 | 2.77 ± 0.03 |
| 0.78 | 0.11 ± 7.29E-03 | 0.7 | 1.48E-01 ± 9.35E-03 | 9.35E-04 ± 5.10E-04 | 0.9 | 1.72E-02 ± 3.61E-03 | 9.80E-02 ± 3.62E-03 | 0.92 | 0.56 ± 0.01 | 2.78 ± 0.06 |
| 0.8 | 0.17 ± 2.20E-02 | 0.7 | 2.24E-01 ± 5.04E-02 | 1.76E-02 ± 2.73E-03 | 0.9 | 5.13E-02 ± 8.48E-03 | 1.33E-01 ± 2.73E-02 | 0.92 | 0.39 ± 0.05 | 2.77 ± 0.04 |

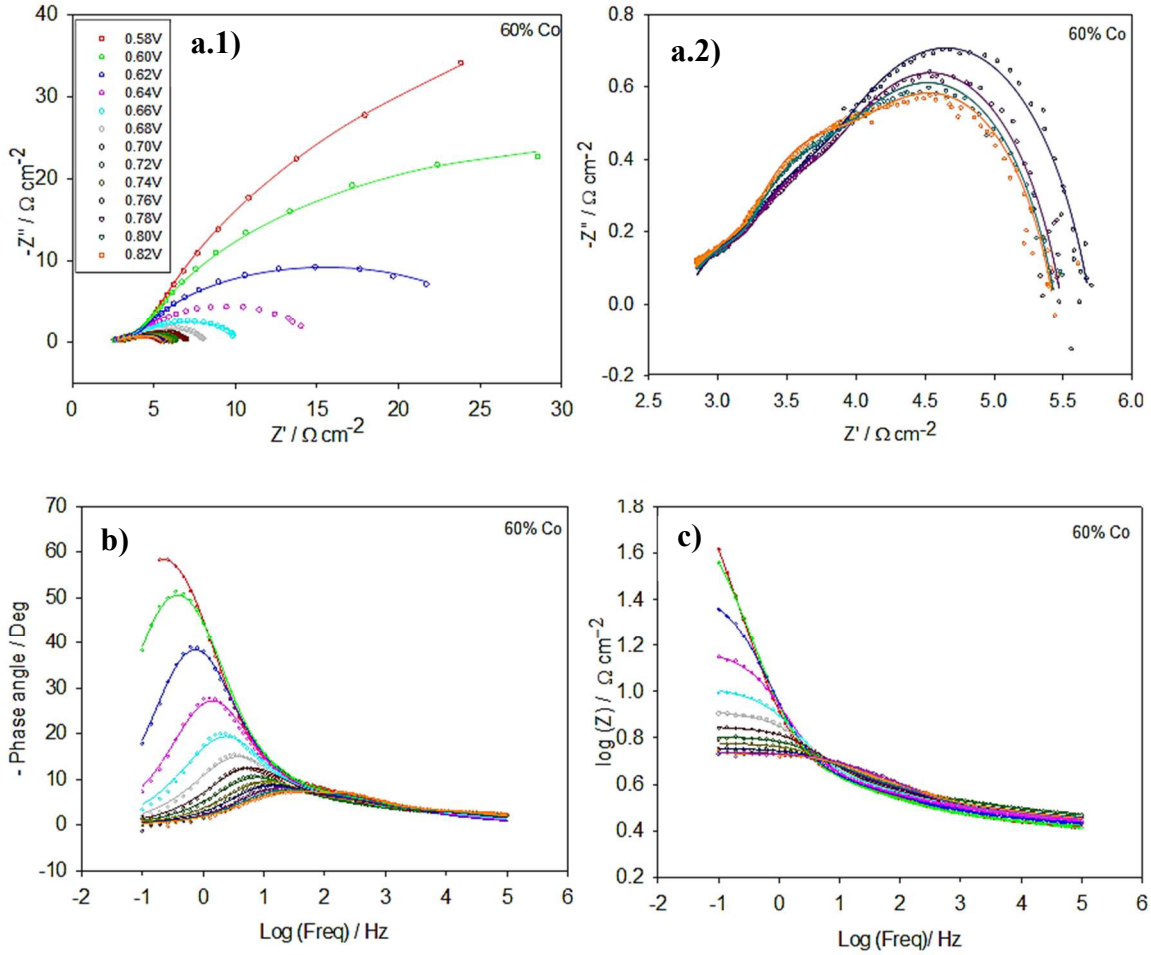
Figure 6.4.3 Electrochemical impedance spectra recorded in 1.0 M NaOH at 25°C for a series of potentials associated with active oxygen evolution for a nickel cobalt mixed oxide electrode with 40 % M Co content in the Nyquist (a.1-a.2) and Bode (b-c) format. The experiment data is represented by discrete points and the simulated impedance response is represented by a continuous line. Image a.2 represent a zoomed in version of the Nyquist plot for potentials between 0.76 - 0.82 V. Table d) presents the optimum fit parameters for the CNLS fitting to circuit in fig. 6.2.1 of the raw impedance response.




**d)**

| E/V | Qfilm / $\Omega^{-1}$ $cm^{-2}$ $s^{\alpha}$ | α film | R film /Ω | Qdl / $\Omega^{-1}$ $cm^{-2}$ $s^{\alpha}$ | α dl | Rp /Ω | Qsq / $\Omega^{-1}$ $cm^{-2}$ $s^{\alpha}$ | α sq | Rsq /Ω | Rs |
|---|---|---|---|---|---|---|---|---|---|---|
| 0.58 | 4.66E-03±1.59E-04 | 0.79 | 0.38±0.01 | 6.10E-02±4.93E-03 | 0.96 | 0.73±0.20 | 6.37E-02±4.35E-03 | 0.84 | 27.06±0.88 | 1.68±0.68 |
| 0.6 | 5.28E-03±1.53E-04 | 0.79 | 0.38±0.01 | 6.21E-02±4.03E-03 | 0.96 | 0.86±0.20 | 5.86E-02±3.09E-03 | 0.84 | 15.55±0.37 | 1.72±0.72 |
| 0.62 | 5.05E-03±1.35E-04 | 0.79 | 0.36±0.01 | 5.34E-02±2.94E-03 | 0.96 | 0.66±0.11 | 6.62E-02±2.08E-03 | 0.84 | 8.47±0.15 | 1.73±0.73 |
| 0.64 | 5.54E-03±1.30E-04 | 0.79 | 0.35±0.00 | 5.23E-02±2.86E-03 | 0.96 | 0.59±0.09 | 6.89E-02±1.66E-03 | 0.84 | 4.52±0.10 | 1.77±0.77 |
| 0.66 | 1.11E-02±1.36E-04 | 0.79 | 0.47±0.01 | 7.14E-02±2.32E-03 | 0.96 | 1.16±0.13 | 9.93E-02±1.18E-02 | 0.84 | 1.66±0.14 | 1.75±0.75 |
| 0.68 | 1.02E-02±1.09E-04 | 0.79 | 0.46±0.01 | 6.54E-02±2.98E-03 | 0.96 | 0.70±0.09 | 1.10E-01±1.34E-02 | 0.84 | 1.02±0.09 | 1.73±0.73 |
| 0.7 | 5.68E-03±9.16E-05 | 0.79 | 0.38±0.00 | 5.49E-02±2.12E-03 | 0.96 | 0.59±0.05 | 1.35E-01±1.51E-02 | 0.84 | 0.84±0.05 | 1.78±0.78 |
| 0.72 | 5.49E-03±1.38E-04 | 0.79 | 0.39±0.01 | 4.72E-02±7.77E-03 | 0.96 | 0.29±0.08 | 1.05E-01±1.16E-02 | 0.84 | 0.81±0.09 | 1.80±0.80 |
| 0.74 | 5.59E-03±1.25E-04 | 0.79 | 0.38±0.01 | 4.46E-02±3.66E-03 | 0.96 | 0.37±0.04 | 1.67E-01±2.71E-02 | 0.84 | 0.51±0.05 | 1.80±0.80 |
| 0.76 | 6.08E-03±3.15E-04 | 0.79 | 0.35±0.07 | 2.62E-02±2.14E-02 | 0.91 | 0.20±0.05 | 9.56E-02±1.14E-02 | 0.84 | 0.59±0.11 | 1.76±0.76 |
| 0.78 | 5.43E-03±1.52E-04 | 0.79 | 0.40±0.01 | 5.00E-02±6.16E-03 | 0.91 | 0.35±0.04 | 1.96E-01±6.10E-02 | 0.88 | 0.29±0.05 | 1.77±0.76 |
| 0.8 | 1.14E-02±9.36E-04 | 0.79 | 0.19±0.06 | 1.20E-02±4.75E-03 | 0.91 | 0.25±0.05 | 1.64E-01±1.08E-02 | 0.84 | 0.36±0.02 | 1.75±0.75 |

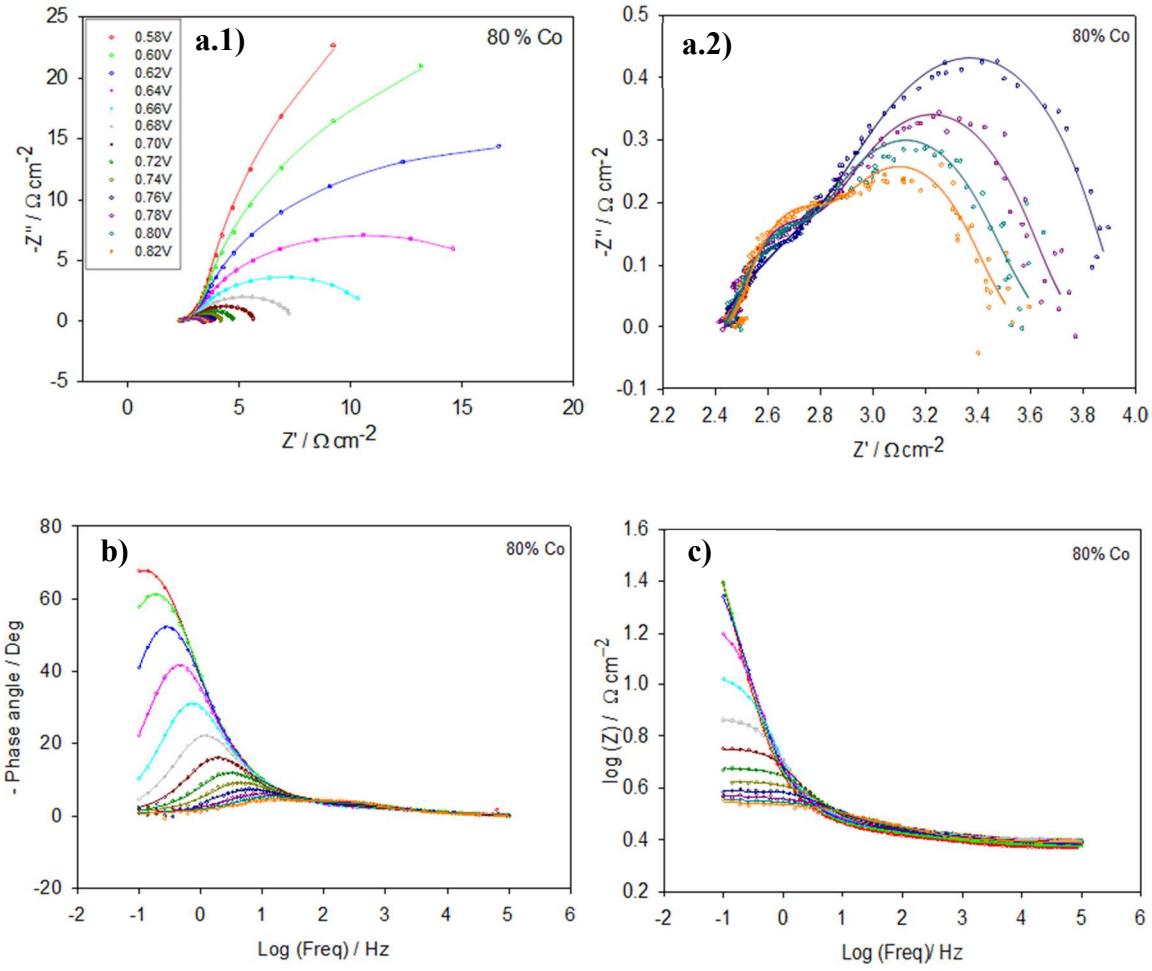
Figure 6.4.4 Electrochemical impedance spectra recorded in 1.0 M NaOH 25°C for a series of potentials associated with active oxygen evolution for a nickel cobalt mixed oxide electrode with 50 % M Co content in the Nyquist (a.1-a.2) and Bode (b-c) format. The experiment data is represented by discrete points and the simulated impedance response is represented by a continuous line. Image a.2 represent a zoomed in version of the Nyquist plot for potentials between 0.76 - 0.82 V. Table d) presents the optimum fit parameters for the CNLS fitting to circuit in fig 6.2.1 of the raw impedance response.




**d)**

| E/V | Qfilm / $\Omega^{-1}$ $cm^{-2}$ $s^{\alpha}$ | α film | R film /Ω | Qdl / $\Omega^{-1}$ $cm^{-2}$ $s^{\alpha}$ | α dl | Rp /Ω | Qsq / $\Omega^{-1}$ $cm^{-2}$ $s^{\alpha}$ | α sq | Rsq /Ω | Rs |
|---|---|---|---|---|---|---|---|---|---|---|
| 0.58 | 3.58E-02±8.95E04 | 0.55 | 2.09±0.08 | 2.21E-02±2.21E-03 | 0.96 | 3.53±2.83 | 1.35E-02±1.70E-03 | 0.74 | 120.79±10.39 | 2.59±0.39 |
| 0.6 | 3.56E-02±1.15E-03 | 0.55 | 1.83±0.10 | 1.80E-02±2.60E-03 | 0.96 | 2.28±1.86 | 1.55E-02±1.95E-03 | 0.74 | 57.72±4.33 | 2.59±0.39 |
| 0.62 | 3.42E-02±1.42E-03 | 0.55 | 1.66±0.10 | 1.70E-02±2.68E-03 | 0.96 | 2.12±1.65 | 1.81E-02±1.02E-03 | 0.74 | 20.70±2.12 | 2.68±0.48 |
| 0.64 | 2.70E-02±1.71E-03 | 0.55 | 1.33±0.11 | 1.04E-02±2.82E-03 | 0.96 | 0.89±0.51 | 2.43E-02±1.40E-03 | 0.74 | 10.19±0.74 | 2.73±0.53 |
| 0.66 | 1.96E-02±2.12E-03 | 0.55 | 0.95±0.08 | 4.46E-03±9.19E-04 | 0.96 | 0.62±0.07 | 3.12E-02±7.75E-04 | 0.74 | 6.14±0.15 | 2.76±0.56 |
| 0.68 | 1.35E-02±1.31E-03 | 0.55 | 0.80±0.03 | 2.70E-03±3.33E-04 | 0.96 | 0.52±0.03 | 3.10E-02±6.09E-04 | 0.74 | 4.14±0.06 | 2.79±0.59 |
| 0.7 | 1.26E-02±9.16E-04 | 0.55 | 0.78±0.02 | 2.56E-03±2.11E-04 | 0.96 | 0.59±0.02 | 2.87E-02±7.02E-04 | 0.74 | 2.98±0.04 | 2.73±0.53 |
| 0.72 | 1.28E-02±9.57E-04 | 0.55 | 0.86±0.03 | 2.96E-03±3.49E-04 | 0.96 | 0.51±0.03 | 3.06E-02±1.06E-03 | 0.74 | 2.25±0.05 | 2.80±0.60 |
| 0.74 | 1.04E-02±1.04E-03 | 0.55 | 0.79±0.03 | 1.75E-03±2.17E-04 | 0.96 | 0.47±0.02 | 2.54E-02±8.91E-04 | 0.74 | 2.03±0.04 | 2.70±0.50 |
| 0.76 | 1.57E-02±1.15E-03 | 0.55 | 0.87±0.05 | 2.35E-03±3.30E-04 | 0.96 | 0.48±0.02 | 2.66E-02±1.27E-03 | 0.74 | 1.62±0.05 | 2.74±0.54 |
| 0.78 | 1.05E-02±1.25E-03 | 0.55 | 0.76±0.03 | 1.46E-03±1.92E-04 | 0.96 | 0.50±0.03 | 2.36E-02±1.26E-03 | 0.74 | 1.53±0.04 | 2.71±0.51 |
| 0.8 | 1.16E-02±1.05E-03 | 0.55 | 0.77±0.03 | 1.51E-03±1.33E-04 | 0.96 | 0.62±0.02 | 2.54E-02±1.42E-03 | 0.74 | 1.36±0.04 | 2.71±0.51 |

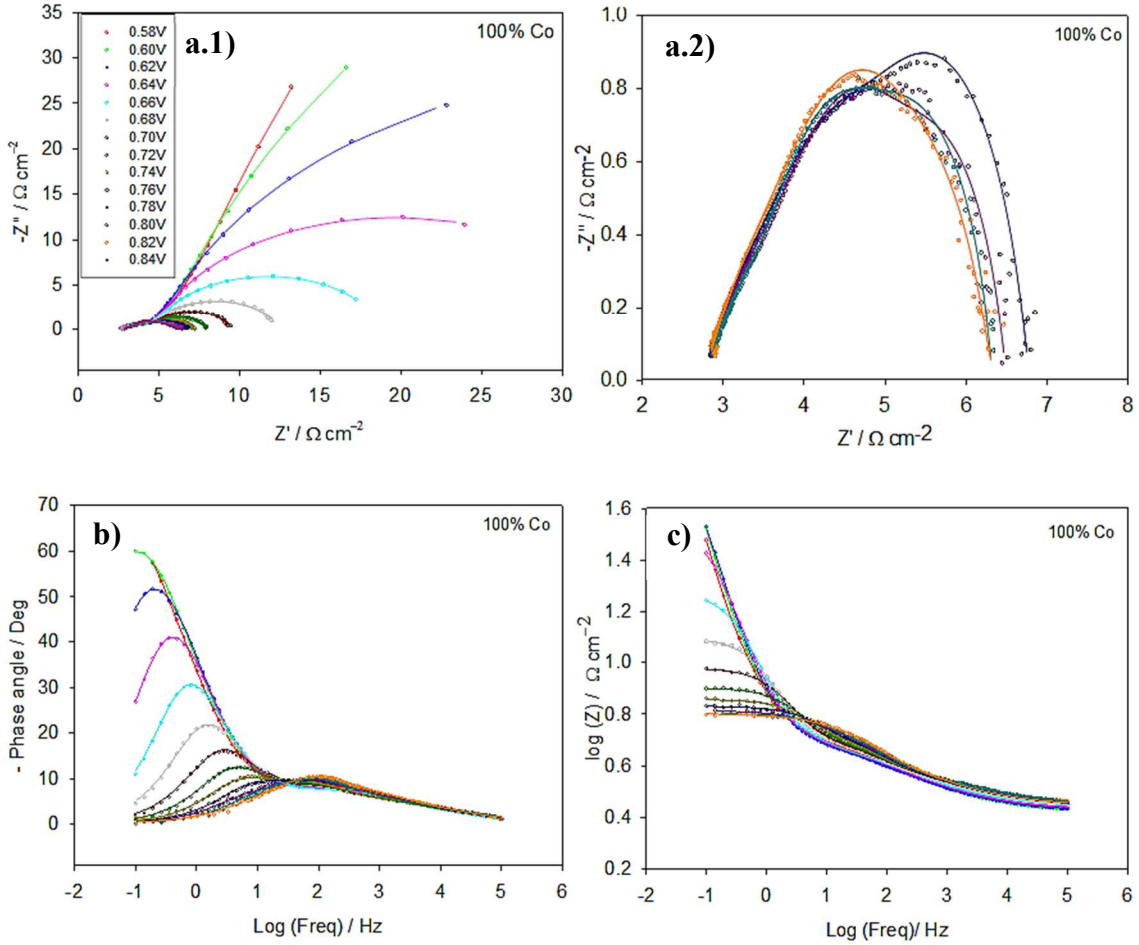
Figure 6.4.5 Electrochemical impedance spectra recorded in 1.0 M NaOH at 25°C for a series of potentials associated with active oxygen evolution for a nickel cobalt mixed oxide electrode with 60 % M Co content in the Nyquist (a.1-a.2) and Bode (b-c) format. The experiment data is represented by discrete points and the simulated impedance response is represented by a continuous line. Image a.2 represent a zoomed in version of the Nyquist plot for potentials between 0.76 - 0.82 V. Table d) presents the optimum fit parameters for the CNLS fitting to circuit in fig. 6.2.1 of the raw impedance response.




**d)**

| E/V | Qfilm / $\Omega^{-1}$ $cm^{-2}$ $s^{\alpha}$ | α film | R film /Ω | Qdl / $\Omega^{-1}$ $cm^{-2}$ $s^{\alpha}$ | α dl | Rp /Ω | Qsq / $\Omega^{-1}$ $cm^{-2}$ $s^{\alpha}$ | α sq | Rsq /Ω | Rs /Ω |
|---|---|---|---|---|---|---|---|---|---|---|
| 0.58 | 1.44E-01 ± 4.79E-03 | 0.45 | 0.77 ± 0.03 | 3.95E-02 ±1.16E-03 | 0.95 | 3.14 ± 0.26 | 2.75E-02 ± 1.05E-03 | 0.91 | 112.77 ± 3.35 | 2.31 ± 0.19 |
| 0.6 | 1.38E-01 ± 4.43E-03 | 0.45 | 0.79 ± 0.03 | 3.84E-02 ± 1.17E-03 | 0.95 | 2.94 ± 0.27 | 2.57E-02 ± 1.01E-03 | 0.91 | 57.78 ± 0.91 | 2.36 ± 0.19 |
| 0.62 | 1.41E-01 ± 3.98E-03 | 0.45 | 0.83 ± 0.03 | 3.98E-02 ± 1.12E-03 | 0.95 | 3.27 ± 0.32 | 2.45E-02 ± 8.03E-04 | 0.91 | 27.01 ± 0.43 | 2.40 ± 0.17 |
| 0.64 | 1.43E-01 ± 5.03E-03 | 0.45 | 0.69 ± 0.03 | 3.60E-02 ± 1.19E-03 | 0.95 | 2.40 ± 0.22 | 2.93E-02 ± 7.23E-04 | 0.91 | 12.56 ± 0.26 | 2.47 ± 0.19 |
| 0.66 | 1.41E-01 ± 6.10E-03 | 0.45 | 0.70 ± 0.03 | 3.31E-02 ± 1.69E-03 | 0.95 | 1.67 ± 0.18 | 3.34E-02 ± 9.78E-04 | 0.91 | 6.04 ± 0.21 | 2.46 ± 0.22 |
| 0.68 | 1.54E-01 ± 4.05E-03 | 0.45 | 0.98 ± 0.04 | 4.40E-02 ± 1.85E-03 | 0.95 | 2.38 ± 0.26 | 6.78E-02 ± 1.70E-02 | 0.91 | 1.62 ± 0.29 | 2.47 ± 0.16 |
| 0.7 | 1.35E-01 ± 7.41E-03 | 0.45 | 0.71 ± 0.05 | 3.00E-02 ± 2.61E-03 | 0.95 | 1.03 ± 0.13 | 5.22E-02 ± 6.18E-03 | 0.91 | 1.52 ± 0.16 | 2.43 ± 0.27 |
| 0.72 | 1.32E-01 ± 5.41E-03 | 0.45 | 1.02 ± 0.07 | 4.66E-02 ± 4.42E-03 | 0.95 | 1.16 ± 0.17 | 7.56E-02 ± 3.62E-01 | 0.91 | 0.24 ± 0.20 | 2.42 ± 0.27 |
| 0.74 | 1.34E-01 ± 5.90E-03 | 0.45 | 1.02 ± 0.10 | 4.73E-02 ± 9.55E-03 | 0.95 | 0.67 ± 0.27 | 9.28E-02 ± 2.72E-01 | 0.91 | 0.22 ± 0.32 | 2.42 ± 0.27 |
| 0.76 | 1.25E-01 ± 6.60E-03 | 0.45 | 0.96 ± 0.09 | 4.63E-02 ± 1.05E-02 | 0.95 | 0.50 ± 0.14 | 1.13E-01 ± 4.26E-01 | 0.91 | 0.14 ± 0.19 | 2.41 ± 0.32 |
| 0.78 | 1.98E-01 ± 2.07E-02 | 0.45 | 0.74 ± 0.07 | 3.17E-03 ± 5.38E-04 | 0.95 | 0.15 ± 0.02 | 2.41E-01 ± 4.50E-03 | 0.91 | 0.47 ± 0.04 | 2.43 ± 0.35 |
| 0.8 | 2.08E-01 ± 2.81E-02 | 0.45 | 0.71 ± 0.07 | 2.82E-03 ± 6.05E-04 | 0.95 | 0.15 ± 0.02 | 2.65E-01 ± 4.63E-03 | 0.91 | 0.37 ± 0.04 | 2.43 ± 0.43 |

Figure 6.4.6 Electrochemical impedance spectra recorded in 1.0 M NaOH 25°C for a series of potentials associated with active oxygen evolution for a nickel cobalt mixed oxide electrode with 80 % M Co content in the Nyquist (a.1-a.2) and Bode (b-c) format. The experiment data is represented by discrete points and the simulated impedance response is represented by a continuous line. Image a.2 represent a zoomed in version of the Nyquist plot for potentials between 0.76 - 0.82 V. Table d) presents the optimum fit parameters for the CNLS fitting to circuit in fig. 6.2.1 of the raw impedance response.




**d)**

| E/V | Qfilm / $\Omega^{-1}$ $cm^{-2}$ $s^{\alpha}$ | α film | R film /Ω | Qdl / $\Omega^{-1}$ $cm^{-2}$ $s^{\alpha}$ | α dl | Rp /Ω | Qsq / $\Omega^{-1}$ $cm^{-2}$ $s^{\alpha}$ | α sq | Rsq /Ω | Rs |
|---|---|---|---|---|---|---|---|---|---|---|
| 0.58 | 1.98E-02 ± 8.18E-05 | 0.46 | 2.79 ± 1.00E-02 | 3.88E-02 ± 2.59E-04 | 0.91 | 16.35 ± 0.68 | 1.76E-02 ± 1.99E-04 | 0.85 | 386.68 ± 0.73 | 2.62 ± 0.12 |
| 0.6 | 2.03E-02 ± 1.63E-04 | 0.46 | 2.62 ± 1.56E-02 | 3.51E-02 ± 4.01E-04 | 0.91 | 14.83 ± 1.16 | 1.49E-02 ± 3.00E-04 | 0.85 | 157.88 ± 4.93 | 2.63 ± 0.23 |
| 0.62 | 2.05E-02 ± 3.14E-04 | 0.46 | 2.52 ± 3.05E-02 | 3.38E-02 ± 8.67E-04 | 0.91 | 13.68 ± 2.67 | 1.37E-02 ± 6.48E-04 | 0.85 | 57.01 ± 2.78 | 2.64 ± 0.28 |
| 0.64 | 2.07E-02 ± 3.41E-04 | 0.46 | 2.53 ± 3.52E-02 | 3.37E-02 ± 1.18E-03 | 0.91 | 13.13 ± 4.37 | 1.57E-02 ± 5.78E-03 | 0.85 | 15.99 ± 4.37 | 2.68 ± 0.32 |
| 0.66 | 1.99E-02 ± 3.30E-04 | 0.46 | 2.39 ± 4.69E-02 | 2.84E-02 ± 2.20E-03 | 0.91 | 4.69 ± 2.62 | 1.30E-02 ± 3.26E-03 | 0.85 | 9.04 ± 2.68 | 2.72 ± 0.26 |
| 0.68 | 1.69E-02 ± 5.78E-04 | 0.46 | 1.77 ± 9.04E-02 | 7.28E-03 ± 1.03E-03 | 0.91 | 0.85 ± 0.05 | 2.51E-02 ± 7.85E-04 | 0.85 | 7.18 ± 0.10 | 2.72 ± 0.29 |
| 0.7 | 1.58E-02 ± 5.18E-04 | 0.46 | 1.53 ± 6.19E-02 | 4.77E-03 ± 4.25E-04 | 0.91 | 0.90 ± 0.03 | 2.47E-02 ± 3.81E-04 | 0.85 | 4.35 ± 0.05 | 2.76 ± 0.43 |
| 0.72 | 1.74E-02 ± 4.86E-04 | 0.46 | 1.67 ± 7.46E-02 | 5.52E-03 ± 5.45E-04 | 0.91 | 0.93 ± 0.04 | 2.64E-02 ± 8.04E-04 | 0.85 | 2.60 ± 0.06 | 2.80 ± 0.15 |
| 0.74 | 1.53E-02 ± 4.97E-04 | 0.46 | 1.60 ± 6.27E-02 | 4.94E-03 ± 4.19E-04 | 0.91 | 1.15 ± 0.04 | 3.15E-02 ± 2.16E-03 | 0.85 | 1.70 ± 0.06 | 2.78 ± 0.36 |
| 0.76 | 1.79E-02 ± 5.66E-04 | 0.46 | 1.90 ± 1.31E-01 | 5.07E-03 ± 7.29E-04 | 0.91 | 0.94 ± 0.06 | 2.92E-02 ± 2.82E-03 | 0.85 | 1.21 ± 0.09 | 2.77 ± 0.35 |
| 0.78 | 1.55E-02 ± 5.30E-04 | 0.46 | 1.79 ± 8.64E-02 | 4.52E-03 ± 4.28E-04 | 0.91 | 1.18 ± 0.05 | 5.65E-02 ± 8.69E-03 | 0.85 | 0.78 ± 0.06 | 2.77 ± 0.34 |
| 0.8 | 1.43E-02 ± 6.71E-04 | 0.46 | 1.38 ± 6.89E-02 | 2.81E-03 ± 2.19E-04 | 0.91 | 1.30 ± 0.04 | 2.92E-02 ± 3.62E-03 | 0.85 | 0.89 ± 0.06 | 2.78 ± 0.34 |

Figure 6.4.7 Electrochemical impedance spectra recorded in 1.0 M NaOH at 25°C for a series of potentials associated with active oxygen evolution for a nickel cobalt mixed oxide electrode with 100 % M Co content in the Nyquist (a.1-a.2) and Bode (b-c) format. The experiment data is represented by discrete points and the simulated impedance response is represented by a continuous line. Image a.2 represent a zoomed in version of the Nyquist plot for potentials between 0.76 - 0.82 V. Table d) presents the optimum fit parameters for the CNLS fitting to circuit in fig. 6.2.1 of the raw impedance response.

Having presented the results of the EIS studies on various Ni/Co electrodes, we turn our attention to the task of extracting useful information from this data regarding the nature of the OER and the physical nature on these surfaces. Similar to that noticed for Mn electrodes, it is apparent for nickel cobalt electrodes that all fitted parameters are affected by oxygen evolution. An interesting aspect of the fitting parameters, presented in figs. 6.4.1d - 6.4.7d, is the fact that the double layer capacitance decreases with potential. This decrease in capacitance at higher oxygen evolution potentials is most readily understood. Vigorous oxygen bubble formation is obvious at higher potentials, and this is likely to lead to a drop in the value of the double layer capacitance due to a decrease in the effective electrode surface area. This might occur due to the exclusion of some of the "inner" surface area associated with the pores and fissures in oxide surface, as these regions become occupied by gaseous oxygen bubbles.[8] In addition, the geometric surface area might be somewhat diminished by the momentary adhesion of gas bubbles to the oxide layer - an effect that would lead to a time-average decrease in surface area over the course of the periods of imposition of the perturbation signal at a given frequency. The latter effect would also explain the slightly increase in the uncompensated solution resistance at higher OER current densities.[9] This observation might be attributed to two possible scenarios: (i) to a time-average decrease in the effective area for interfacial charge transfer, and/or (ii) to an increase in the resistivity of the electrolyte solution in the immediate vicinity of the electrode owing to the high concentration of bubbles.

Contrary in Mn electrodes, the modelled double layer capacitance is a more "pure" capacitance element than the simulated film capacitance, in that the α exponent for the latter is closer to the ideal value of unity for a capacitor displaying no frequency dispersion Mahjani[10] found that for porous conducting polymers, the parameter α from the CPE was ca. 0.6. Other authors related the presence of porous surfaces with $\alpha_{CPE} \sim 0.5$.[11] Taking into account the aforementioned results described by Mahjani[10] and Laisa[11] along with the results outlined in section 5.4.3, it can be assumed that the calculated values from the fitting impedance data are valid, since these were bound to be $\sim 0.5$. The calculation of the effective double layer capacitances $C_{dl,eff}$ was performed following the same approach than that done in section 6.3 for Mn electrodes. Fig. 6.4.8 shows the evolution of the double layer capacitance as a function of potential for a series of nickel cobalt mixed oxide with various % M Co content.

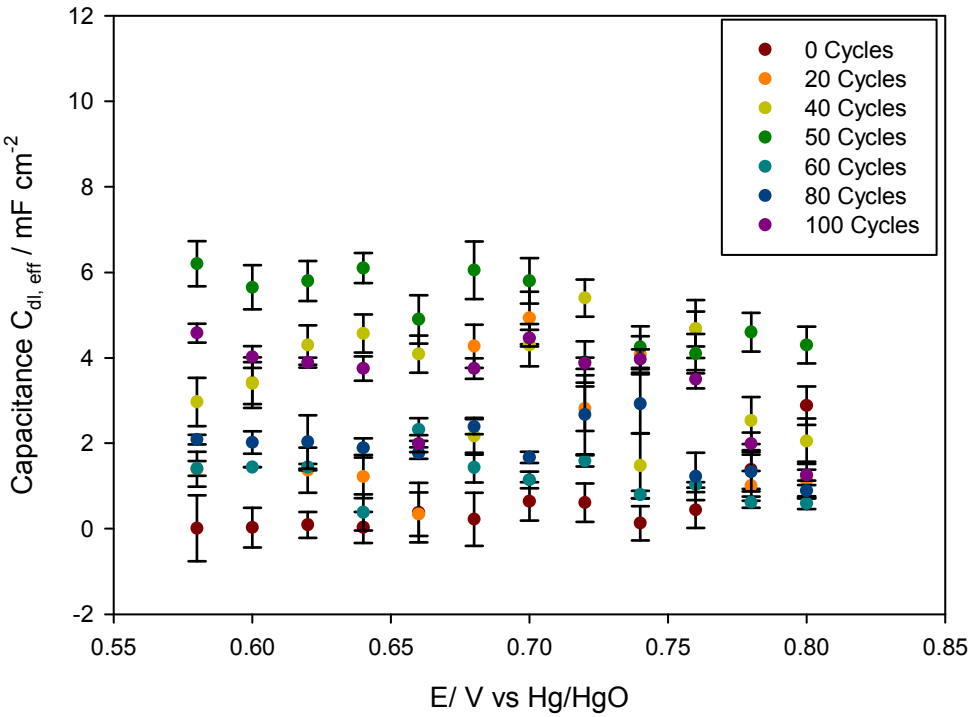



Figure 6.4.8 The optimum fitting values of $C_{dl,eff}$ plotted as a function of applied potential for various nickel cobalt mixed oxide electrodes with different % M Co content. These values were obtained from the fitting tables presented in figs. 6.4.1 - 6.4.7. Error bars represent standard deviations of three different samples.

It is apparent from fig. 6.4.8 that the double layer capacitance behaviour varies with the % M Co content on the electrode but showing little alteration with respect to the applied potential. If one compares fig. 6.3.6 with fig. 6.4.8, it will be observed a clear different capacitance behaviour between Mn and Ni/Co electrodes. This difference in the double layer capacitance behaviour may be related with the current density observed for each type of electrode. Note from fig. 4.5.5 and from fig. 5.5.14 that the current density for nickel cobalt mixed electrodes is one order of magnitude larger than that for Mn electrodes. This is particularly important since typically, the higher of the current density at a given equal overpotential, the greater of evolution of oxygen bubbles. In this perspective, it would be reasonable to ascribe the relatively lower double layer capacitance values for nickel cobalt mixed oxide electrodes with the greater production of oxygen bubbles. The double layer capacitance values outlined in fig. 6.4.8 agree with those calculated by potential step method in Table 5.7.1, although they do not match perfectly. We believe that the latter may be related to the large amount of oxygen gas produced on the surface of the electrodes which disturbs the homogeneity of the electrode surface and causes a similar surface nature for the different electrodes. That mentioned in section 6.3 regarding the precautions of analysing $C_{sq}$ values

also holds for nickel cobalt mixed oxides. The CNLS fitting data corresponding to $C_{sq}$ as function of % M Co content, during the OER is presented in fig. 6.4.9.

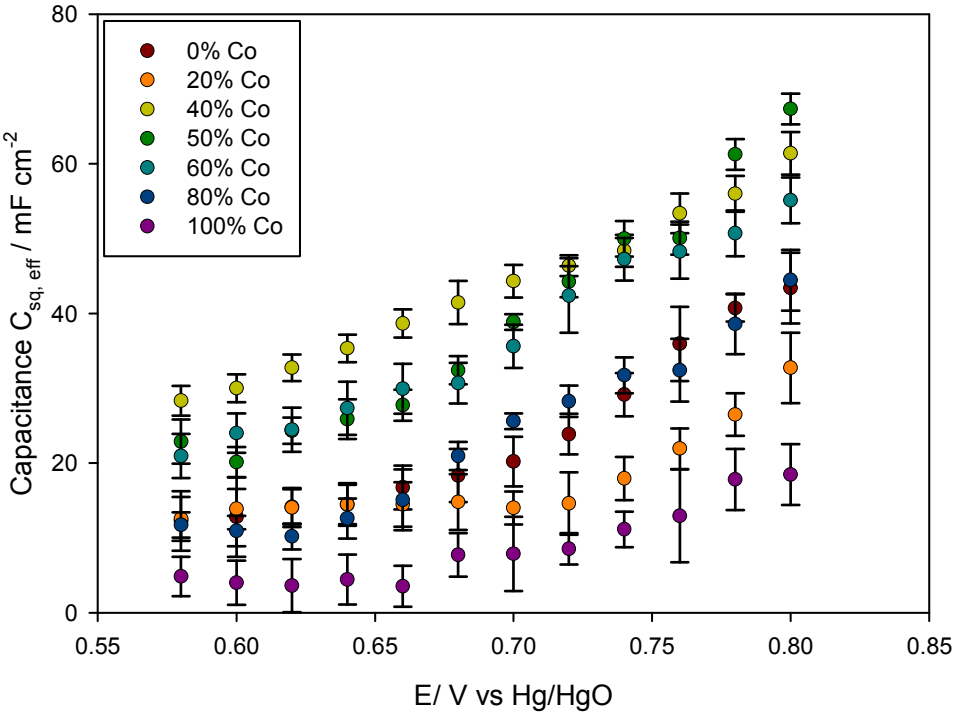



Figure 6.4.9 The optimum fitting values of $C_{dl,eff}$ plotted as a function of applied potential for various nickel cobalt mixed oxide electrodes with different % M Co content. These values were obtained from the fitting tables presented in figs. 6.4.1 - 6.4.7. Error bars represent standard deviations of three different samples.

We would like to remark again that the following discussion should be treated with caution since it is considered that only one intermediate specie was adsorbed on the surface. It is clear from fig. 6.4.9 that $C_{sq, eff}$ increases with applied potential. This trend was observed for all the samples regardless their % M Co content. The magnitude of the surfaquo group capacitance was found to be one order of magnitude larger than that observed for Mn electrodes (see fig. 6.3.7). The significant increment of capacitance behaviour on nickel cobalt mixed oxide electrodes may lie on the nature of the film surface of such electrodes. As previously mentioned in section 5.3.3, the surface of these type of electrodes was found to display surface nanoparticles of between 15 – 50 nm in diameter distributed uniformly across all faces of the oxide film. Such nanoparticles would give rise to the highly active surface area for the surfaquo groups to react in the surface of the film. Further, it was mentioned that electrodes with 40, 50 and 60 % M Co content possess larger and more compact nanoparticles distribution than the other samples. Taking into account that observed

in SEM images in section 5.4.3 and that in the kinetic analysis outlined in section 5.5.3, that observed in fig. 6.4.9 may be considered to be in line with the latter observations. The discussion of the resistance $R_{sq}$ and $R_p$ is now presented. The interpretation of these resistances, which was previously mentioned for Mn electrodes in section 6.3 also holds for Ni/Co electrodes. We present the evolution of both resistances, $R_{sq}$ and $R_p$ as a function of % M Co content for various nickel cobalt mixed oxide electrodes in fig. 6.4.10.

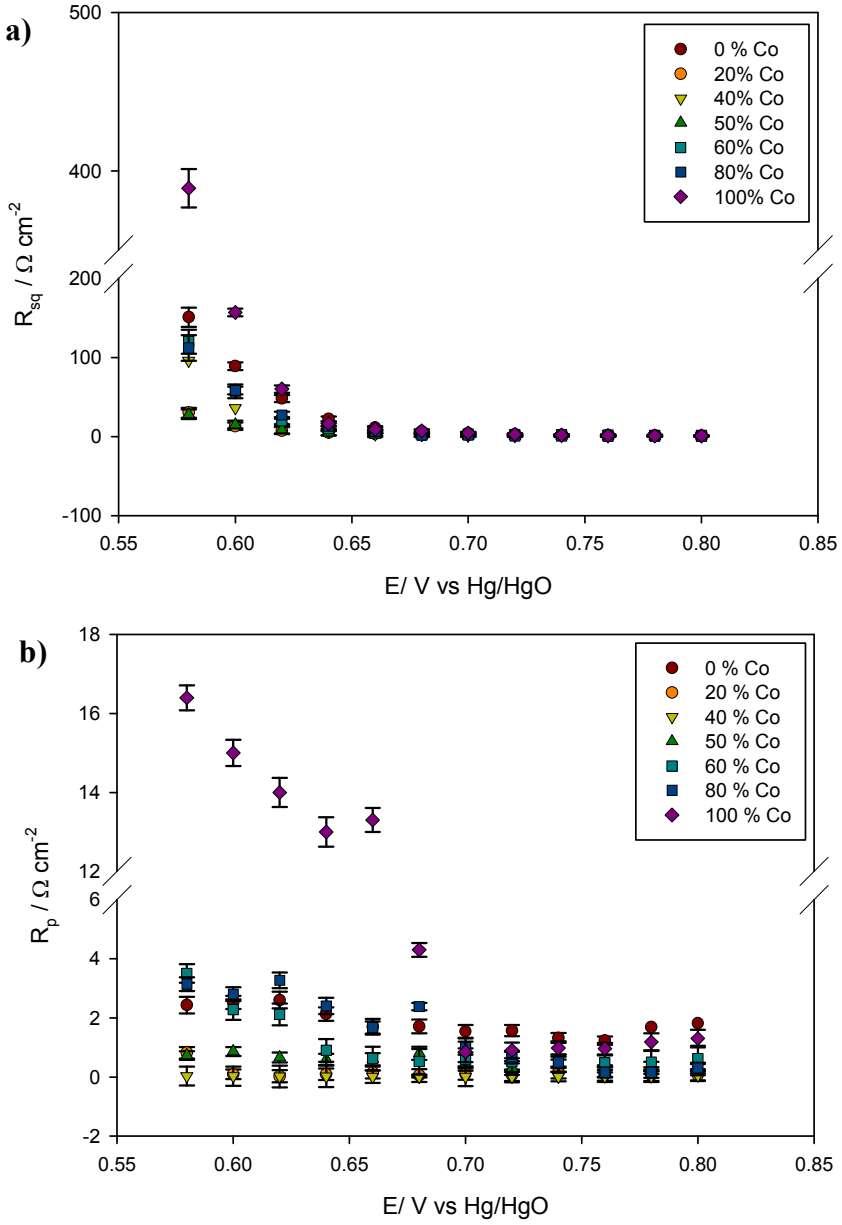



Figure 6.4.10 The optimum fitting values of a) $R_{sq}$ and b) $R_p$ plotted as a function of applied potential for various nickel cobalt mixed oxide electrodes with different % M Co content. These values were obtained from the fitting tables presented in figs. 6.4.1 - 6.4.7. Error bars represent standard deviations of three different samples.

Fig. 6.4.10 display the same $R_p$ and $R_{sq}$ trend found for Mn electrodes. At a potential range of 0.7 V to 0.8 V the surfaquo resistance reaches a plateau for all the electrodes. The latter may be explained by the fact that as the potential is increased, the intermediate species are more readily formed and therefore $R_{sq}$ decreases. As expected for a Faradaic process, the polarisation resistance for each electrode with increasing potential produced an enhancement of electron transfer kinetics. It was found little difference in the $R_p$ values as potential was increased for all the electrodes except for the pure nickel oxide electrode (0 % M Co content).

As mentioned previously, the $R_p$ is related to the overall rate of the OER, thus the observation of approximately constant $R_p$ values regardless the potential suggests that the overall rate remains constant in such potential range. Interestingly, it was found that for both $R_p$ and $R_{sq}$, the electrode with 0 % M Co exhibits significant differences with respect to the other electrodes. The surfaquo resistance and the polarisation resistance were found to be one order of magnitude higher than the other electrodes. The significant difference between the latter and the other electrodes may arise from the fact that NiO possesses different conductivity proprieties that $NiCo_2O_4$ or $Co_3O_4$ as it was previously mentioned in section 1.4. The latter would result in a slow electron transfer, confirmed in fig. 6.4.10b, which would yield to a slow surfaquo group's consumption on the surface and therefore, a large surfaquo resistance should be expected. This is also confirmed in fig. 6.4.10a which displays a large $R_{sq}$ resistance for the samples with 0 % M Co content.

## 6.5 Derivation of Tafel Slopes from Impedance Data

In this section the Tafel slope values obtained using EIS are presented. A summary of that introduced in section 3.7.5, regarding the determination of Tafel slopes form impedance data, is presented first followed by the presentation of results for both manganese oxide and nickel cobalt mixed oxide electrodes. Recall from section 3.7.5 that it should be possible to extract the value of the oxygen evolution Tafel slope, $b$, from the value of the total Faradaic resistance. The relevant expression is presented below:

$$log\left(\frac{1}{R_{far}}\right) = \frac{\eta}{b} + log\left(\frac{2.303 i_0}{b}\right) \tag{6.5.1}$$

Eqn. 6.5.1 implies that the slope of a plot of $\log\left(\frac{1}{R_{far}}\right)$ against η is equal to the inverse of the Tafel slope. In preparing the plots presented below, the value of the $R_{far}$ was extracted directly from the $R_{sq}$ and $R_p$ fitting parameters presented in fig. 6.4.1d - 6.4.7d. Therefore, the $R_{far}$ may be expressed as:

$$R_{far} = R_{sq} + R_p \tag{6.5.2}$$

The plots of $\log\left(\frac{1}{R_{far}}\right)$ vs. $\eta$ generated for the various thickness of hydrous manganese oxide films are presented in figs. 6.5.1 and 6.5.2. It is evident that there is a satisfactory agreement between the Tafel slopes presented in fig. 6.5.1 and 6.5.2 obtained from the impedance data, $b_{EIS}$, and those obtained by the steady-state polarisation method in fig. 4.5.1.

The observed agreement between the two methods suggests that the measured slopes do indeed characterise the oxygen evolution reaction in the steady-state. In addition, the fact that the ac impedance technique also distinguishes between the Tafel slopes characteristic of various Mn film thicknesses indicates authenticity of the existence of different types of kinetic behaviour for these systems, as was postulated and discusses in chapter 4.

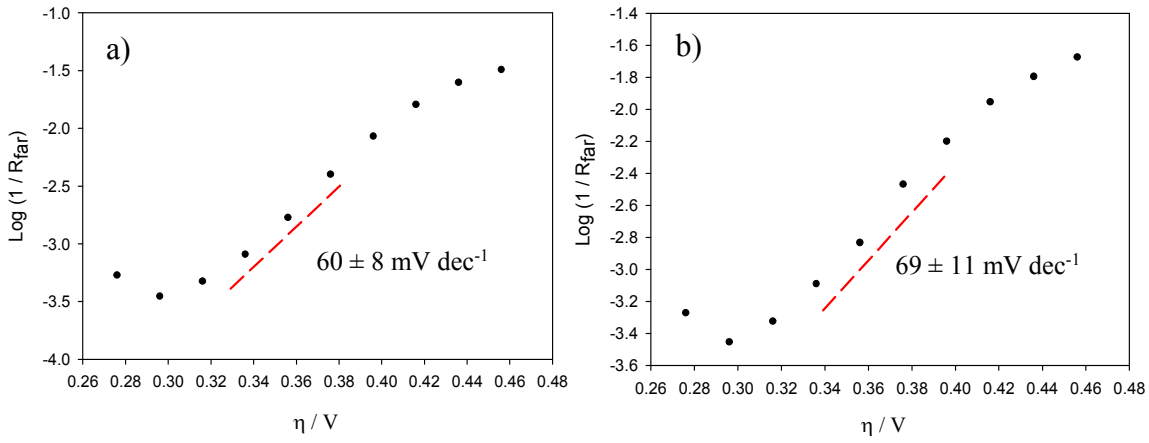



Figure 6.5.1 Log $(R_{far})^{-1}$ *vs.* $\eta$ of a) 25, and b) 250 potential cycles Mn electrodes in 1.0 M NaOH at 25°C. Plots were constructed from the impedance data presented in fig. 6.3.1 and fig. 6.3.2, respectively. These Tafel plots should be compared to those in fig. 4.5.1, which were obtained from steady-state polarisation measurements on the same system.

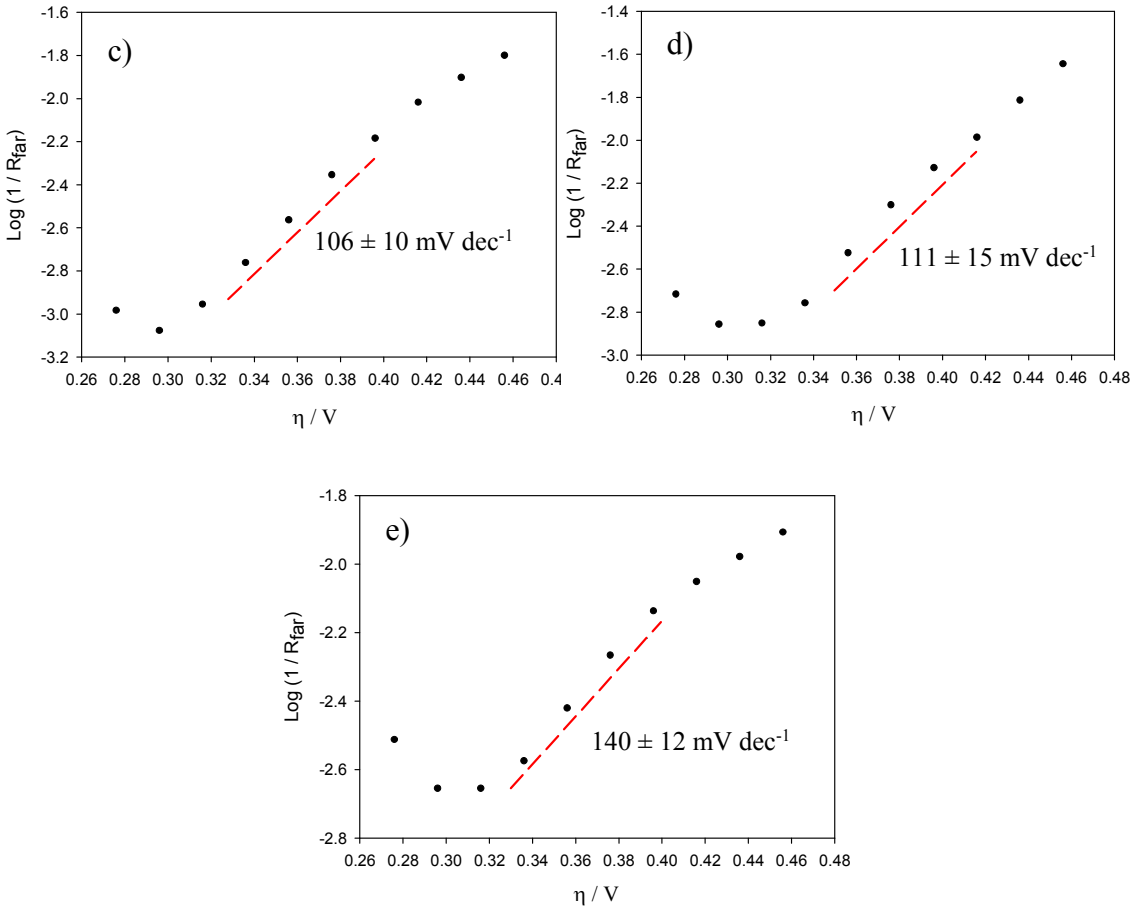



Figure 6.5.2 Log $(R_{far})^{-1}$ *vs.* $\eta$ of c) 500, d) 750, and e) 1000 potential cycles Mn electrodes in 1.0 M NaOH at 25°C. Plots were constructed from the impedance data presented in fig. 6.3.3, fig. 6.3.4, and fig. 6.3.5, respectively. These Tafel plots should be compared to those in fig. 4.5.1, which were obtained from steady-state polarisation measurements on the same system.

To conclude the discussion on the EIS measurements, and analogous to that done to Mn electrodes, we compare the Tafel slopes, $b_{EIS}$, obtained for Ni/Co electrodes using impedance measurements with those measured by steady-state polarisation methods. The same procedure was used for preparing the plots of log $(1/R_{far})$ against $\eta$ for the nickel cobalt electrodes as that used for Mn electrodes early in this section. The plots of log $(1/R_{far})$ against $\eta$ for a series of nickel cobalt mixed oxide electrodes with different % M Co content are presented in fig. 6.5.3. It is clear that there is excellent agreement between the values of $b_{EIS}$ and $b_{ss}$. As was previously remaqued the agreement in the values of the Tafel slopes obtained independently by dc and ac techniques, points out the genuine kinetic significance of the concensus Tafel slope values.

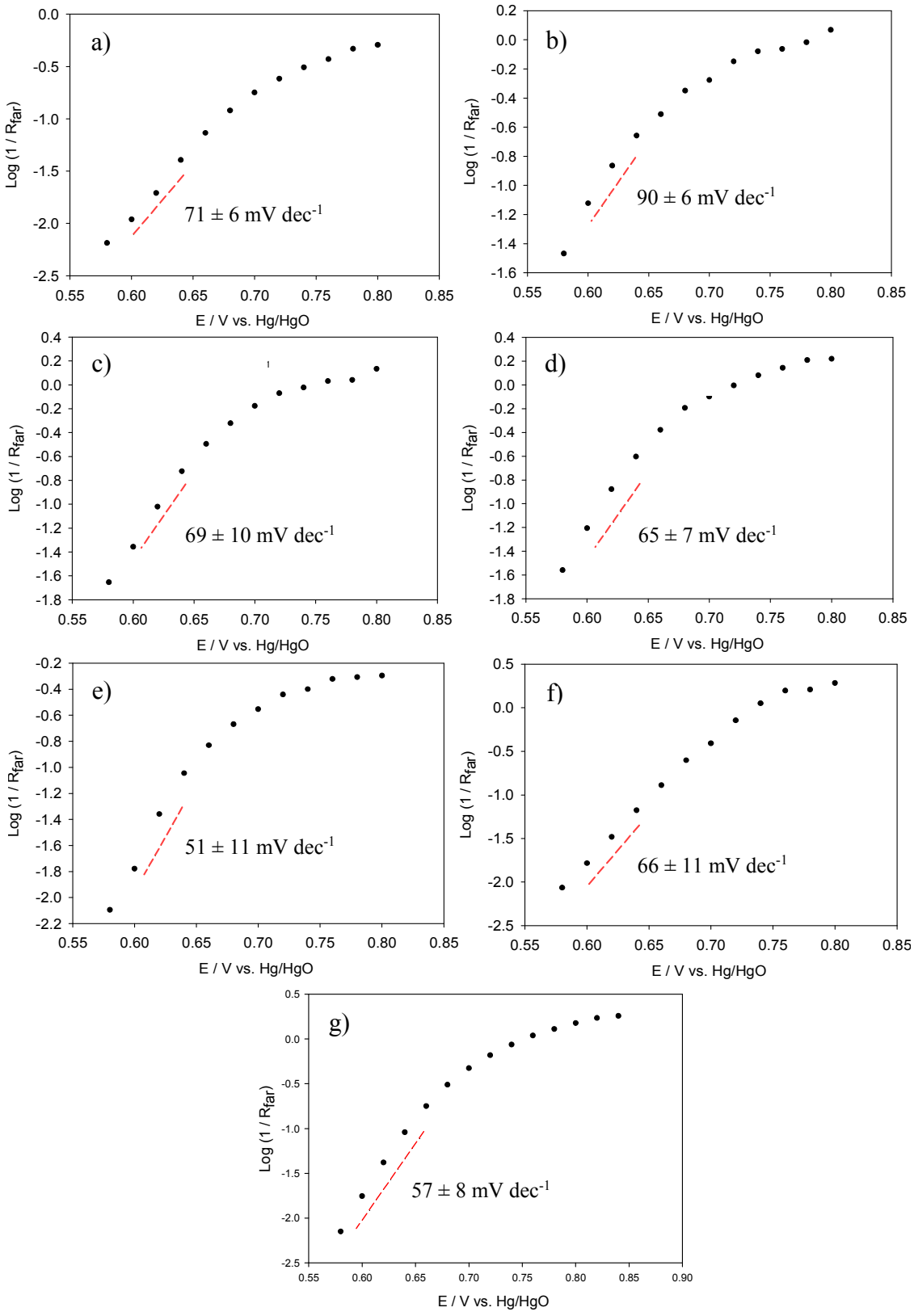



Figure 6.5.3 Log $(R_{far})^{-1}$ *vs.* $\eta$ of a) 0, b) 20, c) 40, d) 50, e) 60, f) 80, and g) 100 % M Co content electrodes in 1.0 M NaOH at 25°C, respectively. These Tafel plots should be compared to those in fig. 5.5.12, which were obtained from steady-state polarisation measurements on the same system.

## 6.6 References Chapter 6


[1] M. E. G. Lyons, M. P. Brandon, *Journal of Electroanalytical Chemistry* **2009**, *631*, 62-70; R. L. Doyle, M. E. G. Lyons, *Journal of The Electrochemical Society* **2013**, *160*, H142-H154.

[2] R. L. Doyle, M. E. G. Lyons, *Physical Chemistry Chemical Physics* **2013**, *15*, 5224-5237; H. Willems, A. G. C. Kobussen, J. H. W. De Wit, G. H. J. Broers, *Journal of Electroanalytical Chemistry and Interfacial Electrochemistry* **1984**, *170*, 227-242.

[3] J. Bisquert, *Physical Chemistry Chemical Physics* **2000**, *2*, 4185-4192; J. Bisquert, *The Journal of Physical Chemistry B* **2002**, *106*, 325-333.

[4] J. Bisquert, G. Garcia-Belmonte, F. Fabregat-Santiago, N. S. Ferriols, P. Bogdanoff, E. C. Pereira, *The Journal of Physical Chemistry B* **2000**, *104*, 2287-2298.

[5] R. de Levie, *Electrochimica Acta* **1963**, *8*, 751-780.

[6] G. J. Brug, A. L. G. van den Eeden, M. Sluyters-Rehbach, J. H. Sluyters, *Journal of Electroanalytical Chemistry and Interfacial Electrochemistry* **1984**, *176*, 275-295.

[7] D. A. Harrington, B. E. Conway, *Electrochimica Acta* **1987**, *32*, 1703-1712.

[8] L. A. da Silva, V. A. Alves, M. A. P. da Silva, S. Trasatti, J. F. C. Boodts, *Electrochimica Acta* **1997**, *42*, 271-281.

[9] B. E. Conway, L. Bai, *Journal of the Chemical Society, Faraday Transactions 1: Physical Chemistry in Condensed Phases* **1985**, *81*, 1841-1862.

[10] A. Sharifi-Viand, M. G. Mahjani, M. Jafarian, *Journal of Electroanalytical Chemistry* **2012**, *671*, 51-57.

[11] A. Lasia, in *Modeling and Numerical Simulations*, Springer New York, New York, NY, **2009**, pp. 67-137.

# CHAPTER 7

# CONCLUSIONS
# AND
# FUTURE WORK

## 7.1 Conclusions

Chapter one introduces general concepts of electrochemistry, focusing on the theory of interfaces and electrode kinetics. Consideration on the state-of-art of the surface electrochemistry of transition metal oxides in aqueous solutions, including concepts of electrocatalysis focusing on the OER and HER of the surface electrochemistry of nickel, cobalt, iron and manganese oxide electrodes was also presented.

Chapter two deals with the theory underpinning the various electrochemical techniques utilized throughout this thesis, such as steady-state polarization, cyclic voltammetry and pulse decay measurements. Various analytical techniques used along this work are also described.

Chapter three analysis the specifics of the various materials, methods and instruments used throughout this thesis. Among them, special attention was given to the electrochemical impedance spectroscopy technique.

Chapter four deals with electrochemical redox and charge transfer proprieties of the hydrous oxy-hydroxide films growth on polycrystalline manganese metal prepared by potential multicycling in alkaline solution. Results aim to investigate the catalytic surfaces on which the OER takes place, assign a more accurate stoichiometry to represent the redox switching reaction exhibited by the surface bound oxy-manganese species in the oxide thin film, and to determine the optimal number of potential cycles at which the Mn electrode should be subjected to exhibit higher catalytic activity towards the OER.

The growth of the Mn oxide film, somewhat analogous to the growth of iron oxide by potential multicycling, consisted in an inner compact oxide layer and an outer hydrous layer. The peak potential-pH response of the hydrous oxide was shown to exhibit a super-Nernstian shift greater than -59 mV per $pH^{-1}$ against a constant potential reference electrode. We assumed that this behaviour may arise because of the high acidity of the manganese oxy-cation. Regarding its kinetics, the Tafel slope changed significantly with film thickness so the thicker the Mn oxide film, the greater the Tafel slope observed. Contrarily, the overpotential, the onset potential and the current density exhibit enhancement as the oxide

film became thicker due to the formation of tunnelled or porous structures at the electrode surface at high number of potential cycles. These structures were proven to have high intrinsic activities towards the OER since they allow intimate contact between solid and liquid phases. The observed increase in Tafel slope values as the film becomes thicker is suggested to be related to the magnitude of the film resistance and the resistance contribution of surfaquo groups adsorbed on the electrode surface. The Tafel slope of ca. 120 mV $dec^{-1}$ observed for many Mn oxides coated electrodes can be associated with the first electron transfer step in the overall sequence describing oxygen evolution being slow and rate determining. Tafel slopes for thin and intermediate thickness multicycled electrodes were found to be ca. 80 mV $dec^{-1}$ indicating that the rate-determining step is mainly due to the second electron transfer step in tandem with a partially difficult electron transfer occurring at the first step of the mechanistic proposed in this work.

Regarding the effect of pH on the kinetic belabour of Mn oxide electrodes, the reaction order values were independent of the hydrous oxide charge capacity. Significant differences were observed when comparing the slopes from the OCP curves decay with the Tafel slopes obtained by steady-state polarisation measurements. Such differences were assigned to the decrease in the surfaquo group's concentration on the electrode surface. Capacitance studies revealed a dependence of double layer capacitance with the film thickness. The observed increase in capacitance behaviour was associated with the formation of a porous layer, resulting in an enhancement of active electrode surface. The influence of the extent of electrode aging was also investigated and similar oxide growth/charge behaviour was observed between a fresh and an aged electrode, noting that after 1000 growth cycles, the aged electrode possesses ca. 40 % more charge storage capacity than a fresh Mn electrode. Since the growth of the subsequent layer occurs on top of the previous one, it is suggested that the initial Mn electrode morphology affects the following Mn oxide layers. However, SEM images did not display surface differences between the electrodes, suggesting that differences may arise from the bulk layers of the electrode. Redox peak potentials of the aged Mn oxide film were found to coincide with those for the fresh one though exhibiting higher current densities. Equal Tafel slope values were found between both types of electrodes, suggesting that the OER mechanism remains equal regardless of the Mn electrode being aged or fresh. That is because, after a few growth cycles, the oxidation state of the electrode surface is similar in both cases. Finally, corrosion was found to occur at elevated anodic potentials, indicating that corrosion competes with oxygen evolution.

Chapter five focuses on electrochemical redox and charge transfer proprieties of nickel cobalt mixed oxide electrodes in alkaline solutions. Results aim the investigation of the catalytic surfaces on which the OER takes place and the determination of the optimal % M Co concentration and annealed temperature at which the nickel cobalt mixed oxide exhibits the highest catalytic activity towards the OER. The first section of the chapter investigates the effect of annealing temperature on a 1:1 molar ratio nickel cobalt mixed oxide electrode while the second section studies the influence of % M Co content on the electrocatalysis behaviour of the electrodes annealed at a fixed annealing temperature of 400°C.

The structural analysis was carried out using XRD, XPS and SEM-EDX analysis. XRD patters revealed the presence of three oxide phases: (i) NiO, (ii) $Co_3O_4$, and (iii) $NiCo_2O_4$. Electrodes annealed at temperatures below 350°C exhibit the largest lattice parameter, the lowest degree of crystallinity, and the larger crystallite size. Contrarily, electrodes annealed at temperatures over 450°C, exhibit smaller lattice parameter, higher degree of crystallinity, and smaller crystallite size. Remarkably, electrodes annealed at 400°C showed intermediate values for the above-mentioned parameters. XRD patters were used to quantitatively analyse the oxide film. The $NiCo_2O_4$ phase was found to increase until 400°C while above 400$^o$C it decomposed, originating the formation of both $Co_3O_4$ and NiO phases. XPS analysis demonstrated the presence of nickel oxide (II/III) and cobalt oxide (II/III) in the surface and also revealed that the surface composition of samples differ significantly to that determined on the bulk, suggesting surface segregation. Therefore, the samples did not exhibit a uniform composition through the different depths of the oxide layer.

Two different morphologies were observed from SEM analysis. At relatively low annealing temperatures, electrodes exhibit widely spaced-cracked layer morphology whereas at relatively high temperatures the electrode revealed a compact mud-cracked morphology. The annealing temperature was found to play a significant role in the electrocatalytic behaviour of electrodes. The increment of temperature, until reaching 400°C, results in a decrease in overpotential from ca. 0.335 V to ca. 0.320 V. However, as the temperature is further increased, the overpotential increases sharply, from ca. 0.320 V to ca. 0.34 V. This variation is due to changes in the conductivity of the oxide film attributed to changes in the film composition. The electrode prepared at 400°C was found to have the best electrocatalytic properties for the OER. Thus, 400°C was chosen to further investigate the effect of % M Co content on the OER of nickel cobalt mixed oxide materials.

By combining the results of XRD, SEM EDX, and contact angle with those of the kinetic analysis and capacitance studies, one can easily relate the % Co content on the electrode with the OER catalytic activity. The SEM images in the macroscale revealed cracked surface for all electrodes with nanoparticles of between 15 – 50 nm in diameter distributed uniformly across the surface, which gave rise to the highly active catalytic behaviour by increasing the active surface area of the electrodes in the nanoscale. Additionally, porous with an average diameter of 1 μm. were also observed, which allowed the electrolyte to penetrate the oxide film increasing its catalytic activity. Thus, XRD results show that the formation of mixed oxide NiO and $NiCo_2O_4$ nanocrystals occurs with increasing up to 60 % M Co content on NiO electrodes. Further increases of % M Co result in the disappearance of the NiO phase, leading to the formation of a major $Co_3O_4$ phase and, in a lesser extent, of a $NiCo_2O_4$ phase. The trend of the overpotential of the samples in decreasing order of increasing $NiCo_2O_4$ phase content was found to be: $60\% > 50\% > 40\% > 20\%{\sim}80\% \gg 0\% \sim 100\%$.

Electrodes with a high content of $NiCo_2O_4$ phase exhibit lower Tafel slope values than those with poor $NiCo_2O_4$ content due to the distribution of $Ni^{2+}$ species in the octahedral sites of the $Co_3O_4$ spinel structure. The reaction order was somewhat dependent of the phase composition. The electrode with 60 % M Co content was found to exhibit the greatest OER electrochemical activity, being comparable to those reported as the best transition metal oxide-based catalysts in the literature. Several points can be made from the above observation: (i) the presence of both NiO and $NiCo_2O_4$ enhances the OER efficiency, and (ii) the presence of $NiCo_2O_4$ enhances the OER efficiency more than NiO or $Co_3O_4$.

Chapter 6 deals with the electrochemical impedance analysis of Mn and Ni/Co oxide electrodes. EIS provides means to obtain additional and complementary information on the OER to that accessible by traditional dc measurements. Using CNLS fitting program, the raw EIS data was fitted to an appropriate equivalent electrical circuit model and the optimum fit values of the various elements tabulated. Values of the total Faradic resistance, $R_{far}$, ($R_{far} = R_{sq} + R_p$), were evaluated from the optimum fitted parameters, and values for the OER Tafel slope were calculated from plots of the log $(R_{far})^{-1}$ *vs.* $\eta$ according to eqn. 3.6.38. This showed that the Tafel slope, measured for our electrodes, either by steady-state polarisation or derived from EIS measurements, is truly characteristic of the kinetics of the OER since they were found to be equal.

## 7.2 Future Work

Considering the results presented in this work, it is our belief that traditional electrochemical techniques cannot yield further information on the oxygen evolution reaction occurring in alkaline media and on the nature of catalytically active surface than that presented in this thesis for polycrystalline Mn, Ni/Co oxide electrodes. Bearing this in mind, and from an industrial perspective, we propose new research paths involving the investigation of the transition metal oxides, such as those investigated in this thesis, for the oxygen evolution reaction in sea water. During seawater electrolysis, both oxygen and chlorine evolve at the anode at similar potentials which causes large amounts of toxic and corrosive $Cl_2$ gas as by-product. The latter may be overcome using selective anodes which inhibit the evolution of chlorine but allowing the oxygen evolution. Therefore, would be a great advantage to perform selective electrolysis of saline water, using abundant and inexpensive anode materials. It has been mentioned that selectivity can be modulated through variation of surface and electronic structure of the electrocatalyst. In this perspective, we propose the use of the electrodes used in this thesis for selective OER in sea water.

Another promising perspective of these transition metal oxides, despite they were designed for the OER catalysis, is the possible use of these electrodes as a potential pH electrode aiming to substitute the traditional glass pH electrodes. The traditional glass electrodes suffer many disadvantages, particularly in strong alkaline solutions. Transition metal oxides have been demonstrated to exhibit extremely fast response times even in strong alkaline solutions. Also, and finally, a complimentary set of experiments which can be carried out using our transition metal oxide electrodes for the detection of organic compounds such as glucose or ascorbic acid. In this sense, other metal-oxides have been extensively explored to develop biosensors with high sensitivity, fast response times, and stability for the determination of organic compounds by electrochemical oxidation.